WILEY-VCH

Klaus-Werner Benz and Wolfgang Neumann

Introduction to Crystal Growth and Characterization

Klaus-Werner Benz and
Wolfgang Neumann

Introduction to Crystal Growth and Characterization

Related Titles

Herlach, D. M., Matson, D. M. (eds.)

Solidification of Containerless Undercooled Melts

2012
Print ISBN: 978-3-527-33122-2,
also available in digital formats

Nikrityuk, P. A.

Computational Thermo-Fluid Dynamics

In Materials Science and Engineering

2011
Print ISBN: 978-3-527-33101-7,
also available in digital formats

Duffar, T. (ed.)

Crystal Growth Processes Based on Capillarity

Czochralski, Floating Zone, Shaping and Crucible Techniques

2010
Print ISBN: 978-0-470-71244-3,
also available in digital formats

Capper, P., Rudolph, P. (eds.)

Crystal Growth Technology

Semiconductors and Dielectrics

2010
Print ISBN: 978-3-527-32593-1,
also available in digital formats

Zolotoyabko, E.

Basic Concepts of Crystallography

2011
Print ISBN: 978-3-527-33009-6

Klaus-Werner Benz and Wolfgang Neumann

Introduction to Crystal Growth and Characterization

With a contribution by Anna Mogilatenko

WILEY-VCH
Verlag GmbH & Co. KGaA

The Authors

Prof. Dr. Klaus-Werner Benz
Freiburger Materialforschungszentrum
(FMF), Albert-Ludwigs-Universität
Freiburg
Stefan-Meier-Str. 21
79104 Freiburg
Germany

Prof. Dr. Wolfgang Neumann
Humboldt-Universität zu Berlin
Institut für Physik
Newtonstr. 15
12489 Berlin
Germany

All books published by **Wiley-VCH** are carefully produced. Nevertheless, authors, editors, and publisher do not warrant the information contained in these books, including this book, to be free of errors. Readers are advised to keep in mind that statements, data, illustrations, procedural details or other items may inadvertently be inaccurate.

Library of Congress Card No.: applied for

British Library Cataloguing-in-Publication Data
A catalogue record for this book is available from the British Library.

Bibliographic information published by the Deutsche Nationalbibliothek
The Deutsche Nationalbibliothek lists this publication in the Deutsche Nationalbibliografie; detailed bibliographic data are available on the Internet at <http://dnb.d-nb.de>.

© 2014 Wiley-VCH Verlag GmbH & Co. KGaA, Boschstr. 12, 69469 Weinheim, Germany

All rights reserved (including those of translation into other languages). No part of this book may be reproduced in any form – by photoprinting, microfilm, or any other means – nor transmitted or translated into a machine language without written permission from the publishers. Registered names, trademarks, etc. used in this book, even when not specifically marked as such, are not to be considered unprotected by law.

Print ISBN: 978-3-527-31840-7
ePDF ISBN: 978-3-527-68436-6
ePub ISBN: 978-3-527-68434-2
Mobi ISBN: 978-3-527-68435-9
oBook ISBN: P-010-18947-1

Cover-Design Adam-Design, Weinheim, Germany
Typesetting Laserwords Private Limited, Chennai, India
Printing and Binding Markono Print Media Pte Ltd., Singapore

Printed on acid-free paper

Contents

Preface *IX*
Acknowledgments *XIII*

1 Fundamentals of Crystalline Materials *1*
1.1 Crystalline State *1*
1.2 Fundamentals of Geometrical Crystallography *12*
1.2.1 Crystal Lattices *12*
1.2.2 Crystal Axes Systems, Crystal Systems, and Crystal Families *14*
1.2.3 Crystal Faces and Zones *15*
1.2.4 Indexing in the Hexagonal Crystal Family *24*
1.3 Morphological Symmetry of Crystals *25*
1.3.1 Crystallographic Point Groups *40*
1.3.2 Some Basic Facts of Group Theory *52*
1.4 Structural Symmetry *60*
1.4.1 Crystal Lattices, Motifs, and Crystal Structures *60*
1.4.1.1 Bravais Lattices *61*
1.4.1.2 The Reciprocal Lattice *62*
1.4.1.3 Lattice Transformations *68*
1.4.2 Crystallographic Space Groups *71*
1.4.2.1 General Remarks *72*
1.4.2.2 The International Tables for Crystallography – The Reference Book for the Representation of Space Group Symmetries *76*
1.4.2.3 Mathematical Description of the Space Group Symmetry *93*
1.4.3 Generalized Crystallographic Symmetry *101*
1.5 Crystal Structures *104*
1.5.1 Sphere Packings *108*
1.5.2 Selected Examples of Inorganic Structure Types *112*
1.5.2.1 Polymorphism and Polytypism *124*
1.5.3 Selected Examples of Molecular Crystals *126*
1.5.4 Symmetry Relations between Crystal Structures *145*

1.6 Crystallographic Databases and Crystallographic Computer Programs *152*
Appendix: Supplementary Material S1 Special Crystal Forms of Cubic Crystal Classes *159*
References *164*

2 Basics of Growth Mechanism and Solidification *171*
2.1 Nucleation Processes *171*
2.1.1 Homogeneous Nucleation *175*
2.1.2 Heterogeneous Nucleation *177*
2.1.3 Metastable Zone Regime *179*
2.1.4 Equilibrium Shape of Crystals *180*
2.2 Kinetic Processes and Growth Mechanism *182*
2.2.1 Molecular Kinetic Theory of Crystal Growth *183*
2.2.2 Interfaces and Roughening of Surfaces *185*
2.2.3 Vapor–Liquid–Solid (VLS) Mechanism *189*
2.2.4 Crystal Growth from Ambient Phases on Rough Surfaces: Vapor Phase, Solution, and Melt Media *190*
2.2.5 Crystal Growth on Flat Surfaces *193*
2.3 Phase Diagrams and Principles of Segregation *195*
2.3.1 Phase Diagrams with a Continuous Miscibility in the Solid and Liquid Phases *196*
2.3.2 Segregation and Segregation Coefficients *201*
2.3.3 Constitutional Supercooling and Morphological Stability *212*
2.4 Principles of Flow Regimes in Growth Melts *214*
2.4.1 Buoyancy Convection *215*
2.4.2 Marangoni Convection *216*
References *218*

3 Growth Techniques in Correlation with Related Growth Mechanism *221*
3.1 Overview on Main Growth Techniques *221*
3.2 Principles of Melt Growth Techniques *224*
3.2.1 The Czochralski Crystal Growth Process *224*
3.2.2 Growth Method after Bridgman *234*
3.2.3 The Float Zone Crystal Growth Process *244*
3.2.4 Bulk Crystal Growth from Metallic Solutions *253*
3.2.4.1 Traveling Solvent Method (TSM) *253*
3.2.4.2 Traveling Heater Method (THM) *255*
3.2.4.3 The Solute, Synthesis, Diffusion Method (SSD) *259*
3.3 Bulk Crystal Growth of II–VI Compounds from the Vapor *260*
3.3.1 Crystal Growth of CdTe by a Sublimation Traveling Heater Method, STHM, in Closed Ampoules *262*
3.3.2 Crystal Growth of CdTe by the Markov Method in Semiclosed Ampoules *264*

3.4 Epitaxial Growth Techniques *267*
3.4.1 Liquid Phase Epitaxy (LPE) *270*
3.4.2 Vapor Phase Epitaxy (VPE) *279*
3.5 Supplementary Material: Principles of Verneuil Technique, Growth from High and Low Temperature, Nonmetallic Solutions *295*
3.5.1 Verneuil Technique *295*
3.5.2 Growth from High Temperature Solutions (Flux Growth) *295*
3.5.3 Growth from Low Temperature Solutions (Aqueous Solutions) *296*
References *298*

4 Characterization of Crystals *301*
4.1 Crystal Defects *302*
4.1.1 Zero-Dimensional Defects *303*
4.1.2 One-Dimensional Defects *314*
4.1.3 Two-Dimensional Defects (Planar Defects) *326*
4.1.3.1 Grain Boundaries *328*
4.1.3.2 Stacking Faults *336*
4.1.3.3 Antiphase Boundaries *340*
4.1.3.4 Twins *342*
4.1.3.5 Domain Boundaries *355*
4.1.3.6 Crystal Surfaces *363*
4.1.4 Three-Dimensional defects *368*
4.1.4.1 Inclusions *369*
4.1.4.2 Precipitates *370*
4.1.4.3 Voids *374*
4.2 Crystal Quality *375*
4.2.1 Criteria of Crystal Quality *376*
4.2.2 Crystal Quality and Application *378*
4.3 Selected Methods of Crystal Characterization *382*
4.3.1 Etching of Crystals *382*
4.3.2 X-Ray Topography *383*
4.3.3 Electron Microscopy *385*
4.3.3.1 Scanning Electron Microscopy *387*
4.3.3.2 Transmission Electron Microscopy *388*
4.4 Materials Engineering by Correlation of Crystal Growth and Characterization *392*
Anna Mogilatenko
4.4.1 Epitaxial Growth of GaN on $LiAlO_2$ Substrates *393*
References *408*

Index ***415***

Preface

Crystalline materials play an important role both in science and industry in the development of modern materials such as semiconductors for electronic devices, solar cells, and lasers. New fields of application require a consequent improvement of crystal quality, which is covered with a thorough understanding of the basics of crystal growth and characterization.

The main aim of this book, therefore, is to provide an introduction to Crystal Growth where the fundamentals of both the crystallization processes and the various growth procedures of technical importance will be treated in detail. Furthermore, selected methods for the characterization of the grown crystals as well as their properties will be discussed.

The actual question may arise: Is it really necessary to have a new book on crystal growth when numerous books already exist in the market describing the basics and thermodynamics of crystal growth and the growth technologies?

Our longstanding experience as academic teachers in the fields of crystallography and crystal growth has shown us that the majority of students whom we have taught in more than two decades had sufficient knowledge either in crystallography or in crystal growth technology. For the students and their subsequent activities in materials science, it would be much more advantageous and effective to have knowledge in both fields of study.

With this textbook, our idea is to provide a compendium where the basics of crystallography as well as crystal growth will be outlined in a unified manner. We have carefully chosen the content of this textbook in such a way that students of natural sciences, materials science, and technology should all be equally interested in this subject. The state-of-the-art content should also be useful for crystal growers, material science researchers and engineers, solid state physicists, and crystallographers.

This book will give a description about the fundamentals on an actual basis of crystals, their growth and production technologies. The crystal properties strongly depend on their real structure. Therefore, the characterization of the grown crystals by various methods will be outlined. Furthermore, the different steps from growth to characterization and description of material properties will be discussed on selected examples.

The content of the book is divided into the following four chapters:

- Fundamentals of crystalline materials
- Basics of growth mechanisms and solidification
- Growth techniques in correlation with related growth mechanisms
- Characterization of crystals.

The chapter "Fundamentals of crystalline materials" begins with the definition of the crystalline state where the various stages of order from the ideal periodic arrangement to the topological disorder are described in detail. Thus, the different types of periodic as well as aperiodic crystals are considered. In addition, the possible transitional stages between crystals and liquids are briefly mentioned. In order to get a thorough understanding of the morphological symmetry of crystals, the fundamentals of symmetry operations necessary for the treatment of the polyhedral shape are described. Within this framework, terms such as crystal coordinate systems, crystal faces, and zones are defined. In order to represent the three-dimensional crystal in the two-dimensional space the commonly used crystal projection, the stereographic projection will be illustrated. To show the correspondence between the morphological and structural symmetry, the lattice concept in crystal space and Fourier-space is explained.

After a phenomenological treatment of symmetry, the fundamentals of group theory for the description of point groups and space groups are comprehensively discussed. The reader will be familiarized with the application of crystallographic point and space groups for the explanation of morphology and structure of periodic crystals, respectively. The extension of the symmetry concept (crystallography in higher dimensions, black-white symmetry) will be considered briefly. Furthermore, the usage of the "International Tables for Crystallography" as the important among reference books in the various branches of crystallography will also be demonstrated particularly for the description of crystal structures.

The various possibilities for the classification of structures (structure types according to the Strukturbericht designation, Pearson symbol, geometric and analytical descriptors) will be introduced. Selected examples of inorganic and organic crystal structures will be described in detail.

Chapter 2 "Basics of growth mechanism and solidification" describes the fundamentals of nucleation processes, the kinetics, and main growth mechanisms. The basic equations for homogeneous and heterogeneous nucleation are derived. Furthermore, the importance of the Oswald-Miers-Regime as a function of supersaturation with respect to the equilibrium shape of crystals is represented. The kinetic processes of crystal growth from vapor phase, solution, and melt media are illustrated. A special point of interest is the role of interfaces for the morphology of surfaces formed. In order to get a thorough understanding of the growth mechanism phase, diagrams with continuous miscibility in the solid and liquid phases are treated in detail. The various aspects of segregation of dopants and residual impurities on a macro- and microscale

for the growth process and growth mechanism are discussed. The influence of the different types of convection regimes in the nutrients on growth and segregation numerically given by specific dimensionless numbers is outlined. The methods that are mainly applied for growing crystals are comprehensively treated in Chapter 3 "Growth techniques in correlation with related growth mechanism." Numerous modern materials are grown from melt and metallic solutions. The Czochralski and the Bridgman methods, as the most versatile melt growth techniques for semiconducting materials, are described in detail. Specific crystals may be grown only by means of the containerless Float Zone Technique. The role of external fields (magnetic fields, microgravity) as an additional tool to improve the crystal quality via flow control within the melt is described for different semiconductor materials. Possibilities and limitations for the methods of bulk crystal growth from metallic solutions are described for a selection of III–V and II–VI semiconductors. Crystal growth experiments using the Traveling Heater Method (THM) under earth and microgravity conditions are compared. The specific mechanisms of THM are outlined and illustrated by concrete examples for the growth of InP and GaSb. The advantages of bulk crystal growth methods from the vapor phase for high quality crystals are explained in detail for CdTe and related II–VI compounds. Nowadays, growth processes of epitaxial films are of great importance for innovative industrial applications such as LEDs and detectors. Therefore, an elaboration of terms and concepts of Liquid Phase Epitaxy (LPE), Vapor Phase Epitaxy (VPE), and Molecular Beam Epitaxy (MBE) is given. Fundamental chemical reactions and growth processes are discussed and illustrated for the III–V semiconductors InP an GaSb.

Chapter 4 "Crystal characterization" outlines under which criteria the grown crystals have to be evaluated. The defect analysis is an essential part of the evaluation of crystals. The main characteristics of following structural defects classified according to their dimensionality are described in detail:

- Zero-dimensional defects
  - point defects
- One-dimensional defects
  - dislocations
- Two-dimensional defects
  - grain boundaries, stacking faults, antiphase boundaries, twins, domain boundaries, crystal surfaces
- Three-dimensional defects
  - inclusions, precipitates, voids.

The essential crystal features that mainly determine the quality of a crystal are outlined. The correlation between crystal quality and field of application is discussed for diamond and protein crystals.

Among the numerous characterization techniques of crystals, the methods of selective etching, X-ray topography, and electron microscopy play a specific role, particularly for defect analysis. The fundamentals of those methods are briefly

discussed. The possibilities and limitations for the defect analysis are illustrated by selected examples. Finally, the correlation between crystal growth, characterization, and the feedback to the growth process for improving the crystal quality (defect engineering) is illustrated for the case study of epitaxial growth of GaN on $LiAlO_2$ substrates.

Acknowledgments

We are grateful to many friends, colleagues, our former PhD students, post-docs, and co-workers who contributed with their research to the growth and characterization of crystal, which are discussed in this book.

In particular, we are very thankful to Dr. I. Häusler and F. Krahl for their tremendous support with preparing the drawings and figures. We gratefully acknowledge the revision of the language of selected parts of this book by Prof. P. Moeck, a German-British applied crystallographer.

KWB is thankful to former colleagues of the Semiconductor Crystal Growth Laboratory (4. Physical Institute, University of Stuttgart) for an excellent cooperation in the time period 1974–1986: in particular, Prof. M. Pilkuhn as head of the institute; Profs G. Baumann and F. Scholz; and Drs H. Eisele, H. Haspeklo, W. Jakowetz, W. Koerber, R. Linnebach, G. Nagel, N. Stath, and Th. Voigt. Several common publications have been an important guide to this book. Thanks also to Prof. J. Weidlein and Drs G. Laube and H. Renz of the Anorganic Institute, University of Stuttgart, for their interdisciplinary cooperation (MOVPE with metal organic adducts).

The cooperation and helpful discussions with active and former members of the Crystallographic Institute and the Freiburg Materials Research Center, FMF, of the Albert-Ludwigs-Universität, Freiburg, is gratefully acknowledged. Special thanks to Profs A. Croell, M. Fiederle, and P. Dold, as well as to Drs V. Babentsov, A. Danilewsky, A. Fauler, Th. Kaiser, M. Laasch, N. Salk, and P. Sickinger for supplying scientific results and figures.

Some of the TEM experiments and results discussed in this book were carried out in the Institute of Solid State Physics and Electron Microscopy of the Academy of Sciences in Halle (Saale) and since 1992 in the newly founded Max Planck Institute of Microstructure Physics (at the same place). For the excellent working conditions in these institutes, WN would like to thank the late Prof. H. Bethge, Prof. V. Schmidt, Prof. J. Heydenreich, his PhD supervisor at Halle, and the late Prof. U. Gösele. WN is indebted to his former colleagues Drs H.-Chr. Gerstengarbe, H. Hofmeister, and K. Scheerschmidt for collaborative results, which will be discussed to some extent in this book.

For valuable discussions and contributions of joint research carried out at the Humboldt University in Berlin, WN is grateful to Drs I. Häusler, I. Hähnert, A. Mogilatenko, Th. Höche, H. Kirmse, the late U. Richter, Private Docent R. Schneider, and Ch. Zheng.

WN appreciates very much the opportunity of having worked together with his colleague and friend Prof. R. Köhler at the Humboldt University, Berlin. RK and WN taught together courses on "Real Structure of Solids" and "Methods of Materials Characterization" over more than a decade. WN wants to thank RK for his permission to reproduce some figures of his part of the joint lecture manuscripts in this book.

We are grateful to the following colleagues for granting permission to reproduce figures from their work or to use their computer programs for generating figures:

Prof. W. Kaminsky (Figures 1.98, 1.99, S1.1 – S1.10 program: WinXMorph),
Dr. R. Scholz (Figure 4.24), Prof. N.D. Browning (Figure 4.27), Prof. D. Hesse (Figure 4.32),
Prof. K. Hermann (Figures 4.52, 4.53, program: Surface explorer), Dr. K.W. Keller (Figure 4.54), Dr. M. Schmidbauer (Figure 4.59).

K.W. Benz
W. Neumann

1
Fundamentals of Crystalline Materials

> Es liegt etwas Atemberaubendes in den Grundgesetzen der Kristalle.
> Sie sind keine Schöpfungen des menschlichen Geistes.
> Sie sind – sie existieren unabhängig von uns.
> In einem Moment der Klarheit kann der Mensch höchstens entdecken,
> dass es sie gibt und sich Rechenschaft davon ablegen
>
> M.C. Escher (1959)

> There is something breathtaking about the basic laws of crystals.
> They are in no sense a discovery of the human mind;
> they just "are" – they exist quite independently of us.
> The most that man can do is become aware, in a moment of clarity,
> that they are there, and take cognizance of them.
>
> M.C. Escher (1959)

The beauty of natural crystals as caused by the regular polyhedral shape, their symmetry, beautiful color, brightness, and, in some cases, clarity has been fascinating human beings all the time. Nowadays, a wide range of modern materials can be synthesized or grown artificially as crystals. The broad spectrum of crystalline materials includes metals, semiconductors, superconductors, ceramics, polymers, organic molecular crystals, proteins, and so on. First of all, we have to answer the following fundamental questions: What are the characteristic features of the crystalline state? What is a crystal? What defines the degree of crystallinity?

1.1
Crystalline State

Our fundamental knowledge about crystals on a macroscopic scale goes back to the early extensive studies of the morphology of natural crystals, the minerals. Historically, these studies of external faces and the measurement of the precise angles between them were the key for the derivation of the fundamental laws of morphological symmetry of crystals. However, we should be aware of the fact that the regular polyhedral shape of a crystal (form or a combination of them) is, of course, a major characteristic macroscopic feature of crystals but not a proper feature for

Introduction to Crystal Growth and Characterization, First Edition.
Edited by Klaus-Werner Benz and Wolfgang Neumann.
© 2014 Wiley-VCH Verlag GmbH & Co. KGaA. Published 2014 by Wiley-VCH Verlag GmbH & Co. KGaA.

their definition. Both natural as well as synthetic crystals will grow only with an idiomorphic shape under definite growth conditions. Figure 1.1 shows examples of individual gypsum crystals that illustrate the variety of different crystal "habits," which define the general shape. The collection of synthetic single crystals shown in Figure 1.2 were grown using a growth technology that do not allow for a polyhedral growth of the crystals.

The most fundamental macroscopic properties of crystals are

- homogeneity
- anisotropy
- symmetry.

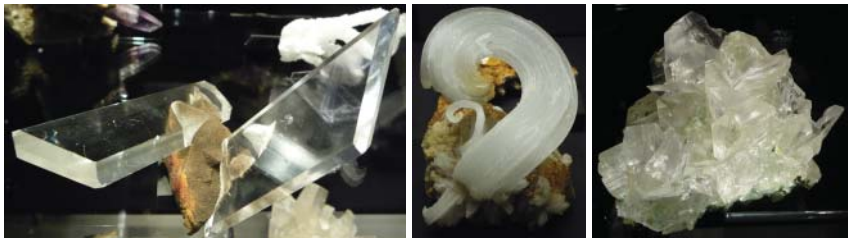

Figure 1.1 (a–c) Gypsum crystals shown in the world-renowned mineral collection "terra mineralia" in castle Freudenstein Freiberg/Saxonia, Germany (*www.terra-mineralia.de*).

Figure 1.2 Collection of synthetic single crystals (Leibniz Institute for Crystal Growth Berlin, Germany).

Macroscopic homogeneity means the crystal is chemically and physically uniformly built. We can consider it as a continuum. The physical properties in different volume elements will show equal characteristics in parallel directions. It is obvious that this treatment is an abstraction and approximation that is applicable only at the macroscopic scale. Anisotropy means for us directional dependence of physical properties. All crystals are anisotropic with respect to some of their physical properties. When we try to determine the thermal expansion of a calcite crystal along the threefold *c*-axis and perpendicular to it, we will measure different values of different signs. Along the *c*-axis, we will find an expansion of the calcite crystal, and perpendicular to it, the crystal shows the anomaly of thermal dilatation with increasing temperature. Anisotropy of crystals does not mean that all crystal properties have to show a different physical behavior in different directions. For example, cubic crystals are optically isotropic. They will, therefore, show neither polarization nor double refraction.

In general, the concept of symmetry is a key to the description of crystals. When we consider "symmetry" as one of the main macroscopic features of crystals, we mean the symmetry concept (symmetry operations and symmetry elements) for describing external forms of crystals, the morphological symmetry of crystals. It is quite clear that there is a basic correspondence between the morphological symmetry (outer symmetry) and the structural symmetry (inner symmetry) of crystals. The fundamentals for the description of the outer and inner symmetries of a crystal will be outlined in Sections 1.2–1.4.

Strictly speaking, all the fundamental macroscopic features of crystals such as homogeneity, anisotropy, and morphological symmetry are the result of the internal order of the crystals at the microscopic level. It should be noted that a periodic arrangement of building units (atoms, groups of atoms, ions, and molecules) of crystals was already predicted by scientists from their comprehensive studies of macroscopic properties of crystals long before von Laue, Friedrich, and Knipping confirmed the periodic order of crystals experimentally by their famous X-ray diffraction experiments in 1912. A year later, father William H. Bragg and son William L. Bragg solved the first crystal structures (NaCl, KCl, CaF_2, ZnS, FeS_2, $NaNO_3$, and $CaCO_3$) from X-ray data (for comprehensive historical survey of crystallography, see, e.g., [1–4]). Nowadays, crystal structure analysis by means of X-ray and electron and neutron diffraction is well developed and routinely applied. Furthermore, modern microscopic techniques such as high-resolution transmission electron microscopy (HRTEM) allow the direct imaging of the atomic arrangement in crystalline structures. Figure 1.3a shows a HRTEM image of a (100) oriented GaAs crystal and the corresponding electron diffraction pattern. For the applied imaging conditions and the specimen thickness given, the white spots represents the projected atomic rows along the [100] zone axis. We can easily construct a lattice were the nodes are occupied by atoms, reflecting their periodic arrangement. The corresponding diffraction pattern (Figure 1.3b) consists of sharp spots (Bragg peaks) situated also on a lattice. This is the so-called *reciprocal lattice* of the crystal.

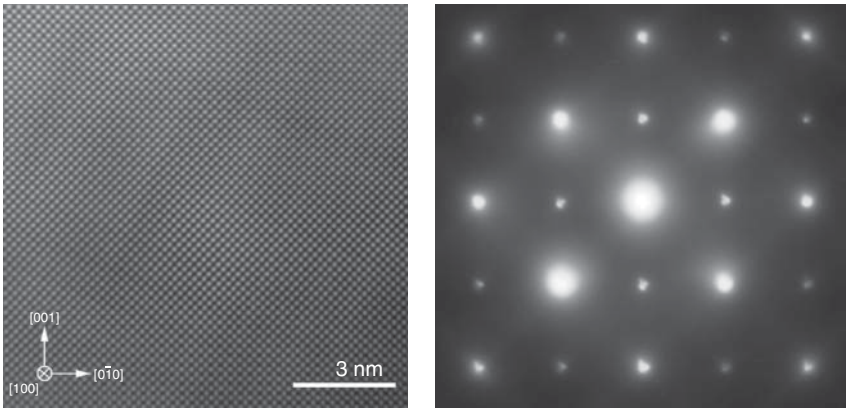

Figure 1.3 HRTEM micrograph of [001] oriented GaAs (a) and the corresponding electron diffraction pattern (b).

With respect to the macroscopic features, we can simply define crystals as homogeneous anisotropic solids. These solids are composed of a three-dimensional periodic arrangement of matter, which forms the microscopic structure of the crystal. As we will show in Sections 1.2 and 1.4, the periodic order can mathematically be described by translation lattices. A "decoration" of the lattice points with matter (atoms, ions, and molecules) generates then the crystal structure. So far, such a definition of crystals is strictly connected with order and periodicity. Periodicity means a periodic infinite repetition of some basic structural unit in all directions by translation. The macroscopic feature of homogeneity is only strictly fulfilled when we consider an infinite space lattice with identical lattice points and identical surrounding. The definition given above within the framework of "classical crystallography" describes what we mean with the term *ideal crystal*. The following questions arise when we are dealing with real crystals, which are finite: What are the boundary conditions that allow for the application of the symmetry concept of an ideal crystal for the description of real crystals? How has one to define ordered structures that lack three-dimensional periodicity within our concept of crystalline matter?

A real crystal is always finite. When we have large-sized crystals, the deviations from the infinity of the underlying lattice concept are negligible. The separation of the matter decorating the lattice points is in the order of 10^{-8} cm (1 Å). Thus, for a crystal size of 1 cm, we have $\sim 10^8$ periodically arranged atoms. However, our real crystal may contain local deviations of chemical composition and various kinds of crystal imperfections (crystal defects) of different dimensions, which may disturb or even destroy the symmetry of our crystal.

A real crystal consisting ideally of only one grain (a continuous lattice without any grain boundary) is called a *perfect single crystal*. Practically, all single crystals are imperfect crystals, containing various kinds of crystal defects. A crystal containing a few grain boundaries is still a single, however imperfect, crystal. Contrary

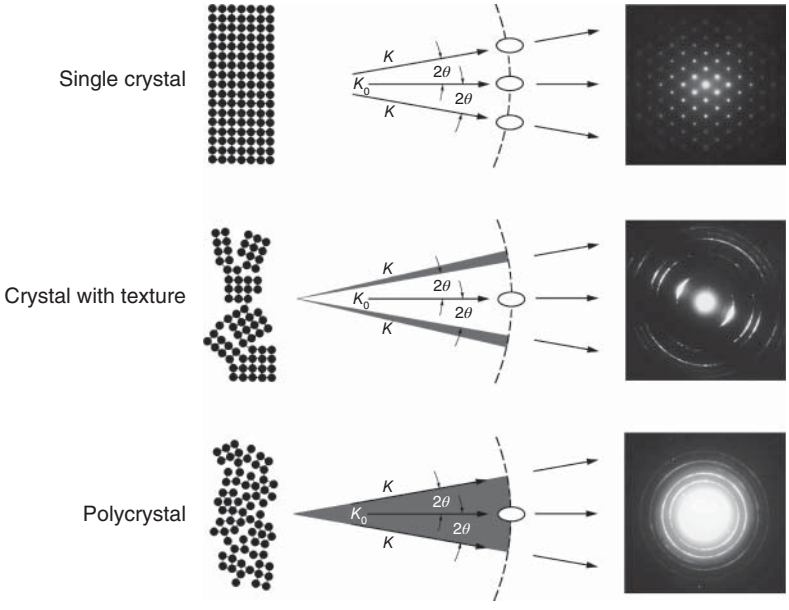

Figure 1.4 Correlation of real structure of crystals and the corresponding diffraction patterns.

to this, a polycrystal is composed of many crystallites (grains) of different size and orientations with an equal probability for all possible orientations. The entity of crystallite orientations is called *texture*. The different stages of crystallinity from single crystalline via a texture to polycrystalline can be determined by means of diffraction as shown in Figure 1.4.

Another important classification criteria for real crystals is connected to their grain size, where the terms *microcrystalline* (diameter of the grains, $d > 1\,\mu m$), *subfine grain-sized crystals* ($d < 1\,\mu m$), and *nanocrystalline* ($d < 100\,nm$) are used.

Nanocrystalline materials are particularly of great interest because the reduced dimensionality may drastically change their physical properties. Transmission electron microscope (TEM) images of an isolated ZnTe nanowire grown on GaAs via a vapor–liquid–solid (VLS) growth process realized in a molecular beam epitaxial system (MBE) are shown in Figure 1.5a,b [5]. The interpretation of the structural image (Figure 1.5b) shows that this one-dimensional nanocrystal has the sphalerite structure just as ZnTe bulk crystals. This nanowire is an imperfect single crystal containing a large number of stacking faults (SF) in the growth direction.

The crystalline state that we have explained until now has always shown the property of periodicity. These crystals should be denoted as "periodic crystals." During the last decades, numerous materials were investigated where their structures have a long-range order but lack translational periodicity. Contrary to the periodic crystals, this class of crystals is referred to as *aperiodic crystals*. A change of the lattice periodicity can be generated by a periodic plane wave modulation of

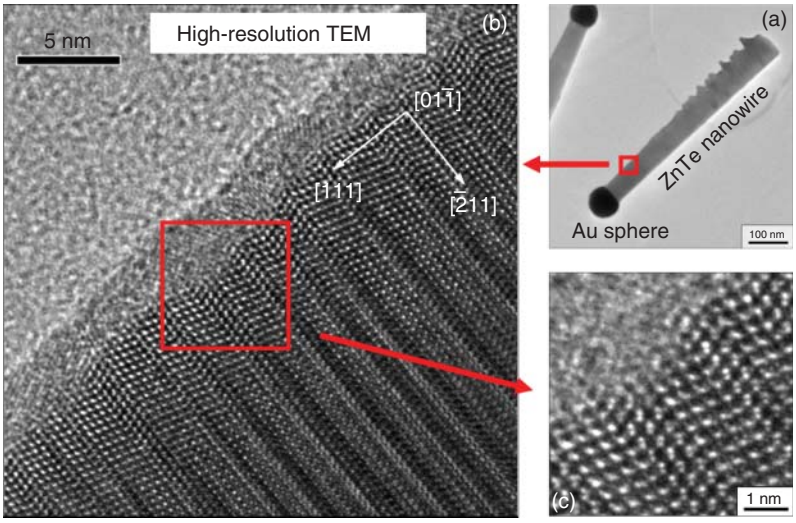

Figure 1.5 TEM images of a ZnTe nanowire: (a) overview image of a "harvested" ZnTe nanowire (the arrow marks the growth direction <111>); (b) HRTEM image of the nanowire [marked area in (a)].

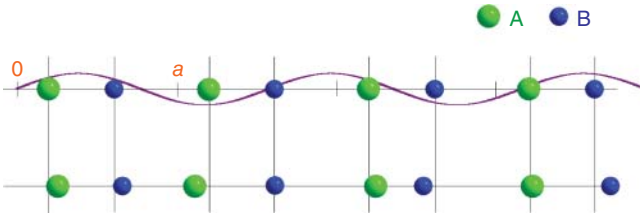

Figure 1.6 Illustration of one-dimensional incommensurate modulation.

a normal crystal as illustrated in Figure 1.6, where a one-dimensional modulation is carried out.

If the modulation period belongs to the rational periodicities of the "basic structure," we speak about a *commensurate-modulated crystal.* If the modulation period is irrational, an *incommensurate-modulated crystal* is given. The diffraction pattern of an incommensurate-modulated structure consists, therefore, of main reflections belonging to the basic structure and additional weaker satellite reflections. Owing to the irrational modulation, the sharp diffraction spots cannot be described by means of a three-dimensional reciprocal lattice. The problem can be solved by means of using the concepts of a superspace description. According to the number d of the dimension of modulations, $(3+d)$ symmetries have to be taken into consideration [6]. The incommensurate crystals can be divided into modulated crystals, composite or intergrowth crystals, and quasicrystals (QCs). Two types of incommensurate modulations are known. A displacive modulation is given when a periodic displacement from the atomic positions of the basic structure occurs. Occupation modulation means the atomic

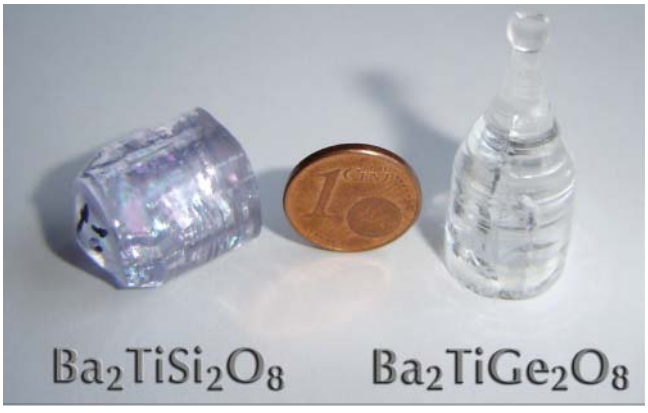

Figure 1.7 Individual crystals of $Ba_2TiSi_2O_8$ (BTS) and $Ba_2TiGe_2O_8$ (BTG). (Crystal growth: Uecker, R., Leibniz Institute for Crystal Growth Berlin, Germany.)

positions of the basic structure are occupied with a periodic probability function. Figure 1.7 shows two synthetic incommensurate crystals of $Ba_2TiSi_2O_8$ (BTS) and $Ba_2TiGe_2O_8$ (BTG), which were grown by Czochralski pulling. Both compounds are members of incommensurate-modulated structures with a basic structure of the fresnoite type [7]. The HRTEM image of BTG in [001] orientation exhibits a one-dimensional modulation along the *b*-axis (Figure 1.8a). The corresponding electron diffraction pattern (Figure 1.8b) clearly shows the existence of main reflections of strong intensity and satellites of weak intensity.

According to the one-dimensional modulation ($d = 1$), four indices ($3 + d$) are necessary to describe the diffraction pattern by means of the reciprocal lattice in a

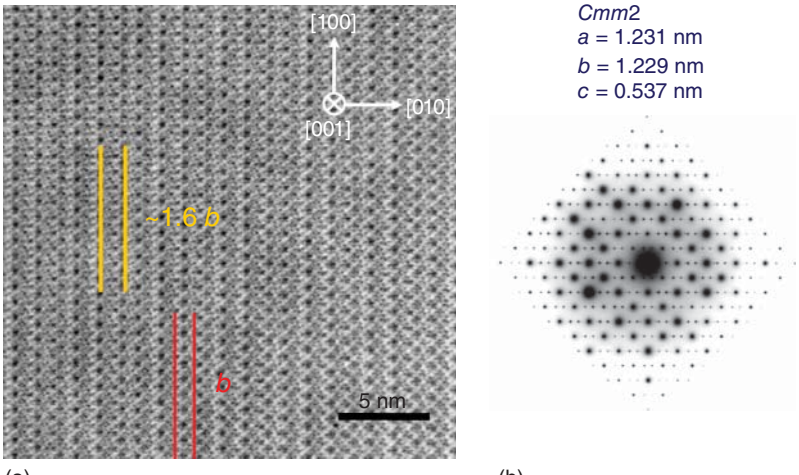

Figure 1.8 HRTEM image of [001] oriented BTG (a) and the corresponding electron diffraction pattern (b). (Courtesy of Höche, Th. [7].)

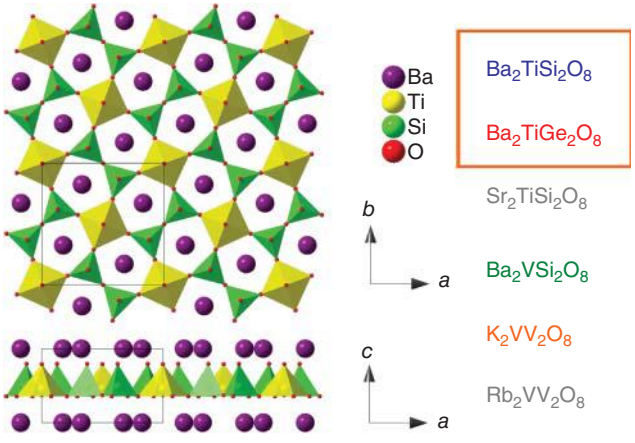

Figure 1.9 Structure model of the ideal basic fresnoite structure projected along [001]. (Courtesy of Höche, Th. [7].)

$(3+d)$-dimensional space. Just for the sake of illustration, the fresnoite framework structure and various members of this structure type are shown in Figure 1.9. The ideal fresnoite basis structure is characterized by layers of corner-connected SiO_4 tetrahedra and TiO_5 square pyramids interspersed with layers of barium atoms.

The crystal structure of BTG was solved by means of highly resolved neutron diffraction [8]. Atomistic representations of the incommensurate-modulated structure for different initial phases of the modulation waves are given in Figure 1.10. The images are time-dependent snapshots of the inherently displacive-modulated ideal basic BTG structure.

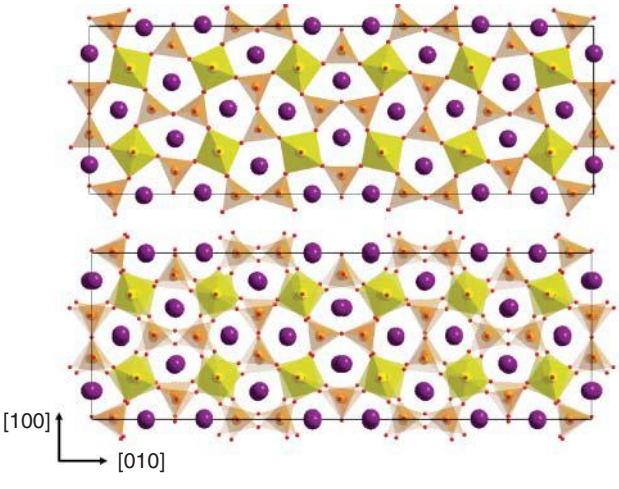

Figure 1.10 Representation of the modulated structure of BTG for different initial phases of the modulation phase parameter *t*. (Courtesy of Höche, Th. [7].)

Composite or intergrowth crystals consist of two or more modulated subsystems. The basic structures of them are mutually incommensurate.

The phenomenon of QCs was experimentally discovered by Shechtman *et al.* [9] while investigating the structure of rapidly cooled $Al_{86}Mn_{14}$ alloys in 1982. The name quasicrystal as an abbreviation for quasiperiodic crystals was introduced by Levine and Steinhardt in 1984 [10]. Since that time, numerous quasicrystalline materials were grown and investigated. A typical electron diffraction pattern of a QC is shown in Figure 1.11.

If we were to try to index this diffraction pattern using the concept of the reciprocal lattice (as applicable to a periodic crystal), we would, of course, fail completely. The QC has a long-range positional (translational) order that is not periodic but only quasiperiodic. This is obvious from the diffraction pattern. The separation between the Bragg peaks in any direction has not a translational symmetry. Very often, the diffraction patterns of QCs show noncrystallographic rotational symmetries (i.e., the existence of 5-fold, 8-fold, 10-fold, and 12-fold rotation axes) as illustrated in Figure 1.11. As we will demonstrate in Section 1.3, a periodic tiling of the space is only consistent with one, two, three, four, and sixfold rotation axes. It can be shown that the mass density of QCs can be described as a discrete sum of incommensurate functions. Contrary to the modulated structures where a basic crystallographic structure exists (main strong Bragg peaks in the diffraction pattern) and the incommensurate modulation (weak satellites in the diffraction pattern), the separation of all discrete diffraction spots of the QCs are incommensurate. There is no regular reciprocal lattice connected with the quasiperiodic structures. As already mentioned for the case

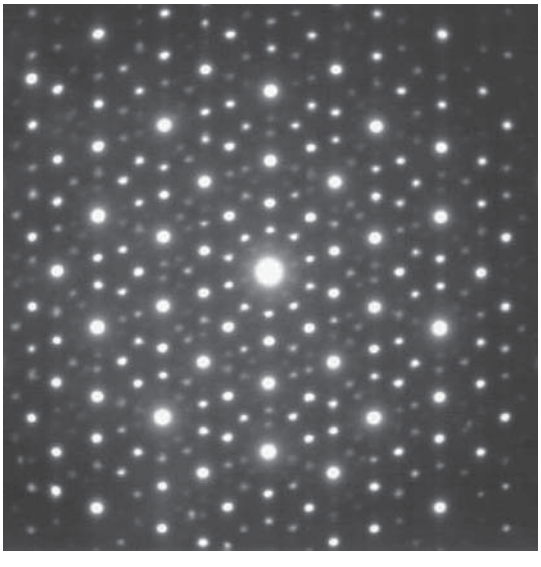

Figure 1.11 Electron diffraction pattern of an icosahedral QC along the fivefold axis. (Data from [9], Copyright 1984 by The American Physical Society.)

of modulated structures, one can also successfully apply crystallography in higher dimensions for the description of QCs.

In general, *d*-dimensional quasiperiodic structures can be constructed as irrational cuts of objects, which are periodically distributed in a higher-dimensional superspace. An icosahedral QC can be described periodically in a six-dimensional space where the projection onto the three-dimensional physical space provides us an icosahedral QC. A one-dimensional QC, for instance, can be generated when a two-dimensionally square lattice will be projected onto one-dimensional space along a straight line (strip) with an irrational slope of the line (strip). A one-dimensional periodic structure will be generated when the slope is rational with respect to the lattice rows.

In addition to the abovementioned aperiodic crystals, there exist other types of deviations from the periodic order in a crystal. In this connection, we will briefly mention the class of "order–disorder structures," abbreviated as OD structures. OD structures consist of layers/slabs with their own symmetry, which are described by partial symmetry operations that are not valid for the whole crystal [11, 12].

A further reduction of the long-range order leads to a statistical arrangement of the atoms. Thus, such a solid has no long-range order but a statistically short-range order and is referred to as an *amorphous solid*. The different stages of order from a three-dimensionally periodic crystal, via a polycrystal to the amorphous state, are clearly visible in the electron diffraction patterns. Figure 1.12 shows a diffraction pattern of an amorphous material.

As shown in Figure 1.4, the electron diffraction pattern of a crystal consists of sharp Bragg peaks, whereas we obtain for a polycrystalline specimen a system of sharp rings. Each ring corresponds to a fixed interplanar spacing within the

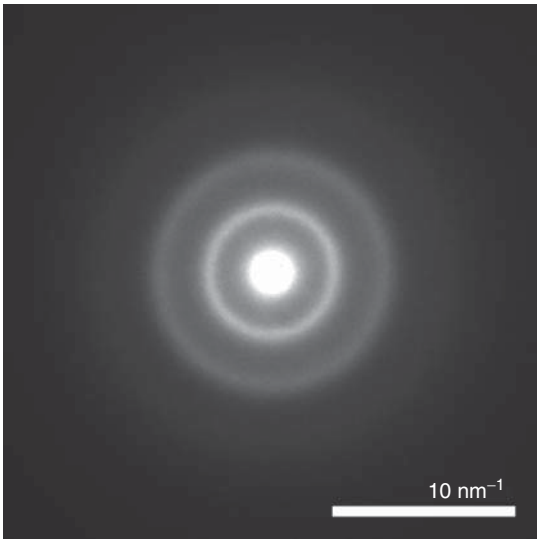

Figure 1.12 Electron diffraction pattern of amorphous silicon.

crystal. When the long-range order is lost, a set of diffuse rings will be obtained in our diffraction pattern. This is caused by the statistical arrangement of the atoms (topological disorder). Similar to liquids, amorphous solids are isotropic.

When we are dealing with the different states of order of solids, we have also to take into account the possible transitional stages between true crystals and true liquids, which can be considered as "soft matter." As we have seen, the main feature of the anisotropic crystals is the long-range positional order, whereas isotropic liquids have neither a long-range periodic positional nor orientational order. The state of matter in between is denoted as "mesomorphic state." *Liquid crystals* (*LCs*), also named as crystalline liquids, are mesophases [13]. LCs have a long-range orientational order, and either only partial positional order or the positional order is completely missing. LCs can be formed either by heating or cooling processes (*thermotropic LCs*) or by dissolving a material in a liquid (*lyotropic LCs*). The existence range of the mesophase depends on the suitable conditions of temperature, pressure, and concentration. The structure of the LCs has at least in one direction a liquid-like arrangement of the molecules and shows certain anisotropy. According to the existence of positional order, the LCs are divided into

- columnar phases (positional order in two directions)
- smectic phases (positional order in one direction)
- nematic phases (no positional order). Chiral nematic phases are also denoted as cholesteric LCs.

In addition to the abovementioned LC phases, there can also be formed "soft crystals" with long-range positional order, which are also described as "anisotropic plastic crystals."

Genuine *plastic crystals* are another example for a transition stage and closely related to LCs. Plastic crystals consists of molecules with long-range order but short-range disorder, which comes from the rotational motions of parts of the structure. They are optically isotropic because of the molecule motions.

The different states of order of a solid including possible transition stages to liquids, which we have discussed, are illustrated in Figure 1.13.

What are the characteristic features of a crystal when we do not restrict our consideration to the properties of "order" and "periodicity"? Typical features characterizing the crystalline state are

- long-range positional order
- a discrete diffraction diagram
- an atomic structure that can be generated as a cut of an n-dimensional periodic structure.

The International Union of Crystallography (IUCr) published the following definition of a crystal in 1992 [14]:

> In the following ***by "crystal" we mean any solid having an essentially discrete diffraction diagram,***
> *and* ***by "aperiodic crystal" we mean any crystal in which three-dimensional lattice periodicity can be considered to be absent***.

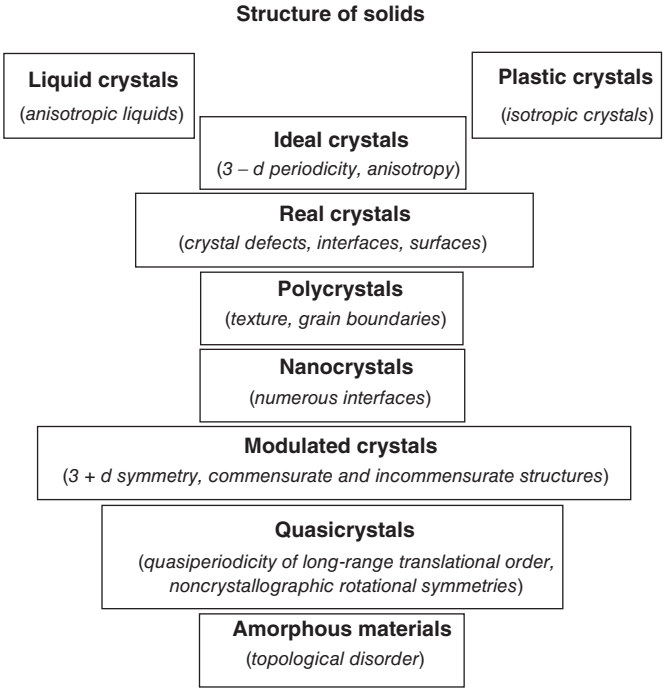

Figure 1.13 Schema of structural states of solids.

It should be noted that there is an ongoing discussion if the definition should be reconsidered or not (for pros and cons of this discussion, see the contributions published in [15]).

1.2 Fundamentals of Geometrical Crystallography

Before dealing with the external and internal symmetries of crystals in detail, we will explain the main concepts used for the geometrical description of crystals. In the previous section, we have shown that a characteristic feature of the periodic crystals is a three-dimensional periodic arrangement of the atomic building units. This periodic order can be described by means of the mathematical concept of translation lattices.

1.2.1 Crystal Lattices

In general, a space lattice is an infinite array of points, where each lattice point has identical neighborhood conditions, that is, all lattice points are identical. An example of a three-dimensional lattice (space lattice) is shown in Figure 1.14.

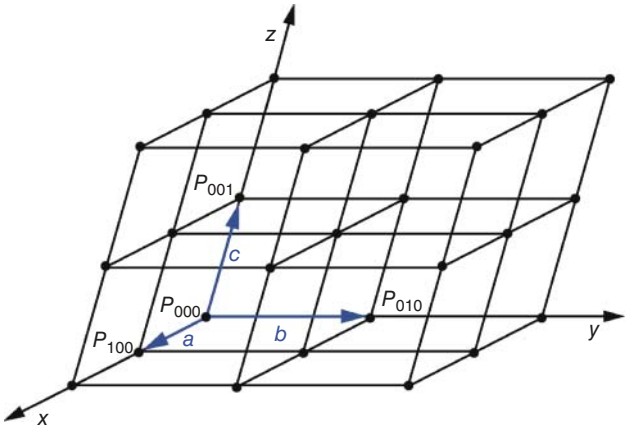

Figure 1.14 Space lattice (the unit cell is defined by the vectors ***a***, ***b***, and ***c***).

When we move from a lattice point to another along a lattice row, the magnitude of the repeating distance $|d_0|$ has always the same value. The parallel movement from a lattice point to another is denoted as ***translation***. Using a coordinate system (origin O; basis vectors ***a***, ***b***, and ***c***), each lattice vector ***t*** of the space lattice L can be expressed as

$$\boldsymbol{t} = l_1\boldsymbol{a} + l_1\boldsymbol{b} + l_1\boldsymbol{c} \in L \qquad (l_1, l_2, l_3 = 0, \pm 1, \pm 2, \ \ldots \ \pm \infty)$$

All vectors of the vector lattice L terminate at lattice points, which form the point lattice. Our three-dimensional point lattice can be decomposed into lattice planes (two-dimensional point lattices) and lattice rows (one-dimensional point lattices) as illustrated in Figure 1.15. The three basis vectors ***a***, ***b***, ***c*** of our space lattice define a primitive parallelepiped, the unit cell of the lattice. The repetition

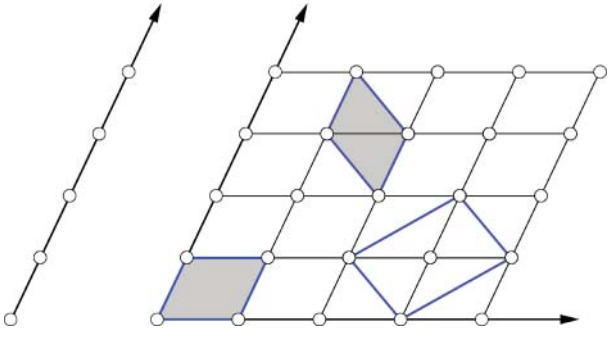

Figure 1.15 Lattice row (a) and lattice plane (b). Various possible unit meshes are selected; primitive meshes marked in gray.

of the unit cell along the three spatial directions leads to the infinite lattice. The number of possible unit cells is infinite because of the infinite number of possible lattice bases. The choice of different unit meshes (two-dimensional unit cells) as repetition units of a two-dimensional lattice is illustrated in Figure 1.15.

A lattice is called *primitive* if it contains no interior lattice points, being otherwise a nonprimitive lattice. All primitive unit cells have the same volume. The volumes of nonprimitive cells are multiples of the volumes of primitive ones. Each unit cell is defined by the following metric parameters: lengths $|\boldsymbol{a}|$, $|\boldsymbol{b}|$, $|\boldsymbol{c}|$ of the basis vectors $\boldsymbol{a}, \boldsymbol{b}, \boldsymbol{c}$ and the angles $\alpha \angle (\boldsymbol{b}, \boldsymbol{c})$, $\beta \angle (\boldsymbol{c}, \boldsymbol{a})$, $\gamma \angle (\boldsymbol{a}, \boldsymbol{b})$, respectively. The volume of the unit cell is

$$V = \boldsymbol{a} \cdot (\boldsymbol{b} \times \boldsymbol{c}) = \begin{vmatrix} \boldsymbol{a} \cdot \boldsymbol{a} & \boldsymbol{a} \cdot \boldsymbol{b} & \boldsymbol{a} \cdot \boldsymbol{c} \\ \boldsymbol{b} \cdot \boldsymbol{a} & \boldsymbol{b} \cdot \boldsymbol{b} & \boldsymbol{b} \cdot \boldsymbol{c} \\ \boldsymbol{c} \cdot \boldsymbol{a} & \boldsymbol{c} \cdot \boldsymbol{b} & \boldsymbol{c} \cdot \boldsymbol{c} \end{vmatrix}^{\frac{1}{2}}$$
$$= \boldsymbol{abc}\,(1 - \cos^2\alpha - \cos^2\beta - \cos^2\gamma + 2\cos\alpha \cdot 2\cos\beta \cdot 2\cos\gamma)^{\frac{1}{2}} \qquad (1.1)$$

We should be aware of the fact that the lattice is a mathematical concept useful for the description of the periodicity of crystal structures. Therefore, the term *crystal lattice* with respect to crystal structures is used. The relationships between lattices and crystal structures are discussed in Section 1.4. The lattice itself is not an object with physical meaning.

We will illustrate later that the existing correspondence between the morphology (external symmetry) and the structure (internal symmetry) of crystals can, therefore, be expressed by identical analytical descriptions. This correspondence means a crystal face is lying parallel to a set of lattice planes and a crystal edge is parallel to a set of lattice rows.

1.2.2
Crystal Axes Systems, Crystal Systems, and Crystal Families

For the analytical description of the geometry of crystals, it is advantageous to use coordinate systems that correspond to the symmetrical arrangement of faces forming the crystal. The crystallographic axes systems were introduced by Christian Samuel Weiss in 1815 and independently found by Friedrich Mohs (1822/1824). We use a right-handed axes system (a, b, c) with interaxial angles α, β, and γ as shown in Figure 1.16.

According to the axes system used, we can classify crystals into seven crystal systems (syngonies) and six crystal families as shown in Table 1.1. The hexagonal crystal family incorporates the trigonal and hexagonal crystal systems. The usage of either the rhombohedral axes system or the hexagonal axes system for the description of trigonal crystals will be discussed later in detail.

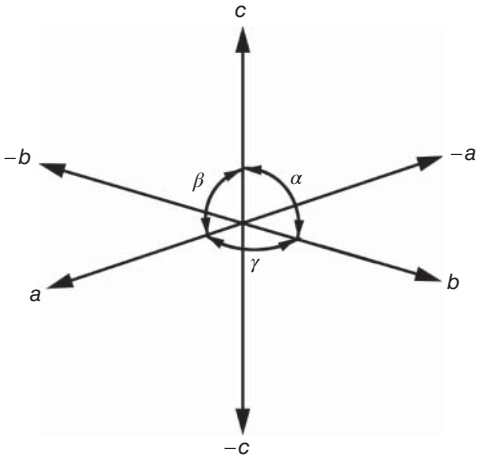

Figure 1.16 System of crystal axes.

1.2.3
Crystal Faces and Zones

A characteristic feature of crystals grown with polyhedral shape is expressed in the ***law of the constancy of interfacial angles*** (first basic law of crystallography, Nicolaus Steno, 1669):

> *The angles between corresponding crystal faces of different crystals of the same species are constant independent of the size of these faces.*

Unequal growth rates in different directions of the crystal are responsible for the diverse sizes of crystal faces, whereas the angular relationships between the faces are constant as illustrated in Figure 1.17. Nowadays, it is clear that the constancy of angles results from the fact that crystal faces are growing parallel to lattice planes as illustrated in Figure 1.17. The law of constancy of interfacial angles is preserved under definite thermodynamic conditions (constant temperature and pressure). This means that the angles between equivalent faces can be used as diagnostic feature for a crystal. In general, the angular measurements are carried out by means of optical two-circle reflection goniometers.

The crystal drawing of an orthorhombic sulfur crystal is shown in Figure 1.18. The question arises how we can analytically describe the various faces and edges of such a crystal? We see some of the faces cut the three rectangular coordinate axes, other faces are parallel to the *a*- and *b*-axes and so on.

Using a crystal-own coordinate system, the position of a particular crystal face is defined by its intercepts OA, OB, and OC with the axes *a*, *b*, and *c*, respectively (Figure 1.19). The direction of the crystal face is fixed by the direction of its normal. A parallel translation along the normal changes the absolute values of the intercepts. However, the ratio of OA : OB : OC will be constant.

Table 1.1 Crystal families, crystal systems, and crystallographic coordinate systems.

Crystal family	Symbol	Crystal system	Crystallographic coordinate system
			System of crystal axes
Triclinic (anorthic)	*a*	Triclinic (anorthic)	$\boldsymbol{a} \neq \boldsymbol{b} \neq \boldsymbol{c}$ $\alpha \neq \beta \neq \gamma \neq 90°$
Monoclinic	*m*	Monoclinic	$\boldsymbol{a} \neq \boldsymbol{b} \neq \boldsymbol{c}$ $\alpha = \gamma = 90°$, $\beta \neq 90°$ ***b**-unique setting* $\boldsymbol{a} \neq \boldsymbol{b} \neq \boldsymbol{c}$ $\alpha = \beta = 90°$, $\gamma \neq 90°$ ***c**-unique setting*
Orthorhombic	*o*	Orthorhombic	$\boldsymbol{a} \neq \boldsymbol{b} \neq \boldsymbol{c}$ $\alpha = \beta = \gamma = 90°$
Tetragonal	*t*	Tetragonal	$\boldsymbol{a} = \boldsymbol{b} \neq \boldsymbol{c}$ $\alpha = \beta = \gamma = 90°$
Hexagonal	*h*	Trigonal	$\boldsymbol{a} = \boldsymbol{b} \neq \boldsymbol{c}$ $\alpha = \beta = 90°$, $\gamma = 120°$ (*Hexagonal axes*) $\boldsymbol{a} = \boldsymbol{b} = \boldsymbol{c}$ $\alpha = \beta = \gamma \neq 90°$ (*Rhombohedral axes*)
		Hexagonal	$\boldsymbol{a} = \boldsymbol{b} \neq \boldsymbol{c}$ $\alpha = \beta = 90°$, $\gamma = 120°$
Cubic	*c*	Cubic	$\boldsymbol{a} = \boldsymbol{b} = \boldsymbol{c}$ $\alpha = \beta = \gamma = 90°$

Crystal faces correspond to lattice planes as already mentioned. The interceptions on the axes are then described by multiples of the lattice translations a_0, b_0, and c_0. When we are concerned with the intercepts of the axes in the crystal lattice, the relationship is then given by

$$\mathrm{OA} : \mathrm{OB} : \mathrm{OC} = m \cdot a_0 : n \cdot b_0 : p \cdot c_0$$

where m, n, and p are integers. The intercepts m, n, and p on the axes are called ***Weiss symbols***.

The relationships between the intercepts on the crystal axes and the direction of face normal are expressed by the following direction cosines:

$$\cos\varphi_a = \mathrm{ON/OA}, \quad \cos\varphi_b = \mathrm{ON/OB}, \quad \cos\varphi_c = \mathrm{ON/OC} \tag{1.2}$$

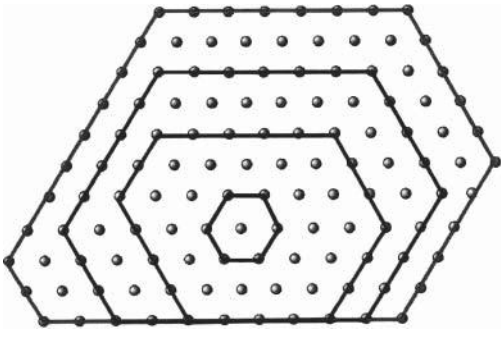

Figure 1.17 Schematic illustration of the law of constancy of interfacial angles.

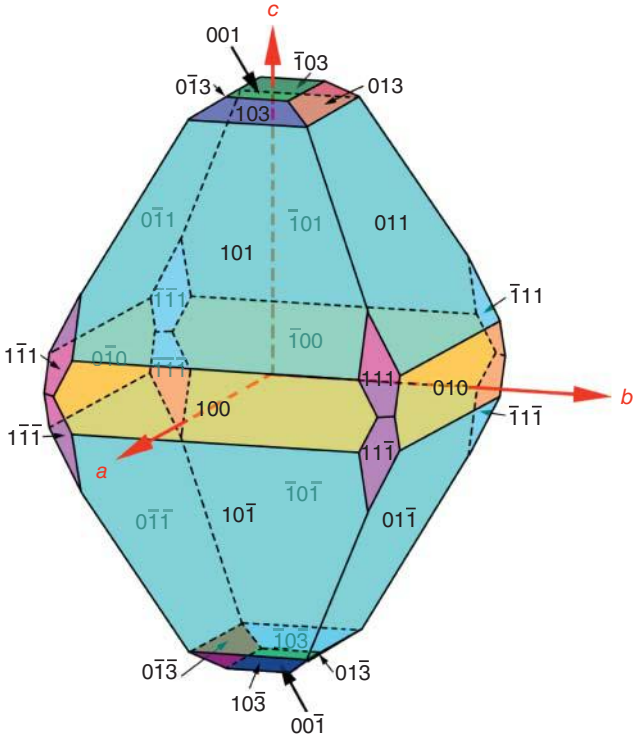

Figure 1.18 Crystal drawing of a sulfur crystal.

Combining the three equations, the following ratio results:

$$\cos\varphi_a : \cos\varphi_b : \cos\varphi_c = \frac{1}{\mathrm{OA}} : \frac{1}{\mathrm{OB}} : \frac{1}{\mathrm{OC}} \tag{1.3}$$

After substituting $\mathrm{OA} : \mathrm{OB} : \mathrm{OC} = m{\cdot}a_0 : n{\cdot}b_0 : p{\cdot}c_0$, it follows:

$$\cos\varphi_a : \cos\varphi_b : \cos\varphi_c = \frac{1}{m \cdot a_0} : \frac{1}{n \cdot b_0} : \frac{1}{p \cdot c_0} \tag{1.4}$$

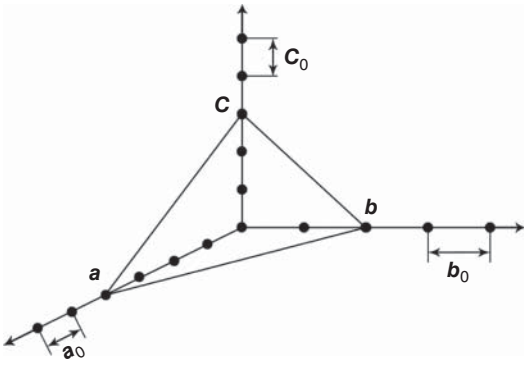

Figure 1.19 Intercepts of a crystal plane on the crystallographic axes.

The direction cosines of the face normal are inversely proportional to the axial intercepts of the face. For the analytical description of faces (lattice planes), the coprime reciprocal values h, k, l of the axial intercepts are used. The hkl are called ***Miller indices*** and the symbol (hkl) is the face symbol.

$$h : k : l = \frac{1}{m} : \frac{1}{n} : \frac{1}{p} \tag{1.5}$$

If the axial intercepts of the face (net plane) of Figure 1.19 are $4a_0 : 2b_0 : 4c_0$, then the corresponding Millers indices (coprime) are (121).

Let the Weiss symbols for a particular face $m : n : p = 2 : 3 : 4$; then, $1/m : 1/n : 1/p = 1/2 : 1/4 : 1/3 = 6 : 3 : 4$ and the Miller indices are (634).

The Miller indices for particular positions of pyramid, prism, and end faces are illustrated in Figure 1.20. A pyramid face intercepts all axes [Weiss symbols: $m{\cdot}a_0 : n{\cdot}b_0 : p{\cdot}c_0$; Miller indices ($hkl$)]. If a face lies parallel to one axis, that is, cutting this axis at infinity, a so-called prism face is given [Weiss symbols: $\propto{\cdot}a_0 : n{\cdot}b_0 : p{\cdot}c_0$; $m{\cdot}a_0 : \propto{\cdot}b_0 : p{\cdot}c_0$; $m{\cdot}a_0 : n{\cdot}b_0 : \propto{\cdot}c_0$ with the corresponding Miller indices (0kl); (h0l); (hk0), respectively]. End faces are lying parallel to two axes [Weiss symbols: $m{\cdot}a_0 : \propto{\cdot}b_0 : \propto{\cdot}c_0$; $\propto{\cdot}a_0 : n{\cdot}b_0 : \propto{\cdot}c_0$; $\propto{\cdot}a_0 : \propto{\cdot}b_0 : p{\cdot}c_0$ with the corresponding Miller indices (100); (010); (001), respectively].

The rational nature of Weiss symbols or Miller indices is expressed in the second basic law of crystallography, ***the law of rational indices* (*Haüy's law, 1774*)**:

> *The ratio between the intercepts on the axes for the occurring faces on a crystal can be expressed by rational numbers.*

Hence, the Miller indices hkl or the Weiss symbols mnp are integers.

The existence of lattice with a parallelepiped as unit cell follows directly from this law.

According to this law, a regular pentagon–dodecahedron with Miller indices (01τ) is not consistent with this law because the golden mean $\tau = (1 + \sqrt{5})/2$ results in an irrational interception. Therefore, the regular

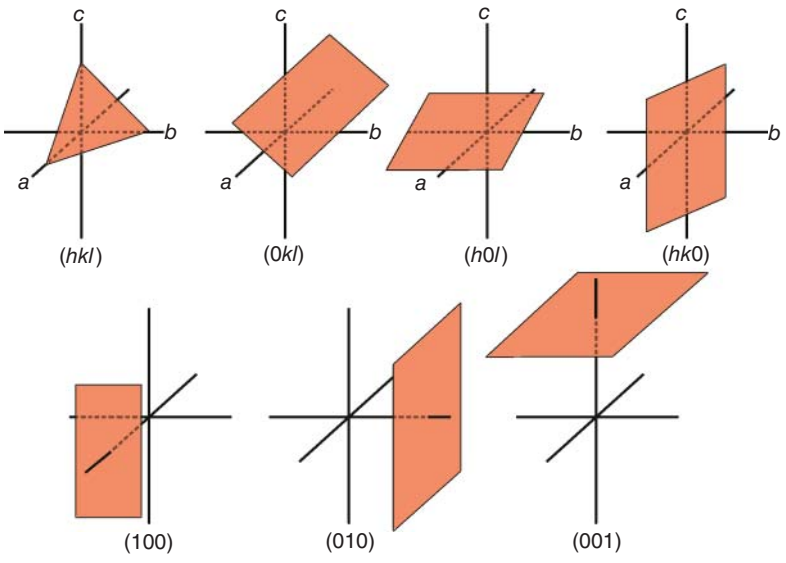

Figure 1.20 The Miller indices of pyramid, prism, and end faces.

pentagon–dodecahedron is not a possible polyhedron for periodic crystals. However, it is a possible form of a QC.

The usage of Miller indices to index crystal faces allows a simple and an elegant description of the morphology of crystals. When we describe an ideal crystal face at structural level, then the two-dimensionally periodic array of lattice points (net planes) expresses the correspondence between Miller's indices and occupation density of lattice planes. Figure 1.21 illustrates this correspondence for some

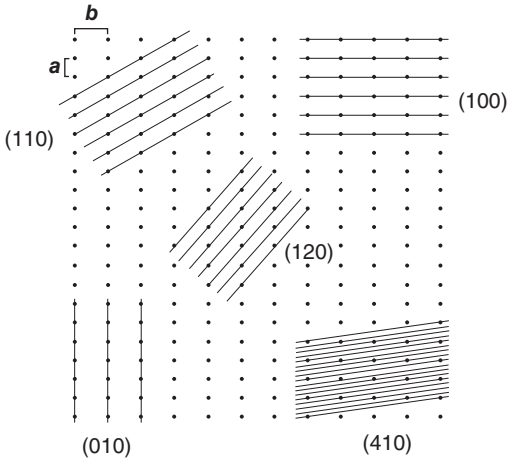

Figure 1.21 Correspondence between Miller's indices and occupation density of lattice planes.

particular faces. It is also obvious that the faces are parallel to sets of lattice planes, where the lattice points in a real crystal are decorated with atomic building blocks. The occupation density of lattice planes, that is, the number of lattice points on a lattice plane, is proportional to the interplanar distance d_{hkl}. According to the ***Bravais–Friedel rule*** [16, 17] derived from numerous statistical investigations of the morphology of natural crystals, faces with low Miller indices (high occupation density and large d_{hkl} values) are of higher importance (more commonly developed on a crystal) than faces with high Miller indices. This pure morphological rule was extended by taking into account the structural symmetry of crystals by ***Donnay and Harker*** [18]. Various computer programs (e.g., Mercury of the Cambridge Crystallographic Database [19], GULP [20], WinXMorph [21]) can be applied to predict the possible crystal morphology for a crystal structure on the basis of the ***Bravais–Friedel–Donnay–Harker*** (***BFDH***) ***law***. Calculations of BFDH morphology do not take into account the real structure or the growth conditions. The ***periodic bond chains*** (***PBC***) ***method*** developed by ***Hartman and Perdok*** [23] was a first successful attempt to calculate the importance of a crystal face on an energetic hypothesis (for a detailed description, see Chapter 2). The PBC theory was later expanded by the "connected net model" [24]. The kinematic-geometric formulation of the morphology by Prywer and Krasinski [25] has clearly demonstrated that the size of a crystal face can also be influenced by the growth rate of neighboring faces and the interfacial angles between them and the original face. Thus, growth conditions can exist where faster growing faces will be evolved and vice versa, that is, slower growing faces will disappear. This also means that the morphological importance of a face is not always inversely proportional to the growth rate as assumed by the BFDH law.

As already discussed, there is a close correspondence between the morphology and the structure of a crystal. The law of constancy of interfacial angles has expressed the correspondence between crystal faces and lattice planes (net planes). In an analogous manner, there is a correspondence between crystal edges (zone axes) and lattice directions (lattice point rows). The existing correspondence between the morphology (external symmetry) and the structure (internal symmetry) of crystals can, therefore, be expressed by identical analytical descriptions, as discussed further.

A set of crystal faces whose face normal lie in a plane is called a ***zone*** with the ***zone axis*** perpendicular to this common plane (Figure 1.22). Faces are denoted as ***tautozonal faces*** if they belong to the same zone. It is obvious from Figure 1.22 that all intersections of the faces of the zone are parallel to each other and parallel to the zone axis.

All directions in crystals are possible zone axes. Directions in crystals are represented by vectors $\boldsymbol{r}_{uvw} = u\boldsymbol{a} + v\boldsymbol{b} + w\boldsymbol{c}$ (where u, v, and w are integers) and can be shortly symbolized by the indices $[uvw]$. A crystal face (hkl) belongs to a zone $[uvw]$ if the so-called zone equation is satisfied:

$$hu + kv + lw = 0 \tag{1.6}$$

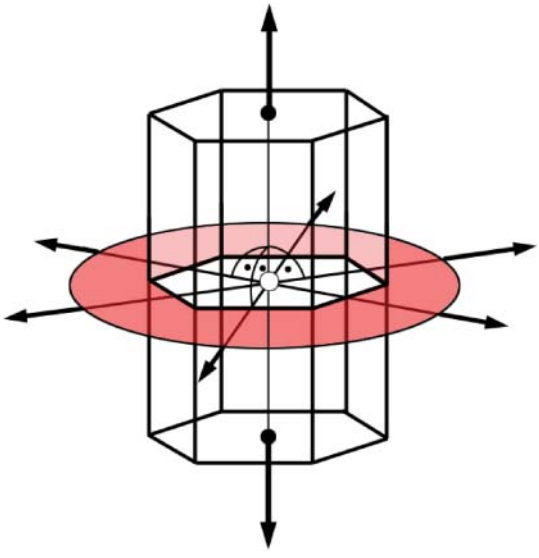

Figure 1.22 Illustration of the term *crystal zone*.

The indices of the zone axis can be determined by calculating the common edge (line of intersection) of two faces belonging to the zone. Both faces have to satisfy the following zone equation:

$$h_1u + k_1v + l_1w = 0 \quad \text{and} \quad h_2u + k_2v + l_2w = 0 \tag{1.7}$$

The solution of the two equations provides the indices [*uvw*]:

$$u = k_1l_2 - k_2l_1; \quad v = l_1h_2 - l_2h_1; \quad w = h_1k_2 - h_2k_1 \tag{1.8}$$

The indices of the common zone axis of two faces can easily be calculated by means of following scheme:

$$\begin{array}{c|cccc|c} h_1 & k_1 & l_1 & h_1 & k_1 & l_1 \\ & \times & \times & \times & & \\ h_2 & k_2 & l_2 & h_2 & k_2 & l_2 \\ \hline & [u & v & w] & & \end{array} \tag{1.9}$$

In an analogous manner, the Millers indices (*hkl*) of a face can be calculated by means of two bounding edges (zone axes and lattice directions lying parallel to the face):

$$\begin{array}{c|cccc|c} u_1 & v_1 & w_1 & u_1 & v_1 & w_1 \\ & \times & \times & \times & & \\ u_2 & v_2 & w_2 & u_2 & v_2 & w_2 \\ \hline & (h & k & l) & & \end{array} \tag{1.10}$$

It can be shown that any linear combination of two faces (two net planes related to the internal structure) $F_1(h_1k_1l_1)$ and $F_2(h_2k_2l_2)$ of the zone $Z[uvw]$ provides an additional face of this zone. In this manner, all the faces of the zone can be derived by successive addition (***complication rule*** of ***Goldschmidt***).

$$h = \lambda_1 h_1 + \lambda_2 h_2, \quad k = \lambda_1 k_1 + \lambda_2 k_2, \quad l = \lambda_1 l_1 + \lambda_2 l_2, \quad \lambda_1, \lambda_2 - \text{arbitrary integers} \tag{1.11}$$

Alternatively, any linear combination of two zone axes $Z_1[u_1v_1w_1]$ and $Z_2[u_2v_2w_2]$ provides an additional zone axis, which lies in the face $F(hkl)$ bounded by Z_1 and Z_2.

$$u = \lambda_1 u_1 + \lambda_2 u_2, \quad v = \lambda_1 v_1 + \lambda_2 v_2, \quad w = \lambda_1 w_1 + \lambda_2 w_2, \quad \lambda_1, \lambda_2 - \text{arbitrary integers} \tag{1.12}$$

The condition that three crystal faces $(h_ik_il_i)$, $i = 1, 2, 3$, belong to one zone, that is, they are tautozonal, or related to the internal structure that three net planes $(h_ik_il_i)$ intersection in parallel lattice directions is fulfilled if

$$\begin{vmatrix} h_1 & k_1 & l_1 \\ h_2 & k_2 & l_2 \\ h_3 & k_3 & l_3 \end{vmatrix} = 0 \tag{1.13}$$

In analogous manner, three zones $[u_iv_iw_i]$, $i = 1, 2, 3$, have a common face or, related to the internal structure of crystals, three lattice directions $[u_iv_iw_i]$ are parallel to a net plane (hkl) if

$$\begin{vmatrix} u_1 & v_1 & w_1 \\ u_2 & v_2 & w_2 \\ u_3 & v_3 & w_3 \end{vmatrix} = 0 \tag{1.14}$$

The zone law plays an important role for the interpretation of crystal faces and crystal forms. From the mutual relationships between crystal faces and crystal edges as illustrated above, we have seen that two crystal faces define a crystal edge and vice versa. When Christian Samuel Weiss (1819) derived the zone law, he could show that all faces of a crystal among each other belong to the ***assembly of zones*** [the zone law is denoted in German also as law of assembly of zones (Zonenverbandsgesetz)]. In principle, this fact allows the derivation of all possible faces of a crystal if four faces are known of which no three belong to the same zone (tautozonal). Then, new zones can be generated by combination of pairs of faces. The combination of pairs of new zones provides then new faces. In this manner, all possible rational faces of a crystal can be derived. This procedure is also a useful tool to determine the indices of unknown faces of a crystal. The crystal drawing of a zircon crystal ($Zr[SiO_4]$) where the faces $F_1(100)$, $F_2(110)$, $F_3(111)$, and $F_4(1\bar{1}1)$ are known is shown in Figure 1.23.

Now, we will illustrate how we can determine the unknown Miller indices of faces x and u by means of the zone law. The combination of $F_3(111)$ and $F_1(100)$ provides the zone $Z_1[01\bar{1}]$; the combination of $F_4(1\bar{1}1)$ and $F_2(110)$ gives $Z_2[\bar{1}12]$.

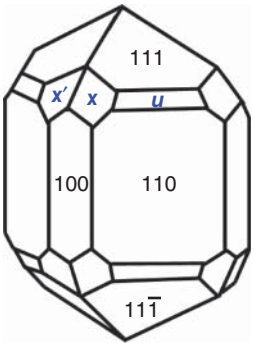

Figure 1.23 Crystal drawing of a zircon crystal ($Zr[SiO_4]$).

The face x with Miller indices (311) results from the combination of $Z_1[01\bar{1}]$ and $Z_2[\bar{1}12]$. The zone $Z_3[\bar{1}10]$ is calculated by combining $F_3(111)$ and $F_2(110)$. From the face $x(311)$ and the mirrored face $x'(3\bar{1}1)$, we calculate $Z_4[10\bar{3}]$. Then, the combination of the zones $Z_3[\bar{1}10]$ and $Z_4[10\bar{3}]$ generates the face $u(331)$.

For the description of crystallographic planes and directions, the following symbols are used:

(hkl) – Miller indices of a crystal face or a single net plane.
{hkl} – Miller indices of a set of all symmetrically equivalent crystal faces (crystal form) or net planes.
[uvw] – Indices of a zone axis or a lattice direction.
<uvw> – Indices of a set of all symmetrically equivalent lattice directions.

In general, the symbols and the conventions with the different kind of brackets may be used for crystals of all crystal coordinate systems. Some specifics have to be considered for the hexagonal axes system. Therefore, the indexing procedure for the hexagonal axes system will be treated separately. Some examples should illustrate the concept of indexing. Let us consider the hexahedron (cube) of the cubic crystal system. The six faces of the cube are (100), ($\bar{1}$00), (010), (0$\bar{1}$0), (001), and (00$\bar{1}$). The symbol {100} in curly brackets denotes the crystal form of the cube consisting of six symmetry equivalent faces.

For example, the symbol {100} for a tetragonal crystal denotes the crystal form of a tetragonal prism and consists of the four symmetry equivalent faces: (100), ($\bar{1}$00), (010), and (0$\bar{1}$0). Crystal forms and their symmetry will be treated in detail in Section 1.3.

The positive and negative directions of the crystallographic coordinate axes a, b, and c are expressed in square brackets as follows: [100], [$\bar{1}$00]; [010], [0$\bar{1}$0]; and [001], [00$\bar{1}$], respectively. In the cubic crystal system, the three coordinate axes are symmetry equivalent. For a cubic crystal, <100> in triangular brackets denotes the abovementioned six symmetry equivalent directions. When we consider an orthorhombic crystal where the coordinate axes a, b, and c are not symmetry equivalent, <100> concludes only the directions [100] and [$\bar{1}$00].

1.2.4
Indexing in the Hexagonal Crystal Family

For crystals of the hexagonal crystal family (trigonal and hexagonal crystal system), some characteristics have to be considered when indexing faces and directions of crystals. In addition to the principal axis c, the hexagonal axes system has three symmetry equivalent axes a_1, a_2, and a_3 perpendicular to c (Figure 1.24). Between the a-axes is an angle of 120°. According to the four axes, the four ***Bravais–Miller indices*** (***hkil***) are used to define a face of a trigonal or hexagonal crystal [16]. It can easily be shown that

$$h + k + i = 0 \quad \text{and} \quad i = -(h + k) \tag{1.15}$$

The traces of the two kinds of hexagonal prisms $\{10\bar{1}0\}$ (pyramids of first position) and $\{11\bar{2}0\}$ (prisms of second position) and the corresponding lattice directions are shown in Figure 1.24. The symbols $\{hkil\}$ are often represented as $\{hk.l\}$ because the third index i is defined by h and k.

We should be aware of the fact that the algorithm $h + k + i = 0$ cannot be directly transferred to the determination of zone indices. In general, one can use the three term symbol $[uv.w]$, where the dot means 0.

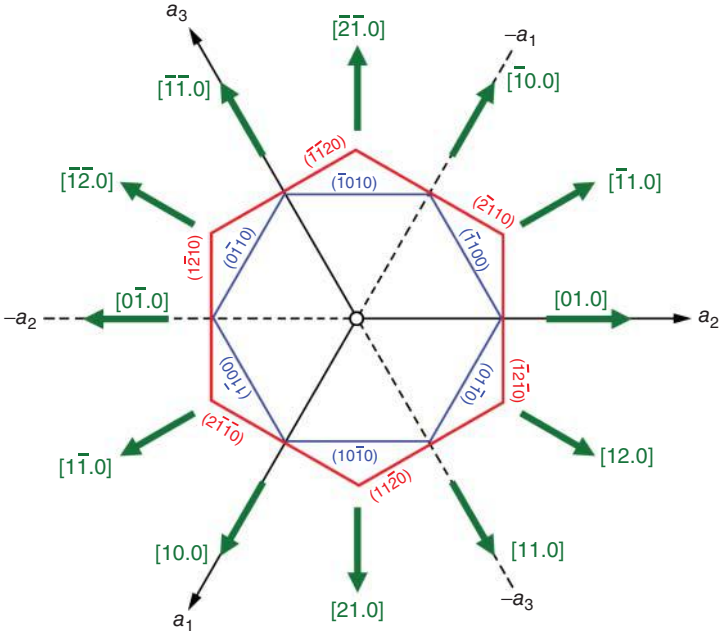

Figure 1.24 Indexing of faces and directions in the hexagonal crystal family (trigonal and hexagonal crystal systems).

The following examples illustrate how we can determine the common zone of two faces and vice versa, the common face of two zones, of crystals of hexagonal crystal family:

The faces $(10\bar{1}0)$ and $(51\bar{6}1)$ were indexed on a quartz crystal. What is the common zone?

First, we reduce the four term symbols to three term symbols (100) and (511). Second, we apply the usual procedure:

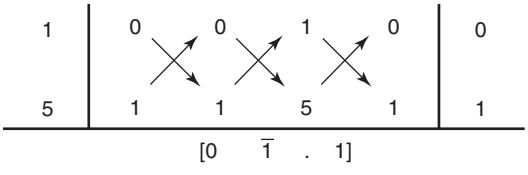

(1.16)

The common zone of the two faces $(10\bar{1}0)$ and $(51\bar{6}1)$ is $[0\bar{1}.1]$.

What is the common face of the two zones [00.1] and [10.0] of the quartz crystal?

Again, we apply the usual procedure:

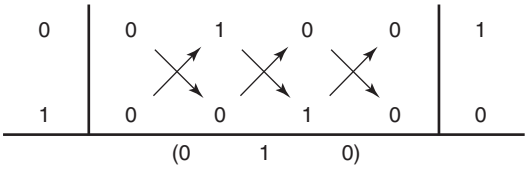

(1.17)

The three term face symbol corresponds to the four term symbol $(01\bar{1}0)$. For the sake of completeness, it should be mentioned that one can use four term direction symbols $[u'v't'w']$.

Then, $[uv.w] = [uv0w] = [u+t', v+t', t', w] = [u'v't'w']$, with t' as random number. If we assume that $u'+v'+t=0$ in analogy to $h+k+i=0$, then the following identities are given:

$$u' = (2u-v)/3, \quad v' = (2v-u)/3, \quad t' = -(u+v), \quad w' = w \tag{1.18}$$

The reverse transformation is given by

$$u = u' - t', \quad v = v' - t', \quad w = w' \tag{1.19}$$

Crystals of the trigonal crystal system can be described in the four term hexagonal axes system or in the three term rhombohedral axes system. The transformation relationships between the hexagonal and rhombohedral axes system are described in detail in Section 1.4.1.2.

1.3 Morphological Symmetry of Crystals

One of the remarkable features of natural and artificially grown crystals is the possible occurrence of a convex polyhedral shape. From such developed morphology

Figure 1.25 Cubic crystals: (a) fluorite (CaF_2, octahedra); (b) fluorite (CaF_2, cubes); and (c) garnet (almandine, $Fe_3Al_2[SiO_4]_3$, rhombic dodecahedra); collection terra mineralia in castle Freudenstein Freiberg/Saxonia, Germany (*www.terra-mineralia.de*).

of crystals, one can deduce a particular external symmetry. In the following, we will discuss what kind of symmetry determines the morphology (external shape) of a crystal. Thus, we have to figure out the kind of motion (symmetry operation), which will transform the crystal shape onto itself. The three crystals shown in Figure 1.25 have external forms of a cube {100}, rhomb-dodecahedron {110}, and octahedron {111}, respectively.

For the description of the polyhedra, we use a cubic axes system. It is obvious from the drawings (Figure 1.26) that the three different polyhedra can be mapped onto itself by three different kind of rotations around lines (rotation axes) through an angle $\alpha = 360°/n$, where the integer n determines the multiplicity of the axes. The position of the axes is marked by the symbols, ⬮, ▲, and ⧫, respectively.

A common feature of the morphological symmetry of the cube, rhomb-dodecahedron, and octahedron is that all of them have three fourfold axes (rotation through 90°, $n = 4$), four threefold axes (rotation through 120°, $n = 3$), and six twofold axes (rotation through 180°, $n = 2$). In addition, the polyhedra contain as symmetry elements three main mirror planes and six secondary mirror planes (Figure 1.27). The crystals are mapped then onto itself by reflection.

Finally, there is a center of symmetry also denoted as inversion center within the crystal polyhedra located at the origin. The mapping operation of inversion produces to each face of the crystal a second parallel face opposite to the initial face. We can see that cube, rhomb-dodecahedron, and octahedron have the same eigensymmetry represented by the symmetry framework of three fourfold, four threefold, and six twofold rotation axes, three main and six secondary mirror

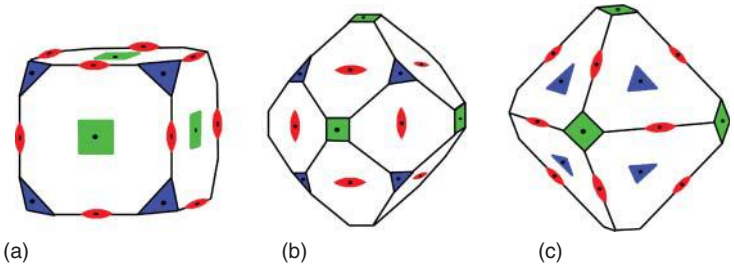

Figure 1.26 (a–c) Rotation axes of cube, octahedron, and rhomb-dodecahedron.

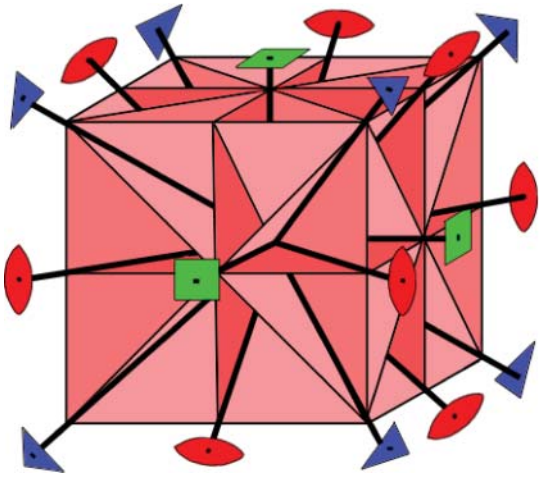

Figure 1.27 Eigen-symmetry framework of cube, octahedron, and rhomb-dodecahedron.

planes, and the center of symmetry. The question arises if these polyhedra can also be generated by less symmetry elements and connected with it less symmetry operations than that of the eigensymmetry?

The complete set of symmetry operations for the description of the morphological symmetry of crystals consists of *rotations*, *reflections*, and *inversions* and the combined operations *rotoinversions* (rotation + inversion) and *rotoreflections* (rotation + reflection). Before dealing with the symmetry elements and their possible combinations, we will briefly describe the fundamentals of the stereographic projection as a very useful tool for the graphical representation of both crystal forms and the action of the abovementioned symmetry operations. The stereographic projection can be derived from a spherical projection (Figure 1.28).

The crystal is positioned within the sphere in such a way that the center of sphere and crystal coincide. All crystal faces are substituted by their normals. The set of normals intersects the surface of the sphere at points representing the poles of crystal faces. All poles of crystal faces will be projected onto the equatorial plane as projection plane with respect to the South Pole as projection point. This means the position of all poles of the crystal in the stereographic projection is determined by the intersection points in the equatorial plane of the lines from the poles on the surface of the sphere to the projection point (Figure 1.29).

In order to avoid that poles of crystal faces of the lower hemisphere are outlying of the equatorial circle, all faces of the lower hemisphere are projected to the North Pole (Figure 1.30). In general, the poles of faces from the upper and lower hemispheres are plotted in the stereogram as dots and open small rings, respectively.

The stereographic projection has two main important properties:

– First, it is angle-preserving but not area-preserving. This means the angular relationships between the faces of crystals will be correctly projected.

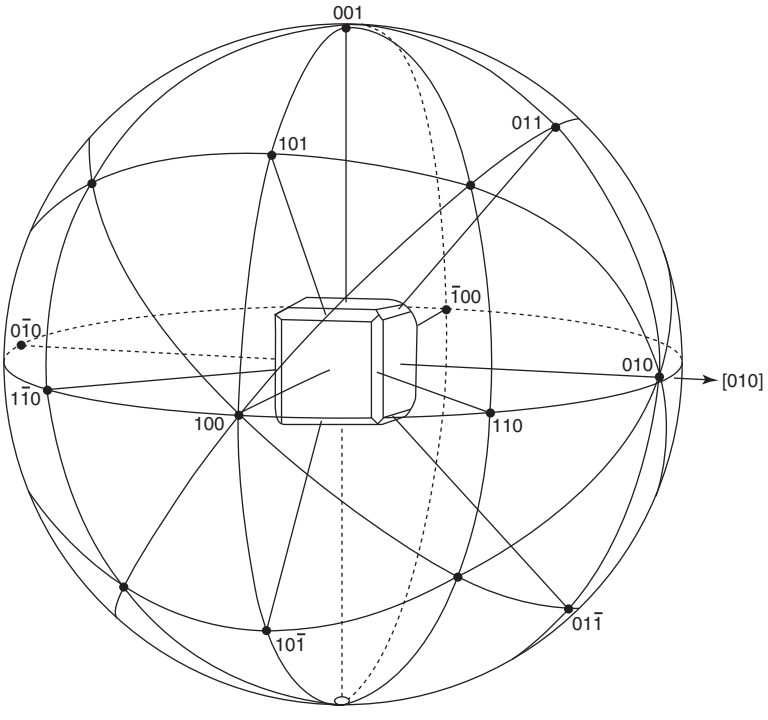

Figure 1.28 Spherical projection of a crystal.

Therefore, one can measure the true angles between the faces or zone axes of the crystal from their stereographic projection.

– Second, all circles on the surface of the sphere will be projected as circles or as straight lines in the projection plane.

A very useful graphic tool for the practical application of the stereographic projection is the Wulff net (Figure 1.31). This net itself is a particular stereographic projection of one half of the terrestrial globe onto the equatorial plane, where the lines of latitude and magnitude of the sphere are projected as ***small circles*** (with the exception of the equator) and ***great circles***, respectively. The outer circle of the net is denoted as the ***primitive***. The lines of the N–S-axis, the E–W-axis, and the primitive are also great circles. Angular relationships between poles can only be measured on great circles.

For practical application, a sheet of translucent paper is laid on the Wulf net and fixed by a tack in such a manner that it can be freely rotated around the center of the Wulf net. The position of any pole in the stereographic projection is fixed by the two angles φ and ρ. The azimuth φ ($0 \leq \varphi \leq 2\pi$) is measured around the primitive, while the pole distance ρ ($-\pi/2 \leq \rho \leq +\pi/2$) is measured from the center of the net along a diameter (N–S-axis, E–W-axis). Faces of the upper hemisphere have positive ρ-values ($0 \leq \rho \leq +\pi/2$) and faces lying in the lower hemisphere have negative ρ-values ($-\pi/2 \leq \rho \leq 0$). For any crystal face with the spherical coordinates

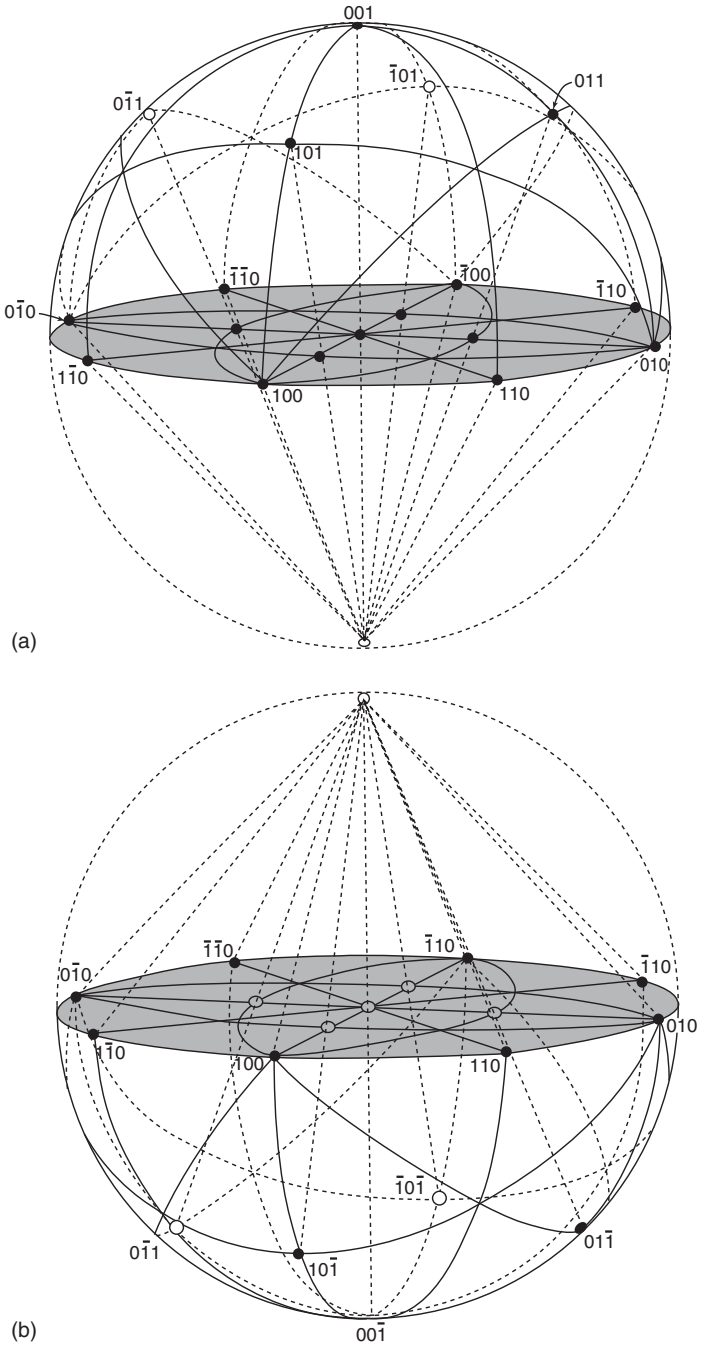

Figure 1.29 (a,b) Stereographic projection.

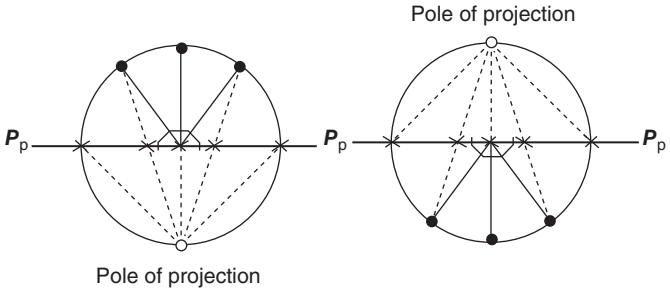

Figure 1.30 (a,b) Principle of stereographic projection.

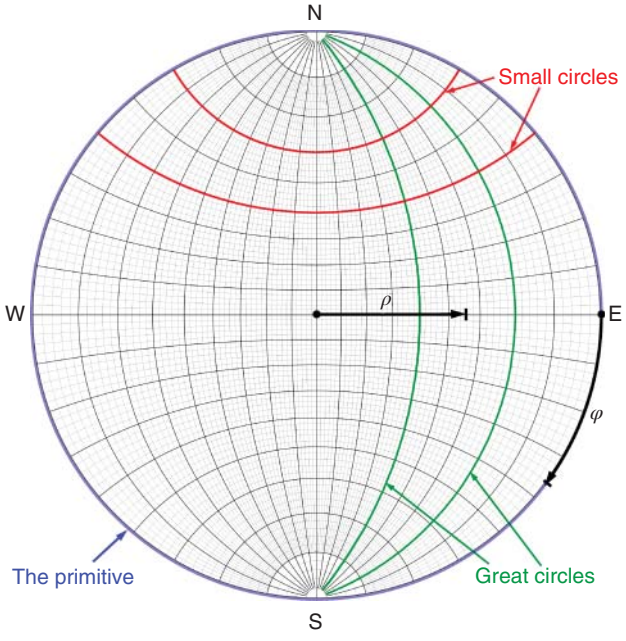

Figure 1.31 The Wulff net (accuracy of projected lines of latitude and longitude 2°).

φ and ρ, one can find the position of the pole as described above and vice versa for any plotted pole in the stereogram one can read out the φ- and ρ-values very easily by means of the Wulff net (Figure 1.32).

A standard construction is the determination of the common zone circle, corresponding zone pole, and the angle between the two faces for which the poles are plotted in the stereogram (Figure 1.33). First, we rotate the stereogram on our translucent paper until the two poles lie on a common great circle. The great circle is the *zone circle* of the two faces. All poles of faces that are lying on this zone circle belong to the same zone, that is, the faces are *tautozonal.* We can directly count the angle between the two faces from the Wulff net with an accuracy of 2° according to the division of the net. However, we should be aware that we measure

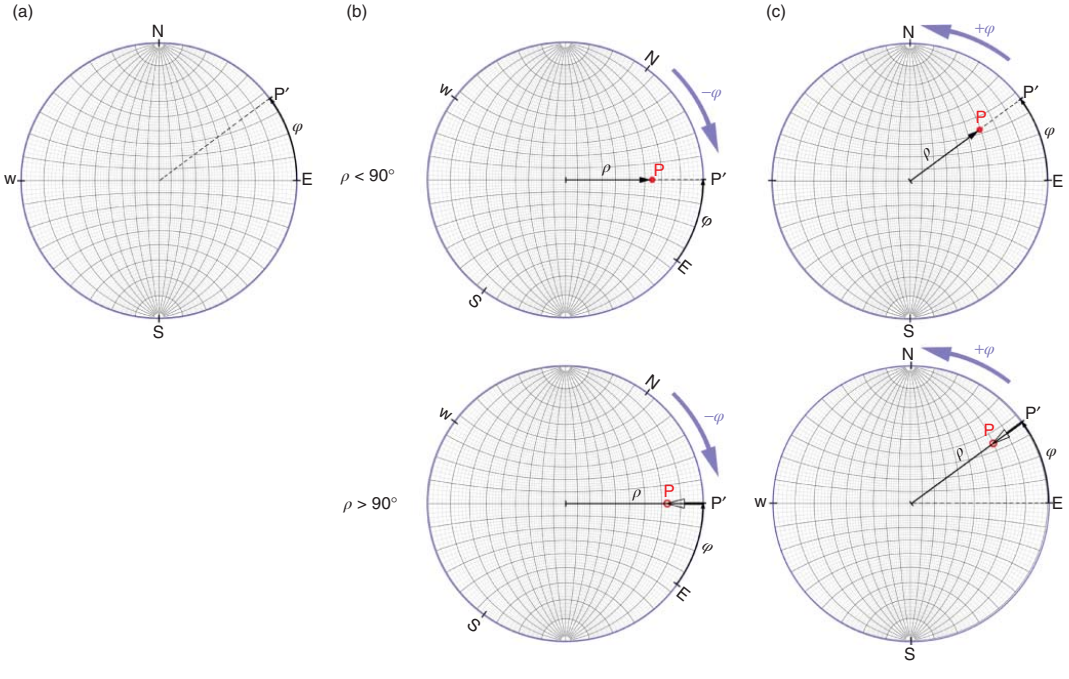

Figure 1.32 (a–c) Construction of projection point of a face for given φ- and ρ-values.

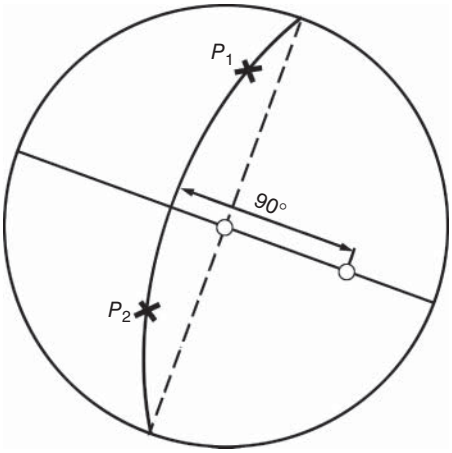

Figure 1.33 Construction of the zone circle and the corresponding zone pole for the two given face poles; measurement of the angle between the faces.

the angle γ between the normals of the two faces. The dihedral angle α, the direct angle between the two faces, is then given by $\alpha = 180° - \gamma$. The corresponding *zone pole* of the *zone circle* lies 90° away on the diameter of the net perpendicular to the diameter of the zone circle (Figure 1.33).

Now, we will use the crystal polyhedra of rhomb-dodecahedron and octahedron to demonstrate that the stereographic projection reflects the morphological symmetry of the crystals. In order to get more familiar with the procedure of stereographic projection, a list of the φ- and ρ-values for all faces of the polyhedra is given besides the images of polyhedra in the lower part of Figure 1.34a. We have to take into consideration that these values are only valid for our chosen standard projection (001) where the faces (001), $(00\bar{1})$ will be projected into the center of the Wulff net. It is obvious that a rotation of our crystals can generate any other standard projection, which will be different if the chosen face is not symmetry equivalent with the initial one. The (001) standard projections of rhomb-dodecahedron and octahedron are shown in the upper part of Figure 1.34a.

In general, a set of symmetry equivalent faces represents a ***crystal form***. In our case, the sets of symmetry equivalent faces {110} and {111} represent the crystal forms of rhomb-dodecahedron and octahedron. Figure 1.34b shows three crystals formed by a combination of the two forms. The morphology of the crystal is determined by the set of crystal forms that occur on the crystal (in German denoted as "***Tracht***"). The term ***habit*** describes the shape of the crystal, which is characterized by the dominant size of a crystal form. In our case, the three crystals consist of the same set of crystal forms (identical *Tracht*) but have different habits (octahedral and rhomb-dodecahedral) owing to the dominant crystal size of one crystal form. There are also some general terms in use for the characterization of the habit such as needle-shaped, prismatic, tabular, and so on. The stereogram gives us an insight what forms are present and how they are positioned

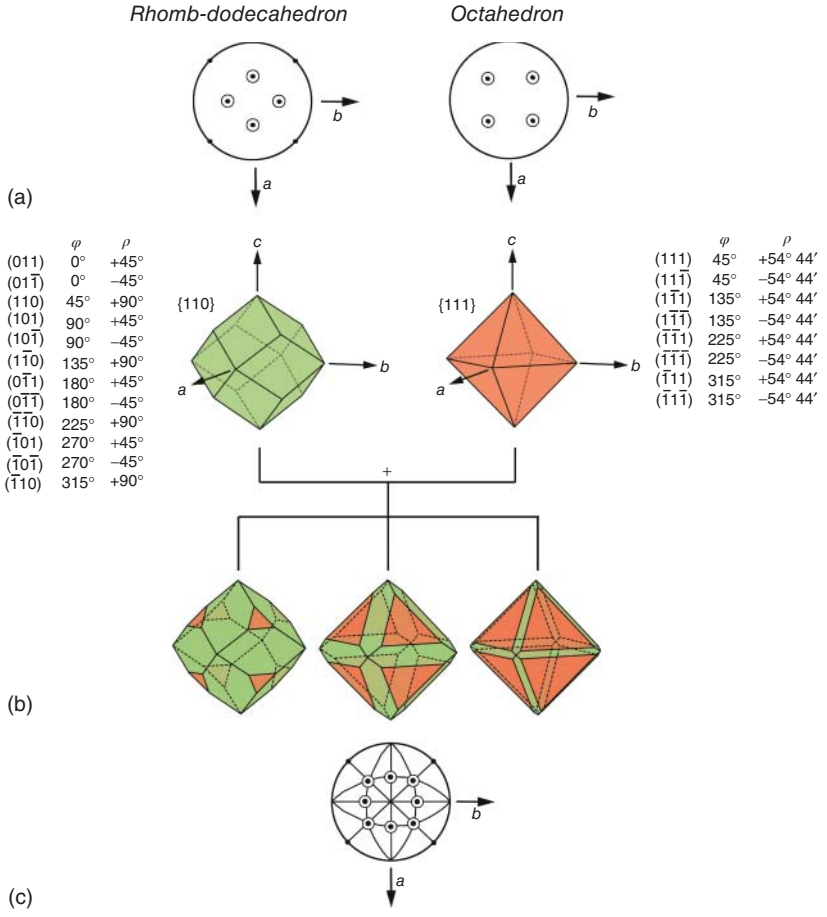

Figure 1.34 Stereographic projection and morphological symmetry (a) upper part: Standard stereographic projections (001) for octahedron and rhomb-dodecahedron, lower part: crystal forms of octahedron{111} and rhomb-dodecahedron{110} and corresponding φ- and ρ-values. (b) Crystals of different habit and identical "Tracht" {110}-rhomb-dodecahedron, {111}-octahedron). (c) (001) stereographic projection of the crystals shown in (b).

with respect to the symmetry framework of the crystal. But, we will not get any information about the habit of crystals.

The symmetry framework of our crystals as a whole and decomposed in rotations and reflections is represented in the stereographic projections of Figure 1.34. When we superimpose the stereogram of our combined crystal, we see that the poles of the rhomb-dodecahedron and the octahedron are exactly located at the position of the twofold and threefold rotation axes, respectively. Furthermore, we see also how the mirror planes are going through the forms. The special position of our three forms, that is, they lie on rotation axes, determines also the face symmetry, as we will describe later.

Our example has shown that the stereographic projection is an appropriate tool for the representation of the morphological symmetry of a crystal. In the following, we will explain how the morphology of the crystal can be represented by means of the various symmetry operations and their possible combinations. The faces of a crystal will be represented by their poles (points) in the stereographic projections. We will analyze the following:

- What kind of crystal forms can be generated by the symmetry operations?
- How many different crystal forms can occur?
- How we can classify the crystals with respect to their morphological symmetry?

Rotations In general, a rotation around an n-fold rotation axis through an angle $\alpha = 360°/n$ (n – integer) will map a particular object onto itself after n-rotations. As an example, the symmetry of the organometallic compound ferrocene $Fe(C_5H_5)_2$ has as principal rotation axis a fivefold rotation axis ($\alpha = 72°$, $n = 5$). The multiplicities n for rotation axes in crystals has to be compatible with the translational periodicity of the crystal lattice. According to the fundamental law with respect to the multiplicity n of rotation axes, only onefold ($n = 1$), twofold ($n = 2$), threefold ($n = 3$), fourfold ($n = 4$), and sixfold ($n = 6$) rotation axes are consistent with lattice periodicity. The limitation of the multiplicity can be proved as follows: Let us assume an n-fold rotation axis located perpendicular to the projection plane at the origin 0. A rotation about this axis through an angle of $\alpha = 360°/n$ (Figure 1.35) should map the whole lattice on itself. Rotations through angles α, 2α, $-\alpha$, and -2α maps the lattice point P_0 in equivalent lattice points P_1, P_2, P_{-1}, P_{-2}. The straight lines $g_1(P_1,P_2)$ and $g_2(P_{-1},P_{-2})$ are parallel and, therefore, identical lattice lines. The distance between P_1 and P_{-1} corresponds to the lattice vector $\boldsymbol{a}$.

It yields that

$$\boldsymbol{a} = P_1P_{-1} = 2r \cdot \sin\alpha \quad \text{and}$$
$$P_2P_{-2} = 2r \cdot \sin 2\alpha = 4r \cdot \sin\alpha \cos\alpha = m\boldsymbol{a}, \quad m - \text{integer} \tag{1.20}$$

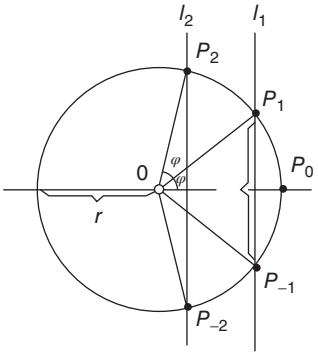

Figure 1.35 Evidence of the fundamental law of restricted multiplicity of rotation axes because of lattice periodicity.

Combining the two equations, we get

$$\cos\alpha = m/2 \tag{1.21}$$

Because cos α lies between +1 and −1, m takes on the values between −2 and +2. The relationships between m, the rotation angles α, and the corresponding multiplicities n are given in Table 1.2.

In addition to the printed symbols, the following graphic symbols are used for the one, two, three, four, and sixfold rotation axes: ●, ▲, ■, ◆, and ⬢, respectively.

Now, we will illustrate the action of the possible crystallographic rotations by means of the stereographic projections. A rotation of an object (whole crystal, crystal face, point, etc.) about a onefold axis by 360° will map the object onto itself. Therefore, this operation is also denoted as identity (symbol 1). An original crystal face that is only mapped onto itself by a symmetry operation, that is, the face will not be duplicated (multiplicity = 1) is called a ***pedion*** (Figure 1.36).

If we rotate a face about a twofold axis by 180°, a second face will be generated. We see in the two stereograms (twofold axis in the projection plane and perpendicular to it) that this operation leads to the identity after a second rotation through 180°. The crystal form generated by a twofold rotation is called ***sphenoid*** (Figure 1.37).

The operations of three, four, and sixfold rotation are shown in Figure 1.38. The symmetry operations give rise to forms consisting of three, four, and six faces, respectively, denoted as ***trigonal***, ***tetragonal***, and ***hexagonal pyramids***.

We have to be aware of the fact that the three forms are open forms because the basal face is missing. We will get closed forms of pyramids only when an additional face, for example, the (001) face, occupies the special position at the intersection point of the rotation axes. Until now, we have treated only ***open crystal forms***. A ***closed crystal form*** is given if its faces form a closed polyhedron. Furthermore, crystal forms are divided into ***general***, ***special***, and ***limiting forms***.

Table 1.2 Possible crystallographic rotations.

m	0	+1	−1	+2	−2
α(°)	90	60	120	360	180
n	4	6	3	1	2

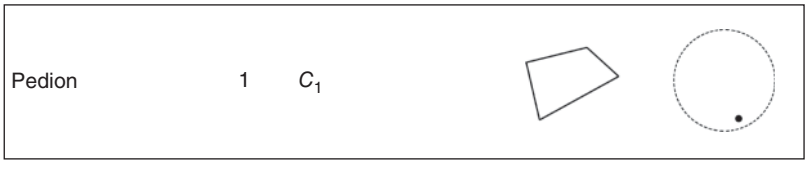

Figure 1.36 The identity operation (onefold rotation axís); general face form: ***pedion*** and corresponding stereogram.

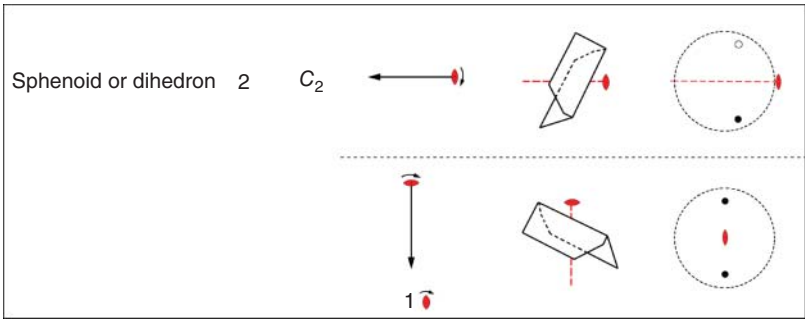

Figure 1.37 The twofold rotation axis; general face form: ***sphenoid*** and corresponding stereogram.

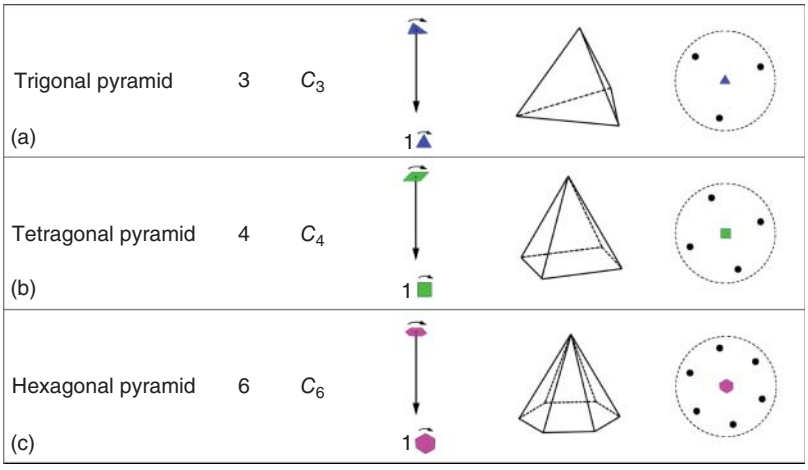

Figure 1.38 The (a) threefold, (b) fourfold, and (c) sixfold rotation axes. General face forms: ***trigonal***, ***tetragonal***, and ***hexagonal pyramids*** and corresponding stereograms.

Crystal forms of trigonal, tetragonal, and hexagonal pyramids are general forms. The face poles do not lie on symmetry elements in the stereographic projection. If our poles move onto the primitive in the stereographic projection, our pyramids will be transformed into ***trigonal***, ***tetragonal***, and ***hexagonal prisms***. The prisms have the same number of faces (identical multiplicity) but a higher eigensymmetry than the pyramids. The prisms are limiting forms. A special form is given if the face pole lies on a symmetry element, in our case on the rotation axis. We will get then a pedion as special form. The special form has always a lower multiplicity.

Reflection The operation of a reflection caused by a mirror plane (symbol: *m*) produces a second face as visualized in Figure 1.39 for *m* perpendicular and parallel to the projection plane. This open form consists of two faces and is called ***dome***. Initial face and mirrored face are related to each other similar to the right hand to the left hand.

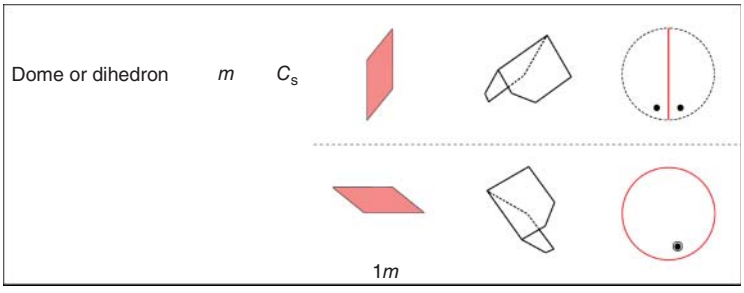

Figure 1.39 The mirror plane; general face form: ***dome*** and corresponding stereogram.

Inversion The inversion operation means a reflection of the initial face through a point, the inversion center, also denoted as center of symmetry, generating a parallel face opposite to the initial one as shown in Figure 1.40. A typical morphological feature of a crystal for the presence of an inversion center is that, for every crystal face, a parallel face exists.

Rotoinversion and Rotoreflection The operation of rotoinversion means we couple the operations of ***rotation*** and ***inversion***. The object will be rotated about the *n*-fold rotation axis and subsequently inverted through the inversion point. The action of the *n*-fold rotoinversions is represented in Figure 1.41. It is obvious that a rotation of the pole by 360° and subsequent inversion is identical to the pure inversion. Therefore, for both operations the symbol $\bar{1}$ is applied. We see also from the stereogram that the twofold rotoinversion is identical to the reflection ($\bar{2} = m$). The three, four, and sixfold rotoinversions generate as closed crystal forms the ***rhombohedron***, ***tetragonal disphenoid***, and the ***trigonal dipyramid***, respectively. The following printed and graphic symbols are used for the rotoinversions ($\bar{1}\circ, \bar{3}\blacktriangle, \bar{4}\blacklozenge, \bar{6}\hexagon$).

We will consider now the possible operations of rotoreflection (S_n) as coupling of ***rotation*** and subsequent ***reflection***. The stereograms of the *n*-fold rotoreflections are given in Figure 1.42. A careful inspection of the stereograms shows us that the operations of rotoreflections have not generated new crystal forms. The following relations are given:

$S_1 \equiv \bar{2} \equiv m$, $S_2 \equiv \bar{1} \equiv$ inversion, $S_3 \equiv 6 \equiv 3/m$ (reflection plane m perpendicular to threefold rotation axis); $S_4 \equiv \bar{4}$ (included 2); and $S_6 \equiv \bar{3} \equiv 3 + \bar{1}$.

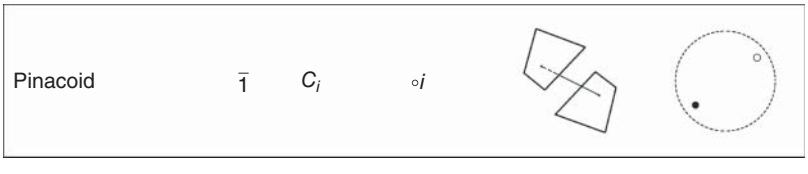

Figure 1.40 The symmetry center (inversion center); general face form: ***pinacoid*** and corresponding stereogram.

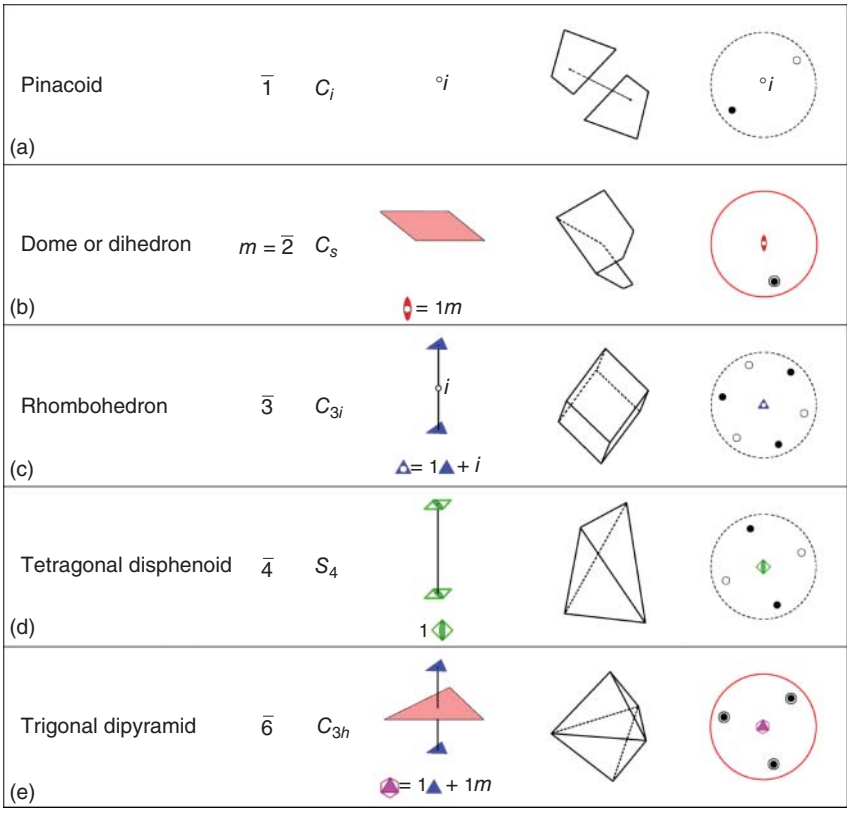

Figure 1.41 (a–f) The *n*-fold rotoinversion axes ($n = 1, 2, 3, 4, 6$). General face forms: pinacoid, dome, ***rhombohedron***, ***tetragonal disphenoid***, ***trigonal dipyramid*** and corresponding stereograms.

The rotation axes X and the rotoinversion axes $\overline{X}$ (including inversion center and mirror plane m) are the possible symmetry elements necessary for the description of the morphological symmetry of crystals. Connected with a symmetry element are a definite number of symmetry operations. A fourfold rotation axis as symmetry element is connected with four symmetry operations, that is, rotations through 90°, 180°, 270°, and 360°. The symmetry analysis of the cube, rhombdodecahedron, and octahedron described at the beginning of this chapter has shown that different kinds of rotation axes, mirror planes, and a symmetry center can form the symmetry framework. The combination of symmetry elements cannot be done arbitrarily. Only combinations compatible with the lattice symmetry of crystals are allowed. A common feature of all symmetry operations that we have described in this chapter is that they leave at least one point fixed after repeated application. Therefore, the symmetry operations are called ***point symmetry operations*** and the corresponding symmetry elements are the ***point symmetry elements***. A systematic analysis of crystallographic relevant combinations of point

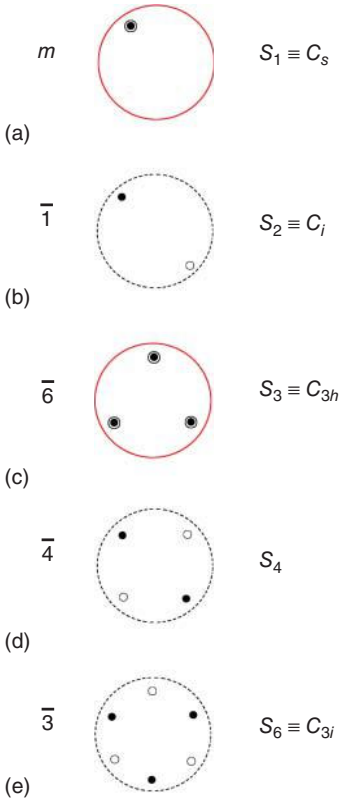

Figure 1.42 (a–e) Stereograms of the *n*-fold rotoreflections ($n = 1, 2, 3, 4, 6$).

symmetry elements, which is always connected with a corresponding set of symmetry operations, leads to the ***32 crystallographic point groups*** in three dimensions. The point groups were firstly derived by Moritz Ludwig Frankenheim (1826) and independently by Johann Friedrich Christian Hessel (1830). In the literature, the two terms ***crystal class*** and ***point group*** are often synonymously used for the description of the morphology of crystals. All crystals that belong to a ***geometric crystal class*** have the same point group symmetry. The symbol of a crystal class is identical with the point group symbol. In addition to the point group symbol, the names of the general forms are commonly used as names for crystal classes. The crystal class is used as a classification scheme for the symmetry group of the external shape of macroscopic crystals. The ***point group*** of a crystal is a set of point symmetry operations. In general, one has to divide point groups into ***crystallographic*** and ***noncrystallographic point groups***. The latter have no restrictions with respect to the multiplicity of rotations and rotoinversions. The ***point groups*** are not only used for the description of the symmetries of external shapes of crystals. They can also be applied to characterize site symmetries

of points in lattices and crystal structures, the symmetry of molecules, and the symmetries of the physical properties of crystals.

1.3.1 Crystallographic Point Groups

Now, we will treat the 32 crystallographic point groups with respect to the generating symmetry elements. Each point group will be represented by its point group symbol (in both the Hermann–Mauguin and Schoenflies notations), by the symmetry framework, by the stereographic projection, and by a crystal drawing of the general form (Figures 1.38–1.41, 1.43–1.48). A general explanation of the Schoenflies symbols is given in Table 1.3. The Hermann–Mauguin symbols also denoted as international symbols exist in parallel as full and short symbols. The symbols

Table 1.3 Explanation of Schoenflies notation.

Schoenflies notation for crystallographic point groups					
n	1	2	3	4	6
C_n	C_1	C_2	C_3	C_4	C_6
C_{nv}	$C_{1v} = C_{1h} = C_S$	C_{2v}	C_{3v}	C_{4v}	C_{6v}
C_{nh}	$C_{1h} = C_S$	C_{2h}	C_{3h}	C_{4h}	C_{6h}
C_{ni}	$C_i = S_2$	$C_{2i} = C_S$	$C_{3i} = S_6$	$C_{4i} = S_4$	$C_{6i} = C_{3h}$
S_n	$S_1 = C_S$	$S_2 = C_i$	$S_3 = C_{3h}$	$S_4 = C_{4i}$	$S_6 = C_{3i}$
D_n	$D_1 = C_2$	D_2	D_3	D_4	D_6
D_{nd}	$D_{1d} = C_{2h}$	D_{2d}	D_{3d}	D_{4d}	D_{6d}
D_{nh}	$D_{1h} = C_{2v}$	D_{2h}	D_{3h}	D_{4h}	D_{6h}

Symbols fort the cubic point groups	
T	Simple tetrahedral group
T_d	Tetrahedral group (T + diagonal mirror planes)
T_h	Full tetrahedral group (T + horizontal mirror planes or symmetry center)
O	Simple octahedral group
O_h	Full octahedral group (O + horizontal mirror planes or symmetry center)

Classification of point groups	
C_n	n-fold rotation axis
C_{nv}	n-fold rotation axis + vertical mirror planes
C_{nh}	n-fold rotation axis + horizontal mirror plane
C_{ni}	n-fold rotoinversion axis
S_n	n-fold rotoreflection axis
D_n	n-fold rotation axis + twofold rotation axes perpendicular to C_n
D_{nd}	D_n + vertical mirror planes
D_{nh}	D_n + horizontal mirror plane

indicate the specific symmetry directions of the generating and indicating symmetry elements of the point group. The primary-, secondary-, and tertiary-specific symmetry directions, also called *Blickrichtungen*, for the crystal systems are listed in Table 1.4. We will describe now the point groups according to the following combinations of symmetry elements: X (rotation axis only), $\overline{X}$ (rotoinversion axis only), X/m (rotation axis and horizontal mirror plane), X_2 (twofold rotation axis perpendicular to X), Xm (rotation axis and vertical mirror plane X), $\overline{X}m$ (rotoinversion axis and vertical mirror plane), X/mm (rotation axis and horizontal and vertical mirror planes), X_1, X_2 (oblique arrangement of rotation axes), and $\overline{X}_1, X_2$ (oblique arrangement of rotation axes X_1, X_2, and addition of center of symmetry or mirror planes).

The first subset of point groups generated by a singular rotation axis X contains the point groups 1, 2, 3, 4, and 6. The rotation axes 2, 3, 4, and 6 are polar axes, which means direction and opposite direction are geometrically different. All general forms are open forms. The number N of equivalent faces for the general forms is $N = X$. (Figures 1.36–1.38).

The point groups of the second subset generated by a singular rotoinversion axis are $\overline{1}$, $\overline{2} \equiv m$, $\overline{3}$, $\overline{4}$, and $\overline{6}$. The twofold rotoinversion is equivalent to a reflection as already described earlier. The point group is always denoted as m in the point group tables. The general forms of $\overline{1}$ and m are open forms, whereas those for $\overline{3}$, $\overline{4}$, and $\overline{6}$ are closed forms (crystal polyhedra) (Figure 1.41) For the number of faces it holds, $N = X$ for X even and $N = 2X$ for X odd.

Table 1.4 Symmetry directions (Blickrichtungen) in the seven crystal systems.

Crystal system	Symmetry direction (Blickrichtung) (position in Hermann–Mauguin symbol)		
	Primary	**Secondary**	**Tertiary**
Triclinic	None	—	—
Monoclinic	±[010] (*unique axis b*) ±[001] (*unique axis c*)	—	—
Orthorhombic	±[100]	±[010]	±[001]
Tetragonal	±[001]	±[100], ±[010]	±[1$\bar{1}$0], ±[110]
Trigonal (hexagonal axes)	±[001]	±[100], ±[010], ±[$\bar{1}$ $\bar{1}$0]	—
Trigonal (rhombohedral axes)	±[111]	±[1$\bar{1}$0], ±[01$\bar{1}$], ±[$\bar{1}$01]	—
Hexagonal	±[001]	±[100], ±[010], ±[110]	±[1$\bar{1}$0], ±[210], ±[120]
Cubic	±[001], ±[010], ±[001]	±[111], ±[$\bar{1}$11], ±[1$\bar{1}$1], ±[11$\bar{1}$]	±[110], ±[1$\bar{1}$0], ±[01$\bar{1}$], ±[011], ±[$\bar{1}$01], ±[101]

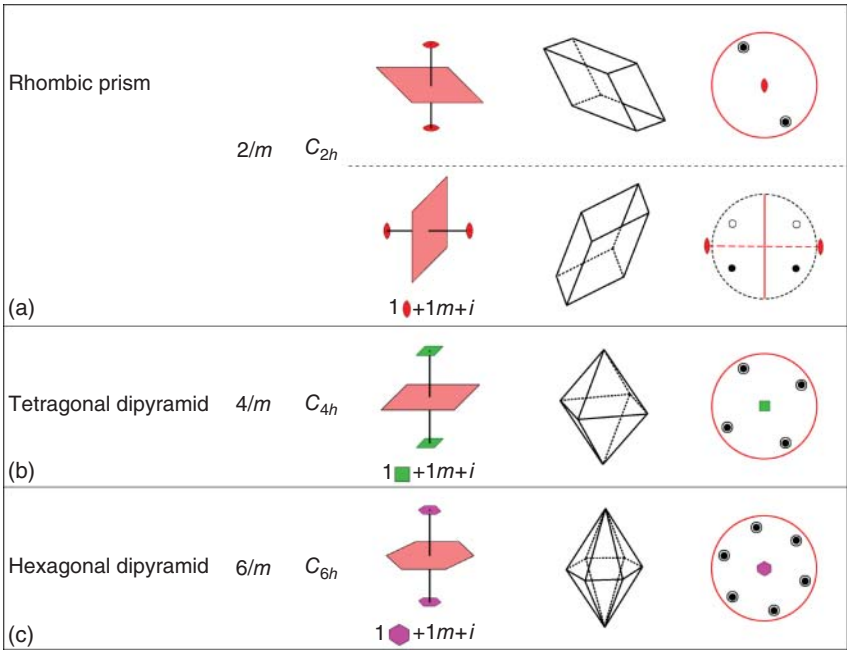

Figure 1.43 (a–c) The point groups generated by the combination X/m.

When we add a reflection plane m perpendicular to the rotation axis (X/m), the point groups $1/m$, 2/m, $3/m$, $4/m$, and $6/m$ will be generated (Figure 1.43). The point groups $1/m \equiv m$ and $3/m \equiv \bar{6}$ have already been generated. Only the general form of $2/m$ is an open form. The number N for the point groups X/m is $N = 2X$. All point groups of this subset have a symmetry center.

The combination X_2, that is, a twofold rotation axis perpendicular to the principal axis X, provides the point groups 12, 22, 32, 42, and 62. We can omit the group 12 because of its equivalence to point group 2. One can easily prove by drawing the stereographic projections for the combinations 22, 42, and 62 that a third twofold axis will be generated. Therefore, the point group symbols are 222, 321, 422, 622 (Figure 1.44). All general forms are polyhedra of $N = 2X$.

The combination of the principal rotation axis X with a vertical mirror plane m leads to the point groups $1m$, $2m$, $3m$, $4m$, and $6m$. The point group $1m$ is equivalent to m. The mirror plane is reproduced by the rotation axis X-times. Thus, we get the point group symbols $mm2$, $3m1$, $4mm$, and $6mm$ (Figure 1.45). The rotation axes are polar axes. The general forms of the point groups are open forms with $N = 2X$.

When we replace the rotation axes by rotoinversion axes, the following groups are generated by combination $\bar{X}m$: $\bar{1}m$, $\bar{2}m$, $\bar{3}m$, $\bar{4}m$, and $\bar{6}m$. The groups $\bar{1}m$ and $\bar{2}m$ are equivalent to $2/m$ and $mm2$, respectively. The combination $\bar{X}m$ causes additional twofold axes perpendicular to $\bar{X}$. The new resulting point groups are

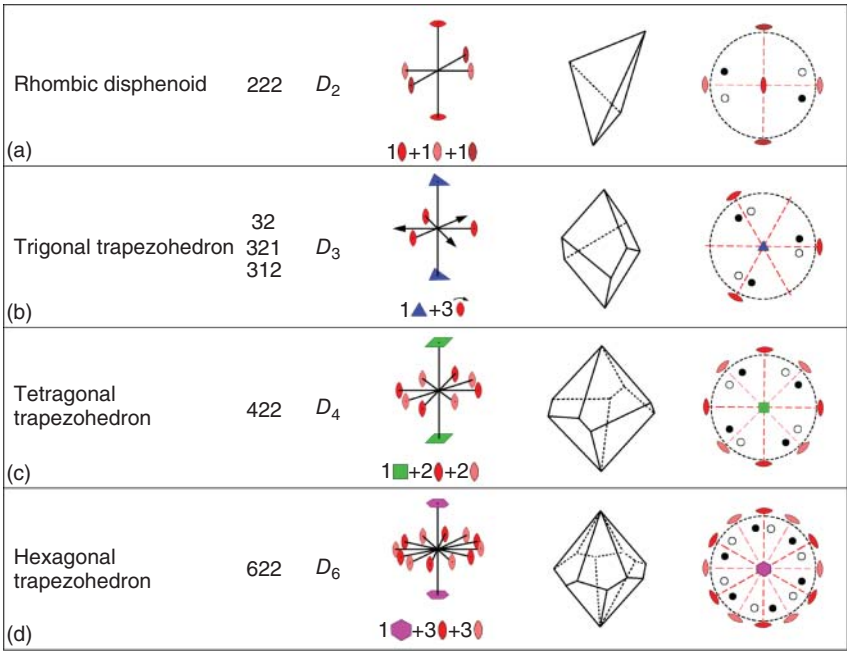

Figure 1.44 (a–d) The point groups generated by the combination X_2.

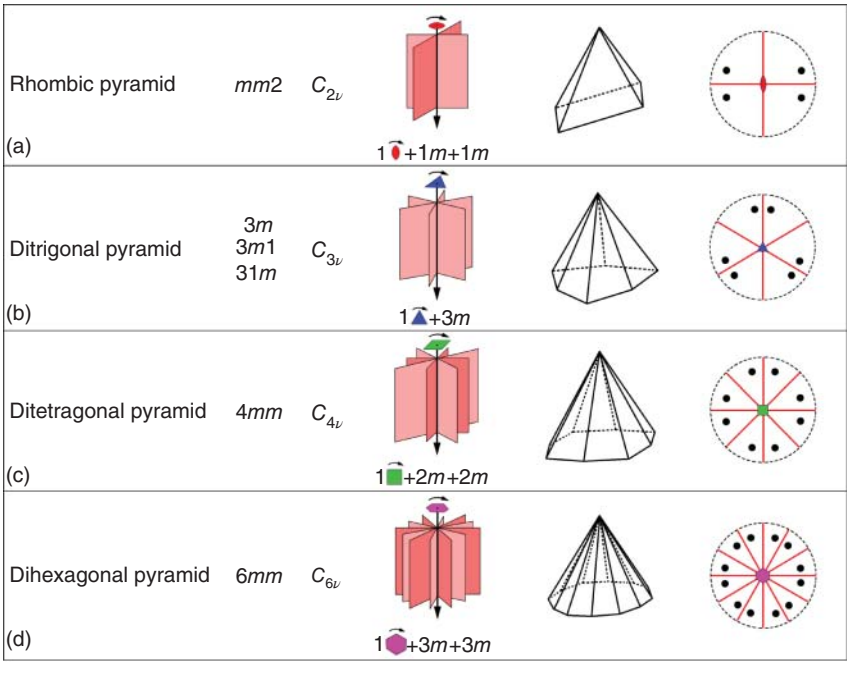

Figure 1.45 (a–d) The point groups generated by the combination *Xm*.

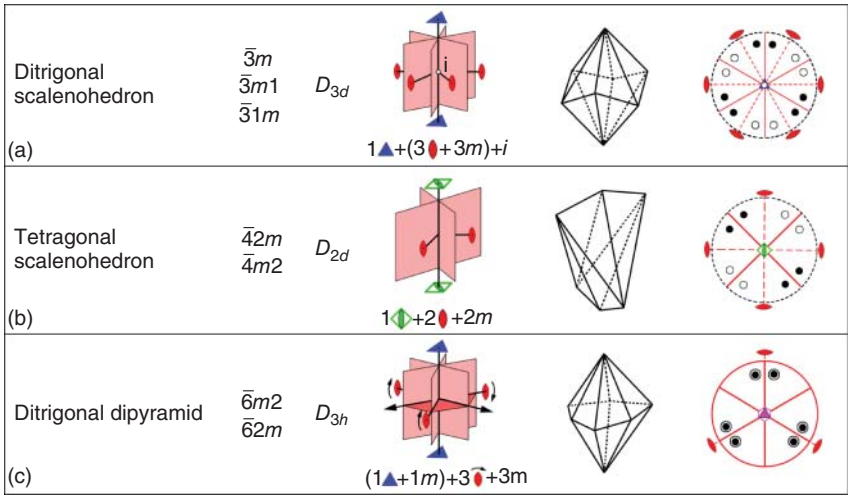

Figure 1.46 (a–c) The point groups generated by the combination $\bar{X}m$.

denoted as $\bar{3}m1$, $\bar{4}2m$, and $\bar{6}m2$ (Figure 1.46). The number of faces of the polyhedra of general forms is $N = 2X$ for X odd and $N = 4X$ for X even.

When we add to the combination X/m a vertical reflection plane m, we will get the point group subset X/mm cover the point groups $1/mm$, $2/mm$, $3/mm$, $4/mm$, and $6/mm$. Here, we have to take into consideration that the combination of a vertical and horizontal reflection planes generates a twofold rotation axis along the intersection line of both reflection planes. Then, we can see that $1/mm = mm2$ and $3/mm = \bar{6}m2$ are no new point groups. The other groups have to be rewritten as follows: $2/mm = 2/m\ 2/m\ 2/m$ (short symbol mmm), $4/mm = 4/m\ 2/m\ 2/m$ (short symbol $4/mmm$), and $6/mm = 6/m\ 2/m\ 2/m$ (short symbol $6/mmm$). All point groups of this subset have a center of symmetry. The number of faces of the polyhedra of general forms is $N = 4X$ (Figure 1.47).

When we combine two symmetry axes X_1, X_2, then a third axis will be generated. A general solution of the problem of combining two rotation axes intersecting at a common point is given using Euler's construction. Here, we will show only the results of permissible combinations and the corresponding intersection angles for possible crystallographic rotation axes (Table 1.5).

All possible combinations of generating crystallographic point groups with one principal rotation or rotoinversion axis are already considered. Under the generating subset X_1, X_2, the combination of two and threefold rotation axes and four- and threefold rotation axes is possible under an oblique angle of 54°44′08″. This is the angle between the edges and body diagonal of a cube. The two point groups that will be formed are 23 and 432. When we add to the point groups 23 and 432 mirror planes (or a center of symmetry), we can generate the new point groups: $2/m\bar{3}$ (short symbol $m\bar{3}$), $\bar{4}3m$, and $m\ \bar{3}m$ (Figure 1.48).

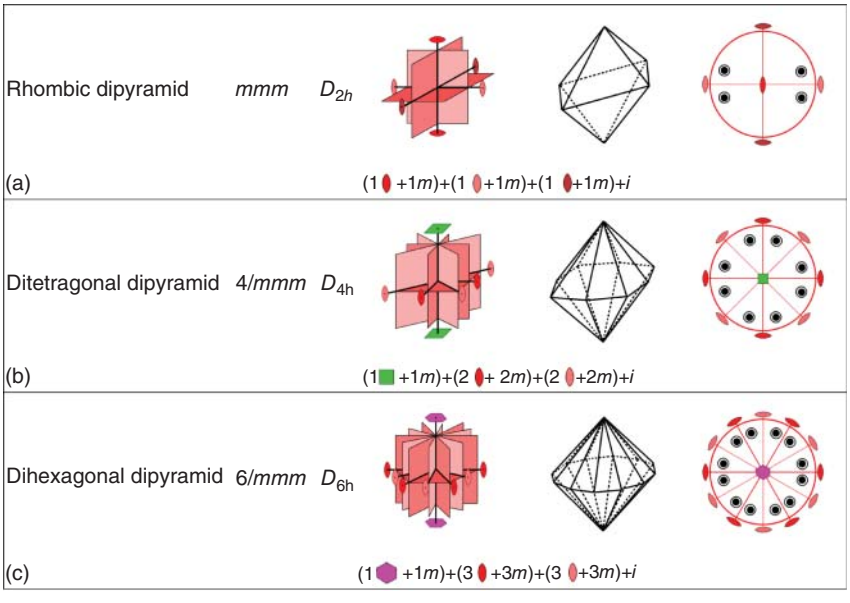

Figure 1.47 (a–c) The point groups generated by the combination *X*/*mm*.

Table 1.5 The six permissible nontrivial combinations of symmetry axes.

Symmetry axes			Angle (°)		
X_1	X_2	X_3	$\angle(X_1, X_2)$	$\angle(X_1, X_3)$	$\angle(X_2, X_3)$
2	2	2	90	90	90
3	2	2	90	90	60
4	2	2	90	90	45
6	2	2	90	90	30
2	3	3	54° 44′ 08″	54° 44′ 08″	70° 31′ 08″
4	3	2	35° 15′ 52″	45	54° 44′ 08″

When we inspect the symmetry framework of the cubic point group $m\,\bar{3}m$, we note a coincidence with the eigensymmetry of the cube, octahedron, and rhomb-dodecahedron. On the other hand, it is also obvious from the stereograms of the cubic point groups that the cube and the rhomb-dodecahedron will be generated in all five cubic point groups as special {100} and {110} forms. The octahedron as special {111} form will be generated in the point groups $m\bar{3}$, 432, and $m\,\bar{3}m$, whereas in the point groups 23 and $\bar{4}3m$, the tetrahedron is generated as {111} form (positive and negative tetrahedrons). An overview about the special forms of the cubic point groups is given in Appendix "Supplimentary material".

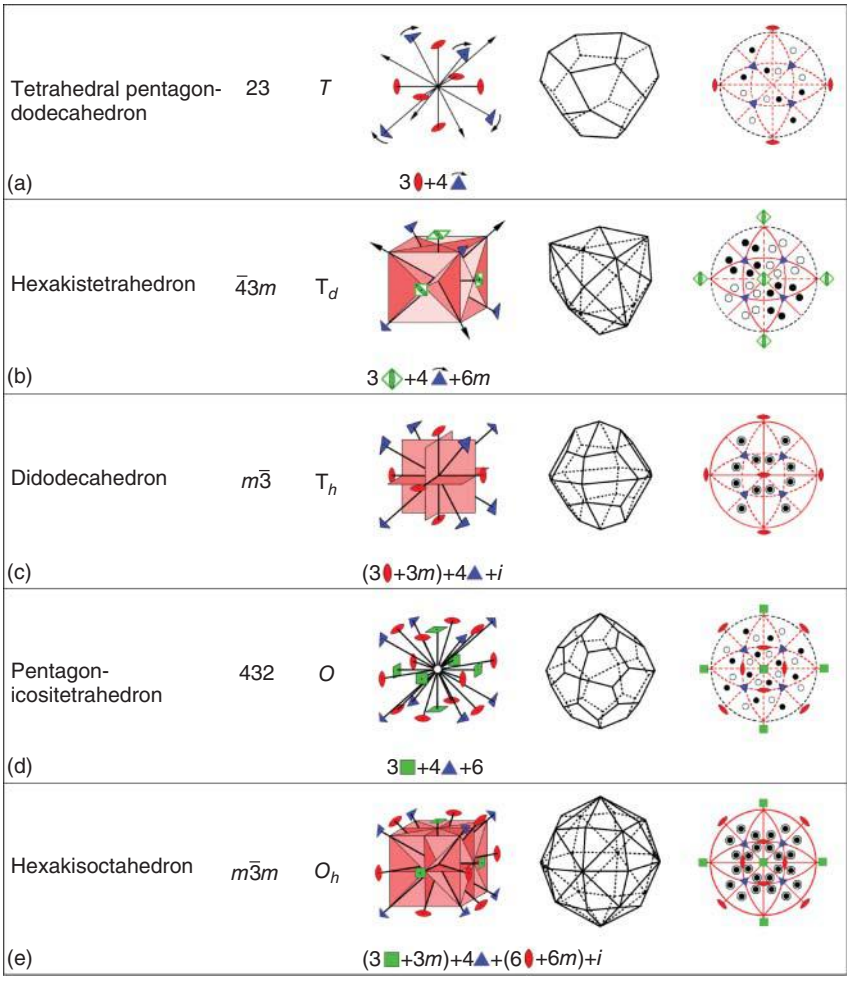

Figure 1.48 (a–e) The cubic point groups.

Altogether 47 different crystal face forms will be generated by the symmetry operations of the 32 point groups, when the ***dome*** (*m*) and ***sphenoid*** (2) are both denoted as ***dihedron*** and not treated separately.

The list of the 32 crystallographic point groups arranged into the seven crystal systems is given in Table 1.6. The point groups can be divided into centrosymmetric and noncentrosymmetric (acentric) point groups. The 11 centrosymmetric point groups $\bar{1}$; $2/m$; mmm; $4/m$; $4/mmm$; $\bar{3}$; $\bar{3}m$; $6/m$, $6/mmm$; $m\bar{3}$; and $m\,\bar{3}m$ correspond to the 11 Laue classes. The Laue classes reflect the point symmetry of diffraction patterns, which are centrosymmetric under kinematical diffraction conditions. According to ***Friedel's law*** are the intensities of hkl and $\overline{hkl}$ reflections equal. If Friedel's law is valid, then one cannot determine if the crystal has a

Table 1.6 The 32 crystallographic point groups.

International symbol (Hermann–Mauguin notation)		Schoenflies symbol	General form (multiplicity)
Short	**Full**		
Triclinic system			
1		C_1	Pedion (1)
$\bar{1}$		C_i	Pinacoid (2)
Monoclinic system			
2		C_2	Sphenoid or dihedron (2)
m		C_s	Dome or dihedron (2)
$2/m$		C_{2h}	Rhombic prism (4)
Orthorhombic system			
222		D_2	Rhombic disphenoid (4)
$mm2$		C_{2v}	Rhombic pyramid (4)
mmm	$\frac{2}{m}\frac{2}{m}\frac{2}{m}$	D_{2h}	Rhombic dipyramid (8)
Trigonal system			
3		C_3	Trigonal pyramid (6)
$\bar{3}$		C_{3i}	Rhombohedron (6)
$3m$ *Rhombohedral axes* $3m1$ *Hexagonal axes* $31m$ *Hexagonal axes*		C_{3v}	Ditrigonal pyramid (6)
32 *Rhombohedral axes* 321 *Hexagonal axes* 312 *Hexagonal axes*		D_3	Trigonal trapezohedron (6)
$\bar{3}m$ *Rhombohedral axes* $\bar{3}m1$ *Hexagonal axes* $\bar{3}1m$ *Hexagonal axes*	$\bar{3}2/m$ $\bar{3}2/m1$ $\bar{3}12/m$	D_{3d}	Ditrigonal scalenohedron (12)
Tetragonal system			
4		C_4	Tetragonal pyramid (4)
$\bar{4}$		S_4	Tetragonal disphenoid (4)
$4/m$		C_{4h}	Tetragonal dipyramid (8)
422		D_4	Tetragonal trapezohedron (8)
$4mm$		C_{4v}	Ditetragonal pyramid (8)
$\bar{4}2m$ $\bar{4}m2$		D_{2d}	Tetragonal scalenohedron (8)

(continued overleaf)

Table 1.6 (*Continued*)

International symbol (Hermann–Mauguin notation)		Schoenflies symbol	General form (multiplicity)
Short	**Full**		
$4/mmm$	$\frac{4}{m}\frac{2}{m}\frac{2}{m}$	D_{4h}	Ditetragonal dipyramid (16)
Hexagonal system			
6		C_6	Hexagonal pyramid (6)
$\bar{6}$		C_{3h}	Trigonal dipyramid (6)
$6/m$		C_{6h}	Hexagonal dipyramid (12)
622		D_6	Hexagonal trapezohedron (12)
$6mm$		C_{6v}	Dihexagonal pyramid (12)
$\bar{6}m2$ $\bar{6}2m$		D_{3h}	Ditrigonal dipyramid (12)
$6/mmm$	$\frac{6}{m}\frac{2}{m}\frac{2}{m}$	D_{6h}	Dihexagonal dipyramid (24)
Cubic system			
23		T	Tetrahedral pentagon–dodecahedron (12)
$m\bar{3}$	$\frac{2}{m}\bar{3}$	T_h	Didodecahedron (24)
432		O	Pentagon–icositetrahedron (24)
$\bar{4}3m$		T_d	Hexakistetrahedron (24)
$m\bar{3}m$	$\frac{4}{m}\bar{3}\frac{2}{m}$	O_h	Hexakisoctahedron (48)

symmetry center or not from the diffraction pattern. Friedel's law is violated for absorbing crystals and dynamical diffraction conditions.

A particular role play the ***holohedral point groups*** (***holoedries***) $\bar{1}$, $2/m$, mmm, $4/mmm$, $\bar{3}m$, $6/mmm$, and $m\bar{3}m$. These are the seven possible point symmetries of lattices as we will describe in Section 1.4. The holohedral point group of each crystal system has the maximal multiplicity, that is, the maximal number of equivalent faces of a crystal form. The point groups 1, 2, 222, 3, 32, 4, 422, 6, 622, 23, and 432 consisting only of proper rotations are called ***enantiomorphic point groups***. In this point groups, right- and left-handed crystal forms can be generated. These crystal polyhedra are mirror image related to each other (Figure 1.49).

This morphological relationship of crystals is denoted as ***enantiomorphism***. The left- and right-handed forms of molecules are commonly denoted as chiral or enantiomeric, respectively. All biological macromolecules (proteins, etc.) crystallize in one of the 11 enantiomorphic point groups.

After the general description of the 32 crystallographic point groups, we will show that the point symmetry operations can be analytically represented by matrices. In general, the action of crystallographic point symmetry operations in

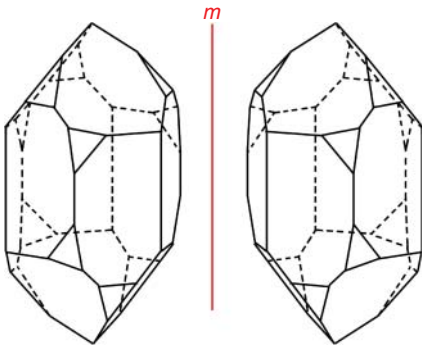

Figure 1.49 Enantiomorphous pair of crystals (left- and right-handed quartzes).

three-dimensional space can be expressed by the following equations:

$$\begin{aligned}\tilde{x}_1 &= W_{11}x_1 + W_{12}x_2 + W_{13}x_3\\ \tilde{x}_2 &= W_{21}x_1 + W_{22}x_2 + W_{23}x_3\\ \tilde{x}_3 &= W_{31}x_1 + W_{32}x_2 + W_{33}x_3\end{aligned} \tag{1.22}$$

In matrix formulation, we can write

$$\begin{pmatrix}\tilde{x}_1\\ \tilde{x}_2\\ \tilde{x}_3\end{pmatrix} = \begin{pmatrix}W_{11} & W_{12} & W_{13}\\ W_{21} & W_{22} & W_{23}\\ W_{31} & W_{32} & W_{33}\end{pmatrix}\begin{pmatrix}x_1\\ x_2\\ x_3\end{pmatrix} \quad \text{or in abbreviated form } \tilde{x} = Wx \tag{1.23}$$

The (3×3) matrix W describes the point symmetry operations, that is, rotations and rotoinversions (including the reflection $m \equiv \bar{2}$). Some examples of matrices for point-group symmetry operations and the orientation of the corresponding symmetry elements are given in Table 1.7. According to the notation given in the International Tables for Crystallography [26], rotations and rotoinversions are given by their printed symbols and a superscript + and −, which defines the sense of rotation (not necessary for twofold rotations). A superscript + means a counterclockwise rotation. In addition, the location of the axes is given.

The symbol $\bar{4}^+$ [001] (positive sense of rotation) means a fourfold rotoinversion with the matrix $\begin{pmatrix}0 & 1 & 0\\ \bar{1} & 0 & 0\\ 0 & 0 & \bar{1}\end{pmatrix}$, that is, the initial point x, y, z is transformed into $y, -x, -z$. The matrix for the fourfold rotoinversion axes $\bar{4}^-$ [001] (negative sense of rotation) is $\begin{pmatrix}0 & \bar{1} & 0\\ 1 & 0 & 0\\ 0 & 0 & \bar{1}\end{pmatrix}$. The initial point x, y, z is then transformed into $-y, x, -z$.

Successive application of point symmetry operations results in a multiplication of the corresponding matrices. The transformation is $W_3 = W_2 W_1$.

Table 1.7 Point group symmetry operations and corresponding matrices.

1 x,y,z	$\begin{pmatrix}1&0&0\\0&1&0\\0&0&1\end{pmatrix}$	$\bar{1}$ $-x,-y,-z$	$\begin{pmatrix}\bar{1}&0&0\\0&\bar{1}&0\\0&0&\bar{1}\end{pmatrix}$
2[100] $x,-y,-z$	$\begin{pmatrix}1&0&0\\0&\bar{1}&0\\0&0&\bar{1}\end{pmatrix}$	m[100] $-x,y,z$	$\begin{pmatrix}\bar{1}&0&0\\0&1&0\\0&0&1\end{pmatrix}$
2[010] $-x,y,-z$	$\begin{pmatrix}\bar{1}&0&0\\0&1&0\\0&0&\bar{1}\end{pmatrix}$	m[010] $x,-y,z$	$\begin{pmatrix}1&0&0\\0&\bar{1}&0\\0&0&1\end{pmatrix}$
2[001] $-x,-y,z$	$\begin{pmatrix}\bar{1}&0&0\\0&\bar{1}&0\\0&0&1\end{pmatrix}$	m[001] $x,y,-z$	$\begin{pmatrix}1&0&0\\0&1&0\\0&0&\bar{1}\end{pmatrix}$
3^+[00.1] $-y,x-y,z$	$\begin{pmatrix}0&\bar{1}&0\\1&\bar{1}&0\\0&0&1\end{pmatrix}$	$\bar{3}^+$[00.1] $y,y-x,-z$	$\begin{pmatrix}0&1&0\\\bar{1}&1&0\\0&0&\bar{1}\end{pmatrix}$
3^-[00.1] $y-x,-x,z$	$\begin{pmatrix}\bar{1}&1&0\\\bar{1}&0&0\\0&0&1\end{pmatrix}$	$\bar{3}^-$[00.1] $x-y,x,-z$	$\begin{pmatrix}1&\bar{1}&0\\1&0&0\\0&0&\bar{1}\end{pmatrix}$
4^+[001] $-y,x,z$	$\begin{pmatrix}0&\bar{1}&0\\1&0&0\\0&0&1\end{pmatrix}$	$\bar{4}^+$[001] $y,-x,-z$	$\begin{pmatrix}0&1&0\\\bar{1}&0&0\\0&0&\bar{1}\end{pmatrix}$
4^-[001] $y,-x,z$	$\begin{pmatrix}0&1&0\\\bar{1}&0&0\\0&0&1\end{pmatrix}$	$\bar{4}^-$[001] $-y,x,-z$	$\begin{pmatrix}0&\bar{1}&0\\1&0&0\\0&0&\bar{1}\end{pmatrix}$
6^+[00.1] $x-y,x,z$	$\begin{pmatrix}1&\bar{1}&0\\1&0&0\\0&0&1\end{pmatrix}$	6^-[00.1] $-y,x-y,-z$	$\begin{pmatrix}0&\bar{1}&0\\1&\bar{1}&0\\0&0&\bar{1}\end{pmatrix}$
3^+[111] z,x,y	$\begin{pmatrix}0&0&1\\1&0&0\\0&1&0\end{pmatrix}$	$\bar{3}^+$[111] $-z,-x,-y$	$\begin{pmatrix}0&0&\bar{1}\\\bar{1}&0&0\\0&\bar{1}&0\end{pmatrix}$
3^-[111] y,z,x	$\begin{pmatrix}0&1&0\\0&0&1\\1&0&0\end{pmatrix}$	$\bar{3}^-$[111] $-y,-z,-x$	$\begin{pmatrix}0&\bar{1}&0\\0&0&\bar{1}\\\bar{1}&0&0\end{pmatrix}$

For example, the symmetry operations of the simple rotation group 3 ($3_z^1, 3_z^2, 3_z^3 = \boldsymbol{I}$) can be represented as follows: The rotation matrix for 3^+ 0, 0, z is $\begin{pmatrix} 0 & \bar{1} & 0 \\ 1 & \bar{1} & 0 \\ 0 & 0 & 1 \end{pmatrix}$.

$$\underset{\begin{pmatrix} 0 & \bar{1} & 0 \\ 1 & \bar{1} & 0 \\ 0 & 0 & 1 \end{pmatrix}}{3_z^1} \cdot \underset{\begin{pmatrix} 0 & \bar{1} & 0 \\ 1 & \bar{1} & 0 \\ 0 & 0 & 1 \end{pmatrix}}{3_z^1} = \underset{\begin{pmatrix} \bar{1} & 1 & 0 \\ \bar{1} & 0 & 0 \\ 0 & 0 & 1 \end{pmatrix}}{3_z^2} \quad , \quad \underset{\begin{pmatrix} 0 & \bar{1} & 0 \\ 1 & \bar{1} & 0 \\ 0 & 0 & 1 \end{pmatrix}}{3_z^1} \cdot \underset{\begin{pmatrix} \bar{1} & 1 & 0 \\ \bar{1} & 0 & 0 \\ 0 & 0 & 1 \end{pmatrix}}{3_z^2} = \underset{\begin{pmatrix} 1 & 0 & 0 \\ 0 & 1 & 0 \\ 0 & 0 & 1 \end{pmatrix}}{\boldsymbol{I}} \tag{1.24}$$

The matrix on the right in the product belongs to the symmetry operation, which is carried out first. From the symmetry matrices of the identity $\boldsymbol{W} = \boldsymbol{I} \equiv 1 = \begin{pmatrix} 1 & 0 & 0 \\ 0 & 1 & 0 \\ 0 & 0 & 1 \end{pmatrix}$ and the inversion $\boldsymbol{W} = -\boldsymbol{I} \equiv \bar{1} = \begin{pmatrix} \bar{1} & 0 & 0 \\ 0 & \bar{1} & 0 \\ 0 & 0 & \bar{1} \end{pmatrix}$, the type of symmetry operation is obvious at first glance. The type of symmetry operation of any point-symmetry matrix can easily be determined by calculating the determinant $\det(\boldsymbol{W})$ and the trace $\mathrm{tr}(\boldsymbol{W}) = \boldsymbol{W}_{11} + \boldsymbol{W}_{22} + \boldsymbol{W}_{33}$ of the matrix as can be recognized from Table 1.8.

Let us consider now the point group *mmm* somewhat more in detail. From the point group symbol and the inspection of the stereogram, we can recognize that there are three twofold axes along the directions [100], [010], and [001] and perpendicular to it three mirror planes. It is obvious that the combination of mirror planes perpendicular to rotation axes causes a symmetry center. The point group *mmm* consists of following symmetry operations: $g_1 = 1$, $g_2 = 2_x$, $g_3 = 2_y$, $g_4 = \bar{1}$, $g_5 = 2_z, g_6 = m_x, g_7 = m_y, g_8 = m_z$, The point group can already be derived from the operations g_1, g_2, g_3, g_4, which are called ***generators*** for the point group *mmm.* The generation of point group *mmm* can be represented as follows:

$$\underset{\begin{pmatrix} 1 & 0 & 0 \\ 0 & \bar{1} & 0 \\ 0 & 0 & \bar{1} \end{pmatrix}}{g_2} \times \underset{\begin{pmatrix} \bar{1} & 0 & 0 \\ 0 & 1 & 0 \\ 0 & 0 & \bar{1} \end{pmatrix}}{g_3} = \underset{\begin{pmatrix} \bar{1} & 0 & 0 \\ 0 & \bar{1} & 0 \\ 0 & 0 & 1 \end{pmatrix}}{g_5} \quad ; \quad \underset{\begin{pmatrix} 1 & 0 & 0 \\ 0 & \bar{1} & 0 \\ 0 & 0 & \bar{1} \end{pmatrix}}{g_2} \times \underset{\begin{pmatrix} \bar{1} & 0 & 0 \\ 0 & \bar{1} & 0 \\ 0 & 0 & \bar{1} \end{pmatrix}}{g_4} = \underset{\begin{pmatrix} \bar{1} & 0 & 0 \\ 0 & 1 & 0 \\ 0 & 0 & 1 \end{pmatrix}}{g_6} \tag{1.25}$$

Table 1.8 Identification of the type of point group symmetry operations.

	$\det(\boldsymbol{W}) = +1$					$\det(\boldsymbol{W}) = -1$				
$\mathrm{tr}(\boldsymbol{W})$	**3**	**2**	**1**	**0**	**−1**	**−3**	**−2**	**−1**	**0**	**1**
Type	1	6	4	3	2	$\bar{1}$	$\bar{6}$	$\bar{4}$	$\bar{3}$	m
Order	1	6	4	3	2	2	6	4	6	2

$$\begin{array}{ccccc} g_3 & \cdot & g_4 & = & g_7 \\ \begin{pmatrix} \bar{1}\,0\,0 \\ 0\,1\,0 \\ 0\,0\,\bar{1} \end{pmatrix} & \circ & \begin{pmatrix} \bar{1}\,0\,0 \\ 0\,\bar{1}\,0 \\ 0\,0\,\bar{1} \end{pmatrix} & = & \begin{pmatrix} 1\,0\,0 \\ 0\,\bar{1}\,0 \\ 0\,0\,1 \end{pmatrix} \\ 2_y & \cdot & \bar{1} & = & m_y \end{array} \quad ; \quad \begin{array}{ccccc} g_5 & \circ & g_4 & = & g_8 \\ \begin{pmatrix} \bar{1}\,0\,0 \\ 0\,\bar{1}\,0 \\ 0\,0\,1 \end{pmatrix} & \circ & \begin{pmatrix} \bar{1}\,0\,0 \\ 0\,\bar{1}\,0 \\ 0\,0\,\bar{1} \end{pmatrix} & = & \begin{pmatrix} 1\,0\,0 \\ 0\,1\,0 \\ 0\,0\,\bar{1} \end{pmatrix} \\ 2_z & \cdot & \bar{1} & = & m_z \end{array} \tag{1.26}$$

Missing products such as $g_2 \cdot g_5 = g_3$, $g_2 \cdot g_6 = g_4$, $g_2 \cdot g_7 = g_8$, and so on provide no additional symmetry operation. We see that any combination (multiplication) of two symmetry operations results in a symmetry operation of *mmm*. The multiplication of any symmetry operation g_i with the identity g_1 lets the element g_i unchanged. When we combine more than two operations, the multiplication is associative, as will be shown for the following combinations:

$$(g_5 \cdot g_3)g_6 = g_5(g_3 \cdot g_6) \rightarrow (g_5 \cdot g_3) = g_2,\ g_2 \cdot g_6 = g_4;$$
$$(g_3 \cdot g_6) = g_8,\ g_5 \cdot g_8 = g_4 \rightarrow g_4 = g_4$$

Another important fact is that the product of any operation g_i with its inverse operation g_i^{-1} is the identity operation $g_1 = 1$.

The properties of the set of symmetry operations of our example *mmm* are consistent with the properties (axioms) of a mathematical group. In the following, some basic facts of group theory and its application to point groups will be outlined.

1.3.2 Some Basic Facts of Group Theory

A set of elements $g \in G$ for which a composition law is defined (often denoted as multiplication) forms a *group G* if the following four postulates are fulfilled:

1) ***Closure***
For each pair of elements $g_i, g_j \in G$ exists exactly one element $g_k \in G$ according to

$$g_i \circ g_j = g_k \in G \tag{1.27}$$

2) ***Associativity***
Multiplications in sequence obey the associative law

$$(g_i \circ g_j)g_k = g_i \circ (g_j \circ g_k) = g_i \circ g_j \circ g_k \tag{1.28}$$

3) ***Identity***
Each group has one unit element e also denoted as identity for which holds

$$g_i \circ e = e \circ g_i = g_i \tag{1.29}$$

4) ***Inverse element***
There exists an inverse element $g_i^{-1} \in G$ for each element $g_i \in G$ with composition

$$g_i \circ g_i^{-1} = g_i^{-1} \circ g_i = e \tag{1.30}$$

The number of elements of a group G is called the ***order of the group*** $|G|$. The order can be *finite* or *infinite.* Crystallographic point groups of three-dimensional space are of finite order ($1 \leq |G| \leq 48$). The point group 1 consists only of the unit element (order 1), whereas the point group $m\,\bar{3}m$ has the maximum order of 48. We should always be aware of the fact that ***a set of symmetry operations forms a crystallographic group***, not the symmetry elements. Space groups and translations are groups of infinite order $|G| = \infty$.

Groups for which the commutative law $g_i \circ g_j = g_j \circ g_i$ holds for all pairs $g_i, g_j \in G$ of group G are called ***commutative*** or ***Abelian groups***. For example, the point groups $2/m$, mmm, $mm2$ are Abelian groups, whereas the point groups $3m$, 32, 422, 622 are non-Abelian groups.

The structure of a finite group can be described by a multiplication table (also denoted as group or Caley table). The table consists of $n \times n$ rows and columns containing all possible pair products of the elements of the group. The product $g_i \circ g_j$ is defined as the product of the element of ith row by the element of jth column (Table 1.9). From the product array, one can see whether the group is Abelian or not. An Abelian group is symmetric along the main diagonal.

Two groups G and G' of identical order are called ***isomorphic*** if there exist an invertible one-to-one correspondence between the elements of G and G' in such a way that products $g_i \circ g_j$ in G correspond to products $g_i' \circ g_j'$ in G'. For finite groups, the group tables of isomorphic groups have an identical array with respect to the group products (this does not mean identical elements). Isomorphic groups have the same structural group theory properties. If the group G is Abelian, cyclic, and so on, the group G' is also Abelian, cyclic, and so on. We will prove if there is an isomorphism between the point groups $mm2$, 222, and 4 by inspection of the corresponding group tables given in Table 1.10.

The three point groups $mm2$, 222, and 4 are of order 4. The array of the products indicates that the point groups $mm2$ and 222 are ***isomorphic***, whereas the point group 4 is not isomorphic to either of them. The point groups $mm2$ and 222 have

Table 1.9 Schema of the multiplication table of a group.

G	e	g_2	g_3	g_4	$\cdots$	g_n
e	e	g_2	g_3	g_4	$\cdots$	g_n
g_2	g_2	$g_2 \circ g_2$	$g_2 \circ g_3$	$g_2 \circ g_4$	$\cdots$	$g_2 \circ g_n$
g_3	g_3	$g_3 \circ g_2$	$g_3 \circ g_3$	$g_3 \circ g_4$	$\cdots$	$g_3 \circ g_n$
g_4	g_4	$g_4 \circ g_2$	$g_4 \circ g_3$	$g_4 \circ g_4$	$\cdots$	$g_4 \circ g_n$
$\vdots$	$\vdots$	$\vdots$	$\vdots$	$\vdots$	$\vdots$	$\vdots$
g_n	g_n	$g_n \circ g_2$	$g_n \circ g_3$	$g_n \circ g_4$	$\cdots$	$g_n \circ g_n$

Table 1.10 Group tables of the point groups *mm*2, 222, and 4.

	*mm*2			
	E	m_x	m_y	2
E	E	m_x	m_y	2
m_x	m_x	E	2	m_y
m_y	m_y	2	E	m_x
2	2	m_y	m_x	E

	222			
	E	2_x	2_y	2_z
E	E	2_x	2_y	2_z
2_x	2_x	E	2_z	2_y
2_y	2_y	2_z	E	2_x
2_z	2_z	2_y	2_x	E

	4			
	E	4^1	2	4^{-1}
E	E	4^1	2	4^{-1}
4^1	4^1	2	4^{-1}	E
2	2	4^{-1}	E	4^1
4^{-1}	4^{-1}	E	4^1	2

the same kind of group table and belong, therefore, to the same isomorphism class. The 32 point groups can be assigned into 18 isomorphism classes.

A finite group is called a ***cyclic group Z*** if it consists only of one element and of its powers *n*.

$$Z = \{z, z \circ z = z^2, z \circ z \circ z = z^3, \ \dots \ , z \circ z \circ z \circ \ \dots \ \circ z = z^n = e\} \tag{1.31}$$

The order $|Z|$ of the group Z is n, which is also called the order of the element z.

Typical examples of cyclic groups are the rotation groups $2\{2_z^1, 2_z^2 = \boldsymbol{I}\}$, $3\{3_z^1, 3_z^2, 3_z^3 = \boldsymbol{I}\}$, $4\{4_z^1, 4_z^2, 4_z^3, 4_z^4 = \boldsymbol{I}\}$, $6\{6_z^1, 6_z^2, 6_z^3, 6_z^4, 6_z^5, 6_z^6 = \boldsymbol{I}\}$.

A subset $H \subset G$ of a group G is denoted as subgroup of G if H is a group itself. Alternatively, G is then a supergroup of H. Each group has two ***trivial subgroups***, the group itself and the unit element. The other subgroups $H(H < G)$ are called ***proper subgroups***.

The point symmetry groups 1, 2, 3, $\bar{1}$, m have only trivial subgroups and no proper subgroups.

If H is a subgroup of a finite group $G(H < G)$, then the order of H is a divisor of the order of G (theorem of Lagrange). Thus $[i] = |G|: |H|$, where $[i]$ is called the index of H in G.

A ***coset decomposition*** of a group G into ***left*** and ***right cosets*** with respect to any of its subgroups H is carried out according to the procedure illustrated in Table 1.11 for the calculation of left cosets.

Each column represents one coset. The subgroup itself is the first coset because of $eH = He$, with e unit element of G. The further columns contain the left-hand products of the elements $g_i \in G$ not contained in $H(g_i \notin H)$ by all elements $h_n \in H$ until all elements of group G are exhausted. The same procedure is done for the right-hand products forming the right cosets.

Table 1.11 Coset decomposition of the group *G* into left cosets.

First coset	Second coset	Third coset	⋯	*i*th Coset
eH	g_2H	g_3H	⋯	g_iH
e	g_2e	g_3e	⋯	g_ie
h_2	g_2h_2	g_3h_2	⋯	g_ih_2
h_3	g_2h_3	g_3h_3	⋯	g_ih_3
⋮	⋮	⋮	⋮	⋮
h_n	g_2h_n	g_3h_n	⋯	g_ih_n

Summarizing the procedure in formulae, we can write the decomposition of group G into left and right cosets as

$$G = H + g_2H + g_3H + \cdots + g_iH, \quad G = H + Hg_2 + Hg_3 + \cdots + Hg_i \quad (1.32)$$

The number i of cosets is denoted as index of H in G. This definition is valid for finite and infinite groups.

An element $g_i \in G$ is called ***conjugate*** to an element $g_k \in G$ if there is an element $g_j \in G$ such that $g_i = g_j^{-1} g_k g_j$. Alternatively, g_k is also in conjugate to g_i.

An element $g_i \in G$ is called ***invariant*** or ***self-conjugate*** if it will be mapped by each element $g_k \in G$ into itself: $g_i = g_j^{-1} g_i g_j$ for all $g_j \in G$. Abelian groups contain only self-conjugate elements.

Conjugation of the subgroup $H \subset G$ to another subgroup $H' \subset G$ is given if there exists an element $g_j \in G$ with the relation $H' = g_j^{-1} H g_j$.

Conjugate subgroups are ***isomorph*** and are, therefore, of identical order.

A subgroup H is called a ***normal subgroup H*** if conjugation by all elements $g_i \in G$ maps a subgroup $H \subset G$ onto itself: $g_i H g_j^{-1} = H$. The left and right cosets of a normal subgroup coincide. Each subgroup $H \subset G$ of index 2 is a normal subgroup H of its initial group G.

If H is a normal subgroup of G, then the set of its cosets form a group, the so-called ***factor group*** $F = G/H$ (also denoted as ***quotient group***). The index i of the factor group F is the index of H in G.

The sub- and supergroup relations of the 32 point groups are illustrated in Figure 1.50. Solid line connections indicate normal subgroups. Double or triple lines are given if there exist two or three normal subgroups with the same symbol. From the minimal supergroup 222 can be derived the three normal subgroups 2_x, 2_y, and 2_z. Dashed lines connect the supergroups with maximal conjugate subgroups.

The following practical example should illustrate how one can derive all subgroups for a given point group. In addition, we will determine which particular subgroups are normal and between which subgroups exists a conjugation.

We will derive the subgroup tree for the point group 422. From the stereographic projection (Figure 1.44), we see that the symmetry framework consists of a fourfold rotation axis in [001] and perpendicular to it there are two main twofold axes in [100] and [010] directions and two subsidiary twofold axes in [110] and $[1\bar{1}0]$ directions, respectively. Thus, the point group is of order 8 with the following group elements (symmetry operations):

$$422 = \{1, 4_z^1, 2_z, 4_z^3, 2_x, 2_y, 2_{xy}, 2_{x\bar{y}}\} \quad (1.33)$$

The group table (Table 1.12) shows that the point group 422 is a non-Abelian group because the array of products is not symmetrical along the main diagonal. From the group table, we can derive eight subsets, which form the following proper subgroups (Table 1.13):

The three subgroups of order 4 with index 2 are normal subgroups according to the definition given above. We will prove it for H_1 by means of coset decomposition of 422 related to the subgroup H_1.

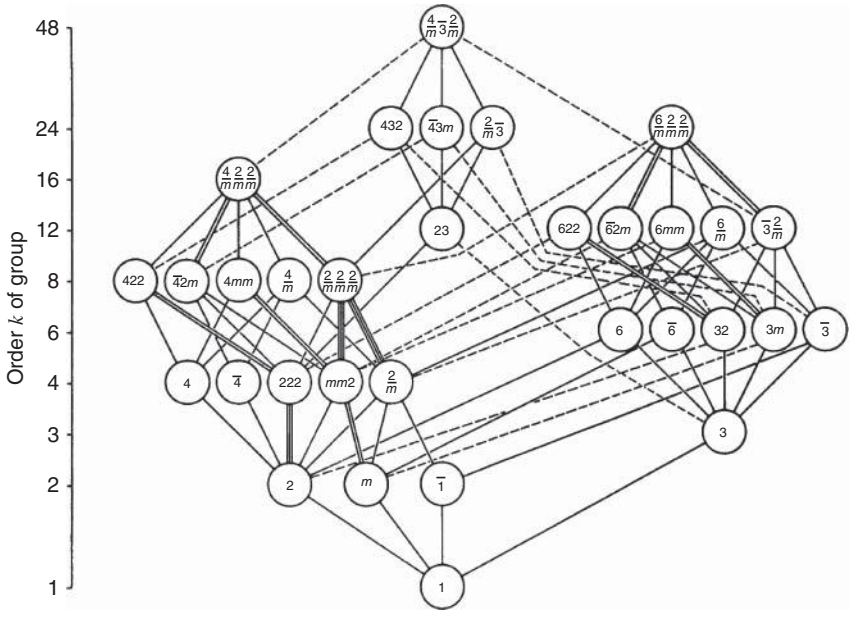

Figure 1.50 Maximal subgroups and minimal supergroups of the 32 point groups. (From the International Tables for Crystallography, Vol. A.)

Table 1.12 Group table of the point group 422.

	1	4_z^1	2_z	4_z^3	2_x	2_y	2_{xy}	$2_{x\bar{y}}$
1	1	4_z^1	2_z	4_z^3	2_x	2_y	2_{xy}	$2_{x\bar{y}}$
4_z^1	4_z^1	2_z	4_z^3	1	$2_{x\bar{y}}$	2_{xy}	2_x	2_y
2_z	2_z	4_z^3	1	4_z^1	2_y	2_x	$2_{x\bar{y}}$	2_{xy}
4_z^3	4_z^3	1	4_z^1	2_z	2_{xy}	$2_{x\bar{y}}$	2_y	2_x
2_x	2_x	2_{xy}	2_y	$2_{x\bar{y}}$	1	2_z	4_z^1	4_z^3
2_y	2_y	$2_{x\bar{y}}$	2_x	2_{xy}	2_z	1	4_z^3	4_z^1
2_{xy}	2_{xy}	2_y	$2_{x\bar{y}}$	2_x	4_z^3	4_z^1	1	2_z
$2_{x\bar{y}}$	$2_{x\bar{y}}$	2_x	2_{xy}	2_y	4_z^1	4_z^3	2_z	1

The left and right cosets are calculated and tabulated (Table 1.14). We see that all left and right cosets are identical. They contain the same elements. The subgroup H_1 is the first coset. Within the second coset ($g_2 \in G$, $g_2 \notin H_1$) is no element of $g_2H_1 \in H_1$ and all elements of g_2H_1 are different. For the third coset ($g_3 \in G$, $g_3 \notin H_1$), all elements of g_3H_1 are identical with the elements of g_2H_1. The same is true for the next cosets. Therefore, these cosets will not be taken into consideration. For the normal subgroup of index 2, the group G can be represented as $G = H_1 + H_1 2_x = 2_x H_1 + H_1$. Thus, $H_1 2_x = 2_x H_1$ or $H_1 = 2_x^{-1} H_1 2_x$.

Table 1.13 Subgroups of the point group 422.

Subgroup	Order	Index
$H_1 = \{1, 4_z^1, 2_z, 4_z^3\}$	4	2
$H_2 = \{1, 2_x, 2_y, 2_z\}$	4	2
$H_3 = \{1, 2_{xy}, 2_{x\bar{y}}, 2_z\}$	4	2
$H_4 = \{1, 2_z\}$	2	4
$H_5 = \{1, 2_y\}$	2	4
$H_6 = \{1, 2_z\}$	2	4
$H_7 = \{1, 2_{xy}\}$	2	4
$H_8 = \{1, 2_{x\bar{y}}\}$	2	4

Table 1.14 Coset decomposition of point group 422 related to $H_1 = 4$.

Left cosets					Right cosets				
H_1	2_xH_1	2_yH_1	$2_{xy}H_1$	$2_{x\bar{y}}H_1$	H_1	H_12_x	H_12_y	H_12_{xy}	$H_12_{x\bar{y}}$
1	2_x	2_y	2_{xy}	$2_{x\bar{y}}$	1	2_x	2_y	2_{xy}	$2_{x\bar{y}}$
4_z^1	2_{xy}	$2_{x\bar{y}}$	2_y	2_x	4_z^1	$2_{x\bar{y}}$	2_{xy}	2_x	2_y
2_z	2_y	2_x	$2_{x\bar{y}}$	2_{xy}	2_z	2_y	2_x	$2_{x\bar{y}}$	2_{xy}
4_z^3	$2_{x\bar{y}}$	2_{xy}	2_x	2_y	4_z^3	2_{xy}	$2_{x\bar{y}}$	2_y	2_x

The subgroup H_1 and its left coset 2_xH_1, corresponding right coset H_12_x, form the factor group $G/H_1 = \{H_1, 2_x H_1\}$. In this case, the normal subgroup is the unit element of the factor group.

With the same procedure of coset decomposition of G related to $H_6 = 2_z = \{1, 2_z\}$, the reader should prove that H_6 is also a normal subgroup and will form with its cosets the factor group $G/H_6 = \{H_6, 4_z^1 \cdot H_6, 2_xH_6, 2_{xy}H_6\}$.

The group structures of $H_4 = \{1, 2_x\}$ and $H_5 = \{1, 2_y\}$ in addition to $H_7 = \{1, 2_{xy}\}$ and $H_8 = \{1, 2_{x\bar{y}}\}$ are quite different. We will illustrate this by means of coset decomposition for the subgroups H_7 and H_8 (Table 1.15).

The left and right cosets for both subgroups are not identical. The cosets also show no group structure. This means, H_7 and H_8 are no normal subgroups. They are conjugate to each other. The following relations are given:

$$H_7 = 4_z^1 \cdot H_8 \cdot 4_z^3 = 4_z^1 \cdot H_8 \cdot 4_z^{-1}, \quad H_8 = 4_z^1 \cdot H_7 \cdot 4_z^3 = 4_z^1 \cdot H_7 \cdot 4_z^{-1} \tag{1.34}$$

The same conjugation relation exists for the subgroups H_4 and H_5. All group–subgroup relations for the point group 422 are illustrated in Figure 1.51. The three subgroups of order 4 and index 2 and the subgroup 2_z of order 2 and index 4 are normal subgroups. Conjugate subgroups are formed by the pairs 2_x, 2_y and 2_{xy}, $2_{x\bar{y}}$, where the following conjugation relations hold:

$$2_x = 4_z^1 \cdot 2_y \cdot 4_z^{-1}, \quad 2_{xy} = 4_z^1 \cdot 2_{x\bar{y}} \cdot 4_z^{-1} \tag{1.35}$$

Table 1.15 Coset decomposition for the subgroups H_7 and H_8.

	Left cosets				Right cosets		
H_7	$4_z^1 \cdot H_7$	$2_z \cdot H_7$	$4_z^3 \cdot H_7$	H_7	$H_7 \cdot 4_z^1$	$H_7 \cdot 2_z$	$H_7 \cdot 4_z^3$
1	4_z^1	2_z	4_z^3	1	4_z^1	2_z	4_z^3
2_{xy}	2_x	$2_{x\bar{y}}$	2_y	2_{xy}	2_y	$2_{x\bar{y}}$	2_x
	Left cosets				**Right cosets**		
H_8	$4_z^1 \cdot H_8$	$2_z \cdot H_8$	$4_z^3 \cdot H_8$	H_8	$H_8 \cdot 4_z^1$	$H_8 \cdot 2_z$	$H_8 \cdot 4_z^3$
1	4_z^1	2_z	4_z^3	1	4_z^1	2_z	4_z^3
$2_{x\bar{y}}$	2_y	2_{xy}	2_x	$2_{x\bar{y}}$	2_x	2_{xy}	2_y

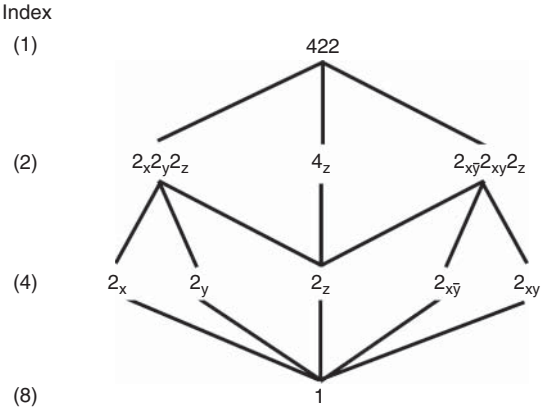

Figure 1.51 Group–subgroup relations for the point group 422.

Now, we will give a brief group theoretical consideration of some fundamental terms of the morphological symmetry of crystals. We have described previously that the crystal forms can be classified as general, special, and limiting forms. The number of symmetry equivalent faces of a crystal form is also called the multiplicity of a form. The multiplicity of a general crystal form is identical to the order of the point group *P*. The multiplicity of a special crystal form is given by the order of the point group divided by the order of the face-symmetry group *F*. The face-symmetry group *F* is a subgroup of *P*. The face-symmetry group *F* is defined as the set of symmetry operations that map the face onto itself. The inherent symmetry of a crystal form independent of the symmetry of the generating point group is the eigensymmetry *E*. The point group describing the eigensymmetry is at least the generating point group or a supergroup of it. A general or special crystal form may be transformed into a limiting form for particular geometric parameters of the form. The limiting form has the same multiplicity and face symmetry as the original form; its eigensymmetry is always higher. Using the

Table 1.16 Face symmetry of cube as function of generating point group.

Generating point group	Face symmetry of cube
$m\,\bar{3}m$	$4m.m$
$\bar{4}3m$	$2.mm$
432	4
$m\bar{3}$	$2m$
23	2

symmetry groups P and E of a crystal form, we can classify the forms as ***characteristic*** (if $P = E$) and ***noncharacteristic forms*** ($E > P$). The following examples should make the facts clear. The general form of the point group $m\,\bar{3}m$ (order $i = 48$) is the ***hexakisoctahedron*** (face symmetry 1), which has a multiplicity of 48. One of the special forms of $m\,\bar{3}m$ is the ***tetrakishexahedron*** (face symmetry m, order 2). Thus, the multiplicity for this form must be 24. The cube (eigensymmetry $m\,\bar{3}m$) can be generated as special form (multiplicity 6) in each of the five cubic point groups. The face symmetry of the cube depends on the symmetry of the generating point group (Table 1.16).

The eigensymmetry of the cube ($m\,\bar{3}m$) is identical with the point group $m\,\bar{3}m$. Only in $m\,\bar{3}m$ is the cube a characteristic form; in all other cubic point groups, it is a noncharacteristic form. The general form of the point group 4 is the tetragonal pyramid (multiplicity 4, face symmetry 1). The tetragonal pyramid $\{hkl\}$ will be transformed into a tetragonal prism for $\{hk0\}$. Both forms have the same multiplicity 4 and the same face symmetry 1. However, the eigensymmetry of the tetragonal pyramid is $4mm$ (order 8) and that of the tetragonal prism is $4/mmm$ (order 16).

The existing correlations between holohedral and merohedral forms of crystals can be described by group–subgroup relations of the point groups. In general, a point group that is a subgroup of the holohedral group within the same crystal family is denoted as ***merohedral*** or ***merohedry***. Merohedries are subdivided into ***hemihedries*** (subgroups of index 2), ***tetartohedries*** (subgroups of index 4), and ***ogdohedries*** (subgroups of index 8). The ***hexakisoctahedron*** (48 faces) is the general form of the cubic holoedry $m\,\bar{3}m$. The ***hexakistetrahedron*** (± correlate forms), ***pentagon–icositetrahedron*** (left-handed- and right-handed correlate forms), and ***disdodecahedron*** (± correlate forms) are the general forms of the cubic point groups $\bar{4}3m$, 432, and $m\bar{3}$, which are subgroups of index $i = [2]$ of $m\,\bar{3}m$. The abovementioned general forms of the three subgroups are merohedral forms, each consisting of 24 faces. The cubic point group 23 is a subgroup of index $i = [4]$ of $m\,\bar{3}m$. The four possible general forms (± left-handed and ± right-handed correlate forms) of ***tetrahedral-pentagondodecahedra*** are tetartohedral forms consisting of 12 faces. Then, it is obvious that we can compose in each case from four correlate forms of the ***tetrahedral-pentagondodecahedron*** or from two correlate forms of the ***disdodecahedron***, ***pentagon-icositetrahedron***, and ***hexakistetrahedron***, respectively, the holohedral form of the ***hexakisoctahedron***.

1.4
Structural Symmetry

In the previous section, we have shown that a crystal can be characterized and classified according to its morphological symmetry by means of the 32 geometric crystal classes, which are denoted by the symbol of the corresponding crystallographic point group.

Now, we will go a step further and deal with the fundamentals of structural symmetry of crystals. The lattice concept as mathematical tool for the description of the periodic arrangement of atoms, ions, and molecules in crystals has been mentioned briefly in Section 1.2. In this section, we will describe the Bravais lattice types and their symmetries. After this, the concept of space groups as the entire set of spatial symmetry operations of a crystal structure will be discussed thoroughly.

1.4.1
Crystal Lattices, Motifs, and Crystal Structures

The translational periodicity of a crystal can be described by the mathematical construct of a lattice as already discussed. We have shown that there are various possibilities to choose a primitive or nonprimitive unit cell in a point lattice.

Let us decorate a two-dimensional lattice with a motif. Owing to the translational symmetry of the lattice, replicas of the motif will be generated by rigid-body translations (Figure 1.52).

The pattern that is formed by the motif is called ***crystal pattern***. If the regular array (crystal pattern) is formed by atoms, ions, or molecules, we use the term ***crystal structure***. The relationship between the crystal lattice and crystal structure can be simply characterized as

$$\textit{lattice} + \textit{motif} = \textit{crystal structure}$$

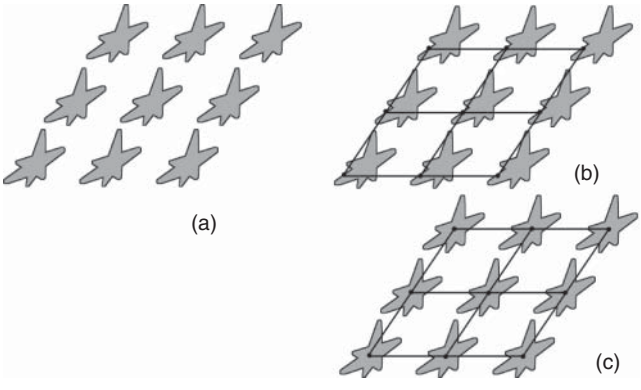

Figure 1.52 Pattern of motif (a) and lattice and motif (crystal pattern) (b and c, respectively).

Our example illustrates also that we can choose different origins for our motif. Necessarily, the motif must not occupy the nodes of our lattice. For the selection of a unit cell we have also to take into consideration the symmetry of the motif. The following exercise illustrates the problem. We will decorate an oblique plane lattice with our motif. We see that the crystal pattern symmetry of our motif is inconsistent with the lattice symmetry. The motif has a fourfold rotational eigen-symmetry; in the oblique lattice, there are only twofold rotation axes. The correct lattice for our motif is only the square lattice as shown in Figure 1.53.

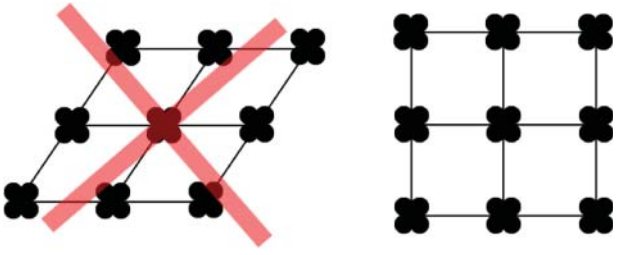

(a) (b)

Figure 1.53 Eigen-symmetry of motif (a) and symmetry of lattice (b) – the right choice of lattice.

The finite number of three-dimensional lattice types, which are consistent with the group of translations, is denoted as Bravais lattices. The term *lattice* goes back to Ludwig August Seeber (1824) who assumed a point lattice, where the nodes of the lattice should be the mass centers of small spherical atoms. Moritz Ludwig Frankenheim (1842) derived 15 possible spatial lattices. Auguste Bravais proved in 1848 that only 14 different space lattice types exist.

1.4.1.1 **Bravais Lattices**

The unit cells of the 14 Bravais lattice types are shown in Figure 1.54. The symbols for the Bravais lattices consist of two letters, where the first letter denotes the crystal family and the second one fixes the centring type. The possible centring types of the Bravais lattices are summarized in Table 1.17. The assignment of the 14 Bravais lattice types into the six crystal families and seven crystal systems, respectively, is represented in Table 1.18. The standard-setting-independent symbols *mS* and *oS* characterize the centered monoclinic and one-face-centered orthorhombic lattices. Alternative settings of these Bravais lattices are given in parentheses.

Among the 14 Bravais lattices are 7 primitive lattices. These seven point lattices correspond to the parallelepipeds of the seven crystal systems. When we consider the symmetry properties of the 14 Bravais lattices classified into seven crystal systems, we notice that the seven holohedral point symmetry groups occur: $\overline{1}$, $2/m$, mmm, $4/mmm$, $\overline{3}m$, $6/mmm$, and $m\,\overline{3}m$. The symmetry framework of an orthorhombic *P*-Bravais lattice is shown in Figure 1.55. Every Bravais lattice point is a center of symmetry; every lattice point has also a twofold axis. The axes of twofold rotation are normal to mirror planes. The symmetry of the holohedral point group $2/m\ 2/m\ 2/m$ (short symbol mmm) is obvious.

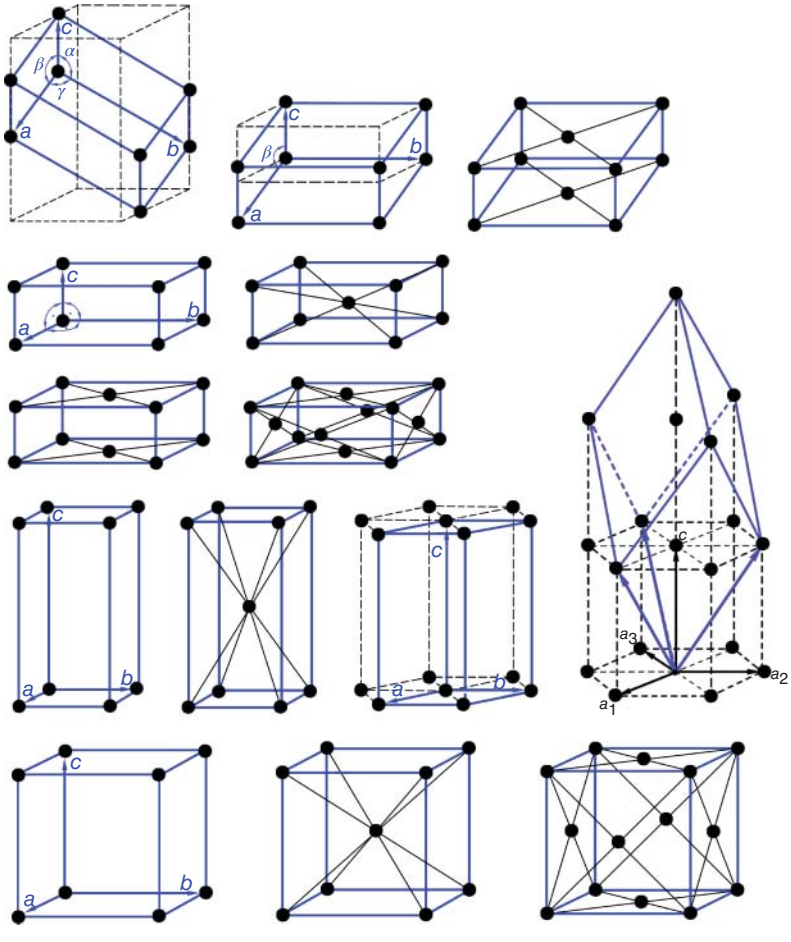

Figure 1.54 The 14 Bravais lattice types.

1.4.1.2 The Reciprocal Lattice

The high resolution transmission electron micrograph of a (100) oriented GaAs crystal (Figure 1.3a) has illustrated the lattice periodicity at atomic scale in direct space. The corresponding electron diffraction pattern (Figure 1.3b) exhibits also the lattice character and symmetry of GaAs, but in reciprocal space. The definition of the reciprocal lattice was introduced by Ewald in 1913 [29] for the description of an orthorhombic lattice and generalized for all crystal systems by von Laue in 1914 [27]. The fundamental relationships between the crystal lattice (direct space) and the reciprocal lattice (reciprocal space) will be outlined in the following.

If L is a crystal lattice with the basis vectors $\boldsymbol{a}$, $\boldsymbol{b}$, $\boldsymbol{c}$, then the assigned reciprocal lattice L^* with the basis vectors $\boldsymbol{a}^*$, $\boldsymbol{b}^*$, $\boldsymbol{c}^*$ is defined by the following equations:

$$(\boldsymbol{a} \cdot \boldsymbol{a}^*) = (\boldsymbol{b} \cdot \boldsymbol{b}^*) = (\boldsymbol{c} \cdot \boldsymbol{c}^*) = 1 \tag{1.36a}$$

Table 1.17 Centering types of Bravais lattices.

Centering type	No. lattice points/ unit cell	Coordinates of lattice points
P – primitive lattices	1	0,0,0
I – body-centered lattices	2	0,0,0; ½,½,½
F – all face-centered lattices	4	0, 0, 0; ½, ½, 0; ½, 0, ½; 0, ½, ½
One–face-centered lattices		
A	2	0, 0, 0; 0, ½, ½
B	2	0, 0, 0; ½, 0, ½
C	2	0, 0, 0; ½, ½, 0
R – rhombohedrally centered (triple hexagonal unit cell)	3	0, 0, 0; 2/3, 1/3, 1/3; 1/3, 2/3, 2/3 (Obverse setting) 0, 0, 0; 1/3, 2/3, 1/3; 2/3, 1/3, 2/3 (Reverse setting)
Primitive (rhombohedral unit cell)	1	0, 0, 0
H – hexagonally centered	3	0, 0, 0; 2/3, 1/3, 0; 1/3, 2/3, 0

$$(\boldsymbol{a}\cdot\boldsymbol{b}^*)=(\boldsymbol{b}\cdot\boldsymbol{c}^*)=(\boldsymbol{c}\cdot\boldsymbol{a}^*)=0 \tag{1.36b}$$

$$(\boldsymbol{b}\cdot\boldsymbol{a}^*)=(\boldsymbol{c}\cdot\boldsymbol{b}^*)=(\boldsymbol{a}\cdot\boldsymbol{c}^*)=0 \tag{1.36c}$$

From relations used as definition (Equation 1.36b and 1.36c), the following relationships between the directions and angles of L and L^* are obvious:

$$\boldsymbol{a}^*\perp\boldsymbol{b} \quad \text{and} \quad \boldsymbol{c},\boldsymbol{b}^*\perp\boldsymbol{c} \quad \text{and} \quad \boldsymbol{a},\boldsymbol{c}^*\perp\boldsymbol{a} \quad \text{and} \quad \boldsymbol{b}$$
$$\boldsymbol{a}\perp\boldsymbol{b}^* \quad \text{and} \quad \boldsymbol{c}^*,\boldsymbol{b}\perp\boldsymbol{c}^* \quad \text{and} \quad \boldsymbol{a}^*,\boldsymbol{c}\perp\boldsymbol{a}^* \quad \text{and} \quad \boldsymbol{b}^*$$

Using these relations, we can derive that the reciprocal basis vectors can be calculated from the basis vectors of the direct lattice and vice versa in the exact manner. Because $\boldsymbol{a}^*\perp\boldsymbol{b}$ and $\boldsymbol{c}$, we can write $\boldsymbol{a}^*=k(\boldsymbol{b}\times\boldsymbol{c})$. For the determination of k, we multiply the equation by $\boldsymbol{a}$. Then, $1=(\boldsymbol{a}\cdot\boldsymbol{a}^*)=k\,\boldsymbol{a}\cdot(\boldsymbol{b}\times\boldsymbol{c})=kV$, and, therefore, $k=1/V$. Thus, $\boldsymbol{a}^*=(\boldsymbol{b}\times\boldsymbol{c})/V$, with V as volume of the unit cell.

Then, the relationships between the basis vectors of the direct and reciprocal lattice can be written as

$$\begin{aligned}
\boldsymbol{a}^* &= \frac{(\boldsymbol{b}\times\boldsymbol{c})}{V}, \quad \boldsymbol{a} = \frac{(\boldsymbol{b}^*\times\boldsymbol{c}^*)}{V^*}\\
\boldsymbol{b}^* &= \frac{(\boldsymbol{c}\times\boldsymbol{a})}{V}, \quad \boldsymbol{b} = \frac{(\boldsymbol{c}^*\times\boldsymbol{a}^*)}{V^*}\\
\boldsymbol{c}^* &= \frac{(\boldsymbol{a}\times\boldsymbol{b})}{V}, \quad \boldsymbol{c} = \frac{(\boldsymbol{a}^*\times\boldsymbol{b}^*)}{V^*}
\end{aligned} \tag{1.37}$$

Table 1.18 Crystal families, crystal systems, and Bravais lattices.

Crystal family	Symbol	Crystal system	Bravais lattice types
Triclinic (anorthic)	*a*	Triclinic (anorthic)	*aP*
Monoclinic	*m*	Monoclinic	*mP* *mS* (*mC*, *mA*, *mI*) *mP* *mS* (*mA*, *mB*, *mI*)
Orthorhombic	*o*	Orthorhombic	*oP oS* (*oA*, *oB*, *oC*) *oI* *oF*
Tetragonal	*t*	Tetragonal	*tP* *tI*
Hexagonal	*h*	Trigonal Hexagonal	*hP* (*hexagonal axes*) *hR* (*rhombohedral axes*) *hP*
Cubic	*c*	Cubic	*cP* *cI* *cF*

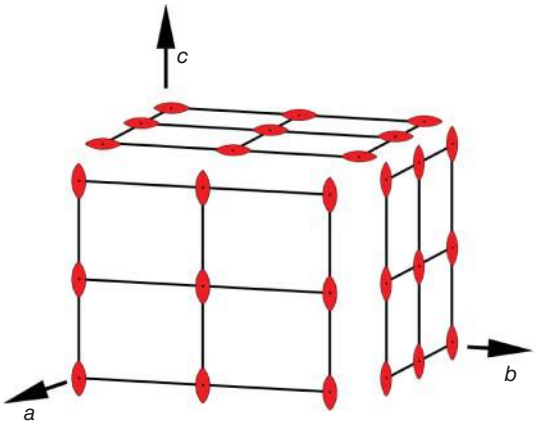

Figure 1.55 Symmetry framework of an orthorhombic *P*-Bravais lattice.

The relationships between the metric parameters (lengths of the basis vectors and interaxial angles) of direct and reciprocal lattices are given by

$$\boldsymbol{a}^* = \frac{\boldsymbol{bc} \cdot \sin\alpha}{V} = \frac{1}{d_{100}}, \quad \boldsymbol{b}^* = \frac{\boldsymbol{ca} \cdot \sin\beta}{V} = \frac{1}{d_{010}}, \quad \boldsymbol{c}^* = \frac{\boldsymbol{ab} \cdot \sin\gamma}{V} = \frac{1}{d_{001}} \tag{1.38}$$

$$\begin{aligned} \boldsymbol{a} &= \frac{\boldsymbol{b}^*\boldsymbol{c}^* \cdot \sin\alpha^*}{V^*} = \frac{1}{d^*_{100}}, \quad \boldsymbol{b} = \frac{\boldsymbol{c}^*\boldsymbol{a}^* \cdot \sin\beta^*}{V^*} = \frac{1}{d^*_{010}}, \\ \boldsymbol{c} &= \frac{\boldsymbol{a}^*\boldsymbol{b}^* \cdot \sin\gamma^*}{V^*} = \frac{1}{d^*_{001}} \end{aligned} \tag{1.39}$$

$$\begin{aligned} \cos\alpha^* &= \frac{\cos\beta \cdot \cos\gamma - \cos\alpha}{\sin\beta \cdot \sin\gamma}, \quad \cos\beta^* = \frac{\cos\alpha \cdot \cos\gamma - \cos\beta}{\sin\alpha \cdot \sin\gamma}, \\ \cos\gamma^* &= \frac{\cos\alpha \cdot \cos\beta - \cos\gamma}{\sin\alpha \cdot \sin\beta} \end{aligned} \tag{1.40}$$

$$\begin{aligned} \cos\alpha &= \frac{\cos\beta^* \cdot \cos\gamma^* - \cos\alpha^*}{\sin\beta^* \cdot \sin\gamma^*}, \quad \cos\beta = \frac{\cos\alpha^* \cdot \cos\gamma^* - \cos\beta^*}{\sin\alpha^* \cdot \sin\gamma^*}, \\ \cos\gamma &= \frac{\cos\alpha^* \cdot \cos\beta^* - \cos\gamma^*}{\sin\alpha^* \cdot \sin\beta^*} \end{aligned} \tag{1.41}$$

The volumes of unit cells of the direct and reciprocal lattices are reciprocal to each other, because

$$1 = (\boldsymbol{a} \cdot \boldsymbol{a}^*) = \frac{(\boldsymbol{b} \times \boldsymbol{c})(\boldsymbol{b}^* \times \boldsymbol{c}^*)}{VV^*} = \frac{(\boldsymbol{b} \cdot \boldsymbol{b}^*)(\boldsymbol{c} \cdot \boldsymbol{c}^*) - (\boldsymbol{b} \cdot \boldsymbol{c}^*)(\boldsymbol{c} \cdot \boldsymbol{b}^*)}{VV^*} = \frac{1}{VV^*} \tag{1.42}$$

Thus,

$$V = \frac{1}{V^*}, \quad V^* = \frac{1}{V} \tag{1.43}$$

In analogy to the volume V of the direct lattice, we can express V^* as

$$\begin{aligned} V^* &= \boldsymbol{a}^* \cdot (\boldsymbol{b}^* \times \boldsymbol{c}^*) = \begin{vmatrix} \boldsymbol{a}^* \cdot \boldsymbol{a}^* & \boldsymbol{a}^* \cdot \boldsymbol{b}^* & \boldsymbol{a}^* \cdot \boldsymbol{c}^* \\ \boldsymbol{b}^* \cdot \boldsymbol{a}^* & \boldsymbol{b}^* \cdot \boldsymbol{b}^* & \boldsymbol{b}^* \cdot \boldsymbol{c}^* \\ \boldsymbol{c}^* \cdot \boldsymbol{a}^* & \boldsymbol{c}^* \cdot \boldsymbol{b}^* & \boldsymbol{c}^* \cdot \boldsymbol{c}^* \end{vmatrix}^{\frac{1}{2}} \\ &= \boldsymbol{a}^*\boldsymbol{b}^*\boldsymbol{c}^*(1 - \cos^2\alpha^* - \cos^2\beta^* - \cos^2\gamma^* + 2\cos\alpha^*2\cos\beta^*2\cos\boldsymbol{\gamma}^*)^{\frac{1}{2}} \end{aligned} \tag{1.44}$$

Another important property is that the reciprocal lattice belongs to the same crystal system as the direct lattice. In the following, the metrical relationships between reciprocal and direct lattices for the seven crystal systems are listed:

Cubic crystal system	$\boldsymbol{a}^* = \boldsymbol{b}^* = \boldsymbol{c}^* = 1/\boldsymbol{a}$	$\alpha^* = \beta^* = \gamma^* = 90^\circ$
Tetragonal crystal system	$\boldsymbol{a}^* = \boldsymbol{b}^* = 1/\boldsymbol{a}, \boldsymbol{c}^* = 1/\boldsymbol{c}$	$\alpha^* = \beta^* = \gamma^* = 90^\circ$
Orthorhombic crystal system	$\boldsymbol{a}^* = 1/\boldsymbol{a}, \boldsymbol{b}^* = 1/\boldsymbol{b}, \boldsymbol{c}^* = 1/\boldsymbol{c}$	$\alpha^* = \beta^* = \gamma^* = 90^\circ$
Trigonal and hexagonal crystal system:		
Rhombohedral axes	$\boldsymbol{a}^* = \boldsymbol{b}^* = \boldsymbol{c}^* = \frac{1}{a \sin\alpha \sin\alpha^*} \cos\alpha^*/2 = \cos\beta^*/2 = \cos\gamma^*/2 = \frac{1}{2\cos\alpha/2}$	

The unit cell of both the direct and reciprocal lattice is a rhombohedron. The more acute the angle α of the direct unit cell, the more obtuse is α^* of the reciprocal unit cell.

Hexagonal axes: $\boldsymbol{a}^* = \boldsymbol{b}^* = \frac{2}{3}\sqrt{3} \cdot \frac{1}{a}, \quad \boldsymbol{c}^* = 1/c, \quad \alpha^* = \beta^* = 90^\circ, \quad \gamma^* = 60^\circ.$

Both unit cells in direct and reciprocal space belong to the same crystal system (trigonal or hexagonal). We have to take into consideration the differences of angles γ (120°) and γ^* (60°).

Monoclinic crystal system:

Unique b-axis setting:

$$\boldsymbol{a}^* = \frac{1}{\boldsymbol{a} \cdot \sin\beta}, \quad \boldsymbol{b}^* = 1/b, \quad \boldsymbol{c}^* = \frac{1}{\boldsymbol{c} \cdot \sin\beta}, \quad \alpha^* = \gamma^* = 90^\circ, \quad \beta^* = 180^\circ - \beta$$

Unique c-axis setting:

$$\boldsymbol{a}^* = \frac{1}{\boldsymbol{a} \cdot \sin\gamma}, \quad \boldsymbol{a}^* = \frac{1}{\boldsymbol{a} \cdot \sin\gamma}, \quad \boldsymbol{c}^* = 1/c, \quad \alpha^* = \beta^* = 90^\circ, \quad \gamma^* = 180^\circ - \gamma$$

As a function of the setting with unique axis *b* or *c*, the angle β^* or γ^* is an obtuse angle if β or γ is an acute angle and vice versa.

Triclinic crystal system:

$$\boldsymbol{a}^* \neq \boldsymbol{b}^* \neq \boldsymbol{c}^*, \quad \alpha^* \neq \beta^* \neq \gamma^* \neq 90^\circ$$

The Bravais lattice types of the direct and reciprocal lattice are identical for *P*-, *A*-, *B*-, *C*-, and *R*-lattices. Direct lattice centring types *I* and *F* correspond to reciprocal lattice centring types *F** and *I** and vice versa $F^* = I$ and $I^* = F$.

The direct and reciprocal lattices belong to the same crystal system and have the same holohedral point symmetry.

In order to get a better understanding of the geometrical relationships between the direct and the reciprocal lattices, we will briefly sketch the graphical construction of the reciprocal lattice for a given direct lattice. We consider a section through a primitive monoclinic lattice perpendicular to the *y*-axis (Figure 1.56a). Perpendicular to this lattice plane, there is an infinite number of families of planes ($h0l$) with the common zone axis [010]. The drawn section (010) is formed by the families of planes (100) and (001), which are parallel to the zone axis *y*. The drawing

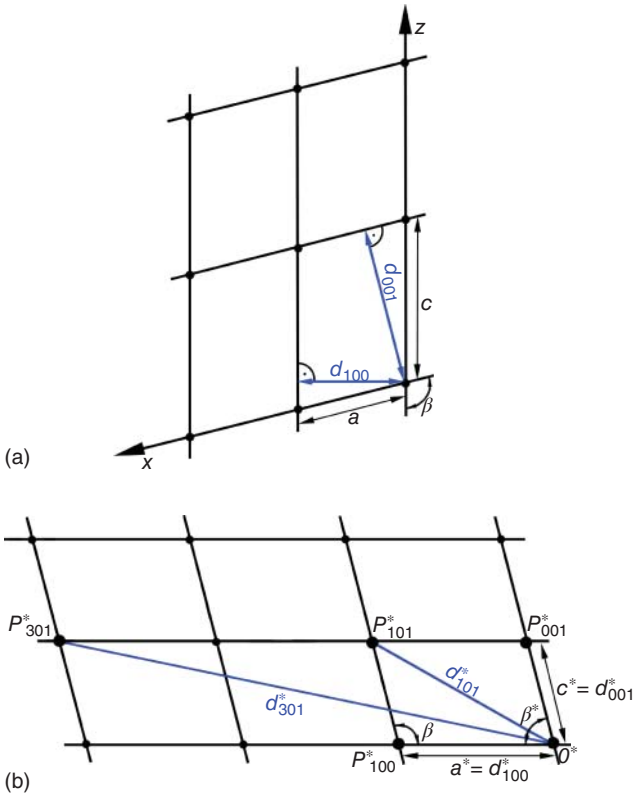

Figure 1.56 Illustration of the graphical construction of the reciprocal lattice. Two-dimensional monoclinic (010) lattice plane (a) and reciprocal lattice plane (b).

shows the traces of the lattice planes of the two families. We construct the normals to our families of planes and determine the interplanar distances d_{hkl}, which are given by: $d_{100} = a{\cdot}\sin\beta$ and $d_{001} = c{\cdot}\sin\beta$. From a common origin O* (Figure 1.56b), the normals of the families of planes (100) and (001) are drawn with lengths, which are inversely proportional to their interplanar distances d_{100} and d_{001}, respectively. Thus, $d^*_{100} = 1/a \cdot \sin\beta = \boldsymbol{a}^*$, $d^*_{00} = 1/c \cdot \sin\beta = \boldsymbol{c}^*$, and $\beta^* = 180° - \beta$. The end points of the two vectors are the reciprocal lattice points P^*_{100} and P^*_{001}.

The same procedure can be applied to construct all other reciprocal lattice points P^*_{h0l} (h,l – coprime). Reciprocal lattice points P^*_{nh0nl} correspond to families of lattice planes ($nh0\,nl$). For example, the lattice points $P^*_{002}, P^*_{003}, P^*_{00n}$ correspond to the families of lattice planes (002), (003), (00n), respectively, with interplanar distances of $d_{001}/2$, $d_{001}/3$, d_{001}/n, respectively. Therefore, the point P^*_{00n} has n-times the distance of P^*_{001}.

We have seen each reciprocal lattice point represents a family of lattice planes. In general, a reciprocal lattice vector can be written as

$$\boldsymbol{r}^* = h\boldsymbol{a}^* + k\boldsymbol{b}^* + l\boldsymbol{c}^* \in L^* \tag{1.45}$$

This means, the reciprocal lattice vector $\boldsymbol{r}^*$ is always perpendicular to the lattice plane (*hkl*) of the direct lattice. Reciprocal lattice vectors have dimensions of reciprocal length (nm^{-1}, $Å^{-1}$).

1.4.1.3 Lattice Transformations

Morphological and structural studies of crystals require often a different choice of unit cell as originally given in the literature. A change of unit cell is always connected with a change of Miller indices (*hkl*) of planes, of indices of directions [*uvw*], and of coordinates *x,y,z* of lattice points. In the following, we will describe the main transformation rules in detail.

The transformation of the original lattice $L(\boldsymbol{a}, \boldsymbol{b}, \boldsymbol{c})$ into the new lattice $L'(\boldsymbol{a'}, \boldsymbol{b'}, \boldsymbol{c'})$, and vice versa, the inverse transformation of L' into L can be described by the following relationships:

$$\begin{aligned} \boldsymbol{a'} &= s_{11}\boldsymbol{a} + s_{12}\boldsymbol{b} + s_{13}\boldsymbol{c}, \quad \boldsymbol{a} = t_{11}\boldsymbol{a'} + t_{12}\boldsymbol{b}' + t_{13}\boldsymbol{c}' \\ \boldsymbol{b}' &= s_{21}\boldsymbol{a} + s_{22}\boldsymbol{b} + s_{23}\boldsymbol{c}, \quad \boldsymbol{b} = t_{21}\boldsymbol{a}' + t_{22}\boldsymbol{b'} + t_{23}\boldsymbol{c'} \\ \boldsymbol{c'} &= s_{31}\boldsymbol{a} + s_{32}\boldsymbol{b} + s_{33}\boldsymbol{c}, \quad \boldsymbol{c} = t_{31}\boldsymbol{a'} + t_{32}\boldsymbol{b'} + t_{33}\boldsymbol{c'} \end{aligned} \tag{1.46}$$

with the transformation matrices $\boldsymbol{S}(s_{ij})$, $\boldsymbol{T}(t_{ij})$, where $\boldsymbol{T} = \boldsymbol{S}^{-1}$. The inverse matrix $\boldsymbol{T}$ is

$$\boldsymbol{T} = \boldsymbol{S}^{-1} = \frac{1}{\det \boldsymbol{S}} \begin{pmatrix} s_{22}s_{33} - s_{23}s_{32} & s_{13}s_{32} - s_{12}s_{33} & s_{12}s_{23} - s_{13}s_{22} \\ s_{23}s_{31} - s_{21}s_{33} & s_{11}s_{33} - s_{13}s_{31} & s_{13}s_{21} - s_{11}s_{23} \\ s_{21}s_{32} - s_{22}s_{31} & s_{12}s_{31} - s_{11}s_{32} & s_{11}s_{22} - s_{12}s_{21} \end{pmatrix}$$

with the determinant

$$\det \boldsymbol{S} = (s_{11}s_{22}s_{33} + s_{12}s_{23}s_{31} + s_{13}s_{21}s_{32}) - (s_{11}s_{23}s_{32} + s_{12}s_{21}s_{33} + s_{13}s_{22}s_{31}) \tag{1.47}$$

The relationships between the corresponding volumes V' and V are given by

$$V' = V \cdot \det \boldsymbol{S} \quad \text{and} \quad V = V' \cdot \det \boldsymbol{T} \tag{1.48}$$

The coordinates of the lattice points are transformed by means of the following relationships:

$$\begin{aligned} \boldsymbol{x'} &= t_{11}\boldsymbol{x} + t_{21}\boldsymbol{y} + t_{31}\boldsymbol{z}, \quad \boldsymbol{x} = s_{11}\boldsymbol{x'} + s_{21}\boldsymbol{y'} + s_{31}\boldsymbol{z'} \\ \boldsymbol{y'} &= t_{12}\boldsymbol{x} + t_{22}\boldsymbol{y} + t_{32}\boldsymbol{z}, \quad \boldsymbol{y} = s_{12}\boldsymbol{x'} + s_{22}\boldsymbol{y'} + s_{32}\boldsymbol{z'} \\ \boldsymbol{z'} &= t_{13}\boldsymbol{x} + t_{23}\boldsymbol{y} + t_{33}\boldsymbol{z}, \quad \boldsymbol{z} = s_{13}\boldsymbol{x'} + s_{23}\boldsymbol{y'} + s_{33}\boldsymbol{z'} \end{aligned} \tag{1.49}$$

with the transformation matrices $\boldsymbol{T}^T(t_{ji})$, $\boldsymbol{S}^T(s_{ji})$, which are the transposed of $\boldsymbol{T}$ and $\boldsymbol{S}$.

The transformation relationships for the cell vectors, Millers indices of planes, indices of directions, and the coordinates of lattice points are summarized in Table 1.19.

Let us consider the following practical example. Corundum (α-Al_2O_3) crystallizes in the point group $\bar{3}m$ and belongs to the hexagonal crystal family (trigonal crystal system). Corundum crystals can be described using a hexagonal or a rhombohedral axes system. For many reasons, it is often necessary to transform the

Table 1.19 Transformation relationships.

		$\cdot h$	$\cdot k$	$\cdot l$
		$\cdot a$	$\cdot b$	$\cdot c$
$h' =$	$a' =$	s_{11}	s_{12}	s_{13}
$k' =$	$b' =$	s_{21}	s_{22}	s_{23}
$l' =$	$c' =$	s_{31}	s_{32}	s_{33}

		$\cdot h'$	$\cdot k'$	$\cdot l'$
		$\cdot a'$	$\cdot b'$	$\cdot c'$
$h =$	$a =$	t_{11}	t_{12}	t_{13}
$k =$	$b =$	t_{21}	t_{22}	t_{23}
$l =$	$c =$	t_{31}	t_{32}	t_{33}

		$\cdot u'$	$\cdot v'$	$\cdot w'$
		$\cdot x'$	$\cdot y'$	$\cdot z'$
$u =$	$x =$	s_{11}	s_{21}	s_{31}
$v =$	$y =$	s_{12}	s_{22}	s_{32}
$w =$	$z =$	s_{13}	s_{23}	s_{33}

		$\cdot u$	$\cdot v$	$\cdot w$
		$\cdot x$	$\cdot y$	$\cdot z$
$u' =$	$x' =$	t_{11}	t_{21}	t_{31}
$v' =$	$y' =$	t_{12}	t_{22}	t_{32}
$w' =$	$z' =$	t_{13}	t_{23}	t_{33}

given crystal data from one axes system into the other one. A particular corundum crystal was described in the rhombohedral axes system. The crystal faces of it were measured and determined to be $(10\bar{1})$, (111), (411), (210), and $(31\bar{1})$. Physical properties of the crystal were measured along the following directions: [111], $[10\bar{1}]$, $[1\bar{1}0]$, $[2\bar{1}\,\bar{1}]$. For further studies, the corundum crystal has to be described in a hexagonal axes system. The relationships between the rhombohedral unit cell and the hexagonal cell are illustrated in Figure 1.57, where the obverse setting of the triple hexagonal cell ($\boldsymbol{a}_H$, $\boldsymbol{b}_H$, $\boldsymbol{c}_H$) with respect to the primitive rhombohedral cell ($\boldsymbol{a}_R$, $\boldsymbol{b}_R$, $\boldsymbol{c}_R$) has been chosen. A detailed description of the two possibilities of *obverse* and *reverse* settings is given in [28].

When we transform the rhombohedral cell (obverse setting) into the hexagonal cell and vice versa, the following relations for the basis vectors are given:

$$\begin{aligned} \boldsymbol{a}_H &= \boldsymbol{a}_R - \boldsymbol{b}_R \\ \boldsymbol{b}_H &= \boldsymbol{b}_R - \boldsymbol{c}_R \\ \boldsymbol{c}_H &= \boldsymbol{a}_R + \boldsymbol{b}_R + \boldsymbol{c}_R \end{aligned} \tag{1.50a}$$

$$\begin{aligned} \boldsymbol{a}_R &= 2/3\boldsymbol{a}_H + 1/3\boldsymbol{b}_H + 1/3\boldsymbol{c}_H \\ \boldsymbol{b}_R &= -1/3\boldsymbol{a}_H + 1/3\boldsymbol{b}_H + 1/3\boldsymbol{c}_H \\ \boldsymbol{c}_R &= -1/3\boldsymbol{a}_H - 2/3\boldsymbol{b}_H + 1/3\boldsymbol{c}_H \end{aligned} \tag{1.50b}$$

Thus, the transformation matrices for a primitive rhombohedral cell R into a triple hexagonal cell H (obverse setting), and vice versa, are

$$R \rightarrow H$$
$$\begin{pmatrix} 1 & -1 & 0 \\ 1 & 0 & -1 \\ 1 & 1 & 1 \end{pmatrix} \tag{1.51a}$$

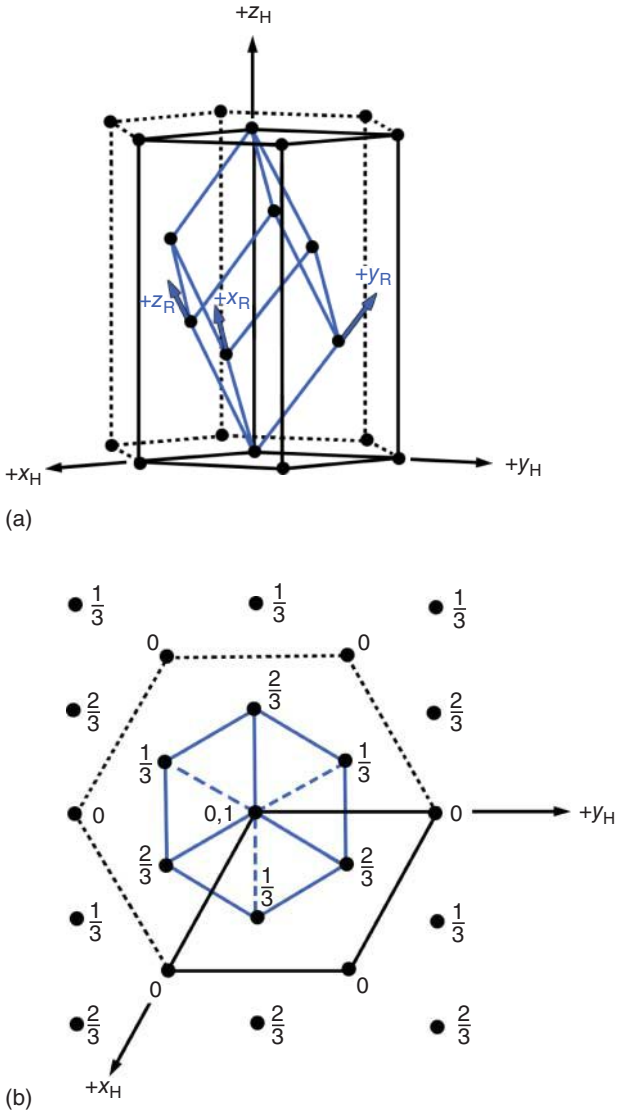

Figure 1.57 Unit cells of the rhombohedral lattice. (a) Obverse setting of primitive rhombohedral unit cell (x_R, y_R, z_R) and triple hexagonal cell (x_H, y_H, z_H). (b) Projection of the two cells along z_H (- - - lower edges of rhombohedron).

$$H \rightarrow R$$
$$\begin{pmatrix} 2/3 & 1/3 & 1/3 \\ -1/3 & 1/3 & 1/3 \\ -1/3 & -2/3 & 1/3 \end{pmatrix} \tag{1.51b}$$

The transformation of indices of lattice planes is given by the following equations:

$$R(hkl) \rightarrow H(h'k'l')$$
$$\begin{pmatrix} h' \\ k' \\ l' \end{pmatrix} = \begin{pmatrix} 1 & -1 & 0 \\ 0 & 1 & -1 \\ 1 & 1 & 1 \end{pmatrix} \cdot \begin{pmatrix} h \\ k \\ l \end{pmatrix} \tag{1.52a}$$

$$H(h'k'l') \rightarrow R(hkl)$$
$$\begin{pmatrix} h \\ k \\ l \end{pmatrix} = \begin{pmatrix} 2/3 & 1/3 & 1/3 \\ -1/3 & 1/3 & 1/3 \\ -1/3 & -2/3 & 1/3 \end{pmatrix} \cdot \begin{pmatrix} h' \\ k' \\ l' \end{pmatrix} \tag{1.52b}$$

Using Equation 1.52a, we will find the following change of Miller indices for the faces mentioned earlier: $(11.0)_H = (10\overline{1})_R$, $(00.1)_H = (111)_R$, $(10.2)_H = (411)_R$, $(11.3)_H = (210)_R$, and $(22.3)_H = (31\overline{1})_R$.

For the transformation of indices of directions, the transposed matrices $\boldsymbol{S}^{\boldsymbol{T}}(s_{ji})$ and $\boldsymbol{T}^{\boldsymbol{T}}(t_{ji})$ have to be used:

$$R(uvw) \rightarrow H(u'v'w')$$
$$\begin{pmatrix} u' \\ v' \\ w' \end{pmatrix} = \begin{pmatrix} 2/3 & -1/3 & -1/3 \\ 1/3 & 1/3 & -2/3 \\ 1/3 & 1/3 & 1/3 \end{pmatrix} \cdot \begin{pmatrix} u \\ v \\ w \end{pmatrix} \tag{1.53a}$$

$$H(u'v'w') \rightarrow R(uvw)$$
$$\begin{pmatrix} u \\ v \\ w \end{pmatrix} = \begin{pmatrix} 1 & 0 & 1 \\ -1 & 1 & 1 \\ 0 & -1 & 1 \end{pmatrix} \cdot \begin{pmatrix} u' \\ v' \\ w' \end{pmatrix} \tag{1.53b}$$

The following relations were calculated for the particular directions in the hexagonal and rhombohedral axes system:

$$[00.1]_{\mathrm{H}} = [111]_{\mathrm{R}}, [11.0]_{\mathrm{H}} = [10\overline{1}]_{\mathrm{R}}, [10.0]_{\mathrm{H}} = [1\overline{1}0]_{\mathrm{R}}, [21.0]_{\mathrm{H}} = [2\overline{11}]_{\mathrm{R}}$$

1.4.2 Crystallographic Space Groups

The concept of ***space groups*** enables the description of the whole spatial symmetry of a crystal at the atomic level. Thus, space groups can be applied to describe the symmetry of crystal structures. The 230 space group types in three dimensions were mathematically derived by the Russian crystallographer E.S. Fedorov and the German mathematician A. Schönflies in 1891. The space group concept assumes lattice periodicity. The experimental evidence for three-dimensional lattice periodicity of crystals was adduced by the famous X-ray diffraction experiment of W. Friedrich, P. Knipping, and M. von Laue in 1912 [30]. It should be noted that structures that exhibit deviations from lattice periodicity (e.g., aperiodic structures, OD

structures) have to be classified by different symmetry concepts (e.g., superspace groups and OD families).

1.4.2.1 General Remarks

The set of all symmetry operations (isometries) of an infinite crystal structure forms a space group. It is assumed as an ideal crystal without any crystal defect or any other distortion of the lattice periodicity. The following isometries can occur in space groups: *translations*, *identity*, *rotations*, ***screw rotations***, *reflections*, ***glide reflections***, *inversions*, and *rotoinversions.* In addition to translations and the well-known point symmetry operations, the list contains two symmetry operations, which we have not treated up to now. They are the result of the combination of a translation with a rotation (screw rotation) or with a reflection (glide reflection), respectively.

Screw Rotations The screw rotation is the combination of a rotation around an axis (screw axis) and a translation by a vector ***s*** (screw vector) parallel to the screw axis. When we rotate an off-axis lattice point around an n-fold proper rotation axis ($n = 1, 2, 3, 4, 6$), we will get an n-fold point arrangement in a plane perpendicular to this axis. Because of the translation periodicity, this arrangement is repeated along the rotation axis after the translation period t. The action of an n-fold screw operation rotates the point through an angle of $360°/n$, followed by a shift of magnitude $|s|$ parallel to the screw axis. If we apply the operation n-times, the point will be mapped in its initial position but shifted n-times of $|s|$, which corresponds to an integral number p of the translation t.

It yields $n \cdot s = p \cdot t$ or $s = (p/n)t$ (p, n – integers).

Because $s < t$, p takes on the values 0, 1, 2, …, $(n - 1)$. For $p = 0$, the screw rotation axis becomes a proper rotation axis. This means also that to every n-fold rotation axes exist $(n - 1)$ screw axes with screw components $s = (1/n)t$, $(2/n)t$, …, $((n - 1)/n)t$. The screw axes are denoted by the symbol n_p. There are 11 screw axes: 2_1, 3_1, 3_2, 4_1, 4_2, 4_3, 6_1, 6_2, 6_3, 6_4, and 6_5, which are illustrated together with the corresponding rotation axes in Figure 1.58.

The following screw axes form enantiomorphic pairs, that is, right- and left-handed screws, which are mirror image to each other: 3_1, 3_2; 4_1, 4_3; 6_1, 6_5; 6_2, 6_4. The 4_2 axis is also a twofold rotation axis (2_0). The 6_2 is at the same time a twofold rotation axis and a 3_2 screw axis. The 6_4 is also a twofold rotation axis and a 3_1 screw axis. The 6_3 is also a threefold rotation axis (3_0) and a twofold screw axis 2_1.

Glide Reflections In general, a glide reflection is the product of a reflection and a translation. We have a reflection through a plane, the so-called glide plane, and a subsequent translation by the glide vector parallel to the glide plane. The glide vector is a fraction of a lattice vector. The main glide operations are axial glides, diagonal glides, diamond glides, and double glides.

– ***Axial glides*** are symbolized by ***a***, ***b***, ***c***, with glide vectors $\frac{1}{2}\boldsymbol{a}$, $\frac{1}{2}\boldsymbol{b}$, or $\frac{1}{2}\boldsymbol{c}$, respectively.

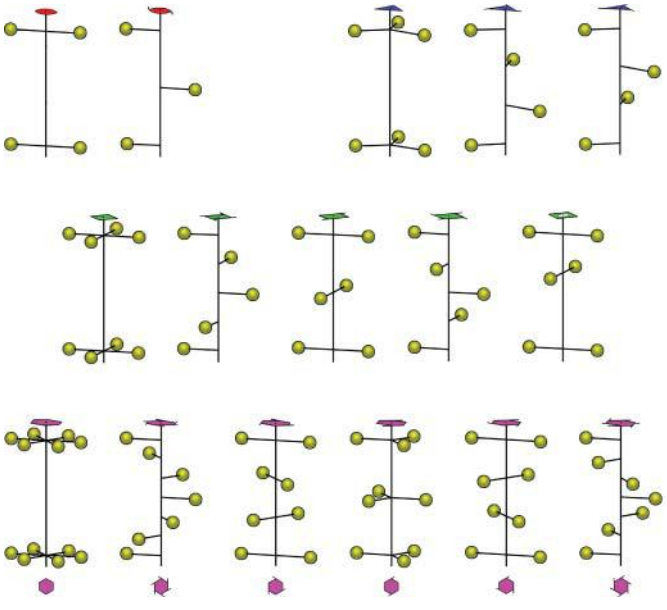

Figure 1.58 Illustration of screw and rotation axes.

- ***Diagonal glides*** are symbolized by *n* with glide vectors $^1/_2(\pm\boldsymbol{a} \pm \boldsymbol{b})$, $^1/_2(\pm\boldsymbol{b} \pm \boldsymbol{c})$, $^1/_2(\pm\boldsymbol{c} \pm \boldsymbol{a})$, or $^1/_2(\pm\boldsymbol{a} \pm \boldsymbol{b} \pm \boldsymbol{c})$,
- ***Diamond glides*** are symbolized by *d* with glide vectors $^1/_4(\pm\boldsymbol{a} \pm \boldsymbol{b})$, $^1/_4(\pm\boldsymbol{b} \pm \boldsymbol{c})$, $^1/_4(\pm\boldsymbol{c} \pm \boldsymbol{a})$, or $^1/_4(\pm\boldsymbol{a} \pm \boldsymbol{b} \pm \boldsymbol{c})$,
- ***Double glides*** (in centered cells only) are symbolized by *e* and have two glide vectors for one glide plane, which are perpendicular to each other with glide vectors $^1/_2\boldsymbol{a}$, $^1/_2\boldsymbol{b}$, or $^1/_2\boldsymbol{c}$, respectively.

The letter *g* is used in three-dimensional space for glide reflections, which can not be described by the abovementioned symbols and translation vectors [e.g., $g(^1/_2, ^1/_4, ^1/_4)$ $x, y - ^1/_4, y$ means a glide reflection with glide part $^1/_2$, $^1/_4$, $^1/_4$ and the glide plane at $x, y - ^1/_4, y$). In two-dimensional space, *g* is used as symbol for glide lines in the plane groups.

The illustration of the action of a *c*-type glide reflection shows that, after applying the glide operation twice, the movement of the motif corresponds to a lattice translation. In Figure 1.59, the action of a twofold screw axis and a *c*-glide plane is illustrated.

At first sight, one can think that the positions are identical with respect to the coordinates. The action of the glide reflection provides a mirror image of the two spheres. We see the same side of the two spheres. The action of the screw turns around the spheres; thus, we see now that the small black sphere is on the backside. This means the spheres are congruently equivalent and not enantiomorphous to each other.

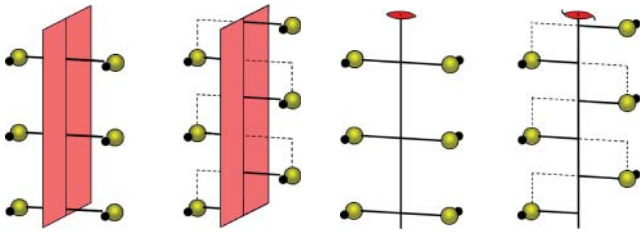

Figure 1.59 Illustration of action of a *c*-glide plane (a) and a twofold screw axis 2_1 (b).

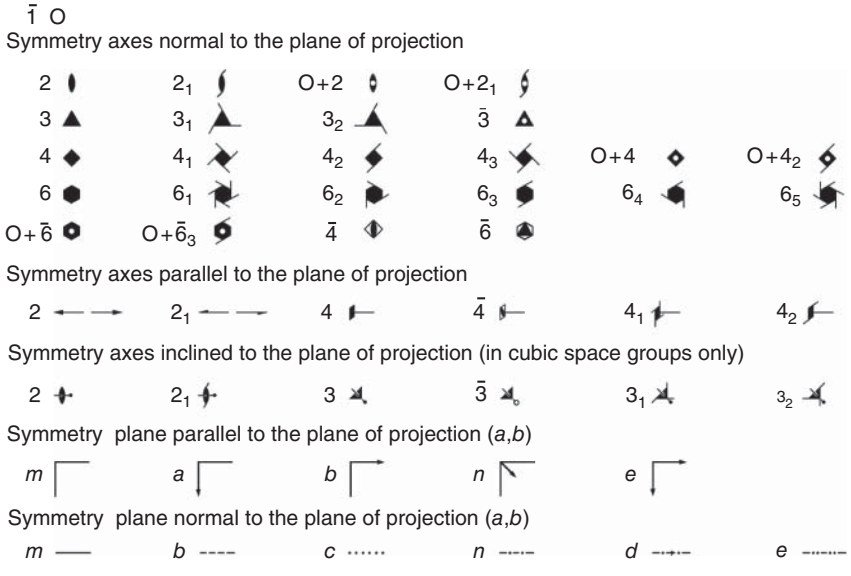
$\bar{1}$ O
Symmetry axes normal to the plane of projection
2 2_1 O+2 O+2_1
3 3_1 3_2 $\bar{3}$
4 4_1 4_2 4_3 O+4 O+4_2
6 6_1 6_2 6_3 6_4 6_5
O+$\bar{6}$ O+$\bar{6}_3$ $\bar{4}$ $\bar{6}$
Symmetry axes parallel to the plane of projection
2 2_1 4 $\bar{4}$ 4_1 4_2
Symmetry axes inclined to the plane of projection (in cubic space groups only)
2 2_1 3 $\bar{3}$ 3_1 3_2
Symmetry plane parallel to the plane of projection (*a*,*b*)
m *a* *b* *n* *e*
Symmetry plane normal to the plane of projection (*a*,*b*)
m *b* *c* *n* *d* *e*

Figure 1.60 Graphical symbols for the description of symmetry elements.

An assembly of the main graphical symbols for symmetry elements as used for the space group diagrams is given in Figure 1.60.

Now, we will give a brief phenomenological explanation for the derivation of space groups in order to get more familiar with the meaning of a space group. When we classified the point lattices into the 14 possible Bravais lattice types, we have shown that the symmetry of the lattices corresponds to the seven holoedries. This means we have the following 14 space group classes that characterize the possible symmetry types of point lattices: $P\bar{1}$; $P2/m$, $C2/m$; $Pmmm$, $Immm$, $Fmmm$; $P4/mmm$, $I4/mmm$; $R3m$; $P6/mmm$; and $Pm\bar{3}m$, $Im\bar{3}m$, $Fm\bar{3}m$. The symmetry types of the point lattices are restricted to the seven holoedries. When we combine (multiply) the Bravais lattice types with the 32 possible crystallographic point groups, 73 ***symmorphic space groups*** will result. Strictly speaking, the symmorphic space groups are mathematically described as the semidirect

product of the translation group T with the point group P. The international space group notation (Hermann–Mauguin symbol) shows us directly whether a ***symmorphic*** or a ***nonsymmorphic*** space group is given. The first letter (P, A, B, C, I, F, R) symbolizes the Bravais lattice type. These letters define the symmetry in one, two, or three specific symmetry directions (Blickrichtungen) as already explained for the description of point groups. If the space group symbol consists of an unmodified point group symbol, a symmorphic space group exist. For a nonsymmorphic space group symbols of glide planes and/or screw axes are given in the notation (e.g., $P2_1/m$, $P2_1/c$, $Pnma$). The unmodified point group symbol of a symorphous space group tells us that the space group can be fully generated by translations and point group operations. However, we should be aware of the fact that symmorphic space groups exist where screw axes and/or glide planes are present (e.g., $C2/m$, $F23$). Similar as for the description of point groups, in addition to the international Hermann–Mauguin symbols, the Schoenflies notation is used. The Schoenflies symbol for a space group consists of the Schoenflies point group symbol with an additional superscript n, where n enumerates the number of the space group belonging to the point group. From the Schoenflies symbol of a space group, we can only retrieve directly the information to which point group the space group belongs. The information on the lattice type and on symmorphic or nonsymmorphic symmetries is only indirectly possible with large restrictions.

From the 73 symmorphic space groups, the 157 nonsymmorphic space groups can be derived by a systematic substitution of the rotation axes (proper and improper) by screw axes and the mirror planes by glide planes. We will illustrate the procedure for the simple tetragonal point group 4. According to the two Bravais lattice types for the tetragonal crystal system, we have the symmorphic space groups $P4$ and $I4$. We replace now the rotation axis by the screw axes, which provides the total of the following six space groups: $P4$, $P4_1$, $P4_2$, $P4_3$, $I4$, and $I4_1$ (the symmetry of formally possible space groups $I4_2$ and $I4_3$ is identical with $I4$ and $I4_1$, respectively, and has, therefore, not to be considered). This procedure of combining the different symmetry operations was applied systematically by Schoenflies using the group theory for the derivation of the 230 space groups. Among them are 65 space group types, which consist only of symmetry operations of the first kind (rotations, screw rotations, and translations). These groups were the result of Leopold Sohncke's (1874) systematical studies of infinite regular point systems. The Sohncke groups are nowadays of great importance because the symmetry of all biological macromolecules can be described by one of the Sohncke groups. The 11 pairs of enantiomorphic space groups belong to these groups:

$$P3_1 - P3_2; P3_112 - P3_212; P3_121 - P3_221; P4_1 - P4_3;$$
$$P4_1\,22 - P4_322; P4_12_12 - P4_32_12;$$
$$P6_1 - P6_5; P6_2 - P6_4; P6_122 - P6_522; P6_222 - P6_422; P4_132 - P4_322$$

Now, we will give a more detailed description of the construction of space groups and will show what kind of structural information can be retrieved from the representation of space groups in the International Tables for Crystallography [31, 32].

1.4.2.2 The International Tables for Crystallography – The Reference Book for the Representation of Space Group Symmetries

A comprehensive overview of the fundamentals of mathematical crystallography for the description of crystals and their symmetry is given in Volume A "Space group symmetry" [31] and Volume A1 "Symmetry relations between space groups" of the International Tables for Crystallography [32]. The 17 two-dimensional space group types (plane groups) and 230 three-dimensional space group types are tabulated in [31]. In addition, there exists a brief teaching edition of Volume A "Space group symmetry," which we highly recommend for readers who are not extensively trained in crystallography [33]. The detailed user guide given in the tables should enable the reader to extract the most relevant information from the tables and the space group diagrams. The 230 space group types are arranged in the International Tables according to the schema shown in Figure 1.61.

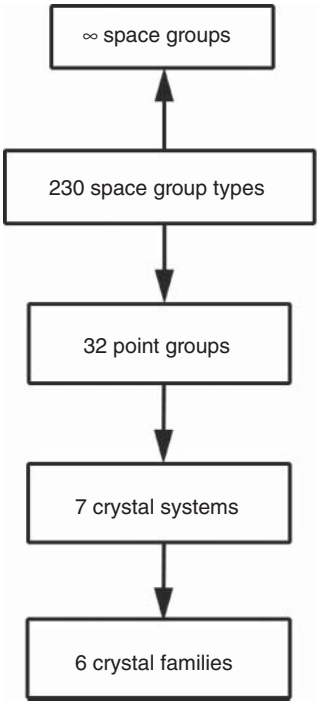

Figure 1.61 Classification schema of crystallographic space groups in the International Tables.

In general, a space group is specified by the following characteristic features

- translational symmetry
- point symmetry
- metric of lattice.

A space group type as tabulated in the International Tables is characterized only by the translational and point symmetry without considering the specific parameters of the unit cell.

Silicon and germanium crystallize both in the space group type $Fd\bar{3}m$. They also occupy the same Wyckoff positions, but they differ in the lattice parameter a_0. Thus, we have two different space groups belonging to the same space group type. The number of crystallographic space group types in three dimensions is restricted to 230, but the number of possible space groups is infinite. The so-called 219 affine space group types are given if the splitting into the 11 enantiomorphic pairs of space group types is neglected by allowing left- and right-handed coordinate systems. The 230 space group types are arranged in the table according to the 32 geometric crystal classes, the corresponding 7 crystal systems, and 6 crystal families, respectively. A detailed description of mathematical classification of space groups, point groups, and lattices is given in [34].

The space groups of the hexagonal crystal family contain the space groups of the trigonal and hexagonal crystal systems. The 25 space groups of the trigonal crystal system incorporate 18 space groups with the hexagonal Bravais lattice *hP* and 7 space groups with rhombohedral Bravais lattice *hR*. The seven rhombohedral space groups are described in the tables for both a hexagonal and a rhombohedral coordinate system. The 13 space groups of the monoclinic system are described for both *b*-unique axis and *c*-unique axis setting for three unit cell choices. For all orthorhombic space groups, six settings exist, which will be shown later. The 230 space group types are listed in Table 1.20.

In the following, we will briefly explain the content and arrangement of the tables using the representation of the orthorhombic space group *Pnma* (Figure 1.62):

(1, 2) Header Section The first line starts with the short Hermann–Mauguin symbol (international symbol) for the space group, followed by the Schoenflies symbol, the short international symbol for the point group, and the type of the crystal system. In our example, *Pnma* is the sixteenth space group of the point group D_{2h}^{16}.The second line of the header section contains the sequential number of the space group (here, number 62 of the 230 space group types), the full international (Hermann–Mauguin) symbol for the space group, and the Patterson symmetry. The Patterson symmetry provides us the space group symmetry of the Patterson function. The Patterson function is the autocorrelation function of the electron

Table 1.20 The 230 crystallographic space groups.

Crystal system	Point group	Space group number	International Symbol (Hermann–Mauguin notation)		Schoenflies symbol
			Short	Full	
Triclinic	1	1	$P1$	$P1$	C_1^1
	$\bar{1}$	2	$P\bar{1}$	$P\bar{1}$	C_i^1
Monoclinic	2	3	$P2$	$P2$	C_2^1
		4	$P2_1$	$P2_1$	C_2^2
		5	$C2$	$C2$	C_2^3
	m	6	Pm	Pm	C_S^1
		7	Pc	Pc	C_S^2
		8	Cm	Cm	C_S^3
		9	Cc	Cc	C_S^4
	$2/m$	10	$P2/m$	$P2/m$	C_{2h}^1
		11	$P2_1/m$	$P2_1/m$	C_{2h}^2
		12	$C2/m$	$C2/m$	C_{2h}^3
		13	$P2/c$	$P2/c$	C_{2h}^4
		14	$P2_1/c$	$P2_1/c$	C_{2h}^5
		15	$C2/c$	$C2/c$	C_{2h}^6
Orthorhombic	222	16	$P222$	$P222$	D_2^1
		17	$P222_1$	$P222_1$	D_2^2
		18	$P2_12_12$	$P2_12_12$	D_2^3
		19	$P2_12_12_1$	$P2_12_12_1$	D_2^4
		20	$C222_1$	$C222_1$	D_2^5
		21	$C222$	$C222$	D_2^6
		22	$F222$	$F222$	D_2^7
		23	$I222$	$I222$	D_2^8
		24	$I2_12_12_1$	$I2_12_12_1$	D_2^9
	$mm2$	25	$Pmm2$	$Pmm2$	C_{2v}^1
		26	$Pmc2_1$	$Pmc2_1$	C_{2v}^2
		27	$Pcc2$	$Pcc2$	C_{2v}^3
		28	$Pma2$	$Pma2$	C_{2v}^4
		29	$Pca2_1$	$Pca2_1$	C_{2v}^5
		30	$Pnc2$	$Pnc2$	C_{2v}^6
		31	$Pmn2_1$	$Pmn2_1$	C_{2v}^7
		32	$Pba2$	$Pba2$	C_{2v}^8
		33	$Pna2_1$	$Pna2_1$	C_{2v}^9
		34	$Pnn2$	$Pnn2$	C_{2v}^{10}
		35	$Cmm2$	$Cmm2$	C_{2v}^{11}
		36	$Cmc2_1$	$Cmc2_1$	C_{2v}^{12}
		37	$Ccc2$	$Ccc2$	C_{2v}^{13}

Table 1.20 (*Continued*)

Crystal system	Point group	Space group number	International Symbol (Hermann–Mauguin notation)		Schoenflies symbol
			Short	Full	
		38	*Amm*2	*Amm*2	C_{2v}^{14}
		39	*Aem*2	*Aem*2	C_{2v}^{15}
		40	*Ama*2	*Ama*2	C_{2v}^{16}
		41	*Aea*2	*Aea*2	C_{2v}^{17}
		42	*Fmm*2	*Fmm*2	C_{2v}^{18}
		43	*Fdd*2	*Fdd*2	C_{2v}^{19}
		44	*Imm*2	*Imm*2	C_{2v}^{20}
		45	*Iba*2	*Iba*2	C_{2v}^{21}
		46	*Ima*2	*Ima*2	C_{2v}^{22}
	mmm	47	*Pmmm*	$P2/m\ 2/m\ 2/m$	D_{2h}^{1}
		48	*Pnnn*	$P2/n\ 2/n\ 2/n$	D_{2h}^{2}
		49	*Pccm*	$P2/c\ 2/c\ 2/m$	D_{2h}^{3}
		50	*Pban*	$P2/b\ 2/a\ 2/n$	D_{2h}^{4}
		51	*Pmma*	$P2_1/m\ 2/m\ 2/a$	D_{2h}^{5}
		52	*Pnna*	$P2/n\ 2_1/n\ 2/a$	D_{2h}^{6}
		53	*Pmna*	$P2/m\ 2/n\ 2_1/a$	D_{2h}^{7}
		54	*Pcca*	$P2_1/c\ 2/c\ 2/a$	D_{2h}^{8}
		55	*Pbam*	$P2_1/b\ 2_1/a\ 2/m$	D_{2h}^{9}
		56	*Pccn*	$P2_1/c\ 2_1/c\ 2/n$	D_{2h}^{10}
		57	*Pbcm*	$P2/b\ 2_1/c\ 2_1/m$	D_{2h}^{11}
		58	*Pnnm*	$P2_1/n\ 2_1/n\ 2/m$	D_{2h}^{12}
		59	*Pmmn*	$P2_1/m\ 2_1/m\ 2/n$	D_{2h}^{13}
		60	*Pbcn*	$P2_1/b\ 2/c\ 2_1/n$	D_{2h}^{14}
		61	*Pbca*	$P2_1/b\ 2_1/c\ 2_1/a$	D_{2h}^{15}
		62	*Pnma*	$P2_1/n\ 2_1/m\ 2_1/a$	D_{2h}^{16}
		63	*Cmcm*	$C2/m\ 2/c\ 2_1/m$	D_{2h}^{17}
		64	*Cmce*	$C2/m\ 2/c\ 2_1/e$	D_{2h}^{18}
		65	*Cmmm*	$C2/m\ 2/m\ 2/m$	D_{2h}^{19}
		66	*Cccm*	$C2/c\ 2/c\ 2/m$	D_{2h}^{20}
		67	*Cmme*	$C2/m\ 2/m\ 2/e$	D_{2h}^{21}
		68	*Ccce*	$C2/c\ 2/c\ 2/e$	D_{2h}^{22}
		69	*Fmmm*	$F2/m\ 2/m\ 2/m$	D_{2h}^{23}
		70	*Fddd*	$F2/d\ 2/d\ 2/m$	D_{2h}^{24}
		71	*Immm*	$I2/m\ 2/m\ 2/m$	D_{2h}^{25}
		72	*Ibam*	$I2/b\ 2/a\ 2/m$	D_{2h}^{26}
		73	*Ibca*	$I2_1/b\ 2_1/c\ 2_1/c$	D_{2h}^{27}
		74	*Imma*	$I2_1/m\ 2_1/m\ 2_1/a$	D_{2h}^{28}

(*continued overleaf*)

Table 1.20 (*Continued*)

Crystal system	Point group	Space group number	International Symbol (Hermann–Mauguin notation)		Schoenflies symbol
			Short	Full	
Tetragonal	4	75	$P4$	$P4$	C_4^1
		76	$P4_1$	$P4_1$	C_4^2
		77	$P4_2$	$P4_2$	C_4^3
		78	$P4_3$	$P4_3$	C_4^4
		79	$I4$	$I4$	C_4^5
		80	$I4_1$	$I4_1$	C_4^6
	$\bar{4}$	81	$P\bar{4}$	$P\bar{4}$	S_4^1
		82	$I\bar{4}$	$I\bar{4}$	S_4^2
	$4/m$	83	$P4/m$	$P4/m$	C_{4h}^1
		84	$P4_2/m$	$P4_2/m$	C_{4h}^2
		85	$P4/n$	$P4/n$	C_{4h}^3
		86	$P4_2/n$	$P4_2/n$	C_{4h}^4
		87	$I4/m$	$I4/m$	C_{4h}^5
		88	$I4_1/a$	$I4_1/a$	C_{4h}^6
	422	89	$P422$	$P422$	D_4^1
		90	$P42_12$	$P42_12$	D_4^2
		91	$P4_122$	$P4_122$	D_4^3
		92	$P4_12_12$	$P4_12_12$	D_4^4
		93	$P4_222$	$P4_222$	D_4^5
		94	$P4_22_12$	$P4_22_12$	D_4^6
		95	$P4_322$	$P4_322$	D_4^7
		96	$P4_32_12$	$P4_32_12$	D_4^8
		97	$I422$	$I422$	D_4^9
		98	$I4_122$	$I4_122$	D_4^{10}
	$4mm$	99	$P4mm$	$P4mm$	C_{4v}^1
		100	$P4bm$	$P4bm$	C_{4v}^2
		101	$P4_2cm$	$P4_2cm$	C_{4v}^3
		102	$P4_2nm$	$P4_2nm$	C_{4v}^4
		103	$P4cc$	$P4cc$	C_{4v}^5
		104	$P4nc$	$P4nc$	C_{4v}^6
		105	$P4_2mc$	$P4_2mc$	C_{4v}^7
		106	$P4_2bc$	$P4_2bc$	C_{4v}^8
		107	$I4mm$	$I4mm$	C_{4v}^9
		108	$I4cm$	$I4cm$	C_{4v}^{10}
		109	$I4_1md$	$I4_1md$	C_{4v}^{11}
		110	$I4_1cd$	$I4_1cd$	C_{4v}^{12}

Table 1.20 (*Continued*)

Crystal system	Point group	Space group number	International Symbol (Hermann–Mauguin notation)		Schoenflies symbol
			Short	Full	
	$\bar{4}2m$	111	$P\bar{4}2m$	$P\bar{4}2m$	D_{2d}^{1}
		112	$P\bar{4}2c$	$P\bar{4}2c$	D_{2d}^{2}
		113	$P\bar{4}2_1m$	$P\bar{4}2_1m$	D_{2d}^{3}
		114	$P\bar{4}2_1c$	$P\bar{4}2_1c$	D_{2d}^{4}
		115	$P\bar{4}m2$	$P\bar{4}m2$	D_{2d}^{5}
		116	$P\bar{4}c2$	$P\bar{4}c2$	D_{2d}^{6}
		117	$P\bar{4}b2$	$P\bar{4}b2$	D_{2d}^{7}
		118	$P\bar{4}n2$	$P\bar{4}n2$	D_{2d}^{8}
		119	$I\bar{4}m2$	$I\bar{4}m2$	D_{2d}^{9}
		120	$I\bar{4}c2$	$I\bar{4}c2$	D_{2d}^{10}
		121	$I\bar{4}2m$	$I\bar{4}2m$	D_{2d}^{11}
		122	$I\bar{4}2d$	$I\bar{4}2d$	D_{2d}^{12}
	$4/mmm$	123	$P4/mmm$	$P4/m\ 2/m\ 2/m$	D_{4h}^{1}
		124	$P4/mcc$	$P4/m\ 2/c\ 2/c$	D_{4h}^{2}
		125	$P4/nbm$	$P4/n\ 2/b\ 2/m$	D_{4h}^{3}
		126	$P4/nnc$	$P4/n\ 2/n\ 2/c$	D_{4h}^{4}
		127	$P4/mbm$	$P4/m\ 2_1/b\ 2/m$	D_{4h}^{5}
		128	$P4/mnc$	$P4/m\ 2_1/n\ 2/c$	D_{4h}^{6}
		129	$P4/nmm$	$P4/n\ 2_1/m\ 2/m$	D_{4h}^{7}
		130	$P4/ncc$	$P4/n\ 2/c\ 2/c$	D_{4h}^{8}
		131	$P4/mmc$	$P4_2/m\ 2/m\ 2/c$	D_{4h}^{9}
		132	$P4/mcm$	$P4_2/m\ 2/c\ 2/m$	D_{4h}^{10}
		133	$P4/nbc$	$P4_2/n\ 2/b\ 2/c$	D_{4h}^{11}
		134	$P4/nnm$	$P4_2/n\ 2/n\ 2/m$	D_{4h}^{12}
		135	$P4/mbc$	$P4_2/m\ 2_1/b\ 2/c$	D_{4h}^{13}
		136	$P4/mnm$	$P4_2/m\ 2_1/n\ 2/m$	D_{4h}^{14}
		137	$P4/nmc$	$P4_2/n\ 2_1/m\ 2/c$	D_{4h}^{15}
		138	$P4/ncm$	$P4_2/n\ 2_1/c\ 2/m$	D_{4h}^{16}
		139	$I4/mmm$	$I4/m\ 2/m\ 2/m$	D_{4h}^{17}
		140	$I4/mcm$	$I4/m\ 2/c\ 2/m$	D_{4h}^{18}
		141	$I4/amd$	$I4_1/a\ 2/m\ 2/d$	D_{4h}^{19}
		142	$I4/acd$	$I4_1/a\ 2/c\ 2/d$	D_{4h}^{20}
Trigonal	3	143	$P3$	$P3$	C_3^1
		144	$P3_1$	$P3_1$	C_3^2
		145	$P3_2$	$P3_2$	C_3^3
		146	$R3$	$R3$	C_3^4

(*continued overleaf*)

Table 1.20 (*Continued*)

Crystal system	Point group	Space group number	International Symbol (Hermann–Mauguin notation)		Schoenflies symbol
			Short	Full	
	$\bar{3}$	147	$P\bar{3}$	$P\bar{3}$	C_{3i}^{1}
		148	$R\bar{3}$	$R\bar{3}$	C_{3i}^{2}
	32	149	$P312$	$P312$	D_{3}^{1}
		150	$P321$	$P321$	D_{3}^{2}
		151	$P3_112$	$P3_112$	D_{3}^{3}
		152	$P3_121$	$P3_121$	D_{3}^{4}
		153	$P3_212$	$P3_212$	D_{3}^{5}
		154	$P3_221$	$P3_221$	D_{3}^{6}
		155	$R32$	$R32$	D_{3}^{7}
	$3m$	156	$P3m1$	$P3m1$	C_{3v}^{1}
		157	$P31m$	$P31m$	C_{3v}^{2}
		158	$P3c1$	$P3c1$	C_{3v}^{3}
		159	$P31c$	$P31c$	C_{3v}^{4}
		160	$R3m$	$R3m$	C_{3v}^{5}
		161	$R3c$	$R3c$	C_{3v}^{6}
	$\bar{3}m$	162	$P\bar{3}1m$	$P\bar{3}12/m$	D_{3d}^{1}
		163	$P\bar{3}1c$	$P\bar{3}12/c$	D_{3d}^{2}
		164	$P\bar{3}m1$	$P\bar{3}2/m1$	D_{3d}^{3}
		165	$P\bar{3}c1$	$P\bar{3}2/c1$	D_{3d}^{4}
		166	$R\bar{3}m$	$R\bar{3}2/m$	D_{3d}^{5}
		167	$R\bar{3}c$	$R\bar{3}2/c$	D_{3d}^{6}
Hexagonal	6	168	$P6$	$P6$	C_{6}^{1}
		169	$P6_1$	$P6_1$	C_{6}^{2}
		170	$P6_5$	$P6_5$	C_{6}^{3}
		171	$P6_2$	$P6_2$	C_{6}^{4}
		172	$P6_4$	$P6_4$	C_{6}^{5}
		173	$P6_3$	$P6_3$	C_{6}^{6}
	$\bar{6}$	174	$P\bar{6}$	$P\bar{6}$	C_{3h}^{1}
	$6/m$	175	$P6/m$	$P6/m$	C_{6h}^{1}
		176	$P6_3/m$	$P6_3/m$	C_{6h}^{2}
	622	177	$P622$	$P622$	D_{6}^{1}
		178	$P6_122$	$P6_122$	D_{6}^{2}
		179	$P6_522$	$P6_522$	D_{6}^{3}
		180	$P6_222$	$P6_222$	D_{6}^{4}
		181	$P6_422$	$P6_422$	D_{6}^{5}
		182	$P6_322$	$P6_322$	D_{6}^{6}

Table 1.20 (*Continued*)

Crystal system	Point group	Space group number	International Symbol (Hermann–Mauguin notation)		Schoenflies symbol
			Short	Full	
	$6mm$	183	$P6mm$	$P6mm$	C_{6v}^1
		184	$P6cc$	$P6cc$	C_{6v}^2
		185	$P6_3cm$	$P6_3cm$	C_{6v}^3
		186	$P6_3mc$	$P6_3mc$	C_{6v}^4
	$\bar{6}m2$	187	$P\bar{6}m2$	$P\bar{6}m2$	D_{3h}^1
		188	$P\bar{6}c2$	$P\bar{6}c2$	D_{3h}^2
		189	$P\bar{6}2m$	$P\bar{6}2m$	D_{3h}^3
		190	$P\bar{6}2c$	$P\bar{6}2c$	D_{3h}^4
	$6/mmm$	191	$P6/mmm$	$P6/m\ 2/m\ 2/m$	D_{6h}^1
		192	$P6/mcc$	$P6/m\ 2/c\ 2/c$	D_{6h}^2
		193	$P6_3/mcm$	$P6_3/m\ 2/c\ 2/m$	D_{6h}^3
		194	$P6_3/mmc$	$P6_3/m\ 2/m\ 2/c$	D_{6h}^4
Cubic	23	195	$P23$	$P23$	T^1
		196	$F23$	$F23$	T^2
		197	$I23$	$I23$	T^3
		198	$P2_13$	$P2_13$	T^4
		199	$I2_13$	$I2_13$	T^5
	$m\bar{3}$	200	$Pm\bar{3}$	$P2/m\bar{3}$	T_h^1
		201	$Pn\bar{3}$	$P2/n\bar{3}$	T_h^2
		202	$Fm\bar{3}$	$F2/m\bar{3}$	T_h^3
		203	$Fd\bar{3}$	$F2/d\bar{3}$	T_h^4
		204	$Im\bar{3}$	$I2/m\bar{3}$	T_h^5
		205	$Pa\bar{3}$	$P2/a\bar{3}$	T_h^6
		206	$Ia\bar{3}$	$I2/a\bar{3}$	T_h^7
	432	207	$P432$	$P432$	O^1
		208	$P4_232$	$P4_232$	O^2
		209	$F432$	$F432$	O^3
		210	$F4_132$	$F4_132$	O^4
		211	$I432$	$I432$	O^5
		212	$P4_332$	$P4_332$	O^6
		213	$P4_132$	$P4_132$	O^7
		214	$I4_132$	$I4_132$	O^8
	$\bar{4}3m$	215	$P\bar{4}3m$	$P\bar{4}3m$	T_d^1
		216	$F\bar{4}3m$	$F\bar{4}3m$	T_d^2
		217	$I\bar{4}3m$	$I\bar{4}3m$	T_d^3
		218	$P\bar{4}3n$	$P\bar{4}3n$	T_d^4

(*continued overleaf*)

Table 1.20 (*Continued*)

Crystal system	Point group	Space group number	International Symbol (Hermann–Mauguin notation)		Schoenflies symbol
			Short	Full	
		219	$F\bar{4}3c$	$F\bar{4}\bar{3}c$	T_d^5
		220	$I\bar{4}3d$	$I\bar{4}\bar{3}d$	T_d^6
	$m\bar{3}m$	221	$Pm\bar{3}m$	$P4/m\ \bar{3}\ 2/m$	O_h^1
		222	$Pn\bar{3}n$	$P4/n\ \bar{3}\ 2/n$	O_h^2
		223	$Pm\bar{3}n$	$P4_2/m\ \bar{3}\ 2/n$	O_h^3
		224	$Pn\bar{3}m$	$P4_2/n\ \bar{3}\ 2/n$	O_h^4
		225	$Fm\bar{3}m$	$F4/m\ \bar{3}\ 2/m$	O_h^5
		226	$Fm\bar{3}c$	$F4/m\ \bar{3}\ 2/c$	O_h^6
		227	$Fd\bar{3}m$	$F4_1/d\ \bar{3}\ 2/m$	O_h^7
		228	$Fd\bar{3}c$	$F4_1/d\ \bar{3}\ 2/c$	O_h^8
		229	$Im\bar{3}m$	$I4/m\ \bar{3}\ 2/m$	O_h^9
		230	$Ia\bar{3}d$	$I4_1/a\ \bar{3}\ 2/d$	O_h^{10}

density and can be written as

$$P(\vec{u}) = \int \rho(\vec{r})\rho(\vec{r} + \vec{u})d\vec{r}$$

$$P(uvw) = \frac{1}{V}\sum_{h,k,l=-\infty}^{+\infty} |F(hkl)|^2 \exp[-2\pi i(hu + kv + lw)] \tag{1.54}$$

This function is very useful for the structure determination. For a detailed description of the Patterson function for crystal structure determination, see, for example, [35]. The relationship between the structure and the corresponding Patterson function is illustrated in Figure 1.63.

The main properties of the Patterson function $P(u)$ are as follows:

- $P(u)$ is always centrosymmetric.
- $P(u)$ has the same unit cell as the electron density.
- For n atoms in the unit cell, there are $n(n-1)$ maxima according to the $n-1$ interatomic vectors from each atom and a maximum at the origin.

One of the practical advantages is that the Patterson function can be directly calculated from the intensities of the reflections of a diffraction pattern without the knowledge of the phases of the scattered waves.

If the space group of a crystal structure is known, one can easily derive the symbol for the Patterson symmetry of the space group. For nonsymmorphic space groups, the symbols of screw axes and glide planes have to be replaced by symbols of rotation axes and mirror planes. Thus, we have then generated the symbol of a symmorphic space group. Because the Patterson function has to be centrosymmetric, we have to add an inversion center if the symmorphic space group is noncentrosymmetric. The combination of the 11 centrosymmetric point groups (Laue

classes) with the possible Bravais lattices of the crystal families results in 24 different Patterson symmetries for the 230 space group types. We should be aware of the fact that the combination of the hexagonal Bravais lattice P with the point group $3m$ provides two different Patterson symmetries $P31m$(space group number 162) and $P3m1$(space group number 164).

(3) Space Group Diagrams In general, the diagrams provide us the information about the symmetry elements within the unit cell and illustrate the arrangement of a set of symmetry equivalent points located at general position. For all orthorhombic space groups, four diagrams for the standard setting *abc* of the axes are printed as shown in Figure 1.62.

The general position diagram corresponds to the symmetry projection along the [001] axis (diagram upper left). There exist six different settings for the orthorhombic space groups. It is quite clear that each setting results in a different space group symbol as shown below for our example.

Axes setting	*abc*	*ba−c*	*cab*	*−cba*	*bca*	*a−cb*
Space group	*Pnma*	*Pmn*	*Pbnm*	*Pcmn*	*Pmcn*	*Pnam*

The different full space group symbols for these settings are also given in the three projections of the symmetry elements of the so-called standard setting *abc.* We will explain this fact using the [001] projection given in the upper left of Figure 1.62. First, we will read this diagram as projection along c', where the b'-axis is horizontal, a'-axis vertical, and the origin in the upper left corner. Then, this setting leads to the same space group symbol as for the given standard setting. The new space group symbol is printed above the projection. Second, we will read this diagram as projection along c', where now the b'-axis is vertical and the a'-axis is horizontal. The new space group symbol is printed at the left. In order to get the conventional orientation, one has to rotate the projection about 90°, and then, the symbol is given above the projection as usual. This setting corresponds to $a' = b$, $b' = -a$, $c' = c$ with the space group symbol *Pmnb.* This procedure can be done for all three projections. In this way, we can understand the change of the space group symbols with the change of the chosen setting. The projections of the framework of the symmetry elements provide us the location and orientation of the symmetry elements. If any symmetry element of a projection is located in a height above the projection plane, the height is printed next to the graphical symbol of the symmetry element. From the [001] projection, we can see that the a-glide plane parallel to the (x,y)-projection plane is located at $z = 1/4$ and the twofold-screw axes 2(1/2, 0, 0) are also located at $z = 1/4(x, 1/4, 1/4; x, 3/4, 1/4)$.

In the lower right, the general position diagram is given projected onto the (001) plane. A set of symmetrically equivalent points is occupying the *general position* if the site symmetry group of the points is 1. The site symmetry group tells us the symmetry operations, which leave the points fixed. There exists only one general position for each of the 230 space group types. The following symbols are used to represent the different types of points:

1 *Pnma* D_{2h}^{16} *mmm* Orthorhombic

2 No. 62 *P* $2_1/n$ $2_1/m$ $2_1/a$ Patterson symmetry *P mmm*

3

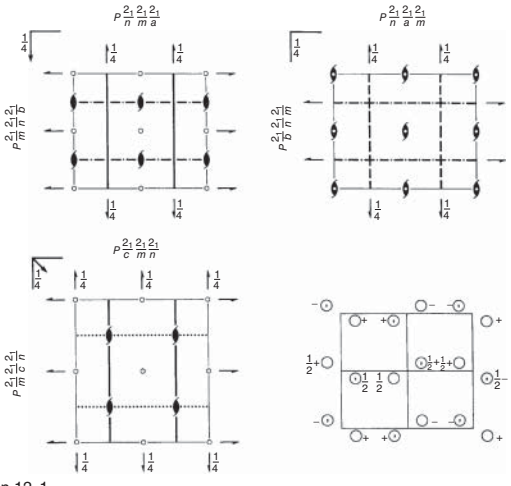

4 Origin at 1 on 12_11

5 Asymmetric unit $0 \le x \le \frac{1}{2}$; $0 \le y \le \frac{1}{4}$; $0 \le z \le 1$

6 Symmetry operations

(1) 1 (2) $2(0,0,\frac{1}{2})$ $\frac{1}{4},0,z$ (3) $2(0,\frac{1}{2},0)$ $0,y,0$ (4) $2(\frac{1}{2},0,0)$ $x,\frac{1}{4},\frac{1}{4}$

(5) $\bar{1}$ 0,0,0 (6) *a* $x,y,\frac{1}{4}$ (7) *m* $x,\frac{1}{4},z$ (8) *n* $(0,\frac{1}{2},\frac{1}{2})$ $\frac{1}{4},y,z$

7 Generators selected (1); *t*(1,0,0); *t*(0,1,0); *t*(0,0,1); (2); (3); (5)

8 Positions

Multiplicity, Wyckoff letter, Site symmetry	Coordinates	Reflection conditions
		General:
8 *d* 1	(1) x,y,z (2) $\bar{x}+\frac{1}{2},\bar{y},z+\frac{1}{2}$ (3) $\bar{x},y+\frac{1}{2},\bar{z}$ (4) $x+\frac{1}{2},\bar{y}+\frac{1}{2},\bar{z}+\frac{1}{2}$	$0kl : k + l = 2n$
	(5) $\bar{x},\bar{y},\bar{z}$ (6) $\bar{x}+\frac{1}{2},y,\bar{z}+\frac{1}{2}$ (7) $x,\bar{y}+\frac{1}{2},z$ (8) $\bar{x}+\frac{1}{2},y+\frac{1}{2},z+\frac{1}{2}$	$hk0 : h = 2n$
		$h00 : h = 2n$
		$0h0 : k = 2n$
		$00l : l = 2n$
		Special; as above, plus
4 *c* .*m*.	$\bar{x},\frac{1}{4},z$ $\bar{x}+\frac{1}{2},\frac{3}{4},z+\frac{1}{2}$ $\bar{x},\frac{3}{4},\bar{z}$ $x+\frac{1}{2},\frac{1}{4},\bar{z}+\frac{1}{2}$	no extra conditions
4 *b* $\bar{1}$	$0,0,\frac{1}{2}$ $\frac{1}{2},0,0$ $0,\frac{1}{2},\frac{1}{2}$ $\frac{1}{2},\frac{1}{2},0$	$hkl : h + l,k = 2n$
4 *a* $\bar{1}$	0,0,0 $\frac{1}{2},0,\frac{1}{2}$ $0,\frac{1}{2},0$ $\frac{1}{2},\frac{1}{2},\frac{1}{2}$	$hkl : h + l,k = 2n$

9 Symmetry of special projections

Along [001] *p*2*gm*
$\boldsymbol{a}' = \frac{1}{2}\boldsymbol{a}$ $\boldsymbol{b}' = \boldsymbol{b}$
Origin at 0,0,*z*

Along [100] *c*2*mm*
$\boldsymbol{a}' = \boldsymbol{b}$ $\boldsymbol{b}' = \boldsymbol{c}$
Origin at $x,\frac{1}{4},\frac{1}{4}$

Along [010] *p*2*g g*
$\boldsymbol{a}' = \boldsymbol{c}$ $\boldsymbol{b}' = \boldsymbol{a}$
Origin at 0,*y*,0

10 Maximal non-isomorphic subgroups

I
[2] $Pn2_1a$ ($Pna2_1$, 33) 1; 3; 6; 8
[2] $Pnm2_1$ ($Pmn2_1$, 31) 1; 2; 7; 8
[2] $P2_1ma$ ($Pmc2_1$, 26) 1; 4; 6; 7
[2] $P2_12_12_1$ (19) 1; 2; 3; 4
[2] $P112_1/a$($P2_1/c$, 14) 1; 2; 5; 6
[2] $P2_1/n11$($P2_1/c$, 14) 1; 4; 5; 8
[2] $P12_1/m1$($P2_1/m$, 11) 1; 3; 5; 7

IIa none
IIb none

Maximal isomorphic subgroups of lowest index
IIc [3] *Pnma* ($\boldsymbol{a}' = 3\boldsymbol{a}$) (62); [3] *Pnma* ($\boldsymbol{b}' = 3\boldsymbol{b}$) (62); [3] *Pnma* ($\boldsymbol{c}' = 3\boldsymbol{c}$) (62)

Minimal non-isomorphic supergroups
I none
II [2] *Amma* (*Cmcm*,63); [2] *Bbmm* (*Cmcm*,63); [2] *Ccme* (*Cmce*,64); [2] *Imma* (*74*); [2] *Pcma* ($\boldsymbol{b}' = \frac{1}{2}\boldsymbol{b}$) (*Pbam*, 55); [2] *Pbma* ($\boldsymbol{c}' = \frac{1}{2}\boldsymbol{c}$) (*Pbma*, 57); [2] *Pnma* ($\boldsymbol{a}' = \frac{1}{2}\boldsymbol{a}$) (*Pmmn*, 59)

Figure 1.62 Representation of space group *Pnma* in the International Tables for Crystallography (Volume A).

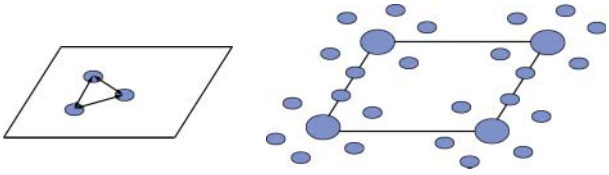

Figure 1.63 Schema of structure (a) and corresponding Patterson function (b).

◯ – asymmetric point

◯, – point connected with a point ◯ – by inversion, rotoinversion, or mirror symmetry

– ◯, + – two superimposed points that are connected by a mirror plane located parallel to the projection plane.

The symbols +, –, ½+, ½– denote the heights of the points. In our example, this means $+z$, $-z$, $\frac{1}{2}+z$, $\frac{1}{2}-z$. In general, the heights of the points are z-coordinates for all noncubic space groups. For rhombohedral space groups, the heights are referred to the hexagonal c-axis. Monoclinic space groups with unique axis b make an exception to this rule. Here, the symbols for the height are referred to the y-coordinates. For instance, the symbol – ◯, + in the general position diagram of the monoclinic space group *Pm* describes the two points with the coordinates $x, y, z; x, -y, z$ for the b-axis setting and $x, y, z; x, y, -z$ for the c-axis setting, respectively. For cubic space groups, the points in the general position diagram are drawn as vertices of transparent polyhedra.

(4) Origin This line tells us where the origin is located and which symmetry elements are going through the origin. In our example, the origin is chosen at the position of the inversion center. The second symbol 12_11 means that, in the [010] direction, a twofold screw axis is going through the origin. Along the [100] and [001] directions, there is only the identity operation. In general, the choice of the origin of the unit cell is arranged according to following rules:

All centrosymmetric space groups are described with an origin at the inversion center. If there exist other positions in a centrosymmetric space group with high site symmetry, which do not coincide with the inversion center, a second description with an origin at the point with highest site symmetry is given in the tables. For 24 centrosymmetric space group types, a description for a second origin is given. For example, the space group $Fd\bar{3}m$ (227) is described with an origin at $\bar{4}3\,m$ (first choice) at $-1/8, -1/8, -1/8$ from the center at $\bar{3}\,m$. The second description is given for an origin at the inversion center with site symmetry $\bar{3}\,m$ at 1/8, 1/8, 1/8 from $\bar{4}\,3m$. For the majority of noncentrosymmetric space groups, the origin is the point of the highest site symmetry. Noncentrosymmetric space groups with low site symmetry positions are described with an origin where symmetry elements are located or crossing each other.

(5) Asymmetric Unit The volume of the unit cell is disjointed by the symmetry framework of the space group into n symmetry equivalent parts, where n is equal to the multiplicity of the general position. One part of n corresponds to the asymmetric unit. Applying the set of symmetry elements of the space group, for our example *Pnma*, there are eight symmetry operations; to the asymmetric unit, this generates the whole unit cell. This means that the volume of the asymmetric unit for *Pnma* is 1/8 of the volume of the unit cell. For all orthorhombic space groups, the asymmetric unit is a parallelepiped where one vertex is the origin of the space group. All boundary faces of the parallelepiped are parallel to the faces of the unit cell. The conditions given in the tables for the direct-space asymmetric units (DAU) are inexact for the boundaries. Exact DAU conditions for the cubic space groups were derived by Koch and Fischer [36]. A complete description of exact DAUs for the 230 space group types was recently given by Grosse-Kunstleve *et al.* [37]. An online gallery of these DAUS with a complete description for all space group types is presented at *http://cci.lbl.gov/asu_gallery/* [38].

(6) Symmetry Operations The number of the symmetry operations for *Pnma* is eight. This number is, of course, equal to the given number of cosets of the space group with respect to its normal subgroup of translations T and equal to the order of the point group *mmm*. The operations are characterized by a symbol for the type of symmetry operation and if necessary by a coordinate triplet defining its location and orientation. The symmetry operations from (1) to (8) have the following meaning:

1) *identity operation,*
2) *twofold screw rotation around the line* $^1/_4$, 0, *z, with a translation* (0,0,1/2),
3) *twofold screw rotation around the line* 0, *y*, 0, *with a translation* (0,$^1/_2$,0),
4) *twofold screw rotation around the line x,* $^1/_4$, $^1/_4$, *with a translation* ($^1/_2$,0,0),
5) *inversion center at* 0,0,0,
6) *glide reflection a with glide part* ($^1/_2$,0,0) *and the glide plane at x, y,* $^1/_4$,
7) *reflection m at the plane x,* $^1/_4$, *z*,
8) *glide reflection n with the glide part* (0, $^1/_2$, $^1/_2$) *at the plane* $^1/_4$, *y, z.*

(7) Generators Selected The set of selected generators allows the derivation of the complete space group. The first generator G_1 is always the identity. Thus, the first coordinate triplet of the general position is *x,y,z*. The generators G_2, G_3, and G_4 are the fundamental translations generating the infinite three-dimensional lattice. For the generation of space groups with centered Bravais lattices one (I, A, B, C, R) or two (F) additional generators are required. The generators G_5 and G_6 correspond to the screw rotations (2) and (3). The last generator of any centrosymmetric space group (in our case G_7) is always the inversion operation (5).

The program GENPOS of the crystallographic databases of the ***Bilbao Crystallographic Server*** (***BCS***) (*http://www.cryst.ehu.es*, see, e.g., Section 1.6) provides the list with the generators or the general positions for each space group [39]. In addition to the information given in the International Tables for Crystallography [31], the user can obtain also these data for different settings.

(8) Positions Here, all Wyckoff positions for the space group *Pnma* (one general position and three special positions) are listed. From left to right, the position list is divided into columns with the headlines: ***multiplicity***, ***Wyckoff letter***, ***site symmetry***, ***coordinates***, and ***reflection conditions***. The first line of the list provides us the information about the general position. The remaining lines contain the information about the special positions. In general, the term *position* (*singular*) is defined as a set of symmetrically equivalent points. This set of points is called a ***general position*** if each point of it is left invariant only by the identity operation. The consecutive numbering for the general point position is identical with the numbering of the symmetry operations (6) in the tables. Thus, we can see how the point with the coordinate triplet *x*,*y*,*z* will be transformed by the eight symmetry operations. For example, glide reflection *n* with the glide part (0, $^1/_2$, $^1/_2$) at the plane $^1/_4$, *y*, *z* (8) transforms the initial point *x*,*y*,*z* into $-x + {}^1/_2$, $y + {}^1/_2$, $z + {}^1/_2$ (8).

A "***special position***" is occupied if each point of the set is left invariant by the identity operation and at least one further symmetry operation.

The term ***multiplicity*** is the number of symmetry equivalent points in the unit cell for the corresponding position. As already mentioned, the multiplicity of the general position is given by the product of the order of the point group and the number of lattice points per unit cell ($P = 1$, A, B, C, $I = 2$, $R = 3$, $F = 4$). Thus, for the general position of *Pnma*, we have a multiplicity of $1 \times 8 = 8$. The multiplicity of a special position is given by the multiplicity of the general position divided by the order of the site-symmetry group. The different positions of a space group are coded by the Wyckoff letter beginning with letter *a* at the bottom line and going upward in alphabetical order. In our case, the Wyckoff letter *d* stands for the general position. Thus, for the space group *Pnma*, four Wyckoff positions exist. The maximum number of 27 positions is given for *Pmmm*. In general, the "site symmetry" of a point of the space group is defined by the set of symmetry operations, which leave the point fixed. This set of symmetry operations forms the "***site-symmetry group***" of the space group, which is isomorphous to a subgroup of the point group belonging to the space group. The site symmetry of all points of general position is 1, whereas the site symmetry of points of a special position is always >1. Our example *Pnma* is a nonsymmorphic space group for which the order of all site-symmetry groups is lower than the order of the point group. The highest order of the site-symmetry groups (special positions 4*a*–*c*) is two; the order of the point group is eight. For symmorphic space groups, there exists at least one special position where the (conjugate) site-symmetry groups are isomorphic to the point group of the space group. Therefore, the order of the site-symmetry group is then identical with the order of the point group. For example, within the symmorphic space group *Pmmm*, there are eight special positions (1*a*–*h*) with the site-symmetry group *mmm* (order 8).

In our example, the special Wyckoff positions 4*a*–*c* have the site symmetry 1 and *m* (order 2). The positions 4*a*, 4*b* have the site symmetry 1. These equivalent positions belong to the same Wyckoff set. The 1731 Wyckoff positions of the 230 space groups can be grouped into 1128 Wyckoff sets. The data of the Wyckoff

positions (program WYCKPOS) and the attribution of the Wyckoff positions to Wykoff sets (program WYCKSETS) for the 230 space groups can be retrieved from the BCS [39].

For the description of the properties of space groups, the explanation of the term ***crystallographic orbit*** [40], also denoted as ***point configuration*** [41], is important. A crystallographic orbit is an infinite set of all points in a space group that are symmetrically equivalent to one particular point. The set of points of Wyckoff position *a* of *Pnma* are completely fixed by symmetry and forms one orbit. In this case, orbit and Wyckoff position are identical. When we are looking at the symmetry equivalent points of Wyckoff position *c* (x, $^1/_4$, z, etc.) with the site symmetry *.m.*, then an infinite number of crystallographic orbits is possible because of the variable x- and z-coordinates. From the relationships between the crystallographic orbits, the concept of ***lattice complexes*** was developed [42–44]. A lattice complex is defined as the set of all crystallographic orbits, which can be generated within one type of Wyckoff set. Altogether 402 lattice complexes are related to the 1128 types of Wyckoff sets. The concept of lattice complexes can be applied to depict existing structural similarities of crystals belonging to different space group types. The same lattice complex may exist in different space group types. A complete list of all lattice complexes for the 230 space groups is given in [44] (for a comprehensive treatment, see also [45]).

The ***reflection conditions*** given at the right most column are useful in X-ray diffraction for space group determination. We should be aware of the fact that these conditions are only valid for kinematical diffraction conditions. In general, electron diffraction patterns exhibit kinematical forbidden reflections owing to the contribution of dynamical scattering effects. Only for very thin crystals, the kinematic diffraction theory can, therefore, be applied. The general conditions are valid for all Wyckoff positions. The special conditions apply only to the corresponding special Wyckoff position in addition to the general conditions. In general, a reflection will be absent if the listed conditions are not fulfilled. The reflection conditions are also denoted as *extinction rules* or *systematic absences* and can be classified into *integral*, *zonal*, and *serial extinctions* according to the symmetry elements leading to the extinctions.

- ***Integral extinctions*** are caused by centered unit cells and act on the whole set of reflections *hkl*. For primitive unit cells, no reflections are extinct.
- ***Zonal extinctions*** exist when glide planes are present. They apply only to a two-dimensional set of reflections (*hk*0, 0*kl*, *h*0*l*, *hhl*).
- ***Serial extinctions*** are caused by screw axes. They act on reciprocal lattice rows (*h*00, 0*k*0, 00*l*, etc.).

It should be noted that symmorphic space groups do not have zonal and serial extinction conditions. As an example we will look at the general reflection conditions for the symmorphic space group $C2/m$, which are $hkl: = h + k = 2n$, $h0l$: $h = 2n$, $0kl$: $k = 2n$, $hk0$: $h + k = 2n$, $0k0$: $k = 2n$, $h00$: $h = 2n$. All these conditions are due to the action of the *C* Bravais lattice, that is, there exist only integral extinction conditions.

For our space group *Pnma*, there are no integral extinctions because of the *P* Bravais lattice type. There exist only zonal extinctions caused by the glide planes of the type *a* and *n*, in addition to the serial extinctions caused by the three twofold screw axes.

(9) Symmetry of Special Projections The projection of a three-dimensional space group along a given direction onto a plane yields a plane group (two-dimensional space group). For each of the three projections along the main symmetry directions, the projection direction, the international symbol of the plane group (two-dimensional space group), the relationship between the basis vectors of the plane group and the three-dimensional space group, and the location of the origin of the plane group are given in the coordinates of the unit cell of the space group.

(10) Subgroup and Supergroup Relationships This section gives a short survey of the sub- and supergroups of the space group *Pnma*. Before discussing the construction of this entry in the International Tables for Crystallography, some of the fundamental definitions of group–subgroup relations of space groups will be explained. Here, we will only deal with such subgroups, which are also space groups. We will show what kind of relations can exist between a space group G with its normal subgroup of translations $T(G)$ and the associated point group $P(G)$ and a subgroup H with corresponding $T(H)$ and $P(H)$.

A so-called "translationengleiche" *subgroup H* (*t-subgroup*) is given, if $T(H) = T(G)$ and $P(H) < P(G)$ holds. The set of all translations in the space group G is also present in the subgroup H. The point group $P(H)$ is a subgroup of $P(G)$.

A so called "klassengleiche" *subgroup H* (*k-subgroup*) means $P(H) = P(G)$ and $T(H) < T(G)$. Group G and subgroup H belong to the same point group, but some of the translations are lost in the subgroup H. *Isomorphic k-subgroups* are given if G and H belong to the same space group type, that is, they have the same space group symbol or the related symbol to the enantiomorphic partner.

The subgroup H is called a *general subgroup* if both the translation symmetry and the point group symmetry is reduced, that is, $T(H) < T(G)$ and $P(H) < P(G)$.

The subgroup H of G is called a *maximal subgroup* if there is no group Z for which the relation holds $H < Z < G$. A maximal subgroup H is either a *t-subgroup* or a *k-subgroup* because either $H = Z$ or $Z = G$ is fulfilled (theorem of C. Hermann). If H is a maximal subgroup of G, then $G > H$ is called a *minimal supergroup of H*.

If H of G is a *t-*, *k-*, *isomorphic* or *general subgroup*, then G is a *t-*, *k-*, *isomorphic* or *general* supergroup of H. Now, we will see what kind of information about sub- and supergroups for *Pnma* is listed.

The entry "**Maximal nonisomorphic subgroups**" comprise the *t-subgroups* (*translationengleiche*, type **I**) and the *k-subgroups* (*klassengleiche*, type **II**). The *k*-subgroups are subdivided into **IIa** (the conventional cell of *Pnma* and the subgroup are the same) and **IIb** (the conventional cell of the subgroup is larger than the cell of *Pnma*). For *Pnma*, seven *t*-subgroups are quoted. The following information is listed: [*i*] – index of the subgroup in *Pnma*, the international symbol of

the subgroup referred to the setting and coordinate system of *Pnma*, conventional short international symbol of the subgroup (only given if the previous symbol is not a conventional one), sequence of numbers with identical enumeration schema for the symmetry operations and coordinate triplets of the general position specifying the retaining coordinate triplets of the general position of *Pnma* in the subgroup. For **IIa** and **IIb**, no data are given. The block **IIc** comprises the **Maximal isomorphic subgroups**. The subgroups listed here are of the same space group type as *Pnma* (see identical international symbol). The different cell enlargements for the subgroups are given after the space group symbol.

Under the last headline "**Minimal nonisomorphic supergroups**," the information on *t-supergroups* (I) and *k-supergroups* (II) of *Pnma* is given.

It is beyond the scope of this book to give a more detailed description of group–subgroup relations of space groups. The reader will find a very comprehensive and detailed description of this topic in Volume A1 "Symmetry relations between space groups" of the International Tables for Crystallography [32]. In addition to the fundamentals of group theory and mathematical crystallography with respect to space groups and their subgroups, this volume contains tables of maximal subgroups of the plane groups and space groups, graphs for the *t-subgroups* and *k-subgroups*, and tables of the relations of Wyckoff positions for all space groups. Guides to all tables and graphs where the content and arrangement are explained in detail are also given. The examples of the graph of the *k-subgroups* of the space groups of crystal class *mmm* (Figure 1.64) and of the

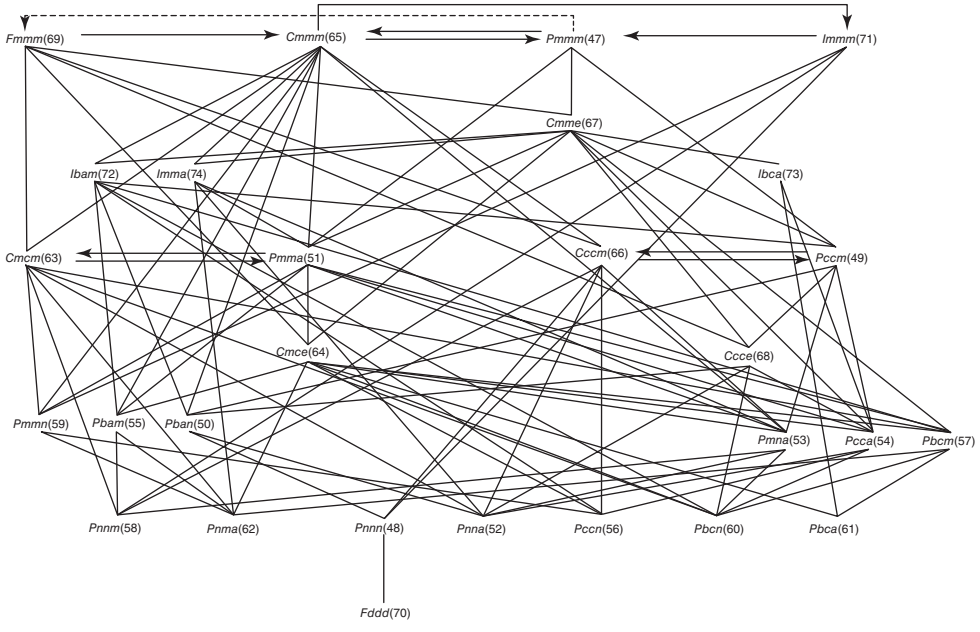

Figure 1.64 Graph of the *k-subgroups* of the space groups of crystal class *mmm*. (From the International Tables for Crystallography, Vol. A1 [32].)

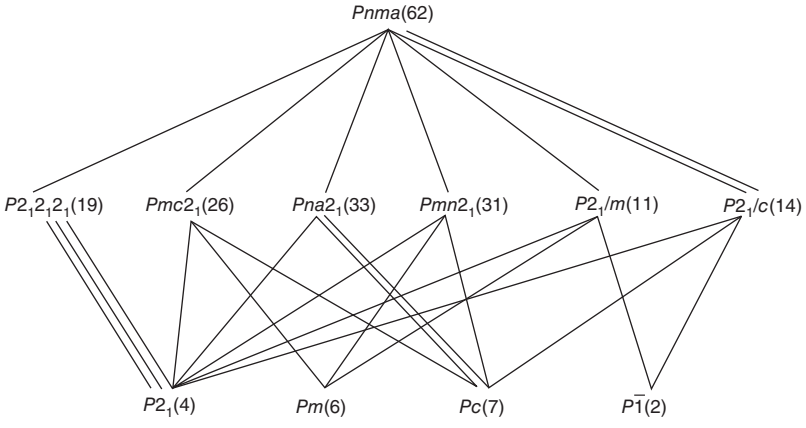

Figure 1.65 Graph of the *t-subgroups* of space group *Pnma*. (From the International Tables for Crystallography, Vol. A1 [32].)

t-subgroups of the space group *Pnma* (Figure 1.65) illustrate the group–subgroup relations for our example of a space group.

In order to get a thorough understanding of the three-dimensional symmetry framework of one of the 230 space groups and the action of the various symmetry elements, the use of the interactive "*3D Space Group Visualizer* (*SGV*)" is a very helpful tool [46]. SGV can be used as standalone program or can be combined with the online version of the space group tables of the International Tables for Crystallography [31]. With a two window technique, the space group table and the 3D image of the selected space group can be simultaneously inspected. SGV allows various useful operations including the rotation and shift of the unit cell, variation of the number of different cells in three dimensions, the selection of subsets of symmetry elements, and the animation of the action of the related symmetry operation. Figure 1.66 shows a 3D SGV image of our space group example *Pnma* with the entire symmetry framework. By moving the cursor onto a single glide plane, the corresponding symmetry operation will be animated. This is an excellent tool to visualize the symmetry operations of a space group in three-dimensional space.

1.4.2.3 Mathematical Description of the Space Group Symmetry

In Section 1.4.1, the space group was defined as the set of all symmetry operations (isometries) of an infinite crystal structure. Now, we will show how the crystallographic symmetry operations, which map an object (e.g., point, crystal face, crystal structure, and crystal) onto itself, can be described mathematically. In a three-dimensional coordinate system with the basis vectors $\boldsymbol{a}_i$ ($i = 1, 2, 3$) and the origin O, an affine mapping (distance-preserving) can be written as

$$\begin{aligned}\widetilde{x}_1 &= \boldsymbol{W}_{11}x_1 + \boldsymbol{W}_{12}x_2 + \boldsymbol{W}_{13}x_3 + \boldsymbol{w}_1\\ \widetilde{x}_2 &= \boldsymbol{W}_{21}x_1 + \boldsymbol{W}_{22}x_2 + \boldsymbol{W}_{23}x_3 + \boldsymbol{w}_2\\ \widetilde{x}_2 &= \boldsymbol{W}_{31}x_1 + \boldsymbol{W}_{32}x_2 + \boldsymbol{W}_{33}x_3 + \boldsymbol{w}_3\end{aligned} \tag{1.55}$$

The coordinates of the initial point x, y, z will be mapped onto $\widetilde{x}_1, \widetilde{x}_2, \widetilde{x}_3$.

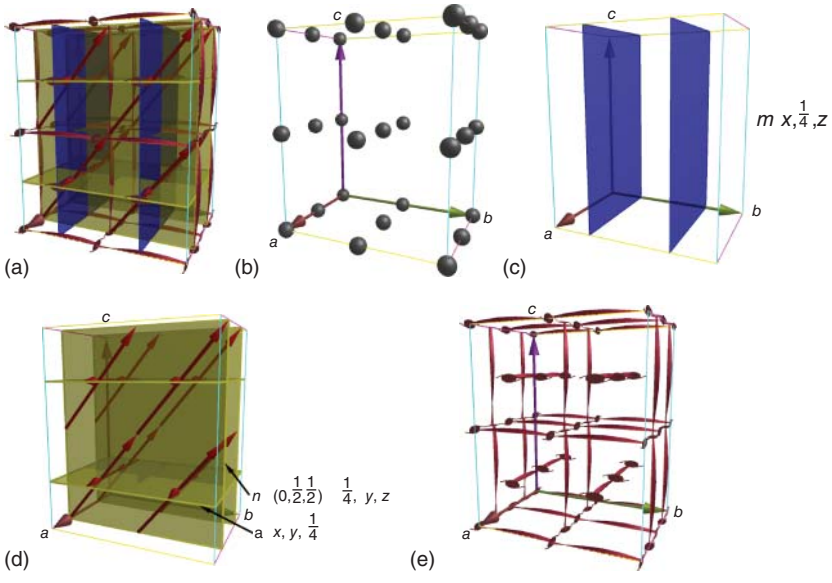

Figure 1.66 Space group visualizer (SGV) images ([46], program SGV by Perwas, C., Hitzer, E.) of space group *Pnma*: (a) whole symmetry frame, (b) location of inversion centers, (c) location of mirror planes, (d) location of glide planes, and (e) location of twofold screw axes.

Using the matrix calculus, we can write

$$\begin{pmatrix}\widetilde{x}_1\\ \widetilde{x}_2\\ \widetilde{x}_3\end{pmatrix}=\begin{pmatrix}W_{11} & W_{12} & W_{13}\\ W_{21} & W_{22} & W_{23}\\ W_{31} & W_{32} & W_{33}\end{pmatrix}\begin{pmatrix}x_1\\ x_2\\ x_3\end{pmatrix}+\begin{pmatrix}w_1\\ w_2\\ w_3\end{pmatrix} \tag{1.56}$$

or in the abbreviated form

$$\widetilde{x}=\boldsymbol{W}x+\boldsymbol{w}=(\boldsymbol{W},\boldsymbol{w})x \tag{1.57}$$

The (3×3) matrix part $\boldsymbol{W}$ and the (3×1) column part $\boldsymbol{w}$ fix the affine mapping. The symmetry operation is characterized by the matrix part $\boldsymbol{W}$ (rotation part) and the translation part $\boldsymbol{w}=\boldsymbol{w}_g+\boldsymbol{w}_l$, where $\boldsymbol{w}_g$ (glide or screw part) is the intrinsic translation part and $\boldsymbol{w}_l$ the location part.

The coordinate triplet (2) of the general position of *Pnma* is $-x+{}^1\!/_2, -y, z+{}^1\!/_2$. This corresponds to a symmetry operation with $\boldsymbol{W}=\begin{pmatrix}\overline{1}&0&0\\0&\overline{1}&0\\0&0&1\end{pmatrix}$ and $\boldsymbol{w}=\begin{pmatrix}1/2\\0\\1/2\end{pmatrix}$.

The combination of two symmetry operations $\boldsymbol{W}_3=\boldsymbol{W}_2\boldsymbol{W}_1$ provides a new symmetry operation, which can be expressed by

$$\widetilde{x}=\boldsymbol{W}_1x+\boldsymbol{w}_1,\quad \widetilde{\widetilde{x}}=\boldsymbol{W}_2\widetilde{x}+\boldsymbol{w}_2=\boldsymbol{W}_2\boldsymbol{W}_1x+\boldsymbol{w}_3 \tag{1.58}$$

$$\widetilde{\widetilde{x}}=\boldsymbol{W}_3x+\boldsymbol{w}_3,\quad \boldsymbol{W}_3=\boldsymbol{W}_2\boldsymbol{W}_1,\quad \boldsymbol{w}_3=\boldsymbol{W}_2\boldsymbol{w}_1+\boldsymbol{w}_2 \tag{1.59}$$

In the abbreviated matrix–column notion, we can write:

$$(\boldsymbol{W}_3,\boldsymbol{w}_3)=(\boldsymbol{W}_2,\boldsymbol{w}_2)(\boldsymbol{W}_1,\boldsymbol{w}_1)=(\boldsymbol{W}_2\boldsymbol{W}_1,\boldsymbol{W}_2\boldsymbol{w}_1+\boldsymbol{w}_2) \tag{1.60}$$

It is obvious that the inverse operation $(\boldsymbol{X}, \boldsymbol{x}) = (\boldsymbol{W}, \boldsymbol{w})^{-1}$ of the operation $(\boldsymbol{W}, \boldsymbol{W})$ is the identity operation $(\boldsymbol{I}, \boldsymbol{o})$.

$$(\boldsymbol{X}, \boldsymbol{x})(\boldsymbol{W}, \boldsymbol{w}) = (\boldsymbol{W}, \boldsymbol{w})^{-1}(\boldsymbol{W}, \boldsymbol{w}) = (\boldsymbol{I}, \boldsymbol{o}) \tag{1.61}$$

Using Equation 1.60, we can write

$$(\boldsymbol{X}, \boldsymbol{x})(\boldsymbol{W}, \boldsymbol{w}) = (\boldsymbol{XW}, \boldsymbol{Xw} + \boldsymbol{x}) = (\boldsymbol{I}, \boldsymbol{o}) \tag{1.62}$$

From this, it follows:

$$\boldsymbol{XW} = \boldsymbol{I}, \;\; \boldsymbol{X} = \boldsymbol{W}^{-1}; \;\; \boldsymbol{o} = \boldsymbol{Xw} + \boldsymbol{x}, \;\; \boldsymbol{x} = -\boldsymbol{Xw} = -\boldsymbol{W}^{-1}\boldsymbol{w} \tag{1.63}$$

Thus, we can write:

$$(\boldsymbol{W}, \boldsymbol{w})^{-1} = (\boldsymbol{W}^{-1}, -\boldsymbol{W}^{-1}\boldsymbol{w}) \tag{1.64}$$

The types of isometries that can occur in a space group can be classified into ***symmetry operations of first kind*** and ***symmetry operations of second kind***. Translations, rotations, and screw rotations are ***symmetry operations of first kind***. They relate the initial and the mapped object into a congruent manner. Inversion, reflections, glide reflections, and rotoinversions are ***symmetry operations of second kind***. They relate enantiomorphous objects, that is, the initial and the mapped object are mirror image.

The matrices $\boldsymbol{W}$ of symmetry operations of first kind are $\det(\boldsymbol{W}) = +1$ (Table 1.21).

Successive application of n-operations of the first kind will not change the value of the determinant. This means, the resulting symmetry operation independent on the number n is an operation of first kind.

The matrices $\boldsymbol{W}$ of symmetry operations of second kind are $\det(\boldsymbol{W}) = -1$ (Table 1.22). An even number of successive operations of second kind leads to a symmetry operation of first kind, whereas an odd number of successive operations will remain a symmetry operation of second kind.

Now, we will characterize the various types of isometries by their $(\boldsymbol{W}, \boldsymbol{w})$ matrix–column pairs.

Identity: $\boldsymbol{I}$ $(\boldsymbol{I}, \boldsymbol{o})$

The identity operation $\boldsymbol{I}$ characterized by the unit matrix $\boldsymbol{I} = \begin{pmatrix} 1\,0\,0 \\ 0\,1\,0 \\ 0\,0\,1 \end{pmatrix}$ and $\boldsymbol{w} = 0$ takes each point x, y, z onto itself. Thus,

$$\boldsymbol{x}' = \boldsymbol{Ix} + \boldsymbol{o} = \boldsymbol{x} \tag{1.65}$$

Table 1.21 Characterization of $\boldsymbol{W}$ for rotations and screw rotations by $\mathrm{tr}(\boldsymbol{W})$.

$\mathrm{tr}(\boldsymbol{W})$	−1	0	1	2	3
Type	2	3	4	6	1
Order n	2	3	4	6	1

Table 1.22 Characterization of $\boldsymbol{W}$ for rotoinversions by tr($\boldsymbol{W}$).

tr($\boldsymbol{W}$)	−3	−2	−1	0	1
Type	$\bar{1}$	$\bar{6}$	$\bar{4}$	$\bar{3}$	$\bar{2} \equiv m$
Order n	2	6	4	6	2

Translation: $\boldsymbol{T}$ $(\boldsymbol{I}, \boldsymbol{t})$

The translation operation is characterized by the translation vector $\boldsymbol{t}$, which causes a displacement of the mapped object. Thus,

$$\boldsymbol{x}' = \boldsymbol{I}\boldsymbol{x} + \boldsymbol{t} \tag{1.66}$$

Rotation and screw rotation: $\det(\boldsymbol{W}) = +1$, $\mathrm{tr}(\boldsymbol{W}) = 1 + 2\cos\varphi < 3$, $\boldsymbol{W}^n = \boldsymbol{I}$.

As already discussed in Section 1.3, the type of point group symmetry operations can be determined by the value of the determinant $\det(\boldsymbol{W})$ and the value of the trace $\mathrm{tr}(\boldsymbol{W})$. For a pure rotation, we have $\boldsymbol{x}' = \boldsymbol{W}\boldsymbol{x}$, $\boldsymbol{w} = 0$. The rotation axis is the line of fixed points. The direction of the line of rotation axis $\boldsymbol{x}$ (for $n > 1$) can be determined from the equation

$$(\boldsymbol{W}, \boldsymbol{w})\boldsymbol{x} = \boldsymbol{x} \tag{1.67}$$

For the screw rotation, we can write $\boldsymbol{x}' = \boldsymbol{W}\boldsymbol{x} + \boldsymbol{w}$, where we have to take into account that $\boldsymbol{w}$ consists of two parts, the screw part and the location part. Screw axes do not have fixed points. The screw component can be calculated as follows:

$$\boldsymbol{t}/n = 1/n(\boldsymbol{W}^{n-1} + \boldsymbol{W}^{n-2} + \cdots + \boldsymbol{W} + \boldsymbol{I})\boldsymbol{w} \tag{1.68}$$

The location of the screw axis can be determined by solving the equation $(\boldsymbol{W},\boldsymbol{w}_l)\boldsymbol{x} = \boldsymbol{x}$ with $\boldsymbol{w}_1 = \boldsymbol{w} - \boldsymbol{w}_g$. Now, we will give an example for the procedure. The number (4) of the general position of space group *Pnma* has the following coordinate triplet: $x + {}^1/_2$, $-y + {}^1/_2$, $-z + {}^1/_2$.

It corresponds to the following matrix–column pair: $\boldsymbol{W} = \begin{pmatrix} 1 & 0 & 0 \\ 0 & \bar{1} & 0 \\ 0 & 0 & \bar{1} \end{pmatrix}$, $\boldsymbol{w} = \begin{pmatrix} 1/2 \\ 1/2 \\ 1/2 \end{pmatrix}$ with $\det(\boldsymbol{W}) = +1$, $\mathrm{tr}(\boldsymbol{W}) = -1$. This means a twofold rotation or screw rotation is given. The order of such symmetry operations is two. Therefore, we write $(\boldsymbol{W},\ \boldsymbol{w})^2 = (\boldsymbol{W}^2,\ \boldsymbol{W}\boldsymbol{w} + \boldsymbol{w})$ and $\boldsymbol{W}\boldsymbol{w} + \boldsymbol{w} = \boldsymbol{t} = \begin{pmatrix} 1 \\ 0 \\ 0 \end{pmatrix}$. Because $\boldsymbol{t} \neq 0$, a twofold screw axis with $\boldsymbol{w}_g = {}^1/_2\boldsymbol{t} = \begin{pmatrix} 1/2 \\ 0 \\ 0 \end{pmatrix}$ is given. The location part yields $\boldsymbol{w}_1 = \begin{pmatrix} 1/2 \\ 1/2 \\ 1/2 \end{pmatrix} - \begin{pmatrix} 1/2 \\ 0 \\ 0 \end{pmatrix} = \begin{pmatrix} 0 \\ 1/2 \\ 1/2 \end{pmatrix}$. $(\boldsymbol{W},\ \boldsymbol{w}_1)\boldsymbol{x} = \boldsymbol{x}\begin{pmatrix} 1 & 0 & 0 \\ 0 & \bar{1} & 0 \\ 0 & 0 & \bar{1} \end{pmatrix}\begin{pmatrix} x \\ y \\ z \end{pmatrix} + \begin{pmatrix} 0 \\ 1/2 \\ 1/2 \end{pmatrix} = \begin{pmatrix} x \\ y \\ z \end{pmatrix}$, Then, we get $x = x$, $y = -y + {}^1/_2$, $z = -z + {}^1/_2$.

From this, the location of the twofold screw axis at x, $^1/_4$, $^1/_4$ follows. This agrees with the data given for the symmetry operation (4) for *Pnma*.

Inversion: $\bar{1}$, $(-\boldsymbol{I}, \boldsymbol{w})$

This symmetry operation, which can also be regarded as a onefold rotoinversion, inverts an object in the inversion center, which is the fixed point for this operation. The mapping is $\boldsymbol{x}' = -\boldsymbol{x} + \boldsymbol{w}$. The location of the inversion center can be determined by $\boldsymbol{x}_f = {}^1/_2\boldsymbol{w}$. The inversion center of *Pnma* is located at the origin. It is obvious that the point with the coordinates x, y, z is inverted at the inversion center into a point with the coordinates $-x$, $-y$, $-z$. In the first setting of the space group $Fd\bar{3}m$, the inversion center is located at 1/8, 1/8, 1/8. This means the point x, y, z is inverted into $-x + {}^1/_4$, $-y + {}^1/_4$, $-z + {}^1/_4$.

Rotoinversion: $\det(\boldsymbol{W}) = -1$, $\mathrm{tr}(\boldsymbol{W}) = -(1 + 2\cos\varphi)$, $\boldsymbol{W}^2 \neq \boldsymbol{I}$

The rotoinversion is a combined operation of a rotation and an inversion. The one and twofold rotoinversions are special cases and are, therefore, treated separately as inversion and reflection, respectively. With the exemption of $\bar{2}$, all other n-fold rotoinversions have one fixed point, the center of rotoinversion. This inversion point can be determined by means of $(\boldsymbol{W}, \boldsymbol{w})\boldsymbol{x} = \boldsymbol{x}'$. The determination of the location of the rotoinversion axis requires the solution of the equation

$$(\boldsymbol{W}, \boldsymbol{w})^2\boldsymbol{x} = (\boldsymbol{W}^2, \boldsymbol{W}\boldsymbol{w} + \boldsymbol{w})\boldsymbol{x} = \boldsymbol{x}' \tag{1.69}$$

Reflection and glide reflection: $\det(\boldsymbol{W}) = -1$, $\mathrm{tr}(\boldsymbol{W}) = 1$, $\boldsymbol{W}^2 = \boldsymbol{I}$.

The type of operation can be determined by means of the equation

$$(\boldsymbol{W}, \boldsymbol{w})^2 = (\boldsymbol{W}^2, \boldsymbol{W}\boldsymbol{w} + \boldsymbol{w}) = (\boldsymbol{I}, \boldsymbol{t}) \tag{1.70}$$

For $\boldsymbol{t} = \boldsymbol{o}$, a reflection is given. The mirror plane is the plane of fixed points. Its location can be determined by means of Equation 1.67.

For $\boldsymbol{t} \neq \boldsymbol{o}$, a glide reflection is given. For the glide reflection, there are no fixed points. The procedure for the determination of the glide vector and the location of the glide plane is demonstrated using the coordinate triplet of space group *Pnma* (8) $-x + {}^1/_2$, $y + {}^1/_2$, $z + {}^1/_2$. The matrix–column pair is $\boldsymbol{W} = \begin{pmatrix} \bar{1} & 0 & 0 \\ 0 & 1 & 0 \\ 0 & 0 & 1 \end{pmatrix}$, $\boldsymbol{w} = \begin{pmatrix} 1/2 \\ 1/2 \\ 1/2 \end{pmatrix}$ with $\det(\boldsymbol{W}) = -1$, $\mathrm{tr}(\boldsymbol{W}) = 1$. As shown above, the translation vector is calculated according to $\boldsymbol{W}\boldsymbol{w} + \boldsymbol{w} = \boldsymbol{t}$. $\boldsymbol{W} = \begin{pmatrix} \bar{1} & 0 & 0 \\ 0 & 1 & 0 \\ 0 & 0 & 1 \end{pmatrix}$

$$\begin{pmatrix} 1/2 \\ 1/2 \\ 1/2 \end{pmatrix} = \begin{pmatrix} -1/2 \\ 1/2 \\ 1/2 \end{pmatrix}; \begin{pmatrix} -1/2 \\ 1/2 \\ 1/2 \end{pmatrix} + \begin{pmatrix} 1/2 \\ 1/2 \\ 1/2 \end{pmatrix} = \begin{pmatrix} 0 \\ 1 \\ 1 \end{pmatrix} = \boldsymbol{t}; \boldsymbol{w}_g = {}^1/_2\boldsymbol{t} = \begin{pmatrix} 0 \\ 1/2 \\ 1/2 \end{pmatrix}.$$

Table 1.23 Space group generation of $G = Pnma$ (No. 62).

G_1	x, y, z (1)	Identity I
G_2	$t(100)$	Translation
G_3	$t(010)$	Translation
G_4	$t(001)$	Translation
(G_2, G_3, G_4 – generating all translations of *Pnma*)		
G_5	$-x+\frac{1}{2}, -y, z+\frac{1}{2}$ (2)	Twofold screw rotation
$G_5 \cdot G_5$	t (001)	
G_6	$-x, y+\frac{1}{2}, -z$ (3)	Twofold screw rotation
$G_6 \cdot G_5$	$x+\frac{1}{2}, -y+\frac{1}{2}, -z+\frac{1}{2}$ (4)	Twofold screw rotation
$G_6 \cdot G_6$	t (010)	
G_7	$-x, -y, -z$ (5)	Inversion
$G_7 \cdot G_5$	$x+\frac{1}{2}, y, -z+\frac{1}{2}$ (6)	***a*** glide reflection
$G_7 \cdot G_6$	$x, -y+\frac{1}{2}, z$ (7)	Reflection
$G_7 \cdot G_6 \cdot G_5$	$-x+\frac{1}{2}, y+\frac{1}{2}, z+\frac{1}{2}$ (8)	n-glide reflection
$G_7 \cdot G_7$	x, y, z	Identity I

The location of the glide plane follows from the solution of the equation $(\boldsymbol{W}, \boldsymbol{w}_1)\,\boldsymbol{x} = \boldsymbol{x}$ with

$$\boldsymbol{w}_l = \boldsymbol{w} - \boldsymbol{w}_g \cdot \begin{pmatrix} \bar{1} & 0 & 0 \\ 0 & 1 & 0 \\ 0 & 0 & 1 \end{pmatrix} \begin{pmatrix} x \\ y \\ z \end{pmatrix} + \begin{pmatrix} 1/2 \\ 0 \\ 0 \end{pmatrix} = \begin{pmatrix} x \\ y \\ z \end{pmatrix}$$

Then, we get $x = -x + \frac{1}{2}$, $y = y$, $z = z$.
From these data follows an $n(0, \frac{1}{2}, \frac{1}{2})$ glide plane located at $\frac{1}{4}, y, z$, which agrees with the data for the symmetry operation (8) of *Pnma*.

After discussing the relationships between the symmetry operations and their corresponding coordinate triplets as given in the International Tables for Crystallography [31] and the procedures for the determination of the type and location of the symmetry elements from the coordinate triplets, we will illustrate how the whole set of symmetry operations of the space group *Pnma* is derived by means of the generators selected (Table 1.23). The generators selected are underlined; the numbers in parenthesis correspond to the enumeration of the list of general position, respectively.

We should be able now to read out the main information content from a space group diagram of the International Tables. In addition, with the mathematical formalism described above, we can specify the symmetry operations and their modes of action of a space group onto a motif. The location of the motif is specified by the coordinate triplet. Now, we will show that the construction or architecture of a space group can be explained instructively using a group theoretical description. The set of all translations $(\boldsymbol{I}, \boldsymbol{t})$ of the infinite three-dimensional lattice forms an Abelian group T ($(\boldsymbol{I}, \boldsymbol{t}_i)\,(\boldsymbol{I}, \boldsymbol{t}_k) = (\boldsymbol{I}, \boldsymbol{t}_k)\,(\boldsymbol{I}, \boldsymbol{t}_i)$) of infinite order. The unit element is given by $(\boldsymbol{I}, 0)$, the negative translation $(\boldsymbol{I}, -\boldsymbol{t})$ of $(\boldsymbol{I}, \boldsymbol{t})$ is the inverse element. The infinite translation group T is a subgroup of the space group G. Furthermore, the

Table 1.24 Schematic representation of the coset decomposition of the space group G with respect to its subgroup of translations T.

$(I, 0)$	(W_2, w_2)	(W_3, w_3)	…	(W_i, w_i)
(I, t_1)	$(W_2, w_2 + t_1)$	$(W_3, w_3 + t_1)$	…	$(W_i, w_i + t_1)$
(I, t_2)	$(W_2, w_2 + t_2)$	$(W_3, w_3 + t_2)$	…	$(W_i, w_i + t_2)$
(I, t_3)	$(W_2, w_2 + t_3)$	$(W_3, w_3 + t_3)$	…	$(W_i, w_i + t_3)$
…	…	…	…	…
(I, t_j)	$(W_2, w_2 + t_j)$	$(W_3, w_3 + t_j)$	…	$(W_i, w_i + t_j)$
…	…	…	…	…

conjugation by all elements $(\boldsymbol{W}, \boldsymbol{w}) \in \boldsymbol{G}$ results always in a translation.

$$(\boldsymbol{W}, \boldsymbol{w})^{-1}(\boldsymbol{I}, \boldsymbol{t})(\boldsymbol{W}, \boldsymbol{w}) = (\boldsymbol{I}, \boldsymbol{W}^{-1}\boldsymbol{t}) = (\boldsymbol{I}, \boldsymbol{t}') \tag{1.71}$$

Therefore, the translation group is not only a subgroup of the space group G. It is also a *normal subgroup* $T \trianglelefteq G$.

Now, we will illustrate the architecture of the space group by means of a coset decomposition of the space group (into right or left cosets) with respect to the subgroup T of translations (Table 1.24).

In general, this array consists of a finite number of i columns and an infinite number of rows.

The number i is fixed by the order i of the point group belonging to the space group. The simplest case is given for $i = 1$ (point group 1, with the space group $P1$ only). The maximum number of columns ($i = 48$) exist for space groups belonging to point group $m\bar{3}m$ (order 48). The point group P is represented by the matrices $(\boldsymbol{I})$, $(\boldsymbol{W}_2)$, $(\boldsymbol{W}_3)$, … $(\boldsymbol{W}_i)$. Each column represents one coset and has an infinite length owing to the infinite number of translations. The first coset is the subgroup T. The other cosets are given by multiplication of all elements of T with an element $(\boldsymbol{W}_i, \boldsymbol{w}_i)$ of G according to the multiplication law described in Chapter 1.3.2.

$$\begin{aligned} G &= T + (\boldsymbol{W}_2, \boldsymbol{w}_2)T + (\boldsymbol{W}_3, \boldsymbol{w}_3)T + \cdots + (\boldsymbol{W}_i, \boldsymbol{w}_i)T \quad \text{(left cosets)} \\ G &= T + T(\boldsymbol{W}_2, \boldsymbol{w}_2) + T(\boldsymbol{W}_3, \boldsymbol{w}_3) + \cdots + T(\boldsymbol{W}_i, \boldsymbol{w}_i) \quad \text{(right cosets)} \end{aligned} \tag{1.72}$$

The index of T in G ($[G{:}T] = i$), that is, the number of cosets is equal to the number of the order of the point group. As described above, the translation group T is a *normal subgroup*. A coset decomposition of a group with respect to a normal subgroup results in identical left and right cosets. The cosets are elements of a new group, the ***factor group*** G/T, which is isomorphic to the point group P.

Now, we will illustrate the right coset decomposition for the monoclinic space group $P2/m$ (Table 1.25). It is obvious that the left cosets will have identical coordinate triplets of the elements.

This form of coset decomposition gives us an interesting insight into the composition of the space group $P2/m$. There are four cosets, that is, the index $[i]$ of T in G is 4. This is equal to the order of the point group $2/m$. According to the number of cosets, the general position has the multiplicity 4. All elements of each column

Table 1.25 Right coset decomposition of space group $P2/m$ to the subgroup of translations T.

T_i1	T_i2	$T_i\bar{1}$	T_im
$x, \quad y, \quad z$	$-x, \quad y, \quad -z$	$-x, \quad -y, \quad -z$	$x, \quad -y, \quad z$
$x+1, \quad y, \quad z$	$-x+1, \quad y, \quad -z$	$-x+1, \quad -y, \quad -z$	$x+1, \quad -y, \quad z$
$x+2, \quad y, \quad z$	$-x+2, \quad y, \quad -z$	$-x+2, \quad -y, \quad -z$	$x+2, \quad -y, \quad z$
$\vdots$	$\vdots$	$\vdots$	$\vdots$
$x, \quad y+1, \quad z$	$-x, \quad y+1, \quad -z$	$-x, \quad -y+1, \quad -z$	$x, \quad -y+1, \quad z$
$x+1, \quad y+1, \quad z$	$-x+1, \quad y+1, \quad -z$	$-x+1, \quad -y+1, \quad -z$	$x+1, \quad -y+1, \quad z$
$x+2, \quad y+1, \quad z$	$-x+2, \quad y+1, \quad -z$	$-x+2, \quad -y+1, \quad -z$	$x+2, \quad -y+1, \quad z$
$\vdots$	$\vdots$	$\vdots$	$\vdots$
$x, \quad y+2, \quad z$	$-x, \quad y+2, \quad -z$	$-x, \quad -y+2, \quad -z$	$x, \quad -y+2, \quad z$
$x+1, \quad y+2, \quad z$	$-x+1, \quad y+2, \quad -z$	$-x+1, \quad -y+2, \quad -z$	$x+1, \quad -y+2, \quad z$
$x+2, \quad y+2, \quad z$	$-x+2, \quad y+2, \quad -z$	$-x+2, \quad -y, \quad -z$	$x+2, \quad -y+2, \quad z$
$\vdots$	$\vdots$	$\vdots$	$\vdots$
$x, \quad y+1, \quad z+1$	$-x, \quad y+1, \quad -z+1$	$-x, \quad -y+1, \quad -z+1$	$x \quad -y+1 \quad z+1$
$x+1, \quad y+1, \quad z+1$	$-x+1, \quad y+1, \quad -z+1$	$-x+1, \quad -y+1, \quad -z+1$	$x+1 \quad -y+1 \quad z+1$
$x+2, \quad y+1, \quad z+1$	$-x+2, \quad y+1, \quad -z+1$	$-x+2, \quad -y+1, \quad -z+1$	$x+2 \quad -y+1 \quad z+1$
$\vdots$	$\vdots$	$\vdots$	$\vdots$
$x+r, y+s, z+t$	$-x+r, y+s, -z+t$	$-x+2r, -y+s, -z+t$	$x+r, -y+s, z+t$
$\vdots$	$\vdots$	$\vdots$	$\vdots$

have the same $\boldsymbol{W}$ matrix representing the corresponding point group symmetry operation. As an example in each line of column 2, we have $\boldsymbol{W} = \begin{pmatrix} \bar{1} & 0 & 0 \\ 0 & 1 & 0 \\ 0 & 0 & \bar{1} \end{pmatrix}$ for the twofold rotation (coordinates referred to *b*-axis setting of $P2/m$) and for the inversion operation of the third column $\boldsymbol{W} = \begin{pmatrix} \bar{1} & 0 & 0 \\ 0 & \bar{1} & 0 \\ 0 & 0 & \bar{1} \end{pmatrix}$. When inspecting the matrices in the cosets, we obtain directly the point group $P(I,2,\bar{1},m)$ of the space group. The coset decomposition of the space group allows us directly to derive the *translationengleiche subgroups* of $P2/m$. Subgroups can be formed by the union of cosets. The following *t*-subgroups can be derived: $P2 = T_i\,1 \cup T_i\,2$, $P\bar{1} = T_i\,1 \cup T_i\,\bar{1}$, $Pm = T_i\,1 \cup T_i\,m$.

1.4.3 Generalized Crystallographic Symmetry

Within Sections 1.2–1.4, we have treated the fundamentals of the classical symmetry concept for the description of periodic crystals. This concept has to be extended when dealing with *n*-dimensional aperiodic crystals as briefly illustrated in Section 1.1. One way of generalizing the concept of symmetry is given using crystallographic groups in higher dimensions. The possibilities and applications of both *higher-dimensional* and *multimetrical crystallography* are outlined by Janner [47].

A comprehensive description and collection of tables for crystallographic groups in four dimensions is given in the book by Brown *et al.* [48]. Classification data of crystallographic groups in dimensions up to six are described by Opgenorth *et al.* [49], Plesken and Schulz [50], and Souvignier [51]. Table 1.26 contains the numbers of main crystallographic classes in dimensions up to six.

Table 1.26 Number of main crystallographic classes for dimensions 1–6 (enantiomorphic pairs in parentheses).

Classification	Dimension					
	1	2	3	4	5	6
Crystal families	1	4	6	23 (6)	32	91
Crystal systems	1	4	7	33 (7)	59	251
Bravais lattice types	1	5	14	64 (10)	189	841
Geometric crystal classes	2	10	32	227 (44)	955	7 104
Symmorphic space groups	2	13	73	710 (70)	6 079	85 311 (30)
Affine space group types	2	17	219 (11)	4 783 (111)	222 018 (79)	28 927 922 (7 052)
Space-group types	2	17	230	4 894	222 097	28 934 974

Table 1.27 Number of crystallographic groups G_n^m.

Dimension of space	Periodicity in subspace n			
m	0	1	2	3
1	2 point groups	2 one-dimensional space groups	—	—
2	10 point groups	7 frieze groups	17 plane groups (two-dimensional space groups)	—
3	32 point groups	75 rod groups	80 layer groups	230 space groups

It is obvious that, for dimensions $n > 3$, the number and complexity of groups is tremendously increased.

For particular structural investigations such as the analysis of a layer package of a crystal structure or of crystal defects (e.g., domain walls, twin boundaries, and grain boundaries), the knowledge of subperiodic groups is very useful. Table 1.27 gives an overview about the possible groups G_n^m, with $m \geq n$. The parameter n denotes the dimension of periodicity of subspace. The 7 frieze groups, 75 rod groups, and 80 layer groups are listed and described in detail in the International Tables, Volume E [52]. The point groups and space groups for $m = 2$, 3 are tabulated in [31], as already mentioned earlier.

The combination of geometric symmetry operations with parameters describing changes of crystal properties is another way of symmetry generalization. The black–white groups and color groups are conclusive examples for this type of symmetry generalization [53]. We will briefly illustrate the concept of antisymmetry (black–white symmetry groups), which is used for the description of magnetic point and space groups. The black and white color is used to characterize the two possible spin states (spin up – spin down). For this kind of symmetry generalization, the symmetry matrix $\boldsymbol{W}$ is augmented to

$$\boldsymbol{W} = \begin{pmatrix} \boldsymbol{W}_{11} & \boldsymbol{W}_{12} & \boldsymbol{W}_{13} & 0 \\ \boldsymbol{W}_{21} & \boldsymbol{W}_{22} & \boldsymbol{W}_{23} & 0 \\ \boldsymbol{W}_{31} & \boldsymbol{W}_{32} & \boldsymbol{W}_{33} & 0 \\ 0 & 0 & 0 & \boldsymbol{W}_{44} \end{pmatrix}, \quad \boldsymbol{W}_{44} = \pm 1 \tag{1.73}$$

The variable $\boldsymbol{W}_{44}$ is +1 for symmetry operations (proper and improper rotations) and is −1 for antisymmetry operations (proper and improper antirotations). The operation changing only $\boldsymbol{W}_{44}$ is the anti-identity $1'$ (E'). When we combine a symmetry operation with the anti-identity operation, an antisymmetry operation (connected with a change of color) will result

$$\boldsymbol{W}_i' = \boldsymbol{W}_i \circ 1' \tag{1.74}$$

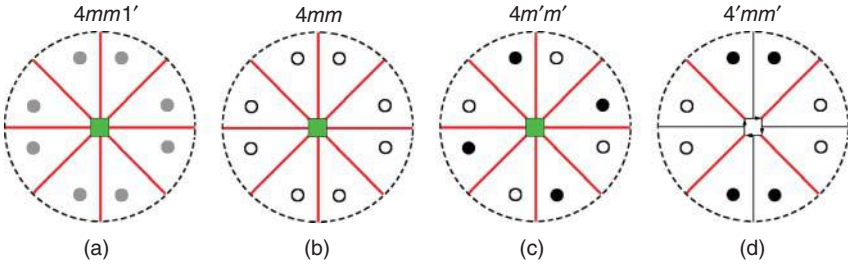

Figure 1.67 Stereographic projections of the tetragonal point groups $4mm1'$ (a), $4mm$ (b), $4m'm'$ (c), and $4'mm'$ (d).

Antisymmetry operations are labeled with a prime. The following relations exhibit that an antisymmetry operation will only result when we combine a symmetry operation with an antisymmetry operation.

$$\begin{aligned} W_i \circ W_j &= W_k \rightarrow \text{symmetry operation} \\ W_i' \circ W_j' &= W_k \rightarrow \text{symmetry operation} \\ W_i' \circ W_j &= W_k' \rightarrow \text{antisymmetry operation} \end{aligned} \tag{1.75}$$

The stereographic projections of the tetragonal magnetic point groups $4mm1'$, $4mm$, $4m'm'$, and $4'mm'$ shown in Figure 1.67 illustrate the various combinations of symmetry and antisymmetry operations.

The group $4mm1'$ is a so-called gray group (all $W_{44} = \pm 1$), $4mm$ is the white group (classical point group, all $W_{44} = +1$), and the groups $4m'm'$ and $4'mm'$ are black–white groups (half of the elements $W_{44} = +1$ and half of the elements $W_{44} = -1$), also denoted as proper magnetic groups.

It should be mentioned that the 122 three-dimensional magnetic point groups were already classified by Heesch in 1930 when he treated these groups as four-dimensional subgroups [54]. Later, the antisymmetry concept of the Russian crystallographers (Shubnikov, Belov, Zamorzaev) [53, 55] was used to describe the magnetic point groups and the magnetic space groups.

Table 1.28 Number of magnetic point and space groups for dimensions 1–4.

Magnetic point and space groups	Dimension *n*			
	1	2	3	4
Point groups	5	31	122	1 025 (177)
White/gray	2	10	32	227 (74)
Proper magnetic (black and white)	1	11	58	571 (89)
Affine space group types	7	80	1 594 (57)	61 553 (674)
White/gray	2	17	219 (11)	4 783 (11)
Proper magnetic (black and white)	3	46	1 156 (35)	51 987 (452)
Space group types	7	80	1 651	62 227

The number of possible magnetic point and space groups for dimensions 1–4 is listed in Table 1.28 (data adopted from Souvignier [56]). A detailed description of crystallographic properties of magnetic space groups is given by Litvin [57].

1.5 Crystal Structures

The mainly applied methods for the determination of the atomic arrangement in crystals, that is, the structure analysis of crystals, are diffraction techniques using X-rays, electrons, or neutrons. Furthermore, methods of electron crystallography are more and more applied to solve the structure of crystalline materials. The branch "electron crystallography" contains all methods and applications, which use electron scattering and imaging to study the structure of matter. Electron crystallography is particularly powerful to solve the structure of nanocrystalline materials where X-ray synchrotron-based methods fail because of the limited size of crystals [58, 59]. Both new developments of aberration-corrected electron microscopes and diffraction methods such as precession electron diffraction (PED) [60–62], nanobeam electron diffraction (NBED) and scanning-nanobeam electron diffraction (SNBED) [63], and automated electron tomography (ADT) [64] have created new possibilities for structural investigations of complex materials and materials systems.

Nowadays, the structure data of solved crystal structures are deposited in one of the crystallographic databases (see Section 1.6). In general, we know the main crystallographic features of the crystal structure when the following parameters are given:

- Chemical formula of the compound
- Number of formula units contained in the unit cell
- Lattice parameters
- Space group
- Cell content (coordinates of the atoms according to the occupied Wyckoff positions).

According to the diversity of the crystal structures as a function of the nature of the different material classes (e.g., inorganic, organic, macromolecules, etc.), we have to retrieve additional information on given structural features (e.g., local and global properties of the crystal structure). In the following, we will explain some of the main concepts and geometrical models for the classification and description of the structures of inorganic materials.

However, we should be aware of the fact that there are different equivalent structure descriptions possible because the Wyckoff sequence depends on the choice of the origin of unit cell. Furthermore, also an inversion or rotation of the coordinate system will cause a change of the structure data. Therefore, a standardization of crystal structure data is absolutely necessary, which can be done by means of

the program STRUCTURE TIDY [65]. Structure databases such as the Inorganic Crystal Structure Database (ICSD) uses standardized structure data entries and offer various search criteria (structure descriptors) for the identification of representative structure types of the compounds stored in the ICSD (for a detailed description, see [66]).

Generally, a crystal structure can be designated by the chemical formula and/or a colloquial name of the compound. Historically, the first classification scheme for crystal structure types was the ***Strukturbericht*** designation. According to this classification scheme, two structures belong to the same structure type if they coincide in lattice symmetry, occupied Wyckoff positions and formula type. The designation after the structure reports consists of a letter and a number (Table 1.29). The letter indicates the composition; the number is a reference number for the structure type (e.g., A1 – Cu, A2 – W, C1 – CaF_2, $H1_1$ – $MgAl_2O_4$). The notation is still in use particularly for the classification of metal and intermetallic structures. Nowadays, structures are mostly classified by means of the Pearson code, the space group, and the Wyckoff sequence. The Pearson code consists of three symbols for the crystal family, the Bravais lattice, and the number of atoms in the unit cell (e.g., cF4 – Cu, cI2 – W, cF8 – CaF_2, cF56 – $MgAl_2O_4$). For a more detailed description, particularly when various crystal structures will be compared with respect to structural relationships and similarities, it is useful to define a set of structural descriptors (analytical and geometrical descriptors) [67]. The analytical descriptors enable the mathematical description of the crystal structure. For this, one has to know:

1) the crystallographic basis of the structure (lattice parameters and metric tensor),
2) the space group symmetry,
3) atomic coordinates of the occupied Wyckoff positions.

Geometrical descriptors are used to describe the short-range order (nearest neighbor connectivity) and global properties of the crystal structure. An important local structure descriptor is the coordination number [N] and the corresponding coordination polyhedron. The symbols for the main important

Table 1.29 Definition of the Strukturbericht (structure report) symbols.

Strukturbericht designation	Structure type
A	Elements
B	AB compounds
C	AB_2 compounds
D	A_mB_n compounds
E, *F*, *G*, *H*, *J*, *K*	More complex compounds
L	Alloys
O	Organic compounds
S	Silicates

coordination polyhedra are given in Table 1.30. The coordination number of an atom specifies the number of nearest neighbor atoms, which form a polyhedron around the central atom. For more complicated structures, special methods for a "weighted coordination number" were discussed (references are given in [68]). Two coordination polyhedra can be connected via a common vertex, common edge, or common face. The coordination symbols can be added in the *crystal-chemical formulae* (e.g., spinel – $MgAl_2O_4$, crystal-chemical formulae: $Mg^{[4t]}Al_2{}^{[6o]}O_4$, $Mg^{[4t]}Al_2{}^{[6o]}O_4{}^{[1,3;12co]}$). The dimensionality of the connection of coordination polyhedra is expressed by the following symbols:

- $^{3}_{\infty}$ for three-dimensional framework structures, $^{3}_{\infty}$[C] diamond;
- $^{2}_{\infty}$ for a layer structure, $^{2}_{\infty}$[C] graphite;
- $^{1}_{\infty}$ for a linear structure (e.g., chain and fiber) $^{1}_{\infty}$[Se];
- $^{0}_{\infty}$ for a molecular structure, $^{0}_{\infty}$[CO_2].

For the characterization of the shape of molecules, extra symbols are used in addition:

- ^[…] for a chain molecule of finite length, $^{\wedge}_{n}$[C_2H_4], polyethylene;
- ○[…] for a cyclic molecule, $^{\bigcirc}$[C_6H_{12}], cyclohexane;
- •[…] for a cage molecule, $^{\bullet}$[C_{60}], Buckminster fullerene.

In order to describe existing similarities between inorganic crystal structures, the following definitions are important (for further details, see the IUCr report [68]):

Table 1.30 Important coordination polyhedra and their symbols.

Coordination polyhedron around atom A	Complete symbol
Two atoms collinear with atom A	[1l]
Two atoms noncollinear with atom A	[2l]
Triangle coplanar with atom A	[3l]
Square coplanar with atom A	[4l] or [4s]
Tetrahedron	[4t] or only [t]
Tetragonal pyramid with atom A in the center of base	[5y]
Tetragonal bipyramid	[5by]
Octahedron	[6o] or only [o]
Trigonal prism	[6p]
Monocapped trigonal prism	[6p1c]
Tetragonal prism	[8p]
Cube	[8cb] or [cb]
Anticube	[8acb] or [acb]
Dodecahedron with triangular faces	[8do] or [do]
Cubeoctahedron	[12co]
Anticubeoctahedron (twinned cubeoctahedron)	[12aco]
Icosahedron	[12i]

1) ***Isopointal*** structures:
   Two structures are ***isopointal*** if the following conditions are fulfilled:
   (i) same space-group type or belong to a pair of enantiomorphic space group types,
   (ii) same complete sequence of occupied (fully or partially at random) Wyckoff positions.
   Both geometric arrangements and atomic coordinations of isopointal structures may be different because there are no restrictions with respect to the lattice parameters and the adjustable position parameters (x, y, z).
2) ***Isoconfigurational*** structure:
   Two structures are ***isoconfigurational*** (*configurationally isotypic*) if it holds, that
   (i) both are ***isopointal***,
   (ii) for all corresponding Wyckoff positions, the crystallographic point configurations and their geometrical interrelations [e.g., axial ratios, unit cell angles, values of adjustable atomic positions (x,y,z), and coordination polyhedra] are similar.
   Let us compare the structures of pyrite FeS_2, CO_2, and PtP_2. The compounds are cubic with space group $Pa\bar{3}$ with identical occupied Wyckoff positions 4*a* 0, 0, 0, and 8*c* *x*,*x*,*x*. Therefore, the structures are isopointal. Are the three structures also isoconfigurational isotypic? Now, we have to prove if the abovementioned condition (ii) is fulfilled or not. The lattice constants are similar (FeS_2 $a = 5.42$ Å, CO_2 $a = 5.62$ Å, PtP_2 $a = 5.69$ Å). The free parameter x of the Wyckoff position 8*c* takes on the values $x = 0.384$ for pyrite, $x = 0.118$ for CO_2 and $x = 0.389$ for PtP_2, respectively. All free parameters between FeS_2 and PtP_2 are fitting very well. Both compounds are isoconfigurational isotypic. Contrary to this, the structure of CO_2 is neither isoconfigurational isotypic to FeS_2 nor to PtP_2. The deviation of the parameter x of CO_2 from the parameters x of FeS_2 and PtP_2, respectively, is too large. Thus, the separations between C–O, Fe–Se, and Pt–P are quite different.
3) ***Crystal-chemically isotypic*** structures:
   Two structures are ***crystal-chemically isotypic*** if:
   (i) both are ***isoconfigurational***; and
   (ii) the corresponding atoms and bonds have similar physical and chemical characteristics (e.g., bond strength and character, atomic radius ratios, and electronic states).
   A special case of ***isotypy*** is given for a pair of structures, which can be denoted as "***type–antitype pair***" if some of the physical/chemical characteristics in (ii) are reversed.
   In the structure type of fluorite (CaF_2, C1, cF12), the Ca cations occupy the Wyckoff position 4*a* and the F anions the position 8*c*. Some Me_2X compounds (Me = Li, Na, K; X = O, S, Se, Te) crystallizes also in this structure type. However, the Me cations occupy the position 8*c* and the X anions the position 4*a*. Thus, we have an exchange of the cation and anion positions. Those members of MeX_2 structures form with the fluorite structure *type–antitype* pairs.

4) ***Homeotypic*** structures:
Two structures are ***homeotypic*** if they are structurally similar and the conditions for isotypy are not fulfilled because:
(i) their space groups are different and between them a group/subgroup relation exist;
(ii) a Wyckoff position occupied by one atomic species in the first structure will be occupied by different atomic species in the second structure (splitting of the original Wyckoff position);
(iii) geometric properties are different [e.g., variations in axial ratios, axial angles, values of adjustable atomic positions (x,y,z), and coordination polyhedra).

Later on, we will derive from the diamond structure (C), the derivative structures sphalerite (ZnS), chalcopyrite ($CuFeS_2$), and stannite (Cu_2FeSnS_4) by substitution as described earlier (ii). Those structures are among each other *homeotypic*.

When we compare the crystal structures and figure out similarities between them, we have to be sure that the crystal structure data are standardized as mentioned earlier.

There are different methods and concepts, which were applied to describe crystal structures. The crystallographic Bauverband (connectivity pattern) introduced by Laves [69] can be divided into frameworks, layers, chains, and isolated groups. As an example, such framework of a structure is given if a part of the structure forms a sphere packing and the other part occupies voids in the sphere packing. Another attempt for the crystal structure description is the application of lattice complexes.

In addition, theoretical methods such as the graph theory or the group theory can be applied to describe and classify crystal structures. In the following, we will discuss the concept of sphere packings.

1.5.1 Sphere Packings

The concept of sphere packing is an appropriate tool for the description and classification of many crystal structures. In the context of mathematical crystallography, a *sphere packing* is defined as a three-dimensional periodic arrangement of spheres with the symmetry of a space group [70]. Preconditions that a set of spheres forms a sphere packing are

- each sphere has a contact at least with one other sphere;
- there is no overlapping of spheres;
- any pair of spheres is connected by a chain of spheres with mutual contact.

Sphere packings are divided in *homogeneous* and *heterogeneous* ones. A *homogeneous sphere packing* consists of symmetry equivalent spheres. This assumes also that all spheres have an equal size.

Sphere packings are classified into types because there exist an infinite number of *homogeneous* and *heterogeneous* sphere packings. Two sphere packings belong to the same type if the sphere packings can be mutually mapped onto each other without any change of the existing contact relationships. The short symbol $k/m/fn$ is used for the classification of sphere packing types [71], where the number k gives the contacts per sphere, m is the length of the shortest mesh within the sphere packing, and f denotes the highest crystal family for the sphere type followed by an arbitrary number n for the differentiation of sphere types with equal $k/m/f$. The number k for homogeneous sphere packings is limited within the range $3 \geq k \leq 12$.

An important parameter is the ***packing density*** ρ of the sphere packing, which is given by the ratio of the volume of all spheres in the unit cell to the volume of the unit cell. It is $\rho = (4/3)\pi(ZR^3/V)$ (Z – number of spheres within the unit cell; R – radius of the spheres; V – volume of the unit cell).

Homogeneous sphere packing types were systematically derived for the cubic (199 types [72, 73]), tetragonal (394 types [71, 74–76]), hexagonal (170 types [77–80]), orthorhombic (365 types [81, 82]), and triclinic (30 types [83]) crystal systems.

In the following, we will describe some selected examples of homogeneous sphere packing types (Table 1.31). The first two examples are the types of the ***cubic closest packing*** (***ccp***) (12/3/*c*1) and the ***hexagonal closest packing*** (***hcp***) (12/3/*h*1). The most dense packing in a plane is a ***hexagonal layer of circles*** where each circle has six contacts and the length of the mesh is 3 (net: 3^6, 6 triangles meet at one vertex; density $\rho = 0.9069$). In analogy, we generate a hexagonal layer of spheres with six contacts of each sphere within the layer (Figure 1.68). The positions of the centers of spheres are labeled by A. We can also see that there are holes between three adjacent spheres in the layer. The holes are sometimes denoted as ***interstices***, ***vacancies***, or ***voids***. With respect to ***crystal structures***, we will use voids and the terms ***interstices*** and ***vacancies*** only with respect to zero-dimensional crystal defects (point defects). The different void positions are labeled by B and C, respectively. The next close-packed layer can be deposited in such a way that the centers of the spheres are at B or C, generating a two layer packing of AB or AC, respectively. By the way, both the packings

Table 1.31 Selected examples of sphere packing types.

Sphere packing type *k/m/fn*	Symmetry Lattice complex		Density, ρ
12/3/*c*1	***F*** $Fm\bar{3}m$	4(*a*) 0, 0, 0	0.7405
12/3/*h*1	***E*** $P6_3/mmc$	2(*c*) 1/3, 2/3, 1/4	0.7405
8/4/*c*1	***I*** $\boldsymbol{Im\bar{3}m}$	2(*a*) 0, 0, 0	0.6802
6/4/*c*1	***P*** $\boldsymbol{Pm\bar{3}m}$	1(*a*) 0, 0, 0	0.5236
4/6/*c*1	***D*** $\boldsymbol{Fd\bar{3}m}$	8(*a*) 0, 0, 0	0.3401
3/3/*c*1	$I4_132$	24(*h*) 1/8, *y*, $^1/_4 - y$	0.0580

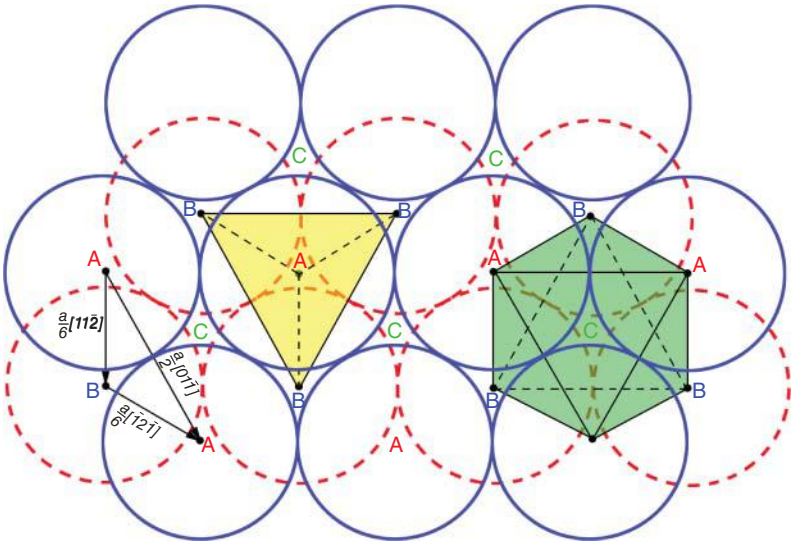

Figure 1.68 Closest homogeneous sphere packings (***hcp*** and ***ccp***).

AB and AC have an identical arrangement. When we have a two layer packing AB, the third layer can be placed only at A or C. This leads to the ABAB … and ABCABC … stacking sequences if we repeat the stacking order periodically. The … ABAB … packing shows hexagonal symmetry with dense-packed (00.1) oriented layers (hexagonal-closed packed). The periodic three layer stacking sequence … ABCABC … has cubic symmetry where the dense-packed planes are {111} planes (cubic-closed packed). In general, we have always two stacking possibilities to place a layer onto a previous one. This means one can derive an infinite number of densely packed stacking sequences. However, only the ***hcp*** and ***ccp*** stacking sequences are leading to homogeneous sphere packings.

Thus, the ***closest homogeneous sphere packing*** (contact number k: 12, each sphere has 6 sphere contacts within the layer, 3 sphere contacts to the parallel layer above and below) are

– (12/3/h1) ***hcp***, stacking sequence: … ***ABAB*** … and
– (12/3/c1) ***ccp***, stacking sequence: … ABCABC ….

Now, we will examine what kind of voids and how many of them occur in ***hcp*** and ***ccp***.

A closer inspection of our arrangement of parallel hexagonal layers of spheres shows us there are two different kinds of voids. Between two layers with four nearest neighbors (coordination number [4]), there are "***tetrahedral voids***," and between two layers with six nearest neighbors, there are "***octahedral voids***" (coordination number [6]). The voids can be filled with smaller spheres of radius R_V touching the surrounding spheres of the sphere packing with radius R. From the geometrical arrangement of our densest sphere packing, we can calculate that the

largest sphere that can be placed in a ***tetrahedral void*** has a radius R_V of 0.225R and a radius of 0.414R for an ***octahedral void***.

The strict mathematical derivation of the homogeneous sphere packing type ***hcp*** shows that it refers to the hexagonal lattice complex $P6_3/mmc2(c)$. Thus we have a hexagonal unit cell where the two spheres occupy the Wyckoff position 2*c* 1/3, 2/3, 1/4 and 2/3, 1/3, 3/4 of space group $P6_3/mmc$. The octahedral voids are then located at the Wyckoff position 2*a* 0, 0, 0; 0, 0, 1/2, whereas the tetrahedral voids occupy the position 4*f* (1/3, 2/3, *z*; 2/3, 1/3, *z* +1/2; 2/3, 1/3, −*z*; 1/3, 2/3, −*z* +1/2) with $z = -1/8$.

The advantage of the above-chosen description is that the space group symmetry of the sphere packing is obvious and in coincidence with the setting of $P6_3/mmc$ in the International Tables for Crystallography, Vol. A [31].

It should be noted that, in several books, the positions 0, 0, 0 and 2/3, 1/3, 1/2 are chosen for the two spheres of ***hcp***. Then, the two octahedral voids are located at 1/3, 2/3, 1/4 and 1/3, 2/3, 3/4, and the four tetrahedral voids are located at 0, 0, 3/8; 0, 0, 5/8; 2/3, 1/3, 1/8, and 2/3, 1/3, 7/8.

The ***ccp*** type corresponds to the cubic invariant lattice complex *F*. The four spheres occupy the position 4*a* of space group $Fm\bar{3}m$ (0, 0, 0; 1/2, 1/2, 0; 1/2, 0, 1/2; 0, 1/2, 1/2). There are four octahedral voids in the unit cell (Wyckoff position 4*b*). One void lies at the center of the unit cell (1/2, 1/2, 1/2), and the three others lie at the middles of the edges (1/2, 0, 0; 0, 1/2, 0; 0, 0, 1/2).

The eight tetrahedral voids (Wyckoff position 8*c*) are occupying the centers of eight cubes with an edge length $a/2$ within the unit cell (1/4, 1/4, 1/4; 1/4, 1/4, 3/4; 1/4, 3/4, 1/4; 3/4, 1/4, 1/4; 3/4, 3/4, 1/4; 3/4, 1/4, 3/4; 1/4, 3/4, 3/4).

In ***hcp*** and ***ccp***, we have altogether n octahedral voids and $2n$ tetrahedral voids per sphere where n is the number of spheres per unit cell (hcp: $n = 2$, ccp: $n = 4$).

The body-centered cubic lattice corresponds to the cubic invariant lattice complex *I* and the sphere packing 8/4/*c*1, with a packing density of 68.02%. In this sphere package exists 12 voids at (1/2, 1/4, 0) and the symmetry equivalent positions. This type of void has four nearest neighbors. The coordination polyhedron is a distorted tetrahedron (tetragonal disphenoid or tetragonal tetrahedron). The radius ratio R_V/R of 0.291 is larger than for an undistorted tetrahedral void. In addition, there are voids at the centers of the cube faces (1/2, 1/2, 0 and the symmetry equivalent positions, $6 \times 1/2 = 3$) and at the midpoints of the the 12 edges of the cube (0, 1/2, 0 and the symmetry equivalent positions, $12 \times 1/4 = 3$). The voids are surrounded by six spheres (coordination number: [6]), where two of them have a shorter distance than the other four. The coordination polyhedron is a distorted octahedron (obtuse tetragonal dipyramid). The largest sphere that can be placed in such a void has a radius of 0.155R.

The sphere packing type 6/4/*c*1 corresponds to the primitive cubic lattice with a packing density of 52.4%. In the center of the unit cell is a large void, which is surrounded by the eight spheres lying at the corners of cube (hexahedral coordination, coordination number: [8]). The radius of such a big sphere is 0.732R. In addition, there exist quadratic voids (coordination number: [4]) at the centers of the faces of the cube. The radius of a sphere filling the quadratic void is

0.414*R*, which is equal to the radius of octahedral coordination. Strictly speaking, the quadratic voids are not real self-contained voids. The position of them is marking the tightest connection between two hexaedric voids. In the sphere packing type 6/4/*c*1, the proportion is one quadratic void and three hexaedric voids per one sphere.

The type 4/6/*c*1 corresponds to the diamond structure and can be derived from the cubic invariant lattice complex *D*. The packing density amounts to only 34.01%.

The packing type 3/3/*c*1 with a packing density of 5.8% was derived by Heesch and Laves [84]. This packing is the thinnest possible (least dense packed) homogeneous sphere packing with three contacts per sphere (for a proof, see [85]). However, this sphere packing is unstable due to the low contact number $k = 3$. A stable sphere packing needs at least $k = 4$.

1.5.2
Selected Examples of Inorganic Structure Types

The goal of crystal chemistry and in broader sense of structural chemistry or structural crystallography in general is the study of the relationships between the crystal structures and the corresponding physical and chemical properties. A main task of crystal chemistry is the structure analysis, structure description, and classification of structures. In the following part, we will describe some of the basic structure types of inorganic materials. For a more comprehensive and detailed description of inorganic crystal structures, the following books are recommended [86–90].

- **Simple cubic structure**, A_{H}, *cP*1, prototype: αPo, $Pm\overline{3}m$
  Atomic coordinates: *Po* 1*a* 0 0 0.
  The simple cubic structure corresponds to the cubic invariant lattice complex *P* and to the sphere packing 6/4/*c*1. The prototype αPo is the sole representative for this structure type (Figure 1.69a).
- **bcc structure**, *A*2, *cI*2, prototype: W, $Im\overline{3}m$
  Atomic coordinates: W 2*a* 0 0 0

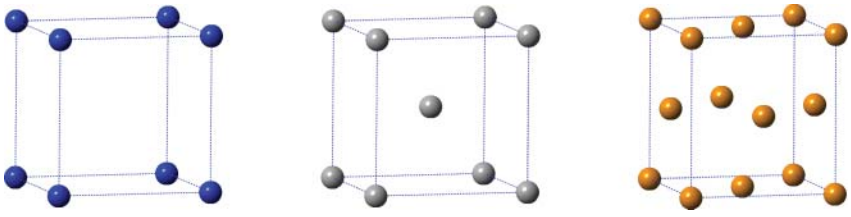

(a) (b) (c)

Figure 1.69 Crystal structures of (a) polonium, (b) tungsten, and (c) copper.

The structure corresponds to the cubic invariant lattice complex *I* and to the sphere packing 8/4/*c*1 (Figure 1.69b). Examples of representatives of this structure types are the alkali metals Li, Na, K, Rb, and Cs and the transition metals V, Cr, Fe, Nb, Mo, Ta, and W.

- **fcc structure**, *A*1, *cF*4, prototype: Cu, $Fm\bar{3}m$,
  Atomic coordinates: Cu 4*a* 0 0 0; coordination formula: ${}^{3}_{\infty}[Cu^{12co}]$
  The *A*1 structure type corresponds to the ccp 12/3/*c*1 and to the cubic invariant lattice complex *F*. The closest-packed layers are the {111} planes; the closest-packed directions are the <110> directions.
  The coordination conditions for ***fcc*** structure are
  – 12 nearest neighbors in <110> directions,
  – 6 second nearest neighbors in <100> directions,
  – 24 third nearest neighbors in <211> directions,
  – 12 fourth nearest neighbors in <110> directions.
  Representatives of structure type *A*2: Cu, Ag, Au, Ni, Rh, Pd, Ir, and Pt.
- **hcp structure**, *A*3, *hP*2, prototype: Mg, $P6_3/mmc$
  Atomic coordinates: Mg 2*c* 1/3 2/3 $^1/_4$
  The *A*3 structure type corresponds to the hcp 12/3/*h*1 and to the hexagonal invariant lattice complex *E*. The closest-packed layers are the {00.1} planes; the closest-packed directions are the <11.0> directions. An ideal ***hcp*** structure is given if the separations of the 12 nearest neighbors of a sphere are identical. The axial ratio *c*/*a* is then $\sqrt{8/3} = 1.633$. Magnesium as the prototype of the *A*3 structure type has an axial ratio of $c/a = 1.624$. Some hcp metals and their *c*/*a* ratios are given in Table 1.32. The primitive hexagonal unit cell (drawn in red) of Mg contains two atoms (Figure 1.70). The hcp stacking sequence … ABAB … is obvious if multiple cells with shifted origin are shown.
- **Diamond structure**, *A*4, *cF*8, prototype: C (diamond), $Fd\bar{3}m$
  Atomic coordinates: C 8*a* 0 0 0; coordination formula: ${}^{3}_{\infty}[C^{4t}]$
  The diamond structure corresponds to the cubic invariant lattice complex *D* and to the sphere packing 4/6/*c*1. The unit cell contains eight atoms. In addition to the four atoms decorating the *F*-lattice, there are four atoms located at four centers of the eight octants of the unit cell. All atoms are tetrahedrally coordinated.

Table 1.32 Axial ratios of hcp metals.

Metal	*c*/*a*	Metal	*c*/*a*
Cd	1.882	Mg	1.624
Zn	1.856	Zr	1.593
Li	1.637	Ti	1.588
Na	1.634	Y	1.571
Ni	1.634	Be	1.567

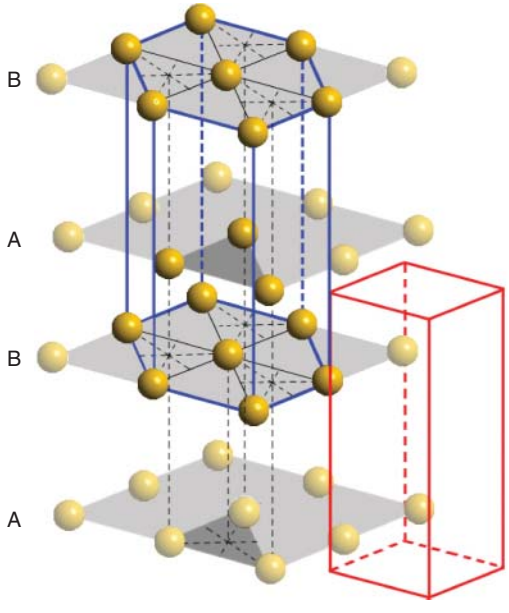

Figure 1.70 Structure of Mg.

There exists also a hexagonal modification of diamond, the ***lonsdaleite*** (space group: $P6_3/mmc$). The structure corresponds to a configuration of the hexagonal univariant lattice complex $E2_Z$ and to the sphere packing type 4/6/*h*2.
In addition to the cubic carbon, white α-Sn, Si, and Ge crystallize in the diamond structure (Figure 1.71).

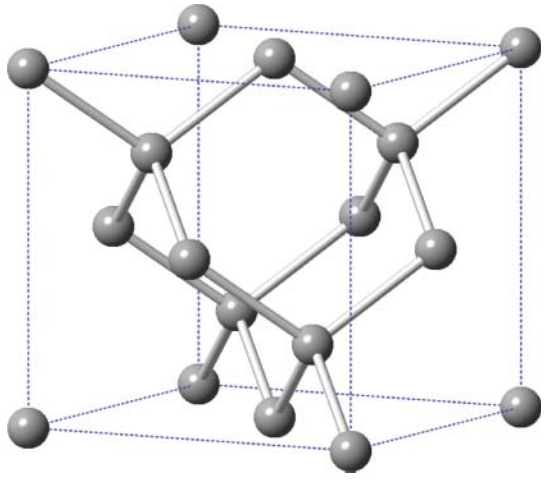

Figure 1.71 Diamond structure.

- **Graphite structure**, *A*9, *hP*4, prototype: C (graphite), $P6_3/mmc$

  Atomic coordinates: $\begin{matrix} \text{C1} & \text{C} & 2c & 1/3 & 2/3 & 1/4 \\ \text{C1} & \text{C} & 2b & 0 & 0 & 1/4 \end{matrix}$; coordination formula: $^{2}_{\infty}[\text{C}^{3\text{l}}]$

  The graphite structure consists of planar hexagonal layers where each carbon atom has three nearest neighbors at a separation of $a\sqrt{3}$. The parallel layers are stacked along the [00.1] direction. As we can see in Figure 1.72, the hexagons of the layers are identically oriented but shifted in such a way that only half of the atoms have identical x_1, x_2-positions with the atoms in the layer above and below. Graphite is a layer structure with a separation of 1.42 Å for the nearest neighbors in the (00.1) layer and a separation of 3.35 Å along the [00.1] stacking direction. The large c/a ratio and the great discrepancies of the bond strength within the layer and perpendicular to it make the good cleavage (00.1) and the low hardness of graphite clear.
- **NaCl structure**, *B*1, *cF*8, prototype: NaCl, $Fm\bar{3}m$

  Atomic coordinates: $\begin{matrix} \text{Na} & 1a & 0 & 0 & 0 \\ \text{Cl} & 1b & 1/2 & 1/2 & 1/2 \end{matrix}$; coordination formula: $^{3}_{\infty}[\text{Na}^{(6o)}\text{Cl}^{(6o)}]$

  This structure type is an example for a ccp structure where one atom species is occupying the octahedral voids. Both atom species have an octahedral coordination. It is regardless if we describe the NaCl structure as a homogeneous sphere packing of Na ions where the Cl ions are located at the octahedral voids or vice versa, the Cl ions form the ccp and the Na ions are filling the octahedral voids. This means the NaCl structure is its own antitype structure. Numerous derivative structures can be generated from the NaCl structure (Figure 1.73).

  Many AB-compounds crystallize in the sodium chloride structure. Examples are LiF, KCl, KBr, PbS, BaO, EuS, HfC, and so on.

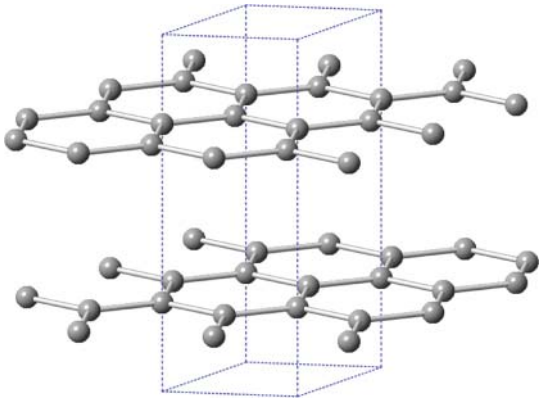

Figure 1.72 Graphite structure.

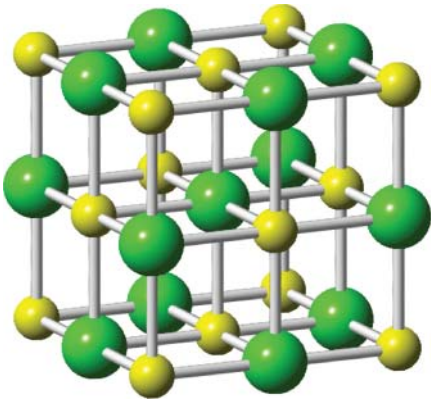

Figure 1.73 NaCl structure.

- **CsCl structure**, *B*2, *cP*2, prototype: CsCl, $Pm\bar{3}m$
  Atomic coordinates: $\begin{matrix} \text{Cs} & 1a & 0 & 0 & 0 \\ \text{Cl} & 1b & 1/2 & 1/2 & 1/2 \end{matrix}$; coordination formula: ${}^{3}_{\infty}[\text{Cs}^{(8cb)}\text{Cl}^{(8cb)}]$
  This structure as a hole can be treated as a heterogeneous sphere packing where two different atom species are packed similarly to a homogeneous cubic body-centered sphere packing. The halogenides CsCl, CsBr, and CsJ and a large number of intermetallic compounds (e.g., NiAl, CuZn, CdCe, AgMg, etc.) crystallize in this structure type (Figure 1.74).
- **CuAu structure**, $L1_0$, *tP*2, prototype: CuAu, $P4/mmm$
  Atomic coordinates: $\begin{matrix} \text{Cu} & 1a & 0 & 0 & 0 \\ \text{Au} & 1d & 1/2 & 1/2 & 1/2 \end{matrix}$
  $a = b = 2.8143$ Å, $c = 3.72$ Å, $c : a = 1.322$.
  The CuAu structure type as given above in standardized crystallographic data can be described as slightly distorted CsCl structure ($c : a = 1.32$). We have an

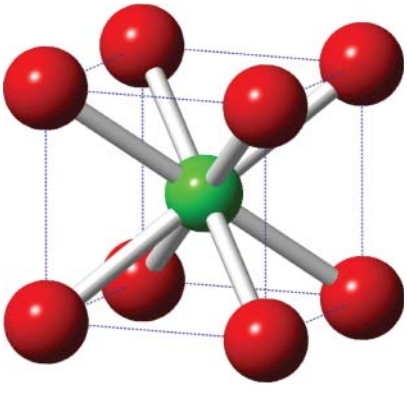

Figure 1.74 CsCl structure.

ordered intermetallic structure where the planes parallel to (001) are alternately occupied by Cu and Au atoms, respectively. On the other hand, the ordered CuAu structure type can also be derived from the fcc structure. The structural relationships between the Cu structure type and CuAu are obvious if following data set is used:

Nonstandard setting of space group $C4/mmm$, atomic coordinates:
Cu $2a$ 0,0,0; Au $2d$ ½,0,½: $a = b = 3.98$ Å, $c = 3.72$ Å, $c : a = 0.935$.
The following coordinate transformation leads to the standard setting (axes a_s, b_s, c_s): $a_s = a/2 - b/2$; $b_s = a/2 + b/2$; $c_s = c$.
Altogether, 75 binary alloys (e.g., CuTi, FePt, FePd, etc.) crystallize in this structure type (Figure 1.75).

- **Cu_3Au structure**, $L1_2$, $cP4$, prototype: Cu_3Au,

Atomic coordinates:

Cu	$3c$	0	1/2	1/2
Au	$1a$	0	0	0

The Cu and Au atoms occupy the positions of a cubic F-Bravais lattice. Owing to the ordered occupation of the vertices positions by Cu atoms and all face centers by Au atoms, a symmetry reduction to $Pm\bar{3}m$ result. A statistical occupation of the F-Bravais lattice positions by Au and Cu atoms exist at temperatures above 663 K. Therefore, the structure of the high-temperature phase of Cu_3Au belong to the space group $Fm\bar{3}m$. Figure 1.76 illustrates the structural relationships between the fcc structure, CuAu, and Cu_3Au.

It should be noted that the transition from the statistical occupation of lattice positions to an ordered occupation leads to the formation of so-called ***superstructures***. The distinction between fcc Cu_3Au ($Fm\bar{3}m$) and the superstructure of ordered Cu_3Au ($Pm\bar{3}m$) can be carried out by means of extinction rules of diffraction experiments, as already described in Section 1.4. For the F-Bravais lattice, only even (e.g., 200, 422, etc.) or odd (111, 315, etc.) hkl reflections are kinematically allowed, whereas no reflections are extinct for a P-lattice. For

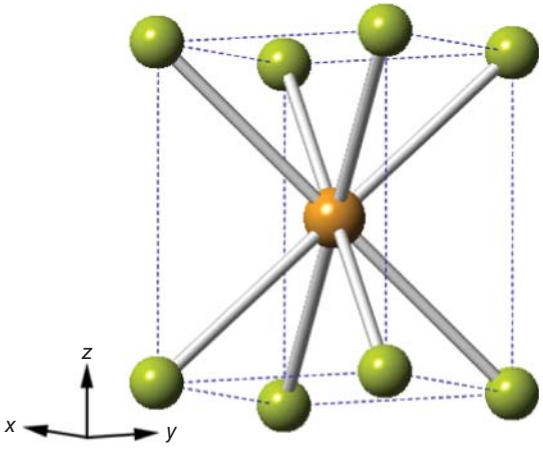

Figure 1.75 Structure of CuAu.

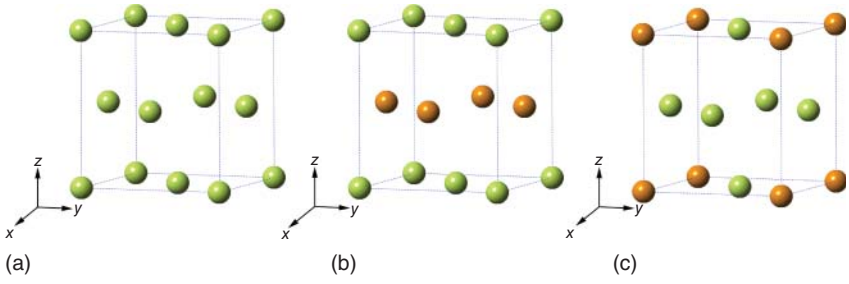

Figure 1.76 Structural relationships between (a) fcc (Cu type), (b) CuAu, and (c) Cu_3Au.

example, 100, 010, 001 reflections are extinct for $Fm\bar{3}m$ but will occur for the superstructure symmetry $Pm\bar{3}m$. In this case, those reflections are denoted as ***superreflections*** and allow the discrimination between the two structure types. The Cu_3Au structure type belongs to the most common structural types of intermetallic phases (386 representatives, e.g., $FeNi_3$, $AlCo_3$, $FePd_3$, Au_3Cd, etc.).

- **Zincblende (sphalerite) structure**, *B*3, *cF*8, prototype: ZnS, $F\bar{4}3m$

  Atomic coordinates: $\begin{matrix} \text{Zn} & 4a & 0 & 0 & 0 \\ \text{S} & 4c & 1/4 & 1/4 & 1/4 \end{matrix}$ coordination formula: ${}^{3}_{\infty}[\text{Zn}^{(4t)}\text{S}^{(4t)}]$

  The sphalerite structure type with the occupation of the Wyckoff position as given above is a ccp structure of Zn where S is occupying one-half of the tetrahedral voids. We can also exchange the positions of Zn and S; thus, we have a ccp structure of S where Zn is occupying one-half of the tetrahedral voids. The following stacking sequences with respect to the tetrahedral voids are possible:
  – AαBβCγAαBβCγ
  – AβBγCαAβBγCα.

  The void sequences αβγαβγ … and βγαβγα … show us that either tetrahedral "down" or tetrahedral "up" voids are occupied.

  Examples: ZnS, CdS, AlAs, ZnTe, CdTe, GaAs, GaSb, InP, CuCl, and so on (Figure 1.77).

- **Wurtzite structure**, *B*4, *hP*4, prototype: ZnO, $P6_3mc$

  Atomic coordinates: $\begin{matrix} \text{Zn} & 2b & 1/3 & 2/3 & 0.381 \\ \text{S} & 2b & 1/3 & 2/3 & 0 \end{matrix}$; coordination formula: ${}^{3}_{\infty}[\text{Zn}^{(4t)}\text{S}^{(4t)}]$

  The wurtzite structure type may be described as hcp structure of Zn where S is occupying one-half of the tetrahedral voids or vice versa. The following stacking sequences with respect to the tetrahedral voids are possible:
  AαBβAαBβ
  AβBαAβBα.

  The void sequences αβαβ … and βαβα … show us that either tetrahedral "down" or tetrahedral "up" voids are occupied as in the sphalerite structure.

  Examples: ZnS, CdS, CdSe, ZnTe, ZnO, GaN, AlN, SiC, and so on (Figure 1.78).

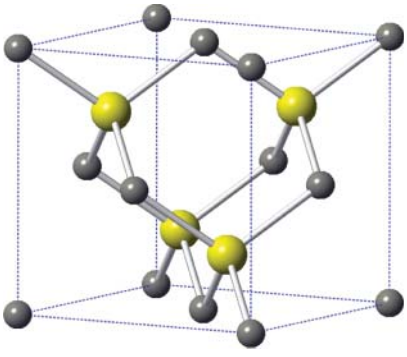

Figure 1.77 Sphalerite structure.

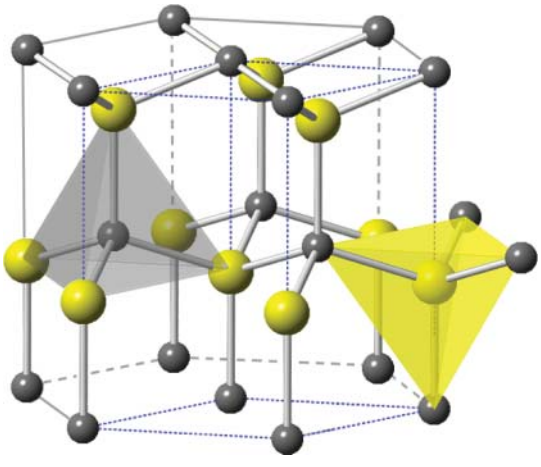

Figure 1.78 Wurtzite structure.

- **Fluorite structure**, $C1$, $cF12$, prototype: CaF_2, $Fm\bar{3}m$

  Atomic coordinates: $\begin{matrix} \text{Ca} & 4a & 0 & 0 & 0 \\ \text{F} & 8c & 1/4 & 1/4 & 1/4 \end{matrix}$; coordination formula: ${}^{3}_{\infty}[\text{Ca}^{(8cb)}\text{F}_2^{(4t)}]$

  This structure type can be described as follows: The cations form a ccp structure where all tetrahedral voids are filled with anions (Figure 1.79). From this structure type, various derivative structure types can be derived by a partial occupation of the tetrahedral voids in the original unit cell or in enlarged unit cells.

  For this structure type, there exists also the antifluorite type where the positions of the cations and anions are exchanged.

  Examples for the fluorite structure: CaF_2, CuF_2, $SrCl_2$, and $BaCl_2$.

  Examples for the antifluorite structure: Li_2O, Na_2Se, K_2O, and K_2Te.

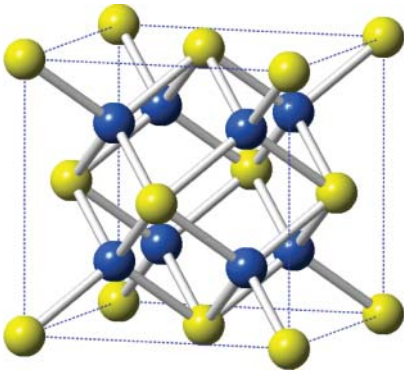

Figure 1.79 Crystal structure of fluorite.

- **Chalcopyrite structure**, $E1_1$, $tI16$, prototype: $CuFeS_2$, $I\bar{4}2d$

  Atomic coordinates:

Cu	$4b$	0	0	1/2	
Fe	$4a$	0	0	0	$^3_\infty[Cu^{(4t)}Fe^{(4t)}S^{(2,2,t)}]$
S	$8d$	0.23	1/4	1/8	

  The structure of the most common copper mineral chalcopyrite represents the prototype of the structure type $E1_1$. Many ternary semiconductor compounds ABX_2 (A = Cu; B = In, Ga; C = S, Se, Te) are crystallizing in this structure type. They are promising candidates for the development of thin film solar cells. The chalcopyrite structure can be derived from the sphalerite structure. The structural relationships between both structure types are illustrated in detail in Section 1.5.4. Comparing both structures, we can see that the length of the c-axis of $CuFeS_2$ is doubled (tetragonal symmetry instead of cubic) and two zinc atoms of ZnS are replaced by one Cu and one Fe atom (see the splitting of Wyckoff position in the symmetry tree, Section 1.5.4).

  Another important structural feature of the chalcopyrite structure is that the cations can form special ordered structures (superstructures). Figure 1.80 shows unit cells of the sphalerite structure, the chalcopyrite structure, and the CuAu-type ordering and the CuPt-ordering of chalcopyrite [91]. The ordered domains

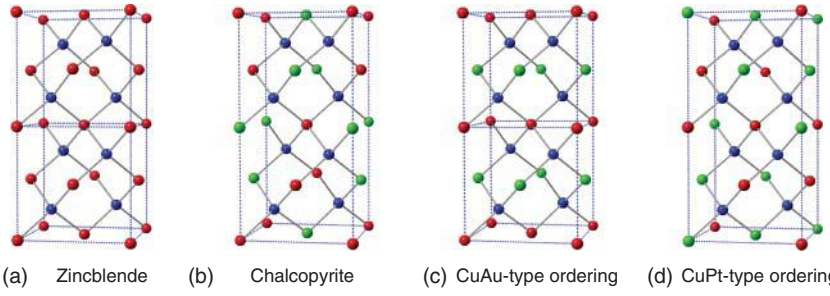

Figure 1.80 Structure relationships between ZnS (sphalerite) and $CuFeS_2$ (chalcopyrite): (a) ZnS structure (a, b, $2c$), (b) $CuFeS_2$, (c) CuAu-ordered $CuFeS_2$, and (d) CuPt-ordered $CuFeS_2$.

in the structure can be directly imaged by means of HRTEM. In addition, in the electron or X-ray diffraction patterns, the ordering phenomena can be determined by the appearance of so-called super reflections.

- **Perovskite structure**, $E2_1$, $cP5$, prototype: $CaTiO_3$, $Pm\bar{3}m$

  Atomic coordinates (standardized data):

Ca	1*b*	1/2	1/2	1/2	
Ti	1*a*	0	0	0	; coordination formula:
O	3*d*	1/2	0	0	

  ${}^{3}_{\infty}[Ca^{(8cb,12co;0)}Ti^{(8cb,6o;0)}O_3^{(4l,2l;8p)}]$

  Origin shift: 1/2 1/2 1/2

  Atomic coordinates:

Ca	1*a*	0	0	0
Ti	1*b*	1/2	1/2	1/2
O	3*c*	0	1/2	1/2

  This structure type is named after the mineral perovskite ($CaTiO_3$). The ideal cubic perovskite structure consists of a cubic-close packing of the Ca^{2+} cations and the O anions. The Ti^{4+} cations fill one-quarter of the octahedral voids. The Ca ions are cubeoctahedrally coordinated by O^{2-} anions. The Ti^{4+} cations are octahedrally coordinated by O^{2-} anions. The structure can also be illustrated by the framework of TiO_6 octahedra, which are connected via vertices in all three dimensions. Always in the center of eight vertex-connected TiO_6 octahedra is a hole, which is occupied by a Ca^{2+} cation (Figure 1.81).

  Only a few compounds such as $SrTiO_3$ crystallize in the ideal cubic perovskite structure. Even $CaTiO_3$ is slightly distorted. Symmetry reduction may be caused by

  – tilting of the anion octahedra
  – distortions of the octahedra
  – displacements of the cations.

  Owing to the abovementioned sources of distortions, many structures with reduced symmetry can be derived from the ideal cubic perovskite. The structural relationship between the aristotype (ideal perovskite) and the derived

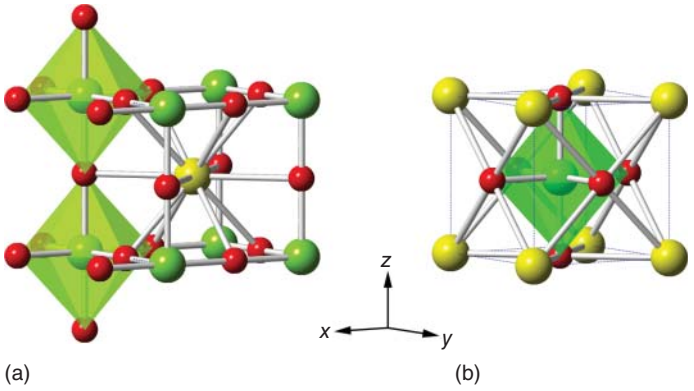

Figure 1.81 Perovskite structure (a) standard setting and (b) second setting, origin shift 1/2, 1/2, 1/2.

structures (hettotypes) can be described by means of symmetry trees (see Section 1.5.4). A detailed derivation and description of symmetry trees for perovskites with tilted octahedra, displaced cations, and distorted octahedra is given by Bock and Müller [92].

A simple estimation of the degree of symmetry reduction of ABX_3 perovskites is possible by means of Goldschmidt's tolerance factor t. The factor describes the geometrical relationships of an perovskite, where r(A), r(B), r(X) are the ionic radii (assumption of pure ionic bonding). The tolerance factor t is expressed as

$$t = \frac{r(\mathrm{A}) + r(\mathrm{X})}{\sqrt{2}(r(\mathrm{B}) + r(\mathrm{X}))} \tag{1.76}$$

An ideal perovskite structure has the value $t = 1$ [e.g., $SrTiO_3$, r(A) = 1.44 Å, r(B) = 0.605 Å, r(O) = 1.40 Å). However, a cubic structure may occur if $0.89 < t < 1$. Perovskites with lower symmetry caused by the abovementioned distortions are given for $0.8 < t < 0.89$. Hexagonal perovskites may occur if $t > 1$ (e.g., $BaNiO_3 = 1.13$).

Materials with perovskite structure exhibit extraordinary electrical and magnetic properties (see Section 4.1.3.5), which are strongly influenced by the symmetry changes due to the structural peculiarities (tilting and distortions of the anion octahedra and displacements of cations). Many perovskites such as $BaTiO_3$ undergo phase transitions. Many important ferroelectric materials crystallize in the perovskite structure. For example, the cubic $BaTiO_3$ ($Pm\bar{3}m$) is paraelectric and undergoes a phase transition below 393 K (Curie temperature) to the ferroelectric tetragonal $BaTiO_3$ ($P4mm$).

Examples:

- Cubic perovskites: $SrTiO_3$, $GdMnO_3$, $CeFeO_3$, **$BaTiO_3$**, and so on.
- Tetragonal perovskites: $SrTiO_3$ (78 K), **$BaTiO_3$**, $SrZrO_3$ (1175 K), and so on.
- Rhombohedral perovskites: $BiFeO_3$, $LaNiO_3$, **$BaTiO_3$**, NdAlO3, and so on.
- Hexagonal perovskites: $BaNiO_3$, **$BaTiO_3$**, $CsNiCl_3$, and so on.
- Orthorhombic perovskites: $PrFeO_3$, $YFeO_3$, $GdFeO_3$, **$BaTiO_3$**, and so on.

• **Spinel structure**, $H1_1$, $cF56$, prototype: $MgAl_2O_4$, $Fd\bar{3}m$

Atomic coordinates (standardized data):

Mg	8*b*	3/8	3/8	3/8	
Al	16*c*	0	0	0	($x = 0.238$);
O	32*e*	*x*	*x*	*x*	

coordination formula: ${}^{3}_{\infty}[Mg^{(4t)}Al^{(6o)}_2O^{(1,3;12co)}_4]$

Origin shift: 3/8 5/8 5/8

Atomic coordinates:

Mg	8*a*	0	0	0
Al	16*c*	5/8	5/8	5/8
O	32*e*	3/8	3/8	3/8

The spinel structure consists of a nearly perfect cubic close packing of anions, where the cations occupy 8 tetrahedral and 16 octahedral voids of the existing 64 tetrahedral and 32 octahedral voids per unit cell. In general, the distribution of the cations A and B onto the tetrahedral and octahedral voids can be described

by the following occupation matrix:

$$\begin{matrix} \underline{A} & \underline{B} \\ \begin{pmatrix} S_{11} & S_{12} \\ S_{21} & S_{22} \end{pmatrix} \end{matrix} \tag{1.77}$$

The matrix elements S_{11}, S_{12} and S_{21}, S_{22} specify the fraction of cations occupying the tetrahedral and octahedral voids, respectively. The two extreme cation distributions representing the *normal spinel structure* $A(B_2)X_4$ and the *inverse spinel structure* $B(AB)X_4$ are described by the following occupation matrices:

$$\begin{matrix} \text{Normal} & & \text{Inverse} & \\ \underline{A} & \underline{B} & \underline{A} & \underline{B} \\ \begin{pmatrix} 1 & 0 \\ 0 & 2 \end{pmatrix} & & \begin{pmatrix} 0 & 1 \\ 1 & 1 \end{pmatrix} & \end{matrix} \tag{1.78}$$

Between the normal and inverse spinel structures are various occupation states possible, which are characterized by the inversion degree λ. The occupancy of tetrahedral and octahedral lattice sites is then characterized by the formula $A_{1-\lambda}B_\lambda(A_\lambda B_{2-\lambda})X_4$, where $\lambda = 0$ and $\lambda = 1$ denote the cation distribution for the normal and inverse spinel structures. A completely statistical distribution of the cations is given for $\lambda = 2/3$. The inversion degree λ is a function of temperature. The unit cell of the normal spinel structure contains eight formula units $A(B_2)X_4$ (Figure 1.82), where the A cations themselves occupy lattice sites of the diamond structure. Thus, the eight A cations occupy the position of the F-lattice and alternatively the centers of four octants of the unit cell. The B cations are located at the vertices of the four empty octants of the diamond structure forming tetrahedra. The X anions form also tetrahedra located in each of the eight cubelets. Four of them have an A cation as central atom. The remaining four X tetrahedra share its center with the B tetrahedra in such a way that the vertices of the differently oriented X and B tetrahedra form B_4X_4 cubes.

Many compounds crystallize in the spinel structure. The majority of compounds with spinel structure are oxides. There exist also sulfides, selenides, halides, and

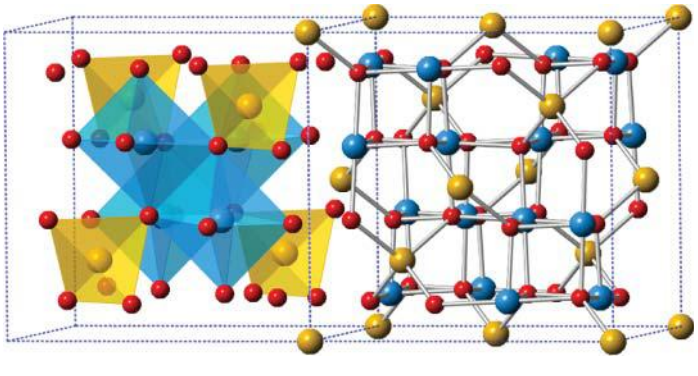

Figure 1.82 Spinel structure.

pseudohalides with spinel structure. The following combinations of oxidation states of the cations are known in spinels: 2^+, 3^+; 4^+, 2^+; 2^+, 1^+; 6^+, 1^+.
Examples:
– Normal spinels: $MgAl_2O_4$, $GeNi_2O_4$, $Mn_3O_4 = Mn^{2+}(Mn_2{}^{3+})O_4$.
– Inverse spinels: $TiMg_2O_4$, $NiLi_2O_4$, $Fe_3O_4 = Fe^{3+}(Fe^{2+}\ Fe^{3+})O_4$.

1.5.2.1 Polymorphism and Polytypism

In the last section, we have seen that elements as carbon and compounds as ZnS can crystallize in different structures. This phenomenon that crystals of the same chemical composition can exhibit different structures is called ***polymorphism***. The different structures are denoted as polymorphic modifications or shortly as **polymorphs**. Polymorphism is an inherent property of the crystalline state and plays an important role for molecular structures. With respect to molecular structures, McCrone [93] defines a polymorph as "*a solid phase of a given compound resulting from the probability of at least two different arrangements of the molecules of that compound in the solid state.*" The different arrangement can be caused by a different packing of the molecules (***packing polymorphism***) or by different conformations (spatial arrangement of a molecule of a given configuration) of the molecules (***conformation polymorphism***).

A special case of polymorphism is ***polytypism***. Structural modifications of elements or compounds, which only differ in their stacking sequence of layers, are denoted as ***polytypes***. The different polytypes of a structure have multiple lattice spacings normal to the layers, which determine the stacking period. Polytypism was firstly discovered in SiC by Baumhauer in 1912. Nowadays, more than 150 different polytypes of SiC were found, which are composed of different slabs of … AB … and … ABC … stacking sequences of the close-packed hcp and fcc structures.

In the following, we will explain the commonly applied notations for the description of close-packed structures and their stacking variants including polytypes. We already used the **ABC notation** for the description of the stacking sequence of the fcc and hcp structure of elements and in a modified version, for example, … AαBβCγAαBβCγ … , for close-packed compounds such as the sphalerite structure. The **Hägg notation** designates the stacking sequence by sequential arrangements of + and − signs. The layer directions A → B, B → C, C → A are designated by + and, vice versa, the opposite directions B → A, C → B, A → C are designated by −. The **Zhdanov notation** consists of a sequence of numbers where each number gives the sum of layers of the same sign. If the layer stacking sequence is composed of multiple repeat units of layers, the repeat unit can be written in parenthesis and the number of repeating symbol is written as subscript. The ***h–c notation***, also known as **Jagodzinski–Wyckoff notation**, consists of a sequence of letters *h* and *c*. The sequence of letters *h* and *c* can be directly derived from the A, B, C sequence. A layer is denoted as *h* if the A, B, C letters on the left- and right-hand side are the same. If the A, B, C letters are different on the left- and right-hand sight, a *c* layer exist. The **Ramsdell notation** is a shorthand two symbol notation (*n*X). The first symbol

n specifies the layer stacking sequence (identity period). The capital letter X (H – hexagonal, C – cubic, R – rhombohedral, T – trigonal, Or – orthorhombic, M – monoclinic, and Tc – triclinic) indicates the crystal system of the structure. Structures with the same *n*X but different stacking sequences (e.g., the two 6H polytypes, Table 1.32) are differentiated by a subscript. For the description of close-packed structures, X is restricted to H, R, and C. However, polytypes can occur in all crystal systems. For example, the layer silicates of mica, muscovite $KAl_2(AlSi_3O_{10})(OH)_2$ and biotite $K(Mg,Fe)_3(AlSi_3O_{10})(OH,F)_2$, exhibit polytypism. Altogether, 23 complex polytypes of mica are known, where $1M$, $2M_1$, $2M_2$ and $3T$ are the most common polytypes [94].

The different notations for describing the hcp, fcc, and some other polytype structures are illustrated in Table 1.33.

The three prototypes for polytypism are SiC, ZnS, and CdJ_2, where SiC is the compound with the largest number of polytypes. The examples of Table 1.33 are typical polytypes of SiC and ZnS. In addition, many **long period polytypes** (**LPP**) were detected for both structures. A LPP **201H/603R** of SiC was observed where the layer width and repeat spacing was determined by synchrotron radiation source X-ray topography [95, 96]. Kelly *et al.* [96] have shown that the correlation between layer thickness *t* and repeat unit *N* of LPPs in SiC can be mathematically described by following general expression:

$$t = kN^n (k = 7000, n = -0.8) \tag{1.79}$$

The constants *k* and *n* were determined from experimental data. The formula shows us that the layer width decreases with increasing repeat unit *N*. Assuming that the limiting layer width is $t = 2c$ ($c_{SiC} = 2.513$ Å), then following expressions can be derived by substitution:

$$t = 2c = 2Nc_o = kN^n, \quad N = (2c_o/k)^{\frac{1}{n-1}} \tag{1.80}$$

For the abovementioned values of *k*, *n*, and *c*, the maximum number of layers is around 2600 with a minimum layer thickness of ~1.3 μm. A higher number of layers would transform the LPP into a one-dimensional disordered layer.

Table 1.33 Notations for describing stacking variants of structures.

Ramsdell	*ABC*	Hägg	Zhdanov	*h-c*
2H	AB	+−	11	*h*
3C	ABC	+++	∝	*c*
4H	ABCB	++−−	22	$(hc)_2$
$6H_1$	ABCACB	+++−−−	33	$(hcc)_2$
$6H_2$	ABCBAB	++−−+−	2 211	*hchchh*
15R	ABCACBCABACABCB	+++−−+++−−+++−−	$323\,232 \equiv (32)_3$	$(hcchc)_3$

1.5.3 Selected Examples of Molecular Crystals

When we decorate the crystal lattice with molecules instead of atoms or ions, a molecular crystal will be formed. The majority of molecular crystals are organic or metallorganic compounds. Some examples for inorganic molecular crystals are described below:

Sulfur forms a variety of molecule structures with S_n, molecules, with $n = 6$, 7, 8, 10, 11, 12, 13, 18, 20, ∝. Probably the most known sulfur structure is the orthorhombic α-sulfur where 16 rings of S_8 molecules are in the unit cell.

The mineral ***calomel*** $\boldsymbol{Hg_2Cl_2}$ is tetragonal and consists of linear Hg_2Cl_2 molecules. The arsenic mineral ***realgar*** $\boldsymbol{As_4S_4}$ is monoclinic with four molecule cages in the unit cell.

The solid forms of fullerene molecules, the ***fullerites***, which will be described later, are a very interesting class of molecular crystals.

A characteristic feature of molecular crystals is the high strength of intramolecular bonds (covalent bonds) on the one hand and the weak intermolecular bonds (van der Waals interaction and in some cases hydrogen bonds) on the other hand. Generally speaking, the weak forces between the molecules require close contacts of the molecular entities. This fact is expressed by the close packing of the molecules. The packing coefficient k (packing density) is given as the ratio of the volume of all molecules in the unit cell to the volume of the unit cell.

It is $k = nV_M/V$, where n – number of molecules, V_M – volume of each molecule, and V – volume of unit cell.

The majority of organic crystals have packing coefficients in the range of 0.70–0.75. A list of the packing density of a selection of polycyclic aromatic hydrocarbon crystals is given in Table 1.34.

In general, the complexity of molecular crystals is caused by the complexity of the geometrical structure of molecules where one has to take into consideration the ***constitution***, ***configuration***, and ***conformation*** of molecules. The molecular ***constitution*** tells us how the atoms in the molecule are interconnected and what kind of bonds (single or multiple bonds) exists between them. The molecular ***configuration*** describes the spatial arrangement of atoms of a molecule not taking into consideration molecular shapes generated by rotations around single bonds. Those arrangements are characterized by the term ***conformation***.

Table 1.34 Packing density of some polycyclic aromatic hydrocarbons.

Substance	Naphthalene	Anthracene	Tetracene	Pentacene	Hexacene
Formula	$C_{10}H_8$	$C_{14}H_{10}$	$C_{18}H_{12}$	$C_{22}H_{14}$	$C_{26}H_{16}$
k	0.704	0.718	0.733	0.743	0.751

Data from [97].

Finally, the complexity of a molecular structure is expressed by the number of possible ***isomers***. Molecules with identical chemical formula but different molecular structure are denoted as isomers. Isomers have different physical and chemical properties. According to the appearing structural aspect ***isomers*** are classified as ***constitutional***, ***configurational***, and ***conformational*** isomers.

The comprehensive studies of molecular crystals by Kitaigorodsky [97] have encouraged the opinion that the properties of a molecular crystal are mainly formed by the structure and properties of the molecules. The packing of the molecules in the unit cell plays a subsidiary role.

In the following, we will describe the crystal structures of some molecular crystals. The sequence of the presentation is arranged to some extent the molecular structures according to the shape of the molecules.

A typical example for a structure with ***chain-like molecules*** is *n*-octane.

n-Octane, C_8H_{18}, $P\bar{1}$, $Z = 1$, Cambridge Structural Database (CSD) identifier OCTAN01, $a = 4.19$, $b = 4.75$, $c = 10.99$; $\alpha = 85.1°$, $\beta = 83.7°$, $\gamma = 74.2°$.

Octane belongs to the alkanes (paraffins) with the general formula C_nH_{2n+2}. There are 18 structural isomers of octane, where *n*-octane is the only unbranched member. Octane is liquid at room temperature. The crystalline form of *n*-octane (melting point: 216.05 K) is triclinic. The linear structure consists of a single chain, where the carbon atoms are connected in a zigzag form (Figure 1.83).

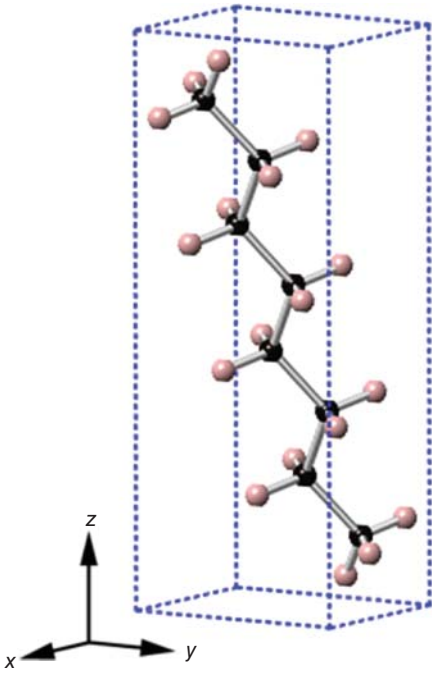

Figure 1.83 Crystal structure of *n*-octane.

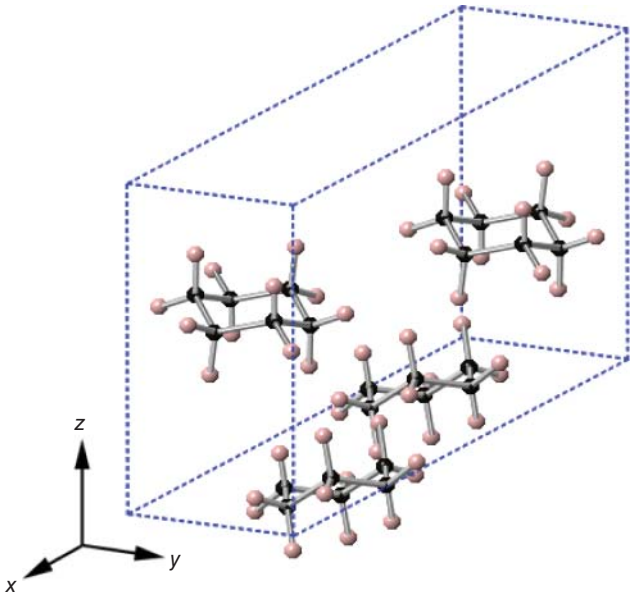

Figure 1.84 Crystal structure of cyclohexane.

Contrary to the alkanes with a chain-like structure, the cycloalkanes have a ring-shaped structure.

Cyclohexane, C_6H_{12}, C2/*c*, $Z = 4$, CSD identifier CYCHEX, $a = 11.23(3)$, $b = 6.44(2)$, $c = 8.20(2)$, $\beta = 108.83°$.

The prefix ***cyclo*** of the molecule C_6H_{12} tells us that the molecule is formed by one six-member ring only. Cyclohexane belongs to class of cycloalkanes (naphthenes), which consist of one or more (polycyclic) rings of carbon atoms. Two stable crystalline phases of cyclohexane (melting point, 279.8 K) exist. The crystal structure of the monoclinic polymorph (phase II) stable below 186 K is shown in Figure 1.84. The cyclohexane molecules in the unit cell have a ***chair conformation***. The high-temperature phase I is stable in the range of 186 and 279.8 K. This phase has cubic symmetry (space group *Fm*3*m*). In this phase, two types of orientational disorder of the molecules were found (plastic crystal) [98].

Polyethylene, $(C_2H_4)_n$, *Pnam*, $Z = 2$, CSD identifier QILHUO01, $a = 7.40$, $b = 4.93$, $c = 2.534$.

Polyethylene $(C_2H_4)_n$ belongs to the semicrystalline polymers, which consist of crystalline and amorphous regions. It should be mentioned that the physical properties of the crystalline regions of the polymer are anisotropic contrary to the isotropic amorphous areas. The crystal structure of the low density polymorph (modification I) is orthorhombic and was already determined by Bunn in 1939 [99]. The rule that the chain axis of polymers should be the *c*-axis leads to the nonstandard setting space group *Pnam.* The standard setting space group is *Pnma* where then the *b*-axis is the chain axis. The carbon atoms form plane zigzag chains where the chain in the middle of the unit cell is differently oriented. The structure

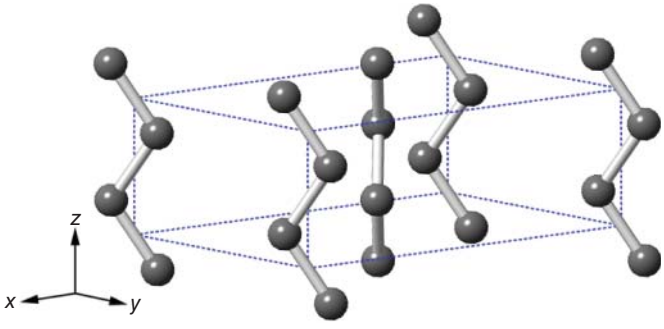

Figure 1.85 Crystal structure of polyethylene.

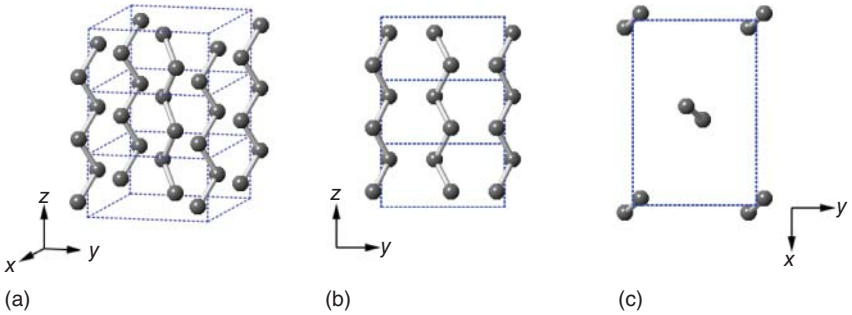

Figure 1.86 (a) Crystal structure of polyethylene, (b) (100) projection, and (c) (001) projection.

images show only the carbon chains without the hydrogen atoms (Figure 1.85). For a better visualization of the chain structure, three unit cells in *c*-direction and the corresponding *bc*-, and *ab*-projections are illustrated in Figure 1.86. In addition to the orthorhombic structure, triclinic and monoclinic polymorphs exist.

In general, polymers are macromolecules that are composed of repeated molecular units. These units are denoted as ***mers*** or ***monomers***. The formation of macromolecules from the repeat units, the monomers, is called ***polymerization***. The number of mers per polymer molecule determines the ***degree of polymerization***. Polyethylene consists of C_2H_4 (ethylene) mers, which form a chain polymer.

Polyethylene is classified into different categories depending on density, molecular weight, and degree of branching of chains.

For example, ultrahigh molecular weight polyethylene (UHMWPE) is composed of extremely long chains and has a molecular weight from 2 to 6 million.

Many molecular crystals consist of ***plane molecules***. Typical examples are polycyclic aromatic hydrocarbons (PAH), urea, quinones, phenol (C_6H_5OH), porphyrins, and phthalocyanines.

Naphthalene, $C_{10}H_8$, $P2_1/a$, $Z = 2$, CSD identifier NAPHTHA12, $a = 8.010(2)$, $b = 5.884(3)$, $c = 8.536(4)$, $\beta = 123.45(3)°$.

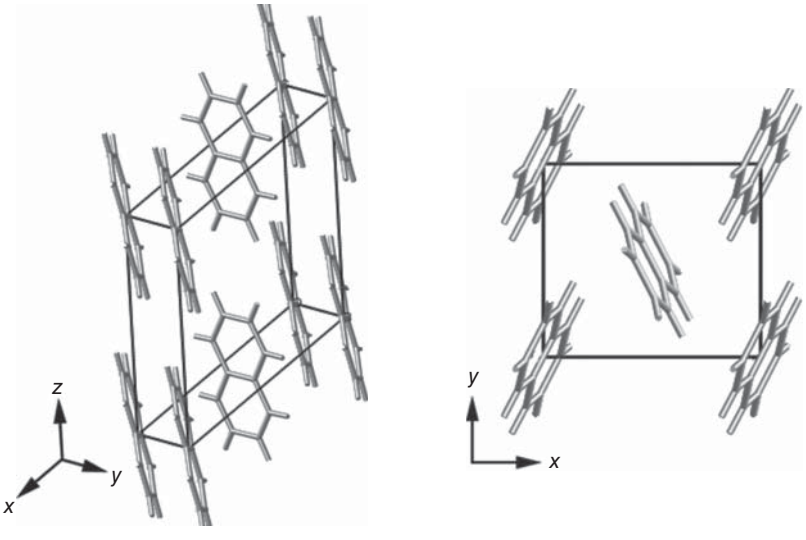

Figure 1.87 (a) Crystal structure of naphthalene and (b) *ab* projection.

Naphthalene is the simplest PAH compound. The molecule consists of two benzene rings sharing an edge and has the symmetry *mmm* (Figure 1.87a). According to the packing of the molecules in the monoclinic naphthalene crystal, the symmetry of the molecule is reduced to $\bar{1}$. The planar layers are stacked along the *c*-axis where we have pairs of inclined layer packages (Figure 1.87b).

Coronene, $C_{24}H_{12}$, $P2_1/a$, $Z = 2$, CSD identifier CORONE, $a = 16.119$, $b = 4.702$, $c = 10.102$, $\beta = 110.90°$.

The PAH compound coronene consists of a six-member benzene ring. The symmetry of the planar molecule is *mmm* (Figure 1.88). The site symmetry of

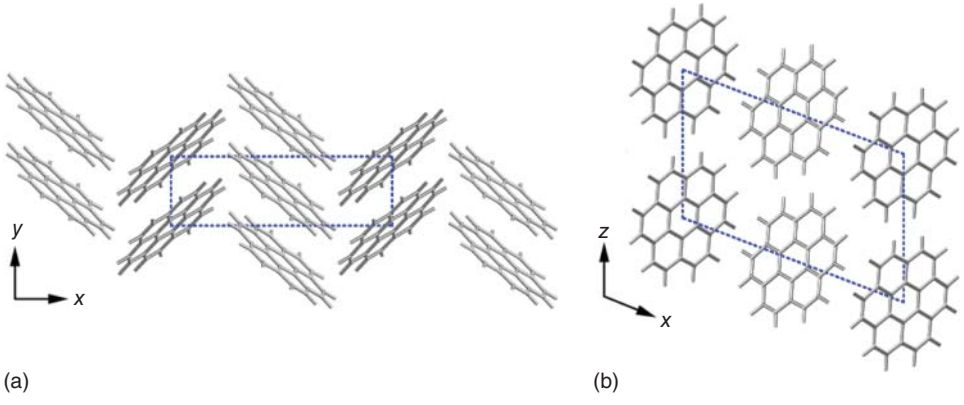

Figure 1.88 Crystal structure of coronene: (a) *ab* projection and (b) *ac* projection.

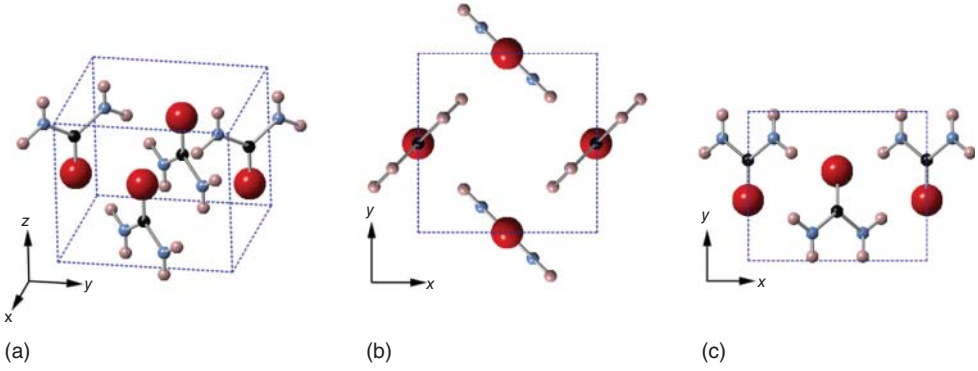

Figure 1.89 Crystal structure of urea: (a) unit cell, (b) *ab* projection, and (c) *bc* projection.

the position of the molecules in the monoclinic unit cell is $\bar{1}$. Similar as in the naphthalene structure, there also pairs of inclined layer packages in coronene. The molecules are arranged in a so-called herringbone pattern.

It should be mentioned that coronene occurs in nature as very rare organic mineral *carpathite* (same composition and structure).

Urea, CH_4N_2O, $P\bar{4}2_1m$, $Z = 2$, CSD identifier UREAXX, $a = b = 5.662$, $c = 4.716$.

Urea was the first organic compound that was synthesized from pristine anorganic precursors (F. Wöhler, 1828). F. Wöhler's successful experiment was the starting point for synthesizing organic molecules occurring in living organisms in the laboratory. The plane urea molecule has *mm*2 symmetry, which is fully preserved in the tetragonal crystal. The symmetry relations of the urea molecules in the tetragonal unit cell are illustrated in Figure 1.89.

Porphyrins and Phthalocyanines Both classes of compounds are heterocyclic macrocycles and structurally closely related to each other, as can be seen in Figure 1.90. Phthalocyanines and porphyrins are composed of four modified pyrrole (C_4H_4NH) rings, which form a 16-membered ring.

The parent structure of the porphyrins is porphin. The crystal structure of porphin is monoclinic with following data.

Porphin, $C_{20}H_{14}N_4$, $P2_1/c$, $Z = 4$, CSD identifier PORPIN01 $a = 10.271(3)$ Å, $b = 12.089(3)$ Å, $c = 12.362(4)$ Å, $\beta = 102.17(2)°$.

From both the *bc*-projection and the molecular arrangement in the unit cell (Figure 1.91), it is obvious that two different stacking directions for the planar porphin molecules are given. The exact symmetry of the planar molecules is $2/m$ (C_{2h}). The average symmetry of the molecules is approximately $4/mmm$ (D_{4h}) [100].

The cavity in the center of the porphyrins can be occupied by metal ions. For example, iron porphyrins are constituents of the protein hemoglobin.

The variety of phthalocyanines is enormously high. Similarly to the porphyrins, phthalocyanines can host nearly all metal ions in its central cavity. In addition, they can also be modified by changing the meso atoms (N bridge atoms). Many

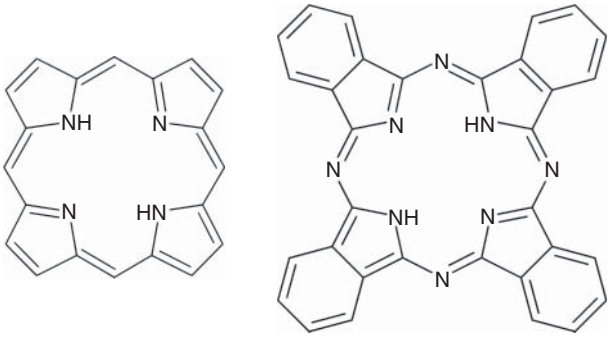

Figure 1.90 Structural formulae of the unsubstituted porphin (a) and phthalocyanine H_2Pc (b).

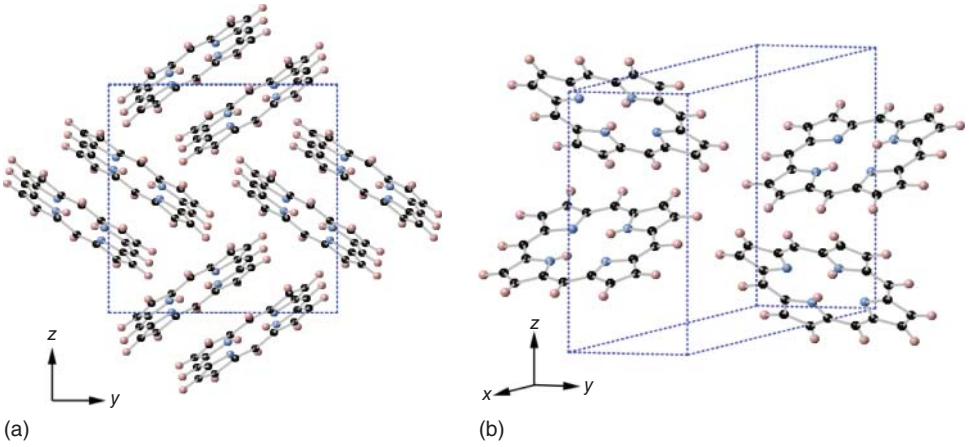

Figure 1.91 Crystal structure of porphin: (a) *bc* projection and (b) unit cell.

new compounds can be synthesized by substituting the peripheral atoms. The peripheral substituents mainly influence the solubility and crystal structure of the phthalocyanines. The shape of the phthalocyanine molecules is not always planar. Highly substituted phthalocyanines can be deformed in different ways. In bisphthalocyanines is a metal atom sandwiched between two phthalocyanine molecules, which are rotated by an angle α, denoted as staggering angle. The upper and lower molecules show convex and concave shapes, respectively.

In general, phthalocyanines are chemically and thermally very stable. Therefore, structural investigations can also be carried out by transmission electron microscopy. A typical example for metal-substituted phthalocyanines is copper phthalocyanine (CuPc), which occurs in various polymorphs (α, β, γ, R, δ, ε, π, ζ, ρ, and σ). We will consider now the molecular arrangements in the crystal structures of the α- and β-phases. Originally, it was assumed that a herringbone arrangement of the molecules is given in both phases. The redetermination of the structure of

α-CuPc by Hoshino *et al.* [101] has evidenced that α-CuPc has a parallel arrangement of the molecules with an inclination angle of 63° to the stacking axis *b*. The β-phase consists of two molecular columns oriented in a herringbone arrangement. A similar structure as for α-CuPc was found earlier by Uyeda *et al.* [102] for the perchloro copper phthalocyanine. This crystal is one of the most stable and electron beam resistant organic crystal. The structural data are as follows:

Chlorinated copper phthalocyanine (CuPc), $CuC_{32}N_8Cl_{16}$, $C2/m$, $Z = 2$, $a = 19.62$ Å, $b = 26.08$ Å, $c = 3.76$ Å, $\beta = 116.50°$.

Figure 1.92 shows the molecular structure image of an epitaxially grown chlorinated CuPc 5 nm thick crystal film taken in the high-voltage high resolution electron microscopy (HRTEM) at 500 kV. The nearly planar CuPc molecules lie parallel to each other. There is no herringbone arrangement of the molecules. The HREM image shows us the projected molecule structure. In order to improve the signal-to-noise ratio, a subsequent image processing (averaging technique) was carried out.

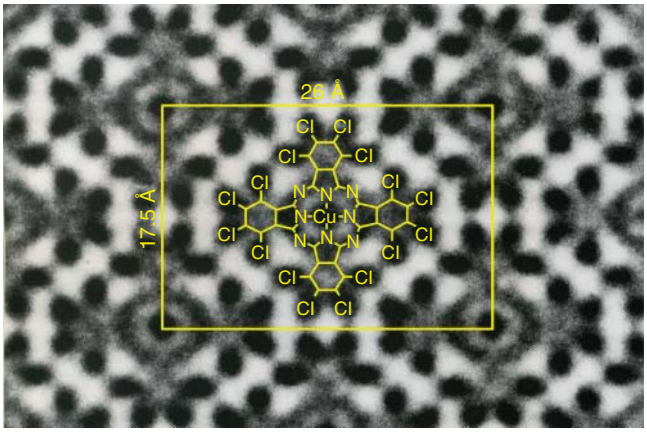

Figure 1.92 Molecular image of chlorinated copper phthalocyanine (Courtesy: Uyeda *et al.* [102]).

In the following, some structures with ***polyhedral molecules*** will be described.

Octanitrocubane, $C_8N_8O_{16}$, $C2/c$, $Z = 4$, CSD identifier CUGDIR, $a = 12.7852$ (8), $b = 8.8395(3)$, $c = 13.9239(8)$, $\beta = 98.03°$.

Octanitrocubane is a derivative compound of cubane C_8H_8 where the hydrogen atoms are replaced by NO_2 groups. The remarkable structural feature of the cubane molecule is that the eight carbon atoms occupy the corners of a cube and each H atom (or NO_2 groups in octanitrocubane) is connected with a C atom as shown in Figure 1.93.

Cubane belongs together with **tetrahedrane** (C_4H_4, not yet synthesized in the pure form) and **dodecahedrane** ($C_{20}H_{20}$) to the so-called **platonic hydrocarbons** because the carbon atoms in these molecules occupy the vertices of a platonic solid (cube, tetrahedron, and dodecahedron). From structural points of view, hydrocarbon molecules with octahedral or icosahedral shape are very unlikely.

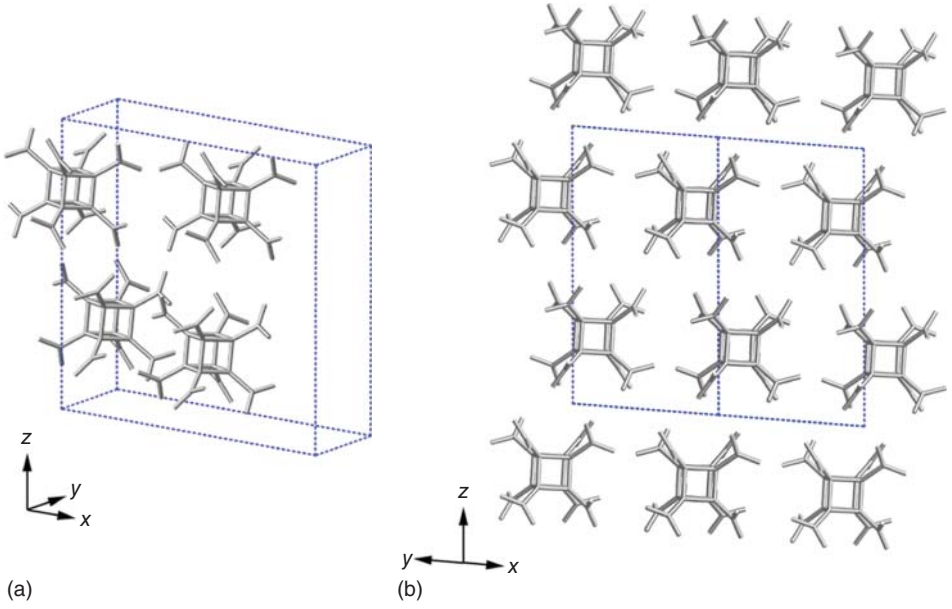

Figure 1.93 Crystal structure of dodecahedrane: (a) unit cell, and (b) octanitrocubane molecule.

It should be mentioned that octanitrocubane is a very high-velocity blasting explosive.

Clathrates Clathrates, also denoted as cage compounds or inclusion compounds, consist of a host structure with cages where atoms or molecules are completely enclosed. An important class of clathrate materials are **gas hydrates**. The host structure is formed by crystalline hydrogen-bonded water molecules, where the cages of the host can be occupied by gas molecules (e.g., N_2, Cl_2, H_2S, CO_2, CH_4, C_2H_6, C_3H_8).

In addition to the hydrate clathrates many other compounds with clathrate structure were crystallized. The structure of the first intermetallic clathrate Na_8Si_{46} was determined by Kasper *et al.* in 1965 [103]. According to their properties anorganic clathrates are also categorized into intermetallic clathrates and semiconducting clathrates. Because of their thermal conductivities, semiconducting clathrates are of great interest for the development of thermoelectrics (e.g., $Sr_8Ga_{16}Ge_{30}$). In 2006, metastable Ge (cF136) with a guest-free clathrate structure type II was firstly synthesized [104].

The characteristic features of the nine clathrate structure types are summarized in Table 1.35. For each structure type, the ideal formula of the unit cell, the space group, the clathrate framework forming polyhedra, and at least one example for the particular structure type are given. The formula $X_mY_n[F_o]$ means in the structure types are m large cages X, n small cages Y, and o host framework atoms F. The

Table 1.35 Characteristic features of clathrate structure types (crystal data collected from [105, 106]).

Type	Formula	Space group	Polyhedra	Compounds
I	$X_6Y_2[F_{46}]$	$Pm\bar{3}\,n$	$[5^{12}6^2]_6[5^{12}]_2$	$Sr_8Ge_{16}Ge_{30}$, $(CH_4)_8[H_2O]_{46}$
II	$X_8Y_{16}[F_{136}]$	$Fd\bar{3}\,m$	$[5^{12}6^4]_8[5^{12}]_{16}$	$Cs_8Na_{16}Ge_{136}$, Na_xSi_{136}, Ge
III	$X_{20}Y_{10}[F_{172}]$	$P4_2/mnm$	$[5^{12}6^2]_{16}[5^{12}6^3]_4[5^{12}]_{10}$	—
IV	$X_8Y_6[F_{80}]$	$P6/mmm$	$[5^{12}6^2]_4[5^{12}6^3]_4[5^{12}]_6$	$Li_{14.7}Mg_{36.8}Cu_{21.5}Ga_{66}$
V	$X_4Y_8[F_{68}]$	$P6_3/mmc$	$[5^{12}6^4]_4[5^{12}]_8$	—
VI	$X_{16}[F_{156}]$	$I\bar{4}3d$	$[4^35^96^27^3]_{16}[4^45^4]_{12}$	$\{(CH_3)CNH_2\}[H_2O]_{156}$
VII	$X_2[F_{12}]$	$Im\bar{3}\,m$	$[4^66^8]_2$	—
VIII	$Y_8[F_{46}]$	$Im\bar{3}\,m$	$[3^34^35^9]_8$	$Ba_8Ga_{16}Ge_{30}$
IX	$X_8Y_{16}[F_{100}]$	$P4_132$	$[5^{12}]_8 + [4^{10}]_4 + \cdots$	Ba_6Ge_{25}

sum $m + n$ is equal to the number of possible guest atoms. The polyhedra notation specifies the kind and number of polyhedra.

The notation $[5^{12}6^2]_6[5^{12}]_2$ means the structure consists of 6 polyhedra having 12 five-member and two six-member faces and two polyhedra having 12 five-membered faces. It should be mentioned that intermetallic and semiconducting clathrates crystallize mainly in the structure types I, II, and IX. Only few examples exist for the structure types III, IV, and VIII. Until now, representatives of structure types V, VI, and VII are only known for gas and liquid hydrates. The main clathrate structure type forming polyhedra are

- pentagondodecahedron $[5^{12}]$, 12 pentagonal faces, 20 vertices;
- tetrakaidodecahedron $[5^{12}6^2]$, 12 pentagonal faces, 2 hexagonal faces, 24 vertices;
- pentakaidodecahedron $[5^{12}6^3]$, 12 pentagonal faces, 3 hexagonal faces, 26 vertices;
- hexakaidodecahedron $[5^{12}6^4]$, 12 pentagonal faces, 4 hexagonal faces, 28 vertices.

$Ba_8Al_{16}Ge_{30}$ is an intermetallic clathrate compound of structure type I and crystallizes in the cubic space group $Pm\bar{3}n$. The unit cell contains six large tetrakaidodecahedra and two small pentagondodecahedra. The 46 tetrahedrally coordinated atoms of Al and Ge form the clathrate framework. The eight Ba atoms are trapped in the eight cages. The structure of $Ba_8Al_{16}Ge_{30}$ is illustrated in Figure 1.94.

In the broader sense metal organic frameworks (MOFs) belong to clathrates because they can form porous structures. The MOF **HKUST-1** is such an example for a highly porous open-framework structure [107].

HKUST-1(Hongkong University of Science and Technology), $(C_{18}\ H_{12}\ Cu_3\ O_{15})_n$,10$n$($H_2O$), name: catena-[bis($\mu_6$-benzene-1, 3,5-tricarboxylato)-triaqua-tri-copper decahydrate clathrate] $Fm\bar{3}m$, $Z = 16$, $a = 26.34$, CSD identifier FIQCEN.

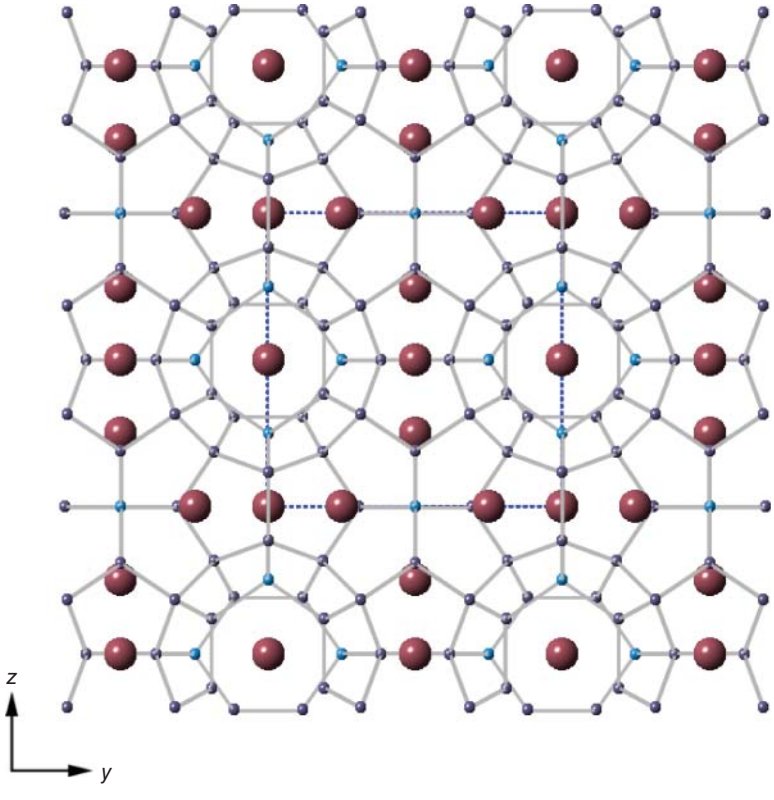

Figure 1.94 Structure of $Ba_8Al_{16}Ge_{30}$.

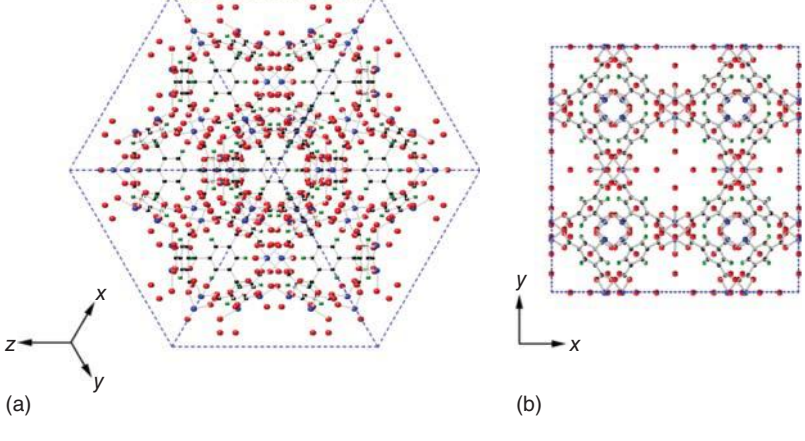

Figure 1.95 Structure of HKUST-1: (a) (111) projection and (b) (001) projection.

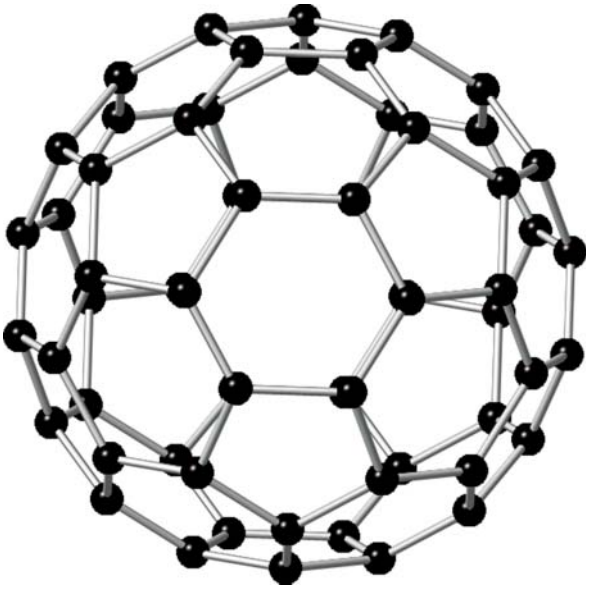

Figure 1.96 Ball-and-stick model of the C_{60} fullerene.

This metal coordination polymer $[Cu_3(C_9H_6O_6)_2\,(H_2O)_{3n}]$ contains large pores (quadratic nanochannels with fourfold symmetry and a size of ~9 Å × 9 Å). In the channels can be stored up to 10 H_2O molecules per formula unit. The structure images shown in Figure 1.95 illustrate the structural features of HKUST-1.

Fullerenes, Fullerides, and Fullerites Polyhedral cage compounds consisting entirely of n-carbon atoms, which form 12 pentagonal and $(n/2-10)$ hexagonal faces ($n \geq 20$) are denoted as ***fullerenes.*** Other polyhedral carbon cages are called ***quasi-fullerenes*** (see IUPAC definition [108]). The prototype of fullerenes, the superstable C_{60}-molecule, was firstly discovered by Kroto *et al.* in 1985 [109]. In remembrance of the famous geodesic domes of the American architect Richard Buckminster Fuller (1895–1983), the inventors named the C_{60} fullerene ***Buckminsterfullerene*** [110]. The molecule is often also denoted as ***buckyball*** because of the symmetrical arrangement of the pentagonal and hexagonal faces similar to that of many soccer balls. The C_{60} molecule (Figure 1.96) has the eigensymmetry of the noncrystallographic full icosahedral point group $m\bar{3}\bar{5}(I_h)$. The carbon atoms occupy the 60 vertices of a truncated icosahedron. The 90 edges between the vertices represent the bonds between the carbon atoms. The diameter of the C_{60} molecule with respect to the carbon atom positions is 7.1 Å, and the density of C_{60} is $\rho = 1.65\ \mathrm{g\,cm^{-3}}$.

In order to get a thorough understanding of the symmetry of fullerenes, we will briefly consider noncrystallographic point groups (for a comprehensive description of this topic the reader is referred to [31]).

Noncrystallographic Point Group Symmetry Molecules such as ferrocene $C_{10}H_{10}Fe$ and many fullerenes have symmetries, which cannot be described by a crystallographic point group. Similarly, the symmetry of QCs where pentagonal, octagonal, decagonal, and dodecagonal symmetries were observed can only be described by means of noncrystallographic point groups.

Let us assume that a molecule or a QC shows pentagonal symmetry. What point groups with pentagonal symmetry are possible? When we combine the different symmetry operations of rotation, inversion, and reflection, as we did for deriving the crystallographic point groups, the noncrystallographic point groups given in Table 1.36 results.

When we have a combination of more than a singular fivefold axis, then the two icosahedral point groups 235 (I) and $m\bar{3}\bar{5}$(I_h) will result. The stereographic projections of the symmetry framework of both point groups are shown in Figure 1.97.

Both groups have 6 fivefold axes, 10 threefold axes and 15 twofold axes. In addition, the full icosahedral group is centrosymmetric and has 15 mirror planes. The order of the groups is 60 and 120, respectively. The general forms are the ***pentagon-hexecontahedron*** (60 faces) and the ***hecatonicosahedron*** or ***hexaicosahedron*** (120 faces). In both point groups, the icosahedron (20 faces)

Table 1.36 Point groups with pentagonal symmetry (single fivefold rotation axis).

Herman–Mauguin symbol	Schoenflies symbol	Order of group	General face form
5	C_5	n	Pentagonal pyramid
$\bar{5}$	C_{5i}	$2n$	Pentagonal antiprism
52	D_5	$2n$	Pentagonal trapezohedron
$5m$	C_{5v}	$2n$	Dipentagonal pyramid
$\bar{5}m$	D_{5d}	$4n$	Dipentagonal scalenohedron

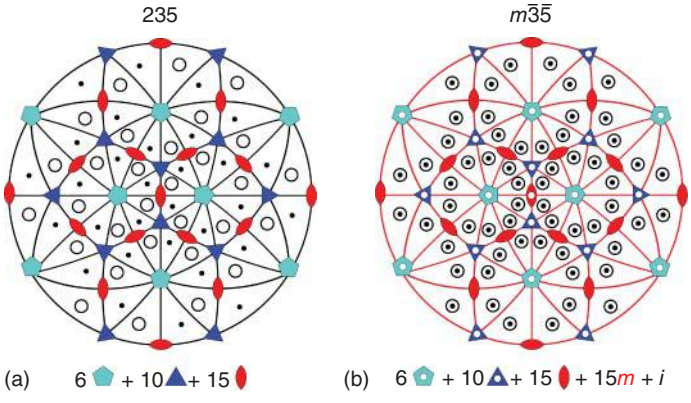

Figure 1.97 Stereographic projections of (a) 235 (I) and (b) $m\bar{3}\bar{5}$ (I_h).

and the dodecahedron (12 faces) will occur as special forms if the face poles are located at the threefold axis (icosahedron) and the fivefold axis (dodecahedron), respectively.

Now, we will explain the icosahedral symmetry and shape of C_{60} a bit more in detail. When we truncate the icosahedron perpendicular to its 12 vertices (perpendicular to the six fivefold axes) to such an extent that the additional 12 faces are regular pentagons and the 20 original triangle faces of the icosahedron are transformed then to regular hexagons, the Archimedean solid of a truncated icosahedron is formed. The shape of our C_{60} molecule is nearly an Archimedean truncated icosahedron. We can also say that the C_{60} molecule is formed by the combination of two special forms of the point group $m\bar{3}\bar{5}$, the two Platonic solids, the regular icosahedron [20 faces, Miller indices $(8\times\{111\}+12\times\{01\tau^2\}]$ and its dual, the regular pentagon–dodecahedron (12 faces, Miller indices $\{01\tau\}$). The shape of the C_{60} can already be generated by means of the icosahedral point group 235 (I), where regular icosahedron and regular pentagon–dodecahedron also occur as special forms. We should be aware of the differences between the cubic pentagon–dodecahedron (limiting form: cubic point group 23, face symmetry 1; special form: cubic point group $m\bar{3}$, face symmetry m.. (Fig. 1.98a)) and of the regular pentagon–dodecahedron (Fig. 1.98b) as special forms of the noncrystallographic point groups 235 (face symmetry ..5) and $m\bar{3}\bar{5}$ (face symmetry 5m). The crystallographic pentagon–dodecahedron $\{0kl\}$ has pentagonal faces (but no fivefold symmetry!), whereas the regular one [$\{01\tau\}$, with $\tau = {}^1/_2\,(\sqrt{5}+1)$] has regular pentagonal faces (fivefold symmetry).

In the cubic point groups 23 and $m\bar{3}$, we can generate an *irregular icosahedron* as a combination of pentagon–dodecahedron $\{0kl\}$ and octahedron $\{111\}$. We have 20 triangular faces (Fig. 1.99a), but only the 8 octahedral faces are equilateral triangular faces. The *regular icosahedron* (point groups 235, $m\bar{3}\bar{5}$) consists of 20 equilateral triangular faces (Fig. 1.99b).

In the meantime, many small ($n<60$) and larger ($n>60$) fullerenes have been identified and comprehensively investigated. Fullerenes with $n>70$ are classified

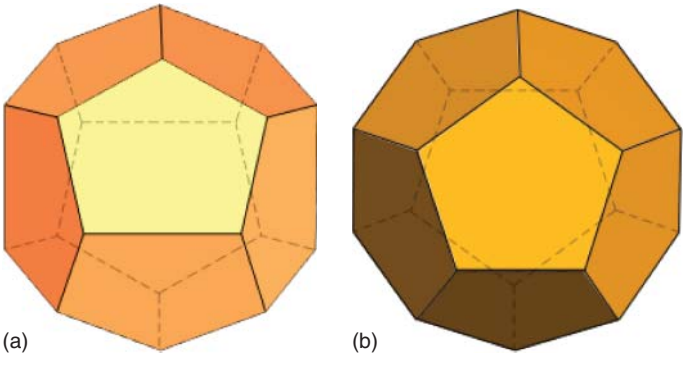

Figure 1.98 (a) Pentagon–dodecahedron $\{0kl\}$ and (b) regular pentagon–dodecahedron $\{01\tau\}$. (crystal polyhedra drawn with the program WinXMorph, Kaminsky, W. [21].)

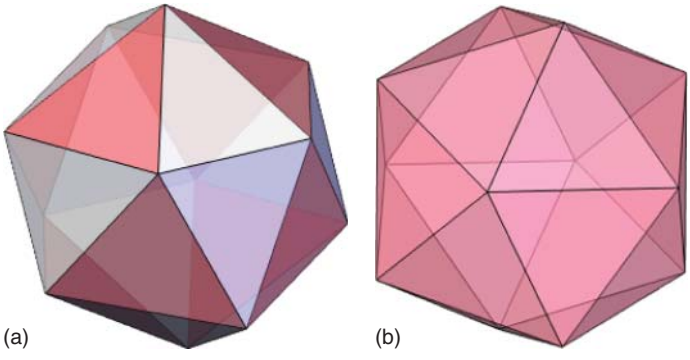

Figure 1.99 (a) Irregular icosahedron (octahedron {111} + pentagon–dodecahedron{0*kl*}) and (b) regular icosahedron ({111}, {$01\tau^2$}). (crystal polyhedra drawn with the program WinX-Morph, Kaminsky, W. [21].)

as ***higher fullerenes***. Very large fullerenes with quasi-icosahedral shape are denoted as ***giant fullerenes***. Some examples of fullerenes and their point group symmetries are shown in Figure 1.100. The smallest possible fullerene is C_{20}. It has the shape of a regular pentagon–dodecahedron [20 vertices (≡ number of atoms), 20 edges (≡ number of bonds), 12 pentagonal faces]. The fullerene C_{22} does not exist. The small fullerenes $C_{20}, C_{24}, \ldots, C_n$ ($n < 60$) are all very unstable. The ***isolated pentagon rule*** (***IPR***), proposed by Kroto [111] and theoretically justified by Schmalz *et al.* [112], is a useful criterion for checking the stability

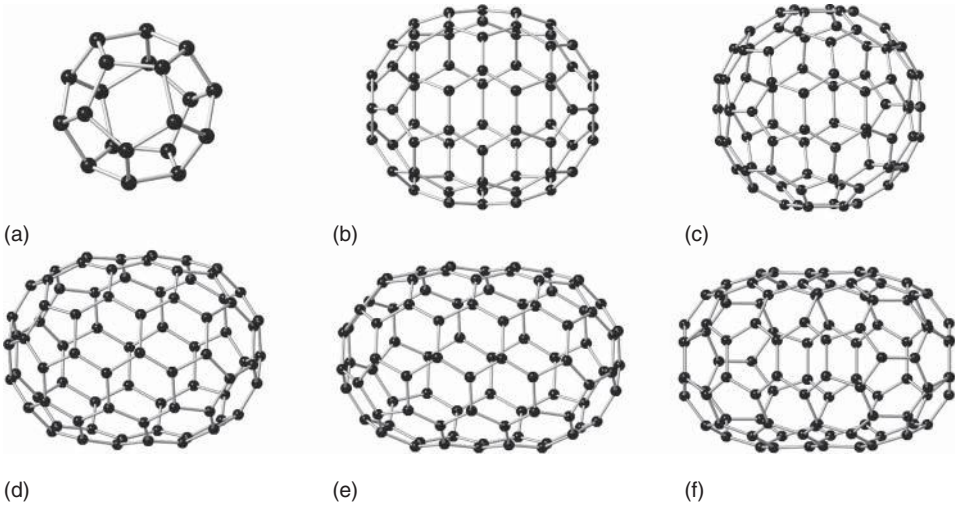

Figure 1.100 A set of ball-and-stick models of fullerenes: (a) C_{20} $m\bar{3}\bar{5}$ (I_h), (b) C_{70} $\bar{1}02m$ (D_{5h}), (c) C_{80} $m\bar{3}\bar{5}$ (I_h), (d) C_{80} $\bar{5}m$ (D_{5d}), (e) C_{90} $\bar{1}02m$ (D_{5h}), and (f) C_{100} $\bar{5}m$ (D_{5d}). (Structure files: Fullerene library, M. Yoshida, web resource: *http://www.nanotube.msu.edu/fullerene/fullerene-isomers.html* (authors: D. Tomanek, N. Frederick, Michigan State University, USA.))

of fullerenes. According to this rule, fullerenes are stable if the pentagons are surrounded only by hexagons. There are no pentagons with shared edges. C_{60} is the first fullerene, which fulfills the IPR criterion. Strictly speaking, the proposed structure of Buckminster fullerene is the only isomer of the 1812 possible isomers of C_{60}, which fulfills the IPR criterion. The number i of IPR isomers increases with increasing number of n: C_{70} $i = 1$, C_{76} $i = 2$, C_{78} $i = 5$, C_{84} $i = 24$. For the fullerene C_{100}, there exist 285 914 isomers from which already 450 fulfill the IPR. Therefore, additional stability criteria have been developed as possible measures for the stability of IPR isomers [113, 114]. Furthermore, numerous studies of structure and stability of hypothetical giant fullerenes up to C_{3840} were carried out [115]. The calculated stable structure for C_{720} is given in Figure 1.101.

The physical and chemical properties of the fullerenes can be modified by changing the cage structure in the following way:

- First, carbon atoms of the cage can be substituted by other atoms. The resulting molecules form the class of ***heterofullerenes*** (e.g., $C_{59}N$, $C_{59}N_2$, $C_{59}NH$, and $C_{59}B$).
- Second, atoms or molecules can be trapped inside the fullerene cage. The new hybrid molecules are denoted as ***endohedral fullerenes*** [e.g., $Na_3@C_{60}$, $Yb@C_{74}$, $Ti_2@C_{80}$, $M@C_{82}$ (M = Sc, Y, lanthanide)].
- Third, ***exohedral fullerenes*** will be formed when atoms, molecules, or organic complexes are attached to the outer shell of the fullerenes (e.g., $C_{76}Cl_{18}$, $C_{60}H_{10}$, $C_{70}M_n$, $n = 12, 25, 37$; M = Be, Mg, Al; $C_{60}[ScH_2(H_2)_4]_{12}$).

Fullerites are the crystalline solids of the fullerenes. Pristine C_{60} crystallizes at room temperature in the fcc structure (lattice parameter $a = 14.17$ Å, space group:

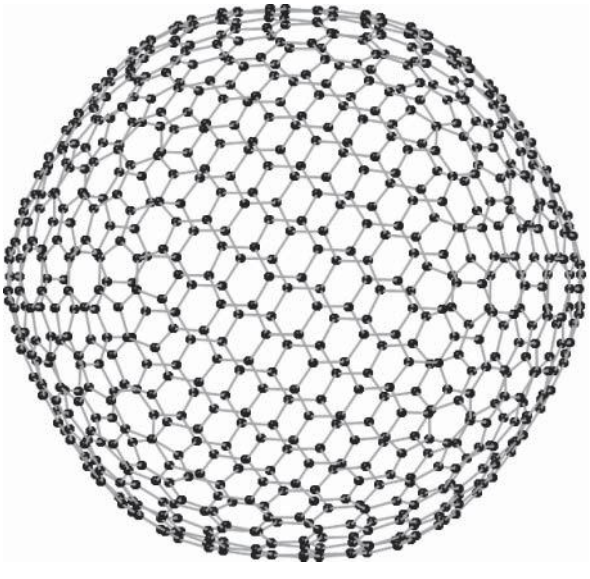

Figure 1.101 Ball-and-stick model of the giant fullerene C_{720}.

$Fm\bar{3}m$). The molecules in the unit cell are not rigid; they are spinning. All spinning molecules in the unit cell are structurally equivalent, that is, the same probability for any three-dimensional possible orientation of all molecules is given. The fullerite C_{60} undergoes a phase transition at 261 K accompanied with a symmetry reduction from $Fm\bar{3}m$ to $Pa\bar{3}$ [$a = 14.067(6)$]. The states of orientational disorder are described in [116].

Figure 1.102 shows the fcc crystal structure of fullerite C_{60}. The molecule with noncrystallographic icosahedral symmetry is decorating the positions of an fcc Bravais lattice forming the fcc crystal structure of C_{60}.

Fullerides are metal-intercalated fullerites. Fulleride structures of alkali metals (Na, K, Rb, and Cs), alkaline earth metals (Mg, Ca, Sr, and Ba), and rare earth metals (Yb, Sm, and Eu) were crystallized and comprehensively investigated.

Now, we will illustrate the main structural features of the alkali metal fullerides A_xC_{60} (A = Na, K, Rb, Cs; $x = 1, 3, 4, 6$). As mentioned above, the fullerite C_{60} crystallizes in the fcc structure at room temperature. The structure consists of four C_{60} molecules and in-between the close-packed molecules are eight tetrahedral and four octahedral voids in the structure as described earlier. For low metal concentrations ($A_1C_{60} - A_3C_{60}$), the metal atoms will successively occupy the octahedral and tetrahedral voids. In the A_1C_{60} fulleride, K, Rb, and Cs occupy the octahedral voids. For the composition of A_3C_{60}, all octahedral and tetrahedral voids are filled with metal atoms. Therefore, the intercalation of higher metal concentrations A_xC_{60} ($x = 4, 6$) leads to new crystal phases of a tetragonal body-centered structure for $x = 4$ and of a cubic body-centered structure for $x = 6$. Owing to the small size of the Na atoms, the stable structure of fullerides Na_xC_{60} ($x = 2, 3, 6, 9.7$) is the fcc structure. The Na atoms are too small to fill the voids. Therefore, Na_4 clusters are formed, which occupy the octahedral voids.

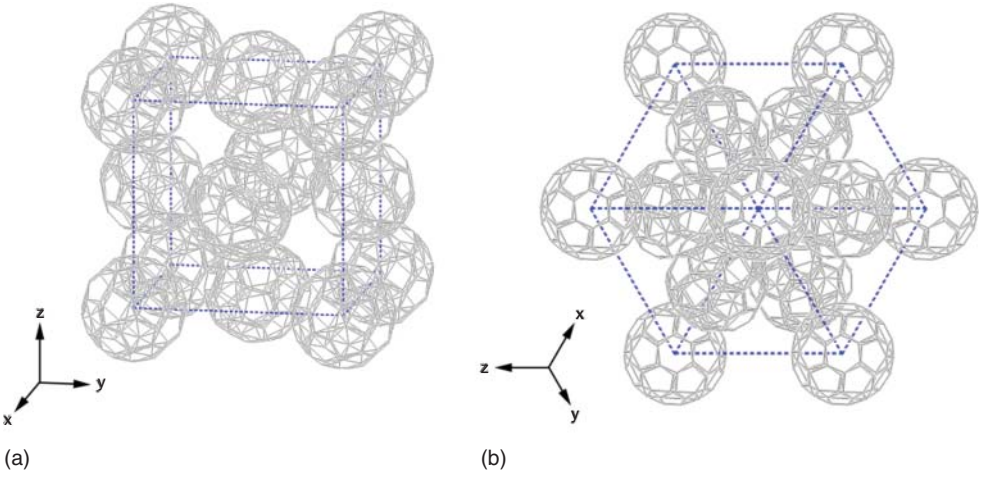

Figure 1.102 (a,b) The fcc-crystal structure of fullerite C_{60}.

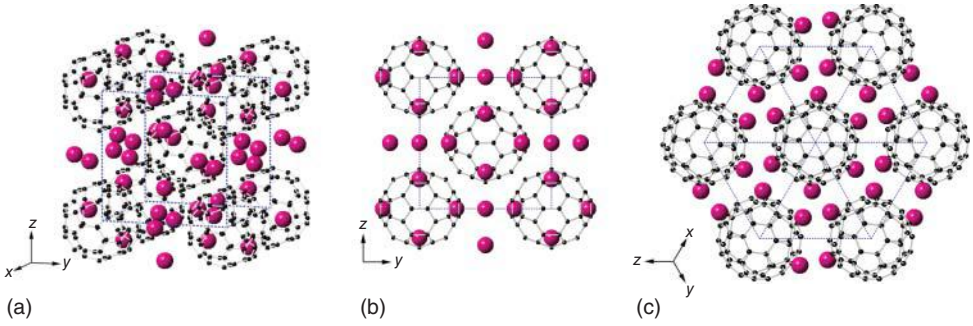

Figure 1.103 Ball-and-stick representation of the structure (a) and the (001) (b) and (111) (c) projections of the fulleride $Cs_6[C_{60}]$.

Fullerides attracted much attention because of the superconductivity of some phases (e.g., critical temperature $T_S = 33$ K for Cs_2RbC_{60} and $T_S = 40$ K for Cs_3C_{60} at high pressure of 15 kbar). In the following, we will illustrate the structure of CsC_{60}.

Hexa-cesium C_{60}-fulleride (hexa-cesium fullerite), $Cs_6[C_{60}]$, $Im\bar{3}$, $Z = 1$, $a = 11.79$, CSD identifier FULLER [117] (Figure 1.103).

Endohedral fullerenes, particularly endohedral metallofullerenes (EMFs), are extensively studied because of their possible applications in the fields of photovoltaics and biomedicine. The technique of cocrystallization with metal organic compounds is a powerful method to obtain crystals with good quality for an X-ray structure analysis. As an example, we will describe the structure determination of the endohedral fullerene $Sc_3N@C_{80}$, which is soluted in benzene. For X-ray analysis, the EMF $Sc_3N@C_{80}$ was cocrystallized with Ni(OEP) [118].

The data of the obtained crystal $\mathbf{C_{128}H_{56}N_5NiSc_3}$ are

$Sc_3N@C_{80}$·Ni(OEP)·2 benzene, Ni(OEP) = nickel octaethylporphyrin = $C_{36}H_{44}N_4Ni$, 2 benzene = $2(C_6H_6)$, $P\bar{1}$, $Z = 2$, $a = 14.505(3)$, $b = 14.878(3)$, $c = 19.855(4)$, $\alpha = 85.052(3)°$, $\beta = 86.758(3)°$, $\gamma = 61.016(3)°$, CSD identifier REJXAG.

The endohedral $Sc_3N@C_{80}$ isomer is surrounded by the Ni(OEP) molecule and the two benzene molecules (Figure 1.104). The X-ray structure analysis provided the exact data of the atomic positions (atom–atom distances and angles between the atoms) of the $Sc_3N@C_{80}$ isomer with noncrystallographic point group symmetry $\overline{10}2m(D_{5h})$.

Closely related to the fullerenes are the **carbon nanotubes** (**CNTs**), which were discovered by Iijima [119] by means of high-resolution electron microscopical studies in 1991. Since their discovery, *in situ* transmission (TEM) and scanning transmission electron microscopy (STEM) at high-resolution has been applied to investigate the growth and structure of CNTs under irradiation. In addition, *in situ* TEM enabled the analysis of irradiation-induced structural modifications and defects in CNTs [120].

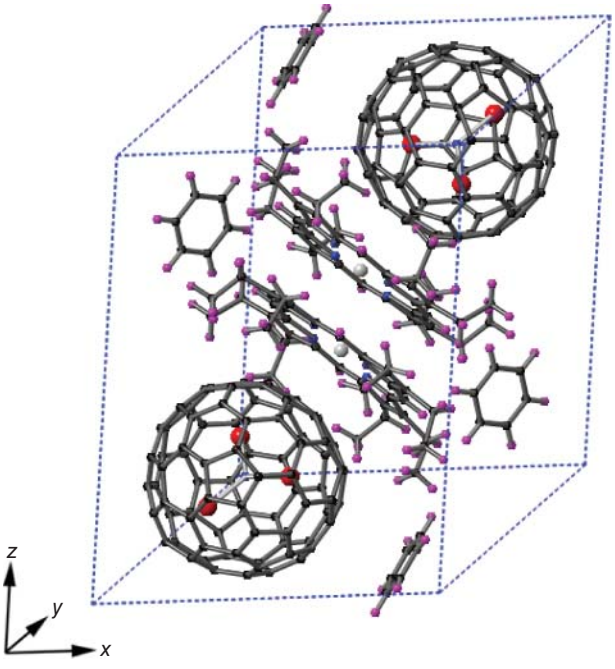

Figure 1.104 Structure of $C_{128}H_{56}N_5NiSc_3$.

CNTs are hollow cylinders with walls formed by one-atom thick graphitic layers (**graphene**). The ends of the cylinder are capped by half of a fullerene molecule. In order to generate open CNTs, the caps can be removed ultrasonically in a suspension of acid. The nanotubes can occur as single-walled nanotubes (**SWNTs**) and multiwalled nanotubes (**MWNTs**). The MWNTs consist of concentric tubular shells arranged similarly to those in the Russian dolls "Matryoskas." In general, the length of the tubes (height of cylinder) is arbitrary, whereas the diameter is geometrically limited. The diameters of CNTs typically range from <1 up to 50 nm and lengths of several microns up to the range of centimeters. CNTs have exceptionally mechanical properties. The tensile strength of CNTs is in the range of 10–60 GPa (high speed (HS) steel has a value of ~4).

The hollow cylinders of CNTs can be generated by rolling up a single graphene layer. As a function of the rolling angle, the following structure types may occur [121]:

- **armchair CNT(*n*,*n*)**
- **zigzag CNT (*n*,0)**
- **chiral CNT (*n*,*m*)**.

The procedure of generating one of the abovementioned nanotube types by rolling up a graphene sheet is illustrated in Figures 1.105 and 1.106. The direction of the resultant vector of the vector sum of the graphene lattice vectors ***n*** and ***m*** defines the direction of rolling up [armchair (***n***,***n***) in Figure 1.105]. After

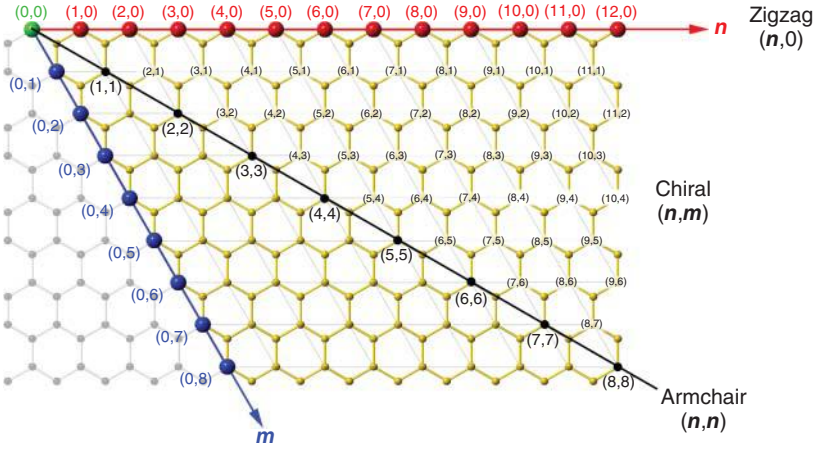

Figure 1.105 Illustration of the procedure for generating carbon nanotubes.

rolling up the graphene sheet, the starting point (0,0) and end point (***n***,***m***) of the resultant vector are located on top of each other (see examples in Figure 1.106). An armchair CNT has identical ***n*** and ***m*** values; for $m = 0$, a zigzag CNT results and arbitrary values of ***m***,***n*** (excluding the cases $n = m$ and $m = 0$) lead to a chiral CNT.

In addition to the CNTs, there are also other carbon nanomaterials such as **nanocones**, **nanobuds**, and nanopeapods. **Nanobuds** are structures where fullerene molecules are docking at the outer wall of a CNT. **Nanopeapods** are CNTs that are filled with fullerene molecules.

1.5.4
Symmetry Relations between Crystal Structures

Structural relationships between crystal structures can be well presented by means of symmetry trees, which outline existing group–subgroup relations of the structures. The concept of symmetry trees for both description and detection of possible structural relations between crystal structures was introduced by Bärnighausen [122]. In general, Bärnighausen trees are the group theoretical description of the relations between the "basic structure and possible derivative structures" [123], which can be derived from the highly symmetric basic structure by symmetry reduction. The terms *aristotype* and *hettotype* are synonymously used instead of basic structure and derivative structure [124]. The flow chart given in Figure 1.107 illustrates which kind of information is required for the comprehensive description of symmetry relations between two structures in a Bärnighausen tree.

Each branch of Bärnighausen tree describes the symmetry reduction from the higher symmetric crystal structure to the structure with lower symmetry. The

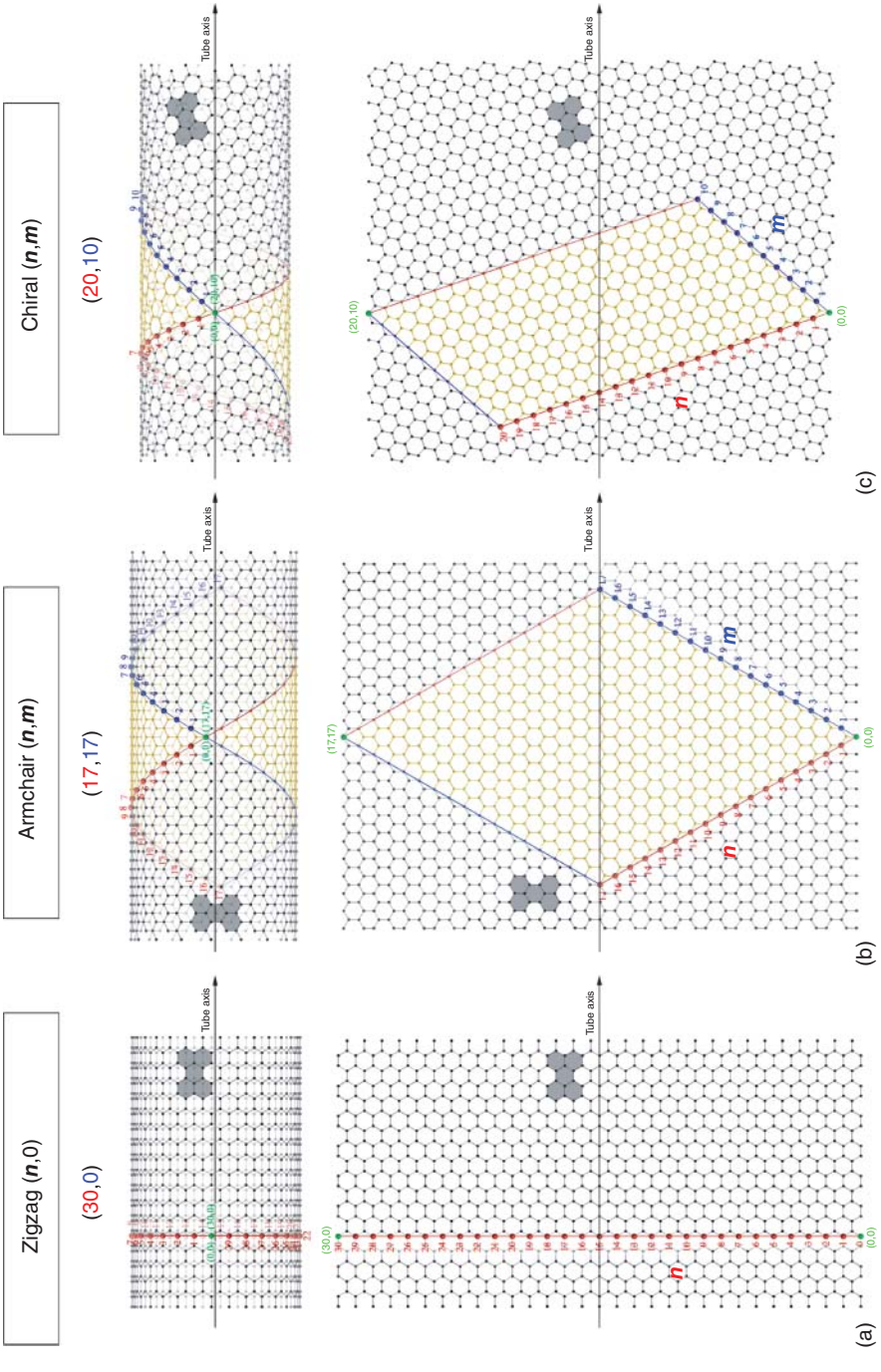

Figure 1.106 (a–c) The three types of carbon nanotubes (graphene sheets and corresponding uprolled NTs).

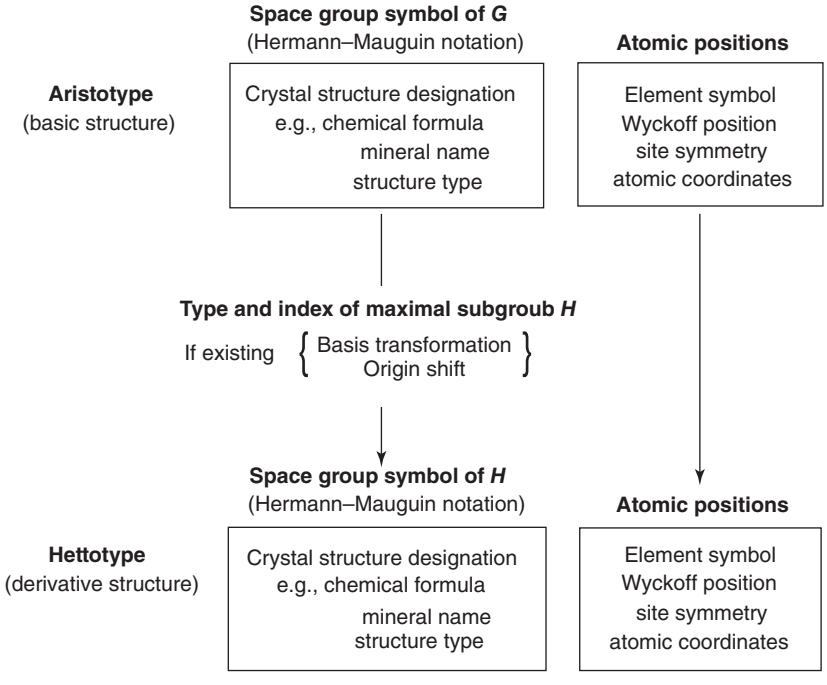

Annotation:

Types of maximal subgroubs:
t – translationengleiche
k – klassengleiche
i – isomorphic

Basis transformation:
basis vectors of H are given as linear combinations of the basic vectors of G

Origin shift:
The origin coordinates of H are given in the coordinate system of G

Figure 1.107 Flowchart and required information content of a branch in a Bärnighausen tree.

structural relations between two structures with the space groups G and H provides us the type of symmetry reduction (kind of maximal subgroup: *t*-, *k*-, *i*-subgroup) by means of the group subgroup relations and the number of lost symmetry operations (index $[i] = |G| : |H|$).

A detailed description of possible group–subgroup relations of space groups was given in Section 1.4.2.2. If the symmetry reduction from G to H is connected with a shift of origin and/or a basis transformation the data for it should also be tabulated. In addition to the space group data of the structures, it is useful to specify the crystallographic data of the structures (element symbol, Wyckoff position,

site symmetry, and atomic coordinates) in the Bärnighausen tree. The inspection of atomic positions exhibits the symmetry changes from the higher symmetric structure to the lower symmetric one by splitting a Wyckoff position into several symmetry-independent positions and/or reduction of the site symmetry.

The following example of a symmetry tree should illustrate the procedure to display relations between crystal structures (Figure 1.108). We will depict the symmetry relations between diamond (C), sphalerite (ZnS), chalcopyrite ($CuFeS_2$), and stannite (Cu_2FeSnS_4). At the top of the symmetry tree is the diamond structure as *aristotype* (space group $Fd\bar{3}m$). The eight carbon atoms in the unit cell

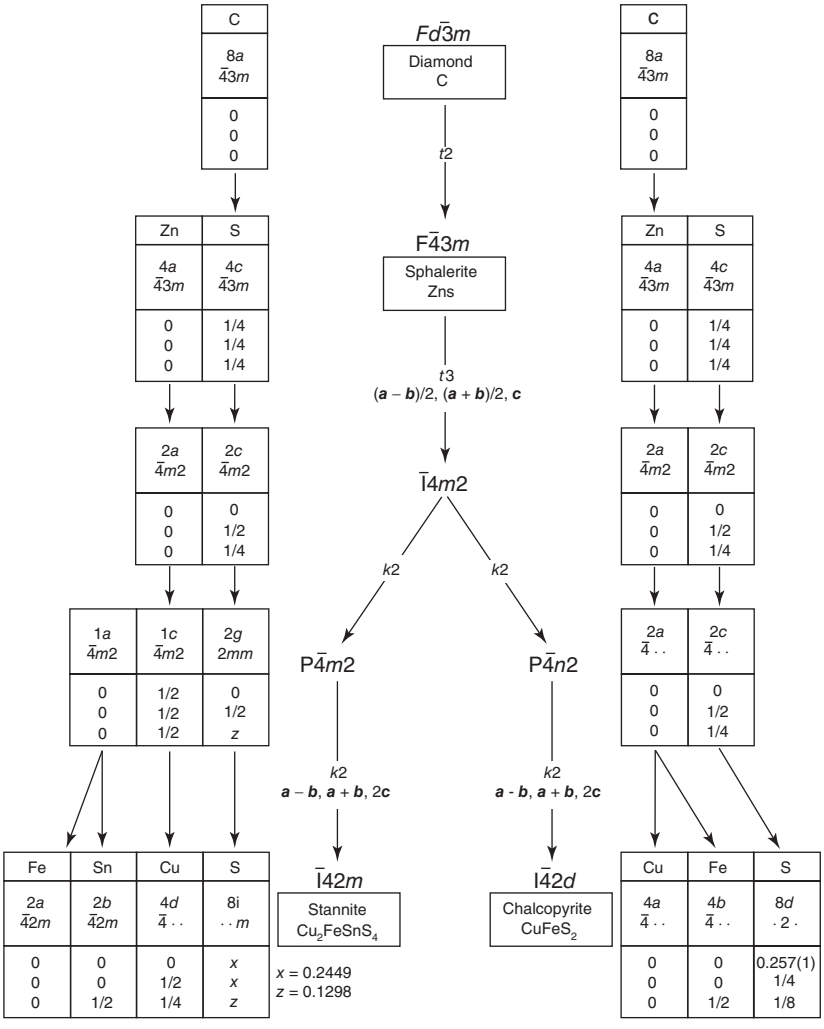

Figure 1.108 Symmetry tree for the structure relations between diamond–sphalerite–chalcopyrite–stannite.

occupy the Wyckoff position 8*a* (site symmetry $\bar{4}3m$). The space group $F\bar{4}3m$ of the sphalerite structure is a *maximal t-subgroup* of index 2. The symmetry reduction from diamond to sphalerite means that half of the point group symmetry operations is lost, including the inversion centers that are present in the diamond structure. The transition from $Fd\bar{3}m$ to $F\bar{4}3m$ is accompanied with the splitting of Wyckoff position 8*a* to the independent positions 4*a* and 4*c*, which are occupied by the elements Zn and S in sphalerite.

The further pathway to chalcopyrite and stannite leads over the *t*-subgroup $I\bar{4}m2$. At this point, the symmetry tree splits into two branches. The branch to the chalcopyrite structure (space group $I\bar{4}2d$) proceeds over the subgroup $P\bar{4}n2$, whereas the pathway over the subgroup $P\bar{4}m2$ leads to the stannite structure (space group: $I\bar{4}2m$).

Main categories of hettotypes are *substitution structures* and *distortion structures*. In our example, the symmetry reduction from diamond to sphalerite and further to chalcopyrite and stannite was a consequence of the substitution of different kind of atoms (Zn, S → C; Cu, Fe → Zn; Fe, Sn, Cu → Zn).

The transition from diamond to sphalerite was connected with a splitting of Wyckoff position 8*a* to two symmetry-independent positions 4*a* and 4*c* with identical site symmetry. However, the splitting of Wyckoff positions along the pathways from sphalerite to chalcopyrite and stannite leads to symmetry-independent positions with lower site symmetry.

Numerous hettotypes can also be derived from the aristotype of a close-packed structure if either tetrahedral and/or octahedral voids are occupied by atoms or voids are generated by removing atoms. Comprehensive and detailed descriptions of the fundamentals of symmetry relationships between crystal structures, including theory and numerous applications can be found in the book and reviews of Müller [125–127].

Symmetry trees can also be a helpful tool for the description of symmetry relations at structural phase transitions of crystals. A phase transition from the high-temperature structure to the low-temperature structure is very often accompanied by the formation of domains. The occurring domain structure can be predicted by group-theoretical considerations (see, e.g., [128, 129]). In the following, we will illustrate only the very basic relationships here. A comprehensive theoretical treatment of phase transitions and corresponding domain structures is given in the International Tables for Crystallography Volume D "Physical properties of crystals" (Part 3: Symmetry aspects of structural phase transitions, twinning, and domain structures).

According to the structural relationships between the high-temperature phase (basic structure and space group *G*) and the low-temperature phase (derivative structure and space group *H*), the following types of domain structures will be formed:

- ***Twin domains***, if *H* is a *translationengleiche* subgroup of *G*,
- ***antiphase domains***, if *H* is a *klassengleiche* subgroup of *G*, and
- a ***complex domain structure***, if *H* is a general subgroup of *G*.

A detailed theoretical description of domain structures is given in [130]. The number of various kinds of domains that are formed at the phase transition are determined by the index *i*. The total number of domains formed in the crystal at a phase transition depends on the nucleation and growth process.

The following examples of structural phase transformations should illustrate the abovementioned facts of domain structure generation. The high-temperature or β-form of quartz crystallizes in one of the enantiomorphic space groups $P6_422$ (left-handed quartz) and $P6_222$ (right-handed quartz) and undergo a phase transition to the low-temperature α-form of quartz via an incommensurate phase (INC) below 573 °C:

$$P6_422 \rightarrow \text{INC} \rightarrow P3_121(\text{left-handed quartz})$$
$$\text{or } P6_222 \rightarrow \text{INC} \rightarrow P3_221(\text{right-handed quartz})$$

The phase transition from α- to β-quartz and vice versa is of *displacive type* [131], that is, the atoms will be slightly shifted without any breaking of primary bonds. The Bärnighausen tree of this structural phase transition given in Figure 1.109 shows that the space group of α-quartz is a *t*2-subgroup of the space group of β-quartz.

The transition from point group 622 (order 12) to 32 (order 6) is accompanied with the loss of the twofold axes parallel *c*. As a result of this symmetry reduction, we observe the formation of two domains, the *Dauphiné twins*. Two left-handed or right-handed α-quartzes penetrate each other where the twofold twin axis is parallel to the [00.1] *c*-axis. The space groups of α- and β-quartzes belong

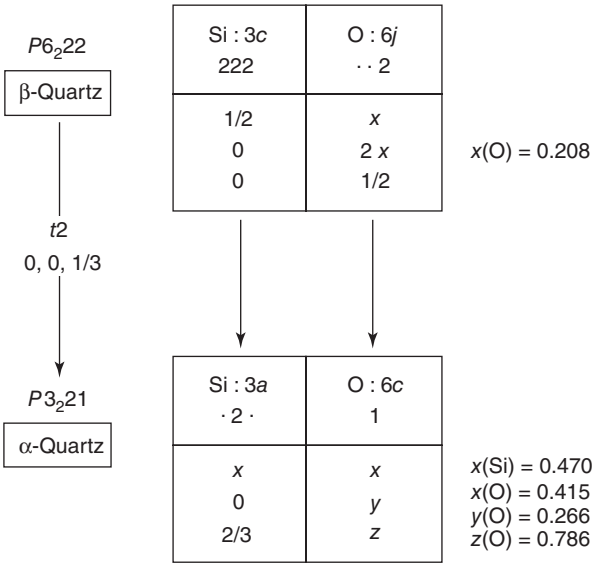

Figure 1.109 Symmetry tree of the α- to β-quartz phase transition.

to the same crystal family (hexagonal). Thus, the *Dauphiné twins* are "merohedral twins," where the two lattices of the two twin components exactly coincide. *Pseudo-merohedral twins* (ferroelastic twins) will be formed at a structural phase transition where the reduction of the point group symmetry is connected with a change of crystal family.

The high-temperature phase of the alloy Cu_3Au crystallizes in the space group $Fm\bar{3}m$ where one gold atom and three copper atoms occupy statistically the positions of a cubic F-Bravais lattice. When cooling down the Cu_3Au phase, an ordering process starts; thus, below 390 °C, the Au atoms occupy the positions of a cubic P-Bravais lattice and the Cu atoms occupy the centers of the cube faces. This "*OD*" structural phase transition is characterized by the symmetry reduction from $Fm\bar{3}m$ (G) to $Pm\bar{3}m$ (H) where H is a $k4$-subgroup of G (Figure 1.110). The ordering process leads to the formation of four different kinds of *antiphase boundaries*, which are also denoted as *translation twins* or *translation domains* in the literature.

The domain structure of a general structural phase transition where H is a general subgroup of G is much more complex. The symmetry tree of the phase transition from the high-temperature phase to the low-temperature phase of β-$Gd_2(MoO_4)_3$ is illustrated in Figure 1.111. The structural data of β-$Gd_2(MoO_4)_3$ given in the Bärnighausen tree were determined by Jeitschko [132]. The high-temperature phase crystallizes in the tetragonal space group $P\bar{4}2_1m$(G) and the low-temperature phase has orthorhombic symmetry [space group *Pba2* (H)]. In our case, H is a general subgroup of G. The transition from G to H proceeds over the intermediate space group *Cmm*2, which is a maximal $t2$-subgroup of $P\bar{4}2_1m$ and a minimal $k2$-supergroup of *Pba*2. It is also interesting to follow how the Wyckoff positions were splitted along the pathway from $P\bar{4}2_1m$ via *Cmm*2 to

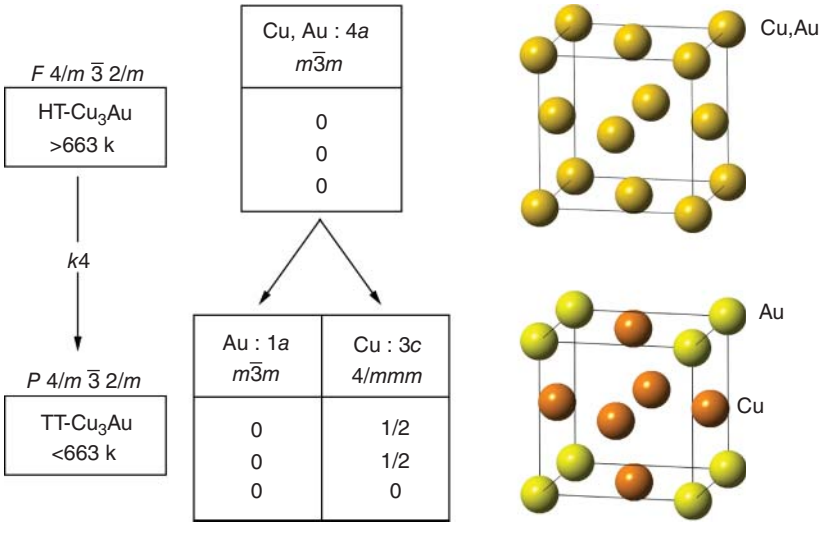

Figure 1.110 Symmetry tree of the order–disorder phase transition of Cu_3Au.

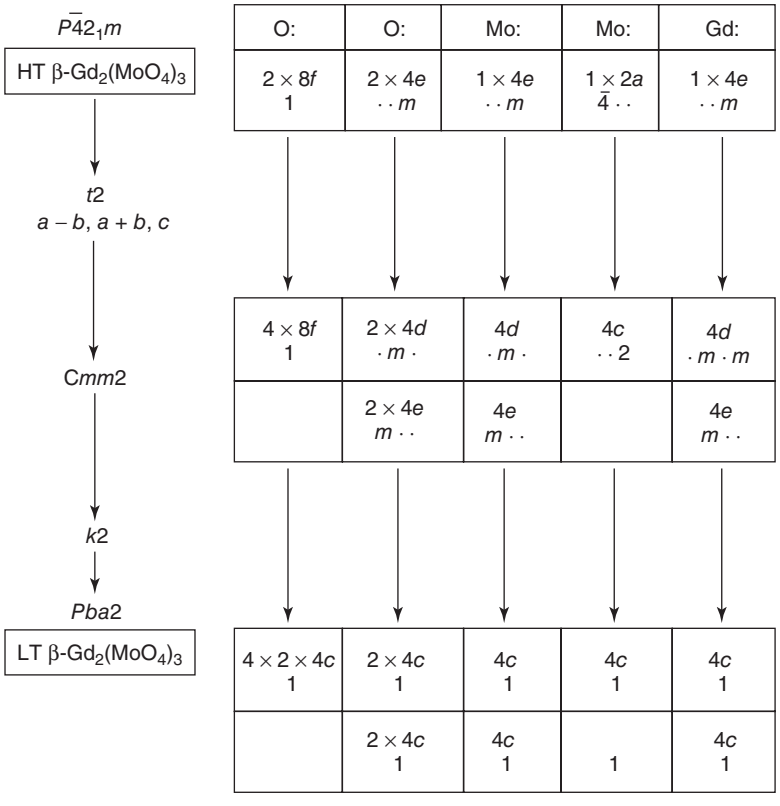

Figure 1.111 Symmetry tree of the phase transition of β-$Gd_2(MoO_4)_3$.

*Pba*2. According to the symmetry relationships, the complex domain structure should consist of twins and antiphase boundaries, which were also experimentally observed in β-$Gd_2(MoO_4)_3$ [133]. However, we should be aware of the fact that a detailed analysis of the domain structure in β-$Gd_2(MoO_4)_3$ needs a deeper and comprehensive theoretical treatment as given above (see, e.g., [130]).

1.6 Crystallographic Databases and Crystallographic Computer Programs

Nowadays, numerous crystallographic databases exist, which are specialized according to the stored information content about crystals. Owing to their historical development, the major crystallographic databases are structural databases that are each concerned with a special class of chemical compounds. In their entirety, they do cover the complete spectrum of chemical compounds, ranging from metals (**CRYSTMET** [134]), through organic and organometallic compounds (**CSD** [135]), over proteins (Protein Data Bank, **PDB** [136]) to

inorganic materials (**ICSD** [137]). Connected with the rapid development of computer technology and software systems, the possibilities of data acquisition, processing, validation, and retrieval have improved enormously.

Moreover, all major databases offer numerous possibilities for the analysis and visualization of the data. Very often, there are also software tools available for the visualization of structures and for the calculation and prediction of properties. In addition to the crystal structure data collection, some of the structural databases have also stored X-ray powder diffraction data as a basis for materials identification.

A tremendous improvement for the exchange of data between the various data sources (authors, journals, and users) and the different databases is because of the implementation of the ***Crystallographic Information File*** (***CIF***) format [138, 139], which is now used in all crystallographic reference databases.

Information about what kind of crystallographic databases exist can be found on the Webpage of the IUCr (*http://www.iucr.org/resources/data*). Here, the databases are classified into primary (major public databases of crystal structures and related data) and secondary (academic or small-scale) databases. A very good insight into the structure, information content, and the fields of application of the major crystallographic reference databases is given in a special issue of *Acta Crystallographica B* [140].

A particular role within the category of crystallographic databases plays the ***Bilbao Crystallographic Server (BCS)***. The ***BCS*** is accessible over the Internet (with any web browser *http://www.cryst.ehu.es*) and contains crystallographic databases and computer programs, which are available online and can be used free of charge. A comprehensive overview about the structure and content of ***BCS*** is given by Aroyo *et al.* [39]. The ***BCS*** set of databases includes space group data, subperiodic groups, *k*-vectors, and Brillouin zones, in addition to the data on incommensurate crystal structures.

Another major advantage of the ***BCS*** is that it provides a large selection of crystallographic programs for the processing of the crystallographic data, which are very helpful for the daily work in crystallography, solid-state physics, and crystal chemistry.

The ***Crystallography Open Database*** (***COD***) was created by a dedicated international group of volunteer scientists [141] in order to provide quick and open (free of charge) access to comprehensive crystallographic structure data off *all* classes of materials for any interested person over the Internet. This database is not a competitor of the well-known crystal structure reference databases, which offer various software tools for data analysis and data handling in addition. The main aim of the ***COD*** is to allow for searches in order to check very quickly if structure data of any particular crystal under investigation are already available (and readily available over the Internet).

The primary place for searching for new crystallographic computer programs is the ***Journal of Applied Crystallography***. The open-access database **SINCris** provides a very good overview about the available numerous crystallographic computer programs. This database contains software for all fields in

crystallography (see Crystallographic Resources and Information Online of the IUCr, *http://ww1.iucr.org/cww-top/crystal.index.html*). The programs are stored in alphabetical order. The program example given below illustrates what kind of information about the software is deposited in **SINCris**.

SHAPE

- *Entered*: Thu Oct 21 10:05:37 DFT 1999
- *Operating systems*: MacOS, Windows
- *Type*: Binary
- *Distribution*: Commercial
- *Application fields*: Graphics, visualization, virtual reality
- *Description*: Drawing the external morphology (faces) of crystals and QCs. In addition, drawing of sections of crystals. The professional edition (Windows only) includes two capabilities beyond those of the standard edition: QCs and sections/growth-zones
- *References: http://www.shapesoftware.com/*

In the following, a very brief description of the main primary and secondary crystallographic databases is given:

Primary Crystal Structure Databases

CRYSTMET Metals Structure Database (*http://www.tothcanada.com*, access: restricted)

CRYSTMET is a structure database for metals, alloys, intermetallic compounds, and minerals. In addition to the structural data, there are also calculated powder diffraction data, which enable the identification of crystal phases.

CSD Cambridge Structural Database (*http://www.ccdc.cam.ac.uk/products/csd/*, access: restricted)

The **CSD** has been developed by the Cambridge Crystallographic Data Center (CCDC). It is the world largest reference structure database for organic molecules and metallorganic compounds. This archive contains bibliographic, chemical, and numerical data from X-ray and neutron diffraction studies. For research and education purposes, any individual can request via the Internet-free structural reference data for any stored organic chemical compound (*http://www.ccdc.cam.ac.uk/products/csd/request/*) for one crystal structure at a time. There is also a 500 entry educational subset of this database [142] openly accessible on the Internet (Figure 1.112).

PDB Protein Data Bank **(***http://www.rcsb.org/pdb/*, **access: free)**

This is the reference structure database of proteins, nucleic acids, and complex assemblies.

NDB Nucleic Acid **Database (***http://ndbserver.rutgers.edu*, **access: free)**

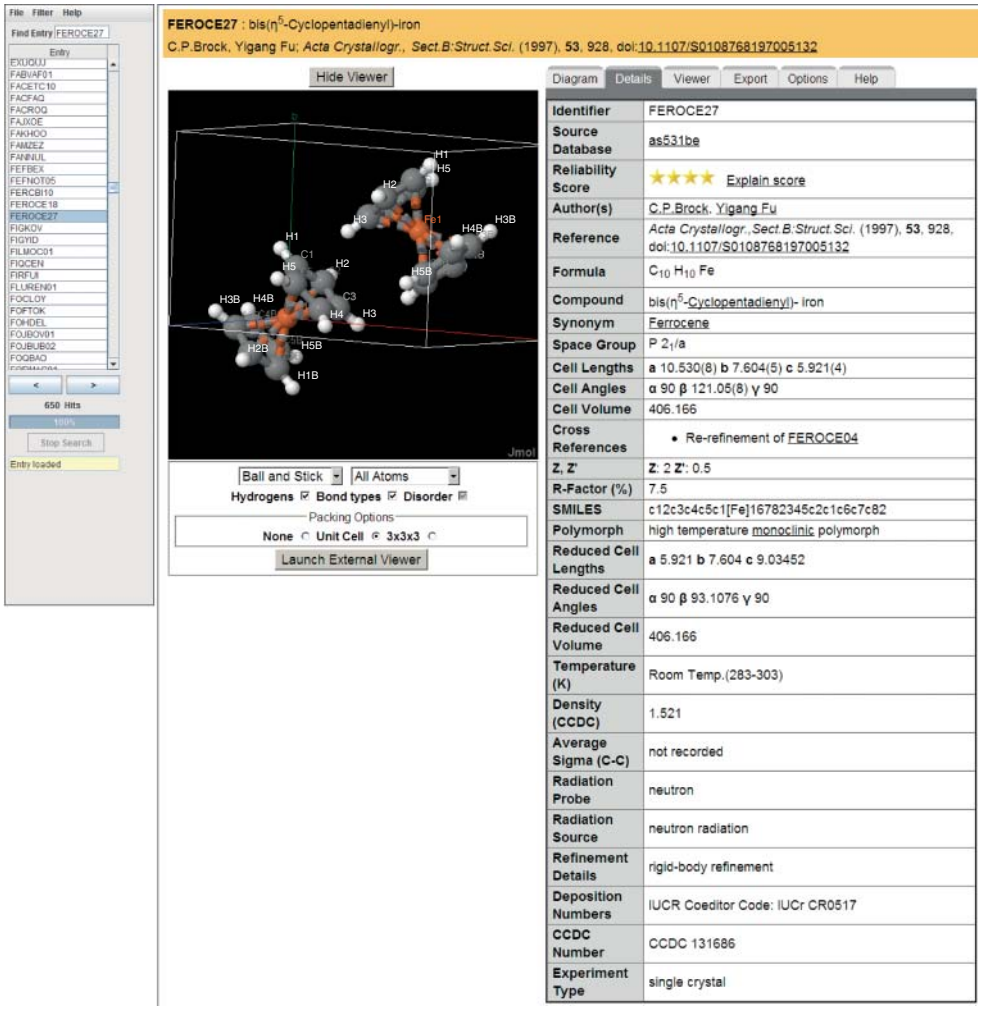
File Filter Help
Find Entry FEROCE27
Entry
FEROCE27
650 Hits
Stop Search
Entry loaded
FEROCE27 : bis(η5-Cyclopentadienyl)-iron
C.P.Brock, Yigang Fu; Acta Crystallogr., Sect.B:Struct.Sci. (1997), 53, 928, doi:10.1107/S0108768197005132
Hide Viewer
Jmol
Ball and Stick
All Atoms
Hydrogens Bond types Disorder
Packing Options
None Unit Cell 3x3x3
Launch External Viewer
Diagram Details Viewer Export Options Help
Identifier FEROCE27
Source Database as531be
Reliability Score Explain score
Author(s) C.P.Brock, Yigang Fu
Reference Acta Crystallogr.,Sect.B:Struct.Sci. (1997), 53, 928, doi:10.1107/S0108768197005132
Formula C10 H10 Fe
Compound bis(η5-Cyclopentadienyl)- iron
Synonym Ferrocene
Space Group P 21/a
Cell Lengths a 10.530(8) b 7.604(5) c 5.921(4)
Cell Angles α 90 β 121.05(8) γ 90
Cell Volume 406.166
Cross References • Re-refinement of FEROCE04
Z, Z' Z: 2 Z': 0.5
R-Factor (%) 7.5
SMILES c12c3c4c5c1[Fe]16782345c2c1c6c7c82
Polymorph high temperature monoclinic polymorph
Reduced Cell Lengths a 5.921 b 7.604 c 9.03452
Reduced Cell Angles α 90 β 93.1076 γ 90
Reduced Cell Volume 406.166
Temperature (K) Room Temp.(283-303)
Density (CCDC) 1.521
Average Sigma (C-C) not recorded
Radiation Probe neutron
Radiation Source neutron radiation
Refinement Details rigid-body refinement
Deposition Numbers IUCR Coeditor Code: IUCr CR0517
CCDC Number CCDC 131686
Experiment Type single crystal

Figure 1.112 Screenshot of the free demo version of the CSD, *http://webcsd.ccdc.cam.ac.uk/teaching_database_demo.php*

Nucleic Acid Database (**NDB**) is a data collection of three-dimensional structural information of nucleic acids.

BMCD Biological Macromolecule Crystallization Database (*http://www.bmcd.nist.gov:8080/bmcd/bmcd.html*, **access: free)**

Biological Macromolecule Crystallization Database (BMCD) is a collection of published crystallization procedures, strategies, and data for all classes of biological macromolecules (e.g., proteins, nucleic acids, various complexes, and viruses) where crystals could be grown suitable for structure analysis.

MPCD Marseille Protein Crystallization Database (*http://www.cinam.univ-mrs.fr/mpcd/*, access: **free)**

The **Marseille Protein Crystallization Database** (**MPCD**) is an online archive of crystallization data of macromolecules, where the users can deposit their own data of new macromolecules and their crystallization conditions.

ICSD Inorganic Crystal Structure **Database** (*http://www.fiz-karlsruhe.de/icsd_content.html*, **access: restricted)**

The ICSD is a large-sized archive of structural data of inorganic materials, where also a comprehensive and searchable list of structure types [66] is included. There exists also an ICSD Web demo version and a downloadable demo database (*http://icsd.fiz-karlsruhe.de/*).

PCD Pearson's Crystal Data – Crystal Structure Database for Anorganic Compounds (*http://www.crystalimpact.com/pcd*, **access: restricted)**

PCD is a relatively new crystallographic database containing structural information about *anorganic* materials. The somewhat unusual word *anorganic* was chosen in order to distinguish this database from the ICSD. In addition to the structural data, there are sets of experimental and calculated powder diffraction patterns archived. A free demo version of **PCD** is also available, see [143].

The Pauling File – a Basic Database for Crystal Structures (*http://crystdb.nims.go.jp/*, **access: free)**

This medium-sized data collection for all classes of nonorganic materials provides online information about the crystallographic structure, diffraction data, physical property data, and phase diagrams.

COD Crystallography Open Database (*http://www.crystallography.net/*, access: free)

The main aim of the COD, founded in 2003, was to create an *open-access* collection of crystal structures covering the whole range of materials in *one* database. In the spring of 2010, the COD possesses more than 100 000 entries and was mirrored by two sites in France and two more sites in the United States [144].

PCOD Predicted Crystallography Open Database (*http://www.crystallography.net/pcod/index.html*, access: free)

The **Predicted Crystallography Open Database** (**PCOD)** contains entries of predicted structures of inorganic materials. A part of this database is P2D2 (Predicted Powder Diffraction Database), which includes all calculated powder diffraction patterns from the PCOD structures.

American Mineralogist Crystal Structure Database (AMCSD) (*http://rruff.arizona.edu/AMS/amcsd.phd*, access: free)

The **American Mineralogist Crystal Structure Database (AMCSD)** contains the crystal structure data that has been published in the *American Mineralogist*,

the *Canadian Mineralogist*, the *European Journal of Mineralogy*, and *Physics and Chemistry of Minerals*. All data of this database are also part of the COD.

Mineralogical Databases

MINCRYST Crystallographic and Crystallochemical Database for Mineral and their Structural Analogs (*http://database.iem.ac.ru/mincryst*, *access: free*)

MINCRYST can be used either as standalone or Internet version. This database contains the structure data of minerals. Furthermore, there are various computer programs included, which allows, for example, the calculation of X-ray diffraction patterns and qualitative and quantitative X-ray diffraction phase analyses.

Mineralogy Database (*http://webmineral.com*, **access: free)**

This database contains entries of individual minerals (4714 species), which are linked to tables containing classification data, crystal data, X-ray powder diffraction data, and data of physical and optical properties.

ATHENA (*http://un2sg4.unige.ch/athena/mineral/min_how.html*, access: free)

ATHENA is a collection of mineral data (name, formula, crystal system, classification, group, reference, type locality, and images).

Special Secondary Structure Databases

National Institute of Standards and Technology (NIST) Crystal Data (*http://www.nist.gov/srd/nist3.htm*, access: restricted)

This large database is a valuable collection of crystallographic, chemical, and physical information across the entire field of solids. The archive is useful for both the identification of materials and for materials design.

Crystal Lattice Structures (*http://cst-www.nrl.navy.mil/lattice/*, access: open)

This small-sized collection of common crystal lattice structures can be searched according to the *Strukturbericht* designation, Pearson symbol, and space group type. A special structure index is reserved for intermetallic alloy phases.

Database of Zeolite Structures (*http://www.iza-structure.org.databases*, access: open)

This archive contains structural information on all of the Zeolite framework types. In addition to the crystallographic data, there are stored powder diffraction patterns for representative materials. There are also links to other zeolite-related databases.

ICSDB Incommensurate Structures Database (*http://www.cryst.ehu.es/icsdb/*)

The **Incommensurate Structures Database** (***ICSDB)*** contains the data of single modulated structures and composites. The chemical information, publication data, the main structural data (cell, symmetry, atom sites, and experimental parameter), both the average structure and the modulated structure and the

modulation parameters are deposited in the ***ICSDB***. Users of the ***ICSDB*** can also add data on new structures.

The NIST Surface Structure Database (SSD) (*http://www.nist.gov/srd/nist42.htm*, access: restricted)

The **Surface Structure Database** (**SSD)** contains a comprehensive collection of crystallographic data of surface and interface structures. Authors who want to include their experimentally determined new surface structures will get access to the SSD free of charge.

Special Database for Phase Identification

PDF: Powder Diffraction File of the International Center for Diffraction Data (ICCD) http://www.icdd.com/ access: restricted)

The main content of the (**Powder Diffraction File**) PDF-2 is a collection of single-phase X-ray powder diffraction data (i.e., characteristic interplanar spacings and corresponding relative intensities) and crystallographic data (lattice constants, reduced cell parameters, number of formula units per unit cell, but not the atomic coordinates) of crystalline materials. The PDF-4 product line incorporates comprehensive databases for inorganic materials, minerals, and organics (and provides atomic coordinates). The PDF data allow structural fingerprinting of crystal phases, for example, the rapid identification of materials by the matching of the PDF data to experimental X-ray powder diffraction data. The PDF database contains software tools for simulating standard X-ray powder diffraction patterns, electron back-scattering diffraction patterns (EBSD), and electron diffraction spot patterns.

(WCD) Wiki Crystallography Database http://nanocrystallography.research.pdx.edu/search.py/search?database=wcd

Following the success of the general Wikipedia community, the **Wiki Crystallography Database** (WCD) was created and initially set up with complete structural information on some 8000 minerals. The search interface possesses additional features that are typical for minerals such as crystal morphology (point group), color, and lustre. As in any Wiki, the mineralogy community is encouraged to upload their own data and to correct errors in the data at any one time. The WCD is located at an open access web site *http://nanocrystallography.research.pdx.edu* that supports usages of crystallographic data for educational purposes [145] in conjunction with interactive structure and morphology visualizations (at the same standards as the commercial databases).

The last comprehensive review about crystallographic databases seems to have been published in 2006 [146]. Newer developments are covered in a dedicated Wikipedia entry *http://en.wikipedia.org/wiki/Crystallographic_database* that has been maintained by the community since 2008.

Appendix: Supplementary Material

S1 Special Crystal Forms of Cubic Crystal Classes

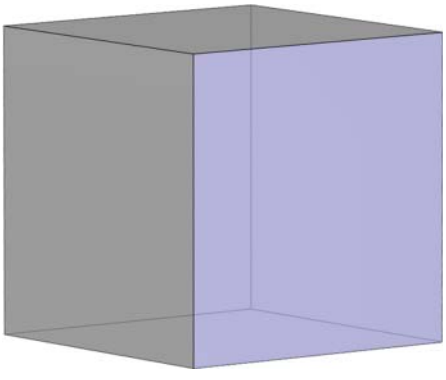

Figure S1.1 Cube.

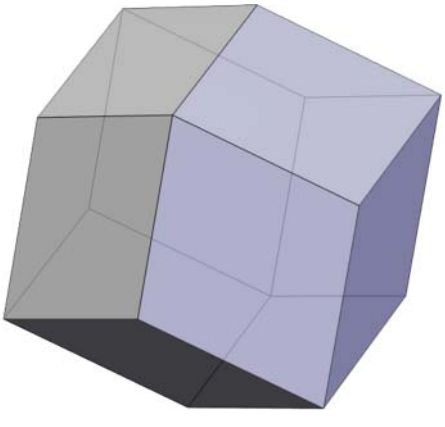

Figure S1.2 Rhomb-dodecahedron.

Table S1.1 The crystal forms of the cubic crystal classes.

Point group	{100}	{110}	{111}	{*hk*0}	{*hhl*} *h* > *l*	{*hll*} *h* > *l*	{*hkl*}
23	Cube	Rhomb-dodecahedron	Tetrahedron	Pentagon-dodecahedron	Deltoid-dodecahedron	Tristetrahedron	Tetrahedral pentagon-dodecahedron
$m\bar{3}$	Cube	Rhomb-dodecahedron	Octahedron	Pentagon-dodecahedron	Trisoctahedron	Deltoid-icositetrahedron	Didodecahedron
432	Cube	Rhomb-dodecahedron	Octahedron	Tetrakis-hexahedron	Trisoctahedron	Deltoid-icositetrahedron	Pentagon-icositetrahedron
$\bar{4}3m$	Cube	Rhomb-dodecahedron	Tetrahedron	Tetrakis-hexahedron	Deltoid-dodecahedron	Tristetrahedron	Hexakistetrahedron
$m\bar{3}m$	Cube	Rhomb-dodecahedron	Octahedron	Tetrakis-hexahedron	Trisoctahedron	Deltoid-icositetrahedron	Hexakisoctahedron

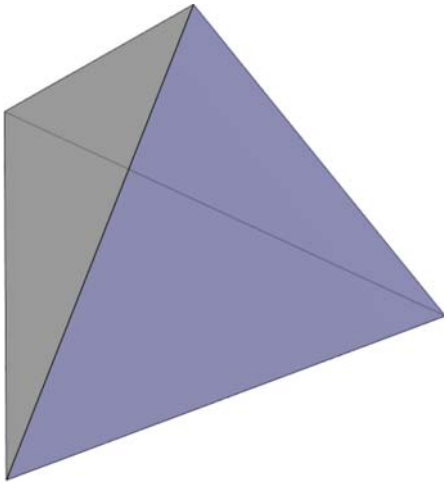

Figure 1.3 Tetrahedron

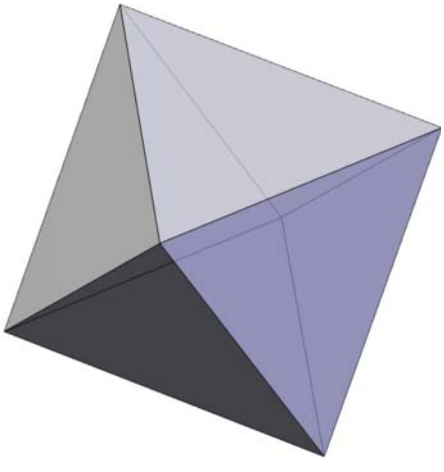

Figure 1.4 Octahedron.

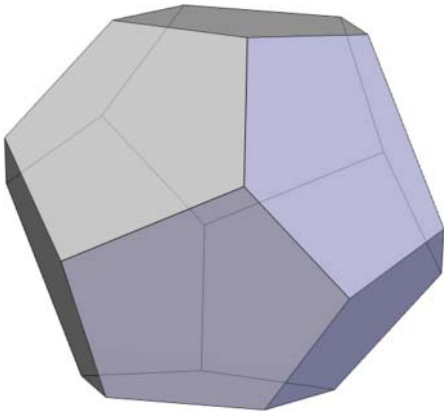

Figure 1.5 Pentagon-dodecahedron.

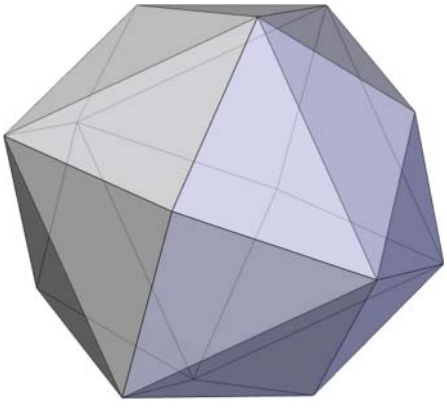

Figure 1.6 Tetrakishexahedron.

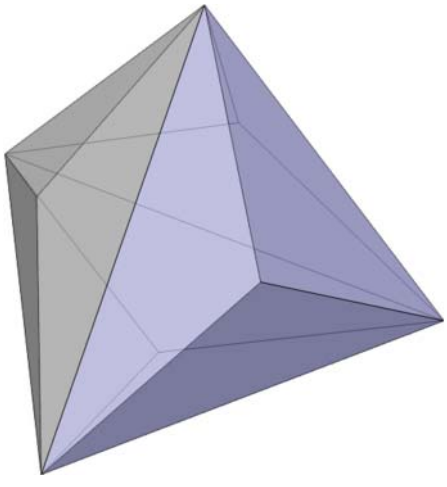

Figure 1.7 Tristetrahedron.

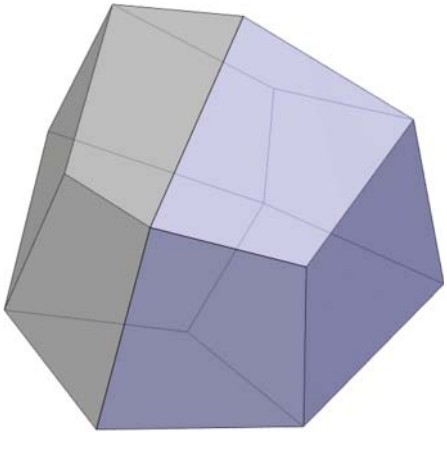

Figure 1.8 Deltoid-dodecahedron.

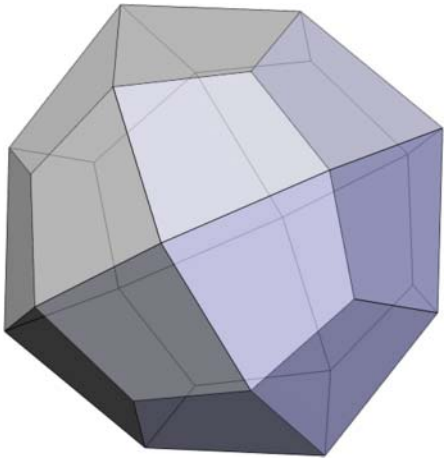

Figure 1.9 Deltoid-icositetrahedron.

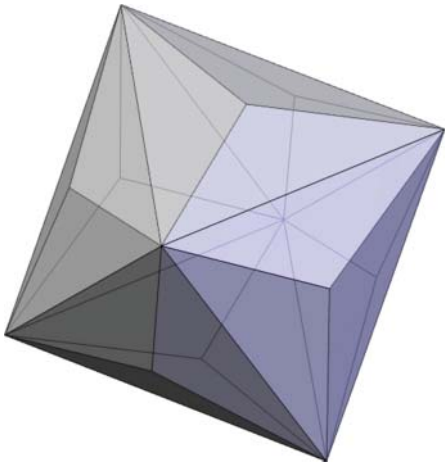

Figure 1.10 Trisoctahedron.

All polyhedra were drawn with the program WinXMorph, Kaminsky, W. [21, 22].

References

1. Burke, J.G. (1966) *Origins of the Science of Crystals*, University of California Press, Berkeley and Los Angeles, California.
2. Ewald, P.P. (ed.) (1962) *Fifty Years of X-Ray Diffraction*, published for the IUCr, N.V.A. Oosthoek's Uitgeversmaatschappij, Utrecht.
3. Burckhardt, J.J. (1988) *Die Symmetrie der Kristalle*, Birkhäuser Verlag, Basel.
4. Lima-de Faria, J. (ed.) (1990) *A Historical Atlas of Crystallography*, Kluwer Academic Publishers, Dordrecht.
5. Kirmse, H., Neumann, W., Kret, S., Dluzewski, P., Janik, E., Karczewski, G., and Wojtowicz, T. (2008) *Phys. Status Solidi C*, **5**, 3780–3784. doi: 10.1002/pssc.200780197

6. Janssen, T., Janner, A., Looijenga-Vos, A., de Wolff, P. M. in: *International Tables for Crystallography*, Vol. C: Mathematical, Physical and Chemical Tables (ed. Prince, E.) 2006**,** 907-955, International Union of Crystallography
7. Höche, T. (2004) Incommensurate structural modulations in fresnoite framework structures, Habilitation thesis, University Leipzig.
8. Höche, T., Esmaeilzadeh, S., Uecker, R., Lidin, S., and Neumann, W. (2003) *Acta Crystallogr., Sect. B*, **59**, 209.
9. Shechtman, D., Blech, I., Gratias, D., and Cahn, J.W. (1984) *Phys. Rev. Lett.*, **53**, 1951.
10. Levine, D. and Steinhardt, P.J. (1984) *Phys. Rev. Lett.*, **53**, 2477.
11. Dornberger-Schiff, K. (1964) *Abh. Dtsch. Akad. Wiss. Berlin, Kl. Chem.*, **3**, 1.
12. Dornberger-Schiff, K. (1982) *Acta Crystallogr.*, **A38**, 483.
13. Demus, D., Goodby, J., Gray, G.W., Spiess, H.-W., and Vill, V. (eds), (1998) *Handbook of Liquid Crystals*, vol. 1–3, Wiley-VCH Verlag GmbH, Weinheim.
14. IUCr: Report of the Executive Committee 1991 (1992) *Acta Crystallogr.*, **A48**, 928.
15. Steurer, W. (2007) *Z. Kristallogr.*, **222** (6), 308.
16. Bravais, A. (1866) *Etudes Cristallographiques*, Gauthier Villars, Paris.
17. Friedel, G. (1907) *Bull. Soc. Fr. Mineral.*, **30**, 326.
18. Donnay, J.D.H. and Harker, D. (1937) *Am. Mineral.*, **22**, 446.
19. CCDC (0000) *http://www.ccdc.cam.ac.uk* (accessed 20 February 2014).
20. Gale, J.D. (2005) *Z. Kristallogr.*, **220**, 552.
21. Kaminsky, W. (2007) *J. Appl. Crystallogr.*, **40**, 382.
22. Kaminsky, W. (2005) *J. Appl. Crystallogr.*, **38**, 566.
23. Hartman, P. and Perdok, W.G. (1955) *Acta Crystallogr.*, **8**, 49, 521–525.
24. Bennema, P. and van der Erden, J.P. (1987) in *Morphology of Crystals, Part A* (ed. I. Sunagawa), D. Reidel, Dordrecht, pp. 1–75.
25. Prywer, J. and Krasinski, M.J. (2007) *Cryst. Res. Technol.*, **42**, 1190.
26. Fischer, W. and Koch, E. (2006) in *International Tables for Crystallography*, Vol. A: Space Group Symmetry (ed. T. Hahn), Wiley-VCH Verlag GmbH, p. 810.
27. Ewald, P.P. (1913) *Z. Phys.*, **14**, 465.
28. Laue, M. (1914) *Jahrb. Radioakt. Elektr.*, **11**, 308.
29. Arnold, H. (2006) in *International Tables for Crystallography*, Vol. A: Space Group Symmetry (ed. T. Hahn), Wiley-VCH Verlag GmbH, p. 78.
30. Friedrich, W., Knipping, P., and Laue, M. (1912) *Sitzungsber. Kgl. Bayer. Akad. Wiss.*, 303, reprinted in *Ann. Phys.* (1913), **41**, 971.
31. Hahn, T. (ed.) (2006) *International Tables for Crystallography*, Vol. A: Space Group Symmetry, 1st online edn, Wiley-VCH Verlag GmbH.
32. *International Tables for Crystallography*, Vol. A1: Symmetry Relations between Space Groups, 2nd online edn, (eds. Wondratschek, H., Müller, U.) John Wiley & Sons, Ltd, 2011.
33. Hahn, T. (ed.) (2005) *International Tables for Crystallography*, Vol. A: Space Group Symmetry: Brief Teaching Edition, Corrected Reprint of 5th edn, John Wiley & Sons, Inc.
34. Wondratschek, H. (2006) in *International Tables for Crystallography*, Vol. A: Space Group Symmetry (ed. T. Hahn), Wiley-VCH Verlag GmbH, p. 726.
35. Buerger, M.J. (1970) *Contemporary Crystallography*, McGraw-Hill Book Company, New York.
36. Koch, E. and Fischer, W. (1974) *Acta Crystallogr.*, **A30**, 490.
37. Grosse-Kunstleve, R.W., Wong, B., Mustyakimov, M., and Adams, P.D. (2011) *Acta Crystallogr.*, **A67**, 269.
38. CCI Gallery of Ddirect-Space Asymmetric Units, *http://cci.lbl.gov/asu_gallery/* (accessed 20 February 2014).
39. Aroyo, M.I., Perez-Mato, J.M., Capillas, C., Kroumova, E., Ivantchev, S., Madariaga, G., Kirov, A., and Wondratschek, H. (2006) *Z. Kristallogr.*, **221** (1), 15.
40. Wondratschek, H. (2006) in *International Tables for Crystallography*,

Vol. A: Space Group Symmetry (ed. T. Hahn), Wiley-VCH Verlag GmbH, p. 726.
41. Fischer, W. and Koch, E. (1978) *Z. Kristallogr.*, **147**, 255.
42. Fischer, W. and Koch, E. (1974) *Z. Kristallogr.*, **139**, 268.
43. Koch, E. and Fischer, W. (1985) *Acta Crystallogr.*, **A41**, 421.
44. Fischer, W. and Koch, E. (2005) in *International Tables for Crystallography*, Vol. A: Space Group Symmetry (ed. T. Hahn), Springer-Verlag, p. 846.
45. Fischer, W., Burzlaff, H., Hellner, E., and Donnay, J.D.H. (1973) *Space Groups and Lattice Complexes*, NBS Monograph, vol. 134, National Bureau of Standards, Washington.
46. Hitzer, E., Perwass, Ch., Ichikawa, D., in: *Geometric Algebra Computing* (eds. Scheuermann, G., Bayo-Correchano, E.), Springer, New York 2010, p. 385
47. Janner, A. (2001) *Acta Crystallogr.*, **A57**, 378.
48. Brown, H., Bülow, R., Neubüser, J., Wondratschek, H., and Zassenhaus, H. (1978) *Crystallographic Groups of Four-Dimensional Space*, John Wiley & Sons, Inc., New York.
49. Opgenorth, J., Plesken, W., and Schulz, T. (1998) *Acta Crystallogr.*, **A54**, 517.
50. Plesken, W. and Schulz, T. (2000) *Exp. Math.*, **9**, 407.
51. Souvignier, B. (2003) *Acta Crystallogr.*, **A59**, 210.
52. *International Tables for Crystallography*, Vol. E: Subperiodic Groups, 2nd online edn (eds. Kopský, V., Litvin, D. B.) Wiley-VCH Verlag GmbH, 2011.
53. Shubnikov, A.V. and Belov, N.V. (1964) *Coloured Symmetry*, Pergamon Press, Oxford.
54. Heesch, H. (1930) *Z. Kristallogr.*, **73**, 325.
55. Zamorzaev, A.M. and Palistrant, A.F. (1980) *Z. Kristallogr.*, **151**, 231.
56. Souvignier, B. (2006) *Z. Kristallogr.*, **221**, 77.
57. Litvin, D.B. (2008) *Acta Crystallogr.*, **A64**, 419.
58. Dorset, D.L. (1995) *Structural Electron Crystallography*, Plenum Press, New York.
59. Zou, X.D., Hovmöller, S., and Oleynikov, P. (2011) *Electron Crystallography: Electron Microscopy and Electron Diffraction*, IUCr Texts on Crystallography, vol. 16, Oxford Science Publication.
60. Vincent, R. and Midgley, P. (1994) *Ultramicroscopy*, **53**, 271.
61. Morniroli, J.P., Stadelmann, P., Ji, G., and Nicolopoulos, S. (2010) *J. Microsc.*, **237**, 511.
62. Benner, G., Niebel, H., and Pavia, G. (2011) *Cryst. Res. Technol.*, **46** (6), 580.
63. Moeck, P., Rouvimov, S., Rauch, E.F., Véron, M., Kirmse, H., Häusler, I., Neumann, W., Bultreys, D., Maniette, Y., and Nicolopoulos, S. (2011) *Cryst. Res. Technol.*, **46** (6), 589.
64. Kolb, U., Mugnaioli, U., and Gorelik, T.E. (2011) *Cryst. Res. Technol.*, **46** (6), 542.
65. Gelato, L.M. and Parthé, E. (1987) *J. Appl. Crystallogr.*, **20**, 139.
66. Allmann, R. and Hinek, R. (2007) *Acta Crystallogr., Sect. A*, **63**, 412.
67. Burzlaff, H. and Malinovsky, Y. (1997) *Acta Crystallogr., Sect. A*, **53**, 217.
68. Lima-De Faria, J., Hellner, E., Liebau, F., Makovicky, E., and Parthé, E. (1990) *Acta Crystallogr., Sect. A*, **46**, 1.
69. Laves, F. (1930) *Z. Kristallogr.*, **73**, 202275.
70. Koch, E. and Fischer, W. (1999) *International Tables for Crystallography*, 3rd revised edn, vol. C, Kluwer Academic Publishers, Dordrecht, Boston, MA, London, pp. 746–751.
71. Fischer, W. (1971) *Z. Kristallogr.*, **133**, 18.
72. Fischer, W. (1973) *Z. Kristallogr.*, **138**, 129.
73. Fischer, W. (1974) *Z. Kristallogr.*, **140**, 50.
74. Fischer, W. (1991) *Z. Kristallogr.*, **194**, 67, 87.
75. Fischer, W. (1993) *Z. Kristallogr.*, **205**, 9.
76. Fischer, W. (2005) *Acta Crystallogr., Sect. A*, **61**, 435.
77. Sowa, H., Koch, E., and Fischer, W. (2003) *Acta Crystallogr., Sect. A*, **59**, 317.
78. Sowa, H. and Koch, E. (2004) *Acta Crystallogr., Sect. A*, **60**, 158.

79. Sowa, H. and Koch, E. (2005) *Acta Crystallogr., Sect. A*, **61**, 331.
80. Sowa, H. and Koch, E. (2006) *Acta Crystallogr., Sect. A*, **62**, 379.
81. Sowa, H. and Fischer, W. (2006) *Acta Crystallogr., Sect. A*, **62**, 413.
82. Sowa, H., Koch, E., and Fischer, W. (2007) *Acta Crystallogr., Sect. A*, **63**, 354.
83. Fischer, W. and Koch, E. (2002) *Acta Crystallogr., Sect. A*, **58**, 509.
84. Heesch, H. and Laves, F. (1933) *Z. Kristallogr.*, **85**, 443.
85. Fischer, W. (1976) *Z. Kristallogr.*, **143**, 140.
86. Vainshtein, B.K., Fridkin, V.M., and Indenbom, V.L. (1994) *Structure of Crystals, Modern Crystallography*, vol. 2, Springer-Verlag.
87. O'Keefe, M. and Hyde, B.G. (1996) *Crystal Structures, I Patterns and Symmetry*, Mineralogical Society of America.
88. Parthé, E. (1996) *Elements of Inorganic Structural Chemistry*, K. Sutter Parthé Publishing.
89. Müller, U. (2006) *Inorganic Structural Chemistry*, 2nd edn, John Wiley & Sons, Ltd, Chichester.
90. De Graef, M. and McHenry, M.E. (2007) *Structure of Materials: An Introduction to Crystallography, Diffraction and Symmetry*, Cambridge University Press.
91. Su, D.S., Tham, P., Schubert-Bischoff, P., Hähnert, I., Neumann, W., Giersig, M., and Zeitler, E. (1998) *Mater. Res. Soc. Symp. Proc.*, **523**, 241.
92. Bock, O. and Müller, U. (2002) *Acta Crystallogr., Sect. B*, **58**, 594.
93. McCrone, W.C.: in: *Physics and Chemistry of Organic Solid State*, Vol. 2 (eds. Fox, D., Labes, M.M., Weissberger, A.), Wiley-Interscience 1965, 726
94. Baronnet, A.: in: Reviews in Mineralogy, vol. 27, *Minerals and Reactions at the Atomic Scale: Transmission Electron Microscopy* (ed. Buseck, P.) 1992, Mineralogical Society of America, Washington, DC, pp. 231–282
95. Kuo, C.-L. (1965) *Acta Phys. Sin.*, **21**, 1089.
96. Kelly, J.F., Fisher, G.R., and Barnes, P. (2005) *Mater. Res. Bull.*, **40** (2), 249.
97. Kitaigorodsky, A.I. (1973) *Molecular Crystals and Molecules*, Academic Press, New York.
98. Kahn, R., Fourme, R., André, D., and Renaud, M. (1973) *Acta Crystallogr., Sect. B*, **29**, 131, Fullerenes.
99. Bunn, C.W. (1939) *Trans. Faraday Soc.*, **35**, 482.
100. Chen, B.M.L. and Tulinsky, A. (1972) *J. Am. Chem. Soc.*, **94**, 4144.
101. Hoshino, A., Takenaka, Y., and Miyaji, H. (2003) *Acta Crystallogr., Sect. B*, **59**, 393.
102. Uyeda, N., Kobayashi, T., Ishizuka, K., and Fujiyoshi, Y. (1978–79) *Chemica Scripta*, **14**, 47.
103. Kasper, J.S., Hagenmuller, P., Pouchard, M., and Cros, C. (1965) *Science*, **22**, 361.
104. Guloy, A.M., Ramlau, R., Tang, Z., Schnelle, W., Baitinger, M., and Grin, Y. (2006) *Nature*, **443**, 320.
105. Mak, T.C.W. and Zhou, G.-D. (1997) *Crystallography in Modern Chemistry: A Resource Book of Crystal Structures*, Wiley-Interscience, Wiley Professional Paperback Edition.
106. Shevelkov, A.V. and Kovnir, K. (2011) in *Principles and Recent Developments in the Field of Zintl Ions and Zintl Phases*, Structure & Bonding, vol. 139 (ed. T.F. Fassler), Springer, p. 97.
107. Chui, S.S.Y., Lo, F., Charmant, J.P.H., and Williams, I.D. (1999) *Science*, **283**, 1148.
108. Godly, E.W. and Taylor, R. (1997) *Pure Appl. Chem.*, **69** (7), 1411.
109. Kroto, H.W., Heath, J.R., O'Brien, S.C., Curl, R.F., and Smalley, R.E. (1985) *Nature*, **318**, 162.
110. Kroto, H.W.: in: *Symmetry 2 Unifying Human Understanding* (ed. Hargittai, I.), Pergamon Press, 1989, p. 417
111. Kroto, H.W. (1987) *Nature*, **329**, 529.
112. 112.Schmalz, T.G., Seitz, W.A., Klein, D.J., and Hite, G.E.J. (1988) *Am. Chem. Soc.*, **110**, 1113.
113. Slanina, Z., Uhlk, F., Lee, S.-L., and Osawa, E. (2001) *Match, Commun. Math. Comput. Chem.*, **44**, 335.
114. Ju, Y., Liang, H., Zhang, J., and Bai, F. (2010) *Match, Commun. Math. Comput. Chem.*, **64**, 419.

115. Itoh, S., Ordejón, P., Drabold, D.A., and Martin, R.M. (1996) *Phys. Rev. B*, **53**, 2132.
116. Schiebel, P., Wulf, K., Prandl, W., Heger, G., Papoular, R., and Paulus, W. (1996) *Acta Crystallogr., Sect. A*, **52**, 176.
117. Zhou, O., Fischer, J.E., Coustel, N., Kycia, S., Zhou, Q., McGhie, A.R., Romanov, W.J., McCauley, J.P. Jr., Amos, B., Smith, A.B. III, and Cox, D.E. (1991) *Nature*, **351**, 462.
118. Cai, T., Xu, L., Anderson, M.R., Ge, Z., Zuo, T., Wang, X., Olmstead, M.M., Balch, A.L., Gibson, H.W., and Dorn, H.C. (2006) *J. Am. Chem. Soc.*, **128**, 8581.
119. Iijima, S. (1991) *Nature*, **354**, 56.
120. *In-situ Electron Microscopy at High Resolution* (ed. F. Banhart), World Scientific Publishing. Singapore 2008
121. Dresselhaus, M.S., Dresselhaus, G., and Eklund, P.C. (1996) *Science of Fullerenes and Carbon Nanotubes*, Academic Press, San Diego, CA.
122. Bärnighausen, H. (1980) *MATCH, Comun.Math. Chem.*, **9**, 139.
123. Buerger, M.J. (1947) *J. Chem. Phys.*, **15**, 1.
124. Megaw, H.D. (1973) *Crystal Structures: A Working Approach*, Saunders Company, Philadelphia, PA.
125. Müller, U. (2013) *Symmetry Relationships between Crystal Structures*, IUCr Texts on Crystallography, vol. 18, Oxford Science Publication.
126. Müller, U. (2004) *Z. Anorg. Allg. Chem.*, **630**, 1519.
127. Müller, U. (2008) *Symmetry Relations between Crystal Structures*, Summer School, on Mathematical Crystallography, Gargagno, *http://www.crystallography.fr/mathcryst/gargnano2008.htm* (accessed 20 February 2014).
128. Van Tendeloo, G. and Amelinckx, S. (1974) *Acta Crystallogr., Sect. A*, **30**, 431.
129. Wondratschek, H. and Jeitschko, W. (1976) *Acta Crystallogr., Sect. A*, **32**, 664.
130. Janovec, V., Přívratská, J., Domain Structures, in: *International Tables for Crystallography*, Vol. D: Physical Properties of Crystals, Chapter 3.4 (ed. A. Authier), Kluwer Academic Publishers Dordrecht 2003
131. Salje, E.K.H., Ridgwell, A., Güttler, B., Wruck, B., Dove, M.T., and Dolino, G. (1992) *J. Phys. Condens. Matter*, **4**, 571.
132. Jeitschko, W. (1972) *Acta Crystallogr., Sect. B*, **28**, 60.
133. Bohm, J. and Kürsten, H.D. (1973) *Phys. Status Solidi A*, **19**, 176.
134. White, P.S., Rodgers, J.R., and Le Page, Y. (2002) *Acta Crystallogr., Sect. B*, **58** (Pt. 3, Pt. 1), 343.
135. Allen, F.H. (2002) *Acta Crystallogr., Sect. B*, **58** (Pt. 3, Pt. 1), 380.
136. Berman, H.M., Battistuz, T., Bhat, T.N., Bluhm, W.F., Bourne, P.E., Burkhardt, K., Feng, Z., Gilliland, G.L., Iype, L., Jain, S., Fagan, P., Marvin, J., Ravichanaran, V., Schneider, B., Thanki, N., Padilla, D., Weissig, H., Westbrook, J.D., and Zardecki, C. (2002) *Acta Crystallogr., Sect. B*, **58** (Pt. 3, Pt. 1), 899.
137. Belsky, A., Hellenbrandt, M., Karen, V.L., and Luksch, P. (2002) *Acta Crystallogr., Sect. B*, **58** (Pt. 3, Pt. 1), 364.
138. Brown, I.D. and Mc Mahon, B. (2002) *Acta Crystallogr., Sect. B*, **58** (Pt. 3, Pt. 1), 317.
139. *International Tables for Crystallography*, Vol. G: Definition and Exchange of Crystallographic Data (eds. Hall, S. R., McMahon, B.) International Union of Crystallography 2006.
140. Crystallographic Databases (2002) *Acta Crystallogr., Sect. B*, **58** (Special issue, Pt. 3, Pt. 1), 317–422.
141. Gražulis, S., Chateigner, D., Downs, R. T., Yokochi, A. F. T., Quirós, M., Lutterotti, L., Manakova, E., Butkus, J., Moeck, P., Le Bail, A., *J. Appl. Crystallogr.* 2009, **42**, 726, *http://journals.iucr.org/j/issues/2009/04/00/kk5039/kk5039.pdf* (accessed 7 March 2014).
142. Thomas, I.R., Bruno, I.J., Cole, J.C., Macrae, C.F., Pidcock, E., and Wood, P.A. (2010) *J. Appl. Crystallogr.*, **43**, 362.
143. Crystal Impact. About 2,600 Entry Demo Version for Free Download, *http://www.crystalimpact.com/pcd/*

download.htm (accessed 20 February 2014).

144. Crystallography Open Database *http://cod.ibt.lt* (In Lithuania, The Current Main Server Site) Mirrors; *http://www.crystallography.net* (in France, the original site); *http://cod.ensicaen.fr* (in France); *http://nanocrystallography.org/* (in Oregon); *http://nanocrystallography.net* (in Oregon) (accessed 20 February 2014).

145. Moeck, P., Čertík, O., Upreti, G., Seipel, B., Harvey, M., Garrick, W., and Fraundorf, P. (2006) *J. Mater. Educ.*, **28**, 87.

146. Moeck, P. (2006) Proceedings of Materials Science and Technology (MS&T) 2006: Fundamentals and Characterization, Vol. 1, p. 529.

2
Basics of Growth Mechanism and Solidification

Single crystals – in its whole shape – are built up from regularly arranged atoms or molecules (compare Chapter 1). Single crystals have a great industrial potential.

For instance, silicon single crystals are the basis of all technical developments in our electronic age; about 50 ktons of single crystals are produced every year worldwide. 200 ktons polycristalline silicon is the market forecast for solar cells by 2013. But other inorganic and organic materials were also grown as single crystals for the development of important applications. Crystal growth needs the careful design and reproducible control of a phase transition

- growth from the melt or solution phase: transition liquid/solid;
- growth from the vapor or gas phase: transition vapor/solid; and
- growth within a solid phase: transition solid/solid.

In Chapter 2, the starting stages of crystal growth – called *nucleation* – as well as processes of growth kinetics and growth mechanism, peculiarities of growth morphology, doping, and impurity segregation will be discussed to understand typical growth phenomena and the resulting physical and chemical properties of the grown crystals. Detailed studies on material science and crystal growth may be found in Refs. [1–4].

2.1
Nucleation Processes

The formation of a three-dimensional nucleus of a new phase is initiated through physical and chemical processes. Physical processes include condensation, crystallization, phase transitions in the solid phase, and so on. Chemical processes are, for example, heterogeneous reactions. All natural and artificial crystallization processes start with a nucleation event with the formation of a solid crystal. If a nucleus of a new phase is not formed in a homogeneous system (e.g., a solution) the new phase is not built up even when it is possible thermodynamically. The process of homogeneous nucleation occurs within a uniform nutrient, which could be a liquid phase (melt or solution) or a vapor (gas) phase.

Liquids cooled below the maximum heterogeneous nucleation temperature – the melting temperature – but which are above the homogeneous nucleation

Introduction to Crystal Growth and Characterization, First Edition.
Edited by Klaus-Werner Benz and Wolfgang Neumann.
© 2014 Wiley-VCH Verlag GmbH & Co. KGaA. Published 2014 by Wiley-VCH Verlag GmbH & Co. KGaA.

temperature are called to be supercooled. Such a system is in a metastable equilibrium. It may, in principle, remain in this metastable state without reaching the minimum free energy, which belongs to the equilibrium state. The new phase can be initiated by introducing a seed of the new phase. In this case, the system reaches the state of real thermodynamic equilibrium which also corresponds to the minimum free energy of the system. As a result, the formation of a nucleus is associated with a change in the free energy of the system.

Nucleation processes may be divided into primary and secondary nucleation.

If primary nucleation happens spontaneously, it is called ***homogeneous*** and if it is induced by foreign particles, it is called ***heterogeneous***. Secondary nucleation is initiated by crystals and plays an important role in industrial crystallization processes [5].

The formation of a nucleus of a new phase in the nutrient can occur only when the supersaturation in the system is sufficiently high. For instance, in metals such as lead the supersaturation values reach up to 80°C, whereas in semiconductor metallic solutions such as Ga–As or In–P, supersaturation values may be only in the range of 5–10 °C.

The difference between the free energy F of the nutrient and the new phase is the driving force for the process of crystallization. Free energy F and free enthalpy G are connected with the following basic equations:

$$F = H - TS \tag{2.1}$$

$$G = U - TS \tag{2.2}$$

H, S, and U are the enthalpy, entropy, and inner energy of the system, respectively.

The enthalpy H can be written as:

$$H = U + PV \tag{2.3}$$

P is the pressure and V the volume of the system.

Crystallization is now a first-order phase transition, for example, from phase 2 (liquid) to phase 1 (solid); and we have for the change of free enthalpy, by neglecting for this consideration the surface energy of the nucleus:

$$\Delta G = G_2 - G_1 = U_2 + PV_2 - TS_2 - U_1 - PV_1 + TS_1 \tag{2.4}$$

$$\Delta G = \Delta U + P\Delta V - T\Delta S \tag{2.5}$$

ΔG must be negative for the onset of crystallization. For a small volume change ΔV, we have $U \approx H$ and $G \approx F$. The change of entropy ΔS is normally very high.

The processes with $\Delta G < 0$ that are responsible for the onset of crystallization cannot be explained by thermodynamic considerations. However, processes connected to the onset of crystallization are discussed in Section 2.1.

In the case of a vapor phase, the difference in free energy is given by (change in volume free energy):

$$\Delta F_V = F_{vapor} - F_{solid} = n\, k_B T \ln(P/P_0) \tag{2.6}$$

F_{vapor} and F_{solid} are the free energies of the vapor and the solid, respectively, P and P_0, the actual and the equilibrium vapor pressure of the gas medium at temperature T, k_B is the gas constant, and n, the number of ions forming a particle.

For solutions, Equation 2.6 may be written as

$$\Delta F = nk_B T \ln(a/a_0)$$
$$= nk_B T[\ln(f/f_0) + \ln(c/c_0)] \tag{2.7}$$

a and a_0 are the activities of supersaturated and saturated solutions, respectively, f and f_0, the corresponding activity coefficients, and c and c_0, the concentrations of the material component in the supersaturated and saturated solutions. For small values of supersaturation, we have $f/f_0 = 1$ and Equation 2.7 can be written as

$$\Delta F = nk_B T \ln(c/c_0) \tag{2.8}$$

For melt and solution, the change in free energy may be also expressed in terms of a temperature difference as

$$\Delta F = \Delta H - T\Delta S \tag{2.1b}$$

where ΔH is the melting or dissolution enthalpy, and ΔS, the entropy change of the system. For a thermodynamic equilibrium ($\Delta F = 0$), we have

$$\Delta S = \Delta H/T_0 \tag{2.9}$$

Using Equations 2.1b and 2.9, we obtain

$$\Delta F = \Delta H - T\Delta H/T_0 = \Delta H(T_0 - T)/T_0$$
$$\Delta F = \Delta H \Delta T/T_0 \tag{2.10}$$

If we introduce the well-known relationship between the free energy F (thermodynamic potential) and chemical potential μ,

$$\Delta F = \Sigma \Delta \mu_i n_i \tag{2.11}$$

Combining Equations 2.11, 2.6, and 2.8, we may write

$$\Delta \mu = k_B T \ln(P/P_0) \tag{2.12a}$$

or by using the ratio of concentrations,

$$\Delta \mu = k_B T \ln(c/c_0) \tag{2.12b}$$

At pressures smaller than P_0 the chemical potential of the crystal is greater than that of the vapor and the crystal may sublime. For $P > P_0$ the vapor will crystallize. The difference $\Delta\mu$, the driving force for the crystallization, is called ***supersaturation***. In this case, the starting phase and the new phase are considered to be infinitively large and that means a flat phase boundary (Figure 2.1).

In practical cases, we have to calculate an equilibrium between phases with finite dimensions. Using our previous example, we will follow the transition from vapor to liquid or solid by forming small droplets or small crystallites. The shape of these new phases is assumed to be a sphere with radius r. As an example, we

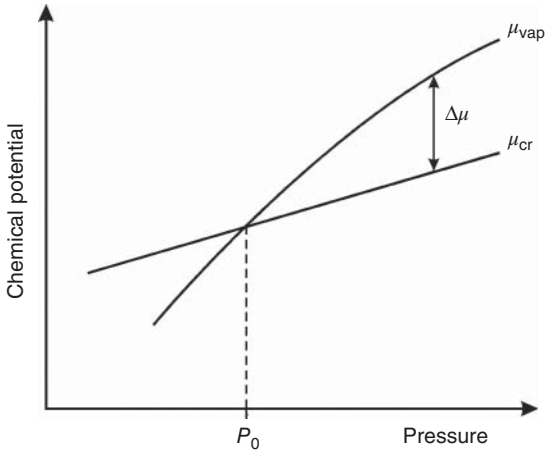

Figure 2.1 Chemical potential of the vapor μ_{vap}, and the crystal μ_{Cr} as function of the pressure. P_0 is the equilibrium pressure.

may use a growth ampoule with a vapor of volume V_{vap} and a liquid droplet with volume V_{liq} and radius r (representative for a small crystallite as well). The vapor pressure in the system is P_{Vap} and in the droplet P_{liq}. The equilibrium is given by the minimum of the free energy in the system:

$$dF = P_{Vap}dV_{Vap} - P_{liq}dV_{liq} + \sigma dA \tag{2.13}$$

σ is the surface tension of the infinitively large liquid and A, the surface area of the droplet. We have $V = V_{Vap} + V_{liq} = \text{constant}$ and $dV_{Vap} = -dV_{liq}$ and Equation 2.13 can be written as

$$P_{liq} - P_{Vap} = \sigma dA/dV_{liq}$$

The surface of the droplet is $A = 4\pi r^2$ and its volume $V_{liq} = (4\pi r^3)/3$.

As a result, we have the well-known Laplace equation:

$$P_{liq} - P_{Vap} = 2\sigma/r \tag{2.14}$$

The pressure in the droplet is always higher than the pressure outside in the vapor. $2\sigma/r$ is called the *Laplace* or *capillary pressure*.

By considering in the same system the free enthalpy G (P, T, n_{Vap}, n_{liq}, A) with respect to the thermodynamic equilibrium, we can write for ΔG ($dP = 0$, $dT = 0$):

$$\Delta G = \mu_{Vap}dn_{Vap} + \mu_{liq}dn_{liq} + \sigma dA = 0 \tag{2.15}$$

n_{Vap} and n_{liq} are the amount of moles in the vapor and liquid phases, respectively. By performing similar calculations as given earlier, we get the important Gibbs–Thomson equation for determining the difference of the chemical potential of the vapor phase and the liquid droplet:

$$\Delta\mu = \mu_{Vap} - \mu_{liq} = 2\sigma v_{liq}/r \tag{2.16}$$

$n = V_{liq}/v_{liq}$ atoms or molecules are transferred from the vapor phase with higher chemical potential to the liquid droplet phase with lower chemical potential.

2.1.1 Homogeneous Nucleation

As mentioned earlier, the formation of a nucleus begins with the appearance of an interface at the boundaries of the new phase. Some energy is needed to form this interface based on the surface energy of each phase. Nucleation involving the beginning of the process was treated from a thermodynamic viewpoint by Volmer [6]. It is assumed, that in a homogeneous solution no impurities are present, the formation of a nucleus is associated with a change in the free energy of the system as described in Chapter 1.

In a supersaturated homogeneous solution, nuclei of a new phase may appear and disappear as a result of statistical fluctuations. But there is always a certain statistical probability that some neighboring particles gain sufficient energy necessary to form a stable critical nucleus of the crystalline phase. The free enthalpy change consists of two parts: (i) the formation of the volume of the new phase (ΔG_1) and (ii) the build up of an interface due to the growing of the size of the nucleus (ΔG_2):

$$\Delta G = \Delta G_1 + \Delta G_2 \tag{2.17}$$

ΔG_1 is negative because of the fact, that the free enthalpy is lowered compared to the initial phase. The transition occurs from an unstable to a stable state. If we consider a spherical nucleus such as a droplet, ΔG_1 may be given by

$$\Delta G_1 = -(4\pi r^3/3V_m)\Delta\mu \tag{2.18}$$

where V_m is the molecular volume.

With the growing nucleus, the surface of the nucleus is increasing as well. The amount of enthalpy change due to the increasing surface of the nucleus is given by

$$\Delta G_2 = 4\pi r^2\sigma \tag{2.19}$$

For ΔG, we now have

$$\Delta G = 4\pi r^2\sigma - (4\pi r^3/3V_m)\Delta\mu \tag{2.20}$$

Owing to the small volume of the nucleus the relative change of its surface is very high compared to the volume change. Therefore, the main component of the change in the free enthalpy involved in the formation of the nucleus will be the surface free enthalpy ΔG_2.

Figure 2.2 shows the total free enthalpy as a function of the radius r. The free enthalpy change ΔG increases with radius r until a maximum r^* is reached. For $r < r^*$, the nucleus is unstable and vanishes because ΔG would increase with increasing size of the nucleus. For $r > r^*$, the free enthalpy change will decrease

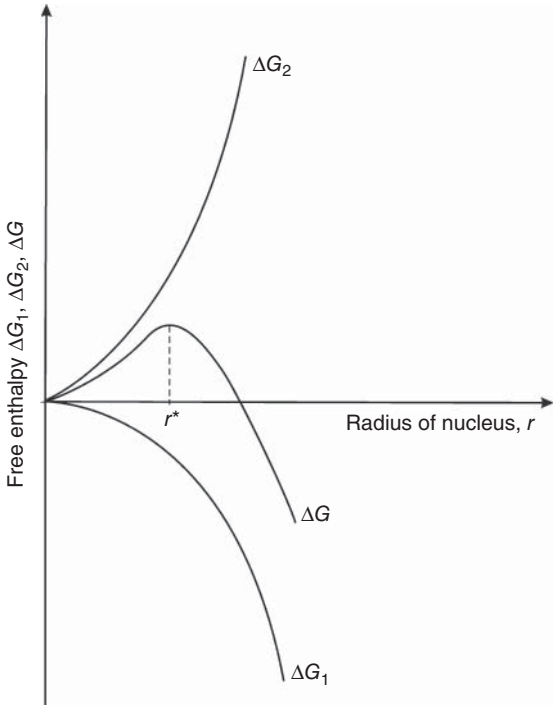

Figure 2.2 Formation of a nucleus. The free enthalpy ΔG_1, ΔG_2, and ΔG as function of the radius of nucleus.

and the nucleus may continue its growth. The maximum value ΔG for a stable radius r^* can be reached by differentiating Equation 2.20:

$$d(\Delta G)/dr = 0 \tag{2.21}$$

For r^*, we get

$$r^* = 2\sigma V_m/\Delta\mu \tag{2.22}$$

It can be seen that Equation 2.22 is the relation given by Gibbs–Thomson (Equation 2.16).

By substituting r^* in Equation 2.20, we obtain the maximum value ΔG^*:

$$\Delta G^* = 16\pi/3 \cdot \sigma^3 {V_m}^2/\Delta\mu^2 \tag{2.23}$$

Equation 2.23 shows the height of the energy barrier for the onset of crystallization. It is inversely proportional to the square of the supersaturation. This result was first obtained by Gibbs in the year 1878. The factor $16\pi/3$ is called the *shape factor* for a spherical nucleus. For nuclei of other shapes, this factor is somewhat different.

By substituting the supersaturation $\Delta\mu$ in Equation 2.23, we obtain the following expression:

$$\Delta G^* = 1/3 \cdot 4\pi {r^*}^2\sigma \tag{2.24}$$

It can be seen from Equation 2.24 that the free enthalpy to build up a critical nucleus is one-third of the surface enthalpy.

Example 2.1: As an example we will consider the homogeneous nucleation of copper. We will calculate the critical nucleation radius r^* and the number of atoms within the critical nucleus. The following properties of Cu will be used:

lattice constant, Cu – fcc $a = 0.3615$ nm;
surface energy $\sigma = 177 \cdot 10^{-7}$ J cm^{-2};
latent heat of crystallization $\Delta H_{Cr} = 1628$ J cm^{-2};
typical supercooling $\Delta T = 236$ K;
melting temperature $T_m = 1358$ K.

Using Equation 2.10, we can write for the critical radius r^* in the case of a melt–solid nucleation process:

$$r^* = 2\sigma T_m / \Delta H_{cr} \Delta T \tag{2.25}$$

With the above-mentioned data , we can calculate the critical radius for the Cu nucleus and its critical volume V^* as

$$r^* = 1.25\ \mu\text{m} \quad \text{and} \quad V^* = 8.2 \cdot 10^{-21} \text{cm}^3$$

with 696 Cu atoms inside this nucleus.

2.1.2
Heterogeneous Nucleation

In Chapter 1, we have seen that the homogeneous nucleation is of fundamental significance. Exceptions are the glass formation and mass crystallization. In practical growth experiments of single crystals, heterogeneous nucleation takes place in the presence of certain sites such as impurity particles, container walls, or substrate crystals. Such types of nucleation centers act as catalytic agents for the reduction of nucleation energy. The effects are often undesirable; however, the process of nucleation on foreign substrates is essential for epitaxial deposition of thin films.

Again we can use the model of a liquid droplet which is growing out of a vapor phase. In a first approximation, the heterogeneous nucleus is considered to be a spherical cap of the nucleating solid on a flat surface.

The cap represents a segment of a sphere with radius of curvature r and a projected radius $r \sin \theta$, the so-called wetting angle θ.

The equilibrium condition is expressed by the Young relation:

$$\sigma_{st} = \sigma_{si} + \sigma \cos \theta \tag{2.26}$$

σ, σ_{st}, and σ_{si} are the specific surface energy of the free surfaces of the droplet (nucleus) and the substrate and of the substrate–droplet interface, respectively (Figure 2.3).

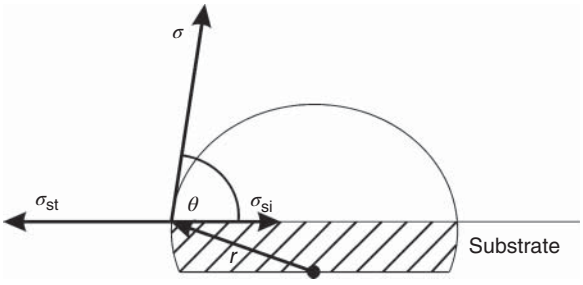

Figure 2.3 Liquid droplet with radius r on a substrate: equilibrium shape with wetting angle θ. σ, σ_{st}, σ_{si} are the specific surface energies between droplet/vapor phase, substrate/vapor phase, and droplet/substrate, respectively.

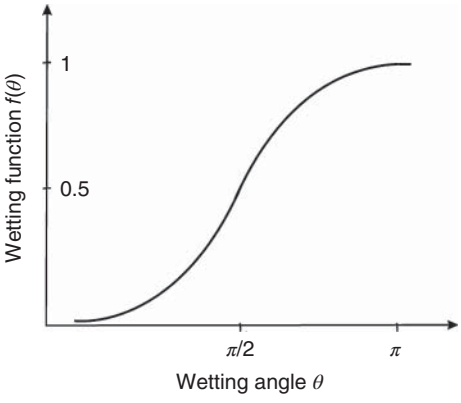

Figure 2.4 Wetting function f in dependence of the wetting angle θ.

It can be shown in Ref. [1], that the critical enthalpy of heterogeneous nucleation $(\Delta G^*)_{het}$ differs from the critical enthalpy of homogeneous nucleation $(\Delta G^*)_{hom}$ by multiplication of the following function $f(\theta)$:

$$f(\theta) = {}^1\!/_4[(1 - \cos\theta)^2(2 + \cos\theta)] \tag{2.27}$$

$$(\Delta G^*)_{het} = (\Delta G^*)_{hom} \cdot f^*(\theta) \tag{2.28}$$

Figure 2.4 depicts a graphic representation of $f(\theta)$ as a function of the wetting angle (θ). It can be seen that $f(\theta)$ varies from 0 to 1 by changing θ from 0 to π.

The case of a complete wetting is $(f(\theta = 0) = 0;\ (\Delta G^*)_{het} = 0)$. A liquid has the tendency to cover the substrate as a continuous film. In the case of the spherical nucleus, a two-dimensional growth takes place. The other extreme means complete nonwetting $(f(\theta = \pi) = 1)$ with $(\Delta G^*)_{het} = (\Delta G^*)_{hom}$ and the substrate has no energetic influence on the droplet/nucleus formation and the droplet/nucleus has the shape of a complete sphere. In this case, we have homogeneous nucleation.

2.1.3 Metastable Zone Regime

In Chapter 1, we have seen that a new phase can crystallize or grow from a liquid or vapor phase only if the latter is supersaturated with respect to the former one. Figure 2.5 shows a schematic drawing of a metastable zone in a concentration temperature diagram.

By cooling a liquid or solution with the composition A′ (T_3) to the composition A (T_2) of the solubility curve shows the equilibrium point of the solid with the solution at temperature T_2. By further reducing the temperature to the point B (T_1), a solid will not be visible. In this case, the solution becomes supersaturated: the solute concentration c exceeds the equilibrium concentration c_0. A further decrease of temperature results in a fast crystallization process. The solution is called *metastable* between the points A and B. The area between curves I and II is called the ***Ostwald–Miers*** *regime*.

The maximum supercooling can be expressed as $\Delta T_{max} = T_2 - T_1$ and $\Delta c_{max} = c_{02} - c_{01}$. Both expressions are related by the following equation:

$$\Delta c_{max} \cong \Delta T_{max}(dc_0/dT) \tag{2.29}$$

Starting from point A″, we can reach point A by evaporating the solvent at T_2 = constant and continue until we reach the boundary of metastability at point C. The value of $(\Delta c_{max})_T = c_{03} - c_{02}$ corresponds to $\Delta T_{max} = T_3 - T_2$.

After reaching the metastable region some time is necessary for the formation of a critical nucleus. This time is called the *induction period of nucleation* and it is the period elapsed from attainment of supersaturation to the formation of the critical nucleus.

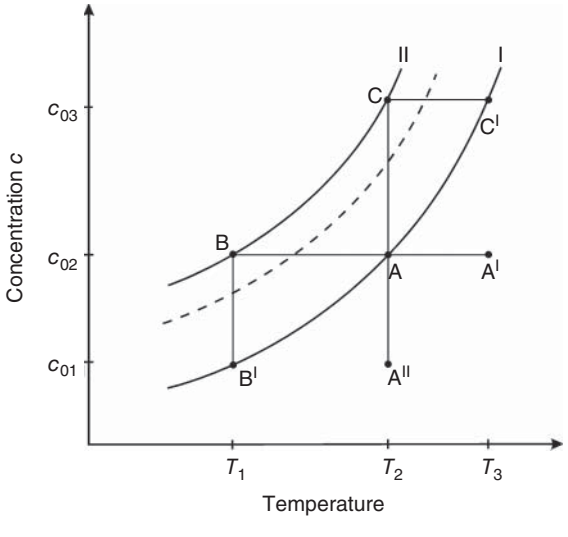

Figure 2.5 Schematic diagram of a metastable zone I solubility curve II limit of Ostwald–Miers regime.

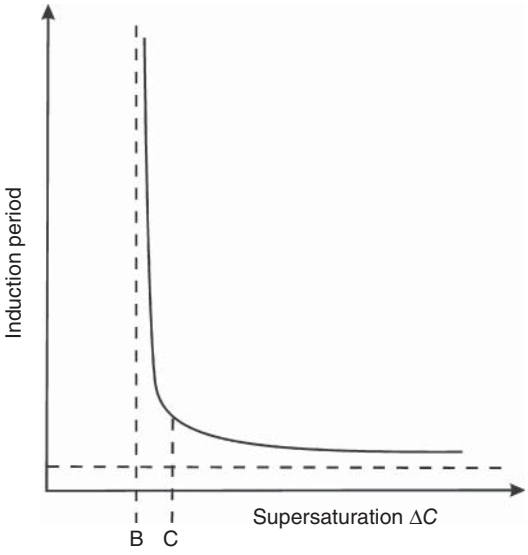

Figure 2.6 Schematic representation of induction time as a function of supersaturation.

In practical systems, the ***Ostwald–Miers Regime*** may be divided in two parts: the area between the solubility curve I and the dashed line of Figure 2.5. In this region, a sudden nucleation does not normally occur. However, between the dashed line and the boundary of metastability II instantaneous nucleation takes place [5]. The principal dependence of the induction period t_N on the supersaturation is shown in Figure 2.6. The regions of supersaturations can be pointed out:

- **Region AB:** where the induction time is long and the formation of a nucleus is nearly impossible.
- **Region BC:** a small increase in supersaturation leads to a decrease in t_N.
- Beyond point **C:** t_N is very small and a sudden nucleation may happen.

The metastable zone may be determined experimentally by direct and indirect methods. Determination of solubility, enthalpy of dissolution, and interfacial tension are used as indirect methods. Well-defined programmed cooling of a solution from equilibrium temperature to a temperature with first visible crystals is used as a direct method.

2.1.4 Equilibrium Shape of Crystals

In Chapter 1, we have described the conditions for the formation of a nucleus from a thermodynamic point of view. If we consider the equilibrium of such a small crystal with its surrounding phase, there exists obviously a shape that is thermodynamically the most favorable. The process of formation of a nucleus

consists of a volume part and a surface part, which is necessary to create a new phase dividing surface. The volume part of the work of formation is $n\ (\mu_v - \mu_{Cr})$ with n atoms or molecules passing from the vapor or liquid phase with a higher chemical potential μ_v to the crystal phase with a lower chemical potential μ_{Cr}. The volume part depends only on the volume of the nucleus or the number of atoms, which are transferred from one phase to the other. The surface part depends mainly from the surface energy and the crystal shape. Therefore, the equilibrium shape can be reached by minimizing only the surface energy. The equilibrium shape of a liquid droplet is clearly a sphere. A crystal is demarcated by individual faces that exhibit well-defined crystallographic orientations with different specific surface energies. As a result, we have an anisotropic surface energy.

In determining the specific surface energy σ of the faces of a crystal with a cubic lattice, a so-called ***Kossel*** crystal, we will take into account the bonds between first, second, and third nearest-neighbor atoms. To determine the surface energy of a face (*hkl*), we construct a prismatic column with a form of the base, which follows the symmetry of the crystal phase, that is, a cubelet for (100) or rhombohedron for (110) faces of cubic crystals [1]. To detach the column from the crystal face (*hkl*), the work Ψ_{hkl} divided by the doubled contact area has to be calculated (Figure 2.7). The factor 2 has to be used because two surfaces are involved during the detachment.

For the surface energy we can write

$$\Psi_{100} = (\Psi_1 + 4\Psi_2 + 4\Psi_3/2b^2) \tag{2.30}$$

where Ψ_1, Ψ_2, and Ψ_3 are the works required to break the bonds (broken bonds per unit area) between the first, second, and third neighbors , respectively. The parameter b is the interatomic distance.

For the rhombohedra face (110), we have

$$\sigma_{110} = (2\Psi_1 + 6\Psi_2 + 4\Psi_3)/2b^2\sqrt{2} \tag{2.31}$$

The greatest contribution to the energy is given by the neighbors with the shortest distance, followed by the second neighbors which are normally not greater than 10% of the first-neighbor bonds (covalent and metallic bonds). The contribution of the third-neighbor bonds can be neglected.

Following the contributions from the above-mentioned text, we have $\sigma_{100} < \sigma_{110} < \sigma_{111} < \sigma_{211}$.

The theorem of ***Gibbs–Curie–Wulff*** gives an expression for the equilibrium shape of single crystals from the general conditions of the minimum of free energy of the system at $T =$ constant and $V =$ constant. It states as a result that the difference between the inner pressure P_{Cr} of the crystal phase and the pressure of the vapor phase P_V does not depend on the crystallographic orientation. One can show the following validity of the pressure difference $P_{Cr} - P_V$ as

$$P_{Cr} - P_V = 2\sigma_n/h_n \tag{2.32}$$

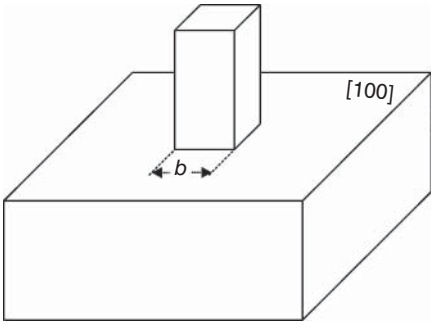

Figure 2.7 Schematic drawing for the determination of the specific surface energy σ_{100} for a Kossel crystal with cubic lattice.

For the equilibrium shape, one obtains

$$\sigma_n/h_n = \text{constant} \tag{2.33}$$

Here h_n is the height of the pyramid of Figure 2.7. Using Equation 2.33, we can write

$$\sigma_1 : \sigma_2 : \sigma_3 \ldots = h_1 : h_2 : h_3 \ldots \tag{2.34}$$

This relationship is known as the ***Wulff rule*** or the ***Gibbs–Curie–Wulff*** theorem. The basic content of Wulff's rule is that in equilibrium, the distances of the crystal faces from a point (Wulff point) within the crystal are proportional to the specific surface energies of these faces. Using this rule we can construct the equilibrium shape in the following way: from an arbitrary point of the crystal, we draw vectors to all possible crystallographic faces. The length of these vectors is proportional to the specific surface energies σ_n. At the end of this vector, planes normal to the vectors are constructed. The resulting closed polyhedron is the equilibrium form of this crystal.

Equation 2.14 can be written as $(P_{Cr} - P_V)\nu_{Cr} = \Delta\mu$ with $V^0_{Cr} = V_{Cr}/n_{Cr}$ as the molar volume of the crystal phase. Using Equation 2.32, the supersaturation is denoted as

$$\Delta\mu = 2\sigma n V^0{}_{Cr}/h_n \tag{2.35}$$

All crystal surfaces show the same value of supersaturation and determine the size of the crystal. Equation 2.35 has the well known form of the ***Gibbs–Thomson*** relation. We can take the Wulff point at the center of the crystal because it has been arbitrarily chosen.

2.2
Kinetic Processes and Growth Mechanism

In Chapter 1, we have seen the first theories on crystal growth, which were described by thermodynamic considerations initiated by Curie 1885 and

extended by Wulff and others. Its main content was the construction of crystal morphology from crystallographic structural and, closely related, minimum energetic considerations.

2.2.1 Molecular Kinetic Theory of Crystal Growth

A connection between a thermodynamic and a molecular kinetic approach is given by a theory introduced by Volmer 1922, Kossel 1927, and Stranski 1928 [1]. They considered crystal growth in terms of attachments of atoms or molecules at a crystal surface. On the surface of the crystal there are several different positions with distinct binding energies. Figure 2.8 shows the sketch of a crystal with different capture sites.

The atomic positions of Figure 2.8 can be described as follows:

- **Position1:** direct capture of an atom on a full crystal surface, binding energy Φ_3.
- **Position 2:** capture of an atom on a new lattice plane, binding energy $\Phi_3 + \Phi_2$.
- **Position 3:** capture of an atom on a monatomic chain, binding energy $\Phi_3 + \Phi_2 + \Phi_1 = \Phi_H$ the so-called ***half-crystal*** position or ***kink***.
- **Position 4:** capture of an atom on the end of a monatomic chain.
- **Position 5:** capture of an atom on a corner of a full crystal surface, binding energy Φ_C.
- **Position 6:** capture of an atom on an edge of a full crystal surface, binding energy Φ_E.

The following assumptions are the basis for the calculations of the different binding energies.

- The crystal is surrounded by a nutrient, a melt, a solution, or a vapor phase.
- The crystal has no content of impurities and no lattice defects.
- The forces between the atoms are Coulomb forces for ions and van der Waals forces for homopolar crystals.

By calculating these binding energies, it was for the first time possible to make predictions to the growth of crystals and their morphology.

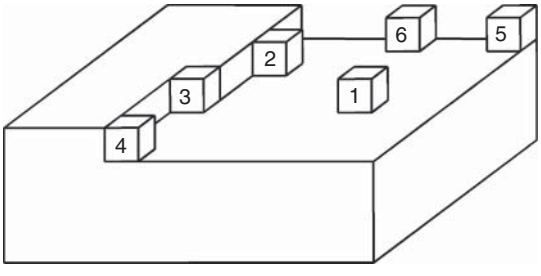

Figure 2.8 Possibilities of capture sites of atoms on the surface of a growing crystal with cubic lattice (***Kossel crystal***).

Example 2.2: We will calculate the capture energies for ionic crystals in a cubic lattice.

The attraction energy between atom1 and atom2 for an ionic crystal is

$$\Phi_0 = \varphi_0 q^2/r \tag{2.36}$$

with q = elementary electric charge and φ_0, geometrical factor.

Now we can calculate Φ_1, the capture-energy part for a linear chain (Figure 2.9a):

$$\begin{aligned}\Phi_1 &= +q^2/r - q^2/2r + q^2/3r - q^2/4r + / - \cdots \\ &= q^2/r(1 - {}^1\!/_2 + {}^1\!/_3 - {}^1\!/_4 + / - \cdots \\ \Phi_1 &= q^2/r \ln 2 = 0.693 q^2/r \end{aligned} \tag{2.37}$$

The energy part Φ_2 can be calculated in the same way (Figure 2.9b):

$$\begin{aligned}\Phi_2 = q^2/r - 2q^2/r\sqrt{2} + 2q^2/r\sqrt{5} - 2q^2/r\sqrt{10} + / - \cdots \Leftarrow \text{first chain} \\ -q^2/2r + 2q^2/r\sqrt{5} - 2q^2/r\sqrt{8} + / - \cdots \Leftarrow \text{second chain}\end{aligned}$$

The influence of the third chain for the calculation of Φ_2 can be neglected.

Now we get for Φ_2 and in a similar way for Φ_3

$$\Phi_2 = 0.1144 q^2/r \tag{2.38}$$

$$\Phi_3 = 0.0662\, q^2/r \tag{2.39}$$

The capture energy of the half-crystal position denotes to

$$\Phi_H = 0.874\, q^2/r \tag{2.40}$$

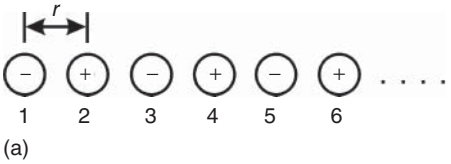

(a)

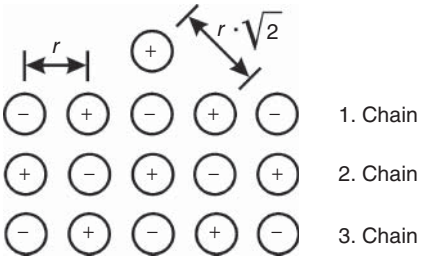

(b)

Figure 2.9 Outline to calculate Φ_1((a) part of a monatomic chain) and Φ_2 ((b) part of a new lattice plain).

The capture energies at the edge and the corner of the crystal have different values:

$$\Phi_E = {}^1\!/_2\Phi_3 + {}^1\!/_2\Phi_2 = 0.0903q^2/r \tag{2.41}$$

$$\Phi_C = {}^1\!/_4\Phi_3 + {}^1\!/_2\Phi_2 + {}^1\!/_4\Phi_1$$

$$\Phi_C = 0.2470\, q^2/r \tag{2.42}$$

As a result, we have for ionic crystals

$$\Phi_H > \Phi_C > \Phi_E > \Phi_3 \tag{2.43}$$

The capture of atoms starts preferably at Position 3 (half-crystal position) of Figure 2.8, followed by edge and corner positions.

Stranski and Kaischew determined the capture energy for different faces of the diamond lattice. It turned out, that the (111) face depicts the lowest energy. This means that the (111) face is the slowest growing face and determines the equilibrium shape of the diamond lattice. It should be noted that natural diamonds occur preferentially in an octahedral shape.

2.2.2
Interfaces and Roughening of Surfaces

Equation 2.43 shows that the capture energy Φ_3 on a flat surface is very small. As a result the crystal in equilibrium is demarcated of a few faces, which are atomically flat. Plane faces of the crystal may be divided in singular and nonsingular faces. Faces that are misoriented by a small angle α from singular faces are called ***vicinal faces*** (Figure 2.10). This classification has been introduced by ***B**urton, **C**abrera, and **F**rank* (***BCF***) [7].

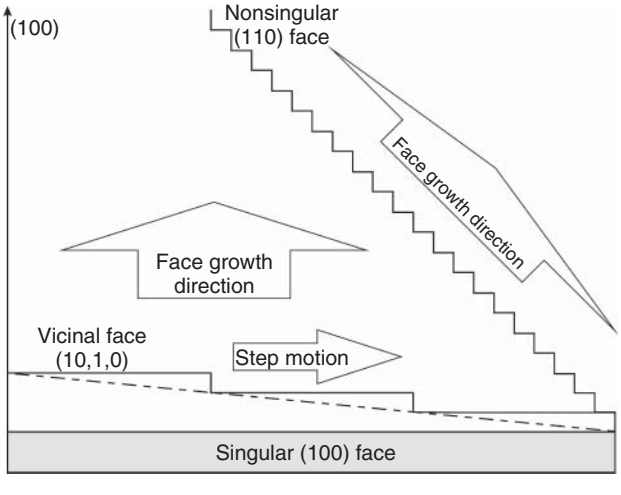

Figure 2.10 Schematic representation of different oriented faces of a cubic crystal.

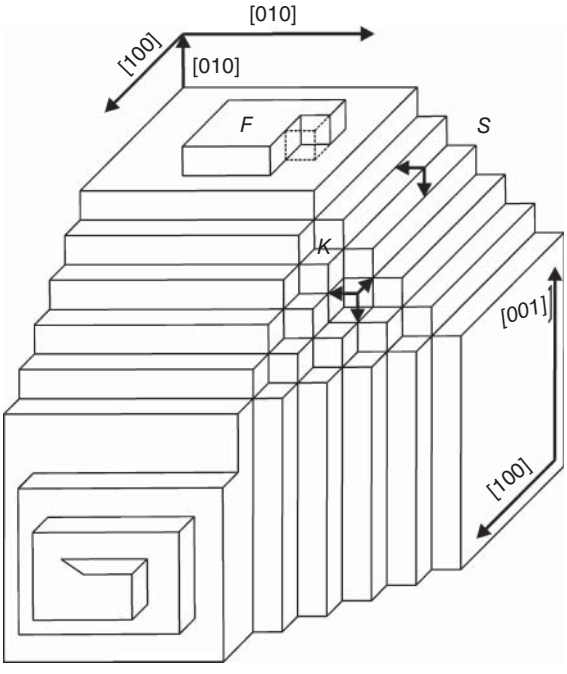

Figure 2.11 Periodic bond chain, PBC, classification of a cubic Kossel crystal F – flat, S – stepped, and K – kinked.

Figure 2.11 depicts another crystal face description, introduced by Hartman and Perdok [8]. They classified the faces of a crystal into F (flat), S (stepped), and K (*kinked*) faces. F-type faces have at least two sets of chains of periodically bonded atoms or molecules, called ***P**eriodic **B**ond **C**hain*s, ***PBC***s. Three PBC vectors are shown in Figure 2.11: vector **A** is parallel to **[100]**, vector **B** parallel to **[010]**, and vector **C** parallel to **[001]**. These PBC-vectors define six F-faces. Any face parallel to only one of the vectors **A**, **B**, and **C** is an S-face. So far S-faces have one such PBC and K-faces do not have any PBC. F-faces as singular faces exhibit a minimum surface free energy, while S and K faces correspond to vicinal (e.g., (011)) and nonsingular (e.g., (111)) faces, respectively.

An important role during crystal growth plays the interface between a solid crystal and the nutrient – a liquid or vapor phase. There are two thermodynamic states of the interface which may be ordered or disordered. The phase transition to this ordering phenomenon is called ***roughening transition*** and was first introduced by Frenkel, see Ref. [9]. The interfaces may be called *sharp interfaces* or *diffuse ones*. Sharp interfaces may be split up due to their type of smoothness. Growth on perfect flat interfaces (compare Figure 2.12) may be possible if they are supplied with kinks (see also Figure 2.8) by two-dimensional nucleation. On a rough interface (surface), a large number of kinks are always present. Individual atoms can be added to the growing surface statistically. A general equation of a growth rate of crystals including the structure of the interface is given by the

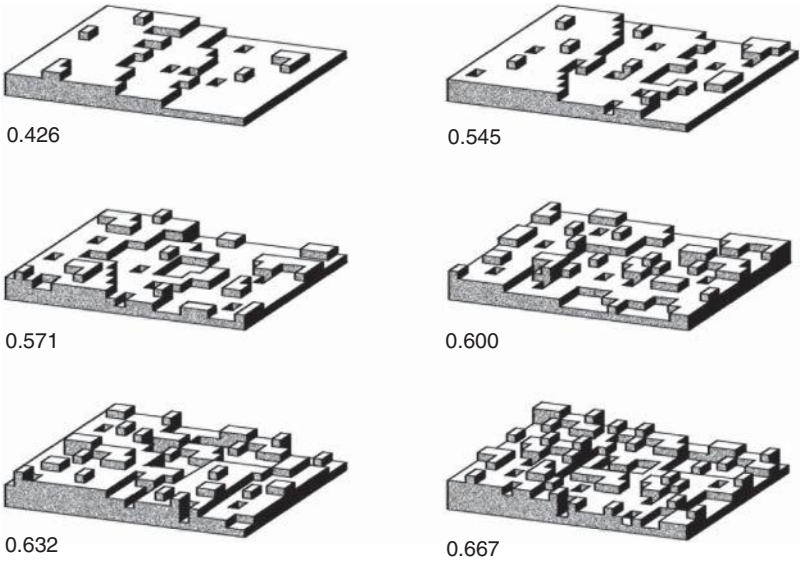

Figure 2.12 Configurations of surfaces from Monte Carlo simulations. The parameter is $k_B T/\phi$. (Redrawn from Jackson, K.A. [9] with permission from Elsevier.)

following expression

$$v = a\nu^{+} f u_k \tag{2.44}$$

a is the distance which is related to the atomic diameter of the growth unit and ν^{+} is the rate at which atoms reach the crystal at active growth sites on the surface.

The parameter f depends on the roughness of the interface and is a measure of the active growth sites. The normalized difference between the rate at which atoms join or leave the crystal is denoted by u_k and can be written as

$$u_k = 1 - \exp(\Delta F/k_B T) \tag{2.45}$$

ΔF, the free energy difference, may be expressed as supersaturation or undercooling or as a vapor pressure difference in the case of a gas environment. The phase into which a crystal is growing governs the rate at which atoms reach the crystal at active growth sites.

If an atom is added to each growth site, the interface will advance by a distance a. The density of active growth sites is strongly temperature dependent if the growth depends on a perfect flat surface on the nucleation of new layers. The term f can be very small on a flat surface and is about a quarter for a rough surface. The density of growth sites on a crystal surface depends mainly on the roughness of the surface, which is an intrinsic property of the crystal surface at equilibrium. It depends also on the properties of the two phases: solid on the crystal site and liquid or vapor on the site of the nutrient separated by the interface. The atomic structure of the interface influences the density of growth sites as well. An important parameter to characterize the roughness of a crystal surface is the α-factor which has been

introduced by Jackson [9] through a two-dimensional model for the equilibrium structure of a crystal interface. This factor is given by

$$\alpha = L/k_B T_M n_i/Z \tag{2.46}$$

L is the latent heat, k_B, the Boltzmann constant, T_M, the melting point, n_i, the number of nearest neighbor sites in the substrate layer and in the surface layer, respectively, and Z, the total number of nearest neighbors. There is a critical value of α, $\alpha_c = 2$ due to a singularity in the surface roughness of this model. Below this surface roughening transition (thermodynamic roughening) the surface is rough and the crystal may easily grow.

Monte Carlo simulations of crystallization, based on the ***Kossel–Stranski model*** have been performed by Jackson [9]. Atoms arrive randomly at sites on the surface and leave the surface determined by a probability factor which depends on the number of adjacent crystalline atoms. Therefore, the computer simulation gives a statistical analysis of this model. When the capture or bond energy is large compared to $k_B T$, an atom on the surface has a high probability of leaving the surface and the formation of nuclei is difficult. Many atoms have to build up a cluster of critical size and they must spread in a lateral way to initiate the motion of steps on the surface and the growth of new layers. Is the bond energy comparable to $k_B T$? Many adsorbed atoms may be present on the surface. In this case the formation of a new layer is not hindered by a nucleation barrier.

Figure 2.12 shows configurations of surfaces from Monte Carlo simulations [9] for different values of $k_B T/\phi$. The configuration for $k_B T/\phi = 0.667$ is a rough surface.

It can be seen from Equation 2.46 that the α-factor consists of an entropy part $\Delta S = L/T_M$ and a geometrical part n_i/Z of the crystal face. The closest–packed face has the largest value for n_i/Z. High values of ΔS on melting will show smooth closest-packed crystal faces with a nucleation barrier for the growth on these faces.

Kinetic Roughening Supersaturation of a solution or a melt has a remarkable influence on the surface roughening. It is well known that at small supersaturations there may be a big difference in growth rates of different crystal faces. Thus faces with α a little greater than 2, which are smooth at the equilibrium temperature, may become rough when the supersaturation increases. This effect has been called *kinetic roughening* and was first described by Temkin [10]. Figure 2.13 shows an example of the effect of kinetic roughening.

Kinetic roughening is often observed during the growth of organic crystals and above a critical supersaturation at an equilibrium temperature. The growth rate of a face depends linearly on the supersaturation [11].

Growth Kinetics of Flat Faces Kinks of existing edges, which may be supplied by two-dimensional surface nucleation, are the basis of the incorporation of atoms or molecules on smooth faces. The formation of a two-dimensional stable nucleus on the perfect surface has to overcome an activation energy barrier. The energy

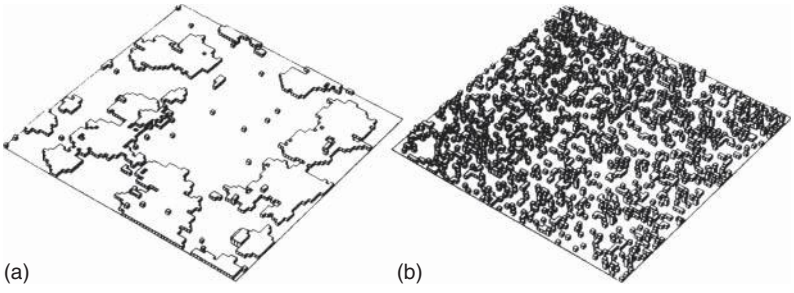

Figure 2.13 Monte Carlo computer simulation of kinetic roughening: $\alpha_C/\alpha = 0.4$. (a) $\Delta\mu/k_BT = 1.5$ and (b) $\Delta\mu/k_BT = 3.5$. (Redrawn from Jackson, K.A. [9] with permission from Elsevier.)

requirement for two-dimensional nucleation and the critical size of a stable nucleus can be derived similar to the homogeneous nucleation, which has been discussed in Section 2.1. The models, which will not be discussed in this chapter predict observable growth rates at supersaturations exceeding 25–50%.

Defect Induced Growth Kinetics of Flat Faces However, in addition to the last mentioned result it is well known that measurable growth rates are also observed at very low undercooling of a nutrient. Frank [12] suggested that defects in a crystal structure may serve as a permanent source of steps and kinks necessary for the capture of atoms or molecules, so that a nucleation process may be no prerequisite for a two-dimensional nucleation. He pointed out that a screw dislocation which has a component of its Burgers vector perpendicular to a growing face could provide a continuous step on a surface for growth.

This is demonstrated in Figure 2.14 where a surface step is winded up in a spiral, starting from a lattice defect as shown in Figure 2.14a. The linear velocity of progress of the step is assumed to be the same at any point of the step during growth (Figure 2.14b). It follows that the angular velocity near the corner of the defect is faster than at the edge. This is the reason why the dislocation proceeds in a spiral form on the propagation of the step (Figure 2.14c).

2.2.3 Vapor–Liquid–Solid (VLS) Mechanism

During experimental growth studies from the vapor phase it has been observed that the beginning of growth on an atomistic scale as described in Section 2.2.1 takes place through liquid droplets on the surface of the growing crystal. Normally it has been understood that growth units captured from liquid or vapor phase onto the growing surface are free to migrate to the kink sites without changing their phase (vapor or liquid) during the integration process into the lattice of the grown crystal. For example, Szurgot and Karniewicz [13] obtained ZnTe crystals by static sublimation in closed silica ampoules with tellurium access in argon gas. On the surface of the grown ZnTe crystals they found tellurium whiskers grown

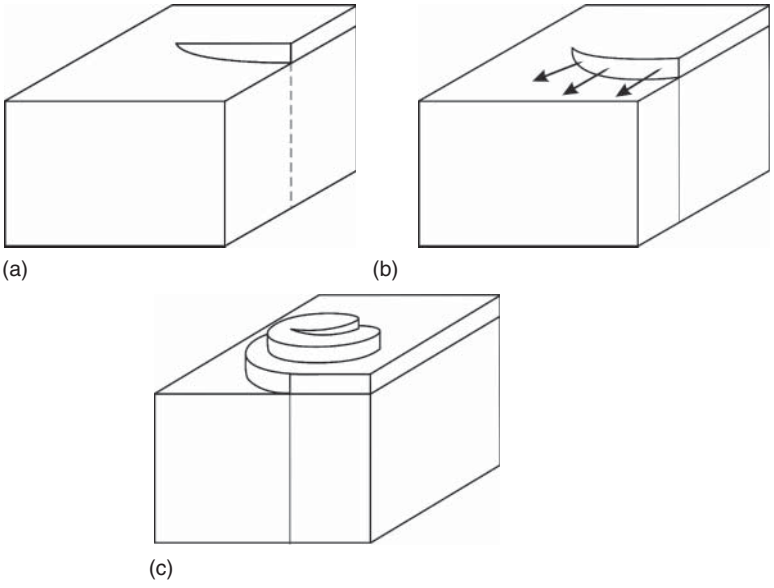

Figure 2.14 Lattice defect (a) and propagation of a screw by forming a screw dislocation (b, c).

from droplets and solidified droplets of tellurium or tellurium solution of ZnTe placed along macrosteps of different height. The mechanism of crystal growth from the vapor phase with participation of a liquid phase is common in whisker growth and described by Givargizov [14]. This type of growth was first proposed by Wagner and Ellis [15]. The role of the liquid droplets is twofold: (i) they serve as a nutrient for growth by dissolving vapor and supplying growth units and (ii) they are in continuous contact with the growing surface.

2.2.4
Crystal Growth from Ambient Phases on Rough Surfaces: Vapor Phase, Solution, and Melt Media

If we consider Figure 2.9 of Section 2.2.1 we can say, if the built units – atoms or molecules – are, for example, attached to a kink position they become part of the crystal or in other words their chemical potential becomes equal to the chemical potential of the crystal. The kink position is a stable position of the crystal, whereas other positions are connected much weaker to the crystal surface. The basis of a crystal growth process is the contact with a surrounding vapor or liquid phase. To initiate crystal growth the ambient phase is supersaturated and its chemical potential must be greater than that of the crystal. From Figure 2.11, we can see that S- and K-faces show enough kink sites to start here with growth processes. Flat F-faces may grow above the roughening transition without overcoming an energy gap. Below the roughening temperature, the F-faces are smooth with no

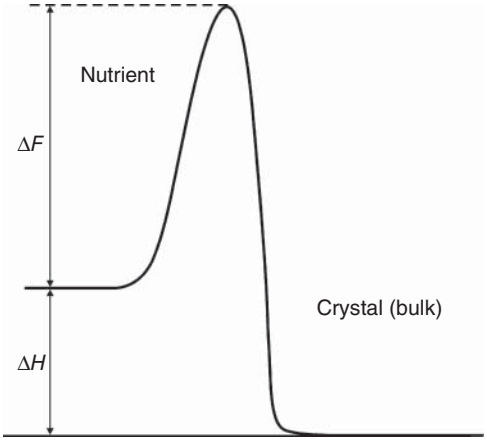

Figure 2.15 Free energy of thermally activated transfer of constituent units (atoms, molecules) across the interface between the vapor or liquid phase.

presence of kink sites. The beginning of growth in this case requires the formation of a two-dimensional nucleus or the existence of screw dislocations to supply the surface with enough kink sites.

Let us consider a thermally activated transfer of atoms or molecules from the ambient phase (vapor, solution, or melt) via the interface to the crystal site. This behavior is shown in Figure 2.15.

- ΔH – enthalpy of the corresponding phase transition, for example, sublimation or melting.
- ΔF – kinetic barrier of the incorporation of a constituent into the crystal.

The right hand side of Figure 2.15 depicts the energy of the constituent unit incorporated at a half-crystal position of the crystal surface. The line at the left hand side represents the average value of the unit in the ambient phase. The gap at the phase boundary ΔF may have different values in different media, for simple monatomic molecules ΔF may be zero.

We will now consider principal mechanism of the growth from melts, solutions, and vapors (Figure 2.16).

Growth from the Melt as Ambient Phase In this case we can define a growth rate R which is proportional to the net flux of attaching and detaching constituent [1]:

$$R = a(a/\delta_S)^2(j_{amb+} - j_{amb-}) \tag{2.47}$$

with

$$j_{amb+} = \nu \exp(-\Delta S_m/k_B) \exp(-\Delta F/k_B T) \tag{2.48}$$

$$j_{amb-} = \nu \exp(-\Delta H_m/k_B T - \Delta F/k_B T) \tag{2.49}$$

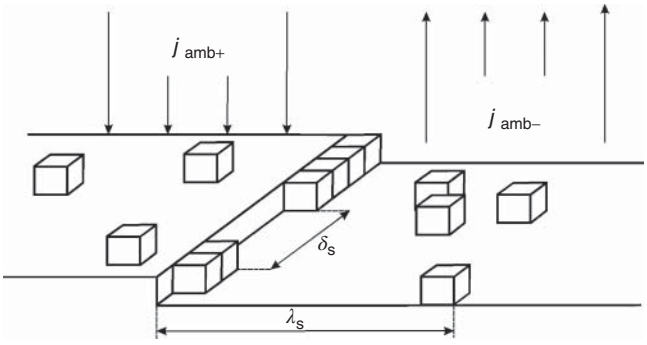

Figure 2.16 Atoms arriving from an ambient phase (melt, solution, or vapor) on a crystal surface with a single step.(j_{amb+} flux of attaching atoms, j_{amb-} flux of detaching atoms, λ_S mean distance of adatoms within their lifetime τ_S).

δ_S is the average distance between kink positions, (a/δ_S), the probability (geometry) of a constituent unit to find a kink site, ν, the vibration frequency of the surface atoms, and j_{amb+} and j_{amb-} are the fluxes of atoms to and from the phase boundary solid/liquid. After some easy mathematical treatment [1], we have for rough faces and small supersaturations ΔT:

$$R = \beta_m \Delta T \tag{2.50}$$

with

$$\beta_m = a\nu(a/\delta_S)^2 \Delta S_m/k_B T \exp(-\Delta S_m/k_B) \exp(-\Delta F/k_B T) \tag{2.51}$$

β_m is the well-known kinetic coefficient for crystallization from melts [2]. It depends on the probability (a/δ_S) as a direct measure of the roughness of the growing surface. It depends also on the entropy ΔS_m of the phase transition and the energy gap ΔF.

If the roughness of the surface may decrease the average spacing of the kink sites is going to infinity and as a consequence β_m and the growth rate R are going to zero. This means that atomically flat and smooth surfaces cannot grow by the normal growth mechanism.

Growth from Solutions as Ambient Phase The growth flux can be written as

$$j_{amb+} = \nu C_{sol} V_c \exp(-\Delta F/k_B T) \tag{2.52}$$

C_{sol} is the concentration of the solute, V_c, the volume of the constituent unit, and $C_{sol}\ V_c$, the probability to find an atom near the half-crystal position. The flux from the interface to the solution is

$$j_{amb-} = \nu(1 - C_{sol}) \exp(-\Delta H_{diss.}/k_B T - \Delta F/k_B T) \tag{2.53}$$

In equilibrium we have $C_{sol} = C_0$ and both fluxes are equal. If we use Equations 2.47, 2.52, and 2.53, we can write for the growth rate R

$$R = \beta_{sol} V_c (C_{sol} - C_0) \tag{2.54}$$

with

$$\beta_{\text{sol}} = a\nu/C_0 V_c (a/\delta_S)^2 \exp(-\Delta H_{\text{diss.}}/k_B T - \Delta F/k_B T) \tag{2.55}$$

β_{sol} is the kinetic coefficient for crystallization in solutions. For dilute solutions ($C_0\ V_c \ll 1$) we have $\exp(-\Delta H_{\text{diss.}}/k_B T) = C_0\ V_c$ and we can write for β_{sol}:

$$\beta_{\text{sol}} \cong a\nu(a/\delta_S)^2 \exp(-\Delta F/k_B T) \tag{2.56}$$

By studying the mechanism of hydrothermal grown α-quartz, Laudise found in 1959 [16], that the growth rate R is proportional to the temperature differences ΔT and concentration differences ΔC as well. At a growth temperature of 347 °C and $\Delta T = 50$ °C a growth rate of 2.5 mm day^{-1} has been measured. Using the equations above a theoretical growth rate of 2.1 mm day^{-1} has been calculated, in good agreement with the measured value.

Growth from the Vapor as Ambient Phase The flux of atoms from the vapor phase via the half-crystal position is given by

$$j_{\text{vap+}} = P/(2\pi m k_B T)^{1/2} a^2 \exp(-\Delta F/k_B T) \tag{2.57}$$

$P/(2\pi m k_B T)^{1/2}$ is the Hertz–Knudsen relation and the flux of atoms per unit area.

The flux from the crystal surface toward the vapor phase (evaporation) is given by:

$$j_{\text{vap-}} = \nu \exp(-\Delta H_{\text{evap.}}/k_B T - \Delta F/k_B T) \tag{2.58}$$

In equilibrium between crystal and vapor phase we have $j_{\text{vap+}} = j_{\text{vap-}}$ and $P = P_{\text{eq}}$.

The growth rate can now be written as

$$R = \beta_{\text{vap}}(P - P_{\text{eq}}) \tag{2.59}$$

with

$$\beta_{\text{vap}} = a\nu/P_{\text{eq}}(a/\delta_S)^2 \exp(-\Delta H_{\text{evap.}}/k_B T - \Delta F/k_B T) \tag{2.60}$$

$$= (a/\delta_S)^2 a^3/(2\pi m k_B T)^{1/2} \exp(-\Delta F/k_B T) \tag{2.61}$$

By comparing the kinetic coefficients β for melts, solutions, and vapor we can conclude that they are proportional to the surface roughness, which is represented by the probability (a/δ_S) to find a half-crystal position.

Growth rates of crystals from solutions or vapors are of the order of micrometers per second whereas growth rate of crystals from the melt are in the range of millimeters per minute or millimeters per hour.

2.2.5 Crystal Growth on Flat Surfaces

When the surface is atomically flat the crystal growth process may start by the formation of laterally moving steps. Before growing vertically to build up a bulk

crystal the surface is growing parallel to itself. One of these growth processes may govern the overall growth rate. In the case of a complete smooth, defect free surface the growth rate is determined by the frequency of the formation of 2D-nuclei. Pyramids of such nuclei are formed. Their side surfaces are shown in Figure 2.17a and called *vicinal surfaces*. Vicinal planes consist of steps with varying height and terraces which are parallel to singular faces.

Slices which are cut from bulk crystals normally show a deviation from exact oriented crystallographic planes. The surfaces of such slices are therefore vicinal planes.

The growth rate R of a layer perpendicular to a singular face can be expressed as follows:

$$R = h/\lambda \nu_{\text{step}} \tag{2.62a}$$

The growth rate ν_{vic} of the vicinal face is given by

$$\nu_{\text{vic}} = R \cos\theta \tag{2.62b}$$

θ is the angle between the selected crystal surface (vicinal face) and the singular plane (compare Figure 2.17b).

The rate of 2D nucleation depends on the magnitude of the supersaturation: the higher the supersaturation, the greater the rate of nucleation. The step density h/λ determines the velocity of steps.

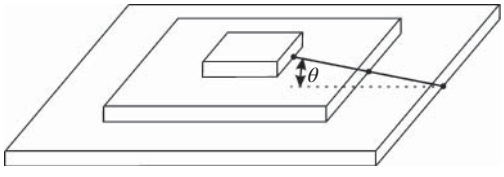

(a)

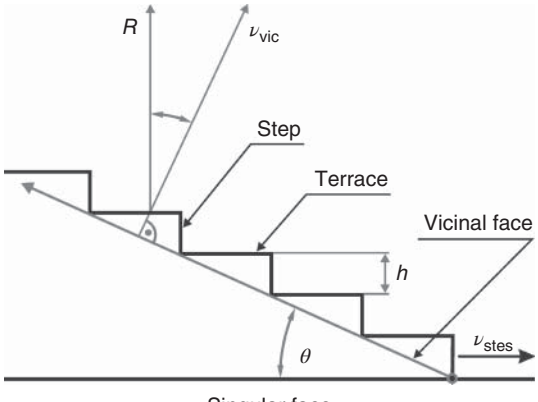

(b)

Figure 2.17 2D growth of a nucleus by forming a pyramid (a). The formation of steps and terraces leads to the basis of a vicinal plane (b).

As in the case of the growth of rough surfaces we will calculate a kinetic coefficient of a step. Toward the step there will be a flux of adatoms related to the half-crystal position:

$$j_{\text{step}+} = \nu n_{\text{step}} a^2 \exp(-\Delta F/k_{\text{B}}T) \tag{2.63}$$

n_{step} is the adatom concentration near the step and a^2 is the area of a kink site. The flux of atoms leaving the half-crystal position is

$$j_{\text{step}-} = \nu \exp(-\Delta W/k_{\text{B}}T - \Delta F/k_{\text{B}}T) \tag{2.64}$$

ΔW represents the energy that is needed to transfer an atom from the kink position onto the flat surface. The step velocity is proportional to the net flux of adatoms:

$$v_{\text{step}\infty} = a\, a/\delta(j_{\text{step}+} - j_{\text{step}-}) \tag{2.65}$$

Using Equations 2.63 and 2.64 in Equation 2.65 one obtains

$$v_{\text{step}\infty} = 2\, a^2 \beta_{\text{step}}(n_{\text{step}} - n_{\text{stepe}}) \tag{2.66}$$

β_{step} is the kinetic coefficient of the step in analogy to the kinetic coefficient of the crystal face (compare Equation 2.61. The factor 2 represents the arrival of atoms from both the upper and lower terraces to the step. Under the condition of equilibrium which means that the fluxes of adsorption and desorption of atoms are equal we have for n_{stepe}:

$$n_{\text{stepe}} = n_0 \exp(-\Delta W/k_{\text{B}}T) \tag{2.67}$$

n_0 is of the order of $1/a^2$ and equal to about 10^{15} cm^{-2} adsorption sites on the crystal surface. β_{step} can be expressed as

$$\beta_{\text{step}} = a\nu a/\delta \exp(-\Delta U/k_{\text{B}}T) \tag{2.68}$$

The mean diffusion length λ_{s} of the adatoms on the surface is related to their lifetime τ_{s} by the Einstein relation:

$$\lambda_{\text{s}} = (D_{\text{s}}\tau_{\text{s}})^{1/2} \tag{2.69}$$

D_{s} is the surface diffusion coefficient. If $D_{\text{s}}/\lambda_{\text{s}}$ – the diffusion rate – is much lower than the rate of crystallization or kinetic coefficient of the step the crystal grows in a diffusion regime. If the constituent units that are incorporated into the kink sites determine the advancing of the steps, the crystal face grows in a kinetic regime.

2.3
Phase Diagrams and Principles of Segregation

In this chapter we will describe phase diagrams in correlation with crystal growth processes. A *phase* may be defined as a homogeneous part of a system that has uniform physical and chemical characteristics. Every solid pure crystal is to be seen

as a phase as well as its melt or a solution of the crystal in a solvent. The understanding of phase diagrams for crystal systems is important. Physical properties or defect structures are often related to the characteristics of its phase diagram.

Most crystals for commercial applications are doped with certain elements to achieve well-defined physical and chemical properties. The distribution of the dopants and residual impurities in the grown crystal is given by the effect of segregation. That means, the dopant concentration in the melt is different from the concentration in the grown crystal. The key parameter is the segregation coefficient k. The dependence of the segregation coefficient of different crystallization parameters will be analyzed.

2.3.1 Phase Diagrams with a Continuous Miscibility in the Solid and Liquid Phases

A system in equilibrium is normally described by a set of intensive or free selectable parameters such as pressure P, temperature T, and composition $x_k{}^i$. $x_k{}^i$ is the molar fraction of each of the components of the system.

According to the Gibb's phase rule for a multicomponent and a multiphase system, the number of possible coexisting phases and the number of components are related to each other by the following equation:

$$f = k_c - i + 2 \tag{2.70}$$

f is the number of degrees of freedom that means the number of free selectable variables describing the state of the system, k_c, the number of components, and i, the number of phases. In a one-component system, f does not exceed two, and the highest number of the coexisting phases is three. The classical diagram of a one–component system is the phase diagram of water, normally shown in a pressure/temperature diagram. The point at which liquid, vapor, and solid phases of water are in equilibrium at $P = 343.5$ Pa and $T = 273.16$ K is called the *triple point* of water. This triple point is important for thermometric measurements and calibrations.

Figure 2.18 shows the principles of a phase diagram of a one–component system. Two phases are simultaneously stable if the following relation is valid:

$$\mu^{\alpha} = \mu^{\beta} = \mu^{\min}$$

The chemical potential of phase α and phase β must show a minimum.

The interface lines in the P/T-diagram of Figure 2.18 are so-called equilibrium lines and may be described using the equation of Clausius–Clapeyron:

$$dP/dT = \Delta H/T\Delta V \tag{2.71}$$

Some important features of the phase diagram of a one-component system can be derived from Equation 2.71:

- A volume change at a transition from a condensed phase to a vapor phase is leading to flat equilibrium lines in the phase diagram.

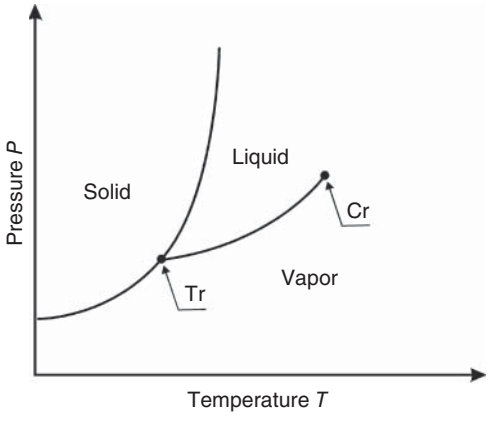

Figure 2.18 Schematic pressure/temperature diagram of a one-component system. Tr – triple point and Cr – critical point.

- At a transition from a solid to a liquid phase, ΔV is very small and the equilibrium lines show a steep slope.

Binary systems are very often an important basis of crystal growth experiments and crystal production: (i) crystal growth from solutions, (ii) growth of doped crystals, and (iii) growth of alloys, for example, Ge – Si crystals.

In the following part, we will describe the basic knowledge of two-component systems for which the vapor pressure may be negligibly small. In this case we do not have to take into account the vapor phase. We suppose an ideal mixing of the two components in its liquid and solid phases. An example of such system is Ge – Si. The system forms solid solutions in the entire range of its components.

The chemical or thermodynamic potential μ as a function of the molar fraction $x_{1,2}$ of the components 1 and 2 is shown schematically in Figure 2.19.

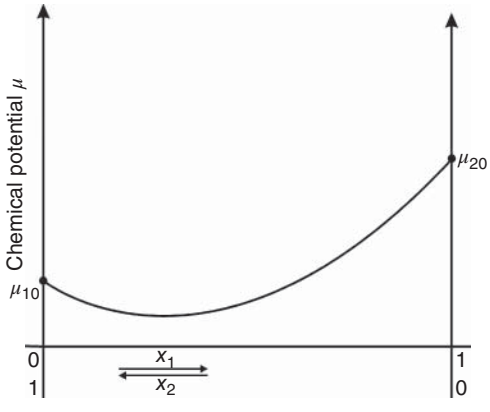

Figure 2.19 Chemical potential of an ideal mixture of two components 1 and 2.

The bending of the chemical potential curvature is due to the entropy of mixture given by the interaction of the two components. The chemical potential of the mixture μ_{mix} can be written as:

$$\mu_{\text{mix}} = \mu_1 x_1 + \mu_2 x_2 \tag{2.72}$$

and

$$\mu_k = \mu_{0k} + k_{\text{B}} T \ln x_k \tag{2.73}$$

μ_{0k} is the chemical potential of the pure components k.

By combining Equations 2.72 and 2.73, we have:

$$\begin{aligned}\mu_{\text{mix}} = {} & (1-x_2)\{\mu_{01} + k_{\text{B}} T \ln(1-x_2)\} \\ & + x_2\{\mu_{02} + k_{\text{B}} T \ln x_2\}\end{aligned} \tag{2.74}$$

If we consider the relation of equilibrium between the phase α (liquid) and phase β (solid) we will study the chemical potential μ_{mix} of a binary system that means a system with two components 1 and 2 at different temperatures as a function of the composition x.

Figure 2.20 shows the chemical potential of the phases liquid and solid of a two-component system as an ideal mixture.

Figure 2.20a shows the chemical potential of a liquid (melt) and solid phase at temperature T_1 as a function of the composition x_1 and x_2. At T_1 and also at $T < T_1$ only the solid phase is the stable phase that means, that the chemical potential of the solid phase is below the chemical potential of the liquid phase over the whole range of composition x_1 and x_2. Only at $T = T_1$ and $x_2 = 1$ ($x_1 = 0$) we have an intersection of both curvatures. This point is the beginning of the phase diagram of this binary system (compare Figure 2.20d). Between $T = T_1$ and $T = T_2$ the system may reach within its equilibrium a two-phase state where the amount of liquid and solid will show a well-defined ratio. This ratio liquid/solid concentration depends on the composition x. Between $T = T_1$ and $T = T_2$ the μ^{α} and μ^{β} curves intersect (compare Figure 2.20b). At $T = T_2$ and $T > T_2$ the curve μ^{α} is below the curve μ^{β} and that means, that the liquid phase is the stable one Figure 2.20c. At T_1 we have the melting temperature of the pure component 2 and at T_2 the melting point of the component 1.

If we consider a system with a temperature T^* with $T_1 < T^* < T_2$ at a composition x^*, the curves μ^{α} and μ^{β} intersect (Figure 2.20b). The system reaches a lowest chemical potential as a two-phase equilibrium consisting of a liquid phase α with a composition x_{A} and a solid phase β with the composition x_{B}. x_{A} and x_{B} may be determined by using the common tangent of both curves μ^{α} and μ^{β}. Figure 2.20b shows also, that for $x < x_{\text{A}}$ only the liquid phase α is stable and for $x > x_{\text{B}}$ we have the solid phase β as a stable one.

The phase diagram of our binary system depicts three main areas: one region above the so-called liquidus line (compare Figure 2.20d), which exists as a liquid phase and a region below the solidus line which is completely solid. Between these two regions there is lens-shaped area of a two-phase state liquid/solid, which gives us the information that a system with an assumed composition $X = x^*$ at T^* will

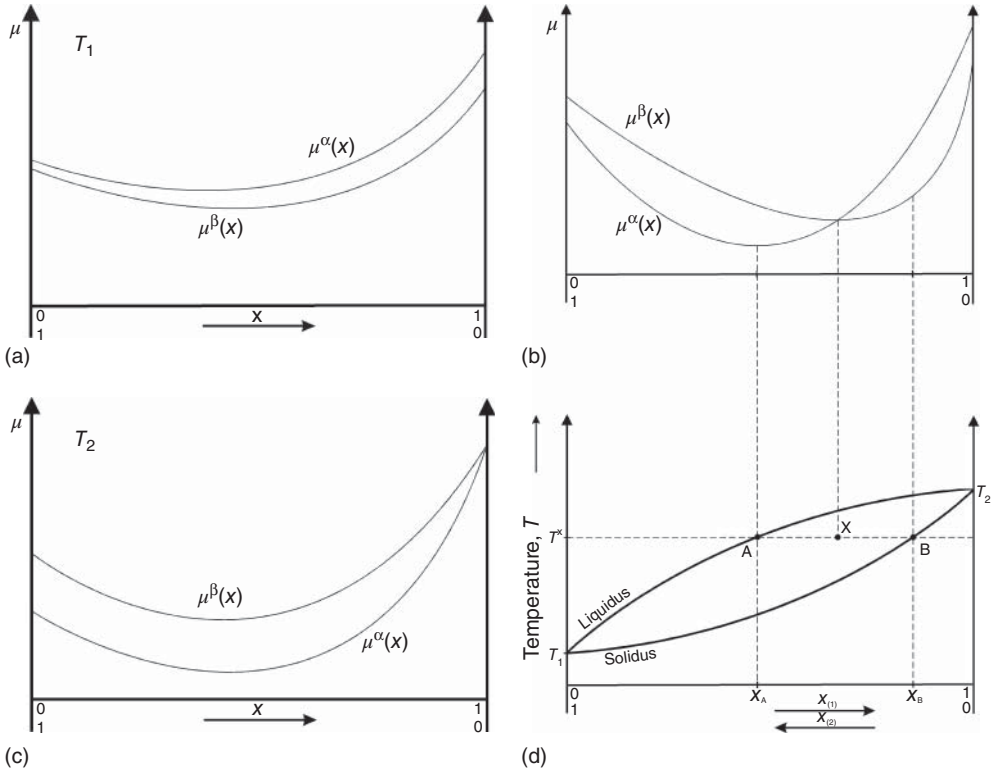

Figure 2.20 Chemical potential of the liquid and solid phases of a two-component system as a function of the composition at different temperatures $T_1 < T^* < T_2$ (a–c) and the resulting phase diagram (d).

be in equilibrium with a liquid phase α of composition x_A and a solid phase β with a composition x_B. For the part of phase α and phase β we have, respectively

$$x^{\alpha} = (x_B - x^*)/(x_B - x_A) \text{ and } x^{\beta} = (x^* - x_A)/(x_B - x_A)$$

and finally

$$x^{\alpha}/x^{\beta} = (x_B - x^*)/(x^* - x_A) \tag{2.75}$$

Example 2.3: We consider a binary phase diagram with a ***Eutectic Point*** that means a phase diagram where the equilibrium solidus and liquidus lines intersection at point E.

Figure 2.21 shows a principle sketch of this eutectic system.

The two solidus lines A–E and E–B have the following behavior:

$$c_{B1} = -0.13T + 93.3 \text{ (A–E)}$$
$$c_{B2} = 0.2T + 10 \text{(E–B)}$$

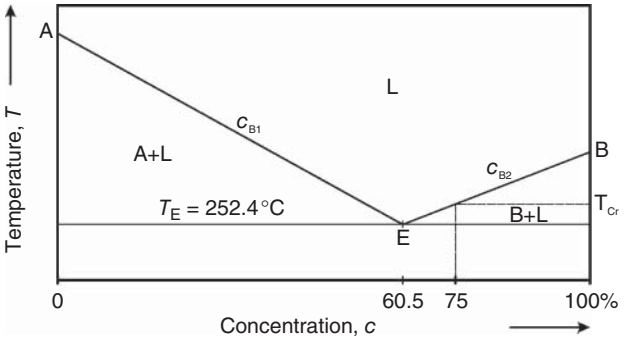

Figure 2.21 Sketch of a binary phase diagram with a eutectic point.

The starting melt is composed of

$$m = 140\text{g A} + 420\text{g B}$$

Now we have to calculate the melting temperatures T_A, T_B, and eutectic temperature T_E

$$T_A : c_{B1} = 0 \quad T_A = -93.3/-0.13 = 717.7\,^{\circ}\text{C}$$
$$T_B = (100-10)/0.2 = 450\,^{\circ}\text{C}$$
$$T_E : -0.13T + 93.3 = 0.2T + 10$$
$$-0.33T_E = -8.3 \quad T_E = 252.4\,^{\circ}\text{C}$$

The concentration of B and A components at the Eutectic Point can be calculated as

$$c_{B1} = c_{B2} = 60.5\% \quad c_A = 100 - c_{B1} = \ 39.5\%$$

The concentration of B in the starting melt and the temperature T_{cr} at which the solidification starts are given by

$$140\,\text{g A} + 420\,\text{g B} = 560\,\text{g} = 100\% \quad c_B(L) = 100/560 \bullet 420 = 75\%$$
$$c_{B2} = 0.2T + 10 \quad T_{cr} = (75 - 10)/0.2 = 325\,^{\circ}\text{C}$$

During this solidification or crystallization process we are finally interested in the amounts $m_A(E)$ and $m_B(E)$ within the Eutektikum. Following Equation 2.75, we have

$$(75-60)\, m(\text{L}) = (100-75)\, m_B \text{ and } m(\text{L}) = m - m_B$$
$$m_B = 0.6\, m(\text{L}) \quad m_B = 0.6(m - m_B)$$
$$m_B = 0.375\, m = 0.375 \cdot 560 = 210\text{g}$$

Total amount of melt at the eutectic point E is

$$m(L,E) = 560-210 = 350\,\text{g}$$
with $m_B(E) = 350 \cdot 0.605 = 211.8\,\text{g}$
and $m_A(E) = 350-211.8 = 138.2\,\text{g}$

2.3.2 Segregation and Segregation Coefficients

From the binary phase diagram of Figure 2.20d we may conclude that a dopant with the concentration x_1 in a thermodynamic equilibrium shows a different solubility in the liquid phase compared to the solid phase. As a result we have different dopant concentrations in the liquid and solid phase at a constant temperature during a solidification process. This behavior is called *segregation*. For many technical applications of inorganic and organic crystals it is important to control the segregation of dopants and residual impurities on a macroscale and microscale as well. Segregation is governed by thermodynamic aspects of the materials system, growth kinetics, and mass transfer in the ambient phase, the latter with the contributions of diffusion and convection.

At a constant temperature, for example, the solidification or growth temperature the ratio of the concentration in the solid divided by the concentration in the liquid is known as the *segregation coefficient* k in general. For the case that the system is in thermodynamic equilibrium it is called the *equilibrium segregation coefficient* k_{0i} of the component i.

$$k_{0i} = c^{\beta}{}_i / c^{\alpha}{}_i \tag{2.76}$$

Normally we will consider only one additional component, for example, an additive or dopant so we can write: $k_0 = c^{\beta}/c^{\alpha}$. k_0 can normally be treated as a constant value independent of the composition if we consider dopants in the typical range of $\leq 10^{18} - 10^{19}$ atom cm^{-3}. At higher values of concentrations, for example, for solid solution systems the segregation coefficient is a function of the concentration. As an example we may describe the solid solution system silicon–germanium: on the germanium-rich side, the segregation coefficient of silicon in germanium amounts to $k_0(\mathrm{Si}) \cong 5$ and on the silicon-rich side, the segregation coefficient is $k_0(\mathrm{Ge}) \cong 0.3$.

In a binary system where the melting point of the component 1 is reduced by solving the component 2 in 1, the segregation coefficient $k_0 = {c_2}^{\beta}/{c_2}^{\alpha}$ reaches a value which is <1. Is the melting point increased by the second component, for example, component 1 in 2, the segregation coefficient $k_0 = {c_1}^{\beta}/{c_1}^{\alpha}$ is >1. This behavior of the segregation coefficient is shown in Figure 2.22.

By reaching temperature T_1 (Figure 2.22), crystals of the composition $k_0 \cdot {c_2}^{\beta}$ appear, a further cooling down to temperature T_2 brings us to a solidification concentration ${c_2}^{\alpha}$. The last solidified part of the melt has the composition ${c_2}^{\alpha}/k_0$.

Concerning the order of magnitude of the segregation coefficient k_0 of a dopant in a host material we can make some simple considerations. As an example, we compare the tetrahedral covalent radius of Si as a host crystal ($a = 0.118$ nm) with the radii of several technological important dopants: P ($a_{\mathrm{P}} = 0.11$ nm), As ($a_{\mathrm{As}} = 0.118$), Cu ($a_{\mathrm{Cu}} = 0.142$), and Au ($a_{\mathrm{Au}} = 0.160$). For a dopant with a higher radius compared to Si we would expect a segregation coefficient <1. In practical experiments we measure $k = 0.35$ and 0.30 for P and As, respectively. For Cu and

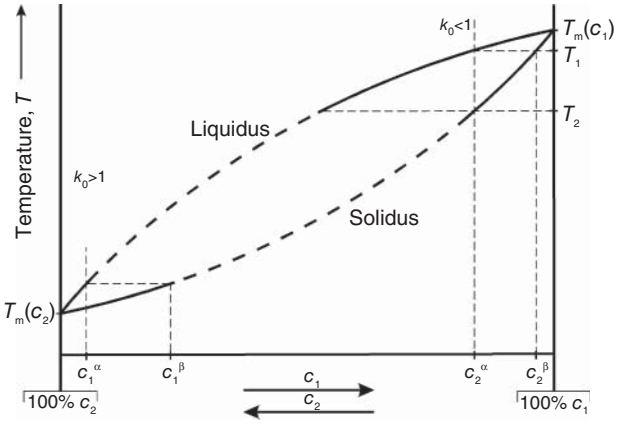

Figure 2.22 Explanation of the segregation coefficient k_0 in a binary system at low dopant concentrations c_1 and c_2.

Au, we have $k = 0.0004$ and 0.000025, respectively due to the higher value of its tetrahedral covalent atomic radius.

The different solubility of a dopant or residual impurity in the solid and liquid phase of a host material (segregation coefficient different from unity!) leads to an axial concentration profile of the additive if the melt is solidified from one end in a crucible.

This process is called *normal freezing* and plays a dominant role during solidification and crystal growth. Normal freezing on the other hand can also be used for the purification of materials which do not decompose at its melting point. Such a purification process is most effective if the segregation coefficient is below and far from unity. A principal sketch of normal freezing is given in Figure 2.23.

The interface solid/liquid moves to the right site. To calculate the concentration profile of the additive in the solidified host material, we will make the following assumptions:

- The additive is homogeneously distributed in the melt during the whole solidification process (complete mixing).
- There is no diffusion in the solid and between liquid and solid phase.

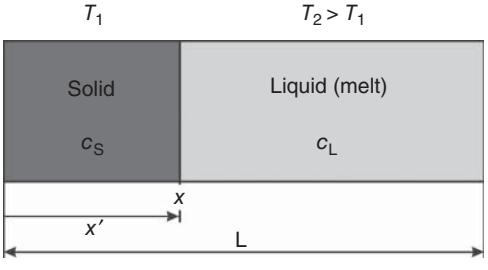

Figure 2.23 Normal freezing (schematically).

- The segregation coefficient k is independent of the additive concentration c.
- The cross section does not change during solidification.

The initial concentration of the additive or dopant in the melt is $c^{l0} = c_0$.
The dopant concentration in the solid is $c^{\beta} = c_s = c_s(x')$
The mass conservation gives the following equation:

$$\begin{aligned} L\,c_0 &= {}_0\int^{x} c_s(x')dx' + {}_0\int^{L} c_L dx' \\ &= {}_0\int^{x} c_s(x')dx' + c_L(L-x) \end{aligned} \tag{2.77}$$

At the phase boundary solid/liquid we have

$$c_s = k \cdot c_L$$

Equation 2.77 turns into

$$(L-x)c_s = k\left[Lc_0 - {}_0\int^{x} c_s\left(x'\right)dx'\right] \tag{2.78}$$

We will transfer this integral equation in a differential equation of first order. By differentiation of Equation 2.78 we have

$$\begin{aligned} Ldc_s/dx - c_s(x) - xdc_s(x)/dx &= -kc_s(x) \\ (L-x)dc_s(x)/dx &= (1-k)c_s(x) \\ dc_s(x)/dx &= (1-k)c_s(x)/(L-x) \\ &= (1-k)c_s(x)/L(1-x/L) \end{aligned} \tag{2.79}$$

Finally, we get

$$\begin{aligned} \ln c_s/A &= (k-1)\ln(1-x/L) \\ c_s &= A(1-x/L)^{k-1} \\ x = 0 &: c_s = kc_0 = A \\ c_s(x) &= kc_0(1-x/L)^{k-1} \end{aligned} \tag{2.80}$$

This equation is often denoted as Scheil's law [17]. One has to point out that the Scheil equation describes the one-dimensional concentration profile for a completely mixed system. Liquid and solid phases may show different densities; this might be considered by multiplying the solidified fraction x/L with the ratio of the respective densities ρ_s/ρ_L.

If there is only a diffusive transport within the liquid part, the concentration profile is described by the following equation, called the *Tiller equation* [18]:

$$c_s(x) = c_0\{1-(1-k)\exp[-kv_x x/D]\} \tag{2.81}$$

where v_x is the interface velocity (Figure 2.23) or growth velocity and D the diffusion coefficient, the other symbols as denoted above.

The solidification process starts with identical concentration as in the case with complete mixing but reaches a plateau with c_0 after an initial transient.

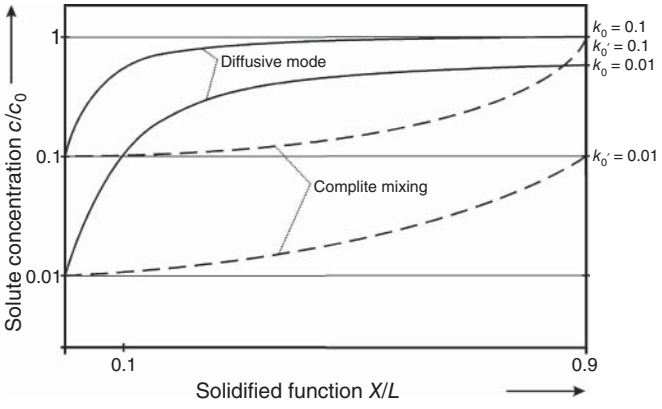

Figure 2.24 Normal freezing: convective and diffusive mass transport, respectively. Calculation after Equations 2.80 and 2.81 for different values of the equilibrium segregation coefficient k_0, $D = 3 \cdot 10^{-8}\ m^2\ s^{-1}$ $v_x = 1.5\ mm\ min^{-1}$ and $L = 100\ mm$, - - - convective mixing, ——— diffusive mode.

The equation does not describe the final part of the solidification process. Equation 2.81 is valid if the remaining characteristic length of the melt is longer than the diffusion boundary layer. Limitations for a diffusive process alone arise for conditions where the flow velocity in the melt approaches the solidification speed or growth velocity (Figure 2.24).

In the case of normal freezing, we have one interface between a solid part and a melt part. If we use a cylindrical shaped ingot and some part of it (Figure 2.25) will be melt, then the configuration of the process of zone melting is given if the liquid zone is transported along the ingot. This process may be used to purify materials and is called *zone refining*. It may be also used for the growth of single crystals in the configuration of a floating zone.

Figure 2.25 depicts schematically the principal configuration of zone melting.

After moving the melt zone from $x = 0$ to $x = L$, we want to calculate the concentration profile of the dopant in the resolidified ingot. This calculation can be done

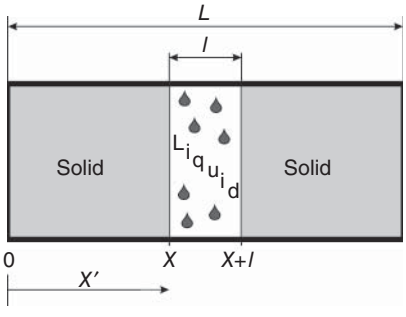

Figure 2.25 Zone melting (schematically), l = zone length.

very similarly to the one done in the normal freezing process using the assumptions, in particular the complete mixing of the dopant in the melt zone. The following equation is given by the conservation of mass:

$$(x+l)c_0 = {}_0\int^{x} c_s(x')dx' + {}_x\int^{x+1} c_L dx' = {}_0\int^{x} c_s(x')dx' + c_L l \tag{2.82}$$

At $x' = x$, we have $c_s(x) = k\, c_L$

$$(x+l)c_0 = {}_0\int^{x} c_s(x')dx' + c_s l/k \tag{2.83}$$

Differentiation of Equation 2.83 gives

$$c_0 = c_s(x) + l/k dc_s(x)/dx$$
$$dc_s(x)/dx = k/l(c_0 - c_s) \tag{2.84}$$

Solution of Equation 2.84:

$$c_s(x) = c_0 + A\exp(-kx/l)$$

With $c_s(0) = k\, c_0$ we have

$$A = c_0(k-1)$$
$$c_s(x) = c_0\{1-(1-k)\exp(-kx/l)\} \tag{2.85}$$

Equation 2.85 is often called *Pfann's law* [19]. It cannot be applied for the concentration profile of the resolidified final zone at the end of the ingot. In this case, Equation 2.80 must be used with L as the remaining zone length.

Figure 2.26 shows the concentration profile for convective mass transport (complete mixing). In comparison with the behavior of normal freezing, the initial

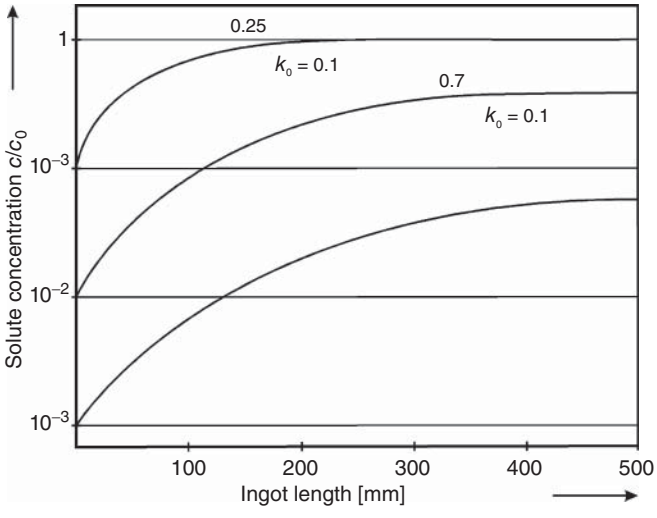

Figure 2.26 Zone melting: concentration profile for complete mixing of the dopant in the melt. Zone length $l = 10$ mm and parameter: segregation coefficient k.

concentration starts at $c_s(0) = k\ c_0$. The shape of the concentration distribution is similar to the diffusive mode of normal freezing. However, the initial transient is shorter and can be influenced by adjusting the zone length.

For zone melting, diffusive mass transport shows similar concentration profiles compared to normal freezing and will not be discussed further.

Under practical conditions, we have to consider convective transport in the liquid phase as well as diffusive transport of the additives. As a result, the segregation behavior during solidification at the interface liquid/solid is not governed just by the properties of the phase diagram of the binary system. The equilibrium segregation coefficient k_0 has to be replaced by an effective segregation coefficient k_{eff}, which is dependent on k_0, on a solute boundary layer δ formed ahead of the growth front and the growth velocity v_x. Considering the case of $k < 1$, we will have an accumulation of the dopant at the interface solid/liquid.

This behavior is demonstrated in Figure 2.27, which shows the solute boundary layer ahead of the advancing (v_x) interface solid/liquid.

If we neglect convection in the liquid or melt during advancing solidification, the solute, or dopant has to be transported back into the melt by diffusive transport mechanism. Therefore, a solute boundary layer δ will be built up ahead of the growth front as a function of the crystallization process. The different interpretation of δ will be discussed later.

The process of diffusion is described by the first and second laws of Fick.

The flux i of dopants in the melt is proportional to the concentration gradient:

$$i = -D\delta c/\delta x \tag{2.86}$$

The continuity equation is

$$\delta i/\delta x + \delta c/\delta t = 0 \tag{2.87}$$

Finally, we have

$$D\delta^2 c/\delta x^2 - \delta c/\delta t = 0 \tag{2.88}$$

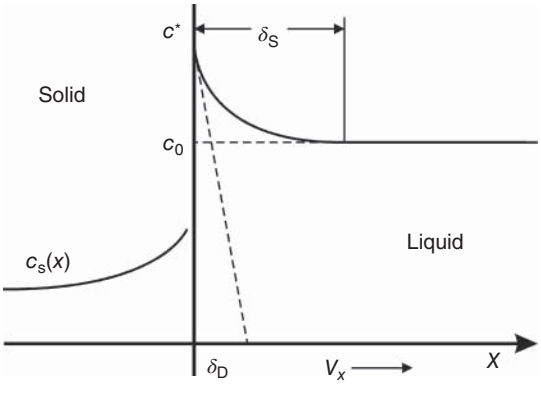

Figure 2.27 Solute boundary layer ahead of the advancing interface solid/liquid. δ_s is the boundary layer given by Burton *et al.* [20] and δ_D follows the interpretation given by Wilson [21].

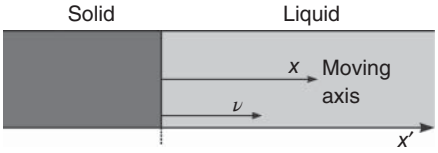

Figure 2.28 Diagram of a moving phase boundary.

To get the one-dimensional transport equation, we introduce a moving phase boundary solid/liquid (Figure 2.28).

We can write now

$$x = x' - vt$$
$$\delta x/\delta x' = 1\delta c/\delta x = \delta c/\delta x'\delta^2 c/\delta x^2 = \delta^2 c/\delta x'$$

and

$$\delta c/\delta t = \delta c/\delta x \cdot \delta x/\delta t = -v\delta c/\delta x$$

Substituting these equations in Equation 2.88, we have

$$\delta^2 c/\delta x^2 + v/D\delta c/\delta x = 0 \tag{2.89}$$

A possible solution may be

$$x = \exp(bx) \tag{2.90}$$

Substituting Equation 2.90 in Equation 2.89, we get

$$Db^2 + vb = 0$$
$$b = 0, -v/D$$

A common solution of Equation 2.89 is

$$c = A + B\exp(-vx/D)$$
$$x \to \infty : c = c_0 \text{ and } A = c_0$$
$$c = c_0 + B\exp(-vx/D) \tag{2.91}$$

The amount of dopant that is not incorporated in the solid must be equal to the amount that is transported by diffusion into the melt volume.

$$C^*(1-k_0)v = -D(\delta c/\delta x)_{x=0} \tag{2.92a}$$

At $x = 0$ we can write

$$c^* = c_0 + B$$
$$(\delta c/\delta x)_{x=0} = -Bv/D\exp(-vx/D) = -Bv/D \tag{2.92b}$$

Substituting these equations in Equation 2.92a:

$$B = (c_0 - c_0k_0)/k_0 \tag{2.92c}$$

Using Equation 2.91 and $x = \delta_s$, we may define an effective segregation coefficient k_{eff}

$$k_{eff} = k_0/(k_0 + (1 - k_0)\exp(-v\delta_s/D) \tag{2.93}$$

This equation has been introduced by Burton, Prim, and Slichter (BPS-Theory) [20].

From Equation 2.93, we can conclude the following:

For $v \to 0$ and $\delta \to 0$, that means for a very low growth rate or an extremely small boundary layer δ (intensive convection), we have

$$k_{eff} = k_0$$

For high growth rates v, by economic reasons often used in industrial applications, or at high diffusion layers (low or no convection), we can write

$$k_{eff} = 1$$

This situation is demonstrated in Figure 2.29.

Until now we have discussed the effects of macrosegregation in an axial direction or the growth- or solidification direction. Normally the solid/liquid interface is slightly curved leading to a lateral solute segregation. First calculations have been performed by Coriell and Sekerka under the assumption of no convection. The results are valid for the case where the solute or diffusion boundary layer is thick compared to the deviation of the solid/liquid interface from planarity. As a result, the lateral segregation in the solid is to a first attempt the product of the interface deflection, the segregation coefficient, and the concentration gradient applicable to a planar interface. The principal behavior of this lateral segregation is schematically shown in Figure 2.30.

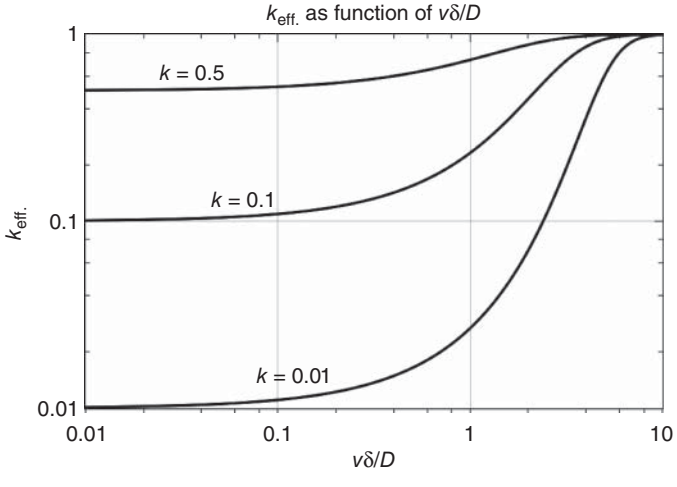

Figure 2.29 Effective segregation coefficient k_{eff} as a function of the standardized growth rate $v\delta/D$.

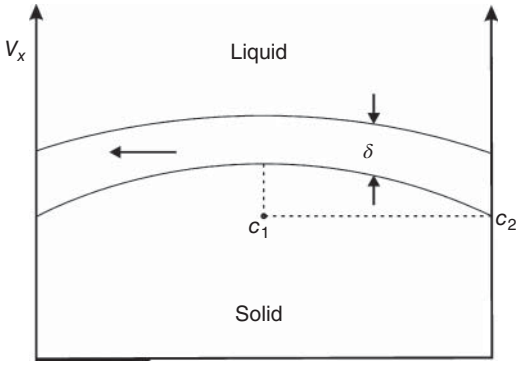

Figure 2.30 Lateral mass transport by diffusion for $k < 1$ in front of a curved interface.

In addition to the segregation governed by diffusion along a lateral concentration gradient, axial concentration gradients may be directly seen in the radial distribution profile. This effect can be demonstrated in Figure 2.30. The point C_2 in Figure 2.30 will be solidified later than the point C_1. Therefore, with $k < 1$, the solute concentration at C_2 is higher than at C_1.

The diffusive mass transport i transports the additives from the center to the edge.

Point C_2 crystallizes at a later time than C_1 and shows a higher concentration during axial segregation.

If we have a solute flow pattern in front of the solid/liquid interface, which is schematically shown in Figure 2.31, the width of the solute boundary layer δ is not uniform but is a function of the solute flow velocities and their directions. The resulting effective segregation coefficient depends on the lateral position. If δ decreases k_{eff} will also decrease.

The segregation behavior is also determined by kinetic effects during crystallization. A solidification process normal to a well-defined crystallographic plane

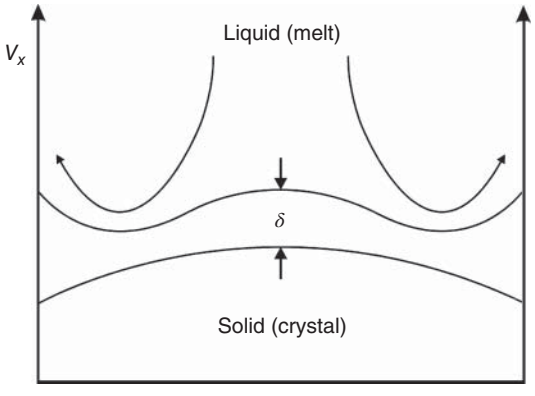

Figure 2.31 Solute boundary layer thickness δ in dependence of the flow regime.

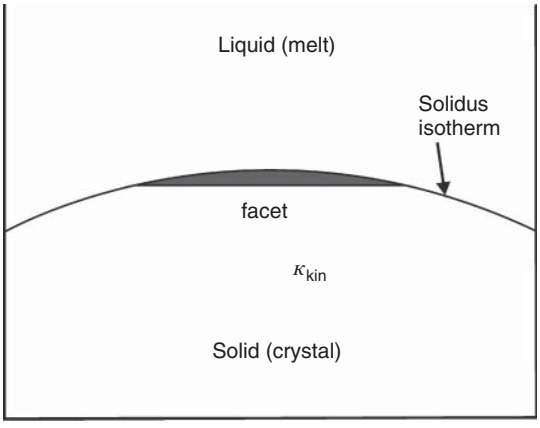

Figure 2.32 Convex-shaped interface and low-index lattice plane (schematically) during crystal growth from the melt black area: undercooled regime.

might result in different values of the segregation coefficients compared to the off-facet region. This effect was studied by Mullin and Hulme [22] during the growth of InSb crystals from the melt. Planar (111)facets have been developed during growth. At growth rates of 20 mm h^{-1} the distribution coefficient for Te in the off-facet region has been measured to $k_0 = 0.5$. The crystallization normal to the (111) facet showed a value of $k_{(111)} = 6$. Figure 2.32 depicts schematically the convex-shaped interface and the low-index lattice plane, which lays tangential to the liquid/solid phase boundary.

Compared to the off-facet region, the facet region shows no kink positions that allow a crystallization process within the thermodynamic equilibrium. On the facet (undercooled regime), a two-dimensional nucleus is necessary to form a new layer, which solidifies with a high lateral growth velocity until the plane is completed. This high lateral growth velocity favors the incorporation of dopants or additives and leads to a so-called kinetic segregation coefficient k_{kin}. The facet or kinetic effect cannot be discussed in connection with a solute enriched boundary layer.

Example 2.4: The equilibrium segregation coefficient of Cu in Si is $k_0 = 4 \cdot 10^{-4}$. Within a zone experiment with a growth velocity of $v = 2.0$ mm min^{-1}, an effective segregation coefficient of $k_{eff} = 2.9 \cdot 10^{-3}$ has been measured.

What is the size of the diffusion boundary layer for a diffusion coefficient of $D = 5.4 \cdot 10^{-4}$ cm^2 s^{-1}?

Putting all data in Equation 2.94 results in $\delta = 3.21$ mm.

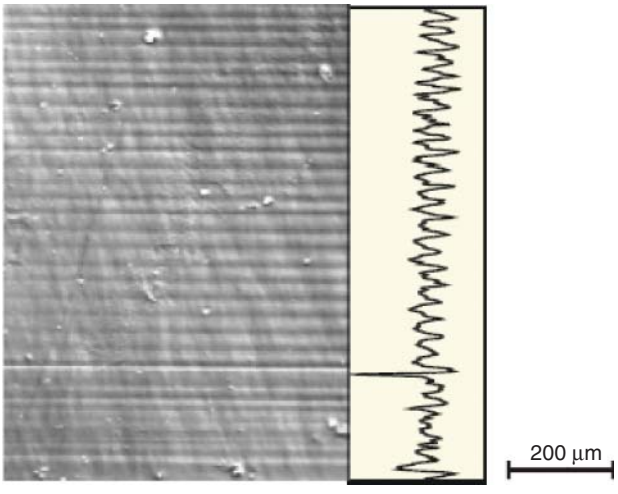

Figure 2.33 Dopant striations in a FZ-silicon crystal.

Microsegregation Microscopic dopant inhomogeneities as a result of microsegregation in grown crystals are related to local fluctuations of the dopant concentration or the crystal composition on a microscale. The spacing of these inhomogeneities is measured from a few micrometers to several hundred micrometers and is called *dopant striations* or simply *striations* (Figure 2.33) [23, 24].

In order to understand the effect of microsegregation, two mechanisms have to be distinguished:

- fluctuation of the growth rate; and
- fluctuation of the size of the solute boundary layer.

By rewriting Equation 2.93, we get the following expression for the boundary layer δ_s:

$$\delta_s = -(D/v_x) \cdot \ln[k_0(1-k_{eff})/k_{eff}(1-k_0)] \tag{2.94}$$

This equation shows that these two mechanisms cannot be separated easily.

With one dopant and small values of fluctuations, and also assuming a constant boundary layer growth rate, fluctuations can be directly correlated to dopant variations. After Brice and Whiffin we may write

$$\Delta c_s = \Delta v\, k_{eff} c_l = \Delta v\, (\delta k_{eff}/\delta v) c_l$$

With $c_l = c_s/k_{eff}$, we get

$$\Delta c_s/c_s = \Delta v/k_{eff} \cdot \delta k_{eff}/\delta v$$
$$\Delta c_s/c_s = \Delta v/v \cdot [(1-k_0) v\delta/D \exp(-v\delta/D)]/[k_0 + (1-k_0)\exp(-v\delta/D)] \tag{2.95}$$

For $v\delta/D \ll 1$ Equation 2.95 may be rewritten as

$$[\Delta c_s/c_s]\Delta v/v = (1-k_0) v\delta/D \tag{2.96}$$

A linear dependence between both the fluctuations of the growth velocity and the dopant can be seen.

As an example, we may use representative values taken from the growth of Si. Growth velocity $v = 2.0\,\text{mm min}^{-1}$, diffusion coefficient $D = 2\ 10^{-8}\ \text{m}^2\ \text{s}^{-1}$, and growth velocity fluctuations of 10%. Using a boundary layer of $\delta = 1.0\,\text{mm}$ and a segregation coefficient of $k_0 = 0.01$, we have $\Delta c/c = 17\%$.

By rearranging Equation 2.92b, we have

$$(\delta c/\delta x)_{x=0} = -\Delta c v/D = G_c \tag{2.92b}$$

an expression of the concentration gradient at the interface liquid/solid. In order to avoid nonsymmetric interfaces, solid/liquid during growth due to temperature asymmetries, crystals may be rotated. In this case, we can reveal equidistant striations, so-called *rotationals*. The distance d of the rotationals is given by

$$d = v/\acute{r} \tag{2.97}$$

where $\acute{r}$ is the rotation rate.

Example 2.5: The growth rate of InP from an In-solution by the **T**raveling **H**eater **M**ethod, *THM* is $v = 2\,\text{mm day}^{-1} = 1.4\,\mu\text{m min}^{-1}$ with a rotation rate $\acute{r} = 2\,\text{rpm}$.

The distance of the rotationals is $d = 0.7\,\mu\text{m}$ [25].

To know the shape and position of the phase boundary of a growing crystal at a certain time as well as the local growth rates, well-defined striations can be used as time markers. The demarcation of the interface may be performed by current pulsing [26], by lamp pulses [27], by controlled vibrations [28], or by rotating the crystal in an inhomogeneous temperature field [25]. The technique of current pulsing requires electrical contacts at the crystal and at the feed or the solution, which may result in disturbances of the growth process.

2.3.3 Constitutional Supercooling and Morphological Stability

During the growth of alloy crystals or doped crystals, it may be possible that a flat growth front becomes unstable and develops a type of macroscopic roughening. This morphological instability is called *constitutional supercooling*. The effect is different from the roughening of surfaces, which is described in Section 2.2.2.

If we grow a crystal with a dopant material, which shows a segregation coefficient $k < 1$, the dopant concentration increases from the melt to the advancing growth front, which is shown in Figure 2.34 (see also Figure 2.27). The dopant concentration is c_0 in the melt and reaches a value c_0/k at the growing interface. Owing to the binary phase diagram for $k < 1$ (compare Figure 2.22), the melting point or solidification temperature follows the liquidus line and is reduced to $T_s(c_0)$ at the interface solid/liquid. If we neglect kinetic undercooling effects, the crystallization temperature at the growing interface must be equal to $T_s(c_0)$.

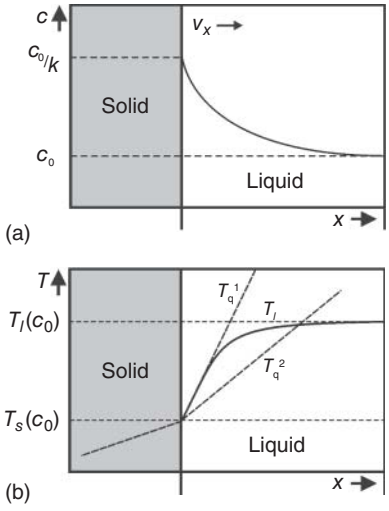

Figure 2.34 (a) Dopant concentration in front of the interface solid/liquid. (b) Effect of constitutional supercooling.

The local equilibrium temperature can be written as

$$T_s(c_0) - T_1 = m\,(c_0 - c_1) \tag{2.98a}$$

with the slope m of the liquidus line

$$m = dT_1/dc \tag{2.98b}$$

and a temperature gradient given by the experimental conditions during growth

$$G = (dT_q/dx)_{x=0} \tag{2.99a}$$

If G is smaller than the gradient mG_c given by the conditions of the phase diagram, the melt is in the regime of constitutional supercooling. G_c is given by Equation 2.92b.

Then we may write

$$G < mG_c = -(mv\Delta c_0)/D \tag{2.99b}$$

To avoid constitutional supercooling, we have

$$G/v = (-m\Delta c_0)1/D$$

By introducing the segregation coefficient k, we can write (Figure 2.35)

$$G/v = ((mc_0)/(kD))(k-1) \tag{2.100}$$

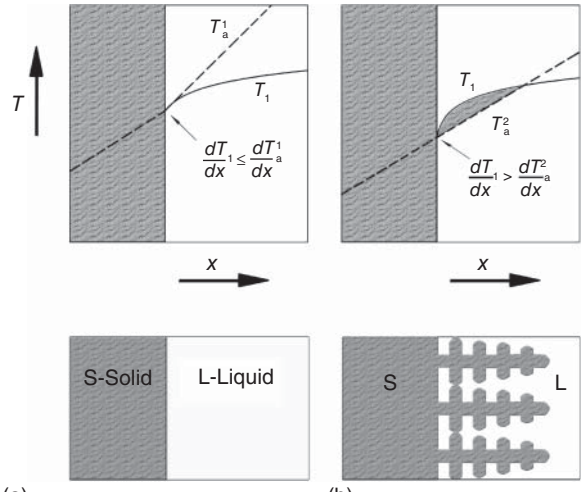

Figure 2.35 (a) Stable growth conditions: ($T_I < T_q$) and (b) $T_I > T_q$ unstable growth conditions and possible appearance of morphological instabilities.

2.4 Principles of Flow Regimes in Growth Melts

In Chapter 1, we have seen that the origin of striations on a microscale is due to fluctuations of the growth rate or to fluctuations of the boundary layer. Possible reasons of such fluctuations besides temperature alterations are instationary time-dependent fluctuations of convective flows in the nutrients. There are many important origins for convective flows. Buoyancy-driven convection may be caused by temperature differences in the melt or solution or concentration gradients due to depletion of a dopant in the melt by the growing crystal. Thermo capillary or Marangony convection may be present whenever a liquid/liquid or a liquid/gas interface is given. Both types of convection represent natural sources.

Artificially introduced forces may lead to a forced convection in the nutrient and are due to

- rotation of the crystal;
- stirring of the melt, accelerated crucible rotation;
- electrodynamic convection;
- external magnetic fields; and
- vibrational convection.

A melt or solution will be handled as an incompressible Newtonian fluid. For incompressible fluids, the viscosity does not depend on the flow velocity. The velocity might be a function of temperature or pressure but is not coupled to the convection itself. A flow in a Newtonian fluid is expressed by a second-order nonlinear partial differential equation system, the Navier–Stokes equations. The equations describe the momentum transport and the conservation of momentum.

Its derivation in time is equal to the sum of acting forces:

$$\rho_l\{\delta v/\delta t + \nu_k \cdot \Delta v\} = -\Delta p + \nu_k \cdot \Delta v^2 + f_{ext} \tag{2.101}$$

ρ_l is the density of the fluid, v the fluid velocity, ν_k the kinematic viscosity, and f_{ext} the external force.

On the left side of Equation 2.97, we have the variation of the momentum; the right side depicts the pressure term, the movement of the fluid and the external forces.

We may emphasize that the Navier–Stokes equations express Newton's second law of motion for a fluid of constant density.

For more information about fluid dynamics, the reader might be referred to the text book by Incropera and de Witt [29].

To describe flow patterns and flow modes in a crystal growth configuration, the introduction of dimensionless similarity parameters is of great importance. These dimensionless parameters are based on the principal of similarity and allow an easy transfer of model experiments to real growth experiments with respect to the fluid flow in the ambient phases. This procedure may be valid only as long as the dimensionless numbers describing the model are set equal to the corresponding ones of the growth process. Of special importance are the so-called critical numbers, describing the transition from one flow state to another. A collection of dimensionless numbers is given in the literature [30].

2.4.1
Buoyancy Convection

In nearly all melt-crystal growth configurations buoyancy convection dominates the overall flow patterns. Buoyancy convection is driven by unstable density structures in the fluid (hot bottom of a crucible filled with a crystal melt). There are two main origins for this type of convection: if the density differences are caused by temperature differences, we have thermal buoyancy convection, and if there are concentration differences, solutal buoyancy convection will arise.

A most important dimensionless number with respect to buoyancy convection in melt growth facilities is the Rayleigh number, written as buoyancy forces divided by the viscous forces:

$$Ra_{th} = (\alpha \cdot g \cdot \Delta T \cdot l^3/\nu_k \cdot \kappa) \quad Ra_s = (\beta \cdot g \cdot \Delta c \cdot l^3/\nu_k \cdot D)$$
$$\text{Thermal} \qquad\qquad \text{Solute} \tag{2.102}$$

with α = thermal volumetric expansion coefficient, β = solute volumetric expansion coefficient, g = gravity vector, ν_k = kinematic viscosity, κ = thermal diffusivity, and D = diffusion coefficient.

Other important numbers related to this subject are the Prandtl *Pr* and Schmidt *Sc* numbers, respectively.

$$\mathrm{Pr} = \nu_k/\kappa \quad Sc = \nu_k/D \tag{2.103}$$

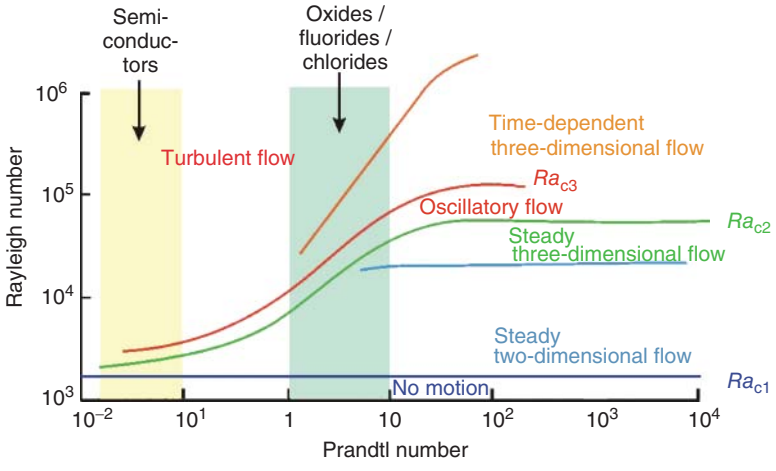

Figure 2.36 Rayleigh and Prandtl number for different flow states ($h/d \to 0$). (Redrawn from Krishnamurti, R. [31], with kind permission from Cambridge University Press.)

The Prandtl number represents the ratio of momentum diffusivity to thermal diffusivity, and the Schmidt number the ratio of momentum diffusivity to the diffusion of species. Instead of the Rayleigh number, the Grashof number is often used:

$$Gr = Ra/\,\mathrm{Pr} = \alpha \cdot g \cdot \Delta T \cdot l^3/\nu_k^2 \tag{2.104}$$

Very important are the critical numbers that describe the transition from one flow state to another. For small aspect ratios (height h of the fluid volume to the diameter d of this volume), Krishnamurti [31] derived the thermal Rayleigh number as a function of the Prandtl number, representing different types of fluids. Figure 2.36 shows various flow states in dependence of the Rayleigh and Prandtl number.

For the classical Bernard configuration with an aspect ratio $h/d \to 0$, the first critical Rayleigh number, which describes the transition from no convection to a steady flow $Ra_{c1} = 1708$ and is independent of the Prandtl number. Carruthers found that for an aspect ratio of 1, this value is shifted to 1 [32].

In the case of semiconductor melts, the transition from both a steady and an oscillatory time-dependent flow to a three-dimensional, unsteady convection occurs at values not far from Ra_{c1}.

For semiconductor melts in Czochralski pullers, we have $5 \cdot 10^7 < Ra_{th} < 10^9$ with the highest value for large-scale silicon pullers.

2.4.2 Marangoni Convection

A specific type of convection was reported by the Italian physicist Carlo Marangoni (1840–1925). This type of convection denoted as Marangoni or thermocapillary convection is driven by gradients of the surface tension caused

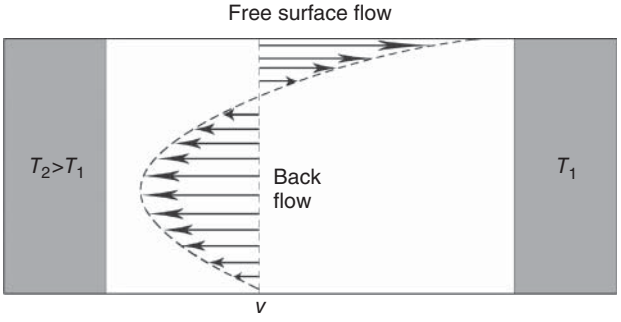

Figure 2.37 Surface tension driven flow (schematically) as a consequence of temperature or concentration differences at the liquid surface.

either by temperature or by concentration dependence of the surface tension. Normally the surface tension decreases with increasing temperature. Free surfaces are present for many crystal growth configurations, for example, float zone or Czochralski arrangements but are also present in bubbles or detached areas in closed ampoules.

Figure 2.37 depicts a schematic representation of a surface tension driven flow due to temperature or concentration gradients [33].

Thermal and concentration-dependent Marangoni convection are characterized by the Marangoni number:

$$Ma_{\mathrm{th}} = -(\delta\gamma/\delta T)\cdot \Delta T x/\nu_{\mathrm{k}}\cdot\rho_{\mathrm{l}}\cdot\kappa \qquad Ma_{\mathrm{c}} = -(\delta\gamma/\delta c)\cdot\Delta c x/\nu_{\mathrm{k}}\cdot\rho_{\mathrm{l}}\cdot D \tag{2.105}$$

Thermal Solute

γ is the surface tension, other symbols as explained earlier.

Similarly to the Grashof number for buoyancy convection, the Reynolds–Marangoni number M is used instead of Ma:

$$M = Ma/\,\mathrm{Pr} = -(\delta\gamma/\delta T)\cdot \Delta T x/\nu_{\mathrm{k}}^2/\rho_{\mathrm{l}} \tag{2.106}$$

An important property of the Marangoni number is the fact that it is not dependent on the gravity vector **g**. If both flow phenomena – buoyancy convection and Marangoni convection – are present in terrestrial experiments, they cannot be separated. However, in growth experiments in space where the earth gravity is reduced by orders of magnitude, Marangoni convection may be studied without a remarkable influence of buoyancy convection [34].

A measure of the relative strength of thermal buoyancy and Marangoni convection is the dynamic Bond number Bo_{d}:

$$Bo_{\mathrm{d}} = Ra/Ma = Gr/M = (\alpha\cdot g\cdot \rho_{\mathrm{l}}\cdot l^2)/(\delta\gamma/\delta T) \tag{2.107}$$

On top of the melt in large-scale Czochralski silicon pullers we have a thermal Marangoni number of $Ma \leq 2\cdot 10^5$.

A critical Marangoni number Ma_{cr1} (in comparison to the critical Rayleigh number!) exists only for temperature gradients perpendicular to the free surface of a fluid (Rayleigh–Bernard configuration): $Ma_{\mathrm{cr1}} \approx 70$. For temperature

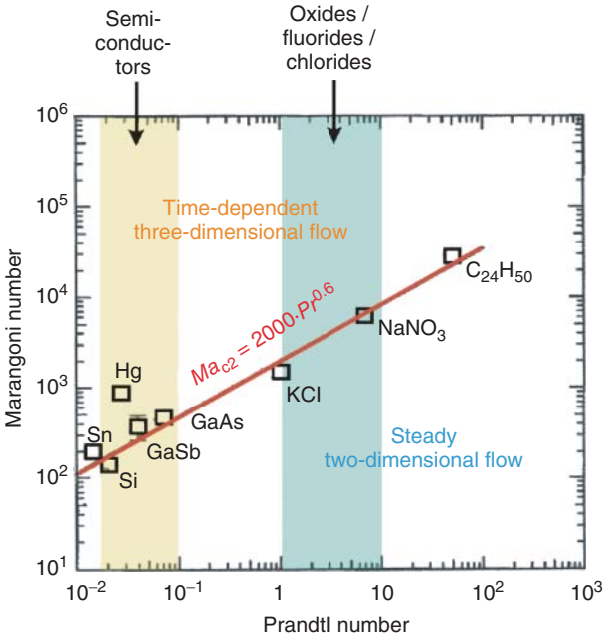

Figure 2.38 The critical Marangoni number Ma_{cr2} as a function of the Prandtl number. (Adapted from Yang, Y.K., Kou, S. [35], with permission from Elsevier.)

gradients with components parallel to a free surface, Ma_{cr1} is zero. That means, if there is even a small temperature gradient at the surface, we will have a significant Marangoni flow.

By this reason, Ma_{cr2} is the most important critical Marangoni number representing the transition from a steady two-dimensional flow to a time-dependent three-dimensional flow. A difference between Ma_{cr2} and Ma_{cr3} is not discussed in the literature.

The critical Marangoni number Ma_{cr2} depends on the Prandtl number and the following correlation was given by Yang and Kou [35]:

$$Ma_{cr2} = 2000 \cdot Pr^{0.6} \tag{2.108}$$

Yang and Kou used a liquid bridge of molten tin between two stainless steel rods to study thermocapillary convection. They carefully avoided the oxidation of the molten tin. Figure 2.38 shows a few critical numbers for selected materials (for details compare Chapter 3).

References

1. Markov, I.V. (1996) *Crystal Growth for Beginners*, World Scientific, Singapore.
2. Chernov, A.A. (1983) *Modern Crystallography: Crystal Growth*, vol. 3, Springer, Berlin.

3. Rosenberger, F. (1979) *Fundamentals of Crystal Growth I, Macroscopic Equilibrium and Transport Concepts*, Springer, Berlin.
4. Callister, W.D. Jr., (2001) *Fundamentals of Materials Science and Engineering/An Interactive e-Text*, 5th edn, John Wiley & Sons, Inc., New York.
5. Nyvlt, J., Söhnel, O., Matuchova, M., and Broul, M. (1985) *The Kinetics of Industrial Crystallization*, Academia Praha.
6. Volmer, M. (1939) *Kinetik der Phasenbildung*, Steinkopff, Leipzig.
7. Burton, W.K., Cabrera, N., and Frank, F.C. (1951) *Philos. Trans. R. Soc. London*, **A243**, 299.
8. Hartmann, P. and Perdok, W.G. (1955) *Acta Crystallogr.*, **8**, 49,521.
9. Jackson, K.A. (2004) in *Crystal Growth – from Fundamentals to Technology* (eds G. Müller, J.-J. Metois, and P. Rudoph), Elsevier B.V., p. 27.
10. Temkin, D.E. (1966) *Crystallization Processes*, Consultant Bureau, New York, p. 15.
11. Jetten, L.A.M.J., Human, H.J., Bennema, P., and van der Erden, J.P. (1972) *J. Cryst. Growth*, **68**, 503.
12. Frank, F.C. (1949) *Faraday Discuss. Chem. Soc.*, **5**, 48.
13. Szurgot, M. and Karniewicz, J. (1981) *J. Cryst. Growth*, **52**, 53.
14. Givargizov, E.J. (1977) *Growth of Crystalline Whiskers and Platelets from the Vapour*, Nauka, Moscow.
15. Wagner, R.S. and Ellis, W.C. (1964) *Appl. Phys. Lett.*, **4**, 89.
16. Laudise, R.A. (1959) *J. Am. Chem. Soc.*, **81**, 562.
17. Scheil, E. (1942) *Z. Metallkunde*, **34**, 70.
18. Tiller, W.A., Jackson, K.A., Rutter, J.W., and Chalmers, B. (1953) *Acta Metall.*, **1**, 428.
19. Pfann, W.G. (1952) *J. Met. Trans. AIME*, **194**, 747.
20. Burton, J.A., Prim, R.C., and Slichter, W.P. (1953) *J. Chem. Phys.*, **21**, 1987.
21. Wilson, L.O. (1978) *J. Cryst. Growth*, **44**, 247.
22. Mullin, J.B. and Hulme, K.F. (1960) *J. Phys. Chem. Solids*, **17**, 1.
23. Burton, J.A., Kolb, E.D., Slichter, W.P., and Struthers, J.D. (1953) *J. Chem. Phys.*, **21**, 1991.
24. Carlson, D.J. and Witt, A.F. (1991) *J. Cryst. Growth*, **108**, 508.
25. Boschert, S., Danilewsky, A.N., and Benz, K.W. (1999) *J. Cryst. Growth*, **205**, 92.
26. Lichtensteiger, M., Witt, A.F., and Gatos, H.C. (1971) *J. Electrochem. Soc.*, **118**, 1013.
27. Danilewsky, A.N. and Benz, K.W. (1990) *J. Cryst. Growth*, **106**, 273.
28. Witt, A.F. and Gatos, H.C. (1968) *J. Electrochem. Soc.*, **115**, 70.
29. Incropera, F.P. and de Witt, D.P. (1996) *Fundamentals of Heat and Mass Transfer*, John Wiley & Sons, Inc., New York.
30. Müller, G. and Ostrogorsky, A. (1994) in *Handbook of Crystal Growth*, vol. 2b (ed D.T.J. Hurle), Elsevier, p. 709.
31. Krishnamurti, R. (1973) *J. Fluid Mech.*, **60**, 285.
32. Carruthers, J.R. (1977) in *Preparation and Properties of Solid State Materials*, vol. 3 (ed W.R. Wilcox), Marcel Dekker, p. 1.
33. Schwabe, D. (1988) in *Crystals – Growth, Properties and Applications* (ed H.C. Freyhardt), Springer, p. 75.
34. Hurle, D.T.J., Müller, G., and Nitsche, R. (1987) in *Fluid Sciences and Materials Science in Space – A European Perspective* (ed H.U. Walter), Springer, p. 313.
35. Yang, Y.K. and Kou, S. (2001) *J. Cryst. Growth*, 135.

3
Growth Techniques in Correlation with Related Growth Mechanism

3.1
Overview on Main Growth Techniques

In this chapter, we will concentrate mainly on the selection of growth methods and growth techniques, which show a high technological and industrial potential but not neglecting some other interesting growth arrangements.

Semiconductor and other application-oriented materials, which are very often used as single crystals in bulk form or as thin epitaxial layers, must exhibit an excellent real structure with a low defect and impurity density. Residual defects and impurities, which are actually unavoidable, should be, in most cases, homogeneously distributed within the grown crystal.

The production of bulk single crystals exceeds more than 50 kton year^{-1}. About 60% of the yearly production is dedicated to semiconductors such as silicon, gallium arsenide, indium phosphide, gallium phosphide, cadmium telluride, and their alloys, for example, cadmium–zinc–telluride. The remaining 40% are shared by optical and acousto-optic crystals, scintillator crystals, laser- and nonlinear-optic crystals, and, finally, crystals for jewelry and watch industry.

The most important growth technology for bulk or volume crystals is the pulling from the melt, in particular from melts contained in crucibles. This method is named after Czochralski [1]. He developed a new method to measure the crystallization velocity of metals.

Historically, the industrial production of ruby and sapphire crystals was introduced by the French scientist Verneuil in 1902 [2]. He developed a flame-fusion process for these materials with melting points above 2000 °C. He could partially control the growth process by forming a neck, followed by an increasing of the crystal diameter.

Materials that exhibit a measurable vapor pressure at its melting point have to be grown in closed ampoules, such as GaAs or CdTe as inorganic materials or naphthalene and anthracene as organic materials. The relevant growth method was introduced by Bridgman [3]. In this case, a liquid (melt) is transported through a temperature gradient in a horizontal or vertical way to achieve a controlled solidification.

Introduction to Crystal Growth and Characterization, First Edition.
Edited by Klaus-Werner Benz and Wolfgang Neumann.
© 2014 Wiley-VCH Verlag GmbH & Co. KGaA. Published 2014 by Wiley-VCH Verlag GmbH & Co. KGaA.

Crystal growth from solutions covers another wide range of various methods and techniques. In particular, solution growth may be important for the growth of a variety of crystals, when the material decomposes at the melting point and a suitable solvent is available to make a saturated solution at a given temperature.

The method of growing crystals from solutions can be roughly divided in the following topics:

- Growth from low temperature solutions
  - growth from aqueous solutions
  - growth by gel method
- Growth from high temperature (HT) solutions
  - growth from flux or top-seeded solution growth
  - growth from metallic solutions (compare Section 3.2.4)
  - hydrothermal growth, often combined with high pressure growth techniques.

A selection of growth methods from solutions will be given in Section S2. The growth from metallic solutions will be discussed in Section 3.2.4.

Bulk crystals may also be grown from the vapor phase by **p**hysical **v**apor **t**ransport (PVT) or HT CVD (**c**hemical **v**apor **d**eposition) . A technologically important candidate from fundamental growth mechanism as well as from practical questions of production is silicon carbide, SiC [4]. SiC is an interesting semiconductor crystal with chemical stability, a high bandgap, high thermal conductivity, and a high breakdown voltage. SiC may replace conventional semiconductors, such as Si or GaAs in high power electronics technology, for example, power distributors, and motor controllers in modern vehicles. SiC bulk crystals are mainly grown by PVT, including sublimation with seed crystals. Other candidates for bulk vapor growth are CdTe and ZnTe, as well as the alloys of these materials.

A survey of the methods of growth suggests that almost 80% of the single crystals are grown from the melt compared with roughly 5% from vapor, 5% from low temperature solution, 5% from HT solution, 2% by hydrothermal methods, and 3% by other methods (e.g., from solid phase).

If a thin crystalline film is grown on a substrate crystal, we call this growth process ***epitaxy*** [5]. Experimentally gained data showed that an epitaxial process may occur if the lattice misfit between the grown layer and the substrate ς, defined as

$$\varsigma = 100(a_l - a_s)/a_s \tag{3.1}$$

is not larger than 15%; a_l and a_s are the lattice constants of the epitaxial layer and the substrate, respectively.

Epitaxial layers or "***epilayers***" are called *homoepitaxial layers*, if substrate and layer are of the same chemical composition, for example, a GaAs layer on a GaAs substrate.

Homoepitaxial layers or layer structures can be grown in a way that the crystallographic orientation of the layer is exactly determined by the substrate crystal. If the chemical composition and/or the structure of layer and substrate are different, we speak of heteroepitaxial layer growth.

In epitaxial growth processes, different phase transformations may be realized. In the case of vapor phase epitaxy (VPE), we have a transition from vapor to solid. Two possibilities may be realized: PVT or CVD, where chemical reactions are involved in the growth process. A transition from liquid to solid leads to liquid phase epitaxy (LPE). Both the epitaxial processes have the advantage that the growth temperature is several hundred degrees below the melting point of the material to be crystallized. The transition solid to solid, solid phase epitaxySPE, may be important for laser or electron beam annealing and will not be discussed in this chapter.

The physical methods of VPE may be divided into the following techniques:

- sublimation and condensation
- flash evaporation
- sputtering
- hot-wall epitaxy
- molecular beam epitaxy, MBE.

The chemical methods are governed by chemical vapor transport and synthesis methods. In chemical vapor transport, the material to be transported and finally deposited is identical with the starting or source material. The source reacts with a transport agent by forming volatile compounds, which are transported in the deposition region where the reverse reaction takes place. An example of this growth process is the Effer-method developed for III–V semiconductors and related compounds. Details of this method will be discussed later in Section 3.4.2.

VPE by transport methods exhibited a big scientific potential for the growth of high purity epitaxial layers of GaAs, GaP, and InP as well as their ternary and quaternary alloys in the time period 1968–1985. It was not possible, with the exception of LPE, to grow such excellent layers by other epitaxial growth techniques [5].

VPE by synthesis methods uses a source material that is chemically different from the material to be epitaxial deposited. This means the epitaxially grown material is the result of a chemical reaction. Important synthesis methods are

- Epitaxy of semiconductors such as Si and GaAs from hydrides and halogenated hydrides (e.g., SiH_4, AsH_4, and $SiHCl_3$).
- Metalorganic vapor phase epitaxy (MOVPE). For the case of GaAs as an example, the transport of a metalorganic Ga compound (which acts as a precursor) by the carrier gas hydrogen (H_2) into the deposition zone occurs. Here, the metalorganic compound is pyrolyzed and reacts with an arsenic-containing compound such as AsH_3.

LPE has been mainly developed for layers of III–V-compound semiconductors by Nelson [6]. It has been used for oxide layers as well. The growth of GaAs and InP from Ga-rich and In-rich solutions, respectively, leads to high purity and high quality (structure and electronic behavior) epitaxial layers. As in the case of VPE, the growth of epitaxial layers is several hundred degrees below the melting point of the binary compounds. The LPE growth process is close to equilibrium.

Sometimes, this may cause problems with the interface sharpness of successive grown layers. This behavior is in contrast to the layer growth in VPE.

3.2 Principles of Melt Growth Techniques

3.2.1 The Czochralski Crystal Growth Process

The principal of the Czochralski growth process will be explained for semiconductor materials, for example, Si, GaAs, or InP. Both III–V compounds crystallize in the zincblende structure. The zincblende (sphalerite) structure was already described in Section 1.5.2 (see Figure 1.77). The four Ga atoms occupy the position of a ccp structure and the four As atoms are located in half of the tetrahedral voids. Each As atom is located at the center of a regular tetrahedron and surrounded by four Ga atoms. This tetrahedral structure implies that the structure does not reveal the center of inversion symmetry. Therefore, crystals with zincblende structure exhibit a polar behavior in the <111> direction of the III-component alternating with atoms of the V-component but with unequal spacing. Thus, two distinct (111) surfaces, a (111)A and a (111)B, can occur. These surfaces are different in etching behavior and growth processes when using such surfaces as seeds for bulk crystal growth or as substrates for epitaxial techniques.

At the beginning of the growth procedure, the raw material – mainly polycrystalline pieces – are filled in a high purity quartz crucible. The procedure must be done in a clean room atmosphere in order to avoid contamination of the melt and the crucible. The crucible is heated by a resistance heater or by radio frequency (RF) heating. The polycrystalline pieces are dissolved in the crucible, and its temperature is kept close to the melting point of the material, normally a few degrees above the melting temperature. Because one cannot avoid temperature gradients in the big crucibles, there may be some buoyancy convection in the melt, and if there are free surfaces, Marangoni (see Chapter 2) convection will be present as well. In order to suppress this unwanted convection, one has to use static or alternating magnetic fields of considerable size.

Important Steps during Czochralski Growth Procedure

- To start the growth process, a seed crystal has to be used. The selection of the seed is very important, in particular for the growth of Si and other technological relevant materials. It must show a very low defect structure, a high crystallographic perfection, and a low content of residual impurities. The seed is fixed on a crystal holder.
- The next step is very crucial. The seed is pulled down and kept some time above the melt surface to reach a temperature slightly below the melting temperature.

Then, the seed is inserted into the melt and withdrawn from it. During this procedure, a small part of the seed may be dissolved. For homogeneity reasons, seed and crucible are rotated in opposite directions.

- Now the growth process starts. In the case of Si growth, the first pulling speed is relatively fast. The diameter of the growing crystal will decrease to a few millimeters. This necking technique was first described by Dash in 1958 [7]. Dislocations and other structural defects can grow out from the crystal and do not reach the further parts of the growing crystal. Such a neck is not used when growing GaAs crystals. Here, we have a higher propagation speed of dislocations than a possible pulling speed of the crystal.
- After the necking process, the pulling speed is increased to reach the desired diameter via a cone.

Figure 3.1 shows the principle arrangement of a Czochralski growth facility.

To grow the crystal with a constant diameter, the growth rate must be synchronic with the pulling rate. An important task is to fix the position of the crystal/melt interface during growth. A high pulling rate shifts this interface toward the crystal, and the crystal diameter may decrease. A low pulling rate brings the interface downward to the melt, and the crystal becomes thicker. During continuous growth, the height of the melt decreases, and we have to distinguish between an effective pulling rate v_{eff} and the applied pulling rate v_{appl} with the following correlation:

$$v_{\mathrm{eff}}\rho_{\mathrm{s}}r_{\mathrm{cr}}^2 = v_{\mathrm{eff}}\rho_{\mathrm{l}}R_{\mathrm{melt}}^2 - v_{\mathrm{appl}}\rho_{\mathrm{sl}}R_{\mathrm{melt}}^2 \tag{3.2}$$

$$v_{\mathrm{eff}} = v_{\mathrm{appl}}R_{\mathrm{appl}}^2/R_{\mathrm{appl}}^2 - (\rho_{\mathrm{s}}/\rho_{\mathrm{l}})r_{\mathrm{cr}}^2 \tag{3.3}$$

where r_{cr}, R_{melt} are the radii of crystal and melt and ρ_{s}, ρ_{l} the densities of crystal and melt, respectively.

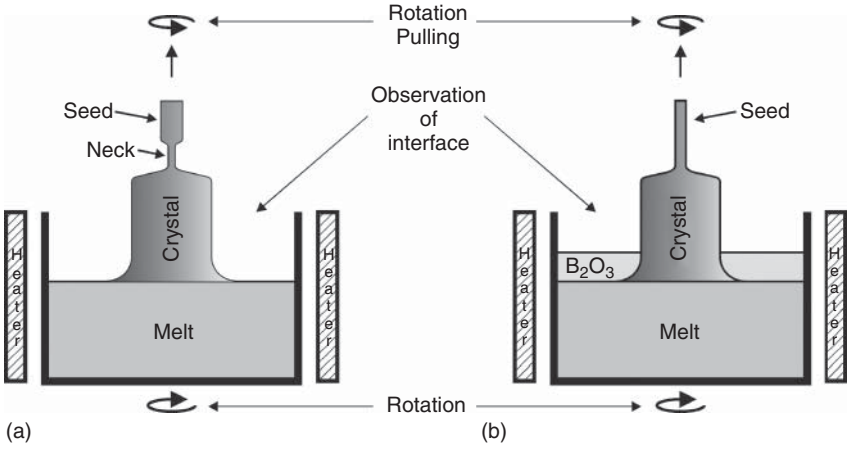

Figure 3.1 Czochralski growth apparatus (schematically): (a) Cz growth for Si with seed and necking structure and (b) GaAs Cz growth with B_2O_3 melt cover and without necking structure.

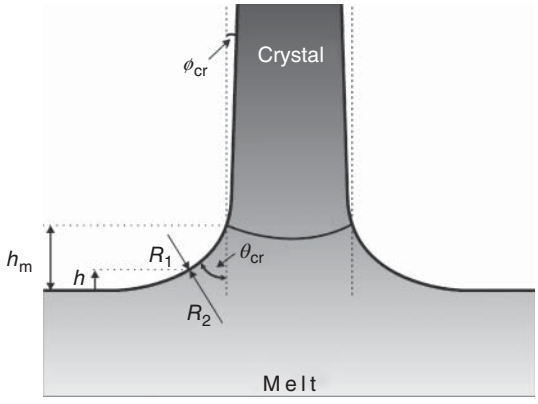

Figure 3.2 Czochralski method: crucible with melt, shape of the melt meniscus, and the grown crystal.

As a consequence, the effective pulling rate is higher than the applied pulling rate. Figure 3.2 depicts schematically grown crystal, melt, and shape of the meniscus for the Czochralski method.

The shape of the meniscus is given by the balance between the surface tension and the gravity. This behavior is expressed by the Laplace–Young equation:

$$-\rho_l g h = \gamma_l (1/R_1 + 1/R_2) \tag{3.4}$$

where g is the gravity vector, h the coordinate of the height, R_1 the curvature perpendicular to the plane, R_2 the curvature in the plane, and γ_l the surface tension.

For the Czochralski geometry, an approximate solution of Equation 3.3 was given by Civinski:

$$h_m = \sqrt{\{\varsigma(1-\sin\Theta_{cr}) + (\varsigma\cos\Theta_{cr}/4r_{cr})^2\}} - \varsigma\cos\Theta_{cr}/4r_{cr} \tag{3.5}$$

with

$$\varsigma = 2\gamma_l/\rho_l g$$

where h_m is the height of the meniscus, Θ_{cr} the meniscus angle. The parameter h_m increases with the increase in crystal radius r_{cr} and becomes independent of r_{cr} for bigger crystal diameter. To grow a Czochralski crystal with a constant diameter, we have to adjust the following conditions:

$$\Theta_{cr} = \Theta^0_{cr} \quad \text{and} \quad \Phi_{cr} = 0; h_m = h^0_m$$

For $\Theta_{cr} > \Theta^0_{cr}$, we have $h_m < h^0_m$ and $\Phi_{cr} > 0$, and the crystal diameter increases.
For $\Theta_{cr} < \Theta^0_{cr}$, we have $h_m > h^0_m$ and $\Phi_{cr} < 0$, and the crystal diameter decreases.

A complete wetting of the crystal by the melt yields $\Theta_{cr} = 0$, and we can rewrite Equation 3.5 as

$$h^0_m = \sqrt{\{\varsigma + (\varsigma/4r_{cr})^2\}} - \varsigma/4r_{cr} \tag{3.6}$$

and, for bigger diameters, as

$$h_m^0 \approx \sqrt{\varsigma} = \sqrt{(2\gamma_l/\rho_l g)} \tag{3.7}$$

The commercial production of technological important crystals needs a diameter control of the grown material. The following techniques are used in practice:

- Reproduction of the crystal diameter through the optical window (compare Figure 3.1) via a TV camera. The crystal diameter can be measured on a TV screen. The alteration of the diameter signal can be used as a feedback for the pulling rate and the temperature. The method is mainly used for crystals with high growth rates, for example, metals such as Cu.
- In the case of silicon, a CCD (charge coupled device) camera is controlling the diameter, including the shape of the melt meniscus precisely usually within ±1 mm. Diameter control on a long term is realized by temperature changes and on a short term by changing the pulling rate.
- The weight of the crystal is measured by a weight sensor and compared with a precalculated standard value. This information is used to control the furnace temperature within a feedback loop. This type of diameter control is used for the growth of many materials, for example, III–V compounds or oxides.

Peculiarities of Czochralski Growth of Different Materials The most important semiconductor material, grown by the Czochralski method, is **silicon**, Si. Modern computer and communication technologies are based on silicon technology. A further demand in increasing the memory capacity, for example, in a laptop computer, needs a higher throughput and yield of large scale integration (LSI) chips.

Silicon wafers with large diameters and high quality are needed. Until now, 450 mm diameter crystals are the standard industrial growth technology. The basis of such high quality crystals is a manufacturing technology of a raw material with an excellent purity. The following processes starting with the mineral silica and ending with the Si-wafer are applied:

- Silicon belongs to the inexhaustible elements with a share of 26% of the earth's crust. Si is obtained by the reduction of SiO_2 at temperature about 2000 °C (arc furnace with graphite electrodes):

$$SiO_2 + 2C = Si + 2CO \tag{3.8}$$

  The achieved purity is about 98% (metallurgical-grade Si).
- The next step is the purification of the metallurgical-grade Si by the reaction with hydrochloric acid (HCl) to form trichlorosilane ($SiHCl_3$):

$$Si + 3HCl = SiHCl_3 + H_2 \tag{3.9}$$

  Several impurities form chlorides that are volatile and can be removed easily. As a result, a high purity trichlorosilane is obtained. A repeating distillation of $SiHCl_3$ increases the purity furthermore (11 N: a purity of 99.99999999999%).

- Finally, the production of polycrystalline Si rods occurs by reduction and thermal dissociation of trichlorosilane with hydrogen as a CVD process on thin Si rods.

$$SiHCl_3 + H_2 \rightarrow Si + 3HCl \tag{3.10}$$

  The polycrystalline Si obtained by this method is an ingot with a diameter of 100–150 mm.
- The silica-crucible of the Cz-growth apparatus is filled up with the polycrystalline Si and melted by a graphite heater at a temperature higher than the melting point of Si (1420 °C). Details of the beginning of growth and the necking process have been described earlier. To grow a crystal without dislocations, a high pulling rate up to 5 mm min^{-1} should be applied. The diameter of the neck is around 3–5 mm, and the neck length is between 100 and 300 mm [8]. To form the shoulder, the temperature of the melt is decreased and the pulling rate reduced to 0.1–0.5 mm min^{-1}. The growth of the main crystal cylinder is carried out by an automatic diameter control as described earlier. Crystals up to a standard diameter of 300 mm are grown with a weight of 50 kg.
  It is interesting to notice that the big crystal is completely supported by the small neck.
  At the end of the growth process, the diameter is slowly decreased to zero. The formation of this tail is necessary to avoid the generation and multiplication of new dislocations into the grown crystal.
  For the future, a further decrease of the production costs of LSI chip fabrication is mandatory. That means an increase in wafer diameter is required. The "International Technology Roadmap for Semiconductors 2005" (ITRS) had already suggested that 450 mm wafers will be used from 2012 on.
- The grown single crystal ingots are sliced by using a sawing machine. Up to 200 mm diameter wafers, internal-diameter blade saws are used. For 300 mm diameter on wafers, multiwire saws are preferred. The thickness of the sliced wafers is about 1 mm.
  The sliced wafers are lapped to remove surface defects and damage induced by the slicing process. Afterward, the wafers are chemically etched to remove the damaged part on the surface. In order to improve further the surface quality, a final mechanochemical polishing of the wafers, using colloidal silica dispersed in NaOH solution, is applied. This final wafer processing is very important to keep the yield of LSI chips high.
  The total production of Si in the year 2013 is predicted to about 200 kton, mainly for solar silicon. Monocrystalline semiconductor silicon production, which is used for the fabrication of computer microchips, may remain below 50 kton.

Example 3.1: We will assess a maximum growth rate or pulling rate for a Si-Czochralski growth experiment. We assume that the growth may take place at a certain temperature in the vicinity of the advancing phase boundary liquid/solid. A maximum growth rate $\boldsymbol{\nu}$ may depend on the following parameters:

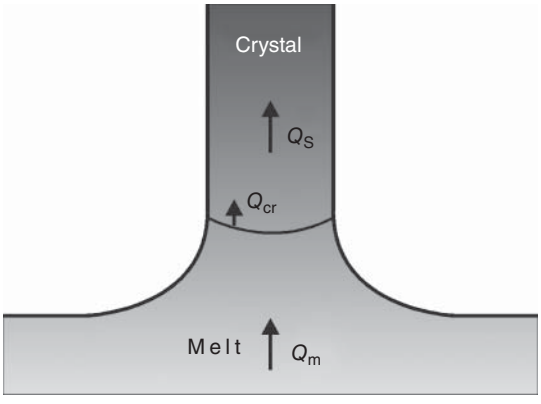

Figure 3.3 Thermal conditions in a growing Si Czochralski crystal.

- kinetic of the growth process
- thermal properties of the melt and the growing crystal
- heat capacity and thermal properties of the growth apparatus.

An upper value of the pulling rate may be calculated by using a thermal equilibrium between melt and growing crystal: the heat transport from the melt (Q_m) via the growing crystal plus the heat of crystallization (Q_{cr}) must be equal to the heat transport through the growing crystal (Q_s) (compare Figure 3.3).

$$Q_{cr} + Q_m = Q_S \tag{3.11}$$

By using the axial temperature gradients along the melt container and the growing crystal (neglecting the loss of heat by radiation), we can write:

$$\rho F v Q_{cr} + \kappa_m F (dT/dx)_m = \kappa_s F (dT/dx)_s \tag{3.12}$$

$$v = 1/\rho Q_{cr} [\kappa_s (dT/dx)_s - \kappa_m (dT/dx)_m] \tag{3.13}$$

Assuming the following experimental condition:

$$\kappa_m (dT/dx)_m < \kappa_s (dT/dx)_s \tag{3.14}$$

we have for the maximum pulling rate:

$$v = \kappa_s / \rho Q_{cr} [(dT/dx)_s] \tag{3.15}$$

Physical properties of Si	
Density	$\rho = 2.5\,\mathrm{g\,cm^{-3}}$
Latent heat of crystallization	$Q_{cr} = 5 \cdot 10^4\,\mathrm{J\,mol^{-1}}$
Thermal conductivity	$\kappa_s = 1.4\,\mathrm{W\,cm^{-1}\,degree^{-1}}$
Molecular weight	$M_{Si} = 28$
Temperature gradient	$(dT/dx)_s \approx 50\,^{\circ}\mathrm{C\,cm^{-1}}$

The maximum calculated pulling rate is $v \approx 10\,\mathrm{mm\,min^{-1}}$.

An experimental value is about $6\,\mathrm{mm\,min^{-1}}$, which fits well with this simple calculation.

The Czochralski growth of **III–V compounds, mainly Gallium arsenide, GaAs and Indium phosphide, InP**, shows a few differences compared to the Cz-growth of Si.

GaAs has a wide range of applications and is mainly used in low noise high frequency opto- and microelectronic devices. Semi-insulating GaAs wafers play an important role in device manufacturing. InP is used as a substrate material for the epitaxial growth of alloys such as (In, Ga)As and (Ga, In)(As, P) for use in emitters and detectors of infrared light at 1.33 and 1.55 μm wavelengths, respectively, matched to optical fiber transmission.

GaAs and InP depict a measurable vapor pressure of the V-component As and P at its melting points. Therefore, it is most important during crystal growth to hinder the evaporation of arsenic or phosphorus, respectively. The solution of this problem has been the use of an inert melt, which covers completely the molten semiconductor material. An inert gas vapor pressure keeps the molten covering material (liquid encapsulate) on top of the semiconductor melt. The liquid encapsulate must fulfill the following conditions:

- The density of the encapsulate must be lower than the density of the molten semiconductor material.
- The vapor pressure of the encapsulate must be negligible at the melting temperature of the semiconductor material.
- The semiconductor material should not be dissolved in the encapsulate.
- The encapsulate should not dope the semiconductor melt and should not react with it.

Boric oxide can be used only above 800 °C owing to its high viscosity. It floats the surface of the materials in the crucible and protects the surface from As loss. Its water content helps to purify the melt. An increase in water content from about 200–2000 ppm decreases the total impurity content in the liquid-encapsulated Czochralski (LEC)-grown GaAs crystals by an order of magnitude to about $10^{15}\,\mathrm{cm^{-3}}$ (with the exception of B, N, O, and C) [9].

LEC-GaAs crystals are grown up to 200 mm diameter and a mass up to 25 kg.

InP, another important representative of III–V compound semiconductor materials, shows as crystal, similar to GaAs, zincblende structure (cubic space

group $F43m$). The melting temperature of InP ($T_m = 1062\,^{\circ}C$) is lower than the melting point of GaAs.

The phosphorus dissociation pressure is 27 bar and is a critical factor to all HT processing such as synthesis and crystallization from the melt.

The LEC growth of InP follows in principle the same procedure as for GaAs. The compound is formed in an InP polycrystalline synthesis system [10] by direct exothermic reaction of In-cast metal ingots and red phosphorus. The internal P vapor pressure is carefully balanced by an inert gas ambient, argon, or nitrogen, maintained in a steel pressure vessel. Direct synthesis in an LEC puller, which is the preferred synthesis method of GaAs, is not possible.

The LEC growth process of InP begins by inserting an InP-seed crystal with a square cross section and the sides normally cut in {110} planes into the melt through the transparent boron trioxide layer. After partially melting the seed, a meniscus is drawn up, and crystal growth is initiated by withdrawing the seed through the boron oxide.

Growing crystal and melt are cocounter- or counter rotated to establish a flow pattern in the melt and to achieve a homogeneous material. By adjusting the furnace temperature, an increase in crystal diameter can be reached. The pulling rate for a 2 in. diameter InP crystal is between 5 and 10 mm h^{-1}. Semi-insulating, iron-doped InP crystals are grown up to a diameter of 4 in. [10].

Modified Czochralski Method with Vapor Pressure Control (GaAs) An inner chamber is the main peculiarity of this modified Czochralski growth method to establish a temperature-controlled As vapor pressure (Figure 3.4). An inert gas pressure and the boron trioxide encapsulate are used as well. Reduced axial and radial temperature gradients are now present compared to the "normal" Czochralski method.

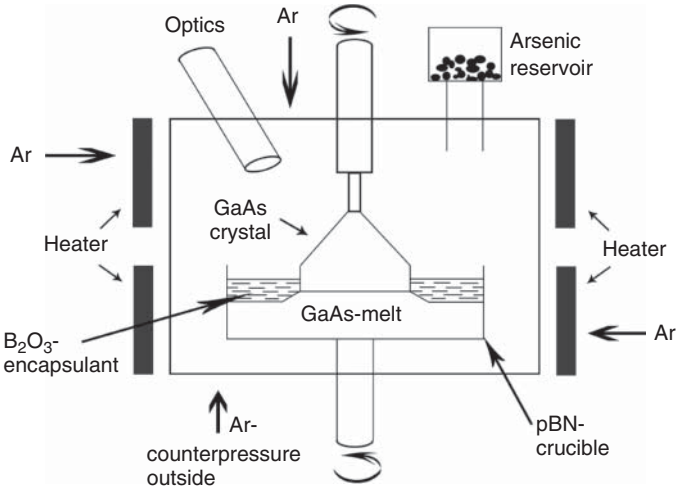

Figure 3.4 Modified CZ method for GaAs with As vapor pressure control.

Low axial temperature gradients of about 15–35 K cm^{-1} for crystal diameters of 100–150 mm have been achieved (100–150 K cm^{-1} for normal GaAs–LEC crystals). As a result, the VCz crystals exhibit a very low thermomechanical stress leading to reduced dislocation densities by one order of magnitude compared to LEC crystals (about 5×10^3 cm^{-2}). Special high frequency electronic devices may be produced by using GaAs–VCz crystals.

Bulk oxide crystals are grown by the Czochralski method in the case that they melt congruently. They are important materials for acoustic, piezoelectric, and optical devices. Important representatives of the oxide materials are $LiNbO_3$ (LN) and $LiTaO_3$ (LT) [11]. LN and LT exhibit a large application potential as surface acoustic wave (SAW) devices and as devices for digital communication technologies. The melting temperature of LT is at 1562 °C; therefore, Pt crucibles cannot be taken for Cz growth. Ir and Pt/Rh crucibles are used to grow crystals with diameters up to 4 in. and a length of 80–120 mm. The growth atmosphere is air, which is an advantage compared to the growth of III–V compounds and other materials. The usual growth conditions are: pulling rate: 5–7 mm h^{-1}, crystal rotation: 8–10 rpm, and the ratio of crystal and crucible diameter is 0.6–0.7. Knowing the exact congruent composition of the melt is of high importance for the reproducible growth of LT crystals with a high uniformity. The crystal composition can be determined by measuring the Curie temperature of LT. The Curie temperature is linearly dependent on the composition.

A new group of oxide crystals, the langasite family, came into attention as new candidates for piezoelectric applications. The reason is that progress in electronic technology requires piezoelectric crystals with large electromagnetic coupling factors and high thermal frequency stability. Interesting langasite candidates are $La_3Nb_{0.5}Ga_{5.5}O_{14}$ (LNG) and $La_3Ta_{0.5}Ga_{5.5}O_{14}$ (LTG). Crystals are grown by a conventional RF-heated Czochralski technique with Pt or Ir crucibles.

In most of the optical and acoustic applications described earlier, single crystals have played a major role in the form of bulk crystals (three dimensional) or epitaxial thin films (two dimensional). The growth of small fiber crystals, which might be viewed being nearly one dimensional, has become the subject of intense studies in recent years. An application has been stimulated, in large part, by their potential for use in a variety of fiber optical applications such as laser sources, electro-optical modulators, switchers, and coupler. There are a variety of melt growth techniques, which have been used to produce single crystal fibers, for example, edge-defined film fed growth, float zone FZ growth, solidification in capillary tubes, and so on.

As an example for the growth of single-crystal fibers, we will describe the micropulling down method, which has been developed at the Tohoku University, Japan.

Figure 3.5 depicts schematically the micropulling down technique. In a Czochralski-like apparatus with two main types of resistance heaters, a crucible containing the oxide melt is additionally heated by RF. At the lower end of the crucible, there is a micronozzle for shaping the growing fiber. The growth of the fiber is initiated by a seed crystal. Fiber crystals grown with small diameters

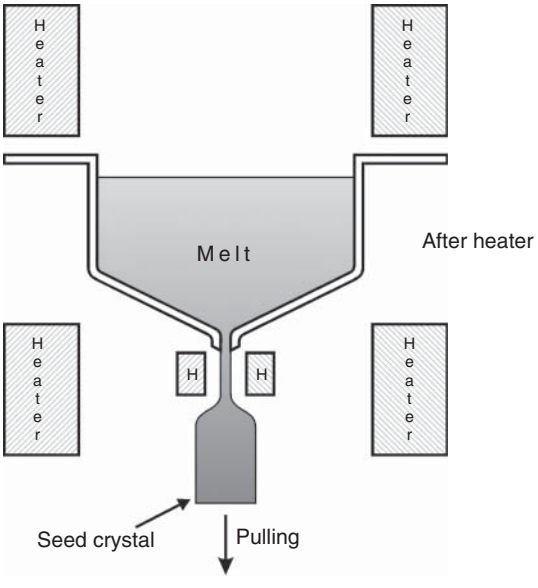

Figure 3.5 Schematic drawing of the micropulling down technique. (Redrawn from Shimamura, K. *et al.* [11], with permission by Wiley.)

ranging from micrometers to millimeters show characteristic features for a wide field of optoelectronic technologies.

A growth technique, which has similarities to the Czochralski technique, is the Kyropoulos technique and is used to grow other oxide material, namely α-aluminum oxide, which belongs to the corundum family. If these crystals contain 1–7% chromium oxide, they are called *red ruby*. Kyropoulos technique is one of the main industrial growth methods to produce sapphire crystals [12] (Figure 3.6).

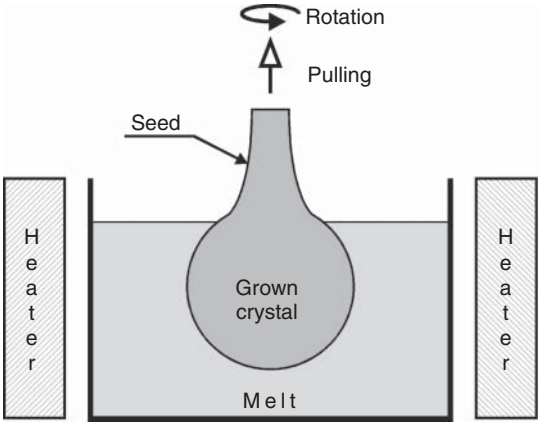

Figure 3.6 Kyropoulos technique (schematically).

This method was first developed by Nacken in 1915 [13], who grew low melting organic materials, salol and benzophenone. For materials with higher melting points, this method was further developed by Kyropoulos [14]. Figure 3.4 shows the principle arrangement of a growth apparatus. A seed crystal is brought into contact with the melt, and after some time – by changing the thermal conditions – the seed is growing into the melt. The Nacken–Kyropulus technique depicts the following interesting features:

- Several necking steps may be used to avoid defects often present in the seed crystal.
- Within the crystallization regime, only low temperature gradients are present.
- The same heating zone may be used for annealing the crystals.

Compared to Czochralski technique, the crystals are not pulled in the part of the growth apparatus with the higher temperature gradients above the melt. Sapphire crystals are grown in more than 300 mm diameter crucibles (70% Mo and 30% W) up to 25 kg.

3.2.2
Growth Method after Bridgman

A further development of the crystal growth from the melt was the normal freezing in a vertical crucible introduced by Bridgman in 1923 [3]. The crucible is pulled down in a furnace with two temperature zones, which is shown schematically in Figure 3.7.

The crystallization starts in the capillary of the ampoule and proceeds through the sphere and the cone to the cylindrical part.

The upper part of the Bridgman facility is heated above the melting temperature of the crystal material; the lower part may consist of a more complex heating system in order to maintain a well-defined temperature gradient at the interface melt/grown crystal. The position and shape of the interface melt/grown crystal mainly depends on the following conditions:

- temperatures and the thermal conductivities of melt and crystal;
- transition of heat between the melt/crystal and the heater system;
- pulling rate of the ampoule (crucible) downward, which leads to an additional heat transport in the same direction;
- heat of crystallization during the growth process.

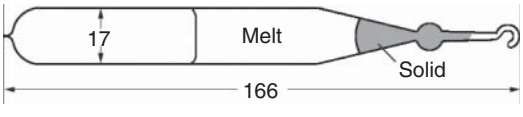

Figure 3.7 Crystal growth (schematically) from the melt after Bridgman. Example ampoule for the growth of naphthalene crystals, melting temperature $T_m = 80\,°C$, pulling rate: $1.2\,mm\,h^{-1}$. Melt: heater temperature T_2, solid: heater temperature T_1, $T_2 > T_1$.

Owing to the influence of these parameters on the growth procedure, the rate of crystallization may be different from the pulling rate of the ampoule. To reach a constant rate of crystallization during the whole crystal growth process, the pulling rate and the temperatures of the heaters must be carefully programmed.

To grow perfect crystals or at least crystals with low defect densities, it is important to establish a convex shape of the solid/liquid interface. As a rough estimation for maintaining this condition, one has to adjust the following ratio between the temperatures T_1, T_2 of the two heaters and the melting temperature T_m:

$$(T_m - T_1)/(T_2 - T_1) > 0.5$$

or

$$T_m > 0.5(T_2 + T_1)$$

We may reach a planar growth front by using these idealized conditions:

$$T_m = 0.5(T_1 + T_2)$$

There are two possibilities to initiate the growth of a single crystal:

- The lower end of the growth ampoule is formed to a capillary (Tammann, 1923). By lowering the ampoule (crystal material is completely molten and liquid), the material starts to crystallize in the capillary of the ampoule (compare Figure 3.7). A crystal with an orientation well suited is formed and extends through the sphere and cone of the ampoule.
- Instead of the self-seeding capillary, there could be a well-prepared and well-oriented seed crystal. Before starting the growth process, the seed crystal may be melted back by a small amount.

For commercial applications, the Bridgman method may be used in horizontal as well as in vertical growth arrangements. The horizontal Bridgman (HB) technique has been mainly used for the growth of GaAs single crystals [8]. A quartz tube containing a quartz boat with molten GaAs and a piece of elemental As is mechanically transported through a temperature gradient maintained in the growth chamber. The withdrawal of the temperature gradient has the disadvantage of being sensitive to mechanical disturbances. The pulling of the growth system may be replaced by reducing the temperature of the growth region electronically. This modified Bridgman method is called the *horizontal gradient freeze* (*GF*) *technique*. It may be also used in a vertically arranged system and is called *vertical gradient freeze* (*VGF*) *technique*. For the growth of GaAs, the melt is located in a vertical crucible made of pyrolytic boron nitride pBN above a GaAs-seed crystal.

In the following text, we will describe the horizontal and vertical Bridgman techniques for the growth of GaAs single crystals and the growth of CdTe crystals by the vertical Bridgman method.

Growth of GaAs by the Horizontal Bridgman or Horizontal Gradient Freeze Technique

Introduced by Weisberg and co-authors, HB method uses a quartz crucible with molten GaAs near the melting temperature of gallium arsenide around 1238 °C

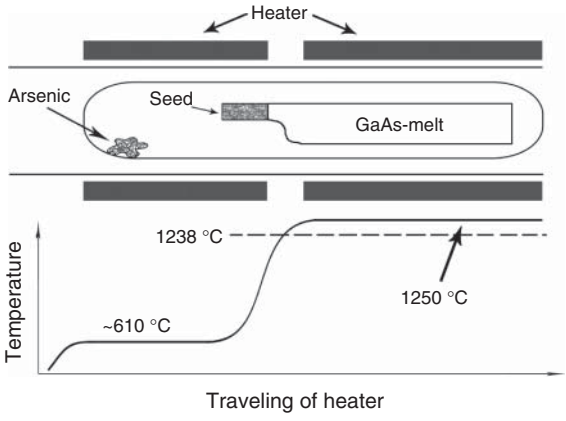

Figure 3.8 Principal arrangement of the horizontal Bridgman technique for growing GaAs.

[8]. At lower temperatures of 617 °C, a piece of solid arsenic is fixed within the crucible. Figure 3.8 depicts a schedule of the HB method in connection with a temperature profile of the furnace.

The As vapor pressure over the melt is controlled by the As piece at the left side of the crucible as in Figure 3.8 (vapor pressure around 1 bar). If the HB or horizontal GF crystals are grown in quartz boats, the main residual impurity is silicon, which makes the material n-type with a donor concentration of about $\leq 10^{16}$ cm^{-3}. By using pBN crucibles instead of quartz boats, residual carrier concentrations of $\leq 10^{12}$ cm^{-3} may be achieved. Now, it is possible to grow p-type GaAs as volume crystals by using Zn as a dopant. Dislocation densities are in the range of 10^3 cm^{-3}, an order of magnitude lower than in typically grown LEC – GaAs. The grown GaAs crystals exhibit a D-shape cross section owing to the geometry of the melt in the quartz boat.

Vertical Gradient Freeze Technique A vertical crucible of pBN contains a seed crystal and, above the seed, the GaAs melt. Boric oxide is used to cover the melt and to avoid wetting of the crucible (Figure 3.9). Highly n- and p-doped crystals as well as semi-insulated crystals may be grown by this technique. To avoid boron contamination, quartz crucibles have to be used. The inner parts of the quartz crucibles must be specially prepared to achieve a dewetting of the melt.

The axial temperature gradient at the interface melt/grown crystal is smaller compared to the LEC growth of GaAs and measures several degree celsius per centimeter.

GaAs crystals up to 200 mm in diameter can be grown by using seeds up to 8 mm in diameter (<111> or <100> orientation). By cutting the crystal into wafers, the dislocation density can be measured by counting the number of pits on the wafer after the wafer was etched by a KOH melt at a temperature of 400 °C for 10 min. Typical values of the **e**tch **p**it **d**ensity, EPD, could be measured to 100 – 1000, which is one to two orders of magnitude lower compared to LEC-grown GaAs crystals.

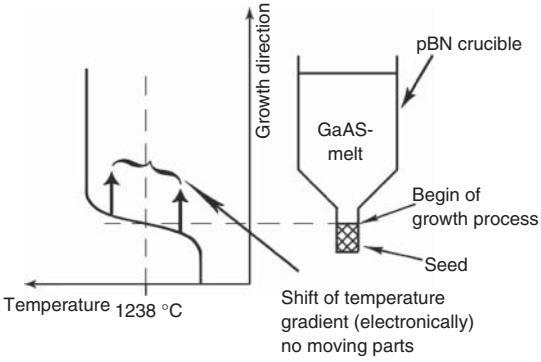

Figure 3.9 Growth of GaAs by the vertical gradient freeze technique. The lower part of the crucible contains the seed crystal. During the heating up phase, the polycrystalline feed melts and a part of the seed as well. Crystal growth will be initiated by shifting the temperature field in vertical direction (region above GaAs melt: borontrioxide).

Another III – V semiconductor, InP, is also grown by the VGF method for technological applications. Conductive InP substrates are needed for **l**ight **e**mitting **d**iodes, LEDs, photodiodes, and optical fiber communication systems. The melting point of InP is 1060 °C with a phosphorus vapor pressure of about 30 bar. This high vapor pressure has to be established during VGF growth of InP, which may lead to some difficulties compared to conventional VGF growth similar to GaAs. Typical growth rates are 2 mm h^{-1}. Moreover, the low stacking fault energy of InP favors the generation of twins. VGF growth of InP leads to single crystals with an excellent quality and a high structural perfection with respect to low dislocation densities ($\leq 5 \times 10^{-3}$ cm^{-2}) and residual stress. InP single crystals up to 100 mm diameter undoped and with many required dopants may be grown by VGF technique.

Growth of CdTe and Related Compounds by the Vertical Bridgman Method CdTe and the ternary compound (Cd, Zn)Te belong to the group of II – VI compounds with zincblende structure. The CdTe bandgap of 1.5 eV in connection with an electron mobility of 1000 – 1200 cm^2 $(V\,s)^{-1}$ and a hole mobility of 50 – 100 cm^2 $(V\,s)^{-1}$ leads to specific resistivity of 10^{10} Ω cm. Such high resistivity values gives CdTe the potential as an interesting material for the application as radiation detectors at room temperature. By adding Zn to the binary CdTe favors the reproducible growth of crystals with specific resistivity greater than $10^9 - 10^{10}$ Ω cm. The high resistivity can only be obtained by controlled compensation of shallow acceptors; the concentration of these shallow acceptors is typically in the range of 10^{16} cm^{-3} [15, 16].

CdTe and (Cd, Zn)Te bulk crystals were grown by different Bridgman-related growth techniques to obtain high resistivity material.

- A lot of crystals described so far in the literature have been grown by the vertical Bridgman method without pressure control. The crucibles consist of

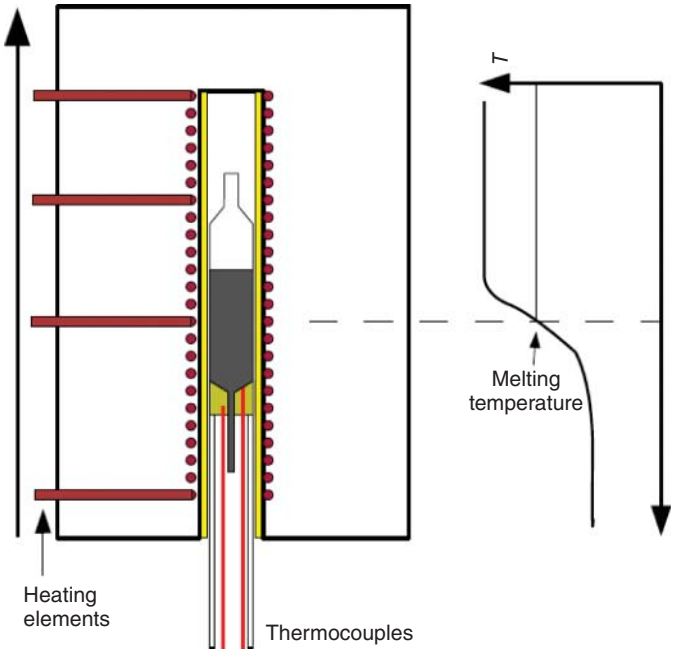

Figure 3.10 Principal arrangement of a vertical Bridgman method for the growth of (Cd, Zn)Te.

carbon-layered fused silica to avoid the sticking of the grown crystal because of the formation of cadmium silicates. Figure 3.10 shows the principal arrangement of a vertical Bridgman configuration for the growth of CdTe and related compounds.

- Crystals have been grown successfully by the HB technique with an additional cadmium source. The growth with an additional Cd source may control the vapor pressure over the melt. This helps to avoid Cd loss during the growth experiment.
- A modified vertical Bridgman method uses a pressure of 10 – 100 bar argon over the melt to grow CdTe and (Cd, Zn)Te, the so-called high pressure method, HPB. This technique is commercially most successfully used to produce high resistivity crystal material for large area X-ray detector material.
- (Cd, Zn)Te crystals with resistivities up to 10^{12} Ω cm have been grown. The HPB facilities may be designed in such a way that crystals up to 140 mm in diameter and with a weight of 16 kg may be grown. The pulling rate is about 10 mm h^{-1} and the complete growth process will be finished after 1 month.
- CdTe and $Cd_{0.97}Zn_{0.03}Te$ crystals up to 100 mm in diameter have been grown with the vertical GF technique under low thermal gradients ranging from 2 to 10 K cm^{-1}. The limitation of this growth method is the length of the grown material, which measures to about 10 mm. Cooling rates of VGF-grown crystals are from 1 to 10 K h^{-1}.

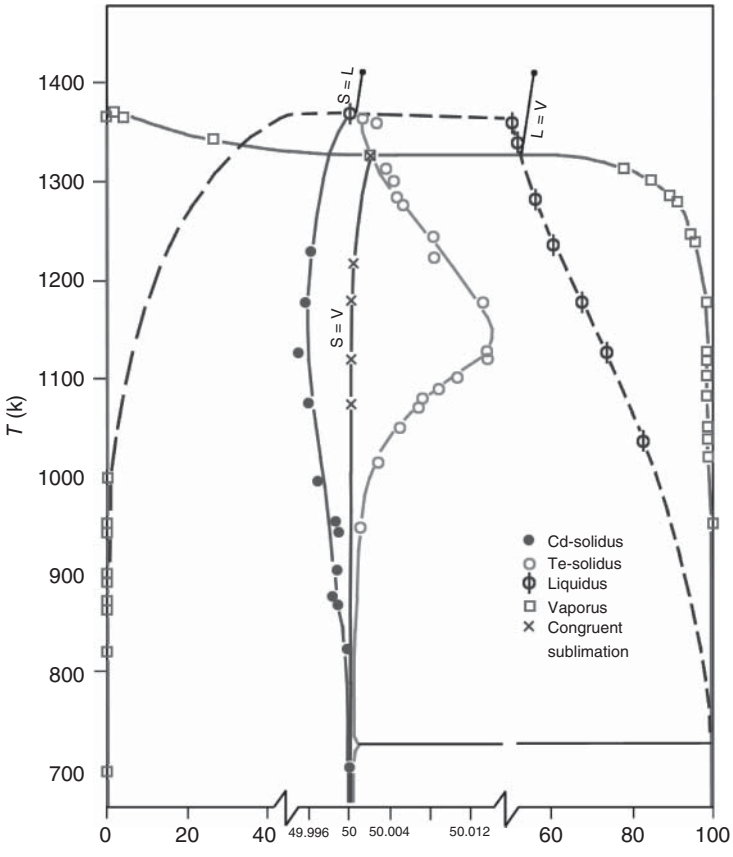

Figure 3.11 *T*/*X* projection of the CdTe phase diagram. The existence region of CdTe is magnified. (Redrawn from Greenberg, H.J., [17], with permission from Elsevier.)

Peculiarities of CdTe with Respect to Bulk Crystal Growth

Phase Diagram of CdTe The phase diagram of CdTe exhibits a narrow region of existence, which is demonstrated in Figure 3.11 as a temperature T/composition X projection.

The existence region is very asymmetric with respect to the tellurium-rich site. It reaches 50.003% Cd on the Cd-rich site and 50.012% Te on the Te-rich site, both values at a temperature of 1123 K.

The congruent melting point ($S = L$), which is important for crystal growth experiments from the melt, is located at 1365 K.

Owing to the retrograde behavior of the solidus on the Te-rich site of the CdTe-phase diagram, Te precipitates with a size of 10–30 nm may appear within the grown crystal. The following possibilities may be applied to reduce the number of precipitates:

- use of an additional Cd source during the crystal growth process and a slow cooling down of the grown crystal;

- annealing of the grown crystal in a separate crucible at evaluated temperatures together with a Cd source.

The appearance of inclusions in the grown crystal is due to the effect of constitutional supercooling and instable phase boundaries during the growth process in connection with the capture of Te droplets from the boundary layer. The boundary layer, mainly a layer with diffusion-controlled processes, is located between the solid and the CdTe melt. The droplets consist of a saturated solution of CdTe and are embedded in cavities with a polyhedral shape. Typical sizes of these inclusions are between 1 and 10 μm.

Typical Growth Defects The growth direction is normally <111>, which reduces or avoids the appearance of parts in the grown crystal – the so-called twins – which show different orientations in comparison with the seed and the main part of the grown crystal. The most important origin of twinning seems to be the variation of the solid/liquid interface position owing to temperature fluctuations. This change in solid/liquid interface position is favored by a low axial temperature gradient.

Twins with other orientations than (111) can easily be observed at the periphery of the grown crystal or by cutting and etching the crystal (Figure 3.12). A good visibility of the growth interface is an additional advantage of this growth technique.

Structure of CdTe Melt Above the congruent melting point, the CdTe melt is not completely dissociated. By the aid of neutron scattering experiments, the existence of three-dimensional objects with a coordination number of 4 of the main components could be demonstrated at a temperature of 1373 K. In order to break up these complex structures or clusters, the melt must be heated up about 20 K above the congruent melting point. A following cooling down of the overheated

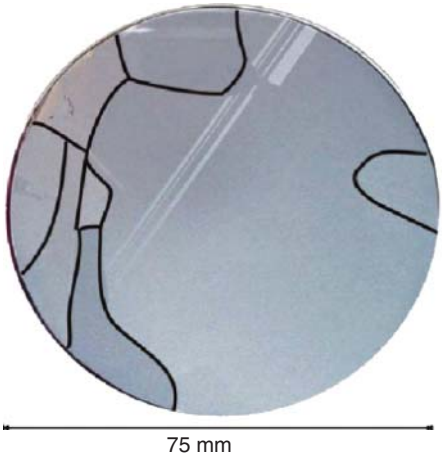

Figure 3.12 CdTe slice with the existence of twins. (Courtesy by M. Fiederle, FMF, University of Freiburg.)

melt leads to an undercooling of about 30 K before nucleation of CdTe. The first to freeze region solidifies suddenly as a polycrystalline material. A renunciation of the overheating of the melt may lead to a better nucleation. However, some still existing clusters may lead to parasitic nucleation and twinning. A solution may be a melting back of the first to freeze region and possibly the seed crystal. As a result, a precise temperature control better than 0.1 K around the seed part of the ampoule or crucible must be applied.

Influence of the Ampoule Wall during Crystal Growth Experiments-Detached Growth
Melt and crystal are in contact with the ampoule wall during Bridgman growth of CdTe.

Several problems may arise from this behavior during crystal growth:

- The ampoule wall is a source of impurities due to dissolving of ampoule material by the hot melt and residual impurities.
- Quartz glass as an ampoule material exhibits a different thermal expansion coefficient as CdTe ($\alpha_{quartz} = 0.55 \cdot 10^{-6}\,K^{-1}$ and $\alpha_{CdTe} = 5.67 \cdot 10^{-6}\,K^{-1}$). This behavior may lead to stress configurations in the grown crystal. It may also result in a cracking of the ampoule.
- The attaching of the crystal at the ampoule wall may be avoided by the use of a pyrolytic graphite layer. However, the incorporation of graphite particles in the grown crystal may lead to polycrystalline growth or twinning.

To avoid the crystal and melt, contact with a graphite-free ampoule wall is an interesting objective for the Bridgman growth of CdTe and related compounds. A contact-free Bridgman growth has been sometimes observed during crystal growth experiments in space under reduced gravity. Details may be found in Ref. [18].

The reason for the contact-free growth is the developing of a meniscus in the melt at the growth front, which leads to a small slit (thickness of several micrometers) between the grown crystal and the inner ampoule wall. This phenomenon is called *detached solidification* or *detached crystal growth*. Another expression in use is dewetting, which describes the wetting of the melt with the ampoule material. In contrast to dewetting, detached solidification refers to the actual state of the grown crystal. Usually, no difference is made between "dewetting" and "detached."

Figure 3.13 describes schematically the detached growth configuration. The enlarged image in Figure 3.13 shows the growth angle α and contact angle θ.

For Bridgman growth with constant diameter, the growth angle is identical with the meniscus angle. The advantage of the detached growth process within a Bridgman configuration may be described as an improvement of the crystal perfection through

- reduced defect density as a result of eliminated mechanical stress caused by differential thermal contraction between the ingot and the ampoule,
- reduced heterogeneous nucleation of grains and twins at the crucible wall,
- reduced heat transfer between the grown crystal and the furnace, leading to lower thermal gradients in the solid.

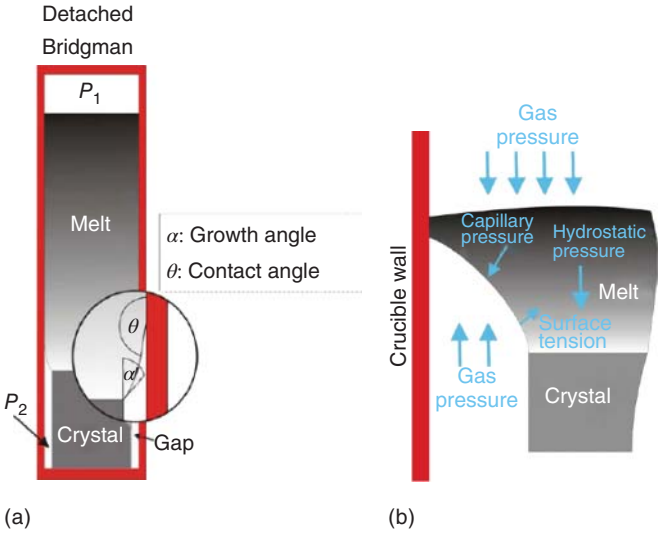

Figure 3.13 Schematic drawing of a detached Bridgman growth configuration (a) and active forces in the system (b).

To achieve detachment during Bridgman growth, the pressure values inside the growth ampoule have to be taken into account. Figure 3.13b depicts a schematic drawing of the active forces in the system with the capillary pressure, surface tension, hydrostatic pressure within the melt, and the external gas pressure outside from the ingot and the melt.

These active forces, as well as the wetting behavior of the ingot material (contact angle), and the growth angle have a significant influence on the detached growth process.

For detached growth under reduced gravity conditions in space, a specific expression was derived by Zemskov [19] and Duffar [18]. Bridgman crystal growth may be detached when the sum of the growth angle α and the contact angle θ exceed 180°:

$$\alpha + \theta \geq \pi \tag{3.16}$$

From Equation 3.16 and the Laplace capillary equation, one may calculate the width of the gap:

$$d_{\text{gap}} = R[(\cos\alpha + \cos\theta)/\cos\theta] \tag{3.17}$$

R is the radius of the ampoule.

High growth angles and high contact angles are necessary to fulfill the condition of Equation 3.16.

The contact angle of a semiconductor melt depends on the ampoule material and its surface structure. A CdTe melt in a carbon-coated quartz ampoule shows a contact angle $\theta = 108°$, whereas in pBN, we have $\theta = 132°$. The growth angle of CdTe measures $\alpha = 30°$. The sum of both angles is still <180°, but as mentioned

earlier, detached Bridgman growth of CdTe has been partially observed in space. It is assumed that impurities in the melt may play an important role toward a higher contact angle to fulfill Equation 3.16.

A further possibility to achieve detached growth in the laboratory on earth may be the built up of a pressure difference inside a sealed growth ampoule by temperature variation. A sealed ampoule filled with an inert gas (e.g., argon) is inserted in the growth furnace. Melting the feed material isolates the top and bottom gas reservoir from each other before growth starts. The pressure in the bottom gas reservoir exceeds the one in the upper gas reservoir by lowering the temperature in the upper part. $P_2 \geq P_1$, shown in Figure 3.14a.

The pressure difference at beginning of growth is self-adjusting. A bubble may rise if the pressure difference exceeds a value of around 20 mbar above the hydrostatic pressure. Owing to the higher gas pressure in the gap next to the growing crystal, a meniscus forms, and the crystal begins growing without contact to the ampoule wall.

However, maintaining the induced pressure difference through temperature change in the upper part of the ampoule is difficult. The temperature in the top part of the furnace has to be reduced further in accordance with the grown length of the crystal.

This active pressure control keeps the pressure difference constant inside the ampoule; detachment over the whole length of the crystal may be possible.

By using external gas sources (Figure 3.13b), a pressure difference can be maintained as well.

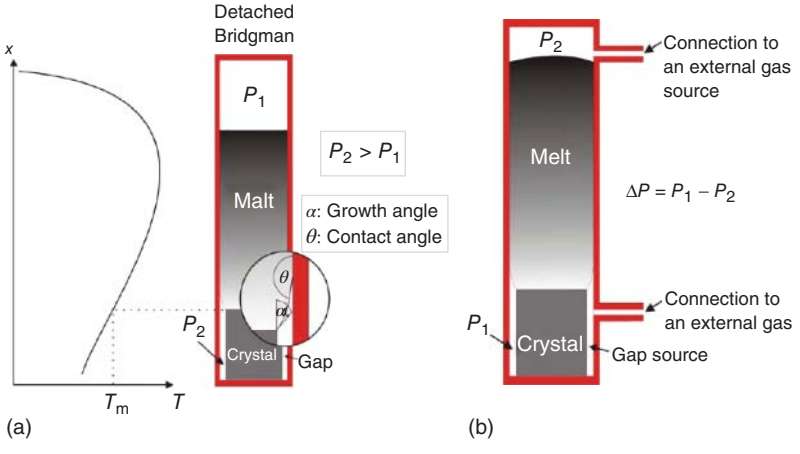

Figure 3.14 Detached growth process induced by a temperature reduction on top of the growth ampoule resulting in a pressure difference inside between the two gas reservoirs on top and next to the seed (a) Bridgman method by using external gas sources to achieve a pressure difference ΔP in the ampoule (b).

3.2.3
The Float Zone Crystal Growth Process

Figure 3.15 shows the principle of the FZ crystal process, which may be compared with the zone refining technique (see Chapter 2).

The growth arrangement consists of a feed crystal, the melt zone, and the grown crystal. In contrast to Czochralski and Bridgman techniques, the FZ method offers the advantage of a crucible free growth. That means, during growth, neither the melt nor the crystal is in contact with any other material except the surrounding atmosphere. This fact may lead to the following peculiarities:

- Tthe FZ process is suitable for materials with high melting points and aggressive melts.
- The growth of high purity crystals with reduced mechanical stress may be favored.

During cooling down of the grown crystal, no ampoule walls with different thermal expansion characteristics are in contact with the crystallized sample.

In many cases, a direct visual observation and control of the melt zone is possible.

A serious disadvantage of the FZ technique is the limitation of the liquid zone under gravity on earth. Under reduced gravity in space, the maximum stable zone length for a cylindrical FZ is given by

$$L_{\max} = 2\pi r \tag{3.18}$$

with $r =$ zone radius. This equation was first theoretically derived by Lord Rayleigh in 1879. For higher length than $L_{\max}$, the stable, smaller energy is not

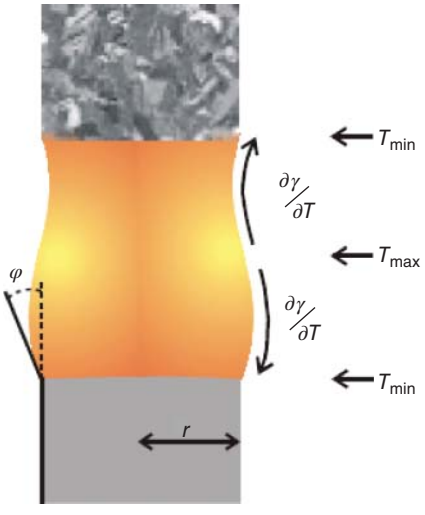

Figure 3.15 Principle of float zone (FZ) crystal growth process, γ surface tension, φ meniscus angle equal to growth angle α. (Courtesy by A. Croell, Crystallographic Institute, University of Freiburg.)

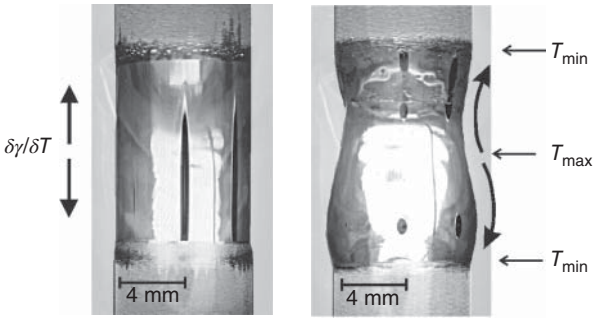

Figure 3.16 Float zone configuration for Si with free positioned melt zones between a seed and a feed crystal. (a) Cylindrical shape in a microgravity environment and (b) "bottle" shape on earth under normal gravity conditions. (Courtesy by A. Croell, Crystallographic Institute, University of Freiburg.)

the cylindrically shaped liquid zone but a configuration with two separated liquid droplets.

Under terrestrial conditions, gravity governs the shape of the liquid zone, which is shown in Figure 3.16b. In a microgravity environment, the liquid zone shows a cylindrical form (Figure 3.16).

On earth, the maximum zone length is given by the Heywang equation (1956):

$$L_{\max} = K(\alpha)\sqrt{\gamma/\rho g} \tag{3.19}$$

where K is a factor depending on the meniscus angle. The angle α is the lower meniscus angle (identical to growth angle α in Figure 3.13), γ the surface tension, ρ the density of the liquid melt, and g the gravity vector, $g = 9.81\,\mathrm{m\,s^{-2}}$.

Example 3.2: With Equation 3.19, we may calculate the maximum zone length of a FZ configuration for two different materials:

$$\text{Si}: \quad \gamma = 718 \cdot 10^{-3}\,\mathrm{N\,m^{-1}}, \quad \rho = 2.52\,\mathrm{g\,cm^{-3}}, \quad \alpha = 6.1 - 8.1, \quad \text{and} \quad K = 2.8$$
$$L_{\max} = 15.1\,\mathrm{mm}$$

$$\text{GaSb}: \quad \gamma = 450 \cdot 10^{-3}\,\mathrm{N\,m^{-1}}, \quad \rho = 6.03\,\mathrm{g\,cm^{-3}}, \quad \alpha = 30.7, \quad \text{and} \quad K = 3.16$$
$$L_{\max} = 8.7\,\mathrm{mm}$$

The higher value of $L_{\max}$ for Si is due to the high surface tension and the low density.

Normally, $L_{\max}$ is limited to several millimeters for most materials. According to Equation 3.19, $L_{\max}$ and the diameter of the crystal are independent of each other. However, in FZ configurations of many growth systems, the maximum diameter cannot exceed the zone length. Otherwise, a solid bridge between seed and feed crystal may be formed.

For technical applications, FZ silicon can be grown with diameters up to 200 mm by the use of additional magnetic fields to maintain diameters bigger than 15 mm.

The maximum growth rate is independent of the special growth process and growth configuration and can be easily explained from the heat flow balance, similar to Example 3.1 of the Si Czochralski process. Si FZ crystals with a diameter of 150 mm show maximum growth rates of about 3 mm min^{-1}.

Today, solar cells fabricated of FZ silicon exhibit the highest efficiencies of silicon-based cells.

In doped Si FZ crystals one always finds, due to the process of segregation, variations of the dopant concentration on a macroscopic as well as on a microscopic scale (compare Section 2.3). Macro- and microsegregations are influenced by flows in the melt zone. Apart from artificial sources, such as rotation and RF heating, these flows are caused either by the gravity-dependent buoyancy convection or by the gravity-independent Marangoni convection. As we have seen in Section 2.4, Marangoni or thermocapillary convection originates in the temperature difference of the surface tension along the free melt zone of the FZ configuration.

As a result of this temperature and flow inhomogeneities, local fluctuations on the crystal composition with spacing ranging from a few micrometers up to several hundred micrometers are present (compare Section 2.3.2). The differences in dopant concentrations may reach up to 40% and are normally not suited for applications of any kind. The description and investigation of "dopant striations" or just "striations" started in the early 1950s.

A reduction of those dopant striations may be achieved by controlling the flow pattern in the melt of a FZ configuration. Two main approaches to control the mechanism for flow instabilities may be pointed out:

- damping the fluid flow and lowering the flow velocities below the critical values,
- superimposing a forced convection of a well-defined velocity and an axis of symmetry.

To reduce flow instabilities, it follows from the Navier–Stokes equation (Equation 2.4) that either the Rayleigh number or the Marangoni number in the case of free melt surfaces has to be reduced. An additional force has to be introduced to transfer the instationary flow conditions in a stable, well-defined flow pattern. In the case of a laminar flow structure within the melt, dopant striations may be avoided.

Static Magnetic Fields for Fluid Flow Damping in Semiconductor Melts Figure 3.17a shows the principle behavior of a conducting material (melt flow of a semiconducting fluid) with a velocity v in a constant magnetic field with a strength B of several hundreds of millitesla. The movement of the conducting fluid generates an electromotive force $v \times B$, which leads to an electric current j in a direction shown in Figure 3.17a. The Lorentz force ($j \times B$) acts on each volume element, which is demonstrated in Figure 3.17b. The Lorentz force can be written as

$$f = \sigma(E + v \times B) \times B \tag{3.20a}$$

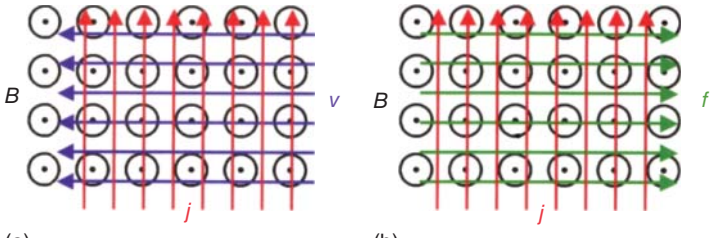

Figure 3.17 Coupling between electromagnetic fields and velocity fields in a semiconductor melt: (a) magnetic field B, velocity v, and direction of electric current j; (b) B, v, and direction of Lorentz force f.

For static magnetic fields and fluids with a high electric conductivity σ and for low velocities in the fluid, the generation of local electric fields is negligible. In this case, we have for the Lorentz force:

$$f = \sigma(v \times B) \times B \tag{3.20b}$$

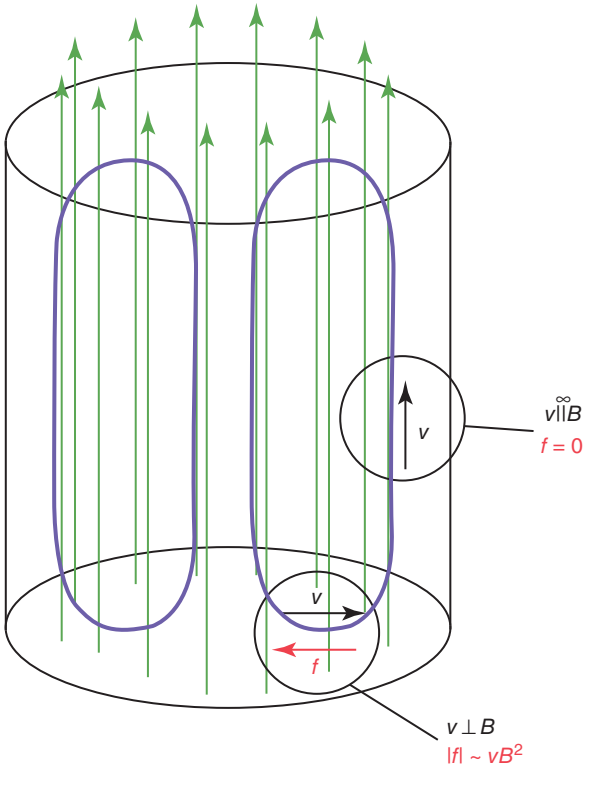

Figure 3.18 Action of Lorentz force in a float zone configuration with two basic flow structures.

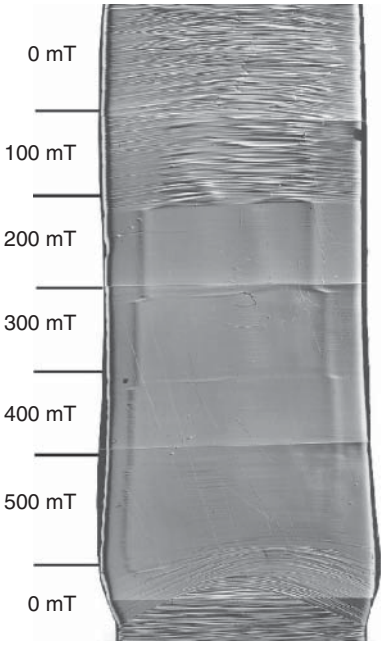

Figure 3.19 Nomarski differential interference contrast (NDIC) micrograph of an etched axial cut of a FZ Si:P crystal grown under different static axial magnetic fields ranging from 100 to 500 mT in 100 mT steps. Phosphorus concentration $c_0 = 6{\cdot}10^{17}$ cm^{-3}. (Reprinted from Croell, A., Benz, K.W., [20], with permission from Elsevier.)

If we consider a floating melt zone with a cylindrical shape and two basic flow configurations in a static magnetic field B as shown in Figure 3.18, we can see the effected area of the Lorentz force f. If the flow velocity is parallel to the direction of the magnetic field B, we have $f = 0$, if v is perpendicular to B, f is given by Equation 3.20b and is opposite to the flow direction. In this case, we have a damping of the flow.

Therefore, the use of static magnetic fields in the FZ crystal growth experiments will result in a reduction or even complete suppression of time-dependent behavior of flows and, thus, weaken or eliminate dopant striations. The elimination of dopant striations by the use of a magnetic field is shown in Figure 3.19. The P-doped FZ Si crystal with an initial concentration of $c_0 = 6{\cdot}10^{17}$ cm^{-3} was grown in a static magnetic field with a strength ranging from 100 to 500 mT. The orientation of the crystal was <111> and the growth rate 4 mm min^{-1}. From 200 mT on, one can see a big reduction of the striation pattern to 500 mT. At the same time, the corresponding reduction of microsegregation can be measured as the reduction of relative concentration fluctuations from 8% to 3%.

Rotating Magnetic Fields for Fluid Flow Damping in Semiconductor Melts In 1917, Kuerth patented a method to stir a melt of a metal by the use of a rotating magnetic field (RMF). The first experiment was carried out 1933 in by Shtanko.

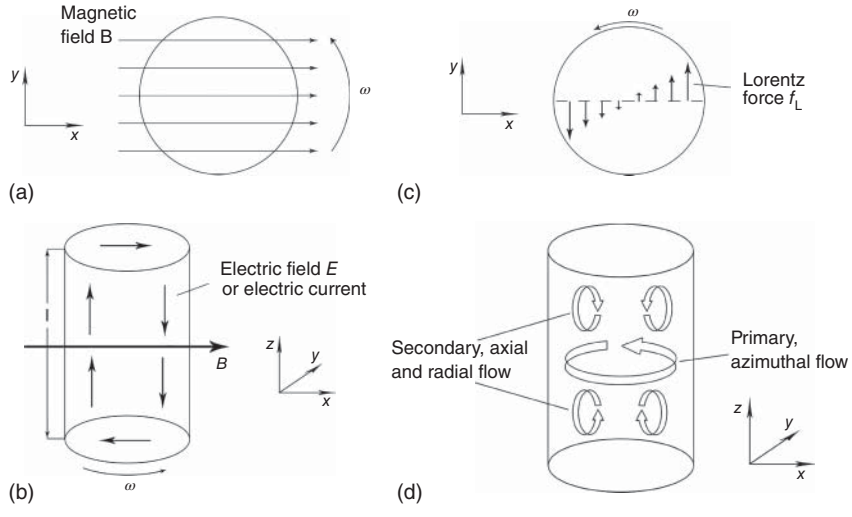

Figure 3.20 (a) Magnetic field lines rotate in the *xy*-plane, (b) induced electric current in an infinite and a finite cylinder, (c) acting Lorentz force f_L, and (d) initiated flow patterns.

Today, electromagnetic stirring by RMFs as well as by traveling or alternating magnetic fields is applied in the steel industry for steel casting processes. A very informative review was given by Birat and Chone [21].

For semiconductor melts within a zone-refining process, Mullin and Hulme used a RMF for the first time in 1958. A review book on the use of static and RMFs for crystal growth was published in 1999 [20].

The influence of an RMF on an electrically conducting melt is shown in Figure 3.20a. We assume a magnetic field rotating in the horizontal *xy*-plane with a frequency ω and acting on a cylindrical melt of height l and radius r. The magnetic field is given by

$$B = B_0(\sin(\omega t)x + \cos(\omega t)y) \tag{3.21}$$

The skin depth of the magnetic field (or penetration depth) should be larger than the radius of the melt.

An electric field E is induced perpendicular to the magnetic field B, leading to an electric current j (Figure 3.20b). The Faraday induction law gives

$$E = \omega B_0 r \sin(\phi + \omega t)z \tag{3.22}$$

Perpendicular to the current j, a Lorentz force f_L is generated (Figure 3.20c):

$$f_L = \sigma(E + v \times B) \times B \approx \sigma(E \times B) \tag{3.23}$$

σ is the electric conductivity.

The angular rotation frequency ω of the magnetic field is higher than the flow velocities within the melt.

The time-averaged Lorentz force can be written in a reduced form as

$$f_L = (1/2)\sigma\omega B_0^2 r \tag{3.24}$$

The Lorentz force is a driving mechanism for a fluid flow in the melt. An azimuthally forced convection is initiated (primary flow) owing to the pressure gradients in the melt. Secondary rolls with axial and radial components are induced (Figure 3.20d).

In Equation 3.24, the strength and frequency of the RMF govern the forced convection and the residual flow pattern in the melt. In order to increase the Lorentz force in a melt configuration, the increase of the frequency of the magnetic field is an important option with respect to the power consumption of the growth facility.

The Lorentz force as a driving force for a melt flow increases with the melt diameter.

This is not the case for static magnetic fields.

Experiments in Low Gravity Environment The role of gravity as an important parameter in the field of crystal growth has been recognized more than 40 years ago. A variety of experiments have been carried out on board of various space flights [22, 23]. Examples are the American Apollo and Spacelab missions, the German D1 and D2 missions, the Russian MIR station or Foton flight, the European EURECA (**Eu**ropean **Re**trievable **Ca**rrier) mission, the International Space Station, and the German and Japanese sounding rocket programs. It is now a common understanding that gravity is one of the experimental parameters such as external forces or fields (compare Section 3.2.2), which may influence the fundamental crystal growth processes mainly via transport phenomena in the nutrients or detached growth in ampoules and containers.

As outlined in the previous sections, microgravity provides an excellent opportunity to study Marangoni convection (surface tension driven flows) without a remarkable influence of buoyancy-driven convection.

Scientific objectives of these studies are in common the explanation of the connection between crystal structure with well-defined physical properties and the parameters of the growth process. During crystal growth from nutrients, which means from melts, solutions, or vapor phase, gravity is playing an important role. Heat and mass transports are essentially influenced by convective flows.

The limited space and power consumption during the early microgravity experiments led to the development of well-defined growth facilities: mono-ellipsoidal as well as double-ellipsoidal mirror furnaces [24, 25] for floating zone growth techniques and resistance heater for the Bridgman method.

Figure 3.21a,b show the principle arrangement of a mono-ellipsoidal (a) and a double-ellipsoidal mirror furnace (b).

Crystal growth by the FZ technique involves a single crystalline rod, which is partially melted. The molten zone remains fixed between the upper and lower crystalline parts and is positioned in the lower focus of the mono-ellipsoidal mirror furnace (compare Figure 3.21a). It is molten by a halogen lamp (~1000 W), which is adjusted in the upper focus. The ratio of the mirror half axes is 90/80 mm. The weight of the liquid zone is limited on earth to about 10 mm owing to the weight of the molten zone. By increasing the diameter, the melt will drop down. In similar space experiments, there is no such limitation, and crystals with bigger

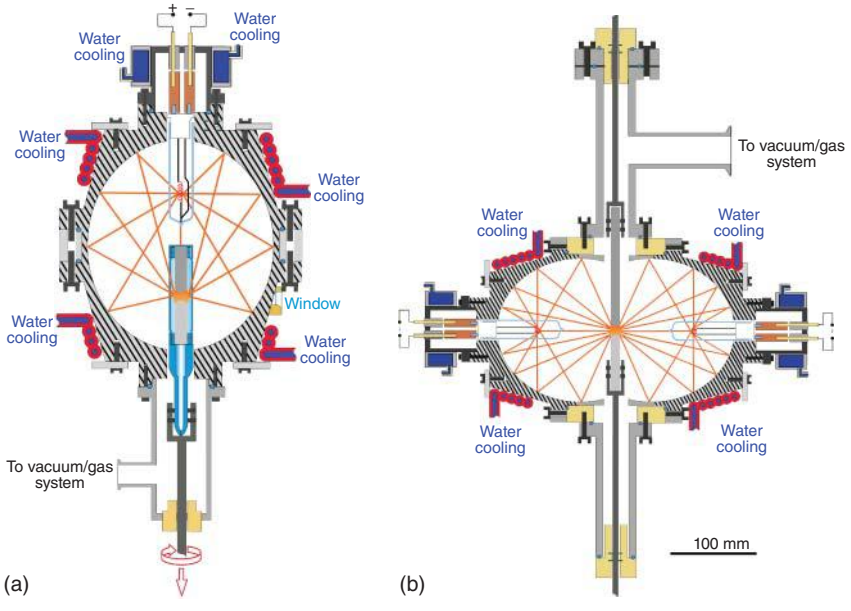

Figure 3.21 (a) Mono-ellipsoidal mirror furnace and (b) double-ellipsoidal mirror furnace. (Adapted from Benz, K.W. *et al.* [24] and Steinborn W., [25].)

diameter – up to 20 mm – may be grown. By moving the furnace with respect to the sample, crystallization at the advancing melt/seed interface is achieved. Simultaneously, feed material is dissolved at the feed/melt interface.

Figure 3.16 shows free Si melt zones on earth and in space (Figure 3.16a). The space experiments have been performed in a German rocket mission, TEXUS 29, **T**echnologische **Ex**perimente **u**nter **S**chwerelosigkeit, Technological Experiments under Reduced Gravity. The Si melt zone on earth is bottle shaped because of its weight.

First space experiments related to the growth of silicon crystals with free melt surfaces showed a strong convection in the melt and led to an inhomogeneous distribution of phosphorus dopants in the grown crystal (striations). The striation formation in the grown crystal was used as a proof for fluid dynamic processes within the molten Si.

Progress in crystal growth in general lies in sophisticated experiments to understand the basic transport mechanism in connection with the properties of the grown crystals.

In addition to scientific interests, such studies may be a basis for improving control and scaling-up terrestrial industrial processes.

Important results of the FZ experiments with silicon under reduced gravity in connection with 1 g-reference experiments are the following:

- Surface tension-driven convection is the dominant flow for the radiation-heated growth of silicon by the floating zone method. Dopant striations are caused by

time-dependent Marangoni convection. If the surface of the molten silicon is covered with a silicon oxide layer, the Marangoni convection can be completely suppressed. This holds not only for silicon but also for other melts and liquids. Bridgman growth experiments in quartz ampoules where the melt wets the inner ampoule do not exhibit Marangoni flows.

- The transition regime from a laminar flow to time-dependent convection could be evaluated by a series of microgravity experiments and 1 g-reference experiments.

Croell *et al.* [26] determined for silicon a Marangoni number:

$$Ma_{c2} = 150 \pm 50$$

This value could be confirmed by numerical simulations [27]. In follow-up experiments, it was possible to quantify the impact of Marangoni convection on the temperature field in the melt, the concentration distribution in the grown crystal, and the growth velocity during the crystallization process itself.

In case of Gallium antimonite, GaSb, the maximum zone height and diameter on 1 g conditions is restricted to about 7 mm. In the German–Canadian–Spacehab 4 mission, crystals with a diameter of 16 mm have been grown [28] (Figure 3.22).

Figure 3.22 Float zone GaSb crystals grown during Spacehab 4 mission (a,b). (c) 1g crystal for comparison. Possible maximum diameter: 7 mm. (Reprinted from Croell, A., [28], with permission from Elsevier.)

The larger melt zones under reduced gravity enabled to analyze the transition from laminar to time-dependent convection as well:

$$Ma_{c2} = 375 \pm 125$$

This critical value fits well in the Pr–Ma relation of Figure 2.37.

3.2.4 Bulk Crystal Growth from Metallic Solutions

Metallic solution growth will be described for a selection of III–V- and II–VI-semiconductors. Growth from metallic solutions exhibits some major advantages over melt growth techniques:

- low or reduced vapor pressure of the V or VI component due to a lower growth temperature,
- no or reduced reactions of the solution with crucibles or container materials,
- the lower growth temperature reduces the deviation from stoichiometric thermodynamic reasons, which may result in more perfect crystals.

Methods for the growth of crystals from metallic solutions are less used compared to crystals grown from the melt. The reason is the low pulling rate during crystal growth procedure when leaving the stoichiometric composition of the melt. This behavior may be seen in Figure 3.23 within the phase diagram of GaSb or InSb.

In both cases, growth is performed on the Ga-rich or In-rich site of the phase diagram. In the case of GaSb crystal, growth may be achieved around 800 K with an Sb content of about 10 at%. In the solution of a metallic group III solvent (Ga or In), the transport of the group V-solute is mainly governed by diffusion processes with low value of diffusion coefficients. The growth rate decreases drastically from several millimeters per hour to several millimeters per day.

Different solution growth techniques will be discussed in the following sections.

3.2.4.1 Traveling Solvent Method (TSM)

The traveling solvent method TSM is shown schematically in Figure 3.24 [29].

A thin solution zone passes through a crystal when a strong temperature gradient is applied. The lower crystal in Figure 3.24 is used as a well-prepared seed. The metallic solution, which is placed between seed and upper feed material, advances through deposition of material at the cooler seed/solution interface. The material is dissolved from the receding feed at the solution/feed interface at higher temperatures.

The interesting point is that crystal growth is achieved without any movement of the crystal or the heater. The migration of a solution zone within TSM has been analyzed by Tiller in 1963 [30]. The traveling rate of the solution zone is proportional to the temperature gradient and depends on thermal conductivity of the solid material and the liquid, as well as upon the atomic kinetics of the freezing

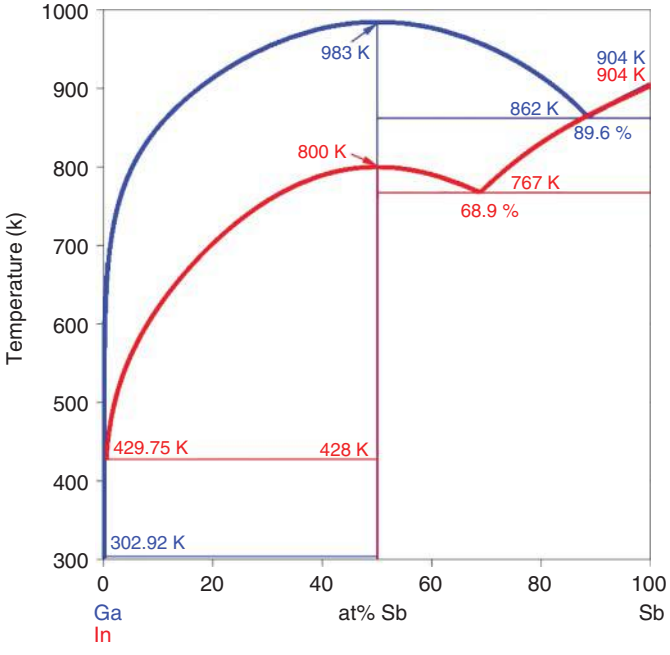

Figure 3.23 Phase diagrams of GaSb and InSb.

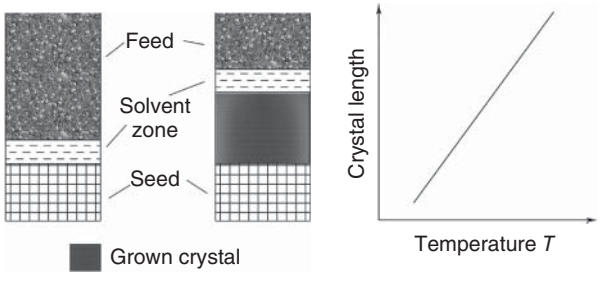

Figure 3.24 Traveling solvent method (TSM; schematically).

and melting process. If $v \times l \ll 1$ (v is the traveling rate of the liquid zone, l is the zone length), the influence of diffusion in the zone can be neglected.

In former time of semiconductor technology, TSM has sometimes been used in the preparation of small-area well-defined crystals and large-area abrupt-rectifying pn-junctions. Binary and ternary III–V-semiconductors have been grown by TSM: for example,: GaAs, GaSb, GaP, and (Ga,In)P. In the case of GaAs, the growth temperature was about 900 °C and the temperature gradient 60–80° mm^{-1}. For GaP within the same temperature range, a temperature gradient of about 200 °C was necessary before significant zone traveling occurred.

An interesting feature of TSM growth is the fact that the dislocation density in the grown crystal can be reduced during growth compared to the seed crystal.

The effect occurs measurable for seed crystals with a dislocation density above $10^4\ cm^{-2}$ within the first 150–200 µm of growth. In the case of a planar growth interface, the mechanism of dislocation removal after the beginning of TSM growth can be explained by either a closed loop formation or by a decrease through a transformation to other types of dislocations, which then propagate alongside to the crystal surface.

3.2.4.2 Traveling Heater Method (THM)

The principle of traveling heater method (THM) is shown in Figure 3.25 [29]. The solvent zone, which is placed between a solid seed crystal and the feed material, may be heated by a resistance heater, by RF heating, or by optical systems (laser heating or mirror heating facilities). By moving the growth ampoule with respect to the fixed heater, crystallization at the advancing seed/metallic solution interface may be achieved. Simultaneously, feed material is dissolved at the feed/metallic solution phase boundary. THM growth has been applied to binary and ternary III–V- and II–VI-compounds. Table 3.1 depicts experimental THM data of several III–V-compounds.

Depending on the zone length, different shapes of the growth interface may be obtained. Figure 3.26 shows the shape of a solidified Ga–Sb solution zone with an effective zone length of 8 mm (a) and 5.5 mm (b). The shape of the interface is

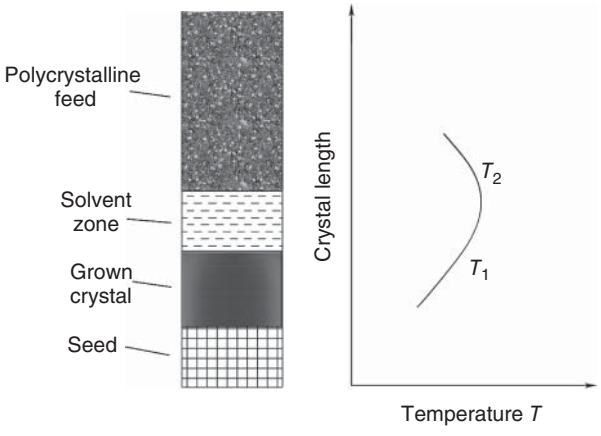

Figure 3.25 Traveling heater method (THM; schematically).

Table 3.1 THM growth of several III–V-semiconductors.

	Melting temperature (°C)	Solution zone (°C)	Traveling rate (mm d^{-1})
GaSb	712	400–600	2–3
GaAs	1238	850–950	1.5 (900 °C)
InSb	500	400	2.0
InP	1070	750–850	≤2.0

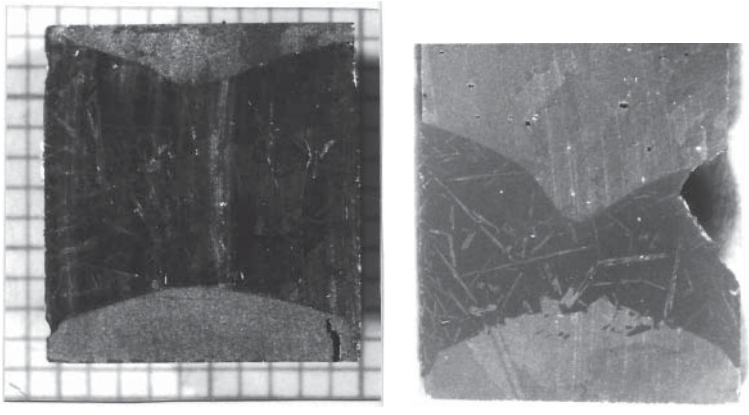

(a) (b)

Figure 3.26 Cross sections of solidified Ga–Sb-solution zones: (a) zone length 8 mm and (b) zone length 5.5 mm. (Reprinted from Benz, K.W., Bauser, E., [29], With kind permission of Springer Science + Business Media.)

important for the success of the crystal growth process. Is the length of the solution zone higher than the effective heater length, a concave interface solid/liquid will be stabilized. This is not practical for a crystal growth process because defect structures can be grown from the ampoule wall inside the material. With a smaller zone length compared to the effective heater length, a convex shaped interface may be formed.

Such an interface is an important basis to achieve a grown crystal with well-defined crystallographic and physical properties. Growing with a convex interface reduces the dislocation density of a seed crystal from about 10^5 cm^{-2} to below 10^3 cm^{-2} within 10 mm growth. A sharp decrease of dislocation density, measured as EPD, within 1–2 mm after the start of growth with <111>-oriented seed crystals can be attributed to the mutual annihilation through dislocations. This annihilation mechanism due to the high dislocation density of the seed crystal is found either in pairs of dislocations of opposite Burger's vector annihilating one another by forming a loop or by their transformation into other types of dislocations, which grow alongside the surface. In the region above 2 mm from the seed, the decrease of EPD is lower and can be explained by an outgrowth via the convex interface.

Example 3.3: The materials transport within the solution zone (antimony in liquid gallium), and as a consequence, the crystal growth rate is mainly governed by a diffusion process. As it can be seen from Table 3.1, the growth rates of III–V-compounds in THM experiments are very similar between 2 and 5 mm day^{-1}. In explaining a value of a maximum growth rate, we may assume diffusion-controlled solute transport.

A relation between the diffusion coefficient D of the solute Sb in the liquid zone and the maximum growth rate v_{max} can be calculated by taking the steady-state

diffusion equation and the conversation of mass. The steady-state diffusion equation can be written as

$$D\frac{dC^2}{dz^2} + v_{\max}\frac{dC}{dz} = 0 \tag{3.25}$$

where D is the diffusion coefficient of Sb in Ga melt, C is the Sb concentration, and $v_{\max}$ is the maximum growth rate.

The equation of mass conservation is

$$D\frac{dC}{dz} + [C_g - C_0]v_{\max} = 0 \tag{3.26}$$

where C_g is the concentration of Sb at the growth interface, C_s is the concentration of Sb at the seed/solution interface, and C_0 is the Sb concentration in the solid.

The diffusion coefficient can be written as

$$D = v_{\max} \cdot h \cdot \ln\frac{C_g - C_0}{C_s - C_0} \tag{3.27}$$

h is the effective length of the liquid zone.

C_g and C_s are taken from the Ga–Sb phase diagram (Figure 3.23) using the measured temperatures T_g and T_s from the calibration experiments. With a solution temperature of about 500 °C, a value of $D = 3 \cdot 10^{-4}$ cm^2 s^{-1} can be calculated. This value is an order of magnitude higher than the diffusion coefficient of Sb in liquid Ga [30]. Therefore, we may assume that, in addition to diffusion, the solute transport in the liquid Ga zone is supported by natural convection.

THM Experiments in a Microgravity Environment The principal objectives of past space experiments was to study the origin of chemical inhomogeneities at a macroscopic (axial and radial segregations) and a microscopic level (striations) in connection with fluid dynamics in the metallic solution.

The details of those inhomogeneity structures are described in Chapter 2. Several experiments have been performed in microgravity to grow single crystals from metallic solutions by the THM for various semiconductors, including Ge, GaAs, InP, CdTe, and ternary compounds. During the German Spacelab Mission D1 (30 October 1985), GaSb and InP THM crystals were successfully grown. Growth rate and growth temperature were taken from 1 g-reference experiments and may be compared in Table 3.1.

InP crystals were sulfur doped ($\sim 10^{19}$ cm^{-3}) in order to study the origin of dopants and compositional inhomogeneities (striations) and defects.

The earth-grown reference crystals show a sulfur concentration as a function of the grown length, which does not follow the diffusion-controlled model of Example 3.1. This behavior is due to the influence of natural convection, which also leads to an irregular striation pattern similar to the seed crystal of Figure 3.27. Such irregular striations are called ***type I striations***.

Figure 3.27 shows a cross section of an InP THM crystal grown in space during the German Spacelab mission D1 in 1985. The seed crystal grown by Czochralski method shows strong striations, which represents changes in the

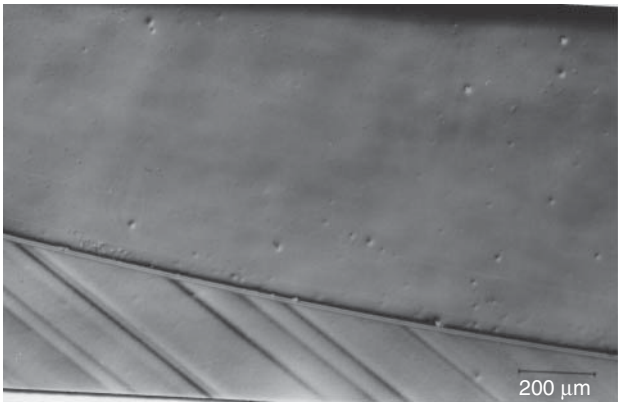

Figure 3.27 Etched cross section of a space grown sulfur-doped InP THM crystal. Seed crystal with striation pattern and grown crystal without convective striations (***type I striations***). Sulfur concentration about 10^{19} cm^{-3}. (Courtesy from A. Danilewsky, Crystallographic Institute, University of Freiburg.)

sulfur concentration. The grown crystal is more homogeneous due to the absence of time-dependent natural convection, which is demonstrated in the upper part of Figure 3.27. As a function of grown length, the sulfur concentration follows the diffusion-controlled transport model. Residual dopant inhomogeneities may be observed, which are associated with gravity-independent growth kinetics (***type II striations***). Such a result is shown in Figure 3.28. It is well known from LPE that a misorientation from the singular lattice plane, for example, (111) or (100), of the substrate crystal is an important parameter in achieving different growth mechanisms. Although facet growth occurs in a fast lateral movement of flat steps on well-oriented substrates (misorientation < 0.1°), the growth mechanism

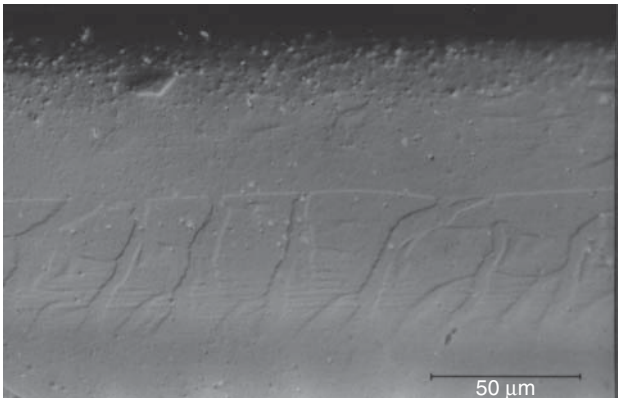

Figure 3.28 Macrostep formation in InP:S crystal with some distance of the seed crystal (seed off orientation >1°) and subsequent ***type II striations*** (S-shape). Not visible: if off-orientation >1°, macrostep formation starts directly at the seed. (Courtesy from A. Danilewsky, Crystallographic Institute, University of Freiburg.)

changes for certain misorientation to near facet and terrace growth. Terrace growth shows a slower lateral movement of macrosteps (compare Figure 2.17) at which the traces of the risers lead to ***type II striations*** [31]. The terrace may produce S-shaped striation segments in the grown THM InP crystal, which can be observed in Figure 3.28. A development of a growth terrace is followed by a subsequent stationary period and its final decay. Because ***type II striations*** are closely related to morphological instabilities, their formation is, therefore, gravity independent. Without disturbances from the time-dependent flows in the metallic solution, it has been possible to measure and calculate a critical growth velocity that is responsible for the formation of ***type II striations***. The critical growth rate for the macrostep formation could be measured to $5\,\mu m\,min^{-1}$. In microgram InP crystals, type II striations occur for growth rates of $9-10\,\mu m\,min^{-3}$. For details, compare Ref. [31].

3.2.4.3 The Solute, Synthesis, Diffusion Method (SSD)

The solute, synthesis, diffusion (SSD) method has been developed by Kaneko *et al.* in 1973 [32] in order to grow high quality GaP crystals and to avoid at that time the expensive high pressure growth apparatus used in the Czochralski liquid encapsulation technique.

The principle setup of the SSD method is shown in Figure 3.29. A crucible containing liquid Ga is placed in a quartz glass tube and positioned in a temperature gradient $T_2 - T_1$.

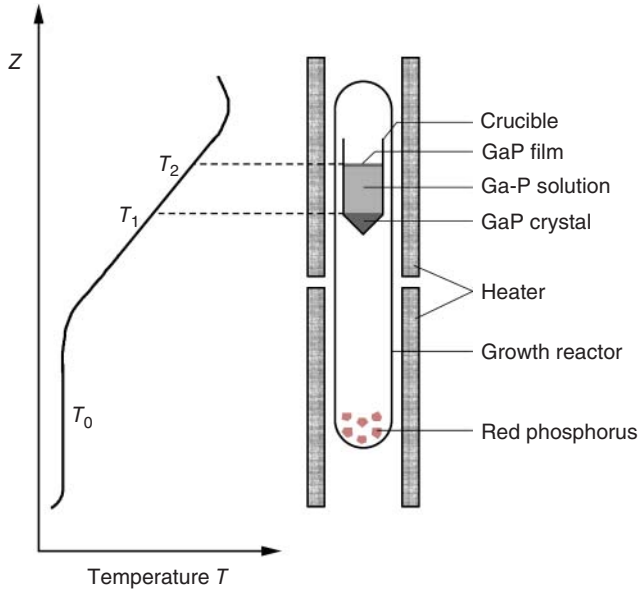

Figure 3.29 Principle of synthesis, solute, diffusion (SSD) method for the growth of high quality GaP crystals. (Redrawn after Benz, K.W., Bauser, E., [33], With kind permission of Springer Science + Business Media.)

The upper liquid Ga surface is exposed to P vapor of about 1 bar. To achieve this pressure value, the red phosphorus must be kept at about 420 °C. GaP synthesized at the Ga surface dissolves in the liquid Ga, and the solute diffuses downward and saturates at the bottom. The crystal starts growing from the bottom. To maintain the GaP film at the surface of the Ga melt, the phosphorus vapor pressure must be higher than the dissociation pressure of GaP at the temperature T_2. Similar to TSM, no moving parts are necessary in SSD growth.

Several modifications to the growth arrangement of Figure 3.29 are possible:

- A charge travel identical to the growth rate can be used, and a constant temperature T_1 (Figure 3.29) can be maintained at the growing interface.
- By using a seed crystal at the bottom of the crucible, growth may be initiated as a single crystal.
- On top of the growth reactor, a condenser to trap the surplus phosphorus can be placed.

A seeding technique has been mainly used for the SSD growth of GaP crystals [32, 33]. The solution temperature in these cases is 1065–1130 °C; the temperature gradient is between 10 and 120 °C. The growth rate varied from about 1–5 mm day^{-1}. The grown crystals were around 30 mm in diameter and 50 mm in grown length. The formation of solvent inclusions in the grown crystals is often a problem within the SSD technique. This can be explained by the existence of the well-known effect of constitutional supercooling. For inclusion-free material means that, in a growth experiment, a certain travel speed related to a certain temperature gradient is maintained.

The low travel rate of the SSD method is a special disadvantage of this technique and cannot easily be improved. To overcome this problem, one has to operate several systems in parallel. Several materials with a high vapor pressure [e.g., III–V-compounds with a high vapor pressure of the V-component (In, Ga)P, etc.] at the melting point may be grown at lower temperatures by the SSD method.

3.3 Bulk Crystal Growth of II–VI Compounds from the Vapor

Growth techniques from the vapor are simple to realize. Crystal growth starts near the thermodynamic equilibrium. II–VI-compounds, similar to other materials, exhibit below the melting point reasonable vapor pressure values. This holds for cadmium as well as for chalcogen elements. Materials of interest are CdTe, CdSe, CdS, or the ternary compounds Cd (Te, Se) and (Cd, Zn)Te.

Applications for these materials are X-ray detectors (CdTe), optic parametric oscillators (CdSe), and electro-optical modulators and switches (CdS).

There are three main PVT techniques:

- The *closed ampoule PVT system.* There is no exchange between reaction chamber and surroundings (compare Figure 3.30a).

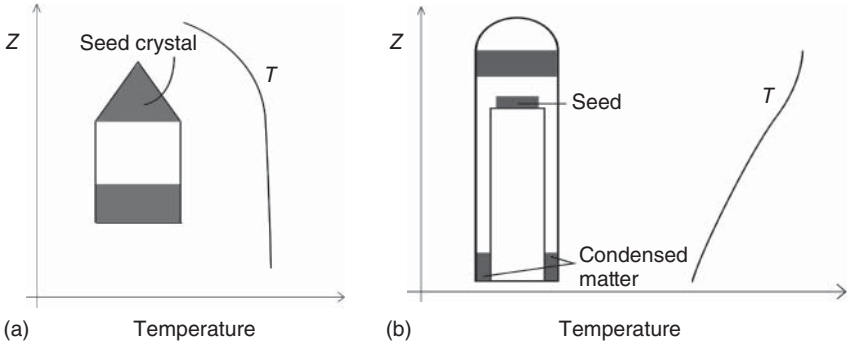

Figure 3.30 Growth ampoules for closed (a) and semiclosed (b) physical vapor transport.

- The *semiclosed PVT system.* Materials exchange between the growth chamber and a reservoir (compare Figure 3.30b).
- The *open ampoule PVT system.* A carrier gas flows through the reactor and governs the material transport.

During PVT growth, the following steps are applied: (i) evaporation of the solid source material, (ii) mass transport through the vapor phase, and (iii) finally, condensation of the vapor at the growing interface. The growth of cadmium chalcogenides such as CdTe or CdSe is generally transport limited. Therefore, properties of grown crystals, crystalline quality in general, and size of crystals must be studied in connection with mass transport phenomena. During growth, a cadmium chalcogenide sublimes as cadmium and diatomic molecule of the chalcogen.

The stoichiometric compound CdTe of the source material or feed evaporates incongruent owing to:

$$2\mathrm{CdTe(s)} = 2\mathrm{Cd(g)} + \mathrm{Te_2(g)} \tag{3.28}$$

where s is the solid and g is the gaseous with an equilibrium constant:

$$K_\mathrm{p} = p_\mathrm{Cd} \cdot \sqrt{p_{\mathrm{Te}_2}} \tag{3.29}$$

and

$$p_\mathrm{Cd}/p_{\mathrm{Te}_2} = 2 \tag{3.30}$$

where $p_{\mathrm{Cd},}\, p_{\mathrm{Te}_2}$ are the partial pressures of Cd and Te, respectively.

The total pressure in this case reaches a minimum. The maximum congruent sublimation point is at $T = 1324\,\mathrm{K}$ after the study by Greenberg [34]. Small deviations δX_Te in Te from the congruent sublimating composition lead to a variation of $p_\mathrm{Cd}/p_{\mathrm{Te}_2}$ by orders of magnitude.

During PVT growth in a closed ampoule, uncontrolled deviation from the composition of stoichiometric gas phase may occur in addition to an irreproducible change in the growth rate. Therefore, the control of the composition in the gas phase is essential for PVT bulk growth of II–VI-compounds. Good results may be obtained by using an ampoule as shown in Figure 3.30b, schematically.

In this arrangement, the ampoule is not sealed off initially. During growth, the excess vapor escapes through an inner quartz tube, which extends far enough into the cooler part of the furnace and condenses at the lower part of the outer tube, sealing off the complete crucible.

In the following, we will describe a crystal growth technique using a closed quartz glass ampoule system as well as a semiclosed ampoule arrangement.

3.3.1
Crystal Growth of CdTe by a Sublimation Traveling Heater Method, STHM, in Closed Ampoules

A sublimation traveling heater method (STHM) with a vapor zone instead of a metallic solution zone as in THM may be used to grow undoped or halogen-doped CdTe bulk crystals or other binary and ternary II–VI-compounds. The ampoule setup is shown in Figure 3.31. It consists of a sealed quartz ampoule with an inner diameter of 15 mm.

Furthermore, the ampoule contains several quartz plugs, the undoped <110>-oriented seed and the undoped or halogen-doped feed, leaving up a free volume corresponding to that of the vapor zone to be formed. In addition, a thin Pt sheet is used as a primary radiation reflector, whereas a Ni net shrouding the ampoule served as a radiation absorber to achieve a leveling-off of the temperature profile. The latter is used to prevent temperature fluctuations, which may cause growth instabilities.

At the first stage of growing the CdTe crystal, the initial feed cone (Figure 3.31a) is kept stationary at the maximum temperature of about 900 °C to obtain a 8 mm vapor zone.

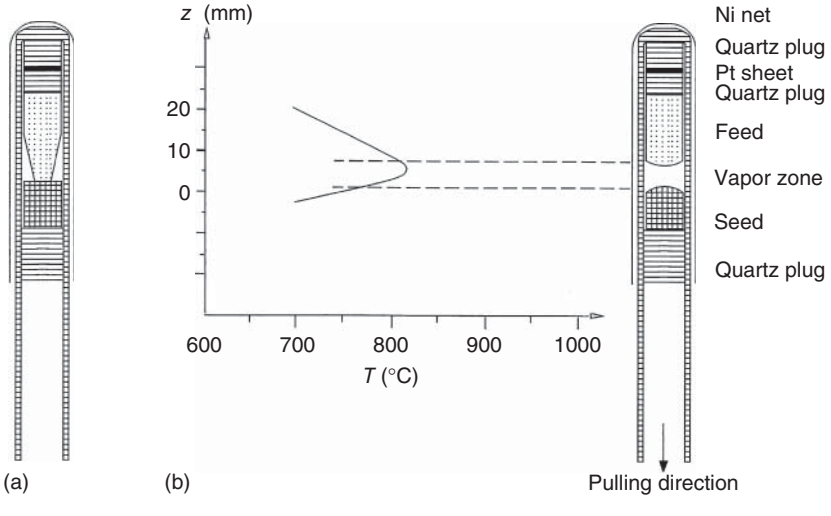

Figure 3.31 Sublimation traveling heater method. Growth ampoule and temperature profile: (a) initial stage and (b) after vapor zone stabilization. (Redrawn after Laasch, M. *et al.*, [35], with permission from Elsevier.)

Deposition of resublimating material between the upper part of the cone and the quartz wall guarantees a stable support of feed in the growth ampoule (Figure 3.31b). After controlled etching the seed surface by 2–3 mm, the growth process is started by pulling the ampoule downward. The pulling rate is about 2 mm day^{-1}. The crystal diameter is about 15 mm, and the length of the vapor zone reaches 8 mm.

The composition of the vapor phase and the behavior of the component's pressures have a strong influence on the transport properties as well as on the quality of the grown crystals. Small stoichiometry deviations of the solid toward Te-rich or Cd-rich composition affect the partial pressures of Cd and Te_2 considerably, as we have seen at the beginning of this chapter. Considering the line of congruent sublimation within the phase diagram determined by Greenberg [34], congruent sublimation only occurs in a small composition range ($0.0008 < \delta_{Te} < 0.002$ at% at $850 \leq T \leq 950$ °C) [36].

Looking at the material transport from feed to seed by using the vertical sublimation arrangement with a closed STHM quartz ampoule, we have to consider Stefan's flow, diffusion, thermal diffusion, and convective flows. It could be demonstrated that diffusion and Stefan flow are dominant in materials transport from feed to seed.

Stefan's flow is a transport phenomenon dealing with the movement of a chemical species by a flowing fluid in a gas phase. The flow is induced by the production or removal of the species at an interface.

This flow process was introduced by the Slovene physicist Joseph Stefan for his early work on calculating evaporation rates. When concentration gradients of the species are also present, diffusion transports the species relative to a mean flow. The total transport rate of the species is then given by the sum of Stefan's flow and the transport by diffusion. It could be shown that turbulent flows in the STHM system can be neglected.

CdTe is an interesting material for radiation detector application. However, existing intrinsic defects require compensation by means of dopants to obtain high resistivity material. As dopants, chlorine, iodine, and bromine have been used in concentrations ranging from $1 \cdot 10^{18}$ cm^{-3} (Cl) to $2 \cdot 10^{20}$ cm^{-3} (Br and J) within the feed material.

Cl-doped CdTe crystals showed the best perfection. Several twins and inclusions could be visualized; up to 20 mm long crystals were grown. Br- and J-doped crystals showed after several millimeters of growth polycrystalline structures due to a forced curvature of the growth front, indicating thermodynamic instability.

The obtained resistivity values were in the range of $10^6 - 10^7$ $\Omega\,cm^{-3}$ of Br-doped and J-doped material; only Cl doping yielded about 10^9 $\Omega\,cm^{-3}$. Responsible for the high resistivity values in Cl-doped CdTe is the so-called A-center, a complex consisting of a Cd vacancy and a neighboring halogen atom ($[V_{Cd}{}^{2-}, Cl_{Te}{}^{+}]^{-}$) [37]. This complex was also detected in Br-doped and J-doped STHM materials.

During the EURECA mission in space [38, 39], two Cl-doped CdTe-STHM crystals of about 10 mm length were successfully grown. They showed a resistivity of about $3 \cdot 10^9 - 1.5 \cdot 10^{10}$ $\Omega\,cm^{-3}$ for the first time in a STHM CdTe crystal. Owing to

Figure 3.32 **Eu**ropean **Re**trievable **Ca**rrier, making possible the successful first EURECA mission from 31 July 1992 to 01 July 1993. STHM experiment CdTe:Cl AM 11/3. Growth temperature $T = 850\,°C$; grown length 11.3 mm. The free vapor zone may be seen in the upper part of the quartz ampoule. Ampoule diameter: 15 mm. Growth furnace: mono-ellipsoidal mirror furnace ELLI. (Courtesy from A. Danilewsky, Crystallographic Institute, University of Freiburg.)

the absence of gravity-dependent convection in the vapor zone, a homogeneous and well-defined crystal could be grown (Figure 3.32).

3.3.2
Crystal Growth of CdTe by the Markov Method in Semiclosed Ampoules

Thermodynamic and experimental studies in closed STHM ampoules [35] indicated the sensitive dependence of mass transfer and crystal perfection on the composition of feed material and gas phase. Smallest deviations of the evaporating feed from the congruently subliming composition cause significant transport-limiting diffusion barriers.

As a consequence, constitutional supersaturation may occur, which result in growth instabilities and polycrystalline growth.

Semiclosed growth systems as shown schematically in Figure 3.30b offer the possibility to control the vapor composition by means of thermodynamic or geometric parameters and may also lead to increased growth rates and improved crystal perfection. The understanding of a semiclosed system is the possibility to exchange material between the growth region and a heat sink. Growth area and heat sink are located within the same sealed quartz glass container. In addition, the use of a seed crystal without wall contact yields a considerable decrease in residual tensions during crystal growth. This semiclosed growth arrangement was introduced by Markov and Davydov [40]. Compared to growth by STHM, we expect an improved crystal quality.

The experimental procedure starts with 1 h annealing of 7 N cadmium and 7 N tellurium at 800 °C under 900 mbar hydrogen pressures. The growth ampoules are evacuated and filled with a mixture of argon and hydrogen. The crystal growth experiments are performed in a multizone resistance heater furnace using an ampoule design and temperature profile shown in Figure 3.33. The complete setup consists of a feed container, which is kept at about 850 °C and closed by a permeable silica disk at its base. The seed crystal, opposite

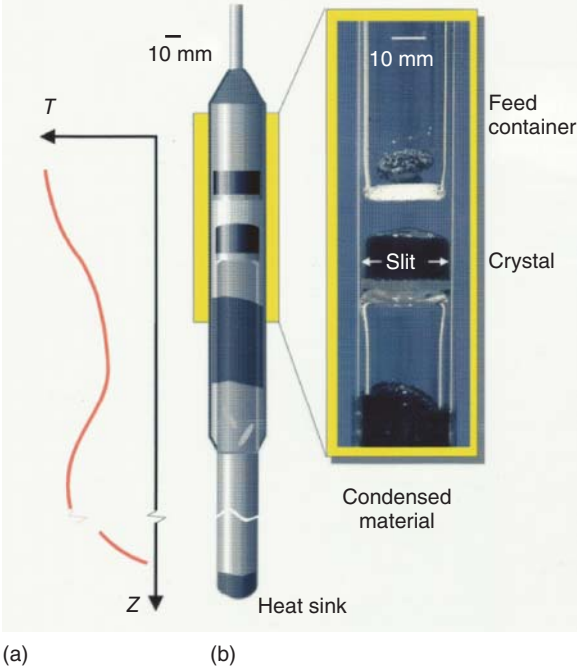

Figure 3.33 Semiclosed ampoule for the growth of undoped and doped CdTe crystals. (a) Temperature profile schematically and growth ampoule with heat sink. (b) Ampoule, magnified, with feed material, grown crystal with seed, and condensed CdTe material.

to the feed, is supported by a platelet of silica. The diameter of the platelet determines the diameter of the growing crystal and finally the ring-like gap between crystal and ampoule wall. This gap, which remains constant during the growth, connects the growth chamber with the heat sink (compare Figure 3.33).

Its width of about 0.5–1 mm is responsible for the amount of material condensing in the sink. The growth runs can be done without any movement of the ampoule.

In order to predict the transport rates as a function of temperatures, other relevant growth parameters (Gibbs enthalpy minimize software) has been used in connection with thermochemical data from Ref. [41].

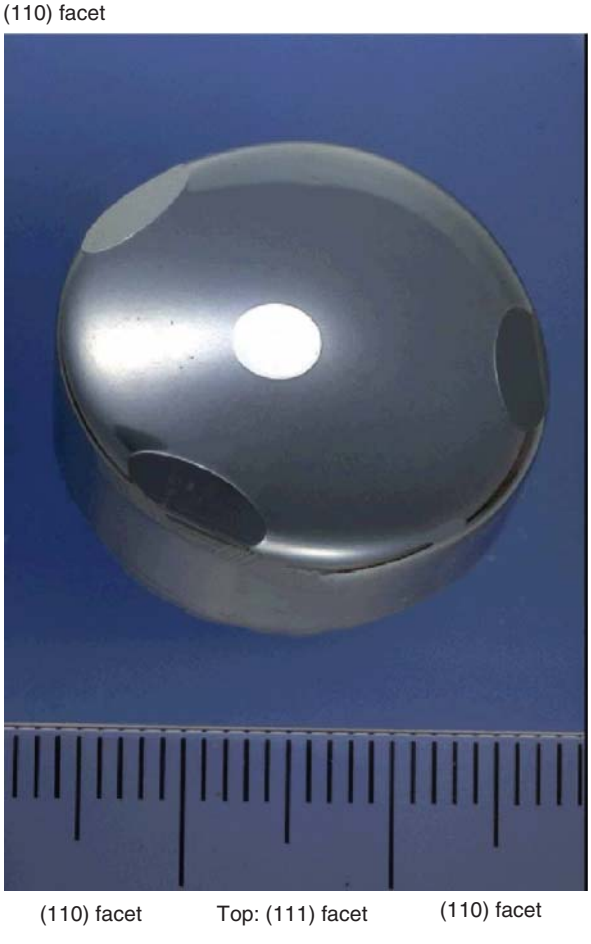

Figure 3.34 CdTe single crystal grown in a semiclosed system. The heat sink was about 100 °C. The growth rate was 1.2 mm day^{-1} at 8 °C cm^{-1} temperature gradient at the growing interface. Feed temperature 850 °C, seed temperature: ~830 °C. The scale is in millimeters. (Reprinted from Laasch, M. *et al.*, [41], with permission from Elsevier.)

The following important data have been achieved from these calculations: all essential parameters are nearly independent of feed material composition, if a heat sink with temperatures <300 °C is applied. Those parameters required to avoid interface instability are

- high growth rate,
- partial pressure ratio p_{Cd}/p_{Te} of 2, and
- low temperature gradient at the growing interface, the best condition.

The pressure control in the growth system by using a low temperature heat sink of about 100 °C leads to high growth stability. The macroscopic growth interface shows in this case a convex shape. Complete single crystals with a diameter of 15 mm and a length of 10 mm could be grown without twins and inclusions, which can be seen in Figure 3.34. Perpendicular to the growth direction, one can see on top of the crystal the formation of a tetrahedral {111} facet. Further facets can be seen at the perimeter of the crystal.

3.4 Epitaxial Growth Techniques

The word epitaxy is derived of the Greek language. "Epi-" means "on" or "over" something and "taxis" means "to arrange" or "to align." In the field of material science, atoms may be arranged regularly on a surface that a crystal structure may be formed. The atoms that are deposited on a single crystalline substrate will be arranged in the structure of the substrate. If the layer has the same atoms as the substrate, the epitaxial process will be called *homoepitaxy*. Is the grown layer another type of material as the substrate, we call it *heteroepitaxy*.

Figure 3.35 shows the processes on an atomistic scale on the surface of the substrate when an epitaxial layer is grown. Atoms that will start to form an epitaxial

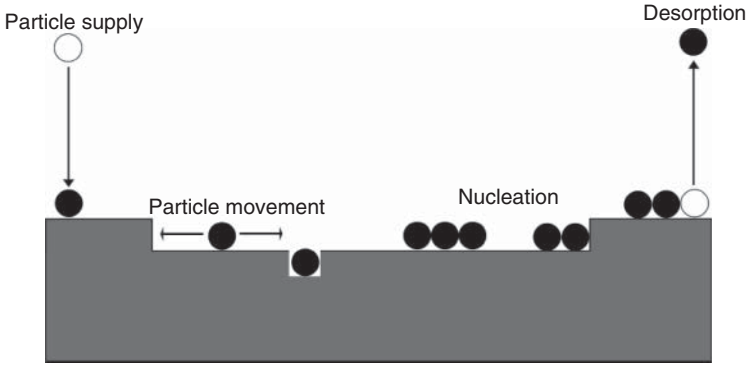

Figure 3.35 Epitaxial growth on the surface of a substrate: possible processes on atomic scale.

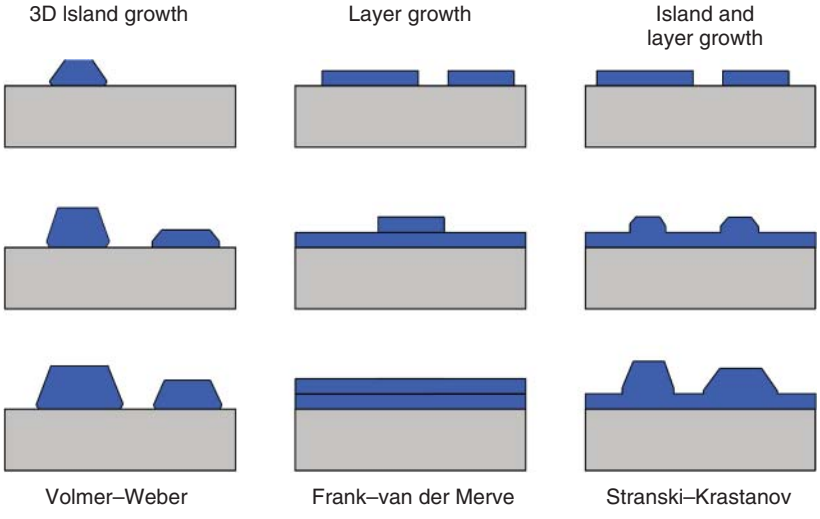

Figure 3.36 Different growth modes of epitaxial layers.

layer may attach at the substrate surface. They have also a chance to be desorbed from the surface. The attached atoms are mobile and may diffuse on the surface. Their mobility increases with increasing temperature. The final attachment at the surface can be realized at steps or crystal defects, which is shown schematically in Figure 3.35.

There are different possibilities to grow up an epitaxial layer, which is shown in Figure 3.36.

In the case of Volmer–Weber mechanism, the binding energy between the mobile atoms is higher than between these atoms and the substrate atoms. Three-dimensional islands are formed on the substrate surface. Is the binding energy between the layer atoms and the substrate atoms greater than between the layer atoms among each other, we will have the growth of a monolayer (Frank–van der Merwe growth). If one layer is complete, the next one will follow. A mixed form of both the growth mechanisms is given by the growth after Stranski and Krastanov. At first, one or several monolayers are formed, followed by an island growth.

As discussed earlier, homoepitaxy is performed with only one material. Normally, a single crystalline film is grown on a single crystalline substrate. The main reason to use such a growth technology is to produce a film, which has a much higher purity than the substrate.

An additional important fact is that one may also grow layers with well-defined dopants. Dopant concentrations in the range from 10^{12} up to $10^{20}\,cm^{-3}$ can be easily achieved.

Examples are epitaxial silicon layers on silicon substrates to fabricate transistor devices with abrupt doping profiles. Such profiles can often not be produced by diffusion or ion implantation.

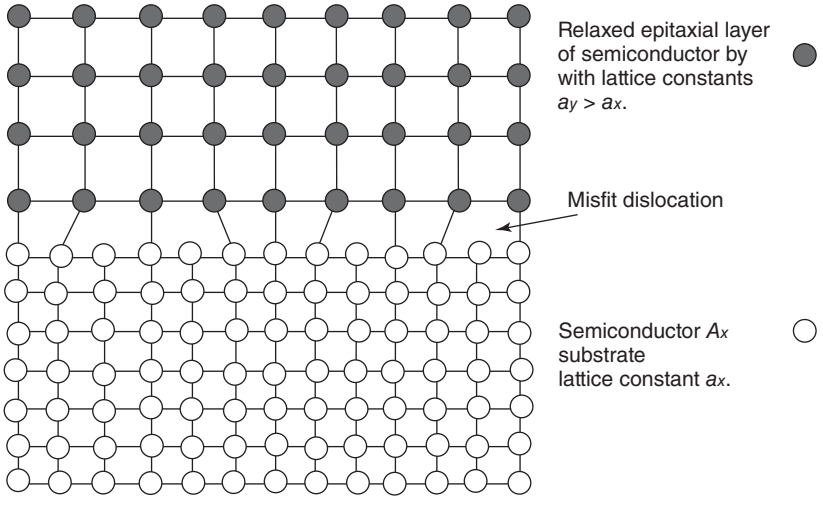

Figure 3.37 Heteroepitaxy: formation of misfit dislocations if lattice constants of substrate and layer are different. Compare Section 4.1.3, Figure 4.19.

In the case of heteroepitaxy, substrate and epitaxial layer have different lattice constants.

As a result, a tension is built up in the epitaxial layer. Is the lattice constant of the layer smaller compared to the substrate, a tensile stress is built up. A compressive stress is active if the lattice constant of the layer is bigger. Such configured tensions at the beginning of layer growth may be compensated by the formation of defects within the crystal structure (compare Section 4.1.3). Figure 3.37 demonstrates this possibility by the set up of misfit dislocations. Several crystal planes of the substrate end at the interface substrate/epitaxial layer.

An example of an application of heteroepitaxy is the system (Ga, Al)As on GaAs, an important representative of the III–V-semiconductors. By changing the composition x of $Ga_xAl_{1-x}As$, one can change the bandgap energy of the new material and, therefore, the emission wavelength of LEDs and lasers. The variation of photon emission energy of ternary and quaternary III–V-semiconductors is shown in Figure 3.38.

In the following section, we will describe the principle mode of operation of the following technical important epitaxy processes:

- LPE
- VPE, CVD
  - Effer method
  - Tietjen method
  - MOVPE
- MBE.

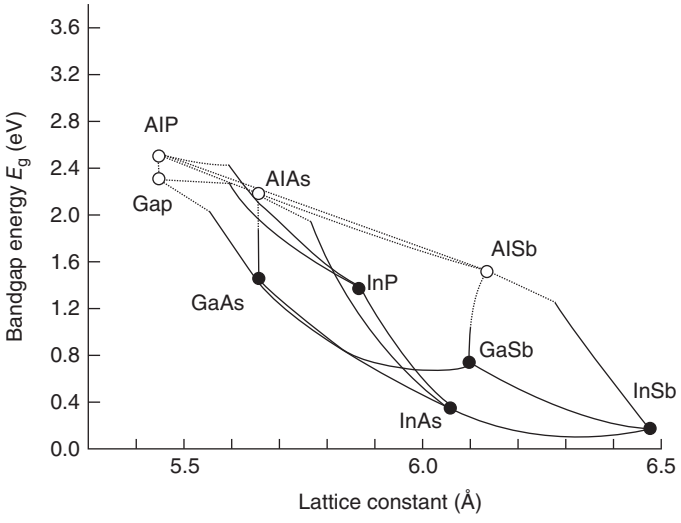

Figure 3.38 Bandgap energy as function of lattice constant of different III–V-semiconductors with zincblende structure: ----------○ indirect bandgap; ----------• direct bandgap.

3.4.1
Liquid Phase Epitaxy (LPE)

LPE, an important solution growth method, has been widely applied to composite semiconductor materials in particular to binary, ternary, and quaternary III–V-semiconductors such as GaAs or InP or related compounds. LPE of GaAs has been investigated intensively from the mid of 1960s. There was an upcoming interest in the development of optoelectronic devices, lasers, and photodiodes. However, the quality and perfection of melt grown crystals did not meet the need for these optoelectronic applications. The growth system had to be able to produce materials with very low unintentional doping, which means a very low impurity concentration.

The growth of III–V-semiconductors from metallic solutions as thin epitaxial layers offered the possibility to build up optoelectronic devices with low carrier concentration and to create large depletion volumes in the devices.

A simple method to grow LPE GaAs has been successfully applied by Nelson in 1963 [6]. A GaAs substrate not in contact with a Ga–As–Sn solution is positioned in a graphite boat and brought in a furnace (compare Figure 3.39). The graphite crucible is heated up to 640 °C. After reaching this temperature, the power is turned off and the furnace tipped so that the molten Ga–As–Sn solution covered the exposed surface of the GaAs substrate. Then, the whole system is cooled down to about 400 °C, and finally, the furnace is tipped back to its original position. Immediately, the graphite crucible is removed, and any remaining solvent is wiped off the epitaxial layer (compare also Figure 3.41).

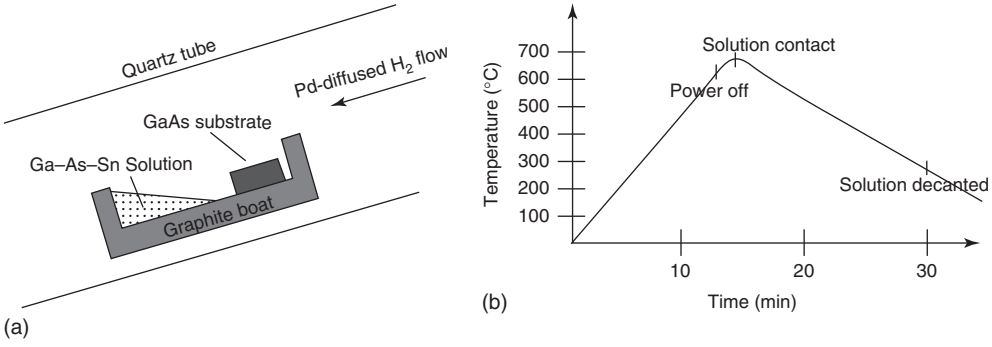

Figure 3.39 (a) Apparatus for LPE growth of GaAs from a Ga–As–Sn solution and (b) Heating schedule for epitaxial deposition of GaAs. (Adapted from Nelson, H., [6].)

The experimental procedure shows that, in LPE growth, parameters can be easily controlled and properties of grown layer can be, therefore, readily reproduced. Careful attention, however, must be focused on all the above-described growth phases to insure that undoped and doped layers of well-defined thickness and flatness combined with low defect density can be grown.

The solvent has a strong influence on the properties of the epitaxial layer. In the case of III–V-semiconductors, normally, a group III element will be used. To grow GaAs, GaP, and GaSb, liquid Ga may be used as solvent. GaSb may be also grown from Sb solvent, but the growth regime on the Sb-rich site of the Ga–Sb phase diagram is relatively small due to the position of the eutectic point at 862 K (Figure 3.23). In summary, we can say that the solvent must dissolve sufficient quantities of the solute in order to obtain layers of usable thickness, and the growth of high purity layers requires solvents, which are themselves components of the solute. If other low melting solvents are used, such as Sn or Pb, atoms of the solvent are mostly incorporated to a high extent in the growing crystals and lead to a highly doped material.

Point defects in III–V-semiconductors (vacancies and interstitials) influence in a high degree their physical properties. The concentration of such defect depends on the composition of the metallic solution. Figure 3.40 depicts the existence regime of GaSb, the deviation of stoichiometry S as a function of temperature is [42]:

$$S = (N_{Ga} - N_{Sb})/(N_{Ga} + N_{Sb}) \tag{3.31}$$

N is the number of atoms.

S is more pronounced on the Ga-rich site compared to the Sb-rich site. This means that the concentration of Sb vacancies is higher than the concentration of the Ga vacancies. Similar results are obtained for GaAs.

Melt grown crystals show always a p-type behavior with a hole concentration of $p = 2 \cdot 10^{17}\ \mathrm{cm}^{-3}$. The reason is the existence of an antisite stoichiometric defect, a Ga atom on a Sb vacancy [Ga_{Sb}]. The formation of this defect may be

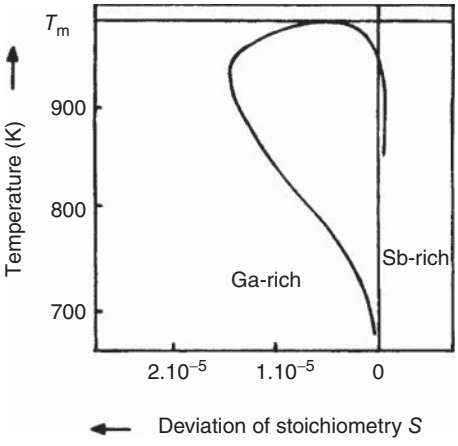

Figure 3.40 Deviation S of stoichiometry as a function of temperature for GaSb. T_m is the melting temperature of GaSb.

qualitatively explained by the fact that the covalent-tetrahedral radius of the Ga atom is smaller than that of the Sb atom, leading to this particular antisite defect. A successful reduction of this defect may be achieved by using a Ga solvent to grow crystals instead of a GaSb melt. The Sb concentration should be $\leq$30 at%.

Process Control and Layer Thickness Nelson reported a thickness of epitaxial layers of about 70 µm. Surfaces of the grown layers were rough because of the rapid growth in the low temperature range near the completion of the process. Large droplets of Ga were also noted at the interface. Goodwin *et al.* in 1968 [43] introduced a temperature gradient of about 10 °C cm^{-1} so that the seed was always colder than the solution by a fixed amount.

A "LPE-tipping system" was described by Bauser [29, 44] (compare also Figure 3.41).

We may now distinguish three methods of LPE growth: *step-cooling*, *equilibrium-cooling*, and *super-cooling*. Equations relating layer thickness to growth time can be derived for semi-infinite growth solutions by expecting that the rate of growth is diffusion limited.

Solution and substrate are in equilibrium at the interface [45] (Figure 3.42).

1) *Step-cooling*: Metallic solution is brought in contact with substrate at t'_A. $T_{growth} = T - \Delta T_S$. The metallic solution is supersaturated.
2) *Equilibrium-cooling*: Metallic solution is brought in contact with substrate at t_A. $T_{growth} = T(R)$. Growth from saturated solution with cooling rate R.
3) *Super-cooling:* Metallic solution is brought in contact with substrate at t'_A. $T_{growth} = (T - \Delta T_S) + T(R)$. Growth from supersaturated solution with cooling rate R.

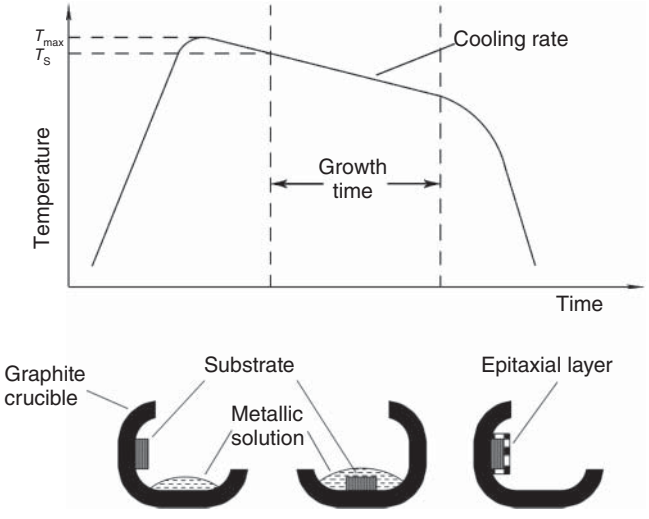

Figure 3.41 Temperature during one growth circle in a tipping furnace. The substrate is exposed to the solution at T_S. (Redrawn after Benz, K.W., Bauser, E., [29], With kind permission of Springer Science + Media.)

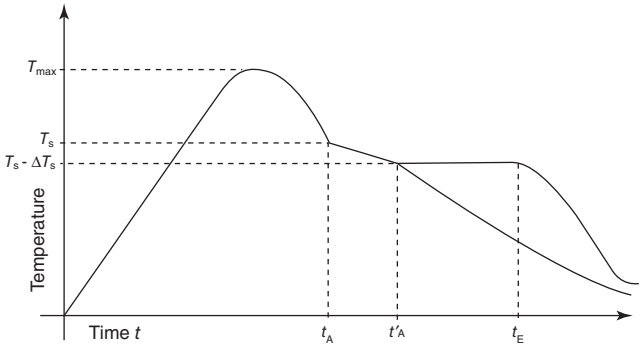

Figure 3.42 Temperature/time diagram to illustrate different LPE growth modes: step-cooling, equilibrium-cooling, and super-cooling.

Example 3.4: We will now calculate the thickness $x(t)$ of the grown layer as a function of the growth time t. At the interface substrate/solution, we may realize the following characteristics:

- c^* solute concentration at the interface (in the case of III–V-compounds, As, Sb, or P) in the solution
- $c_S = k \cdot c^*$ solute concentration in the substrate; k is the segregation coefficient
- $c^* + \Delta c = c_0$; Δc is the concentration of supersaturation.

Particle flow i at the advancing solid/liquid interface during growth:

$$i = -D\frac{\partial c}{\partial x} - vc \tag{3.32}$$

where v is the growth velocity and D is the diffusion coefficient of solute.

The continuity equation of LPE process with particle flow is

$$\frac{\partial i}{\partial x} + \frac{\partial c}{\partial t} = 0 \tag{3.33}$$

$$\frac{\partial c}{\partial t} = D\frac{\partial^2 c}{\partial x^2} + v\frac{\partial c}{\partial x} \tag{3.34}$$

The second term of this equation can be neglected for small growth rates usually achieved in LPE:

$$\frac{\partial c}{\partial t} = D\frac{\partial^2 c}{\partial x^2} \tag{3.35}$$

At the beginning of growth, we have $c(x,t)$ with $t = 0$ and at the interface $c(0,t) = c^*$

$$c(x,0) = c^* + \Delta c$$

$$c\,(x,t) = c_0 + \Delta c\ \ \mathrm{erf}\left[\frac{x}{2\sqrt{Dt}}\right] \tag{3.36}$$

Material flux and growth at the interface boundary $x = 0$

$$D\left.\frac{\partial c}{\partial x}\right|_{x=0} + c^* v = c_S v$$

$$D\left.\frac{\partial c}{\partial x}\right|_{x=0} = (c_S - c^*)\,v = c^*(k-1)v$$

$$\left.\frac{\partial c}{\partial x}\right|_{x=0} = \Delta c\frac{1}{\sqrt{\pi Dt}} \tag{3.37}$$

$$v(t) = \frac{\Delta c}{c^*}\frac{\sqrt{D}}{k-1}\frac{1}{\sqrt{\pi t}} \tag{3.38}$$

For the thickness of the grown layer, we have

$$x(t) = \int_0^t v(t)dt = \frac{2}{\pi^{\frac{1}{2}}}\frac{\Delta c}{(k-1)c^*}(Dt)^{\frac{1}{2}} \tag{3.39}$$

For III–V-semiconductors, we have

$$(c_S - c^*) = c^*(k-1) \quad \text{with } c_S = 1/2 \quad \text{and } c^* \approx 10^{-3}$$

$$\text{and} \quad m = \frac{dT}{dc} = \frac{\Delta T_S}{\Delta c}, \quad \text{Slope of the liquidus line}$$

$$\Delta c = \frac{\Delta T_S}{m}$$

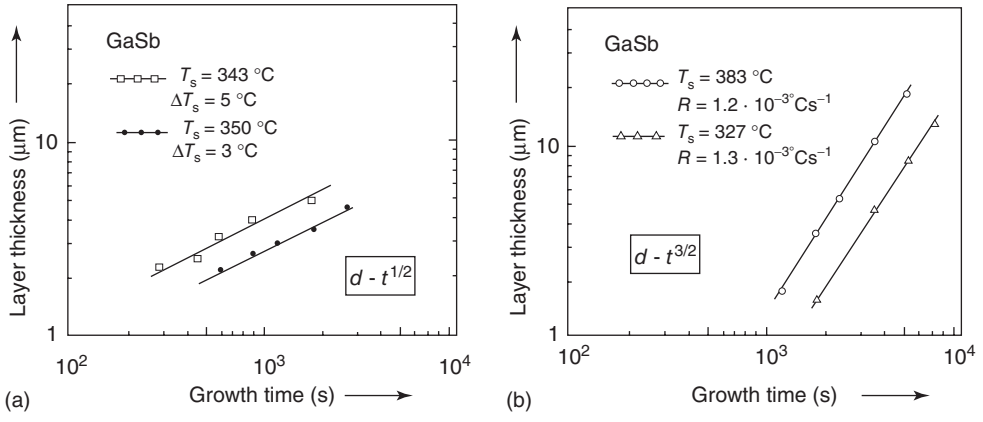

Figure 3.43 Layer thickness as a function of growth time for two growth modes: (a) growth from a supersaturated Ga solution and (b) growth from a saturated Ga solution with linear cooling rate.

We can write for ( )

$$x(t) = 2\frac{D^{\frac{1}{2}}}{\pi^{\frac{1}{2}}}\frac{\Delta T_S}{mc_S}(t)^{\frac{1}{2}} \tag{3.40}$$

$$x(t) \sim \sqrt{t}$$

The thickness of the grown epitaxial layer is proportional to $t^{1/2}$ (step-cooling process).

Growth from a saturated solution (equilibrium cooling) with an additional cooling rate R:

Boundary conditions: $c = c^*$ for $t = 0$ and $c = c^*$ for $t > 0$.

During growth, we have a linear cooling rate R:

$$T = T_S - Rt \tag{3.41}$$

Equilibrium concentration following the liquidus line from the phase diagram:

$$T = T_S - m\Delta c(t)$$
$$m\Delta c(t) = Rt$$
$$\Delta c(t) = R/mt$$

Solute concentration at the interface solid/liquid:

$$c(0,t) = c^* - R/mt$$

To calculate the thickness of the grown layer, we can write (as before):

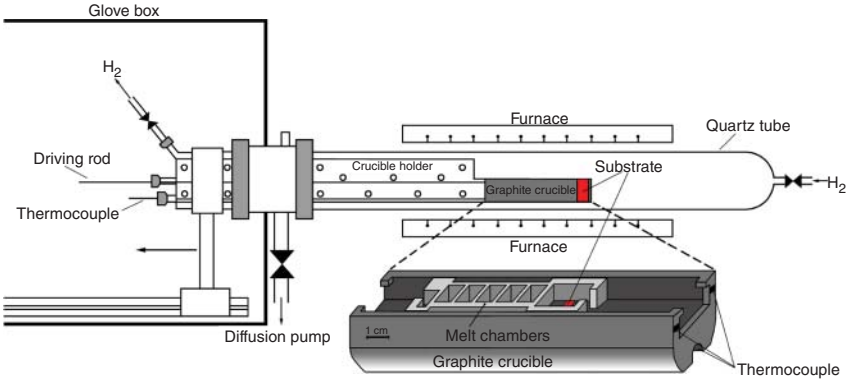

Figure 3.44 Multichamber LPE system for the growth of binary, ternary, and quaternary III–V-semiconductors.

$$c(x,t) = c_0 - \frac{4R}{m}t + i^2 \ \text{erf}\left[\frac{x}{2\sqrt{Dt}}\right]$$
$$x(t) = 4/3\pi^{\frac{1}{2}}R/mt(Dt)^{\frac{1}{2}}\frac{1}{(k-1)c^*}$$
$$x(t) \sim t^{\frac{3}{2}} \tag{3.42}$$

Figure 3.43 shows the results of measured LPE layer thickness for the growth of GaSb from Ga solutions as a function of growth time. Figure 3.43a demonstrates the growth from supersaturated solutions with ΔT_S of 3 and 5 °C. The layer thickness proportional to $t^{1/2}$ is fulfilled. The layer thickness is proportional to $t^{3/2}$ by growing layers from saturated Ga solutions with defined cooling rates (for details, see Figure 3.43b).

In the following section, we will describe the details of the process control to grow a GaSb/$Ga_{1-x}Sb_xAl$ heterostructure (Figure 3.45) using a multichamber system, which is shown schematically in Figure 3.44.

Explanation of Figure 3.45**:**

1) **Position A**
   At the beginning, substrate (left) and solution are baked out at 600 °C for 2 h under Pd-diffused high purity hydrogen to remove Ga oxide and impurities.
2) **Position B**
   Determination of the saturation temperature T_{S1} of the Ga–Sb solution and T_{S2} of the Ga–Sb–Al solution. All solid particles visible through a transparent furnace must be dissolved.
3) **Position C**
   Finally, all solutions are heated to $T_{S1} + 20$ °C to solve residual material in both the solutions.

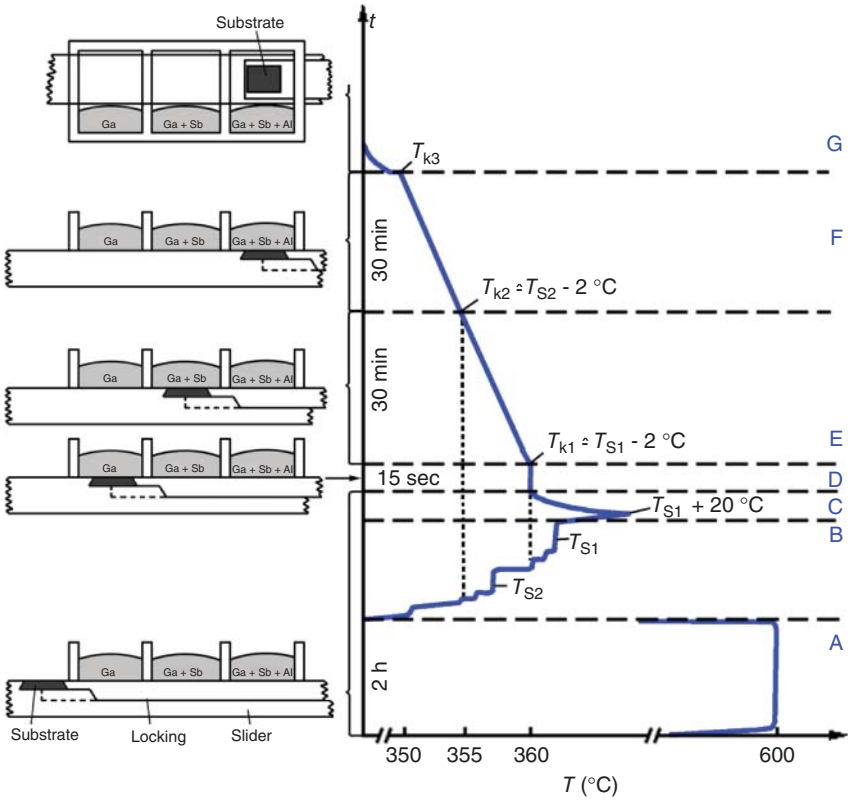

Figure 3.45 LPE process control for the growth of GaSb–(Ga, Al)Sb layers (see text).

4) **Position D**
   At $T_{S1} - 2\,°C$, the substrate is positioned under the pure Ga solution for 15 s to remove about 20 µm substrate surface.
5) **Positions E and F**
   Now, we have a clean, smooth surface to start growth of the GaSb and the (Ga, Al)Sb layers (super-cooling mode) at T_{k1} and T_{k2}.
6) **Position G**
   At T_{k3}, the growth process is finished, and the substrate with the grown layers is tipped off.

Some technical applications such as LEDs use a vertical dipping system for their basic epitaxial structures instead of a horizontal one. A vertical dipping apparatus was introduced by Rupprecht *et al.* [46]. A sketch of such an apparatus is shown in Figure 3.46.

The system includes a resistance furnace and a quartz crucible inside. A graphite substrate holder is attached to the upper end of the quartz tube, which in term passes through an "O-ring" seal in a removable top cap. In the upper part of the quartz tube, there is a gas inlet for introducing Pd-diffused hydrogen.

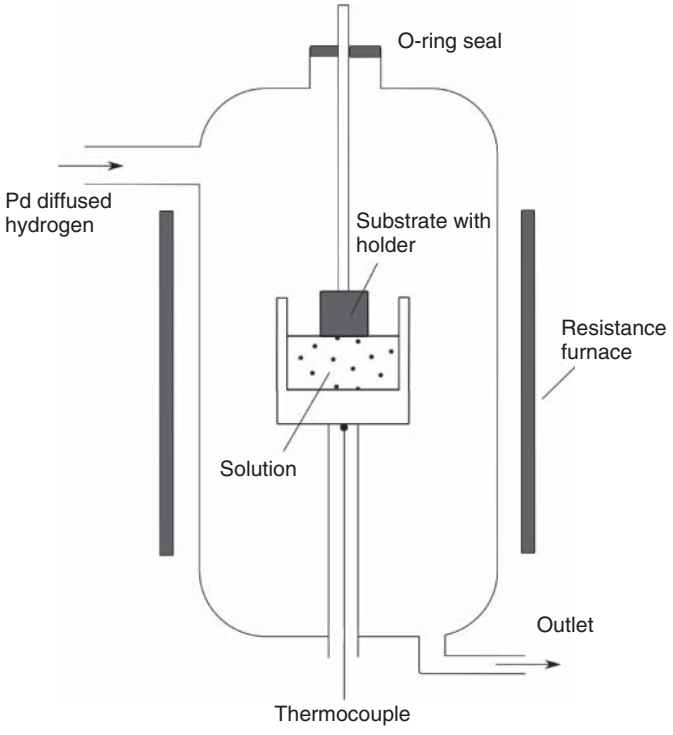

Figure 3.46 Vertical LPE dipping system.

With this LPE technique, pn-junctions can be grown in one growth run and only with one solution in the case of GaAs doped with Si. Silicon shows in GaAs an amphoteric behavior, which means it can be used as both n- and p-dopants. A highly Si-doped substrate with n-type behavior is dipped in a Ga – As + Si-doped solution starting at 930 °C and cooling down to 890 °C. This part of the grown layer is n-type. By further reducing the temperature below 890 °C, a p-type layer will be grown, leading to a pn-junction of high quality.

Final Remarks

LPE has been discussed in this chapter as a method to grow layers from metallic, nonstoichiometric solutions. In the past, LPE has been used mainly for nearly all types of III – V-semiconductors to study basic growth phenomena and to build up electronic and optoelectronic devices and device structures. Growth from a solvent with a group III element such as Ga and In leads to high quality epitaxial layers of III – V-compounds. High quality means low residual impurity concentrations $\leq 10^{15}$ cm^{-3} and low intrinsic point defect concentrations.

Actual interests for LPE growth are directed to the following materials [47]

- Oxides; high temperature superconductors for flat tunnel device technology.
- Nitrides for optoelectronic and high power electronic devices.

- Langasite type materials such as calcium gallium germanate, $Ca_3Ga_2Ge_4O_{14}$, for their outstanding piezoelectric properties.

3.4.2 Vapor Phase Epitaxy (VPE)

Chemical Vapor Deposition (CVD) CVD or VPE is commonly used in mass production of single crystalline layers of silicon and III–V-semiconductors for electronic and optoelectronic devices. Similar to LPE, the growth temperatures are lower compared to melt growth techniques, leading to layers with low concentrations of point defects and unwanted impurities.

There are several methods to realize crystal growth from vapor phase (the growth of bulk crystals by vapor phase has been described in Section 3.3.2):

- Physical methods
  - Condensation and sublimation
  - Flash evaporation
  - Sputtering
  - MBE
- Chemical methods
  - VPE with chlorides of V elements such as PCl_3, $AsCl_3$, or $SbCl_{3.5}$ first reported by Effer in 1965 [48],
  - VPE with hydrides of V elements such as PH_3, AsH_3, and SbH_3 after Tietjen and Amick in 1965 [49], nowadays called *hydride VPE* or HVPE,
  - Close-space transport with transport gases,
  - MOVPE.

All these techniques are different by the type of source material and the mechanism by which it is transported to the growing epitaxial layer surface. The simplest method, therefore, is the sublimation where the source material is positioned at one end of a sealed tube and heated up so that the vapor may be transported to the cooler end of the tube for crystallization.

Vapor phase epitaxial growth is shown principally in Figure 3.47 and consists of a quartz-tube reactor with a graphite susceptor and a substrate crystal as deposition zone.

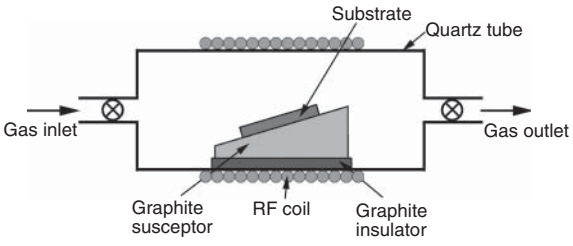

Figure 3.47 Reactor configuration for a VPE growth process (schematically). Quartz reactor with graphite susceptor and a well-prepared substrate crystal, RF coil heating (cold wall reactor), and gas outlet.

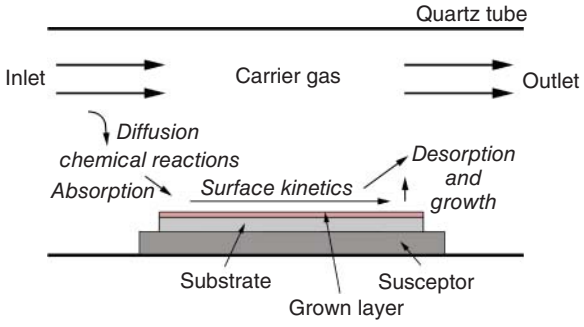

Figure 3.48 Vapor phase epitaxy: operating sequence within the deposition zone.

The materials to be deposited are transported normally by Pd-diffused hydrogen of extreme high purity as gaseous reaction partners of the systems to be grown. Figure 3.48 demonstrates the operating sequence within the deposition zone. From the inlet gas carrier, a diffusion of reaction partners associated with chemical reactions of the crystal product is directed to the substrate surface. On the substrate, surface kinetics are dominant, leading to a growing epitaxial layer and a final desorption of reaction partners (compare also Figure 3.35).

Chloride VPE, introduced by Effer in 1965 [48], has been an important method to grow high purity epitaxial layers with residual carrier concentrations of $\leq(10^{14}-10^{15})\,\mathrm{cm}^{-3}$. The technique is mainly used to grow high quality layers of InP, GaAs, (Ga,In)P, (Ga, As)P, or (In,Ga)(As,P) alloys [50, 51]. The method has been also developed to grow uniform epitaxial layers on large area substrates as vapor levitation epitaxy, VLE. VLE uses reactant vapors and transport gases not only to provide reactants to the substrate surface but also to lift the wafer and keep it suspended above the susceptor during the epitaxial process. The concept of VLE has been first described by Cox [51].

Chloride VPE has some advantages over HVPE. It may lead to simple and inexpensive systems because the method does not use toxic gases such as AsH_3 and PH_3. The chlorine VPE is schematically shown in Figure 3.49. As a carrier gas, Pd-diffused H_2 is used together with a halide of a main group V element of the periodic table. To grow InP or GaP, PCl_3 vapor is introduced in the source zone (Figures 3.49b and 3.50a). PCl_3 reacts with hydrogen to hydrochloric acid and phosphorus (completely above 500 °C):

$$PCl_3 + (3/2)H_2 = (1/2)P_2 + 3HCl \tag{3.43}$$

The phosphorus is transported to the In and Ga sources and dissolves in the source materials. It could be shown that, during the P-dissolving process, Ga- and In-chlorides are formed as well:

$$In + HCl = InCl + (1/2)H_2 \tag{3.44}$$

$$Ga + HCl = GaCl + (1/2)H_2 \tag{3.45}$$

Similar reactions can be written for $InCl_2$, $InCl_3$, and $GaCl_3$.

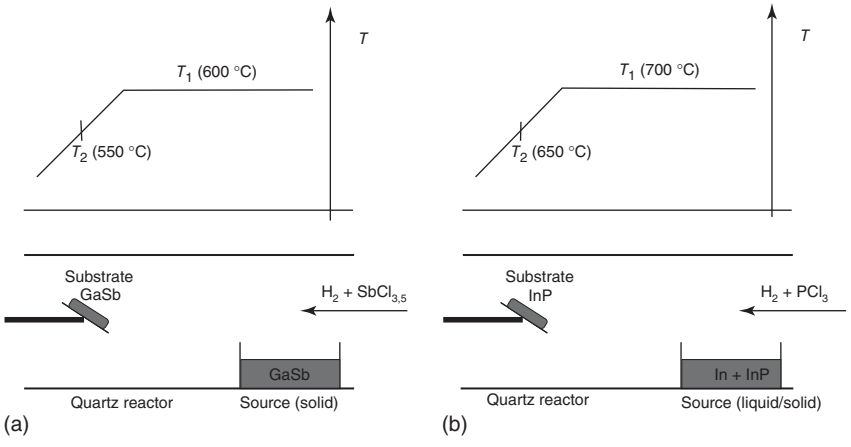

Figure 3.49 Chloride vapor phase epitaxy of (a) GaSb (schematically) and (b) InP (schematically).

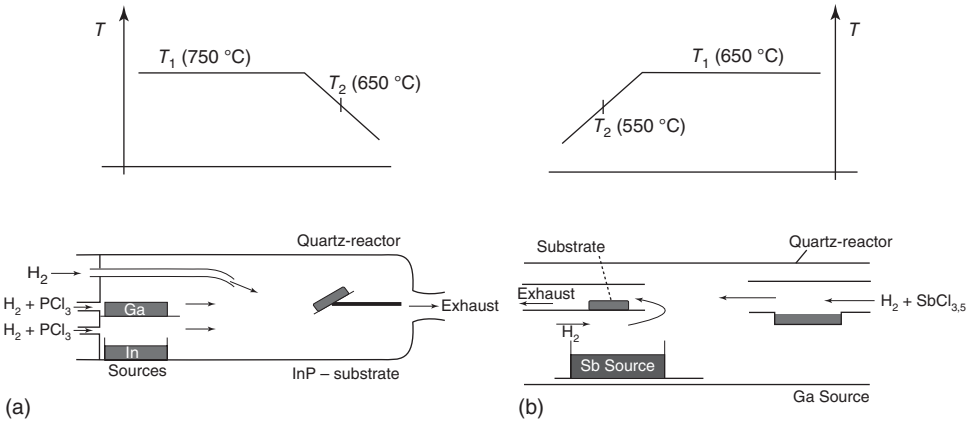

Figure 3.50 Chloride VPE: (a) alignment for the growth of (Ga, In)P ternary system; (b) modified chloride VPE for GaSb with separated Ga and Sb sources.

Before the growth, the saturation process of the In and Ga sources with phosphorus must be finished. In this case, a homogeneous InP or GaP crust is formed over the complete source. The equilibrium between the saturated source and the gas phase is very important for the chlorine VPE. A nonequilibrium situation over the source results in a deviation of HCl and P concentration and will lead to a nonuniform layer growth and a scatter in the composition of the alloys.

The ratio of the sum of the chloride partial pressures to the sum of the *P*-partial pressures depends on the saturation level of the source. If the source is undersaturated, S_{source} is very high. If the source is saturated, we have S_{source}

$$S_{\text{source}} = \left(\sum \text{Cl} / p_{\text{P}}^{0} \right) \tag{3.46}$$

Example 3.5: In order to get some more inside in the transport properties of reactants, we will present a few basic thermodynamic considerations of the GaSb–chlorine VPE system (Figure 3.49a).

The following assumptions have to be made:

- All reactions in the epitaxial growth apparatus are in thermodynamic equilibrium.
- All gases in the system are ideal gases.
- Possible chemical reactions in the system are known.
- In our case, crystal growth is controlled by thermodynamics, not by kinetic processes.

In order to get a statement of the composition of the gas phase during crystal growth, we have to arrange all possible chemical reactions. In the GaSb system, we have a polycrystalline GaSbsource at temperature T_1 and a GaSb substrate at T_2. Hydrogen and $SbCl_3$ or $SbCl_5$ reach the source zone as reactant gases. $SbCl_{3,5}$ becomes decomposed into HCl, Sb_4, and Sb_2 at source temperature T_1.

We have now the following reaction equations in the system $GaSb/SbCl_{3,5}/H_2$:

$$(3/2)H_2 + SbCl_3 \leftrightarrow (1/4)Sb_4 + 3HCl \tag{3.47}$$

$$(5/2)H_2 + SbCl_5 \leftrightarrow (1/4)Sb_4 + 5HCl \tag{3.48}$$

$$2Sb_2 \leftrightarrow Sb_4 \tag{3.49}$$

HCl reacts with the solid GaSb of the source:

$$HCl + GaSb \leftrightarrow GaCl + (1/4)Sb_4 + (1/2)H_2 \tag{3.50}$$

$$2HCl + GaCl \leftrightarrow GaCl_3 + H_2 \tag{3.51}$$

In the substrate zone at T_2, reaction (3.50) is shifted more to the left side, and we have the deposition of GaSb.

The essential components of the gas phase over solid GaSb are H_2, GaCl, Sb_4, Sb_2, and HCl. Neglected are the following components, because they are by orders of magnitude lower: $SbCl_{3,5}$, SbH_3, and Cl_2.

Equations 3.49–3.51 are characterized by the following equilibrium constants (p is the pressure of components):

$$K_{p1} = \frac{p_{Sb_4}}{(p_{Sb_2})^2} \tag{3.52}$$

$$K_{p2} = p_{HCl}/p_{Gacl} \cdot (p_{Sb_4})^{\frac{1}{4}} \cdot (p_{H_2})^{\frac{1}{2}} \tag{3.53}$$

$$K_{p3} = (p_{GaCl_3} \cdot p_{H_2})/p_{GaCl} \cdot (p_{HCl})^2 \tag{3.54}$$

To determine the six unknown components, we need three more equations.

The total pressure in the system must be 1 bar:

$$p_{H_2} + p_{HCl} + p_{Sb_4} + p_{Sb_2} + p_{GaCl} + p_{GaCl_3} = 1 \tag{3.55}$$

All chlorides are gaseous and will not be incorporated in the epitaxial layer. The conservation equation for chlorides is $\sum$Cl

$$\sum \mathrm{Cl} / \sum \mathrm{H_2} = (p_{HCl} + p_{GaCl} + 3p_{GaCl_3})/p_{H_2} + (1/2)p_{HCl} = A \tag{3.56}$$

A is a constant, which is given by the amount of Sb chlorides. In the following, we will use only $SbCl_5$. The calculations can be easily transferred to $SbCl_3$. For A, we have:

$$A = 5p^0_{SbCl_5} / \sum \mathrm{H_2} \tag{3.57}$$

Equation 3.58 is given by the condition of stoichiometry, which is valid over the substrate as well as over the source:

$$\left(\sum \mathrm{Sb^{Source}} - \sum \mathrm{Ga^{Source}}\right) / \sum \mathrm{H_2}$$
$$= \left(\sum \mathrm{Sb^{Substrate}} - \sum \mathrm{Ga^{Substrate}}\right) / \sum \mathrm{H_2} = B \tag{3.58}$$

with

$$\sum \mathrm{Sb} = 4p_{Sb_4} + 2p_{Sb_2} \quad \text{and} \quad \sum \mathrm{Cl} = p_{GaCl} + p_{GaCl_3}$$
$$\sum \mathrm{Sb} = p^0_{SbCl_5}$$

and, finally,

$$B = p^0_{SbCl_5} / \sum \mathrm{H_2} = 0.2A \tag{3.59}$$

The degrees of freedom f of the system are p, T, A, and B. This is consistent with Gibb's phase rule:

$$f = \alpha - \beta + 2 = 4$$

$\alpha = 4$ number of components: Cl, Ga, H, Sb
$\beta = 2$ number of phases: gas phase and solid state.

The temperature dependence of the equilibrium constant is given by

$$\ln K_p = -\Delta G / k_B T \tag{3.60}$$

$$\frac{d \ln K_p}{dT} = \Delta H / k_B T^2 \tag{3.61}$$

$$\Delta G = \Delta H + T \Delta S$$

where ΔG is the free enthalpy, ΔH is the enthalpy of reaction, ΔS is the entropy of reaction, and k_B is the gas constant.

If the enthalpy of reaction is > 0, which holds for III–V-semiconductors, the transport of species will take place from higher to lower temperatures.

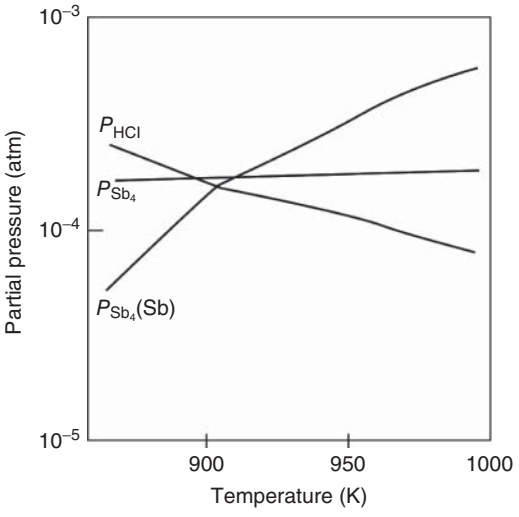

Figure 3.51 $GaSb-SbCl_5-H_2$ system. Temperature dependence of partial pressure of several gasphase components ($A = 8.33 \cdot 10^{-4}$, $B = 1.67 \cdot 10^{-4}$).

Table 3.2 $(GaSb-SbCl_5-H_2)$ system.

***B* value**	**Temperature (K)**
$5 \cdot 10^{-5}$	860
$1 \cdot 10^{-4}$	890
$1.7 \cdot 10^{-4}$	905
$2.5 \cdot 10^{-4}$	940
$3.3 \cdot 10^{-4}$	960
$5 \cdot 10^{-4}$	985
	Melting temperature GaSb

Limiting temperature of supersaturated Sb as a function of $SbCl_5$ concentration (*B*-value).

The partial pressures of the components H_2, GaCl, $GaCl_3$, Sb_4, Sb_2, and HCl are determined by Equations 3.52 – 3.59. The equilibrium constants K_{p1}, K_{p2}, and K_{p3}, were taken from literature or calculated [52].

Figure 3.51 shows the partial pressure of various gas phase components over solid GaSb as a function of temperature for $B = 1.67 \cdot 10^{-4}$. In addition, we can see the vapor pressure of Sb_4 over solid/liquid antimony. The partial pressure p_{Sb_4} exceeds the vapor pressure p_{Sb_4} (Sb) at temperatures below 905 K. In this case, the gas phase is supersaturated with Sb vapor. Solid antimony may crystallize out in the system.

Table 3.2 shows the limiting temperature of supersaturated antimony vapor as a function of $SbCl_5$ (*B*-value) concentration.

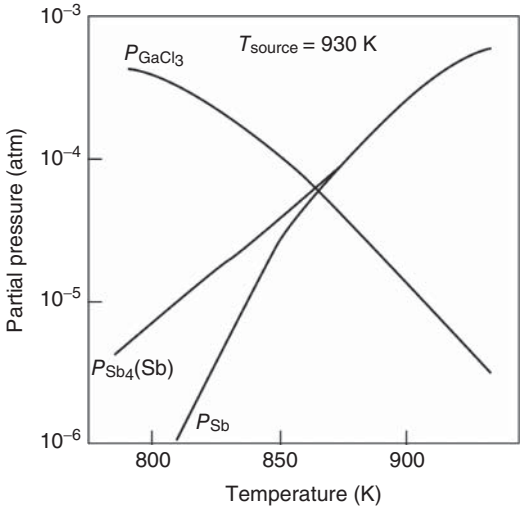

Figure 3.52 (GaSb/Ga–Sb–$SbCl_5$–H_2) system, modified chloride VPE system: partial pressures of various species as a function of temperature for $A = 1{\cdot}10^{-2}$ and source temperature: 930 K.

For $B > 5{\cdot}10^{-4}$, the gas phase is supersaturated even at the melting point of GaSb.

As a summary, we may point out that the chlorine VPE is only possible at low $SbCl_5$ concentrations for growing GaSb epitaxial layers.

This constraint may be avoided by using spatially separated Ga and Sb sources as shown in Figure 3.50b. Equations 3.47–3.51 are still valid. Instead of Equation 3.58, the stoichiometry condition we have to use:

$$4\text{Sb(liquid, solid)} \leftrightarrow \text{Sb}_4\text{(gaseous)} \tag{3.62}$$

and

$$K_{p4} = p_{Sb_4} \tag{3.63}$$

Now, the antimony partial pressures p_{Sb_4} and p_{Sb_2} over the source are independent of the chloride partial pressures. Figure 3.52 depicts the calculated partial pressures of various species in the gas phase as a function of the substrate temperature (source temperature $T = 930$ K).

There is no supersaturation of antimony vapor in the gas phase at temperatures between 800 and 900 K. The antimony transport does not interfere with the Ga transport in the modified chloride VPE system. The sum of the gallium chloride partial pressures is higher than the sum of the Sb pressures. The partial pressure of $GaCl_3$ cannot be neglected in this system in comparison to the "normal" system. It is always possible to avoid the crystallization of solid antimony in the substrate region if the chloride concentration is kept at a high value over the substrate. It could be demonstrated that the transport rates of GaSb are an order of magnitude higher compared to the "normal" chloride VPE system [52].

It should be pointed out that the constraint of free choosable parameters during chloride VPE with a GaSb source is not present in the case of epitaxial growth of arsenides and phosphides. The equilibrium pressure of arsenic (phosphorus) is 1 bar at 876 K (704 K).

Growth experiments with ($GaSb-SbCl_5-H_2$) system [52]:

Source temperature 580–630 °C	$A = 6.5 \cdot 10^{-4} - 1.2 \cdot 10^{-3}$
Layer thickness ~1 µm	Growth rate $\leq 0.1\ \mu m\ h^{-1}$
Net hole concentration: $\sim 10^{17}\ cm^{-3}$	

According to the calculated reaction equilibriums, solid Sb crystallized out in the substrate region for Sb partial pressures $p_{Sb_4} \sim 1.5 p_{Sb_4}$.

Growth experiments with ($GaSb/Ga-Sb-SbCl_5-H_2$) system [52]:

Source temperature 620–690 °C	$A = 1.1 \cdot 10^{-2} - 1.6 \cdot 10^{-3}$
Layer thickness >1 µm	Growth rate: 0.12–1.90 $\mu m\ h^{-1}$
Net hole concentration: $\leq 3 \cdot 10^{16}\ cm^{-3}$	

Hydride Vapor Phase Epitaxy (HVPE) HVPE is a growth technique that has a broad application potential. HVPE is used to grow epitaxial layers of the following materials:

- Si, Ge, and Si–Ge mixed crystals,
- GaAs, (Ga,As)P, GaP, and (Ga,In)P for LEDs and photodetectors,
- GaN, InN, and AlN as thin as well as thick layers.

Thick layers may be used as substrates of high quality for subsequent growth of device structures.

A HVPE reactor for growing III–V-semiconductors and related compounds consists of two main zones: the source zone for producing chloride gas of a group III-metal such as Al, Ga, or In and the growth zone where the chlorides of group III metal are intermixed with the group V hydrides (NH_3, PH_3, AsH_3) to grow the epitaxial film. As in the chlorine VPE, the understanding of the possible chemical reactions is very important (Figure 3.53).

For the growth of (Ga, As)P, we have the following reactions:

Source Zone

$$Ga + HCl \rightarrow GaCl \quad \text{at } 900\,^{\circ}C \tag{3.64}$$

$$AsH_3 \rightarrow (1/4)As_4 + (3/2)H_2 \tag{3.65}$$

$$PH_3 \rightarrow (1/4)P_4 + (3/2)H_2 \tag{3.66}$$

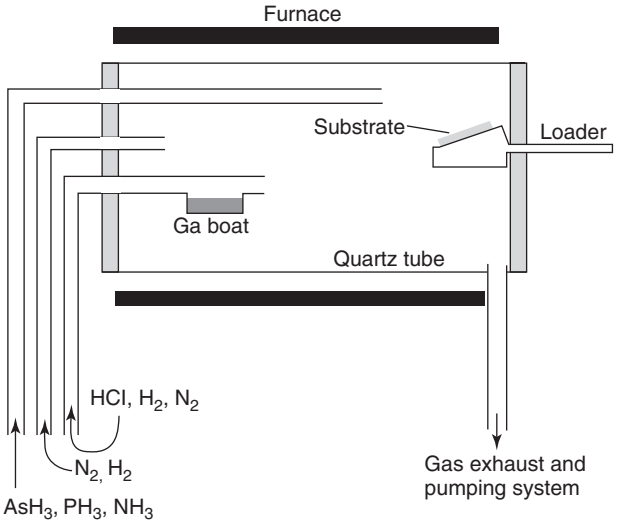

Figure 3.53 HVPE system to grow binary and ternary III–V-semiconductors (schematically).

Deposition Zone

$$\mathrm{GaCl} + (1-x)(1/4)\mathrm{As}_4 + x(1/4)\mathrm{P}_4 + (1/2)\mathrm{H}_2 - - - - \rightarrow \mathrm{GaAs}_{1-x}\mathrm{P}_x + \mathrm{HCl} \quad \text{at } 800\,^{\circ}\mathrm{C} \tag{3.67}$$

Ga is liquid, $\mathrm{GaAs}_{1-x}\mathrm{P}_x$ is solid, and all other species are gaseous.

The equilibrium constant of this reaction ($x = 0$) is

$$K_{\mathrm{HVPE}} = p_{\mathrm{HCl}}/p_{\mathrm{GaCl}} \cdot p_{\mathrm{As}_4}^{\frac{1}{4}} \cdot p_{\mathrm{H}_2}^{\frac{1}{2}} \tag{3.68}$$

Equilibrium partial pressures as a function of temperature can be calculated in the same way as we have done for chlorine VPE of GaSb.

As an example, by growing group III-nitrides, such as GaN, AlN, or InN, one can calculate the equilibrium partial pressures of the gaseous species over group III-metals in the source zone. Assuming $\Sigma p_i = 1$ atm and using $p^0_{\mathrm{HCl}} = 6{\cdot}10^{-3}$ atm with a mole fraction of hydrogen of 0,0 in the carrier gas, we may compare the equilibrium pressure values of the different gas species over the source metals Ga, Al, and In [53]. The temperature was varied between 300 and 1000 °C.

In the Ga source zone, the major gas component of Ga is GaCl. P_{GaCl_2} and p_{GaCl_3} are orders of magnitude lower than p_{GaCl} ($T_{\mathrm{Source}} > 500\,^{\circ}\mathrm{C}$). P_{GaCl} is nearly equal to p^0_{HCl}.

The HCl introduced in the source zone reacts almost completely with liquid Ga.

An In-source zone depicts a similar behavior as the Ga zone. During the growth of AlN, the Al-source zone shows at low temperatures AlCl_3 as the major gas species ($T_{\mathrm{source}} < 700\,^{\circ}\mathrm{C}$).

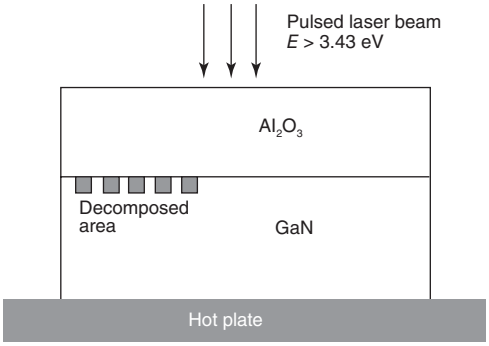

Figure 3.54 Principle of "laser lift-off" process (schematically) [53]; GaN–sapphire interface. (Redrawn from Hemmingson, C., *et al.* [53], with kind permission of Springer Science+Business Media.)

GaN layers up to 300 µm have been grown on sapphire substrates. However, for applications as laser diodes or high power lamps, free-standing GaN substrates are necessary. One possible technique to remove the sapphire substrate from the thick epitaxial layer is a laser lift-off process [53]. This technique is schematically shown in Figure 3.54. A laser beam irradiates the GaN–sapphire wafer through the sapphire with an energy less than the bandgap of sapphire but larger than the bandgap of GaN.

The laser beam will be absorbed at the GaN–sapphire interface as shown in Figure 3.54.

A thin layer of GaN (about 100 nm) at the interface to the sapphire will decompose into liquid Ga and N_2 gas if the power density of the laser beam is sufficient. By scanning the beam, the GaN at the interface can be completely decomposed. As a consequence, the GaN layer can be removed from the sapphire.

Metalorganic Vapor Phase Epitaxy (MOVPE) MOVPE of III–V-semiconductors differs from chloride VPE and hydride VPE. The group III elements are transported as metal alkyls together with the group V hydrides directly to the substrate zone. There is no source zone, and the chemical reactions of the components are over the substrate. Manasevit reported in 1968 [54] the growth of GaAs epitaxial layers by using trimethylgallium $Ga(CH_3)_3$ and arsine. The reaction can be written as

$$Ga(CH_3)_3 + AsH_3 = GaAs + 3CH_4 \tag{3.69}$$

The metal alkyl transported in purified hydrogen was decomposed in the temperature range 600–800 °C in the presence of arsine. Until this time, metal alkyls were well known in chemistry; but this was the first application of the use of these materials for semiconductor epitaxy.

In MOVPE, several parameters of an epitaxial layer such as thickness, carrier concentration, and composition of ternary and quaternary semiconductors can be independently controlled by an exact regulation of the gas flows. The outcome of this is the following specific feature of MOVPE:

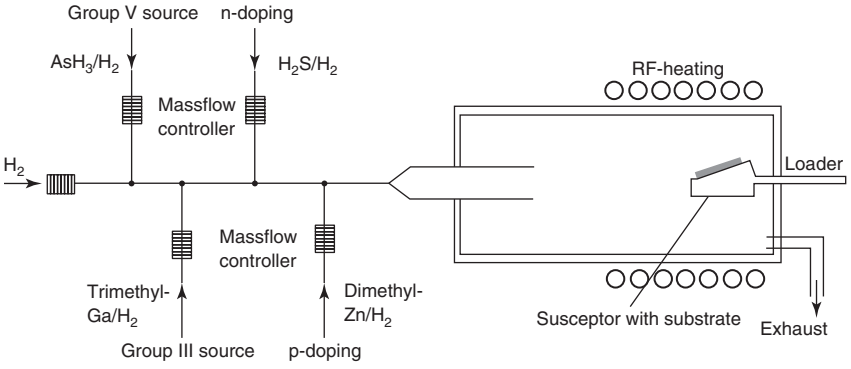

Figure 3.55 Line diagram of a MOVPE reactor with gas supply of group III alkyls, group V hydrides, *p*- and *n*-dopants, and epitaxial reactor.

- Growth of nearly all compound semiconductors, in particular ternary and quaternary semiconductors. Certain compounds such as (Al, Ga, In)P may be obtained by MOVPE only.
- Growth of arbitrary heterostructures with graded layers and abrupt transitions as well as sharpness of transitions within one monolayer.
- Growth of very thin layers, multiquantum well structures, and superlattices.
- Controllable high and low growth rates.
  For a typical growth rate of 10 nm min^{-1}, an epitaxial monolayer ($d = 0.15$ nm) needs about 0.9 s. During this time, the gaseous reactant parts with a flow rate of $v > 10$ cm s^{-1} are completely exchanged for a susceptor length of 5 cm.
- Excellent surface perfection of grown layers with a high uniformity during deposition on large areas. A high productivity with a great number of substrates can be achieved in one run (Figure 3.55).

The MOVPE growth process can be divided in two important parts:

- material transport to the susceptor with substrate,
- releasing semiconductor atoms from the gas molecule and incorporation in the substrate.

The slower part of these two processes dominates the growth rate. Both processes are dependent on temperature. Therefore, the characteristics of the growth rate as a function of temperature can be classified in three parts (compare Figure 3.56):

- *Part I*: the chemical reactions and processes near the substrate surface determine the growth rate. Owing to the strong temperature dependence of these processes, the growth rate increases in part I.
- *Part II*: the growth is mass transport limited. The growth rate is determined by the material transport from the gas flow to the substrate surface. This process is governed by diffusion through a stagnant layer and leads to a nearly constant growth rate. In the case of III–V-semiconductors, the growth rate is limited by the transport of the group III elements.

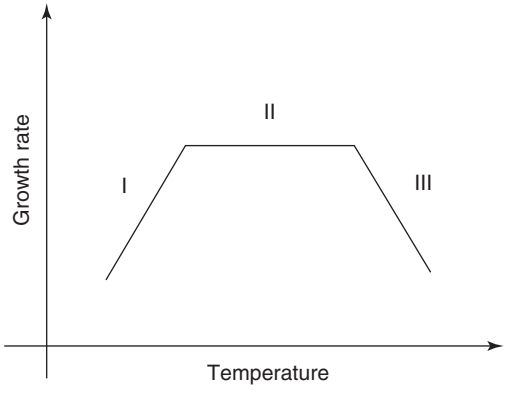

Figure 3.56 MOVPE growth rate as a function of temperature (schematically).

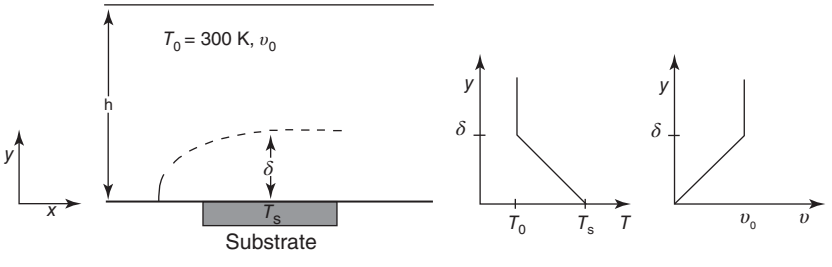

Figure 3.57 Stagnant layer model. (Adapted from Everstein, F.C., *et al.*, [55].)

- *Part III:* owing to the HT, there is still a desorption of the epitaxial layer and the growth rate decreases.

Above the susceptor, there is the formation of a diffusion boundary layer or stagnant layer δ, which is shown in Figure 3.57 [55]. The semiconductor atoms with concentration $c(y)$ diffuse from outside this layer to the susceptor and will be completely incorporated in the epitaxial layer:

$$c(y = 0) = 0 \quad \text{and} \quad v_x(0 < y < \delta)$$

Within the stagnant layer, the flow v has no component in the horizontal direction.

Above the stagnant layer, we have

$$V_x = v_0 = \text{constant}, \quad v_y = 0, \text{and } T = T_0 = 300\,\text{K (ambient temperature)}$$

The particle flux i outside the stagnant layer is given by the continuity equation:

$$\delta i_x(x)/\delta x + \delta i_y(x, y)/\delta y = 0, \quad y > \delta \tag{3.70}$$

i_x does not depend on y.

In the stagnant layer, we have

$$i_y(x) = -D\delta c(x, y)/\delta y, \quad 0 < y < \delta \tag{3.71}$$

Temperature gradient within the stagnant layer:

$$T = T_S - ((T_S - T_0)\delta)/y; \quad T_S = \text{susceptor temperature}$$

Temperature dependence of the diffusion constant D:

$$D = (D_0 T^2)/T_0^2$$

As a result, we have for the material flux to the substrate:

$$i_y(x) = (p_0 T_0 D_0 / k_B T_0^2 \delta) \cdot \exp(-D_0 T_S x / h v_0 \delta T_0) \tag{3.72}$$

where h is the height of the reactor and p_0 is the partial pressure of source material.

With physical data of the semiconductor material, one can calculate the growth rate of the epitaxial layer:

$$r_x \sim i_x(y) \tag{3.73}$$

The model from Si epitaxy [55] can be transferred to compound semiconductors as the growth rate is dependent of one basic material, the group III-alkyl, and if the group V-hydride is oversupplied. This is the case in most epitaxial configurations.

Molecular Beam Epitaxy (MBE) MBE, a PVT method has been developed by Arthur and Cho in 1968/1969, in particular for the growth of GaAs and GaAs/$Ga_xAl_{1-x}As$ structures. In a common publication, Cho and Arthur [56] gave a first review on this new important growth technology. During the time from 1970 to 1978, MBE has been introduced as a multipurpose film growth technique for III–V-compound semiconductors with well-defined device applications, which has been summarized by Ploog [57]. MBE as a physical method has distinctive differences to the considerably older epitaxial methods such as LPE and VPE. These differences are beneficial and include the ability to control the epitaxial growth reproducible to atomic monolayer dimensions and to monitor the growth process in real time.

Figure 3.58 depicts schematically a conventional MBE growth chamber. The MBE process takes place in an ultrahigh vacuum (UHV) of about 10^{-11} mbar. There are two main reasons for using such a low pressure environment to grow thin epitaxial layers.

- Well-defined atomic or molecular beams may only propagate in a vacuum where their mean free path is sufficient high.
- Residual gases may be incorporated in an epitaxial layer if the total pressure in the chamber is increasing. This is particularly the case for oxygen and carbon; their residual pressure should be below 10^{-13} mbar.

The growth chamber exhibits the following specifications:

- Plasma sources provide beams of oxygen radicals and activated ions by RF excitation.
- The substrate is mounted and fixed on a molybdenum block holder. The block holder can be rotated to get flat surfaces and a homogeneous layer thickness.

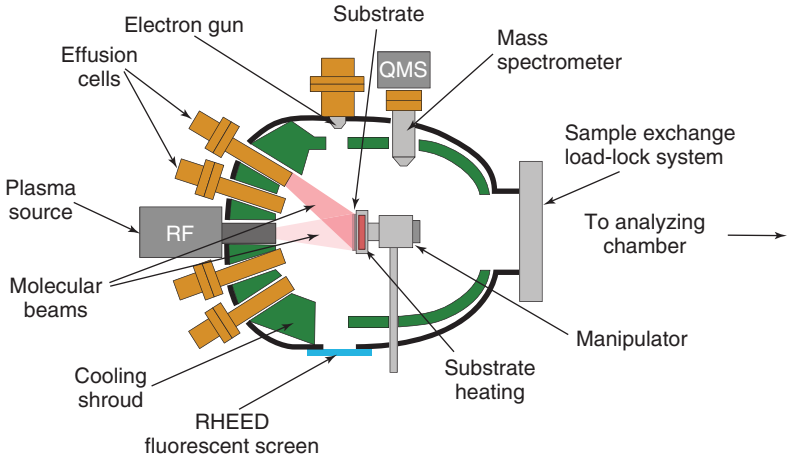

Figure 3.58 Schematic presentation of a MBE growth chamber. (Courtesy by FMF, University of Freiburg.)

The molybdenum block is heated by a high purity tantalum ribbon. The substrate temperatures during epitaxial growth must be high enough to activate surface migration of the species adsorbed on the growing surface.

- The sources of atomic or molecular beams should operate up to about (1200–1400) °C to generate molecular beams with no undesirable impurities and an excellent and uniform layer surface (rotation of the substrate!). Most of the materials that are used for the molecular beam are thermally evaporated or sublimed from effusion cells. The source materials can be elements such as Ga or As or compounds such as InP, which are contained in pBN or high purity graphite crucibles.

Every effusion cell is equipped with a mechanical shutter made of BN. The shutter is used to switch on and off the beams in times in the order of several hundred milliseconds. The shutter allows the abrupt change in composition or doping during epitaxial growth.

Growth of As, P, or Sb components can be achieved as well by using gaseous hydrides as AsH_3, PH_3, or SbH_3, which are injected in the growth chamber via cracker cells by interaction with surfaces of several hundreds of degree celsius. A particular advantage of this gas source molecular beam epitaxy (GSMBE) is the fact that the group V beam fluxes may be controlled more precisely compared to the normal temperature-controlled effusion cells.

In metalorganic molecular beam epitaxy (MOMBE), the basic species are supplied as metalorganics as described earlier in this chapter.

MBE machines for scientific purposes as well as for industrial applications are constructed in a modular design. The growth chamber, an analysis chamber, and a sample preparation chamber are connected via a transfer module under UHV conditions. Before insertion into the growth chamber, substrate, and wafer holders are outgassed in an introduction chamber.

A specific advantage of MBE is the possibility of *in situ* characterization of the growing or grown epitaxial layer. Main diagnostic techniques that are applied are the following:

- **RHEED**: *Reflection high-energy electron diffraction*
  In situ observation of growth morphology of epitaxial layers.
- **AES**: *Auger electron spectroscopy*
  Chemical analysis of surface contamination of substrates; assessing the cleaning process of substrates before epitaxial growth.
- **SIMS**: *Secondary ion mass spectroscopy*
  To identify the properties of the epitaxial layer, for example, composition, doping, and unintentional incorporation of impurities.
- **XPS/UPS**: *X-ray photoemission spectroscopy/ultraviolet photoemission spectroscopy*
  To study electronic states of grown surfaces and interfaces.

The characterization techniques are normally installed in the analysis chamber to avoid cross-contamination of growth environment and analytical instruments. However, RHEED is still used in the growth chamber because it is used *in situ* and in real time.

RHEED takes the advantage of an electron gun (compare Figure 3.58), which produces a collimated electron beam with energies of 5–40 keV. The electrons are diffracted from the growing surface. The diffraction pattern can be observed on a fluorescent screen (Figure 3.59) and analyzed by imaging processing methods. The angle between the beam and the diffracting surface is about 0.2–2°.

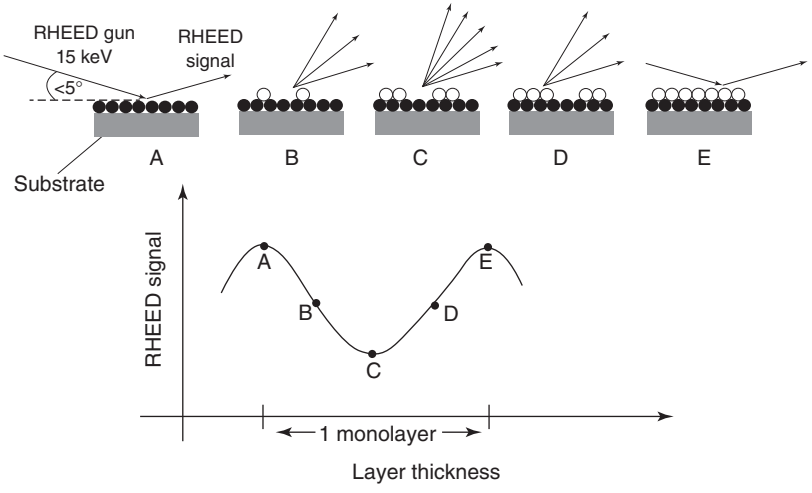

Figure 3.59 RHEED: oscillation of the intensity of the directly reflected beam. The periodicity of the RHEED intensity leads to the monolayer growth time.

With the real-time RHEED picture of the growing surface, we may characterize the growth regime (surface reconstruction, see Section 4.1.3.6) and the microscopic roughness and determine *in situ* the lateral lattice constant of the growing layer. The oscillation of the RHEED intensity of the directly reflected beam leads to the monolayer growth time. We may observe this situation in Figure 3.59: at the beginning of growth, we have a high intensity followed by a decrease in intensity when scattering atoms appear on the surface. When the first monolayer is completed, the intensity increases again. The growth rate is about 1 monolayer s^{-1} that is $<1\,\mu m\,h^{-1}$.

A large number of solid materials have been prepared by MBE: semiconductors such as III–V-, II–VI-, IV–VI-, and IV–IV-compounds and oxides, magnetic materials, and metals. Most basic work on physics, materials properties, and technology has been done on III–V-semiconductors.

For the state of the art of MBE, the reader is referred to the actual book on physics and technology of MBE published by Henini in 2012 [58].

Example 3.6: Vacuum conditions in a growth chamber for a molecular beam coming out of the effusion cells:

- distance exit effusion cell to substrate: 10–30 cm
- mean free path should be about20 cm.

To calculate the mean free path λ, we can use the ideal gas law. There is less interaction among the particles. The particle density at a given pressure can be written as

$$p \cdot V = N k_B T$$

$$n = \frac{N}{V} = \frac{p}{T k_B}$$

where P is the pressure, T is the temperature, V is the volume of the gas, and k_B is the Boltzmann constant.

Each particle has a radius r and a velocity u and a collision-free route $u\delta t$. The collision cross section σ is

$$\sigma = 4\pi r^2$$

Collision-free volume:

$$\delta V = \sigma u \cdot \delta t = 4\pi r^2 u \cdot \delta t$$

If δV reaches $1/n\ m^3$, a propagating particle will meet another one, and we have a collision.

The mean time τ between two collisions is

$$\tau = \delta t \quad \text{and} \quad \frac{1}{n} = 4\pi r^2 u \cdot \tau$$

and for the mean free path λ, we have

$$\lambda = u \cdot \tau = (1/4)\pi r^2 n = k_B T / 4\pi r^2 p$$

The mean free path λ for an air–molecule (molecule diameter about 3.7 Å) at 300 K and a background pressure in the growth chamber of

$$p = 10^{-4}\,\text{hPa}$$

lead to a mean free path $\lambda = 10$ cm.

High vacuum HV would be enough to reach a collimated molecular beam!

The gas impurities from the residual air of 10^{-4} hPa, however, would reach the substrate surface and would be highly incorporated in the epitaxial layer. The properties of the grown semiconductor layers would be in such a case mainly governed by impurities. Therefore, we have a strong request to the conditions of the real vacuum in the MBE chambers of

$$p_{max} \leq 10^{-11}\,\text{hPa}$$

3.5 Supplementary Material: Principles of Verneuil Technique, Growth from High and Low Temperature, Nonmetallic Solutions

3.5.1 Verneuil Technique

A fine dry powder of size 1–20 µm of the crystal material is shaken by a mechanical hammer through a wire mesh and allowed to fall through an oxygen–hydrogen flame. The powder melts, and a liquid film is formed on top of the seed crystal. The liquid film crystallizes progressively as the seed is slowly moved down. The rate of charge feed is balanced by the rate of lowering down the grown crystal. The Verneuil method is commonly used for the growth of synthetic gems and a variety of high melting oxides, for example, ruby crystals are grown up to 90 mm in diameter for jewelry and lasers (see Figure 3.60) [2].

3.5.2 Growth from High Temperature Solutions (Flux Growth)

Controlled cooling down is used for the growth of materials, which have a high solubility in a suitable solvent. The temperature coefficient of the solubility should not be too small. A technique that controls spontaneous nucleation by using a seed crystal has been developed by Tolksdorf and Welz [59]. Figure 3.61 (left) shows the fixed seed crystal outside of the solution. The solution itself is supersaturated for a given growth temperature. In this case, there may be a few crystals at the bottom of the growth vessel until the equilibrium of the solution is reached. Now, the vessel is turned by 180°, and the seed crystal comes into contact with the saturated growth solution. Growth is initiated by cooling down the whole system within a

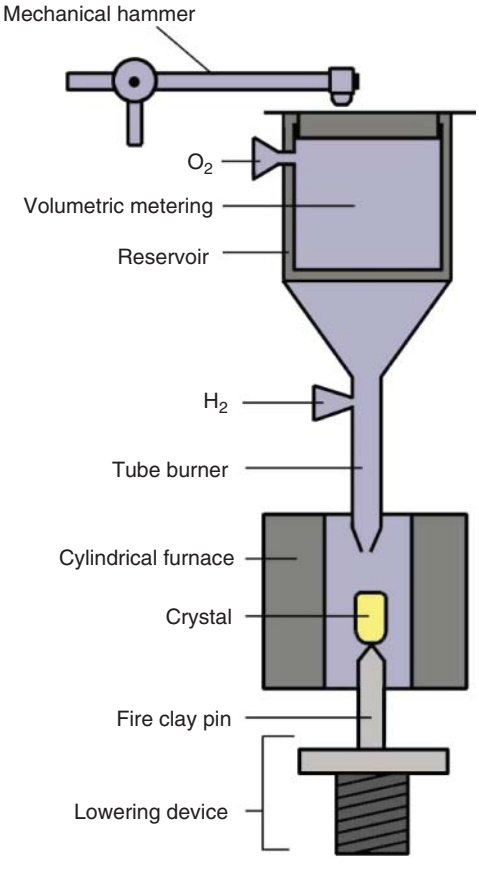

Figure 3.60 Principles of Verneuil technique.

well-defined program. Turning again the whole system by 180°, the seed with the grown crystal can be separated of the solution.

An example of growing bulk crystals with a large size is the growth of high quality quartz crystals by hydrothermal growth technique [60]. By using a Bridgman-type autoclave filled with quartz nutrient and quartz seeds in a line and finally with water and mineralizers (to increase the solubility of quartz in water), the crystals are grown under high pressure at 350 °C; compare Figure 3.62.

3.5.3
Growth from Low Temperature Solutions (Aqueous Solutions)

Figure 3.63 shows an apparatus to grow crystals from aqueous solutions by evaporation of the solvent. The basis of this method is a phase transition in a multicomponent system. One or several components of a liquid phase change over into a crystal phase. A fresh supply of the solution is maintained by vessel I.

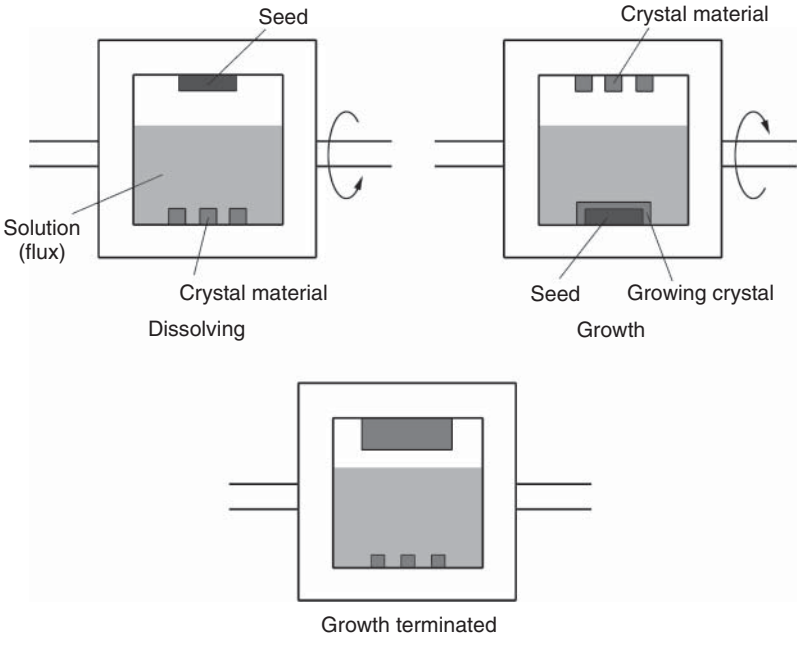

Figure 3.61 Flux growth (schematically). (Modified from Tolksdorf, W., Welz, F., [59].)

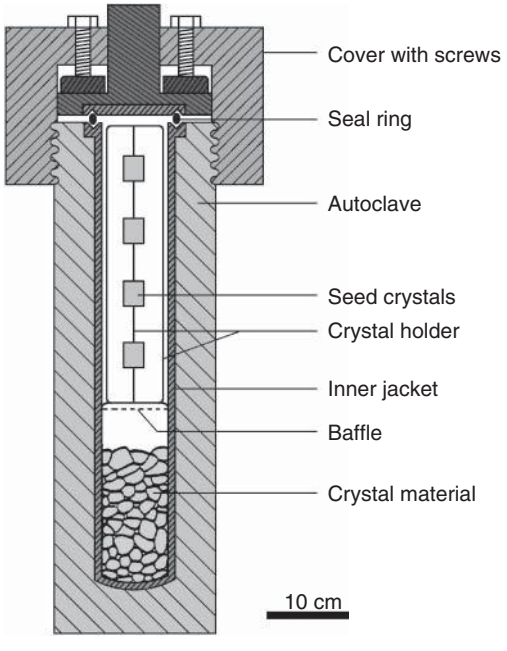

Figure 3.62 Growth of quartz crystals by using a modified Bridgman autoclave (schematically).

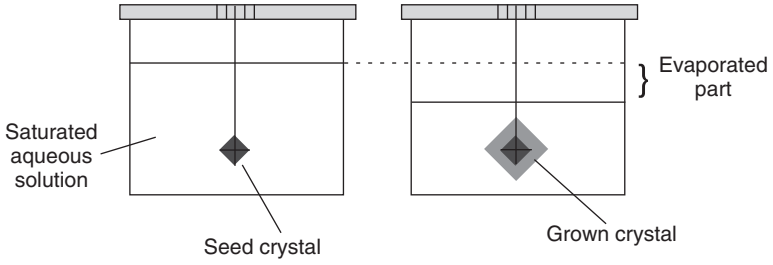

Figure 3.63 Growth from aqueous solutions, schematically.

References

1. Czochralski, J. (1918) *Z. Phys. Chem.*, **92**, 219.
2. Verneuil, A. (1902) *Compt. Rend. (Paris)*, **135**, 791.
3. Bridgman, P.W. (1923) *Proc. Am. Acad. Arts. Sci.*, **58**, 165, and 1925, **60**, 303.
4. Sudarshan, T.S., Cherednichenko, D., and Yakimova, R. (2005) in *Bulk Crystal Growth of Electronic, Optical, and Optoelectronic Materials* (ed P. Capper), John Wiley & Sons, Ltd, Chichester, p. 433.
5. Herman, M.A., Richter, W., and Sitter, H. (2004) *Epitaxy, Physical Principles and Technical Implementation*, Springer.
6. Nelson, H. (1963) *RCA Rev.*, **24**, 503.
7. Dash, W.C. (1958) *J. Appl. Phys.*, **29**, 736.
8. Hibiya, T. and Hoshikawa, K. (2005) in *Bulk Crystal Growth of Electronic, Optical, and Optoelectronic Materials* (ed P. Capper), John Wiley & Sons, Ltd, Chichester, p. 1.
9. Brozel, M.R. and Grant, I.R. (2005) in *Bulk Crystal Growth of Electronic, Optical, and Optoelectronic Materials* (ed P. Capper), John Wiley & Sons, Ltd, p. 43.
10. Grant, I.R. (2005) in *Bulk Crystal Growth of Electronic, Optical, and Optoelectronic Materials* (ed P. Capper), John Wiley & Sons, Ltd, Chichester, p. 122.
11. Shimamura, K., Fukuda, T., and Chani, V.I. (2003) in *Crystal Growth Technology* (eds H.J. Scheel and T. Fukuda), John Wiley & Sons, Ltd, Chichester, p. 429.
12. Tatartchenko, V.A. (2005) in *Bulk Crystal Growth of Electronic, Optical, and Optoelectronic Materials* (ed P. Capper), John Wiley & Sons, Ltd, Chichester, p. 299.
13. Nacken, R. (1915) *Neues Jahrb. Mineral. Geol. Paläontol.*, **2**, 133.
14. Kyropoulos, S. (1926) *Z. Anorg. Allg. Chem.*, **154**, 308.
15. Li, G., Jie, W., Hua, H., and Gu, Z. (2003) *Prog. Cryst. Growth Charact. Mater.*, **46**, 85.
16. Hirano, H. and Kurita, H. (2005) in *Bulk Crystal Growth of Electronic, Optical, and Optoelectronic Materials* (ed P. Capper), John Wiley & Sons, Ltd, Chichester, p. 241.
17. Greenberg, H.J. (1999) *J. Cryst. Growth*, **197**, 406.
18. Duffar, T., Boiton, P., Dusserre, P., and Abadie, J. (1997) *J. Cryst. Growth*, **178**, 397.
19. Zemskov, V.S., Raukham, M.R., Barmin, I.V., Senchenkov, A.S., Shul'pina, I.L., and Sorokin, L.M. (1983) *Fiz. Khim. Obrab. Mater.*, **17**, 56.
20. Benz, K.W., Guest Editor (1999) *Prog. Cryst. Growth Charact. Mater.*, **38**, 1–4 , 1-272.
21. Birat, J.P. and Chone, J. (1982) *Ironmaking Steelmaking*, **10**, 269.
22. Benz, K.W. and Dold, P. (2002) *J. Cryst. Growth*, **237-239**, 1638.
23. Seibert, G. (2001) *A World Without Gravity*, ESA Publication, p. SP-125.
24. Benz, K.W., Duffar, T., and Fiederle, M. (2001) in *A World Without Gravity*, ESA Publication, p. 172.
25. Steinborn, W. (1986) in *Material Sciences in Space* (eds B. Feuerbacher,

H. Hamacher, and R.J. Naumann), Springer-Verlag, p. 227.
26. Croell, A., Mueller-Sebert, W., Benz, K.W., and Nitsche, R. (1994) *Microgravity Sci. Technol.*, **III/4**, 204.
27. Kaiser, Th. and Benz, K.W. (1998) *J. Cryst. Growth*, **183**, 564.
28. Croell, A., Kaiser, Th., Schweizer, M., Danilewsky, A.N., Lauer, S., Tegetmeier, A., and Benz, K.W. (1998) *J. Cryst. Growth*, **191**, 365.
29. Benz, K.W. and Bauser, E. (1980) *Crystals Growth, Properties and Applications*, III – V Semiconductors, vol. 3, Springer-Verlag, p. 1.
30. Tiller, W.A. (1963) *J. Appl. Phys.*, **34**, 2757.
31. Danilewsky, A.N., Benz, K.W., and Nishinaga, T. (1990) *J. Cryst. Growth*, **99**, 1281.
32. Kaneko, K. *et al.* (eds) (1973) *Proc. Inst. Electr. Electron. Eng.*, **61**, 884.
33. Gillessen, K. and Marshall, A.J. (1976) *J. Cryst. Growth*, **32**, 216.
34. Greenberg, J.H., Guskov, V.N., and Lazarev, V.B. (1992) *Mater. Res. Bull.*, **27**, 997.
35. Laasch, M., Schwarz, R., Rudolph, P., and Benz, K.W. (1994) *J. Cryst. Growth*, **141**, 81.
36. Greenberg, J.H., Guskov, V.N., Lazarev, V.B., and Shebershneva, O.V. (1992) *Mater. Res. Bull.*, **27**, 847.
37. Hofmann, D.M., Omling, P., Grimmeiss, H.G., Meyer, B.K., Benz, K.W., and Sinerius, D. (1992) *Phys. Rev.*, **B45**, 6247.
38. Eiche, C., Joerger, W., Fiederle, M., Ebling, D., Schwarz, R., and Benz, K.W. (1995) *J. Cryst. Growth*, **146**, 98.
39. Benz, K.W., Babentsov, V., and Fiederle, M. (2004) *Prog. Cryst. Growth Charact. Mater.*, **49/49**, 189.
40. Markov, E.V. and Davydov, A.A. (1971) *Neorg. Mater.*, **4**, 575.
41. Laasch, M., Kunz, T., Eiche, C., Fiederle, M., Joerger, W., Kloess, G., and Benz, K.W. (1997) *J. Cryst. Growth*, **174**, 696.
42. Edelin, G. and Mathiot, D. (1980) *Philos. Mag. B*, **42**, 95.
43. Goodwin, A.R., Gordon, J., and Dobson, C.D. (1968) *Br. J. Appl. Phys.*, **D1**, 115.
44. Bauser, E. (1974) *J. Cryst. Growth*, **27**, 148.
45. Hsieh, J.J. (1974) *J. Cryst. Growth*, **27**, 49.
46. Rupprecht, H., Woodall, J.M., and Pettit, G.D. (1967) *Appl. Phys. Lett.*, **11**, 81.
47. Klemenz Rivenbark, C.F. (2010) *Handbook of Crystal Growth*, Springer-Verlag, Berlin, Heidelberg, p. 1041.
48. Effer, D. (1965) *J. Electrochem. Soc.*, **112**, 1020.
49. Tietjen, J.J. and Amick, J.A. (1966) *J. Electrochem. Soc.*, **113**, 724.
50. Hoshino, M., Kitahara, K., Kodama, K., and Ozeki, M. (1989) *J. Cryst. Growth*, **96**, 188.
51. Cox, H.M., Hummel, S.G., and Keramidas, V.G. (1986) *J. Cryst. Growth*, **79**, 900.
52. Jakowetz, W., Barthruff, D., and Benz, K.W. (1977) *Inst. Phys. Conf. Ser.*, **33a**, 41.
53. Hemmingson, C., Monemar, B., Kumagai, Y., and Koukito, A. (2010) in *Handbook of Crystal Growth*, Springer-Verlag, Berlin, Heidelberg, p. 869.
54. Manasevit, H.M. (1968) *Appl. Phys. Lett.*, **12**, 156.
55. Everstein, F.C., Severin, P.J.W., van der Brekel, H.L., and Peek, J. (1970) *J. Electrochem. Soc.*, **117**, 925.
56. Cho, A.Y. and Arthur, J.R. (1975) *Prog. Solid State Chem.*, **10**, 157.
57. Ploog, K. (1980) in *Crystals Growth, Properties and Applications*, III – V Semiconductors, vol. 3, Springer-Verlag, p. 73.
58. Henini, M. (ed.) (2012) *Molecular Beam Epitaxy: From Research to Mass Production*, Elsevier.
59. Tolksdorf, W. and Welz, F. (1976) *J. Cryst. Growth*, **35**, 285.
60. Byrappa, K. (2005) in *Bulk Crystal Growth of Electronic, Optical, and Optoelectronic Materials* (ed P. Capper), John Wiley & Sons, Ltd, Chichester, p. 387.

4
Characterization of Crystals

Crystal growth and the comprehensive characterization of the grown crystals are inseparable parts of the fabrication process of high-quality crystals. In general, we can define crystal characterization as the overall assessment of the grown crystal with respect to the following features:

- morphology,
- composition (including elemental purity and homogeneity),
- structure,
- physical properties, and
- crystal quality.

The evaluation of structure must be divided into two main parts. The first part is related to the *crystallographic structure* of the crystal. For a crystal of known crystal structure, one has to prove if this specific structure or another phase (e.g., a polymorph) occurs. For a crystal of unknown structure (e.g., most cases of protein crystals), the crystal structure has to be determined. The second part of the structural characterization is concerned with the analysis of the *defect structure* of the crystal. A detailed defect analysis requires the identification of the existing defect types, their densities, and their distribution. The defect analysis is an essential part of the evaluation of crystals because crystal defects mainly influence their physical properties (e.g., mechanical, electrical, and optical) and the crystal quality.

In this chapter, we will deal with the main crystal defects and their influence on the chemical and physical behavior of crystals. After this, we discuss what criteria define the quality of a crystal for a specific material class and application. The necessary information for the assessment of crystal quality is mainly gained from the numerous applied characterization methods. A brief overview of the main characterization methods is presented. The necessary interplay between crystal growth, characterization, and the feedback to the growth process for improving the crystal quality (defect engineering) will be illustrated for the case study of crystal growth of $LiAlO_2$ substrates for epitaxy of III-nitride films.

Introduction to Crystal Growth and Characterization, First Edition.
Edited by Klaus-Werner Benz and Wolfgang Neumann.
© 2014 Wiley-VCH Verlag GmbH & Co. KGaA. Published 2014 by Wiley-VCH Verlag GmbH & Co. KGaA.

4.1 Crystal Defects

A crystal is named a *real crystal* if many properties of the *ideal crystal* are preserved in it but the *real* and *ideal crystal* differ at least in one property. In Section 1.1, we have denoted a real crystal consisting of one grain as *perfect single crystal*. A perfect crystal means a real crystal in thermodynamic equilibrium, where only intrinsic defects (e.g., lattice vibrations and native point defects) occur. In reality, a real crystal is more or less an *imperfect crystal* where in addition to the equilibrium lattice defects different types of nonequilibrium defects may occur. For the description of the ***real structure*** of a crystal and all its deviations from the ***ideal structure*** (crystal imperfections and crystal defects) various classifications were proposed. A basic classification divides the imperfections into

- chemical defects (cause a modification of the ideal chemical composition);
- physical defects (let the chemical composition unaltered);
- mechanical defects (e.g., cracks, fissures, cleavages, and dislocations).

The crystal imperfections can also be divided into ***substantial*** and ***nonsubstantial defects*** (Table 4.1).

Nonsubstantial defects do not cause an alteration in the type and number of atoms in the unit cell. ***Substantial defects*** may lead to such an alteration or the defect-induced changes of the periodic arrangement of building units (atoms, molecules, etc.) prevent the assignment of the building units to a specific unit cell.

Table 4.1 Defects in crystals.

Defects in crystals	
Nonsubstantial	***Substantial***
Internal stress	Mixed crystals
Lattice vibrations	Inhomogeneities
Phonons in crystals and phasons in quasicrystals	
Electronic defects (quasiparticles)	n-dimensional crystal lattice defects
Excitons, plasmons, polarons, and magnons	($n = 0, 1, 2, 3$)

In the following text, we consider the different types of *crystal lattice defects* in detail. Crystal lattice defects are commonly classified according to their dimensionality. The following list summarizes the main lattice defects as a function of their dimensionality.

1) **Zero-dimensional defects** (point defects)
   Types: Vacancies, self-interstitials, impurity atoms, antisite defects, and point defect agglomerates.
2) **One-dimensional defects** (line defects)
   Types: Dislocations, disclinations, and dispirations.

3) **Two-dimensional defects** (planar defects)
   a. *Homophase interfaces*: Grain boundaries (GBs), twins, stacking faults (SFs), domain boundaries, and antiphase boundaries (APBs). External surfaces.
   b. *Heterophase interfaces*: Intergrowth between crystals, where either the lattices and/or the atomic basis are different.
4) ***Three-dimensional defects*** (bulk defects) Types: Clusters, inclusions, precipitates, and voids.

4.1.1 Zero-Dimensional Defects

Localized disruptions in a crystal with extensions limited to a few interatomic distances around the disruption are treated as zero-dimensional defects. They are called ***point defects***. In a monoatomic crystal, two elementary types of point defects can occur: ***vacancies*** and ***interstitials*** also denoted as ***self-interstitials*** (Figure 4.1a,b). A vacancy is an atomic site in the structure normally occupied by an atom, which is unoccupied (a vacant atomic site). An interstitial site is any site in the structure (e.g., a tetrahedral or octahedral void), which is usually unoccupied by a normal atom of the structure. An extra atom that is occupying such a site is called an *interstitial atom* or shortly an *interstitial*.

Vacancies and interstitials also occur in compound crystals. But we should be aware of the fact that for the formation of point defects in crystals such as NaCl, $MgAl_2O_4$, and MgO the following conditions have to be maintained:

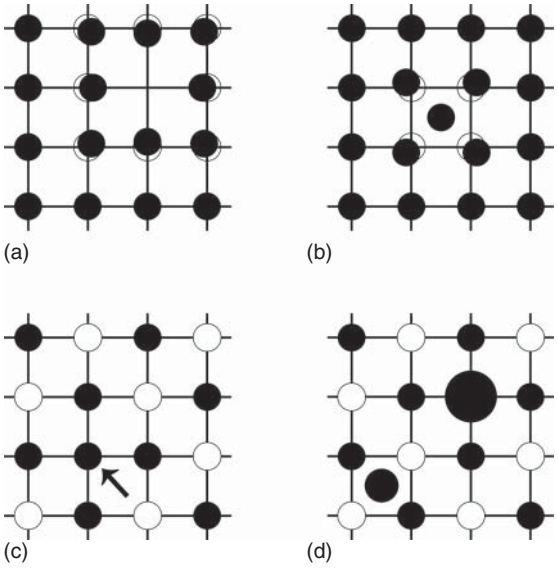

Figure 4.1 Types of point defects: (a) vacancy, (b) interstitial, (c) antisite defect, and (d) interstitial and substitutional impurity.

- charge balance (electroneutrality)
- mass balance
- site balance (the ratio of lattice sites must be conserved).

Therefore, point defects such as vacancies and interstitials occur in ionic crystals in pairs with opposite charge. Before describing the specific types of point defect pairs, we will introduce two other types of isolated point defects. A specific type of a point defect in a compound crystal is the so-called ***antisite defect*** (Figure 4.1c). If in a GaAs crystal, a Ga atom is occupying an As site, or vice versa, and an As atom is located at a Ga site, then an antisite defect is formed. The exchange of the positions of Mg and Al ions in the spinel structure is another example for the formation of antisite defects.

In general, both monoatomic and compound crystals consist of a certain concentration of impurity atoms, which can occupy either a normal lattice site or an interstitial site. The point defects formed by the impurities are called ***substitutional impurities*** or ***interstitial impurities***, respectively (Figure 4.1d).

The four main types of point defect pairs in ionic crystals are the following:

- *Schottky defect*: vacancies in the cation and anion sublattices
- *Anti-Schottky defect*: cation and anion interstitials
- *Frenkel defect*: vacancies in the cation sublattice and cation interstitials
- *Anti-Frenkel defect*: vacancies in the anion sublattice and anion interstitials.

Some of the above-mentioned point defect pairs are schematically illustrated in Figure 4.2.

Point defects will be generated during the growth process of a crystal. A crystal in thermodynamic equilibrium ($T > 0$ K) will always contain point defects. These point defects are called ***intrinsic***. Intrinsic point defects are vacancies and interstitials in a pure monoatomic crystal and the four above-mentioned point defect pairs and the antisite defect in compound crystals. Therefore, it is

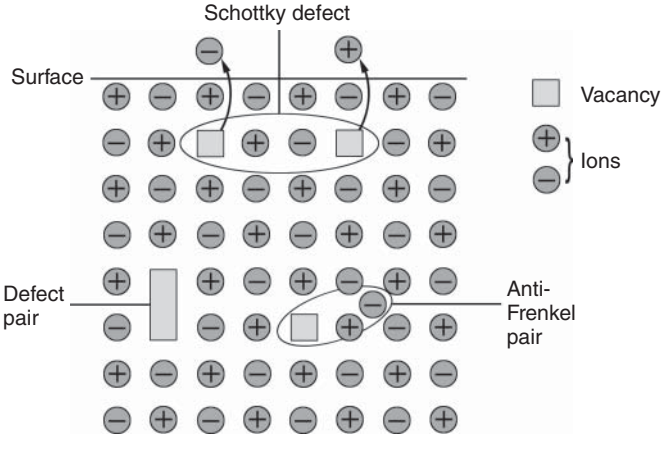

Figure 4.2 Point defect pairs in ionic crystals.

impossible to grow any crystal defect-free of intrinsic point defects. ***Extrinsic point defects*** are ***substitutional*** and ***interstitial impurities***. In general, extrinsic point defects are not in thermodynamic equilibrium. Therefore, a complete removal of extrinsic point defects is theoretically possible, however difficult it is practically. For example, within the Avogadro project, a monoisotopic FZ-silicon crystal was grown from a polycrystalline ^{28}Si with an isotope enrichment of 99.994% for a new kilogram standard in the Leibnitz Institute of Crystal Growth Berlin [1, 2]. By a specific segregation process, the carbon content (extrinsic point defect) could be reduced from 5×10^{15} cm^{-3} to $<3 \times 10^{14}$ cm^{-3}. A complete removal of C impurity is until now not possible in practise.

The formation of point defects in crystals can also be induced by the following processes:

- irradiation of crystals with high-energy particles,
- mechanical treatment of crystals, and
- plastic deformation of crystals.

For the identification of point defects and the description of defect reactions, a specific point defect notation is necessary. The commonly applied system for the description of point defects is the ***Kröger-Vink notation*** [3]. This system consisting of so-called structure elements enables also the comprehension of point defects in equations of chemical reactions for the description of defect chemistry. The general symbol describing a structure element is designated by C_S^Q, where C defines the ***species***, the subscript S describes the location of the defect and the superscript Q represents the ***effective charge*** of the defect**.** We will illustrate the Kröger–Vink notation for some examples of point defects in spinel ($MgAl_2O_4$). The spinel structure and the numerous structural variants between the two extreme cation distributions of the *normal spinel* $A(B_2)X_4$ and the *inverse spinel* $B(AB)X_4$ were already discussed in Section 1.5. The first line gives the notation for ion occupation of an ideal normal spinel. An effective charge of zero is designated by superscript x, a positive effective charge by superscript dot ($^\bullet$) and a negative one by superscript prime ($'$). The effective charge Q of the defect is related to the charge of the perfect crystal. Thus, the Mg, Al, and O ions located at their regular lattice positions have an effective charge of zero. In general, Q is given by

$$Q = q_\mathrm{d} - q_\mathrm{s} \tag{4.1}$$

The parameters q_d and q_s are the real charges of the species at the defect site and at the regular lattice site.

The Mg'_{Al} antisite defect has an effective charge of 1^-. The real charge of Mg at the Al position is 2^+ and the real charge at the Al site in a perfect spinel is 3^+.

$$Q = q_\mathrm{d} - q_\mathrm{s} = (2-3) = -1$$

Conversely, the $Al^\bullet_{Mg}$ antisite defect has an effective charge of 1^+. The real charge of the Al defect at the Mg position is 3^+ and the real charge at the Mg site in the spinel lattice is 2^+.

$$Q = q_d - q_s = (3-2) = +1$$

For the vacancies V''_{Mg}, V'''_{Al}, $V^{\bullet\bullet}_{O}$ in the spinel, the following relations hold for the effective charges:

$$V''_{Mg} \quad Q = q_d - q_s = (0-2) = -2$$

$$V'''_{Al} \quad Q = q_d - q_s = (0-3) = -3$$

$$V^{\bullet\bullet}_{O} \quad Q = q_d - q_s = (0-(-2)) = +2$$

The effective charges of the interstitial defects $Mg^{\bullet\bullet}_i$, $Al^{\bullet\bullet\bullet}_i$, O''_i are given by

$$Mg^{\bullet\bullet}_i \quad Q = q_d - q_s = (2-0) = 2$$

$$Al^{\bullet\bullet\bullet}_i \quad Q = q_d - q_s = (3-0) = 3$$

$$O''_i \quad Q = q_d - q_s = (-2-0) = -2$$

The formation of the eight isolated intrinsic point defects in $MgAl_2O_4$ given in Table 4.2 can be described by the following defect formation equations:

$$\text{Antisite defects}: Mg^x_{Mg} + Al^x_{Al} \rightleftharpoons Mg'_{Al} + Al^{\bullet}_{Mg} \tag{4.2}$$

The number of generated antisite defects determines the inversion degree λ (normal spinel $\lambda = 0$, inverse spinel $\lambda = 1$; $Mg_{1-\lambda}\,Al_\lambda((Mg_\lambda Al_{2-\lambda})O_4)$, for details

Table 4.2 Illustration of the Kröger–Vink notation for the description of point defects.

Kröger–Vink symbol	Type of defect
Mg^x_{Mg}, Al^x_{Al}, O^x_O	Cations Mg, Al, and anion ***O*** on their own lattice sites x – effective charge 0
Mg'_{Al}, $Al^{\bullet}_{Mg}$	Mg ion occupies an Al site ($'$ – effective charge 1^-), Al ion occupies a Mg site ($^\bullet$ – effective charge 1^+),
V''_{Mg}, V'''_{Al}, $V^{\bullet\bullet}_O$	Mg and Al vacancies with an effective charge of 2^- and 3^-, respectively O vacancy with an effective charge of 2^+
$Mg^{\bullet\bullet}_i$, $Al^{\bullet\bullet\bullet}_i$, O''_i	Mg and Al interstitials with an effective charge of 2^+ and 3^+, respectively ***O*** interstitial with an effective charge of 2^-
$(Mg^{\bullet\bullet}_i : Mg'_{Al})^{\bullet}$	Associated defect (defect cluster of a Mg interstitial and a Mg antisite defect) with an effective charge of 1^+
$(V^{\bullet\bullet}_O : Mg'_{Al})^{\bullet}$	Associated defect (defect cluster of an O vacancy and a Mg antisite defect) with an effective charge of $1^{+/-}$
e'	Electron
$h^{\bullet}$	Hole

see Section 1.5). The formation of antisite defects in spinel is energetically more favorable than the formation of any other intrinsic point defect in spinel.

$$\text{Frenkel defects}: \ \mathrm{Mg}_{\mathrm{Mg}}^{x} \rightleftharpoons V_{\mathrm{Mg}}'' + \mathrm{Mg}_{\mathrm{i}}^{\bullet\bullet} \tag{4.3}$$

$$\mathrm{Al}_{\mathrm{Al}}^{x} \rightleftharpoons V_{\mathrm{Al}}''' + \mathrm{Al}_{\mathrm{i}}^{\bullet\bullet\bullet} \tag{4.4}$$

$$\text{Anti-Frenkel defect}: \ \mathrm{O}_{\mathrm{O}}^{x} \rightleftharpoons V_{\mathrm{O}}^{\bullet\bullet} + \mathrm{O}_{\mathrm{i}}'' \tag{4.5}$$

$$\begin{aligned}\text{Schottky defect}: \ \mathrm{Mg}_{\mathrm{Mg}}^{x} + 2\mathrm{Al}_{\mathrm{Al}}^{x} + 4\mathrm{O}_{\mathrm{O}}^{x} &\rightleftharpoons V_{\mathrm{Mg}}'' + 2V_{\mathrm{Al}}''' + 4V_{\mathrm{O}}^{\bullet\bullet} \\ &+ \mathrm{Mg}_{\mathrm{Mg}}^{x} + 2\mathrm{Al}_{\mathrm{Al}}^{x} + 4\mathrm{O}_{\mathrm{O}}^{x}\end{aligned} \tag{4.6}$$

This equation can be simplified and written as follows:

$$0 \rightleftharpoons V_{\mathrm{Mg}}'' + 2V_{\mathrm{Al}}''' + 4V_{\mathrm{O}}^{\bullet\bullet} \tag{4.7}$$

The null value stands for the perfect crystal.

In addition to the single point defects in spinel, many associated point defect types (defect cluster) can be generated. In addition to the isolated interstitials given in Table 4.2, there are also "split interstitials" energetically stable in the spinel structure as evidenced by computer simulation [4]. The "*magnesium split interstitial*" $\mathrm{Mg}_{\mathrm{i}}^{\bullet\bullet} - V_{\mathrm{Mg}}'' - \mathrm{Mg}_{\mathrm{i}}^{\bullet\bullet}$ consists of two magnesium cations, which are transferred from normal tetrahedral sites to two unoccupied octahedral sites. The formed magnesium vacancy is surrounded by the two occupied octahedral sites. In the case of the "*aluminum split interstitial*" $\mathrm{Al}_{\mathrm{i}}^{\bullet\bullet\bullet} - V_{\mathrm{Mg}}'' - \mathrm{Mg}_{\mathrm{i}}^{\bullet\bullet}$, one aluminum and one magnesium cation are transferred from their lattice sites to the previously unoccupied octahedral lattice sites. Two examples of associated defects in spinel are given in Table 4.2.

Besides the structural point defects electronic defects, that is, electrons e' and holes $h^{\bullet}$ can exist.

$$\text{Electronic defects}: \quad \text{null} \rightleftharpoons e' + h^{\cdot} \tag{4.8}$$

Electronic defects play an important role in many cases. For instance, electrical properties such as the conductivity of intrinsic semiconductors can be changed and improved by controlled impurity doping using the methods of diffusion or ion implantation. Semiconductors where the electrical conductivity is determined by impurity atoms are called ***extrinsic semiconductors***. When the intrinsic semiconductor silicon is doped with an ***electron donor*** (e.g., P, As, and Sb), an ***n-type conductivity*** is generated by ***excess electrons e′*** (*n-negative charge*) from the donor atoms (one per donor atom). Conversely, when silicon is doped with an ***electron acceptor*** (e.g., Al, Ga, and In), a ***p-type conductivity*** is caused by ***electron holes h•*** (*positive charge*). One of the possible sources of color in crystals is the so-called color center, where some of them are specific ***electron*** and ***hole color centers***.

A really important aspect is that the formation of point defects in a crystal lowers its free energy to a minimum, whereas the formation of line defects, planar defects, and three-dimensional defects raises the free energy in a crystal.

In the following section, we calculate the number of point defects that are present in a crystal under the condition of thermal equilibrium. The state of a crystal at the thermal equilibrium for a given temperature and pressure corresponds to the minimum of the Gibbs free energy ΔG. Let us assume there were n_V vacancies formed in an otherwise perfect crystal consisting of N atoms. The formation of vacancies is accompanied by a change of Gibbs free energy.

$$\Delta G = \Delta H - T\Delta S \tag{4.9}$$

The formation of point defects in a crystal is an endothermic process. This means the positive enthalpy term ΔH will increase the energy. This increase of energy will be counterbalanced by the entropy term ΔS, which at least causes a reduction of the free energy to a minimum value. The increase of enthalpy is given by the product of the formation enthalpy for a vacancy ΔH_f and the number n of formed vacancies:

$$\Delta H = n \cdot \Delta H_f \tag{4.10}$$

The entropy term consists of two parts. The vibrational entropy ΔS_{vibr} takes into consideration the change of thermal entropy caused by the altered vibrations of atoms surrounding the vacancies. It is assumed that the changes of vibrational entropy are approximately proportional to the number of vacancies. A bit more complex is the treatment of configurational entropy ΔS_{vibr}.

$$\Delta S = n \cdot \Delta S_{vibr} + \Delta S_{conf} \tag{4.11}$$

For a crystal consisting of N atoms and n_v vacancies, numerous different arrangements of point defects are possible and this can be described by

$$W = \frac{N!}{n!(N-n)!} \tag{4.12}$$

The parameter W represents the thermodynamic probability for the distribution of n vacancies among N lattice sites. The configurational entropy ΔS_{conf} is given by

$$\Delta S_{conf} = k \cdot \ln W = k \cdot \ln \frac{N!}{n!(N-n)!} \tag{4.13}$$

The value of the Boltzmann constant k is $1.38 \times 10^{-23}\,\mathrm{J\,K^{-1}}$ or $8.62 \times 10^{-5}\,\mathrm{eV\,K^{-1}}$. The logarithm of factorials in Equation 4.13 can be approximated using the simpler form of Stirling's formula:

$$\ln x! \approx x \cdot \ln x \tag{4.14}$$

Then Equation 4.13 can be rewritten as follows:

$$\Delta S_{conf} = k[N \cdot \ln N - n \cdot \ln n - (N-n) \cdot \ln(N-n)] \tag{4.15}$$

An example of calculation of ΔS_{conf} for vacancy distribution in a monoatomic crystal using the correct expression of Stirling's approximation $\ln n! \approx n \cdot \ln n - n + {}^1/_2 \ln(2\pi n)$ is given in the book of Tilley [5]. The change in free energy caused by the formation process of vacancies can be now written as

$$\Delta G = n \cdot \Delta H_f - T(n \cdot \Delta S_{\text{vibr}} + \Delta S_{\text{conf}}) \tag{4.16}$$

The number of vacancies at thermal equilibrium can be calculated by setting

$$\left(\frac{\mathrm{d}\Delta G}{\mathrm{d}n}\right)_{\mathrm{T}} = 0 \tag{4.17}$$

Inserting the values of ΔS_{conf} (Equation 4.15), the derivative can be written as

$$\left(\frac{\mathrm{d}\Delta G}{\mathrm{d}n}\right)_{\mathrm{T}} = \frac{\mathrm{d}}{\mathrm{d}n}\{n \cdot \Delta H_{\mathrm{f}} - n \cdot T\Delta S_{\text{vibr}} - kT \times [N \cdot \ln N - n \cdot \ln n - (N-n) \cdot \ln(N-n)]\} = 0 \tag{4.18}$$

$$\left(\frac{\mathrm{d}\Delta S_{\text{conf}}}{\mathrm{d}n}\right)_{\mathrm{T}} = k\frac{\mathrm{d}}{\mathrm{d}n}[N \cdot \ln N - n \cdot \ln n - (N-n) \cdot \ln(N-n)] \tag{4.19}$$

$$\left(\frac{\mathrm{d}\Delta S_{\text{conf}}}{\mathrm{d}n}\right)_{\mathrm{T}} = k\left[\left(-\ln n - \frac{n}{n}\right) - \left(-\ln(N-n) + \frac{(N-n)}{(N-n)}\right) \cdot (-1)\right] \tag{4.20}$$

The derivation yields

$$\left(\frac{\mathrm{d}\Delta G}{\mathrm{d}n}\right)_{\mathrm{T}} = \Delta H_{\mathrm{f}} - T\Delta S_{\text{vibr}} - kT[-\ln n - 1 + \ln(N-n) + 1] = 0 \tag{4.21}$$

Equation 4.21 can be clearly arranged as follows:

$$\Delta H_{\mathrm{f}} - T\Delta S_{\text{vibr}} + kT \ln\left(\frac{N-n}{n}\right) = 0 \tag{4.22}$$

Rearranging Equation 4.22 provides

$$n = (N-n) \cdot \exp(\Delta S_{\text{vibr}}/k) \cdot \exp(-\Delta H_{\mathrm{f}}/kT) \tag{4.23}$$

In general, the number of vacancies in a crystal is much smaller than the number of occupied lattice sites ($n_{\mathrm{V}} \ll N$). Thus, we can write

$$\frac{n}{N} \approx \exp(\Delta S_{\text{vibr}}/k) \cdot \exp(-\Delta H_{\mathrm{f}}/kT) \approx \exp(-\Delta G_{\mathrm{f}}/kT) \tag{4.24}$$

Both the vibrational entropy ΔS_{vibr} and the formation enthalpy ΔH_{f} contribute to the equilibrium concentration of vacancies $c_{\mathrm{V}} = n/N$. In most cases, the equilibrium concentration is essentially determined by the enthalpy term.

The main conclusion that we can draw from Equation 4.24 is that at any temperature above absolute zero ($T > 0\,\mathrm{K}$) all crystals will have a certain number of vacancies. We can also see that with increasing temperature the equilibrium concentration of vacancies also increases. Furthermore, a decrease in the value of formation energy ΔG_{f} of the defect causes an increase in the defect concentration. It is neither possible to grow a crystal without such defects nor possible to

Table 4.3 Energy of formation of vacancy, Schottky and Frenkel defects in selected compounds.

Vacancy Compound	ΔE_V (eV)	Schottky Compound	ΔE_S (eV)	Frenkel Compound	ΔE_F (eV)
Al	0.76	LiBr	1.80	SrF_2	0.70
Au	0.98	KCl	2.26	AgBr	1.20
Ag	1.1	NaCl	2.30	AgCl	1.60
Cu	1.14	KBr	2.37	CaF_2	2.80
Mo	3.24	CaO	6.10	UO_2	3.40
W	3.51	MgO	6.60	ZrO_2	4.10

remove all of them by a specific thermal treatment (e.g., annealing at high temperatures and subsequent rapid quenching). Those defects are called *intrinsic* or *thermodynamic* point defects.

The derivation of equations for calculating the equilibrium concentration of Schottky and Frenkel defects can be carried out in a similar manner.

The equation for the calculation of ***Schottky defects*** is given by

$$\frac{n_S}{N} \approx \exp(\Delta S_{vibr}/2k) \cdot \exp(-\Delta H_{fS}/2kT) \approx \exp(-\Delta G_{fS}/2kT) \tag{4.25}$$

The parameter n_S denotes the number of cation and anion vacancies distributed among the possible lattice sites N, and ΔG_{fS} is the formation energy of a pair of vacancies.

A similar equation is valid for the calculation of the number of n_F ***Frenkel defects*:**

$$\frac{n_F}{(NN_i)^{1/2}} \approx \exp(\Delta S_{vibr}/2k) \cdot \exp(-\Delta H_{fF}/2kT) \approx \exp(-\Delta G_{fF}/2kT) \tag{4.26}$$

Here ΔG_{fF} is the formation energy of an interstitial, N is the number of regular lattice positions, and N_i is the number of interstitial positions.

Experimental values of the formation energy of vacancies, Schottky and Frenkel defects in selected compounds are given in Table 4.3.

Now we will illustrate how the concentration of Schottky defects in NaCl is changed as a function of temperature. First, we have to calculate the number of Na and Cl atom sites in the crystal per cubic centimeter. The number of occupied lattice sites in the unit cell is 8. The lattice constant of NaCl is 5.46 Å.

$$N = \frac{8\,\text{atoms/unit cell}}{(5.46\forall \times 10^{-8}\,\text{cm})^3} = 4.47 \times 10^{22}\,\text{atoms cm}^{-3} \tag{4.27}$$

Using Equation 4.25, the number of Schottky defects n_S can be calculated for a given temperature. The formation energy for a Schottky defect in NaCl is 2.30 eV. For a temperature of 500 K, the number of Schottky defects is

$$n_S = 4.47 \times 10^{22} \times \exp\left(-\frac{2.3\,eV}{2 \times 8.62 \times 10^{-5}\,eV/K \times 500\,K}\right) = 1.2 \times 10^{11} \tag{4.28}$$

Table 4.4 Concentrations of Schottky defects in NaCl as a function of time.

Temperature (K)	n_S/N	n_S (cm^{-3})
300	4.8×10^{-20}	2.1×10^{3}
500	2.6×10^{-12}	1.2×10^{11}
600	1.0×10^{-10}	4.5×10^{12}
900	3.6×10^{-7}	1.6×10^{16}
Melting point 1074	4.0×10^{-6}	1.8×10^{17}

The concentrations of Schottky defects in NaCl in the temperature range from 300 K (room temperature) to 1074 K (melting point) are listed in Table 4.4.

Point defects control and modify a multitude of physical phenomena and properties of crystals. Diffusion as the material transport by atomic motion, that is, by a series of jumps of individual atoms, is one the phenomena where the diffusion mechanisms are strongly coupled with the presence of a specific type of point defects. The following basic mechanisms occur:

Vacancy mechanism: An atom is jumping from a normal lattice site to an adjacent vacancy. This means there is an exchange of the positions of the diffusing atoms and the vacancies. Diffusing atoms and vacancies are moving in opposite directions.

Interstitial mechanism: This diffusion type also denoted as ***direct interstitial mechanism*** is given if an atom on an interstitial site jumps to an adjacent interstitial site. Impurity atoms such as H, C, N, and O diffuse by this mechanism because they are small enough to occupy an interstitial site (e.g., tetrahedral or octahedral voids in a structure).

Interstitialcy mechanism: This mechanism is a two-step movement. An interstitial atom is jumping to an occupied normal lattice site bouncing out this lattice atom. The lattice atom is then moving to an adjacent interstitial position. A ***colinear interstitialcy diffusion*** occurs if the interstitial atom and the bounced out lattice atom are moving in the same direction. If the directions of both atoms are different, a ***noncolinear interstitialcy diffusion*** is given.

The three types of diffusion mechanisms are schematically illustrated in Figure 4.3.

There are some other atomic mechanisms of diffusion proposed (for a detailed treatment see, e.g., [6]).

Another example where a change of a physical property is associated with the presence of point defects are the ***color centers***. Nowadays, the term *color center* is used for any defect that causes light absorption. If the absorption bands are in the visible range of a spectrum, a color change of the crystal can be observed. This color is complimentary to the color canceled out by the absorption band. Color centers were first detected when alkali halides were irradiated by X-rays. They

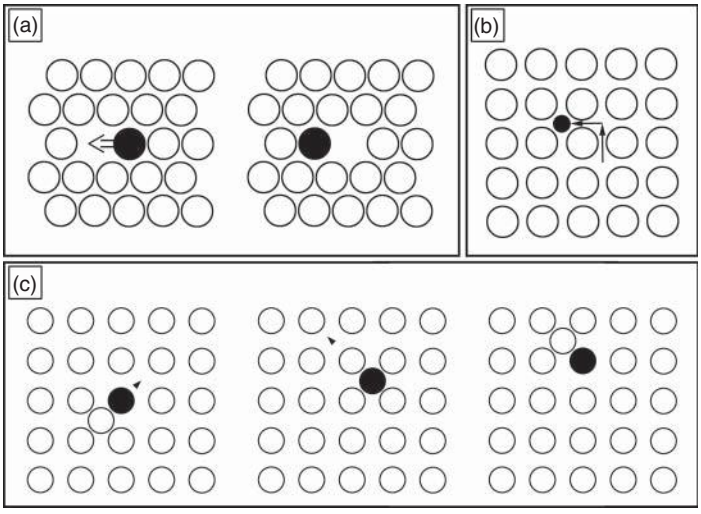

Figure 4.3 Atomic mechanisms of diffusion: (a) vacancy mechanism, (b) interstitial mechanism, and (c) interstitialcy mechanism.

were denoted as "*Farbzentren*" in Germany (color centers). The original F-center is an anion vacancy where an electron is trapped ($V_{Cl}^{\bullet} e'$). There are a variety of F-centers in alkali halides where either electrons or holes are trapped at an anion vacancy site. Two of the F-centers are schematically illustrated in Figure 4.4.

A chemically homogeneous pristine and nearly perfect diamond should be transparent and colorless because of the wide bandgap of 5.47 eV corresponding to a wavelength of 225 nm (deep ultraviolet). Probably diamond is the material with the most color centers where more than 500 color centers are known. Most of these centers occur in synthetic diamond and are associated with impurities. Nitrogen is the most important impurity in diamond. It is present in more than 50 color centers in diamond. In the following section, we exemplarily illustrate how the color of diamonds is related to impurities and specific color centers. An overview of important optical defects in diamond and their effect on color is given in [7, 8].

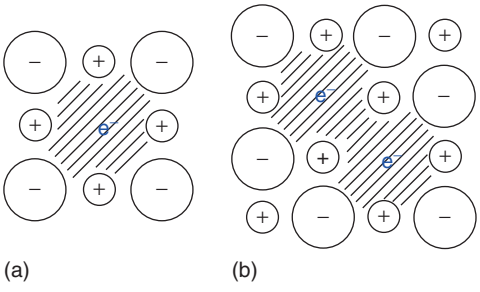

Figure 4.4 (a,b) F-center and F_2 center (pair of adjacent F-centers) in alkali halides.

Brown diamonds: It is not exactly clear until now what causes the brown coloration of diamond. There exist several assumptions about it based on which the evidence of plastic deformation in natural diamonds concluded that dislocations are a possible source. TEM (transmission electron microscopy) and positron annihilation strengthen the suggestion that the brown coloration is caused by multivacancies.

Yellow diamonds: The yellow color is caused by the ***N3 color center***. This center is formed by three substitutional N atoms surrounding a vacancy.

Orange diamonds: The color centers $H4$ and $H3$ cause an orange color. A $H4$ center consists of four substitutional N atoms surrounding two vacancies. An $H3$ center consists of two substitutional N atoms separated by a vacancy in neutral state $(N_i V_C N_i)^x$.

Green diamonds: A dark green color is caused by the so-called ***GR1 color center*** consisting of a neutral vacancy V_C^x.

Blue diamonds: The blue color is caused by an extremely low impurity of boron (<50 ppm). Boron as an acceptor causes a band gap change, which is the physical cause for the color change.

Black diamonds: The black color is often caused by inclusions (e.g., graphite).

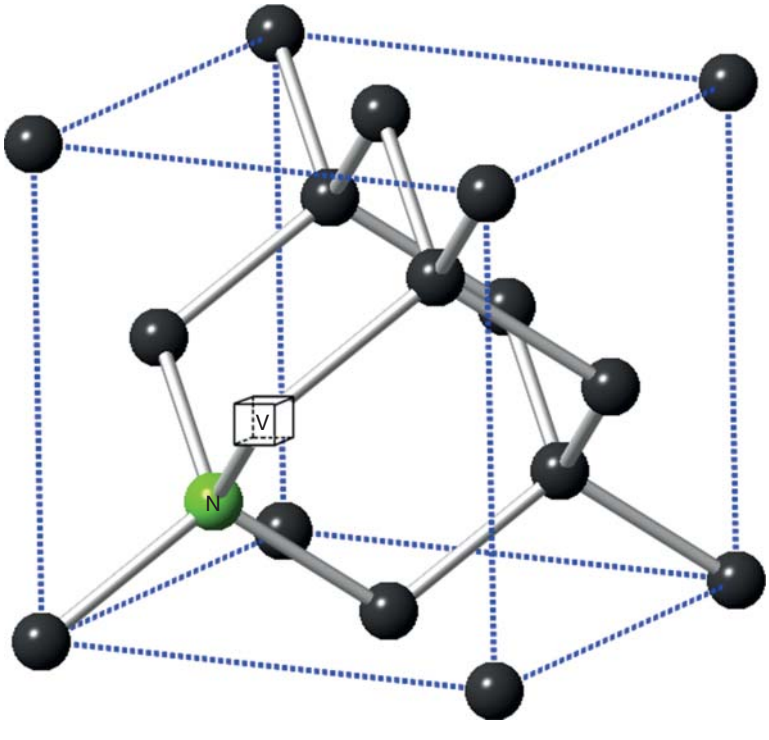

Figure 4.5 Structure of NV-color center.

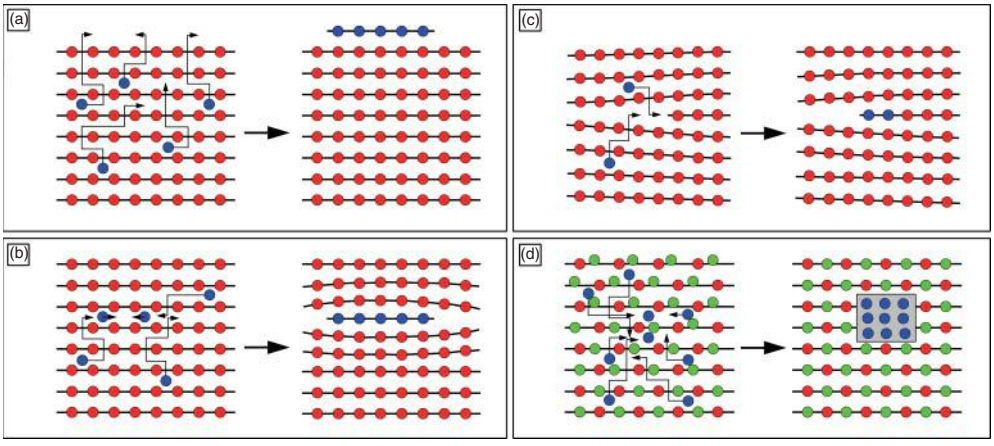

Figure 4.6 Mechanisms of interstitial annihilation: (a) diffusion to surface, (b) formation of a dislocation loop or stacking fault by aggregation of interstitials, (c) absorption at an edge dislocation (negative climb), and (d) formation of a precipitate.

One of the most investigated color centers in diamond is the ***NV***-center. This center is formed by a substitutional N atom and an adjacent vacancy in the diamond structure (Figure 4.5). The NV-center occurs in natural as well as synthetically grown diamond crystals. The NV-center can occur as NV- and NV^0-center. It was found that the very stable NV-center in diamond can be used as a basis for the development of single photon sources for quantum optical experiments (for more detailed information see, e.g., [9]).

Point defects and particular point defect agglomerations at high concentration are the source for the formation of various crystal defects. The condensation of vacancies and interstitials may lead to the formation of SFs with different types of surrounding partial dislocations. The formation of dislocation loops is also very often caused by agglomerated point defects. Furthermore, the precipitation of a new phase can also be caused as a consequence of the reduction of an excess of point defects. The climb process of dislocations (Section 4.1.2) is connected with the diffusion and agglomeration of vacancies and interstitials. Some of the mechanisms that can lead to a reduction of an excess of interstitials are schematically illustrated in Figure 4.6.

4.1.2
One-Dimensional Defects

One-dimensional crystal defects are ***line defects*** that can be divided into three principal categories. They are as follows:

- ***Dislocations***
- *Disclinations*
- *Dispirations*.

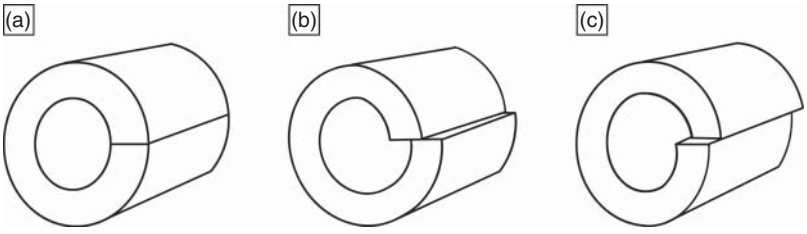

Figure 4.7 Volterra cut in a hollow cut cylinder: (a) cut cylinder, (b) edge dislocation: displacement of the walls perpendicular to cylinder axis, and (c) screw dislocation: displacement of the walls parallel to cylinder axis.

We will use the procedure originally introduced by Volterra for the description of possible deformations in a continuum [10] to explain the differences between the three categories. We will take a hollow cut cylinder as shown in Figure 4.7 and displace the sides of the cut. Then we can add or remove material and put together the walls again. The final deformation state of the cylinder depends on the type of displacement. If we have shifted the two walls along a vector perpendicular or parallel to the cylinder axis, the resulting discontinuities are ***dislocations***. A displacement of the two parts of the crystal by a rotation will cause a ***disclination***. When the displacement is a combination of a vector shift and a rotation (screw rotation), a ***dispiration*** results.

Summarizing the results of the Volterra cut procedure, we can say that ***dislocations***, ***disclinations***, and ***dispirations*** are characterized by symmetry operations of ***translations***, ***rotations***, and ***screw rotations***, respectively (for comprehensive description of Volterra's method see, e.g., [11, 12]).

Dislocations are common in all kinds of crystalline materials. Disclinations are observed as specific defects in some alloys. They are essential defects in liquid crystals. Dispirations were theoretically predicted and derived by Harris in 1970 [13]. In the following section, we treat the basic properties of dislocations.

The main geometrical properties of dislocations are determined by

- the dislocation line $\boldsymbol{l}$
- the Burgers vector $\boldsymbol{b}$.

The two fundamental dislocation types are the ***edge dislocation*** and the ***screw dislocation***. The Burgers vector $\boldsymbol{b}$ of an edge dislocation is perpendicular to the dislocation line $\boldsymbol{l}$, whereas for a screw dislocation, the Burgers vector $\boldsymbol{b}$ is parallel to the dislocation line $\boldsymbol{l}$. The atomic arrangement of a crystal around an edge dislocation is illustrated in Figure 4.8. A characteristic feature of an edge dislocation is the inserted extra half-plane. The bottom of this half-plane defines the *dislocation line* which is perpendicular to the plane of the figure. The region around the dislocation line is characterized by a lattice deformation (displaced atoms), which decreases with increasing distance from the dislocation line. The most distorted area in striking distance of the dislocation line is called the *dislocation core*. The value of the dislocation core radius r_0 is in the range of $\boldsymbol{b}$ to $5\boldsymbol{b}$ depending on the material (e.g., crystal structure and interatomic potential). The lattice distortions

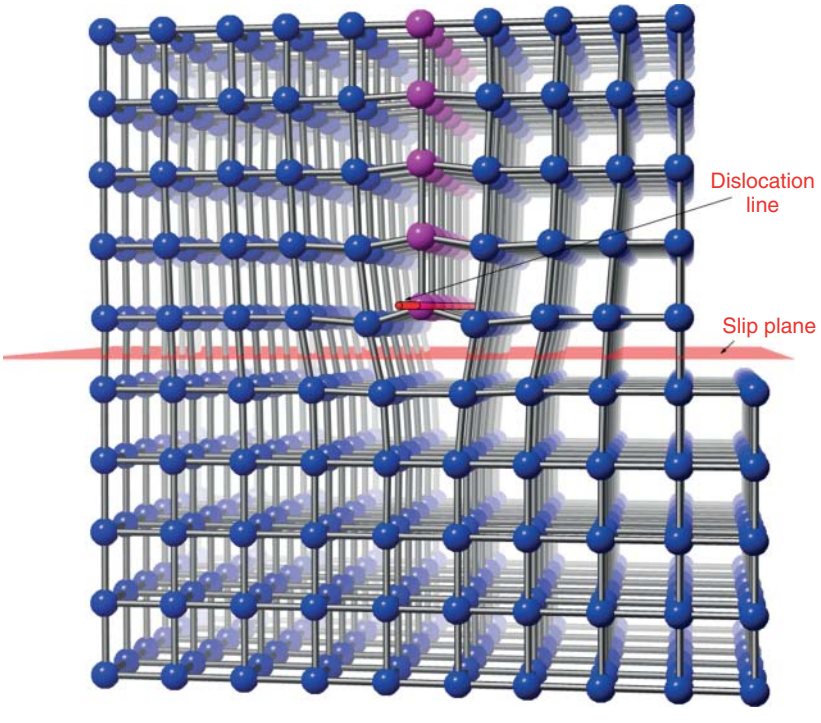

Figure 4.8 Atomic arrangement of an edge dislocation.

outside the core region can be mathematically treated by means of the linear elastic theory.

A model of a screw dislocation is shown in Figure 4.9 where the lattice is distorted along the dislocation line running from top-to-bottom of the crystal. The dislocation line acts as a spiral axis. This means that parallel atomic planes are winded through the crystal around the spiral axis to form a spiral surface. It was already discussed in Chapter 2 that screw dislocations are strongly correlated with the spiral growth of crystals and the occurrence of surface steps.

The general procedure to define the Burgers vector $\boldsymbol{b}$ of a dislocation in a crystal is the ***Burgers circuit*** construction using the finish-start/right-hand (FS/RH) convention. The two equivalent procedures are illustrated in Figure 4.10 for an edge dislocation in a simple cubic crystal. First, we will draw a closed circuit from the ***start*** atom (S) to the ***finish*** atom (F) around the dislocation outside the dislocation core in a clockwise (right-handed screw) direction as shown in Figure 4.10a. The identical circuit is carried out in the perfect reference crystal. The circuit in the reference crystal is not closed. The *vector from F to S*, which closes the circuit, is the Burgers vector (Figure 4.10b). Now we will apply the reversed procedure. First, the Burgers circuit is drawn in the perfect crystal (Figure 4.10c). Then, the identical circuit is carried out in the distorted crystal around the dislocation. Again, the circuit is not closed. Now the Burgers vector is pointing *from S to F* (Figure 4.10d).

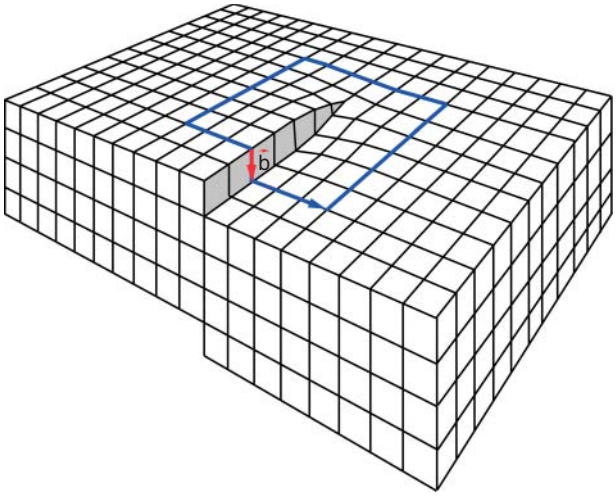

Figure 4.9 A screw dislocation within a crystal.

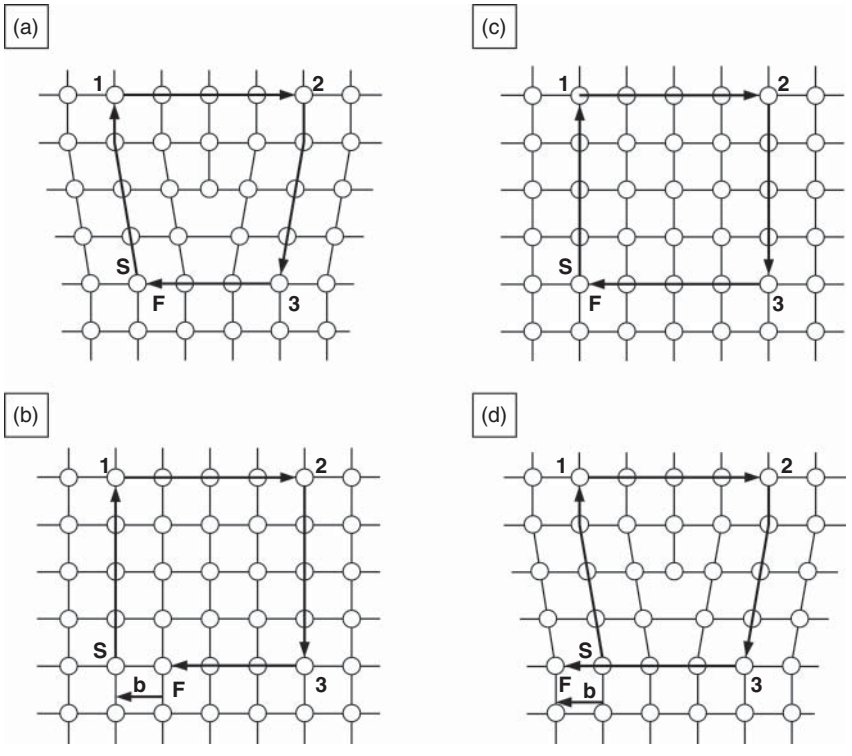

Figure 4.10 The Burgers circuit for the determination of the Burgers vector of an edge dislocation: (a) closed circuit around the dislocation, (b) circuit around the perfect reference crystal, (c) closed circuit around the perfect reference crystal, and (d) circuit around the dislocation.

An edge dislocation is designated by the symbol ⊥ where the vertical stroke shows the inserted half-plane and the horizontal stroke the location of the slip plane. According to the applied FS/RH convention, the symbol ⊥ denotes a *positive edge dislocation* and 𝕋 a *negative edge dislocation* with an inserted half-plane below the slip plane. A right-handed screw dislocation is given if $\boldsymbol{b} \uparrow\uparrow \boldsymbol{l}$ (*positive screw dislocation*) and a left-handed screw if $\boldsymbol{b} \uparrow\downarrow \boldsymbol{l}$ (*negative screw dislocation*). A ***mixed dislocation*** is composed of both edge and screw components. The Burgers vectors of the components are given by

$$\boldsymbol{b}_S = (\boldsymbol{b} \cdot \boldsymbol{l}) \cdot \boldsymbol{l} = (|\boldsymbol{b}| \cdot \cos\alpha) \cdot \boldsymbol{l} \tag{4.29}$$

$$\boldsymbol{b}_e = \boldsymbol{l} \times (\boldsymbol{b} \times \boldsymbol{l}) = (|\boldsymbol{b}| \cdot \sin\alpha) \cdot \boldsymbol{n} \tag{4.30}$$

where $\alpha \angle (\boldsymbol{l}, \boldsymbol{b})$ and $\boldsymbol{n}$ the unit vector perpendicular to $\boldsymbol{l}$. In general, if the Burgers vector of a dislocation is a translation vector of a crystal as shown in Figure 4.10 the dislocation is called a ***perfect dislocation***. It should be noted that the dislocation line cannot start or end inside the crystal. Dislocations must end at the surface of a crystal or at other dislocations like at a GB or may form a closed loop. We should be aware of the fact that the Burgers vector of a dislocation will be not changed along the dislocation line. If a dislocation will change the nature from an edge dislocation to a screw dislocation within the crystal, the Burgers vector remains the same at all points. A curved dislocation like a dislocation loop will have a constant Burgers vector.

A diffraction contrast TEM image of a typical dislocation arrangement in a spinel $MgAl_2O_4$ of low nonstoichiometry (MgO: $Al_2O_3 = 1:1.75$) is shown in Figure 4.11. In addition to isolated singular dislocations of different lengths, dislocation loops were obtained. In this bright-field image, the dislocations appear as dark lines in comparison to the nearly uniform background. The reason for the black contrast is a drastical change of the diffraction conditions caused by the *displacement field* around the dislocations. An essential parameter for the classification of the perfection of a crystal is the ***dislocation density*** ρ_{dis}, which is defined as the total length of dislocation line per unit volume ($\rho_{dis} = l/V$).

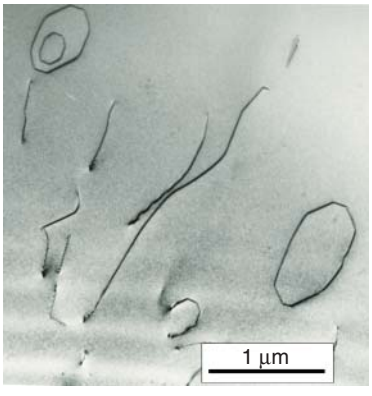

Figure 4.11 Diffraction contrast TEM image of dislocations in spinel $MgAl_2O_4$.

The dislocation density ρ_{dis} of the investigated Verneuil-spinels $MgAl_2O_4$ for nonstoichiometries ranging from MgO·1.75 Al_2O_3 to MgO·3 Al_2O_3 was in the order of $10^7 - 10^9\,cm^{-2}$. Stoichiometric Czochralski-spinels have a much higher degree of perfection with dislocation densities ρ_{dis} between 10^2 and $10^4\,cm^{-2}$.

The Burgers vector will also be conserved if dislocations form a network where different dislocations meet at the nodes. TEM images of a hexagonal dislocation network in spinel $MgAl_2O_4$ are shown in Figure 4.12. The Burgers vectors of the three pairs of dislocations were determined by systematically tilting the specimen and applying the contrast rules (invisibility criterion for dislocations) of the diffraction contrast technique (a description of the technique is given in Section 4.3). The three Burgers vectors of the dislocations are $b_1 = a/4\,[01\bar{1}]$, $b_2 = a/4\,[\bar{1}01]$, and $b_3 = a/4\,[1\bar{1}0]$. The resolution of the image does not allow unambiguously the determination of the exact node configuration. Possible node configurations are shown in Figure 4.12b. According to the *node rule* for dislocations, when N dislocations meet at the node, the sum of the Burgers vectors (outgoing and ingoing) is zero.

$$\sum_{i}^{N} \boldsymbol{b}_i = 0 \tag{4.31}$$

The three Burgers vectors of the dislocations forming the network in spinel fulfill this criterion.

A perfect dislocation in spinel has a Burgers vector of the type $\boldsymbol{b} = a/2\ \langle 110\rangle$. The network dislocations have Burgers vectors of $\boldsymbol{b} = a/4\ \langle 110\rangle$ with a length of $|\boldsymbol{b}| = a/4\sqrt{2}$, which is only half of the length of the lattice translation vector. A dislocation with a Burgers vector, which is only a part of a translation vector, is denoted as ***imperfect*** or ***partial dislocation*** or ***partial*** in short. In the lower diffraction contrast image of Figure 4.12a, black/white fringe patterns are clearly visible between the pairs of partial dislocations. This fringe contrast is caused by

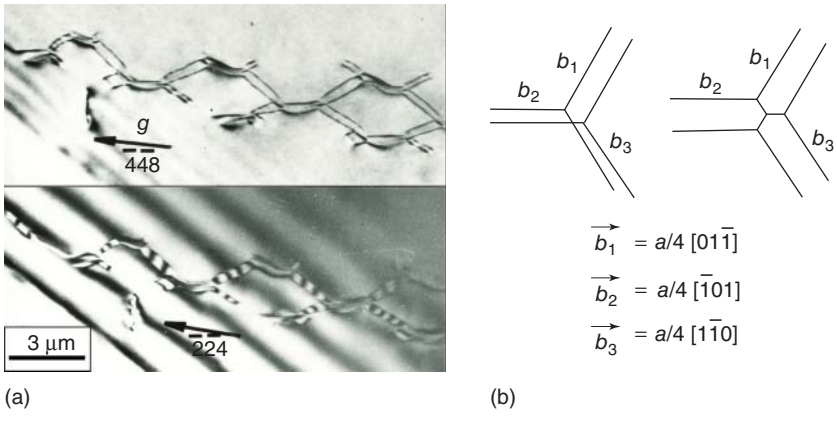

(a) (b)

Figure 4.12 Hexagonal dislocation network in (111) spinel $MgAl_2O_4$. (a) Bright-field images using different ***g***-vectors and (b) possible node configurations.

SFs. Each SF is bounded by two partials (for a detailed description of SFs, see Section 4.1.3.2). The formation of partial dislocations is possible by a dislocation reaction $b_1 \rightarrow b_2 + b_3$. The question arises as to what is the main criterion for the stability of a perfect and imperfect dislocation in a particular crystal. The Burgers vector of a dislocation is, of course, strongly connected with the geometry of the crystal structure. In addition, we have to take into consideration the energy of a dislocation. The formation of a dislocation in a crystal increases the energy of the crystal. We have mentioned earlier that the atoms surrounding the dislocations are displaced. The displacement is connected with a corresponding strain field. The total strain energy of a dislocation is the sum of the strain energy of dislocation core and strain energy of the region outside the core, which is elastically deformed (for a detailed theoretical treatment of the calculation of dislocation energy see, e.g., [11]). The main result is that the strain energy of a dislocation, also denoted as *self-energy of the dislocation*, is proportional to the square of the Burgers vector.

$$\boldsymbol{E} \approx \boldsymbol{b}^2 \tag{4.32}$$

From this relation, it is obvious that dislocations with shortest translation vectors as Burgers vectors are energetically most favorable. The stable Burgers vectors of cubic and hexagonal lattice types are given in Table 4.5. On the basis of Equation 4.32 *F.C. Frank* derived a criterion, nowadays denoted as ***Frank's rule***, which allows determining whether a dislocation will dissociate or not.

Let us consider the dissociation $b_1 \rightarrow b_2 + b_3$. The dissociation reaction will occur if $b_1^2 > (b_2^2 + b_3^2)$. The self-energy of the dislocation will then be lowered. The relation $b_1^2 < (b_2^2 + b_3^2)$ does not minimize the energy. Therefore, the dissociation will not take place. If the reaction is energetically counterbalanced $(b_1^2 = (b_2^2 + b_3^2))$, it cannot be predicted whether a dissociation occurs or not. Now we will describe the formation of the so-called ***Shockley partial dislocations*** in the fcc structure by a dissociation reaction of the stable perfect dislocation of type $a/2$ <110>. In Section 1.5.1 (Figure 1.68), we have shown that the fcc structure corresponds to the cubic closest packing 12/3/c1 and consists of closest-packed {111} planes with closest-packed <110> directions. The location of the vectors of

Table 4.5 Stable dislocations in simple lattice types.

Lattice type	Type of Burgers vector	Number of equivalent vectors
cP	a <100>	6
cI	$a/2$ <111>	8
	a <100>	6
cF	$a/2$ <110>	12
hP	$a/3$ <11.0>	6
	c <00.1>	2

the dissociation reaction

$$\frac{1}{2}[\bar{1}10] = 1/6[\bar{2}11] + 1/6\,[\bar{1}2\bar{1}] \tag{4.33}$$

$$b^2 : \quad a^2/2 > a^2/6 + a^2/6$$

is illustrated in Figure 1.68. According to Frank's rule, the dissociation of the perfect dislocation into two Shockley partials is energetically favorable. It should be mentioned that between the partials a ribbon of SF is created (see description in Section 4.1.3.2). We will discuss later the physical meaning of Equation 4.33 with respect to the movement of dislocations. The two fundamental types of dislocation movements are ***glide*** and ***climb***. The glide motion is a so-called *conservative motion* because no removal or addition of material takes place. The dislocation moves in a plane, its ***glide plane***, along a particular crystallographic direction denoted as ***glide direction***. In literature, the terms ***glide*** and ***slip*** are synonymously used. Strictly speaking, *glide* denotes the motion of one dislocation, whereas *slip* describes the motion of many dislocations as in the case of plastic deformation of a material. Glide plane and glide direction are called ***glide elements*** and form a ***glide system***. The glide surface contains the dislocation line. Glide motion is always possible if $\boldsymbol{b}\cdot n = 0$, where n is the normal to the dislocation line. For a pure edge dislocation, the Burgers vector $\boldsymbol{b}$ and the dislocation line $\boldsymbol{l}$ define a single plane, which is the glide plane. For a screw dislocation, where $\boldsymbol{b}||\boldsymbol{l}$ any plane for which $\boldsymbol{b}\cdot n = 0$ is a possible glide plane. The glide process of a pure edge dislocation is schematically illustrated in Figure 4.13. The glide process in the crystal starts when the applied shear stress τ reaches the value of ***critical shear stress*** $\boldsymbol{\tau_c}$. This stress is necessary to override the so-called *Peierls–Nabarro* stress, which is a barrier to the motion caused by the periodicity of crystal lattice. During the glide process, the atoms above and below the glide plane are displaced against each other by shifts in the order of magnitude of b. We can see if the edge dislocation is moved across the glide plane to the surface of the crystal a surface step with a step height equal to the Burgers, vector $\boldsymbol{b}$ is generated. An important feature of the glide process is the ***velocity of dislocations***, which depends on

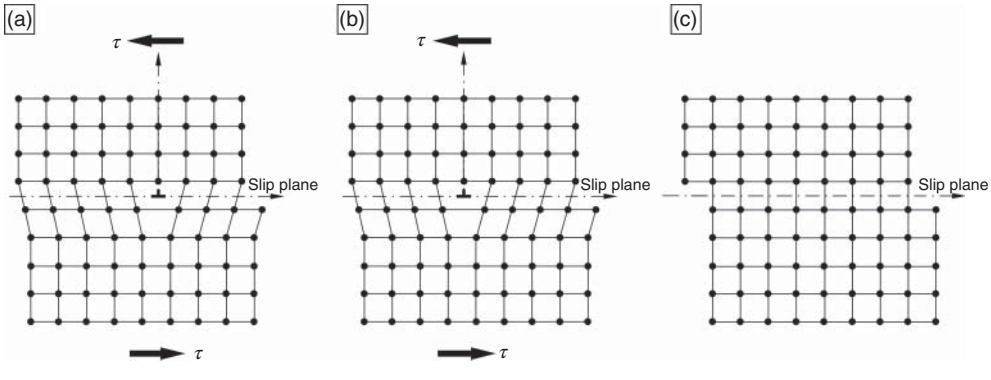

Figure 4.13 (a–c) Glide of an edge dislocation.

Table 4.6 Slip systems in some crystals.

Crystal structure type	Crystal class	Slip system Slip plane	Slip direction
Cu, Ag, Au – ***fcc***	$m\bar{3}m$	{111}	<1$\bar{1}$0>
α-Fe, W, Mo – ***bcc***	$m\bar{3}m$	{110}	<1$\bar{1}$1>
α-Fe, W – ***bcc***	$m\bar{3}m$	{211}	<$\bar{1}$11>
α-Fe, K – ***bcc***	$m\bar{3}m$	{321}	<$\bar{1}$11>
Cd, Zn, Mg – ***hcp***	6/*mmm*	{00.1}	<11.0>
	6/*mmm*	{10.1}	<11.0>
Ti, Zr – ***hcp***	6/*mmm*	{10.0}	<11.0>
NaCl – ***type***	$m\bar{3}m$	{110}	<1$\bar{1}$0>
CsBr, ***CsCl – type***	$m\bar{3}m$	{110}	<001>
Si, Ge, C – diamond type	$m\bar{3}m$	{111}	<1$\bar{1}$0>
GaAs, α-ZnS – sphalerite type	$\bar{4}3m$	{111}	<1$\bar{1}$0>
$MgAl_2O_4$ – spinel type	$m\bar{3}m$	{111}	<1$\bar{1}$0>
Nonstoichiometric spinel, at high temperatures		{110}	<1$\bar{1}$0>
C – graphite type	6/*mmm*	{00.1}	<11.0>

the investigated crystal (e.g., structure and bonding), the applied shear stress, temperature, impurities, type of dislocation, and so on.

The crystallographic parameters of the glide (slip) motion of dislocations are defined by the glide (slip) system as mentioned earlier. Examples of slip systems of some crystals of different structure types are given in Table 4.6. According to the point symmetry of the crystals, a different number of independent slip systems exist for a particular crystal structure. For a gold crystal (structure type A1, fcc structure), there are 12 slip systems according to the 4 unique {111} slip planes with 3 different <110> slip directions in each plane. The number of possible slip systems of type ({321}, < $\bar{1}$11 >) for α-Fe is 24 (24 different {321} planes with 1 < $\bar{1}$11 > direction). For hexagonal crystals with ***hcp*** structure like Cd, only three different slip systems of type ({00.1} <11.0>, 1 slip plane × 3 slip directions) exist. The slip process is the fundamental process of plastic deformation of crystals at normal temperatures. Now let us discuss Equation 4.33 with respect to the slip process. In Figure 1.68, the periodic three-layer stacking sequence *ABC* of the dense-packed (111) planes is illustrated. The slip of the perfect dislocation $\frac{1}{2}[\bar{1}10]$ means that the atoms of A layer move directly from one A point to the next one. If the perfect dislocation splits in the two partials 1/6 [$\bar{2}$11] and 1/6 [$\bar{1}2\bar{1}$], the slip proceeds indirectly from A via C to A by means of a zigzag motion, which is energetically more favorable than the direct slide process.

We have already mentioned that screw dislocations can slip on any plane for which the relation $\boldsymbol{b}\cdot\boldsymbol{n}=0$ is valid. If a screw dislocation is moving on a plane and encounters an obstacle, then it can change the slip plane. This process is called ***cross slip***. The different stages of a double cross slip are illustrated in Figure 4.14. The screw dislocation moves on a (111) plane and circumvent the

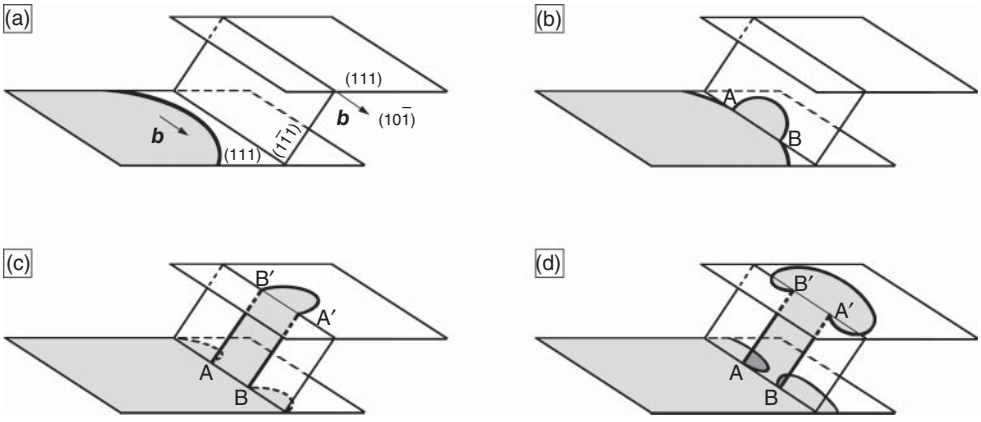

Figure 4.14 (a–d) Double cross slip of a screw dislocation.

obstacle between A and B by cross slip on the (1$\bar{1}$1) plane. The second cross slip of the screw allows it to move onto a plane parallel to the original one.

The motion of an edge dislocation out of its glide plane is called ***climb***. Climb is a nonconservative motion because it involves a rearrangement of atoms. The climb process is always coupled with the motion of point defects (vacancies and interstitials), which takes place at higher temperatures. A ***positive climb*** of the edge dislocation is characterized by a removal of rows of atoms, whereas a ***negative climb*** is caused by an addition of rows of atoms at the bottom of the half-planes. Figure 4.15 illustrates that a positive climb can occur by interstitial formation and emission (1) or vacancy aggregation (2). A negative climb will occur if interstitials are aggregated or vacancies are emitted. It should be noted that pure screw dislocations cannot climb. However, if screws have a small edge component as in the case of the so-called *helical dislocations*, climbing is possible. During the motion and intersection of dislocations, steps of atomic dimensions in the dislocation lines can be generated. Steps that are contained in the glide plane are called ***kinks*** and otherwise ***jogs***.

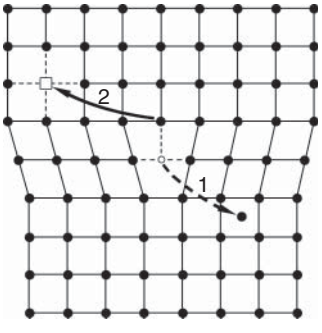

Figure 4.15 Positive climb of an edge dislocation.

Dislocations in crystals are already originated during the growth process where thermal and mechanical stress is a possible source of generation. When a seed crystal with dislocations in it is used for the growing process then these dislocations act as source for additional dislocations. An access of point defects can contribute to the formation and extension of dislocations as already described. Dislocations will also be formed if two regions (grains) in a crystal are slightly misaligned. The strain between the two grains forming the GB will be accommodated by the formation of dislocations as we will describe in Section 4.1.3.1. When a crystal is plastically deformed, the number of dislocations increases drastically. Most of the as-grown crystals have dislocation densities in the range of $10^3 - 10^6\ \mathrm{cm}^{-2}$. For heavily deformed metals, the dislocation density can rise up to $10^{11} - 10^{12}\ \mathrm{cm}^{-2}$. On the other hand, the crystal growth techniques for silicon were optimized that the growth of dislocation-free crystals is nowadays possible.

Dislocation multiplication occurs during the motion of dislocations under the applied shear stress. The already described process of *multiple cross slip* is one source of dislocation multiplication. The other well-known mechanism of dislocation multiplication is the ***Frank-Read source***, which is schematically illustrated in Figure 4.16. Let us assume a segment of a dislocation line, which is pinned at the two points. Under the action of shear stress, it bows out. A semicircle is formed if the applied stress reaches the value of critical stress ($\tau = \tau_c$). We see that a half-loop is formed, which is still anchored. This half-loop will further expand until the two segments touch and annihilate each other because they are of opposite signs. There are now two parts. The loop is no longer pinned and can freely move away from the source. The original pinned segment can start the process again.

The classical example of a Frank-Read source in silicon experimentally observed by W. C. Dash using the decoration technique with copper is shown in Figure 4.17.

The investigation of the dislocation structure of deformed crystals by means of the diffraction contrast method in a conventional TEM has tremendously contributed to the understanding of the processes of plastic deformation of materials. However, conventional TEM at accelerating voltages in the range of 100 – 200 kV is restricted to studies of very thin specimens in the range of 0.1 µm. High-voltage electron microscopes (>500 – 3000 kV) enable the incorporation of a high-temperature straining stage for the *in-situ* deformation of several

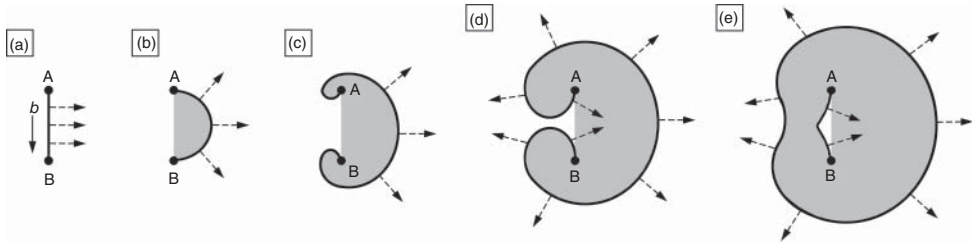

Figure 4.16 (a – e) Mechanism of dislocation multiplication by means of a Frank-Read source.

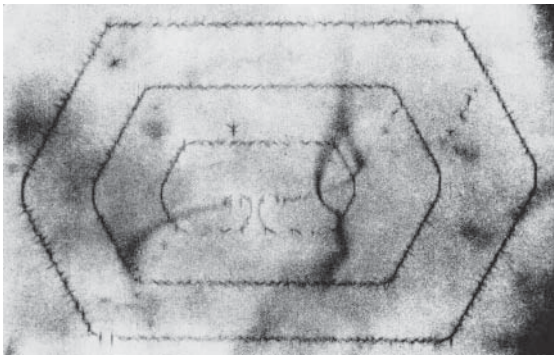

Figure 4.17 Copper decorated Frank-Read source in silicon. (From W. C. Dash in [14].)

micrometers thick specimens (for a comprehensive overview about *in-situ* deformation and dislocation dynamics during plastic deformation see, e.g., [15]). It can be assumed that the information on the dislocation structure retrieved from *in-situ* experiments of thick specimens corresponds to the dislocation structure of bulk crystals. The three high-voltage electron micrographs given in Figure 4.18a illustrate how the number of dislocations of nickel-based superalloy SC16 after heat treatment increases with increasing specimen thickness from left to right. The single-crystal superalloy SC16 consists of ordered cuboidal Ni_3Al precipitates (γ'-phase), which are coherently embedded in the solid solution fcc matrix (γ-phase) in the nondeformed state. *In-situ* high-temperature straining experiments at 1000 °C were carried out in the high-voltage electron microscope at 1000 kV [16]. The micrographs shown in Figure 4.18b clearly demonstrate the dependence of the dislocation and alloy structure of the applied load (at the beginning load 2.8 N, at final stage 14.5 N). The two micrographs of Figure 4.18c show the motion and creation of dislocation during *in situ* deformation after a time interval of 60 s. For a better comparison of the structural features, some points are especially labeled.

Dislocations and their ability to move through a crystal are mainly influencing the mechanical properties of a crystal. Properties such as brittleness and ductility of a material are closely related to the dislocation structure. For example, metals with *fcc* structure have a large number of slip systems and can be easily plastically deformed. They are quite ductile. The low number of slip systems of metals with *hcp* structure causes the brittleness in these materials. It is well-known that ceramics are more brittle than metals. This behavior is not caused by the lower dislocation density. Owing to the covalent bonding in ceramics, the dislocations do not easily slip and this is responsible for the brittleness. The formation of dislocation at higher temperatures is closely connected with point defects. The interaction between point defects and dislocations also influences the electronic properties of dislocations, which is of particular importance in semiconducting materials [17].

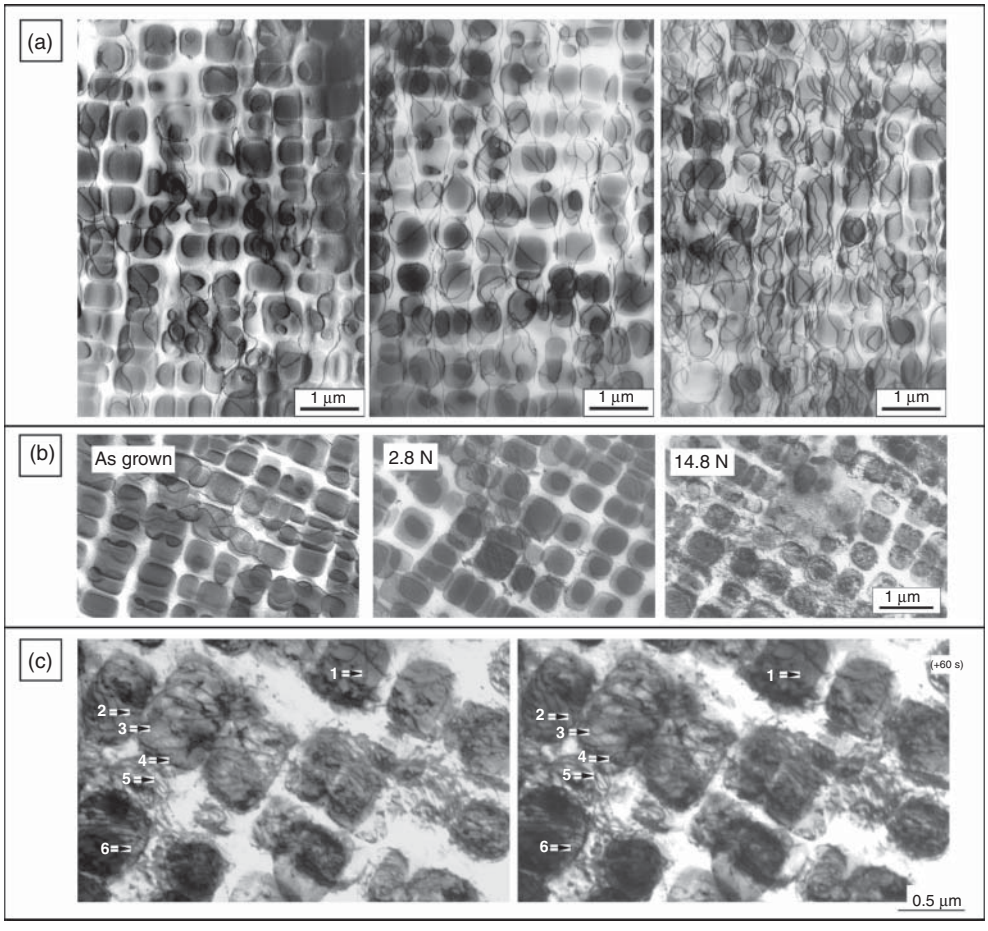

Figure 4.18 *In-situ* high-voltage electron microscopy studies of dislocations in nickel-based superalloy SC16. (a) Dislocation structure as a function of thickness. (b) Microstructure of SC16 at different stages of *in-situ* deformation at 1000 °C. (c) Generation and motion of dislocations during *in situ* deformation of SC16 in the HVEM.

4.1.3 Two-Dimensional Defects (Planar Defects)

A common feature of planar defects in crystals is the existence of internal interfaces. These interfaces are of great importance because they influence and/or even control essential properties of materials. A useful classification scheme for crystalline interfaces is to distinguish between homophase and heterophase boundaries (for a comprehensive treatment of crystalline interfaces see, e.g., [18]).

Homophase boundaries are interfaces between two crystals with the same crystal structure and the same chemical composition. The following planar defects form such type of boundaries: GBs, twins, SFs, APBs, inversion boundaries, and domain boundaries of ferroic crystals.

Heterophase boundaries are interfaces between two crystals where either the lattices and/or the bases are different. Examples of heterophase boundaries are as follows: Interfaces of thin or thick films on bulk crystals, boundaries in the various types of composites, multilayers, precipitates, and so on.

The atomic structure of the interfaces plays a particular role, which is often associated with heterogeneities caused by the interaction between the adjacent crystals as a function of crystal structure, lattice parameters, and bonding. The atomic structure of the interface may contain various structural and chemical defects (e.g., facets, steps, line defects, cracks, voids, atomic disorder, segregation, and precipitates). Therefore, a subclassification of interfaces in ***sharp*** and ***diffuse interfaces*** is useful. An important feature for classifying interfaces is the degree of matching of the lattices along the interfaces. In general, interfaces are divided into ***coherent***, ***semicoherent***, and ***incoherent interfaces*** (Figure 4.19).

A *coherent interface* (Figure 4.19a) is given if there is nearly a perfect two-dimensional lattice matching across the interface. The lattice parameter mismatch expressed by the "***misfit***" is so small that it will be assimilated by elastic coherency strain. The misfit is defined as follows:

$$m_f = (a_B - a_A)/a_A \tag{4.34}$$

where a_A is the lattice parameter of the reference lattice.

A *semicoherent interface* consists of regions with a nearly perfect lattice matching across the interface and regions where the lattice matching is destroyed. The difference in lattice parameters is accommodated by the formation of misfit dislocations. The spacing of formed misfit dislocations d in Figure 4.19b is

$$d = (a_B \cdot a_A)/(a_B - a_A), \text{where } a_B > a_A \tag{4.35}$$

In the case of an *incoherent interface*, there is no lattice matching of the two crystal parts across the interface (Figure 4.19c).

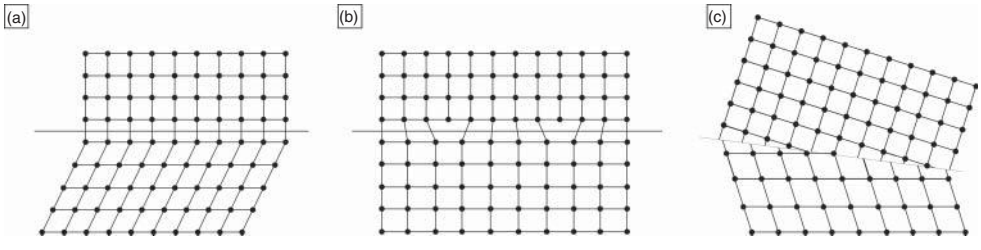

Figure 4.19 (a–c) Schematic illustration of the coherency degree of interfaces: (a) coherent, (b) semicoherent, and (c) incoherent.

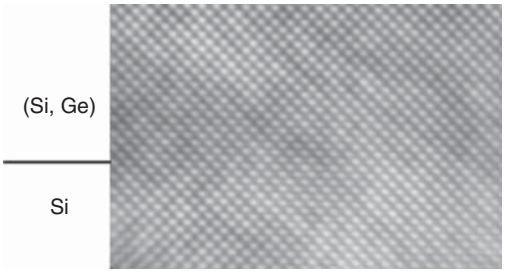

Figure 4.20 HRTEM micrograph of a coherent interface structure of a SiGe – island on silicon.

Concerning the periodicity in the interface plane, one can divide the interfaces of the semicoherent type into ***commensurate*** and ***incommensurate*** ones. A commensurate interface is characterized by a one- or two-dimensional periodicity in the interface plane. An incommensurate interface is given if the translation vectors of the adjoining parts of the bicrystal in each direction within the interface are irrational multiples of each other. An example of a coherent interface structure of a (Si, Ge) island grown by liquid-phase epitaxy on a (100) silicon substrate is shown in Figure 4.20. The misfit between Si and (Si, Ge) can be completely accommodated by an elastic coherency strain (for details, see [19]).

In the following section, we discuss the characteristic features of the main planar defects. The schematical two-dimensional arrangement of atoms given in Figure 4.21 illustrates the various interfaces connected with specific planar defects. From left to right, we have a heterophase boundary (a), for example, an interface between a bulk crystal and a grown layered structure. The following homophase interfaces inside the layer structure illustrate the change of atomic arrangement caused by an SF (b), a twin (c), and an APB (d). Then, we can see that a part of a lattice plane is occupied by foreign atoms (e). This is a two-dimensional precipitation, a so-called Guinier–Preston (GP) zone. One can treat GP zones as planar defects. We discuss this type of defect together with the three-dimensional defects in Section 4.1.4. The interface between the layer and the surrounding vacuum/gas (f) is the external surface (f).

4.1.3.1 Grain Boundaries

A GB is the interface region between two misoriented crystal grains of the same material. In general, the two grains are symmetry related only by rotations and translations when neglecting any deformation between the grains (Figure 4.22a). We can already geometrically describe a GB if we know the following parameters related to a reference coordinate system:

- the normal n of GB plane
- the location d of GB plane.

Then, we can define the following specific types of GBs: A ***tilt boundary*** is given if n is perpendicular to the rotation axis r $[u_r\ v_r\ w_r]$ (Figure 4.22c) and

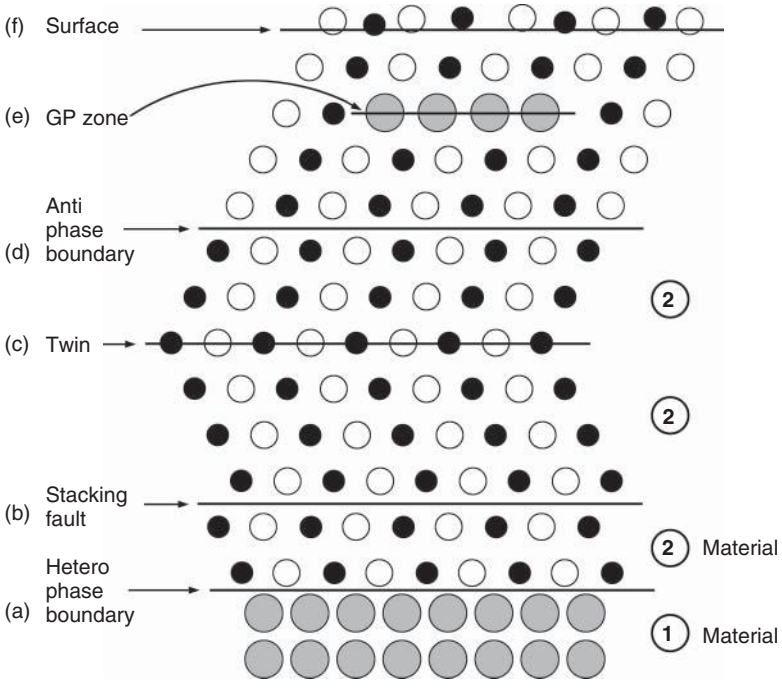

Figure 4.21 Schematic illustration of interfaces in crystalline materials: (a) heterophase bulk crystal/layered structure, (b) stacking fault, (c) twin, (d) antiphase boundary, (e) GP-zone, and (f) external surface.

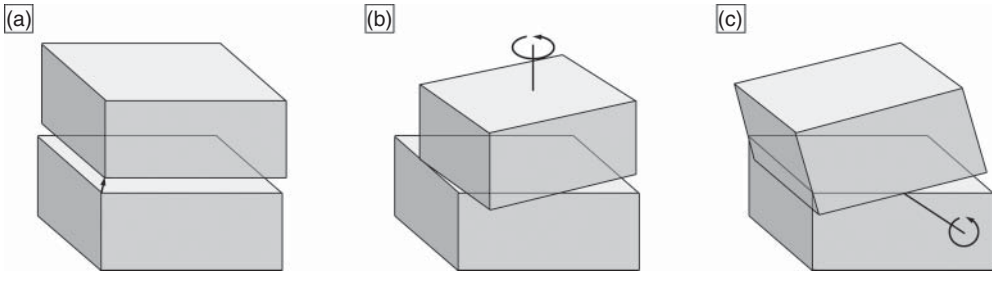

Figure 4.22 (a–c) Schematic illustration of the formation of a grain boundary.

a ***twist boundary*** results if n is parallel to the rotation axis r (Figure 4.22b). Mixed GBs ($n \angle r$) are composed of both a tilt and twist component. A ***GB*** is called ***symmetrical*** if the two planes forming the interface have the same indices $(h_1k_1l_1) \equiv (h_2k_2l_2)$. An ***asymmetric GB*** is given if $(h_1k_1l_1) \neq (h_2k_2l_2)$.

According to the degree of misalignment between the two grains, the GBs are divided into ***low-angle*** (or ***small-angle***) ***GBs*** (misorientation angle $\theta < 15°$) and ***high-angle*** (or ***large-angle***) ***GBs*** ($\theta > 15°$).

An entirely characterization of the geometry of a GB requires the specification of the five ***macroscopic*** and four ***microscopic degrees of freedom*** (DOFs).

Macroscopic DOFs			
CSL-misorientation scheme		*Interface plane scheme*	
Rotation angle θ	1 DOF	GB plane normal n_1 of grain 1	2 DOFs
Rotation axis r [u_r v_r w_r]	2 DOFs	GB plane normal n_2 of grain 2	2 DOFs
Normal n_1 or n_2 of GB plane	2 DOFs	Twist angle φ	1 DOF
Microscopic DOFs			
Translation relations between the two grains (t_1, t_2 in the GB plane, t_3 perpendicular to the GB plane)		3 DOFs	
Vector $\boldsymbol{d}$ fixing the position of GB plane along n		1 DOF	

The five macroscopic DOFs can be classified either by the ***CSL coincidence site lattice misorientation scheme*** or by the ***interface plane scheme*** [20–22]. The CSL-misorientation scheme defines a rotation axis r [u_r v_r w_r], which is identical in both grains with respect to a reference coordinate system. The rotation around the angle θ brings the grains in coincidence. The position of the GB plane is fixed by its normal in one of the grains. The interface plane scheme can be easily explained using Figure 4.22b. The five macroscopic DOFs are fixed by the GB plane normals n_1 and n_2 in the two grains and the twist angle φ. As an example, we define the macroscopic DOFs for a (111) twin boundary in an fcc structure using both schemes:

– *CSL-misorientation scheme*: 70.53°, [110], [111] and
– *Interface plane scheme*: [111], [111], 60°.

Useful geometrical approaches for the description of interfaces, particularly for GBs are based on the concepts of

- the ***CSL***
- the ***displacement shift complete*** (***DSC***) lattice
- the ***O-lattice*** (lattice of origin) [23].

Before describing the commonly applied lattice concepts for the characterization of GBs, we will explain what the term ***derivative lattice*** means. Let us consider two lattices L and L' with bases A and A'.

$$A = \begin{pmatrix} \boldsymbol{a} \\ \boldsymbol{b} \\ \boldsymbol{c} \end{pmatrix}, \quad A' = \begin{pmatrix} \boldsymbol{a'} \\ \boldsymbol{b'} \\ \boldsymbol{c'} \end{pmatrix}, \quad A' = PA \tag{4.36}$$

The following relations hold:

Superlattice L' (p_{ij} – integers, det $(P) > 1$): *All the nodes of the superlattice L' are nodes of the original lattice L, but not all nodes of the original lattice L are nodes of the superlattice L'.*

Sublattice L' ($P = Q^{-1}$, q_{ij} – integers, det $(Q) > 1$): *All nodes of the original lattice L are also nodes of the sublattice L', but not all nodes of the sublattice L' are nodes of the original lattice L.*

Composite lattice L': Some elements of p_{ij}, q_{ij} are fractional (special case).

It should be mentioned that even in literature, the inverse definition is used, that is, superlattice as defined earlier is denoted as sublattice.

Let us assume that two interpenetrating lattices L_1 and L_2 of the two grains of a GB form a CSL. This lattice is a superlattice that contains all the lattice points in common to L_1 and L_2. The CSL represents the intersection of L_1 and L_2. It is characterized by the parameter Σ, which is the volume ratio of the unit cell of CSL to the unit cell of crystal. The value of Σ is the reciprocal density of coincidence lattice sites referred to the original lattice.

$$\mathrm{CSL} = L_1 \cap L_2 \tag{4.37}$$

$$\Sigma = \frac{\text{volume of CSL unit cell}}{\text{volume of crystal unit cell}} \tag{4.38}$$

A low ratio of Σ means a high number of coincidence sites, whereas $\Sigma = \infty$ means an entirely random orientation. A Σ 1 GB represents an ideal bicrystal with no misorientation. For cubic lattices, Σ can be any odd number. A cubic CSL will be generated by a rotation about an axis $[uvw]$ by an angle θ if the conditions

$$\tan\frac{\Theta}{2} = \frac{n}{m}(u^2 + v^2 + w^2)^{\frac{1}{2}} \quad n, m\text{-integers} \tag{4.39}$$

and

$$\sum = n^2 + m^2(u^2 + v^2 + w^2) \tag{4.40}$$

are fulfilled [24]. It should be noted that if Σ is even, it has to be divided by 2. Table 4.7 contains the cubic CSL ($\Sigma \leq 25$), which will be generated by rotations around the main symmetry axes (for substantial tables of cubic CSLs ($\Sigma \leq 49$) and the corresponding $\theta/[uvw]$ see, e.g., [21]).

Special approaches were developed to determine possible coincidence rotations for the cubic, tetragonal, hexagonal, rhombohedral, and orthorhombic lattices [25–28]. In general, the value of Σ depends on the rotation angle and the axial ratio of the lattice. A three-dimensional exact CSL exists only if the rotation matrix has rational elements (for detailed studies of *exact* and *approximate coincidences* as a function of the c/a ratio for hexagonal and rhombohedral crystals, see, e.g., [27, 28]).

The CSL concept was extended to derive coincidence conditions for quasicrystals particularly with icosahedral symmetry. The CSL, the corresponding rotation matrices, and index Σ were derived for a six-dimensional cubic lattice [29]. A CSL

Table 4.7 Cubic CSLs ($\Sigma \leq 25$) for the main rotation axes.

[100]	Σ	θ	[110]	Σ	θ	[111]	Σ	θ
	1	0		1	0		1	0
	5	36.9		3	70.5		3	60.0
	13	22.6		9	38.9		7	38.2
	17	28.1		11	50.5		13	27.8
	25	16.3		17	86.6		19	46.6
				19	26.5		21	21.8

theory was also derived for the description of multiple junctions in grains and multicrystal assemblies with cubic symmetry [30].

The CSL is the finest lattice contained in L_1 and L_2, whereas the *DSC lattice* is the coarsest lattice that contains both crystal lattices as superlattice. The *DSC lattice* is the sublattice with the largest volume of the primitive cell. It is the union of the two lattices. The DSC lattice is the lattice of pattern conserving displacement. A displacement by a DSC vector of one crystal lattice with respect to the second causes a pattern shift that is complete. The DSC lattice defines the Burgers vectors of secondary dislocations (perfect GB dislocations).

$$\mathrm{DSC} = L_1 \cup L_2 \tag{4.41}$$

According to Grimmer's reciprocity theorem, the DSC lattice for the crystal lattices L_1 and L_2 is the reciprocal lattice of the CSL formed by the reciprocal lattices L_1^* and L_2^* [31]. The volume of the DSC unit cell is therefore given by $1/\Sigma$. The relations between the CSL and DSC are illustrated in Figure 4.23, where two two-dimensional squared lattices are rotated about the [001] axis at 36.9°; forming an Σ 5 boundary.

We will briefly mention the O-lattice concept introduced by Bollmann as an extension and generalization of the CSL [23]. It considers coincidences of points

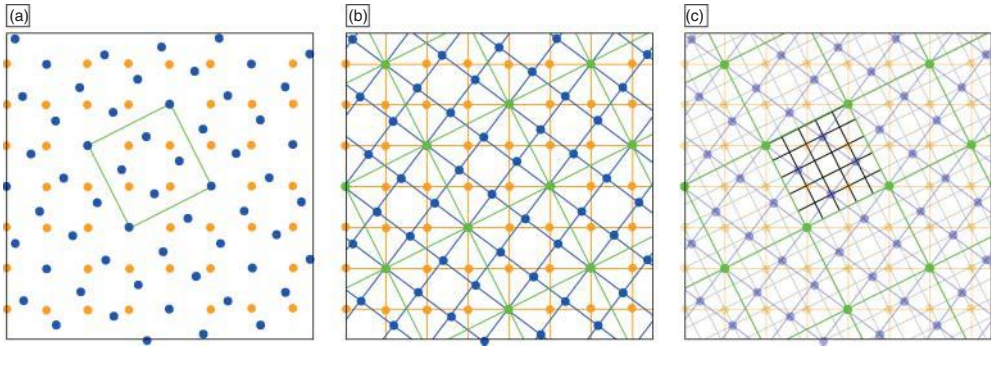

Figure 4.23 CSL and DSC lattices for an [001] Σ 5 boundary: (a) lattices of the two grains, (b) CSL, and (c) DSC.

with the same internal cell coordinates in two interpenetrating lattices. Coincidences of points with the same internal coordinates are called *O-points*. Both crystal lattices are related by a linear transformation $\boldsymbol{x}^{(2)} = \boldsymbol{A}\boldsymbol{x}^{(1)}$. The O-elements are given as solutions of the basic equation $(\boldsymbol{I} - \boldsymbol{A}^{-1})\,\boldsymbol{x}^{(O)} = \boldsymbol{b}^{(L)}$, where $\boldsymbol{I}$ is the identity matrix, $\boldsymbol{A}^{-1}$ the inverse of transformation matrix $\boldsymbol{A}$, $\boldsymbol{x}^{(O)}$ an O-lattice vector, and $\boldsymbol{b}^{(L)}$ a vector of lattice 1. The CSL concept is restricted to well-defined rotation angles where a coincidence of lattice points is given. The CSL determines the best fit of lattice points in an interface. The O-lattice concept allows the calculation of all points in interfaces with a perfect fit (examples of application of O-lattice theory for the description of GBs see, e.g., [32]).

Now we will illustrate a symmetrical low-angle tilt boundary (classical model of Read and Shockley [33], Figure 4.24) in a simple cubic lattice. The small orientation mismatch between the two lattices is completely accommodated by one set of edge dislocations with Burgers vectors parallel to the GB plane. This type of perfect dislocations is denoted as ***intrinsic primary GB dislocations***. The dislocation spacing d is given by

$$d = \frac{|\boldsymbol{b}|}{2 \sin \theta / 2} \tag{4.42}$$

where $\boldsymbol{b}$ is the Burgers vector and θ the rotation angle. When θ is small, one can write $d \approx \boldsymbol{b}/\theta$. The number of dislocations n is $n = 1/d$. An asymmetric low-angle tilt boundary in this cubic crystal is composed of at least two sets of edge dislocations with Burgers vectors which are perpendicular to each other. Low-angle twist boundaries are composed of an array of screw dislocations. Such a boundary in a cubic crystal is formed by at least two sets of intersecting screw dislocations. A low-angle mixed boundary contains both tilt and twist components. Such a boundary will be constructed from at least two sets of intersecting dislocations.

A low-angle GB with a maximum misorientation of 15° can be described as Σ 1 boundary. It was confirmed theoretically and experimentally that the structure of a coincidence boundary will be preserved if a maximum angular deviation of v_m

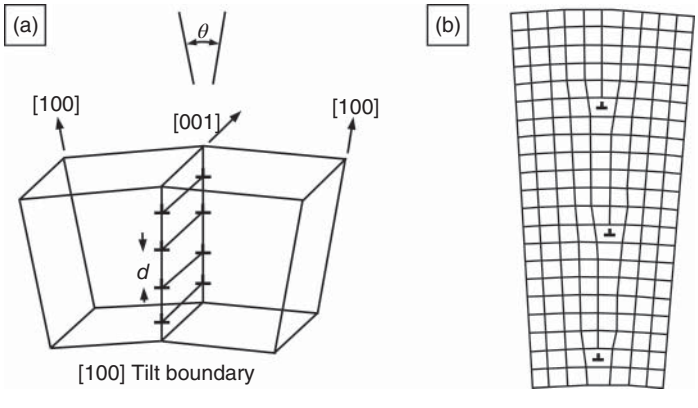

Figure 4.24 (a,b) Schematic illustration of the dislocation structure of a symmetric low-angle tilt boundary.

is not exceeded. The relationship between ν_m and Σ is given by

$$\nu_m = \nu_0 \Sigma^{-n} \tag{4.43}$$

where $\nu_0 \approx 15°$ and $n = 1/2$ (Brandon criterion [34]). It should be mentioned that different values for the exponent n are used in the literature (for details see, e.g., [21]).

A TEM diffraction contrast image of a typical small-angle GB in spinel $MgAl_2O_4$ is shown in Figure 4.25. The GB is a stepped pure tilt boundary. It consists of a set of parallel equidistant dislocations V_1 with the Burgers vector $\boldsymbol{b}_1 = a/2$ [011] between the individual steps S_i. The Burgers vectors are normal to the (011) interface plane, the line direction is $l = [100]$. The Burgers vectors are pure edge dislocations. The tilt axis is parallel to $l = [100]$. The tilt angle θ was calculated to $\theta = 0.65°$ using Equation 4.42. It can be seen that after eight dislocations of type V_1, a second type of dislocations follows (different contrast behavior), which is correlated with the step structure of the GB. The diffraction contrast image analysis enables the determination of the type of GB, the character of dislocations, and the orientation relationships.

Structure information about GBs at an atomic level of magnitude can be gained from the various types of high-resolution transmission electron microscopy (HRTEM) and STEM (scanning transmission electron microscopy) images. Figure 4.26 shows a lattice-fringe image of a 20° [001] tilt boundary in a bicrystal of gold. In both crystal grains, the lattice planes of type (200) with a separation

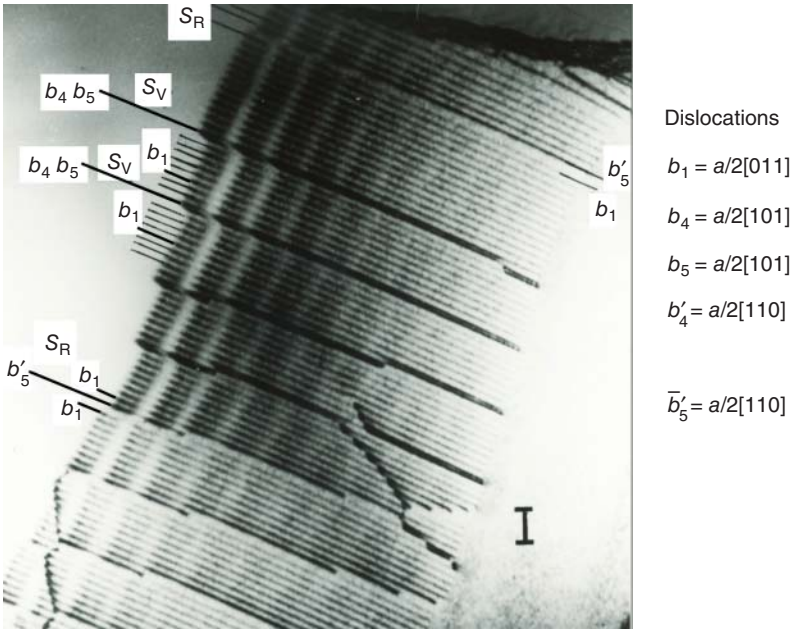

Figure 4.25 Two sets of parallel dislocations in a low-angle tilt boundary in spinel $MgAl_2O_4$.

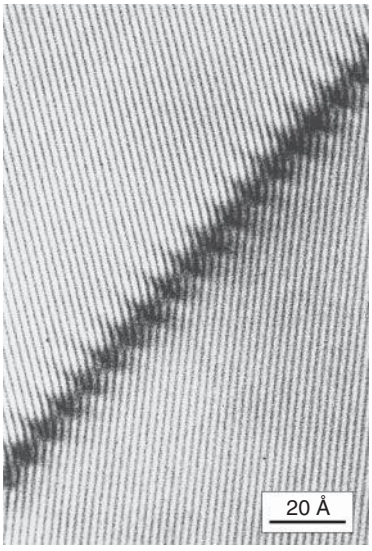

Figure 4.26 Lattice-fringe image of a 20° [001] tilt boundary in gold. (By courtesy of R. Scholz, Halle.)

of 2.04 Å can be imaged without any overlapping effect because the GB region and the dislocations are oriented exactly "edge-on." This image clearly shows the terminating lattice fringes of the upper grain at the row of edge dislocation. One can easily count the number of dislocations and measure the mean spacing between the terminating lattice fringes. It should be mentioned that the phase contrast image of lattice fringes is superimposed by the amplitude contrast (diffraction contrast) caused by the strain around the dislocations. Therefore, we see a row of equidistant black streaks perpendicular to the trace of GB plane, which looks like a slide zippener.

In addition to the possible dislocation structure of a GB, it is necessary to gain information about the real atomic structure of GBs. The *structural unit model*, which was derived from computer simulation of energy-minimized atomic structure of GBs was later experimentally evidenced by HRTEM studies (see, e.g., [35]). The experimental studies by means of HRTEM and HRSTEM have shown that a GB is composed of only a limited number of distinct structural units. A structural unit is a polyhedral cluster of atoms.

With the application of high-resolution electron microscopy, particularly with aberration-corrected microscopy, a true imaging of the atomic core structure of GBs with a minimized delocalization effect is nowadays possible as illustrated in Figure 4.27 (N.D. Browning PNNL, Richland, WA, USA, personal communication).

It should be mentioned that the macroscopic DOFs of a GB can be measured experimentally by means of conventional TEM and electron diffraction (e.g., from Kikuchi-diagrams), BSE (backscattered electron diffraction) in an SEM (scanning

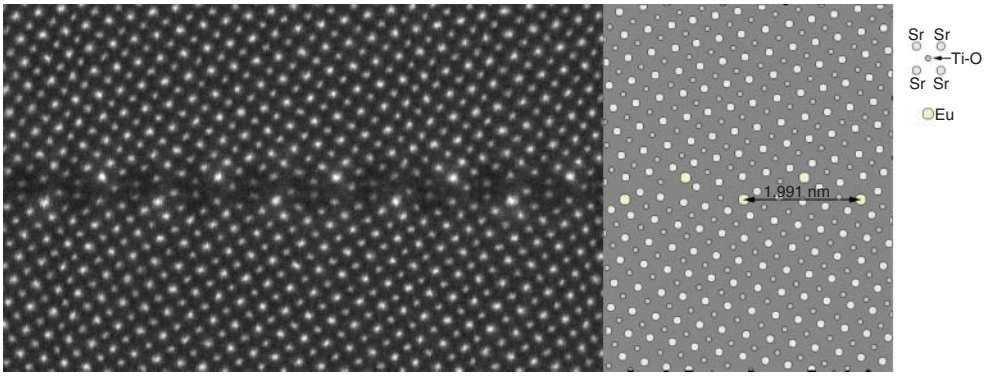

Figure 4.27 Aberration-corrected high-resolution STEM Z-contrast image of an Eu doped symmetrical Σ 13, (510)/[001], 22.6° tilt grain boundary in $SrTiO_3$. (By courtesy of N.D. Browning PNNL, Richland, WA, USA, personal communication.)

electron microscope) and X-ray diffraction. The microscopic DOFs can be determined by means of aberration-corrected HRTEM and STEM or by computer simulation.

4.1.3.2 Stacking Faults

Any interruption of the normal stacking sequence of a basic structure generates an *SF*. Geometrically, an SF is defined by the ***SF plane (hkl)*** and the ***displacement vector R***. The displacement vector ***R*** defines the translation between the two perfect crystal parts A and B as illustrated in Figure 4.28. It is obvious that the vector ***R*** must be a *partial lattice translation vector* because a lattice translation vector maps the lattice onto itself and cannot generate an SF. The displacement vector ***R*** can lie in the SF plane but can also be inclined to it. An SF that ends inside the crystal and not at the surface is surrounded by partial dislocations.

Now we will illustrate the formation of SFs for the *ccp* and *hcp* structure. As already described in Section 1.5.2, the stacking sequence for the ccp structure is … *ABCABC* … and … *ABAB* … for the hcp structure. In addition to the ABC notation stacking operators, Δ (***delta***) and ∇ (***nabla***) proposed by Nabarro are particularly useful for the description of SF arrangements. The stacking sequences

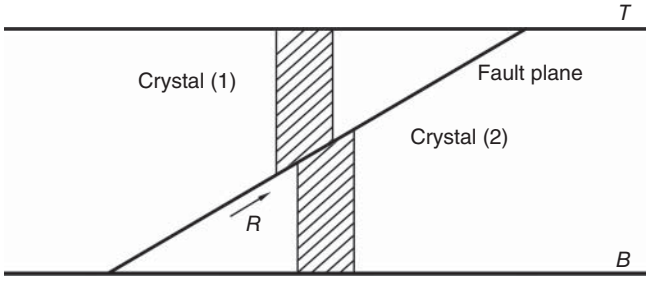

Figure 4.28 Stacking fault running from top to bottom of a crystal.

AB, BC, CA are depicted by Δ and the reversed sequences BA, CB, AC by ∇. The operator sequences ΔΔΔΔΔ and Δ∇Δ∇Δ∇ describe the ccp and hcp structure, respectively.

An easy way to generate an SF in the *ccp* structure is given if we remove or insert a plane of the normal stacking sequence.

An ***intrinsic SF*** is formed when we remove a plane:

ABCA↓CABC ΔΔΔ∇ΔΔΔ

An ***extrinsic SF*** is formed when we insert a plane:

ABCA***C***BCAB ΔΔΔ∇∇ΔΔΔ

The SF planes for *fcc* are the {111} planes, the displacement vector is given by $\boldsymbol{R} = \pm 1/3 \langle 111 \rangle$. An equivalent description is given if $\boldsymbol{R} = 1/6 \pm \langle 211 \rangle$ because the difference between the two vectors is a full lattice vector.

For the *hcp* structure, three basic types of ***SFs*** for the dense-packed basal plane (0001) exists – two intrinsic (I_1, I_2) and one extrinsic (E).

I_1 : BABABCBCB ∇Δ∇ΔΔ∇Δ∇
I_2 : ABABCACA Δ∇ΔΔΔ∇Δ
E : ABABCABAB Δ∇ΔΔΔΔ∇Δ

The SF I_1 is generated by the removal of a plane (in our example, an A plane) and the subsequent displacement of the crystal part above the fault of $1/3 \langle 10.0 \rangle$. This process is illustrated as follows: …BABABABABA… → …BABAB↓BABA … → BABABCBCB.

The displacement vector is given as a sum, $\boldsymbol{R} = {}^1\!/_2 \langle 00.1 \rangle + 1/3 \langle 10.0 \rangle$.

The SF I_2 is generated by a shift of the two halves of the perfect crystal along the displacement vector $\boldsymbol{R} = 1/3 \langle 10.0 \rangle$. In a similar way, as for the *fcc* structure, the extrinsic SF (E) for *hcp* crystals is formed by inserting an extra atomic plane (in the example above a c-plane). The displacement vector is $\boldsymbol{R} = {}^1\!/_2 \langle 0001 \rangle$.

In addition to the geometric classification of SFs [36], the genetic classification into *growth*, *deformation*, and *layer displacement faults* [37, 38] is commonly applied.

Growth fault: During the layer-by-layer growth of the crystal, a layer can violate the stacking rule but the subsequent layers will follow the original sequence.

2H ABABABABAB → ABABACACAC Δ∇Δ∇∇Δ∇Δ∇

Deformation fault: In this case, the two perfect halves of the crystal slip on the (0001) plane along the slip vector $\pm \langle 10.0 \rangle$.

2H ABABABABAB → ABABCACA Δ∇ΔΔΔ∇Δ

Layer displacement fault: This type of fault occurs if a single layer or a pair of adjacent layers (e.g., for ccp crystals) is displaced in the stacking sequence but all others occupy the original positions. In the case below, A is shifted to **C**.

2H ABABABABAB → ABABCBABAB ΔVΔΔVVΔVΔ

The existing coincidences and similarities between the fault types are obvious when we inspect the layer sequences of the geometrically and genetically classified faults using the Nabarro designation.

Stacking faults are closely related to polytypic structures, whose fundamentals are described in Section 1.5.2.1. In the 6H polytype (ABCACB), 18 different arrangements of intrinsic SFs are possible geometrically. Therefore, different classification schemes are necessary for the description of possible SF arrangements in polytypes (for details see, e.g., [39]).

The atomic arrangements of SFs can be directly imaged and investigated by HRTEM. The determination of the nature of SFs in GaN by means of HRTEM will be illustrated in detail in Section 4.4.1. SFs can also be imaged using the method of diffraction contrast in conventional TEM and X-ray diffraction. Figure 4.29a shows a TEM diffraction contrast image of an extrinsic SF in a silicon crystal, which consists of a set of parallel dark-and-bright fringes. The two ends of the SF inside the crystal on the (111) plane are surrounded by partial dislocations. Position and fringe structure of the inclined SF are schematically illustrated in Figure 4.29b. In general, an SF causes a phase shift of $\alpha = 2\pi \boldsymbol{g}\cdot\boldsymbol{R}$ of the scattered electron beam, which is constant for a particular crystal and type of fault. The parameter $\boldsymbol{g}$ denotes the reflection *hkl* used for the imaging. For *fcc* crystals with $\boldsymbol{R} = \pm 1/3 <111>$, the criteria for *v*isibility and *n*on*v*isibility are

$$V:\ \alpha = \pm 2/3\pi(h + k + l) = 2n\pi/3n - \mathit{integer}\, nv:\ \alpha = m\pi\, k - \mathit{integer}$$

The invisibility criterion (use of different $\boldsymbol{g}$-vectors for the imaging) can be applied to determine the exact direction of $\boldsymbol{R}$. From the arrangement of the fringe pattern (e.g., symmetry of the outer and central fringes) in the bright- and dark-field images, the type of the fault (intrinsic or extrinsic) can be determined by simple rules. It should be mentioned that specific procedures of the diffraction contrast-imaging technique can be applied to determine the crystallographic nature of SFs (SF plane, $\boldsymbol{R}$-vector, type of SF, and type of surrounding partial dislocations) in crystals with complex crystal structures where no a priori information about the possible SF defects exist. Conclusions about the formation mechanism of an SF can be drawn from the specific type of surrounding partial dislocation. We have already described in Section 4.1 that two different types of partial dislocations can surround an SF in *fcc* crystals. Extrinsic and intrinsic SFs that are formed by inserting and removing a part of a {111} plane, respectively, are bounded by Frank partial dislocations with a Burgers vector $\boldsymbol{b} = 1/3 <111>$. The Frank partial dislocation is an edge dislocation with a Burgers vector normal to the {111} fault plane. Therefore, the Frank partial is "***sessile***" and cannot glide. However, it can climb by absorption or emission of point defects. An intrinsic SF

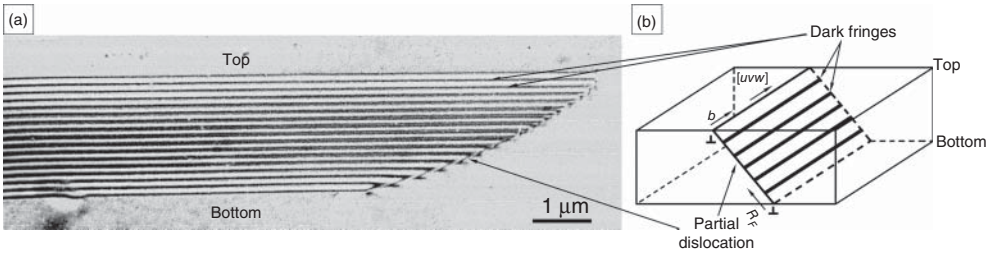

Figure 4.29 Stacking fault in silicon: (a) TEM bright-field image and (b) schematic illustration of SF location and fringe pattern.

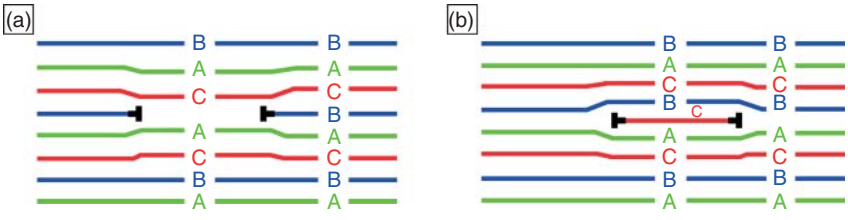

Figure 4.30 Illustration of formation of stacking fault loops: (a) vacancy loop (surrounded by negative Frank partials) and (b) interstitial loop (surrounded by positive Frank partials).

loop can be formed by coalescence of vacancies. A precipitation of interstititals may cause an extrinsic SF loop. The formation process of SF loops in an fcc crystal is schematically illustrated in Figure 4.30.

It should be noted that an intrinsic SF can also be formed by the slip process of a dislocation across one of the {111} planes with a Burgers vector of type 1/6 <211> (Shockley partial dislocation). As already noted in Section 4.1, a perfect dislocation may dissociate into two Shockley partials according to the reaction

$$\boldsymbol{b} = \boldsymbol{b}_1 + \boldsymbol{b}_2, \text{ e.g., } \frac{1}{2}[\bar{1}10] = 1/6[\bar{2}11] + 1/6\,[\bar{1}2\bar{1}] \tag{4.44}$$

These partials are "***glissile***" and move on a {111} plane. The slide process is a two-step process, first along $\boldsymbol{b}_1$ and subsequently along $\boldsymbol{b}_2$. The two partials enclose an SF ribbon with a displacement vector $\boldsymbol{R}$ equal to one of the Burgers vectors of the partials. We should be aware of the fact that an intrinsic fault formed by the coalescence of vacancies and an intrinsic fault formed by the slip process have an identical geometrical arrangement with respect to the stacking sequence of layers. However, the bounded partial dislocations are different. Thus, one can draw conclusions about the formation process if the nature of the partials is analyzed.

The energy of the SF ribbon between two partial dislocations is given by

$$E_{\mathrm{SF}} = \gamma_{\mathrm{SF}} \cdot d \cdot l \tag{4.45}$$

where γ_{SF} is the specific SF energy (additional energy per unit area of fault), d is the width of SF ribbon, and l is the length of the partials. The equilibrium separation d between the partials that minimize the total energy is given by the balance of the

Table 4.8 Calculated fault energies for intrinsic, extrinsic, and twin faults [41].

Material	Ag	Au	Cu	Ni	Al	Pt
γ_{ISF} (mJ m^{-2})	16	25	36	133	112	286
γ_{ESF}	12	27	40	138	112	284
γ_{TF}	8	12	18	65	50	137

repulsive forces between the partials and the attractive force caused by γ_{SF}. For materials with low specific SF energy γ_{SF}, the equilibrium spacing d is large and vice versa; a high value of γ_{SF} causes a very small separation d between the partials. The SF energy can be directly determined by means of ribbon width measurements or dislocation node measurements from TEM diffraction contrast images (for details of the methods see, e.g., [40]). Measurements of ribbon widths <5 nm have to be carried out from HRTEM images. The diffraction contrast images using the weak-beam technique allow studies of pairs of partials with $d > 5$ nm.

Nowadays, various computational approaches exist for the calculation of SF energies. Calculated fault energies using the density functional theory (DFT) for some fcc metals are listed in Table 4.8.

4.1.3.3 Antiphase Boundaries

Stacking faults and APBs are closely related. Both are translation boundaries. Analogous to SFs, the ***geometry of antiphase boundaries*** is characterized by a displacement vector $\boldsymbol{R}$ and a plane, the contact plane (hkl) between the two domains, which define the ***antiphase boundary***. We will illustrate the formation of an APB for a two-dimensional structure consisting of two types of atoms (Figure 4.31). If the displacement vector $\boldsymbol{R}$ is parallel to the boundary, a so-called ***conservative antiphase boundary*** is generated. The formation of a conservative antiphase boundary does not change the chemical composition of

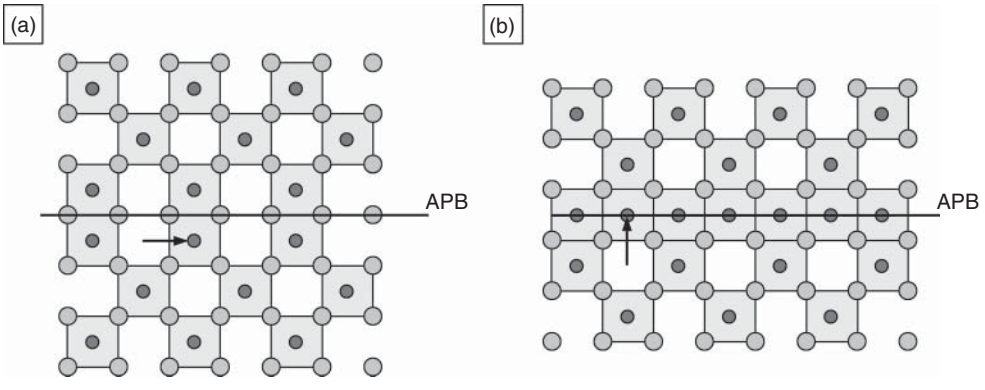

Figure 4.31 Antiphase boundaries in a two-dimensional structure: (a) conservative APB and (b) nonconservative APB.

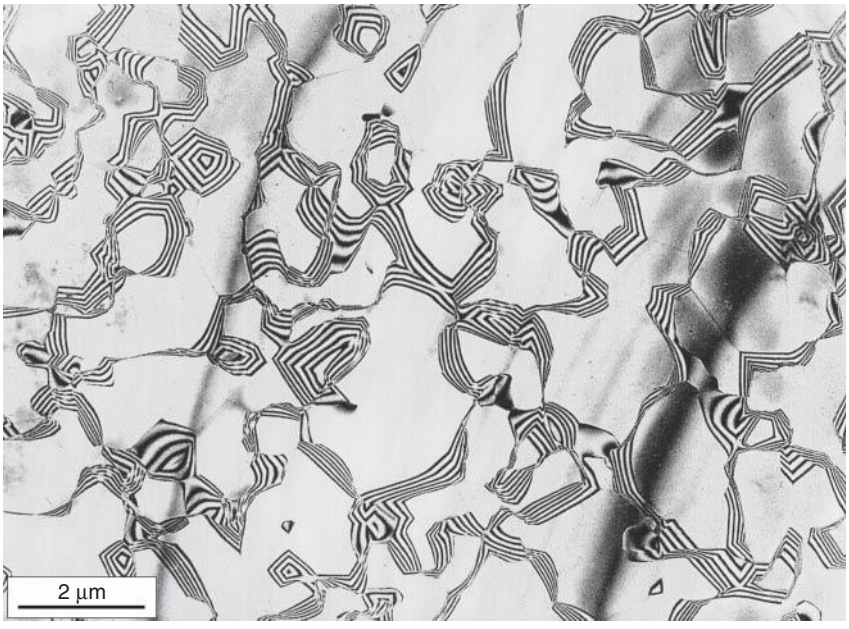

Figure 4.32 Diffraction contrast image of APBs in spinel $MgTi_2O_4$. (Reprinted with permission from Hesse, [42] Copyright 1987, American Vacuum Society.)

the structure (Figure 4.31a). A ***nonconservative antiphase boundary*** is formed if the displacement vector $\boldsymbol{R}$ is perpendicular to the boundary. In this way, the chemical composition is changed.

Similarly to SFs, APBs end at a surface of the crystal or must be bounded by a partial dislocation. The atomic structure of APBs can be directly imaged and investigated by HRTEM. The method of diffraction contrast in conventional TEM and X-ray diffraction is also an appropriate method to study APBs. Figure 4.32 shows a TEM diffraction contrast image of APBs in the spinel $MgTi_2O_4$ [42]. This is a similar fringe contrast image as for SFs. An APB causes a phase shift of $\alpha = 2\pi \mathbf{g}\cdot\boldsymbol{R}$ of the scattered electron beam. The parameter $\boldsymbol{g}$ denotes the reflection *hkl* used for the imaging. Contrary to a common SF, the displacement vector $\boldsymbol{R}$ for an APB is a lattice vector of the fundamental structure but not from the superstructure generated by the APB. For fundamental reflections $\boldsymbol{g}\cdot\boldsymbol{R} = 0, 1, 2, \ldots$ and $\alpha = 0, 2\pi, 4\pi, \ldots$. This means for fundamental reflections an APB is invisible. Conversely, for superlattice reflections $\alpha = 0, \pi, \ldots$, an APB is visible for $\alpha = \pi$. Therefore, APBs are also denoted as π-boundaries. The APB can be considered a particular type of SF.

In Section 1.5.4, we have described in detail that the order–disorder phase transition of Cu_3Au is characterized by the symmetry reduction from $Fm\bar{3}m$ (high-temperature phase) to $Pm\bar{3}m$ (low-temperature phase). In the high-temperature phase, the atoms (1Au, 3Cu) occupy the positions of the F-Bravais lattice statistically. The ordering process of the atoms generates a superstructure where

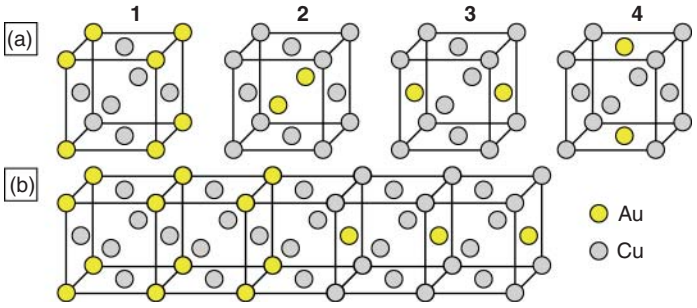

Figure 4.33 (a,b) The four possible domain types of Cu_3Au and one example of an APB.

the Au atoms occupy the positions of a cubic P-Bravais lattice and the Cu atoms are located at the face-centers of the cube. The loss of translational symmetry is accompanied by the formation of four domains (domain states). The unit cells of the four Cu_3Au domains are shown in Figure 4.33. The origin shift between the domain states is expressed by the displacement vectors $\boldsymbol{R}_1 = {}^1/_2$ [110], $\boldsymbol{R}_2 = {}^1/_2$ [011], $\boldsymbol{R}_3 = {}^1/_2$ [101]. When two domains are intergrown, the common contact plane is an APB as shown in Figure 4.33b.

A very important class of structures are the so-called ***long period antiphase boundary structures (LPSs)***. Such LPSs were observed in various binary alloys (e.g., Cu_3Au, Ti_3Al, Pt_3V, $(Pt,Rh)_3V$, $(Pt_{92}Rh_8)_3V$, and $Ti_{27}Al_{73}$). The structures are composed of stable periodic arrangements of conservative (001) APBs in the building blocks [domains in the Cu_3Au structure type (structure report notation: $L1_2$)]. The structures can be composed of domains of equal size or of a mixture of domains of different size. The latter case leads to much more complicated structures. Comprehensive studies of LPS by means of HRTEM and electron diffraction have shown that the structures can be described as one-dimensional modulated structures. In addition to the structural modulation, a chemical modulation was observed in some LPS (for a detailed overview on LPS, see [43]).

4.1.3.4 Twins

The general phenomenon of macroscopic twinning is well known in mineralogy for a long time and was already described as a special feature of crystal morphology in the book of Romé de l'Lisle (1783) [44]. A *twin* can be defined as an intergrowth of two or more single crystals (individuals) of the same species with definite crystallographic orientation relations between them [45]. The individuals forming the twin are denoted as ***twin components*** or ***twin domains***. The geometrical relations between the twin components are described by the ***twin law***. This law specifies all symmetry operations which transforms the different orientation states of the twin components into each other. A twin operation cannot be a symmetry operation of one of the twin components. According to the possible twin operations, the twins can be classified as

- ***reflection twins*** (twin element: mirror plane *m*)
- ***rotation twins*** (twin element: rotation axis, most frequently a twofold axis 2)

- ***inversion twins*** (twin element: inversion center *i*).

It should be noted that in the literature, particularly in the field of crystal defect analysis, *inversion twins* are universally denoted as "***inversion boundaries***." Examples of inversion boundaries will be described in Section 4.4.1.

For the description of the twin law, we have also to take into consideration that the twin elements can be rational (integer indices) or irrational, whereas the irrational indices can be approximated by large integer indices. The following examples should illustrate this fact. A reflection twin can be formed if two twin components are connected by a rational mirror plane (*hkl*), which is normal to an irrational direction. The lattice plane (*hkl*) is then a common plane of the two twin components and represents a two-dimensional CSL of the twin boundary (***two-periodic twin*** with a ***two-dimensional twin lattice***). If the twin components are connected by an irrational mirror plane parallel to a rational lattice row [*uvw*], a reflection twin is formed where the lattice row [*uvw*] is common to the two twin components. In this case, only a one-dimensional CSL is given (***one-periodic twin*** with a ***one-dimensional twin lattice***). The conditions for the existence of a three-dimensional CSL ***three-(periodic twin*** with a ***three-dimensional twin lattice)*** are the following:

- *Reflection twin*: A lattice row [*uvw*] has to be exactly perpendicular to the twin plane (*hkl*).
- *Rotation twin*: A lattice plane (*hkl*) has to be exactly perpendicular to the twofold twin axis [*uvw*].
- *Inversion twin*: Only noncentrosymmetric twin components can form an inversion twin. The twin lattice is always a three-dimensional CSL.

As already described in Section 4.1.3.1, the density of coincidence lattice sites is defined by the CSL index Σ. The CSL index of the two twin components is commonly expressed by the twin lattice index *j*.

$$[j] = \Sigma = V_{\text{twin}}/V_{\text{crystal}} \tag{4.46}$$

$V_{\text{twin}}, V_{\text{crystal}}$ – volumes of the primitive unit cells of twin and crystal, respectively.

The index $[j] = 1$ means a complete coincidence of both lattices, whereas $[j] = n$, $n > 1$ means that only the fraction of $1/n$ lattice sites forms the CSL.

In addition to the index [*j*], a very important parameter for the classification of twins and their lattices is the ***twin obliquity ω***. The angle ω is a measure of the deviation of orthogonality of the twin axis to a lattice plane, or vice versa, a twin plane to a lattice direction. The conditions of mutual perpendicularity of a lattice plane and a lattice direction for the seven lattice systems are summarized in Table 4.9. These conditions are valid independently of the given metric parameters of the crystal. In addition, for particular metric parameters, a lattice plane (*hkl*) may be perpendicular to a lattice direction [*uvw*] if the following equation is satisfied:

$$\begin{aligned}\frac{a}{h}(au + bv\cos\gamma + cw\cos\beta) &= \frac{b}{k}(au\cos\gamma + bv + cw\cos\alpha)\\ &= \frac{c}{l}(au\cos\beta + bv\cos\alpha + cw)\end{aligned} \tag{4.47}$$

Table 4.9 Conditions for mutual perpendicularity of lattice plane/lattice row in the seven lattice systems.

Lattice system	Lattice plane (*hkl*)	Lattice row [*uvw*]
Triclinic	—	—
Monoclinic	$\beta \neq 90°$ (010)	[010]
	$\gamma \neq 90°$ (001)	[001]
Orthorhombic	(100)	[100]
	(010)	[010]
	(001)	[001]
Hexagonal	(*hk*.0)	$[2h+k, h+2k, 0]$
	(00.1)	[00.1]
Rhombohedral	$(h, k, -h-k)$	$(h, k, -h-k)$
	(111)	[111]
Tetragonal	(*hk*0)	[*hk*0]
Cubic	(*hkl*)	[*hkl*]

Data from [46].

Table 4.10 Friedel's classification of twins.

	TLS ($\omega = 0$)	TLQS ($\omega > 0$)
$[j] = 1$	Twins by merohedry	Twins by pseudo-merohedry
$[j] > 1$	Twins by reticular merohedry	Twins by reticular pseudo-merohedry

(a, b, c – lattice constants, α, β, γ – interaxial angles).

The twin obliquity ω is zero if the conditions given in Table 4.9 and in Equation 4 are satisfied.

Three-periodic twins can be divided into four main categories as a function of twin index and twin obliquity (Table 4.10). ***Twinning by merohedry*** means the lattices of the twin components coincide exactly in direct and reciprocal space. Therefore, merohedral twins are often denoted as "parallel lattice twins." An important fact is that the *diffraction patterns* of *merohedral twins* show *no spot splitting* due to the exact coincidence of the reciprocal lattices of the twin components. The meaning of the term *merohedry* with respect to point groups was already described in Section 1.3.2. Merohedral twins can only be formed in crystals with a merohedral point group.

Twinning by pseudo-merohedry means the lattices of the twin components are almost, but not exactly coincident in direct and reciprocal space. The mismatch between the lattices is very small. Therefore, the *diffraction patterns* of *pseudo-merohedral twins* show *spot splitting*. Pseudo-merohedral twins are generated at phase transition where the point groups of the deformed phase and the prototype phase belong to a different crystal family. The point group of the deformed phase is then a *pseudo-merohedral point group*.

Twinning with partial lattice coincidence is given if the lattice index [j] is >1. This means the twin lattice is diluted compared to the lattices of the twin components. In addition, the partial lattice coincidence can be exact or approximate. The relation between the twin component lattice and the diluted twin lattice is expressed by the term *reticular*.

Merohedral twinning is also denoted as "*twinning by twin-lattice symmetry* (*TLS*)" and pseudo-merohedral twinning as "*twinning by twin-lattice quasi-symmetry* (*TLQS*)." It should be mentioned that finer classification schemes of crystal twinning were introduced (see, e.g., [47]).

The interface between the different twin components is denoted as *twin boundary*, *twin interface*, or *composition surface*.

Twins can be divided into *simple* and *multiple twins*. *Simple twins* have only domains of two different orientation states. They can be described by one twin law. *Multiple twins* consist of domains with at least three or more orientation states which cannot be uniquely described by one twin law. A multiple twin is called a *polysynthetic twin* if all twin boundaries are parallel planes. If a multiple twin consists of a circular arrangement of twin boundaries, a *cyclic twin* is given.

We have also to take into consideration if a *macroscopic* or a *microscopic* twinned crystal is given. In most cases, macroscopic twins can be morphologically classified into one of the main categories: contact twins, polysynthetic (lamellar) twins, penetration twins, and cyclic twins.

The dovetail twin of gypsum (Figure 4.34b) is a typical contact twin. The two twin components are in contact across the (100) composition plane. It is obvious that the dovetail twin is a reflection twin where the composition plane is parallel to the twin mirror plane. Figure 4.34a shows an example of a polysynthetic twin of the triclinic feldspar albite, which consists of a linear arrangement of repeated contact twins where all (010) twin composition planes are parallel and in coincidence with the twin mirror planes. Detwinning of the twin domains with two alternating orientation states would generate a parallel intergrowth structure. A twin is called *penetration twin* if two or more twin components penetrate each other. Quartz crystals twinned after Dauphiné and Brazil twin laws are penetration twins. Dauphiné twins (Figure 4.34c) are formed by a 180° rotation around the threefold [00.1] axis. A Dauphiné twin consists of either two left-handed or right-handed intergrown crystals. Dauphiné twins are also denoted as electrical twins because they can be verified by the absence of pyro- and piezoelectricity which are main physical properties of untwinned quartz crystals. Optical measurements do not allow the detection of Dauphiné twins. Brazil twins are commonly described by twin reflections across planes $\{11\bar{2}0\}$ perpendicular to twofold symmetry axes. This twin type is formed by two enantiomorphous (left-handed and right-handed) individuals with reversed polar axes. Brazil twins can also be described as inversion twins. Contrary to Dauphiné twins, Brazil twins are denoted as optical twins because of the reversed rotary dispersion of optical activity of the two twin components.

Now we will classify our examples of twins according to Friedel's classification schema. Dauphiné and Brazil quartz twins are typical examples of merohedral

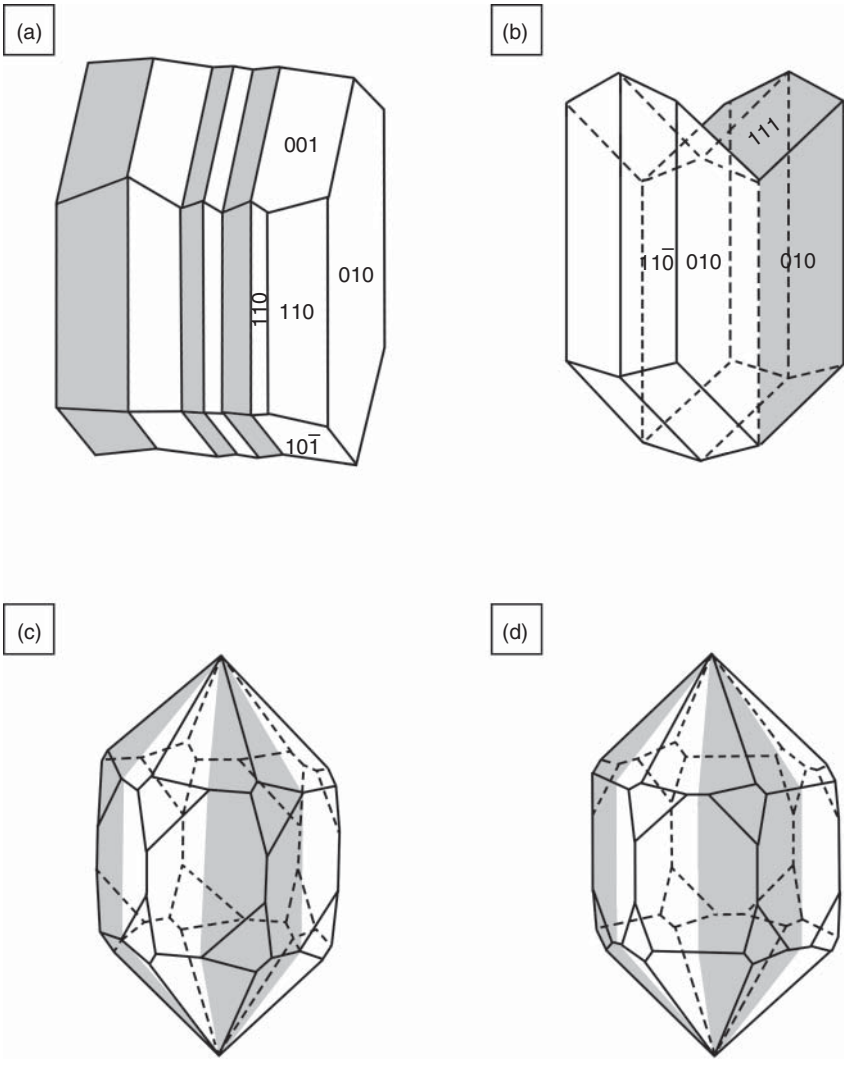

Figure 4.34 Examples of twins: (a) polysynthetic albite twin, (b) gypsum dovetail twin, (c) quartz Dauphiné twin, and (d) quartz Brazil twin.

twins. The lattices of the twin components are parallel and a totally and exact coincident (lattice index $[j] = 1, \omega = 0$) is given (TLS by merohedry). The albite and pericline twin laws are the common twin laws of plagioclase feldspars with the end members $NaAlSi_3O_8$ (albite) and $CaAl_2Si_2O_8$ (anorthite). Twins after albite law are characterized by a rational twin composition and twin reflection plane (010). For all plagioclases, the twin index [j] of albite twinning is equal to one. But in triclinic crystals the vector normal to the (010) plane is not a rational lattice

direction. The deviation ω is also a function of the anorthite content (expressed in atomic percent at.%) of a specific plagioclase. The values for ω are in the range of 3.4° and 4.64° [48]. Thus, TLQS by pseudo-merohedry is given (lattice index $[j] = 1$, $\omega > 0$). The dovetail twin of gypsum is an example for TLQS by reticular pseudo-symmetry (lattice index $[j] > 1$, $\omega > 0$). With the program OBLIQUE of Le Page [49] as most relevant combinations $(hkl)/[uvw]/\omega/j$ were calculated for the dovetail twin the following two: (100)/[302]/2.47°/3 and (100)/[805]/0.42°/4 (see, e.g., [45]).

Twins can be formed during the crystal growth process. In Section 1.5.4, we have shown that twins can also occur as a result of phase transitions. Furthermore, twins can be generated by the mechanical deformation of single crystals. But also during the recrystallization process caused by thermal annealing twins can be formed which are denoted as *recrystallization* or *annealing twins*. However, we should be aware of the fact that this classification with respect to the formation process does not mean there are strict demarcations between the methods. For example, a mechanical twin can be generated under external mechanical load as we will describe a bit later in detail. Microscopically such a twin formation will start with a nucleation process and will subsequently grow into a macroscopic twin. Both processes deformation and twin growth are combined. Dauphiné twins of quartz can occur as growth twins, transformation twins, and mechanical (ferrobielastic) twins.

Growth Twins Contrary to Dauphiné twins, quartz twins after the Brazil law (inversion twins) occur only as growth twins. Other typical examples of growth twins of minerals are the dovetail twin of gypsum, spinel after (111) twin law both as contact and penetration twin and the (00.1) contact twin of calcite, and so on. Twins after the spinel law were commonly detected in synthetically grown cubic semiconductors such as Si, Ge, ZnS, and CdTe.

In general, growth twins can be formed already at the ***nucleation process*** or subsequently during the ***actual growth process***. Twinning by nucleation means that twins are already formed at the first stages of nucleation before the nucleus has reached the critical size. It is assumed that penetration twins, sector twins, and probably also the majority of contact twins are formed at the nucleation stage if they consist of twin domains of nearly the same size.

Numerous HRTEM studies of the growth of multiple twinned particles (MTPs) of cubic crystals have shown that at first nuclei consisting of a noncrystallographic arrangement of atoms are formed which subsequently are transformed to quintuples of twins (for details, see Hofmeister [50]). A similar mechanism was proposed by Senechal [51] for twinning by nucleation of macroscopic twins .

During the actual crystal growth, twinning can be caused by thermal or mechanical stress. Very often, the mechanical stress is closely connected with the occurrence of crystal defects such as impurities, inclusions, and dislocations. Another mechanism of twin formation is given if during the layer-by-layer growth the stacking sequence is accidentally changed (e.g., … ABCAB***C***BACBA …). Growth twins exhibit ***reentrant*** angles as a typical morphological feature.

In general, the twinning probability of a material is correlated with its twin energy. Sometimes, one is also using the SF energy for estimating the probability of twin formation. When we compare the twin energies (Table 4.8 in Section 4.1.3.2) for the fcc metals Ag (8 mJ m^{-2}), Au (12 mJ m^{-2}), Cu (18 mJ m^{-2}), and Al (50 mJ m^{-2}), then it is obvious that the probability of twin formation in Ag, Au, and Cu is much higher than in Al.

Phase Transformation Twins It is quite clear not all phase transitions follow in an easy manner group–subgroup relations. However, very often group–subgroup relations exist between the high- and low-symmetry phases of displacive and order–disorder phase transitions. In Section 1.5.4, we have already explained that twin domains will arise if the group H of the low-symmetry phase is a *translationengleiche subgroup* of the group G of the high-symmetry phase. The number of possible twin domains is defined by the index $[i] = |G|/|H|$ (see Section 1.3.2). We have illustrated by means of the Bärnighausen symmetry tree that the displacive phase transition from β- to α-quartz is accompanied by the formation of two twin domains, the Dauphiné twins (the space group of α-quartz is a $t2$-subgroup of β-quartz). Both space groups belong to the same crystal family, the formed twins are *merohedral twins*.

Phase transitions via a *t-subgroup* with a change of the crystal family are accompanied by the formation of *pseudo-morohedral twins* (*ferroelastic twins*). A typical example of ferroelastic twins is the plagioclase twins. The monoclinic feldspar sanidine $K(Al,Si)_4O_8$ (space group: $C2/m$) undergoes a phase transition at approximately 480 °C to triclinic microcline $KAlSi_3O_8$ (space group: $C\bar{1}$), which is accompanied by an ordering of Si/Al (order–disorder transition). The phase transition from monoclinic monalbite (space group: $C2/m$) to triclinic albite $Na_3\ AlSi_3O_8$ (space group: $C\bar{1}$) at approximately 978 °C is a displacive one. In both cases, the phase transitions proceed via a $t-2$ subgroup with a change of crystal family from monoclinic to triclinic (anorthic). The nonstandard setting of space group $C\bar{1}$ instead of $P\bar{1}$ was chosen to illustrate easily the symmetry relations between the monoclinic high-temperature and the triclinic low-temperature phase. Two pseudo-merohedral twin domains will arise during the phase transition, which can be formed either with the *albite twin law* (reflection twin on (010)) or with the *pericline twin law* (twofold rotation twin along [010], composition plane irrational || [010] denoted as rhombic section; see also Table 4.11). It should be mentioned that plagioclase twins after the albite and periclase law can be formed during the crystal growth, phase transitions, and by mechanical deformation. In general, a crystal is denoted as *ferroelastic* if the various possible orientation states differ in spontaneous strain and one can switch reversibly between the orientation states by an external mechanical stress (for a detailed treatment of ferroelasticity, see, e.g., [52]).

Mechanical Twins Mechanical twinning is caused by a homogeneous shear deformation. This process of plastic deformation of a crystal takes place at low temperatures. The twin formation proceeds very fast with sound velocity by a switching

Table 4.11 Twinning elements of selected materials.

Crystal	Bravais lattice type	K_1 {*hkl*}	η_1 <*uvw*>	K_2 {*hkl*}	η_2 <*uvw*>	*s*	Type of twin
Cu, Ag, Au	*cF*	111	$11\bar{2}$	$11\bar{1}$	112	0.707	C
Fe, W, Mo	*cI*	112	$\bar{1}11$	$11\bar{2}$	111	0.707	C
Si	*cF*	111	$11\bar{2}$	$11\bar{1}$	112	0.408	C
Zn	*hP*	$10\bar{1}2$	$\bar{1}011$	$10\bar{1}\bar{2}$	$10\bar{1}1$	0.140	C
C (graphite)	*hP*	$11\bar{2}1$	$\bar{1}\bar{1}26$	0001	$11\bar{2}0$	0.367	C
α-U	*oC*	130	$3\bar{1}0$	$1\bar{1}0$	110	0.299	C
		$1\bar{7}2$	312	112	*$3\bar{7}2$*	0.228	II
		112	*$3\bar{7}\bar{2}$*	*$1\bar{7}2$*	312	0.228	I
		121	*$\bar{3}2\bar{1}$*	*$\bar{1}4\bar{1}$*	311	0.329	I
Albite	*aP*						
$NaAlSi_3O_8$	Albite law	010	*$\bar{1}010$*	*$\bar{3}05$*	010	0.148	I
	Pericline law	*$\bar{3}05$*	010	010	*$\bar{1}010$*	0.148	II

Data from [53, 54].

of twin domains. Therefore, mechanical twinning of macroscopic crystals is often accompanied by an audible clicking noise. A part of the matrix crystal is switched into a mirror orientation caused by the mechanical load. In general, the twin system is defined by the twin plane {*hkl*} and the shear direction (twin direction) <*uvw*>. The atomic arrangement of an fcc twin is shown in Figure 4.35a. The normal stacking sequence … ABCABC … (ΔΔΔΔΔ) for an fcc structure is changed to … CAB**C**BAC … (ΔΔΔ∇∇∇). In our case, the central C layer is the (111) twin boundary and acts as mirror plane for the stacking sequences of the two twin components. In the language of materials science, it is common to denote the component with the original atomic arrangement as matrix (parent crystal) and the reflected part as twin. This type of twin boundary where the reflection plane is a common plane of matrix and twin is called *coherent twin plane*. All other interfaces between matrix and twin are called *incoherent twin planes*. The orientation relationships of the twin and the matrix parameters are described by the four parameters K_1, K_2, η_1, and η_2, which are called *twin elements* (Figure 4.35b).

The twinning plane (here identical with the composition plane) is labeled K_1. The crystal structure below K_1 is the matrix part, the sheared twin structure is located above K_1. The plane K_1 is in no way affected by the shear (first undistorted plane). The plane K_1 contains the shear direction η_1. The plane K_2 is the second undistorted plane, the plane S containing the normals to K_1 and K_2, and the shear direction η_1 is the shear plane. The intersection of K_2 and S is the conjugate shear direction η_2. The twinning process causes a shear rotation of plane K_2 through the angle 2α. It is obvious from the figure that $|\eta_2| = |\eta'_2|$, that is, η_2 is unchanged in length. The magnitude of the simple shear is given by

$$S = 2\tan\alpha \tag{4.48}$$

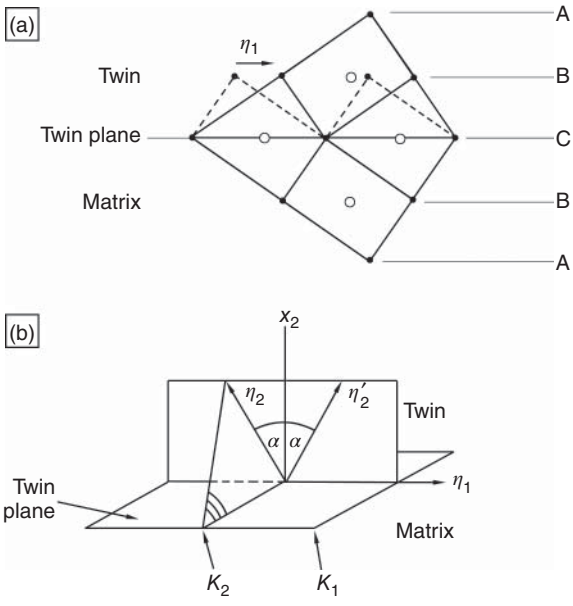

Figure 4.35 Illustration of deformation twinning: (a) atomic arrangement of (110) plane of an fcc twin and (b) geometrical relationships of the parameters K_1, K_2, η_1, and η_2.

There exist different types of deformation twins that are defined by the rational or irrational character of twin elements K_1, K_2, η_1, and η_2. Twins are classified as ***twins of type I*** (reflection twins) if K_1 and η_2 are rational (K_1-lattice plane, η_2-lattice direction), as ***twins of type II*** (rotation twins) if K_2 and η_1 are rational, and as ***compound twins (C)*** if all four twin elements K_1, K_2, η_1, and η_2 are rational. Cubic twins are always compound twins. ***Conjugate*** or ***reciprocal twins*** are given, if the following conditions for the two twin systems are fulfilled:

$$\text{System I} \quad K_1(hkl), K_2(h'k'l'), \eta_1[uvw], \eta_2[u'v'w']$$

$$\text{System II} \quad K_1(h'k'l'), K_2(hkl), \eta_1[u'v'w'], \eta_2[uvw]$$

A list of the four twinning elements and the scalar magnitude of the shear ***s*** for selected materials is given in Table 4.11. Irrational indices of planes and directions are approximated by large integer indices and especially marked by asterisks.

Various models and theories have been developed for the description of the mechanisms of mechanical twinning for the main crystal structure types. The starting point is the formation of a microscopic twin at nucleation stage and its further growth. Very often the twinning mechanism is described by means of a specific dislocation model. A comprehensive overview and critical discussion of the various twinning models can be found in the review of Christian and Mahajan [55]. The process of mechanical twinning is associated with the formation of thin twin bands (twin lamellae) also denoted as Neumann lamellae. In single crystals,

the twin lamellae have sides parallel to the twin plane K_1. Lens-shaped (lenticular) twins are formed in polycrystalline materials and in single crystals with twin intersections. In general, deformation twins are very thin with pointed ends.

Annealing twins are a special kind of twins that are formed during recrystallization and grain growth in (cold-worked) metals and alloys that are already deformed. The growth of annealing twins during the recrystallization process takes place at higher temperatures where self-diffusion can occur. Contrary to mechanical twinning where shear deformation is the driving force for twin formation annealing twins grow by diffusion.

Various models of the formation of annealing twins have been developed. The *growth accident concept* assumes that annealing twins are formed at a GB by errors in the stacking sequence. Other models predict that annealing twins are formed at the interface if well-oriented grains touch each other (*grain encounting)* or twins are nucleated by means of SFs. From the analysis of a multitude of experimental annealing twin studies, it was reasoned that the frequency and occurrence of annealing twins are mainly influenced by the following factors [56]:

- grain size D
- temperature and time of annealing
- velocity of GB migration
- GB energy
- twin boundary or SF energy
- texture of grains
- prestrain or degree of prior deformation
- presence of inclusions.

A higher degree of prior deformation (higher strain level) will cause a higher velocity of GB migration and at least a higher twin density during the recrystallization process will result. The relation between twin density ρ_T (number of twin interfaces/unit length), grain size D, and SF energy E_{SF} is expressed by the following simple equation:

$$\rho_T = \frac{B}{D} \log \frac{D}{D_0} \tag{4.49}$$

The constant B is related to $1/E_{SF}$ and D_0 is the grain size at $\rho = 0$.

The shape of annealing twins differs from that of deformation twins. In general, their shape is characterized by straight edges without pointed ends. Recrystallized grains with annealing twins have a much lower dislocation density than a deformed area.

In the following section, we illustrate how the type and atomic structure of microtwins in nanocrystalline (nc) germanium can be determined by a combined analysis of HRTEM and image simulation [57, 58]. The heavily twinned structure of the (110) oriented nc-Ge film is visible in the HRTEM micrograph (Figure 4.36a). The film contains approximately 3.1×10^{12} twin boundaries per cm^2. The Fourier transform of the HRTEM image (Fig. 4.36b) clearly shows the pseudo fivefold symmetry characteristic for multiple twinning. In the HRTEM image, one can detect circularly arranged microtwins (cyclic twins), which meet

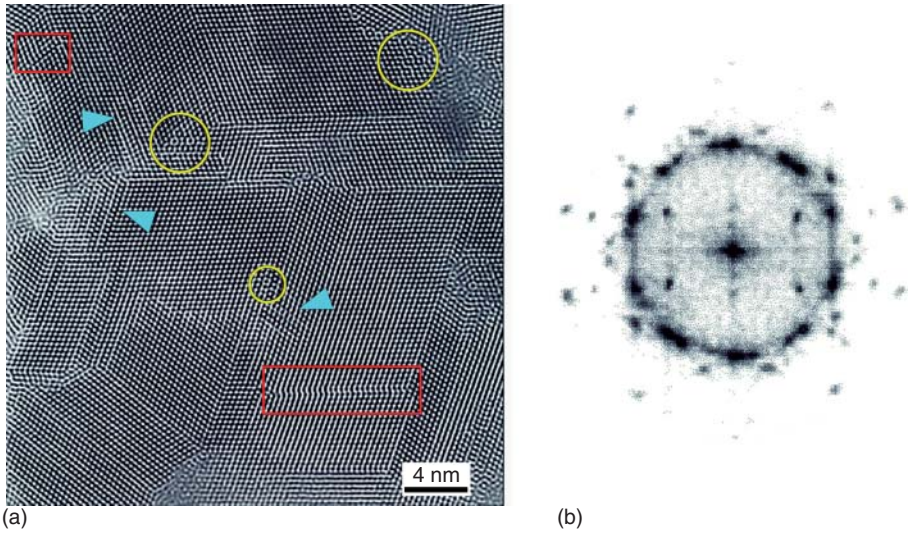

Figure 4.36 HRTEM image (taken at 400 kV) of a nc (110) oriented germanium film with complex twin structures with linear and circular structural features (a). Fourier transform of the HRTEM image (b). (Reprinted with permission from Neumann, *et al.*, [57].)

in three- or fivefold junctions parallel to the growth direction of the film. The intersection regions of the cyclic twins form different types of core structures.

The structure images of the coherent (111) twin boundaries in <110> orientation can be interpreted without computer simulation. It is an already known fact that the (111) twin boundary in the diamond structure falls on a layer of channels (rather than a layer of atoms). This fact may be used to determine whether the HRTEM image shows white channels or white columns of atoms. In our case, the channels were imaged as bright dots (optimum defocus conditions near the Scherzer focus). In addition to the coherent twin boundaries, interface regions of multiple twins with linear and circular contrast features (especially marked by arrows and circles) and SFs (encircled by a rectangular box) are visible in Figure 4.36.

For the interpretation of these special contrast features, we have to take into consideration the crystallography of multiple twinning. The possible twin boundaries in the diamond structure can be classified by means of the CSL theory. The coherent primary twin with {111} as a twin plane is a $\Sigma = 3$ boundary. The phenomenon of circular multiple twinning and the specific properties of $\Sigma = 3^n$ boundaries in crystals with *fcc* and diamond structures was extensively studied (for details see, e.g., [50, 58]). In general, group theoretical methods can be applied to characterize and number the interface operations that leave the given CSL invariant [59, 60]. The possibility of forming circular multiple twins within a fivefold junction type is illustrated in Figure 4.37 showing the computer-simulated atomic structure of a fivefold multiple twin consisting of five tetrahedra.

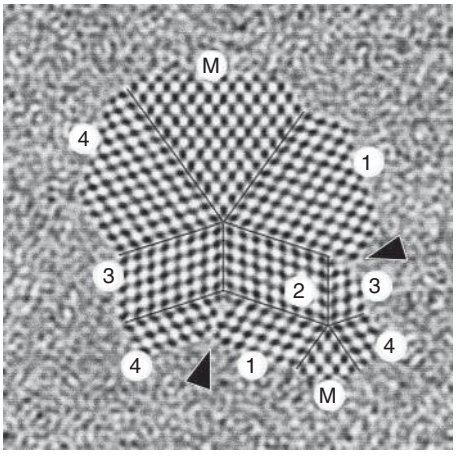

Figure 4.37 Computer-simulated twin quintuplets of germanium in (110) orientation. (Reprinted with permission from Neumann, *et al.*, [57].)

The twin boundaries in the ideal pseudo-pentagonal particle are four $\Sigma = 3$ boundaries with a tilt angle of 70.53° and one $\Sigma = 81$ boundary (not shown in Figure 4.37) with a tilt angle of 77.88°. The $\Sigma = 81$ boundary is formed when there is a mismatch of 7.35° between the {111} planes. In our computer model, the gap was closed by elastic deformation of the twin. In real circular multiple twins, the gap can be closed by crystal defects such as incoherent twin boundaries, SFs, and partial dislocations. Figure 4.38 shows the HRTEM micrograph of an isolated MTP with a fivefold twin junction. In the area of one twin, two couples of SFs (marked by arrows) are present that are tetrahedrally arranged.

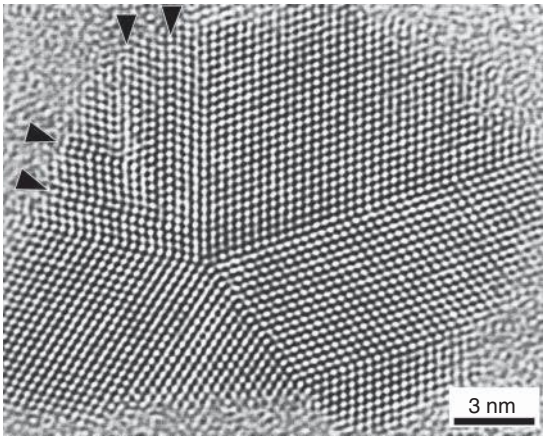

Figure 4.38 HRTEM image (400 kV) of an nc circular multiply twinned particle of germanium. (Reprinted with permission from Neumann, *et al.*, [57].)

In our model, the single tetrahedra are enumerated, where M denotes the matrix and the numbers 1–4 designate the order of twins. The adjacent twin components (e.g., matrix/first-order twin, second-/third-order twin) are structurally related by a rotation of 70.53° ($\Sigma = 3$ boundaries). The various possibilities of combining the matrix with twins of different order lead to superposition structures with CSLs of types $\Sigma = 3$, $\Sigma = 9$, $\Sigma = 27$, and $\Sigma = 81$. The formation rule of those circular multiple twins is $\Sigma = 3^n$, where n is the order of twins. The symmetry of twin boundaries can be analyzed by means of the *bicrystal concept* [61, 62] where black–white (antisymmetry) groups describe simple twin boundaries and polychromatic symmetry groups the more complex multiple twins. Another method applied for the symmetry description of twins is the method of *composite symmetry* (for detailed descriptions of both methods, see, e.g., [45]).

In order to determine the nature of various types of multiple twins in germanium shown in Figure 4.36, HRTEM image simulations of superimposed (111) twins were carried out. The starting point of the contrast simulations was the geometry of the CSL models of $\Sigma = 3^n$ ($n = 1–4$) twin boundaries. Figure 4.39 shows the superposition twin structure of $\Sigma = 3$, $\Sigma = 9$, $\Sigma = 27$, and $\Sigma = 81$ interfaces and the corresponding simulated structure images. The rigid CSL models did not consider the stress strain/state of the real superimposed twinned part. In order germanium and the corresponding simulated structure images for the Scherzer defocus to overcome these disadvantages, molecular dynamics calculations were carried out to determine the relaxed interface structure. The contrast calculations of unrelaxed and relaxed CSL structures enabled a matching of experimental images with computer-simulated ones. It could be demonstrated that linear superstructures are caused by $\Sigma = 3$ interfaces, whereas most of the circular contrast features arise from $\Sigma = 9$ twin interfaces [58].

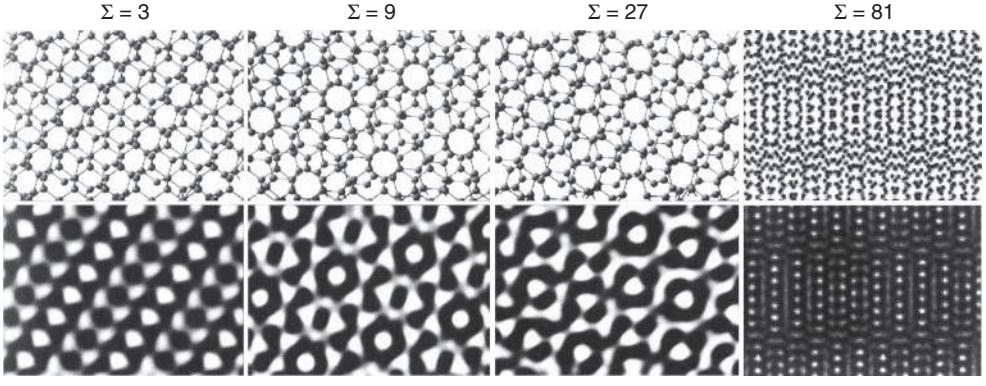

Figure 4.39 Superimposed twin structures of $\Sigma = 3$, $\Sigma = 9$, $\Sigma = 27$, and $\Sigma = 81$ interfaces in (110). (Reprinted with permission from Neumann, *et al.*, [58].)

4.1.3.5 Domain Boundaries

In general, the formation of domain structures is primarily associated with phase transitions. In Section 1.5.4, we have illustrated the group–subgroup relations for the formation of twin boundary and APB at phase transitions. Now we will take into consideration the structure–property relationships of materials, which allow a classification of the domain structures as a function of the directional physical properties (tensor properties) of the domains. The term *ferroic* was introduced to classify crystals, which consist of two or more stable domains that are switchable under an external force field [63]. This force field causes a movement of the boundaries between the domains (*domain walls*) and leads to the reorientation of the domain states. The domain states are characterized by a specific directional physical property, which shows hysteresis behavior as a function of the external field. In general, ferroic crystals arise in a phase transition from a high-temperature *parent phase* to a low-temperature *ferroic phase* (also denoted as daughter phase) with lower point-group symmetry. The domains of the ferroic phase have the same homogeneous crystalline structure, which is differently oriented in different domains. The number n of various kinds of domains (precisely described as single domain states, for a detailed theoretical derivation see, e.g., [64]) in the ferroic phase is given by the index $[i] = |G| : |H|$, where $|G|$ and $|H|$ denote the order of the point groups of the ferroic phase and the parent phase ($H \subset G$), respectively.

The main characteristics of the four types of primary ferroics are given in Table 4.12. *Ferroelectric*, *ferromagnetic*, and *ferroelastic* crystals are well known as *ferroics* for a long time, whereas a *ferrotoroidicity* as a new ferroic property was experimentally approved only in 2007 [65] (for an introduction to ferroic materials see, e.g., [66]).

A typical example of a ferroelectric crystal is $BaTiO_3$. In the high-temperature phase above 120 °C (Curie temperature T_C), $BaTiO_3$ crystallizes in the cubic perovskite structure (point group: $m\bar{3}m$, see Section 1.5.2) and behaves like an insulating material. This phase is called *paraelectric*. A polarization, that is, the formation of electric dipoles, is given only if an electric field is applied. If the field is switched off, the polarization vanishes. On cooling $BaTiO_3$ below the Curie temperature, the *paraelectric* phase undergoes a phase transition to the *tetragonal ferroelectric phase* (point group: $4mm$). The ferroelectric phase consists of domains, that is, regions with a homogeneous structure (*domain states*) with uniform spontaneous polarization. The direction of the spontaneous polarization is different in different ferroelectric domain states. It should be noted that the polarization in

Table 4.12 Classification of primary ferroics.

Type	Microscopic property	Order parameter	Switching force	Example
Ferroelectric	Electric dipole moment	Polarization	Electric field	$BaTiO_3$
Ferromagnetic	Magnetic moment	Magnetization	Magnetic field	Fe_3O_4
Ferroelastic	Deformation	Strain	Mechanical stress	$Pb_3(PO_4)_2$
Ferrotoroidic	Magnetic vortex	Toroidization	Toroidal field	LiCoPO4

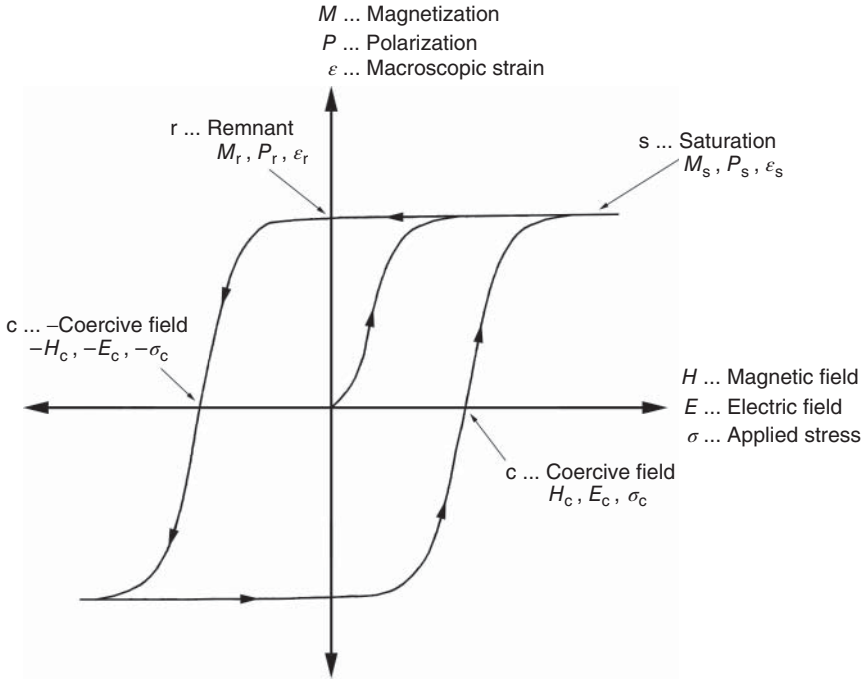
M ... Magnetization
P ... Polarization
ε ... Macroscopic strain
r ... Remnant
M_r , P_r , ε_r
s ... Saturation
M_s , P_s , ε_s
c ... –Coercive field
–H_c , –E_c , –σ_c
H ... Magnetic field
E ... Electric field
σ ... Applied stress
c ... Coercive field
H_c , E_c , σ_c

Figure 4.40 Typical hysteresis curve of ferroic crystals.

the ferroelectric phase is a structural effect and is also present when no electric field is applied. Permanent electric dipoles can occur only in crystals along a polar direction. Therefore, ferroelectricity is possible only in the following 10 crystal classes: 1, *m*, 2, *mm*2, 3, 3*m*, 4, 4*mm*, 6, and 6*mm*. Under the action of an electric field, the *domain walls* (boundaries between domains) can move and the directions of the spontaneous polarization of the differently oriented domains will be aligned along the field. This reorientation of the ferroelectric domains is denoted as *domain switching*. In the paraelectric phase, the electric-field-induced polarization is linearly dependent on the applied electric field. The ferroelectric phase is characterized by a nonlinear and reversible dependence of the structurally induced polarization on the applied field expressed by the hysteresis curve (Figure 4.40). If the electric field is zero, there is still a *remanent polarization* P_r present in the ferroelectric crystal. For a net zero polarization, an electric field of coercive field strength E_C has to be applied. The transition from the cubic point group $G = m\bar{3}m$ to the tetragonal point group $H_1 = 4mm$ is accompanied by the formation of six single domain states ($[i] = |G| : |H| = |48| : |8| = 6$). The vector of spontaneous polarization in the point group 4*mm* lies parallel to the polar tetragonal *c*-axis (Figure 4.41).

The six domain states form three pairs of domains with their polarization vectors parallel to the *x*-, *y*-, and *z*-axes of the cubic parent phase. From Figure 4.41, it is obvious that two types of domain walls exist. Two domains that are polarized

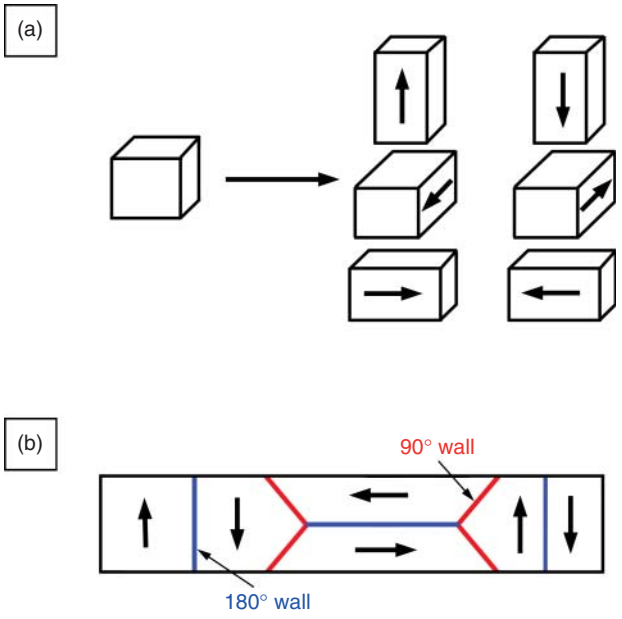

Figure 4.41 Domain states and domain boundaries in tetragonal $BaTiO_3$: (a) orientation relationships of the six single domain states and (b) 90° and 180° domain walls.

perpendicular to each other are separated by a 90° domain wall, whereas a 180° domain wall separates two domains with antiparallel polarization vectors.

The tetragonal ferroelectric phase is stable in the temperature range from 120 to 5 °C. Then it transforms to an orthorhombic phase (point group: $mm2$). This phase can appear in 12 single domain states ($[i] = |G| : |H_2| = |48| : |4| = 12$) with <110> vectors of spontaneous polarization. At about −90 °C, another phase transition from orthorhombic to rhombohedral (point group $H_3 = 3m$) occurs. In the rhombohedral phase, eight single domain states occur ($[i] = |G| : |H_3| = |48| : |6| = 8$) with <111> vectors of spontaneous polarization. In the orthorhombic phase, 60°, 90°, 120°, and 180° domain walls can be formed, whereas 70.5°, 109.5°, and 180° domain walls are possible in the rhombohedral phase. Domain switching, the motion of the walls, and the corresponding strain actuation play an important role in the application of ferroelectric materials [67].

It should be noted that $BaTiO_3$ is ferroelectric and ferroelastic. In the tetragonal phase, the 90° domains are ferroelectric and ferroelastic, whereas the 180° domains are only ferroelectric. This means there is a very high spontaneous strain in the 90° domains and the 180° domains are nearly strain free. The ferroelectric domain structure arising from the phase transition can be treated as a special type of transformation twin domains [64]. In order to get a thorough understanding of the processes of spontaneous polarization and domain switching, it is necessary to gain knowledge about the atomic structure of domains and domain walls. The

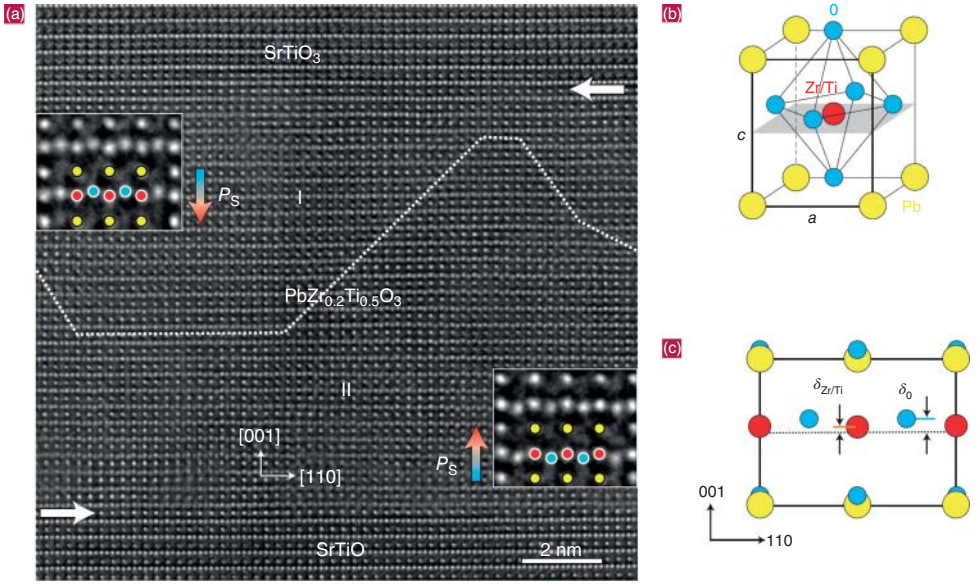

Figure 4.42 Atomic scale imaging of electric dipoles in ferroelectric films: (a) aberration-corrected [$\bar{1}$10] HRTEM structure image of the ferroelectric $SrTiO_3/PbZr_{0.2}Ti_{0.8}O_3/SrTiO_3$ thin film heterostructure, (b) unit cell of $PbZr_{0.2}Ti_{0.8}O_3$, and (c) [$\bar{1}$10] projection of crystal structure. (Reprinted by permission from Macmillan Publishers Ltd: Jia, *et al.*, [58], copyright (2008).)

new generation of aberration-corrected TEMs enables the imaging of ferroelectric domain walls at an atomic scale. Figure 4.42 shows an aberration-corrected [$\bar{1}$10] HRTEM structure image of a thin $PbZr_{0.2}Ti_{0.8}O_3$ layer embedded between $SrTiO_3$ layers [68]. According to the chosen imaging conditions of negative phase contrast, the atoms are bright on a dark background. The horizontal arrows mark the two interfaces between $PbZr_{0.2}Ti_{0.8}O_3$ and $SrTiO_3$. The dotted line marks the 180° domain wall between the two domains designated by I and II. The directions of spontaneous polarization in the two domains are marked by arrows designated by P_S. From the two magnified insets, one can see that the electric dipoles are formed by the displacements of ions (PbO – yellow, Zr/Ti – red, and O – blue) in the unit cell along the [001] direction. It is obvious that the shift of atoms in domains I and II is in opposite directions. Tetragonal structure of ferroelectric $PbZr_{0.2}Ti_{0.8}O_3$ is shown in Figure 4.42b. The shifts of the Zr/Ti atoms and oxygen atoms (Figure 4.42c) lead to a symmetry reduction and cause the formation of electric dipoles.

Ferromagnetic as well as *ferrimagnetic* materials are characterized by magnetic domain states with different spontaneous magnetization, which can be switched by an applied magnetic field. Iron is a classic example of an ordinary ferromagnet. Above $T_C = 1043$ K, α-Fe is *paramagnetic* and crystallizes in the cubic space group $Im\bar{3}m$ (structure type A2, see Section 1.5.2). On cooling

through $T_{C,}$ α-Fe undergoes a phase transition from the paramagnetic state to the ferromagnetic state. We will now consider the group–subgroup relation for this phase transition. In Section 1.4.3, we have briefly illustrated how antisymmetry operations are used for the description of magnetic symmetry. A paramagnetic state of a crystal is described by a gray point group taking into consideration that the magnetic moments at each site are parallel and antiparallel [69]. The paramagnetic–ferromagnetic phase transition of Fe is accompanied by the symmetry change from the gray group $G' = m\bar{3}m1'$ to the black/white point group $H = 4/mm'm'$. In the tetragonal ferromagnetic phase 6, single magnetic domain states occur ($[i] = |G'| : |H| = |96| : |16| = 6$). Owing to the antiidentity $1'$ (each point has two states black- and white = gray) is the order $|G'|$ of a gray point group twice of the order $|G|$ of the ordinary point group.

The magnetic domain structure, particularly the domain configurations as well as their shape and size strongly depend on the microstructure of the material. In the following section, we illustrate the analysis of domain structure of a FeCo-based nc soft magnetic alloy by means of the special TEM techniques of Lorentz microscopy and electron holography [70, 71]. The difference between the conventional TEM and Lorentz imaging mode is illustrated in Figure 4.43. In the Lorentz mode, the normal objective lens (main imaging lens) is switched off and the focus function is taken over by an objective mini lens. Then the sample is located at a nearly magnetic-field-free environment and the natural magnetization inside the specimen is preserved during the investigation. In the conventional TEM imaging mode, the strong magnetic field of the objective lens destroys or modifies the inherent magnetic domain structure. The formation of magnetic contrast using the Fresnel method (defocusing method) of Lorentz microscopy is

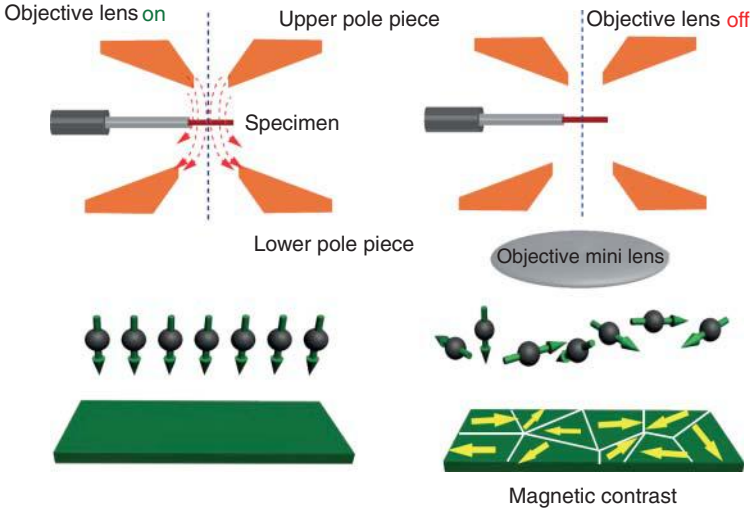

Figure 4.43 Imaging modes in TEM. (a) Conventional TEM mode for structural imaging and (b) Lorentz mode for magnetic domain imaging. (Zheng, C. [70].)

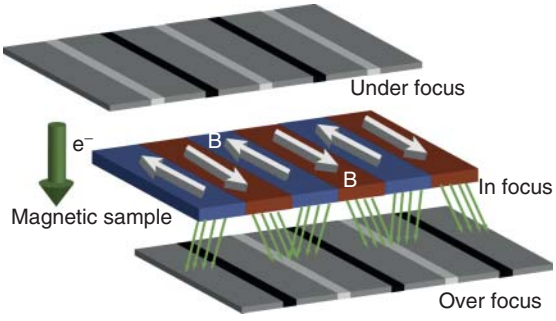

Figure 4.44 The formation of magnetic contrast in the Fresnel mode of Lorentz microscopy. (Zheng, C. [70].)

shown in Figure 4.44. When incident electrons interact with the magnetic sample, they will be deflected by the Lorentz force

$$F = -e(v \times H) \tag{4.50}$$

where e is the electron charge, v is the electron velocity, and H is the magnetic field. The deflection directions are determined by Fleming's left hand rule. In different domains, we have different directions of spontaneous magnetization. When electrons transmit through two adjacent 180° domains, they will be deflected toward opposite directions. Subsequently, the convergent or divergent electrons at the positions of domain walls will form black or white contrast as a function of over- or underfocusing the specimen. Owing to the small deflection angles, the magnetic domains can be observed only under large defocus imaging conditions.

Lorentz microscopy images and the reconstructed phase image of an off-axis electron hologram of magnetic domain structure in a FeCo-based nc soft magnetic alloy are shown in Figure 4.45.

The in-focus image (Figure 4.45a) shows only structure contrast, whereas in the over-focused image (Figure 4.45b), the locations of the domain walls are clearly indicated by white lines. Detailed information about the magnetic flux in

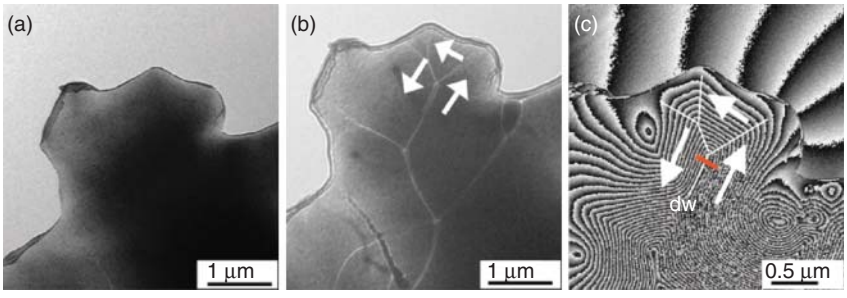

Figure 4.45 Magnetic domain structure of a FeCo-based nanocrystalline soft magnetic alloy: (a) in-focus, (b) over-focused Lorentz microscopy image, and (c) reconstructed phase image of an off-axis electron hologram (decreased field of view). (Zheng, C. [70].)

the domains can be gained from the reconstructed phase image of the off-axis electron hologram (for a detailed description of electron holography, see, e.g., [72]). The black-and-white contour lines in Figure 4.45c visualize the magnetic flux distribution in and around the specimen. Some of the domain walls are marked by white lines and the flux directions in the adjacent domains are marked by white arrows. The domain wall designated by "*dw*" is a 180° wall. Near the edge of the sample, the wall is split in two 90° walls forming a closure structure. The left 90° wall is even further split in two 45° walls. The width of the domain wall designated by "*dw*" was determined from through-focus series images of Lorentz microscopy and amounts to 32.1 nm.

According to the general definition of *ferroics*, a *ferroelastic crystal* consists of two or more domain states with homogeneous spontaneous strain. In different ferroelastic domain states, a different homogeneous spontaneous strain exists. A "ferroelastic switching," that is, a reversible transition from one orientation state to another can be generated if external mechanical stress is applied. The strain curve as a function of the applied stress has the form of a hysteresis loop (Figure 4.40). Ferroelastic domains are a specific form of mechanical twins. *Ferroelastic twins* can be formed at a displacive phase transition from the high-temperature *paraelastic phase* (without spontaneous strain) to the low-temperature *ferroelastic phase* with a group–subgroup relation (see Section 1.5.4, description of *merohedral* and *pseudo-merohedral* twinning).

A *ferroelastic phase transition* accompanied with the formation of *ferroelastic twins* (pseudo-merohedral twins) is given if the point group H of the ferroelectric phase is a subgroup of the point group G of the paraelectric phase. *Both point groups* belong to the *same crystal family*.

$$H \subset G \quad \text{crystal family } H = \text{crystal family } G$$

A *nonferroelastic phase transition* accompanied with the formation of *nonferroelastic twins* (merohedral twins) is given if the point group H of the ferroelectric phase is a subgroup of the point group G of the paraelectric phase. *Both point groups* belong to different *crystal families*.

$$H \subset G \quad \text{crystal family } H \neq \text{crystal family } G$$

A systematic list of group–subgroup relations for ferroelastic phase transitions (t-index) as well as a compilation of ferroelastic and coelastic materials and the transition temperatures is given in the book of Salje [52]. It should be noted that switchable ferroelastic twins can also be formed during the crystal growth and are not always resulting from a phase transition.

A typical example of the formation of ferroelastic twins are the feldspar twins, which were already described in detail in Section 4.1.3.4. Ferroelasticity can be a singular independent property of a crystal. However, it can also be coupled to another ferroic property such as ferroelectricity. We have seen that $BaTiO_3$ and $Gd_2(MoO_4)_3$ (see Section 1.5.4) are both ferroelectric and ferroelastic.

A *ferrotoroidic crystal* contains different domain states with a different spontaneous toroidization, that is, a spontaneous alignment of magnetic vortices.

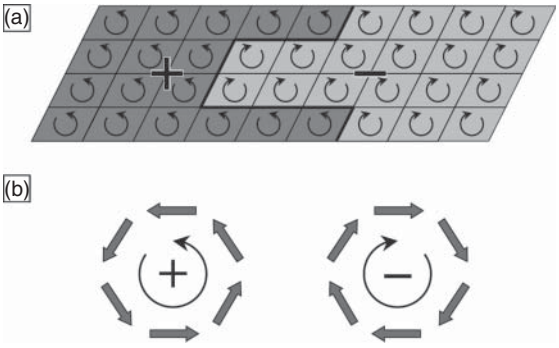

Figure 4.46 Schematic illustration of ferrotoroidic order. (Adapted from [74].) (a) Ferrotoroidic domain structure and (b) arrangement of atomic magnetic moments.

Ferrotoroidic domains can be switched by the application of crossed electric and magnetic fields ($S_i = (E \times H)_i$) by collinear electric and magnetic fields and by a magnetic field alone [73]. Analogous to the other three types of primary ferroic materials, a *ferrotoroidic material* shows a hysteresis behavior of the toroidal moment T as a function of the applied external field $S_i = (E \times H)_i$. We will briefly visualize what a ferrotoroidic order means. Figure 4.46a shows a sketch of a ferrotoroidic domain structure. The curls in the unit cells illustrate the vortices of magnetic moments. We see that the aligned left-handed and right-handed vortices form two domain states. When taking into consideration only the spin ordering and not the orbital ordering of the atoms, the spin part of the toroidal moment can be expressed as $T \infty \sum_n r_n \times S_n$, where r_n is the radius vector and S_n is the spin moment of the n magnetic ions in the unit cell. Figure 4.46b schematically shows how a ferrotoroidic moment is caused by an arrangement of atomic magnetic moments. The left-handed and the right-handed vortex lead to opposite toroidal moments (the vector of toroidization points out of plane and into plane, respectively). Ferrotoroidic domains were firstly experimentally detected by optical second harmonic generation (SHG) in $LiCoPO_{4,}$ where antiferromagnetic domains were also observed.

It is obvious that the brief survey of ferrotoroidicity is only a general introduction to this new field of ferroic materials. For a comprehensive theoretical treatment of ferrotoroidicity with respect to the current state of knowledge about ferrotoroidic materials, including symmetry aspects and physical property tensors, the following references are recommended [73–76]. In addition to the abovementioned primary ferroics, "***multiferroic***" materials exist where two or more ferroic properties are combined in the same phase.

In all ferroic crystals, domain walls act as planar defects, which strongly influence the physical properties of the crystals. Here the word "planar" does not mean that the domain walls are always a plane.

4.1.3.6 Crystal Surfaces

In general, the interface of crystal/vacuum and crystal/gas can be defined as the surface of a crystal. The term *surface* means the transition region between the three-dimensional periodic bulk structure and the vacuum/gas phase. This region includes all atomic layers (sometimes the outermost layer only) whose equilibrium positions of the atoms are different from those of the corresponding atoms in the bulk for ***clean surfaces***. A clean surface exists under ultrahigh vacuum conditions. The surface structure is usually denoted as a substrate structure if it is covered with an adsorbate (adsorption structure and overlayer structure).

A surface or face of a single crystal is characterized by a set (*hkl*) of Miller indices as we have already described in Section 1.2. This means an ideal surface (*hkl*) is structurally correlated with a lattice plane (*hkl*). Macroscopically the symmetry of a crystal face can be mathematically described by 1 of the 10 two-dimensional point groups that belong to the four crystal families/systems (Table 4.13).

The symmetry of a specific crystal face cannot be treated in isolation. The face symmetry is correlated to the point group symmetry of the crystal. For example, a cube {100} occurs as a special form in all five cubic point groups. It is obvious that the face symmetry of a cube is different in each point group (Figure 4.47).

The face symmetry of a crystal can usually be determined by symmetry analysis of etch figures, striations on the faces, or vicinal faces. The mineral pyrite (FeS_2) very often occurs as cubes with striations on the faces. From the symmetry and arrangement of the striations on the faces, it is obvious that pyrite crystallizes in the point group $m\bar{3}$.

The structural symmetry of ideal crystal faces can be described by the 17 two-dimensional space groups (plane groups), which can be classified into the 10-point

Table 4.13 Ten two-dimensional point groups.

Crystal family/crystal system				
Oblique	**Rectangular**	**Quadratic**	**Hexagonal**	
1	*m*	4	3	6
2	2*mm*	4*mm*	3*m*	6*mm*

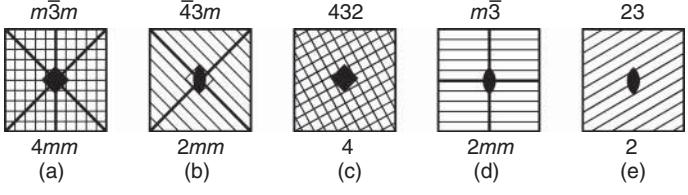

Figure 4.47 (a–e) Striation patterns representing the face symmetries of a cube {100} in the five cubic point groups.

Table 4.14 The two-dimensional space groups (symbol ***g*** – glide line).

Crystal family/ crystal system	Bravais lattice	Lattice parameter	Point group	Space group symmorphic (left) and nonsymmorphic (right)	
Oblique *m*	*mp*	*a*, *b*	1	*p*1	
		γ	2	*p*2	
Rectangular *o*	*op*	*a*, *b*	*m*	*pm*	*pg*
	oc	$\gamma = 90°$	2*mm*	*p*2*mm*	*p*2*mg*, *p*2*gg*
			m	*cm*	
			2*mm*	*c*2*mm*	
Square *t*	*tp*	$a_1 = a_2$	4	*p*4	*p*4*gm*
		$\gamma = 90°$	4*mm*	*p*4*mm*	
Hexagonal *h*	*hp*	$a_1 = a_2$	6	*p*6	
		$\gamma = 120°$	6*mm*	*p*6*mm*	

groups, 5 Bravais lattice types, and the 4 crystal families/systems (Table 4.14). The five two-dimensional Bravais lattice types are illustrated in Figure 4.48.

When one takes into consideration that a surface may consist of several layers (a slab of thickness *z*), the 80-layer groups can be applied to describe the diperiodic surface structure. However, this is not of practical relevance because most of the real surface structures caused by dynamic processes such as ***surface relaxation*** and ***surface reconstruction*** cannot be classified by means of the classical concept of symmetry.

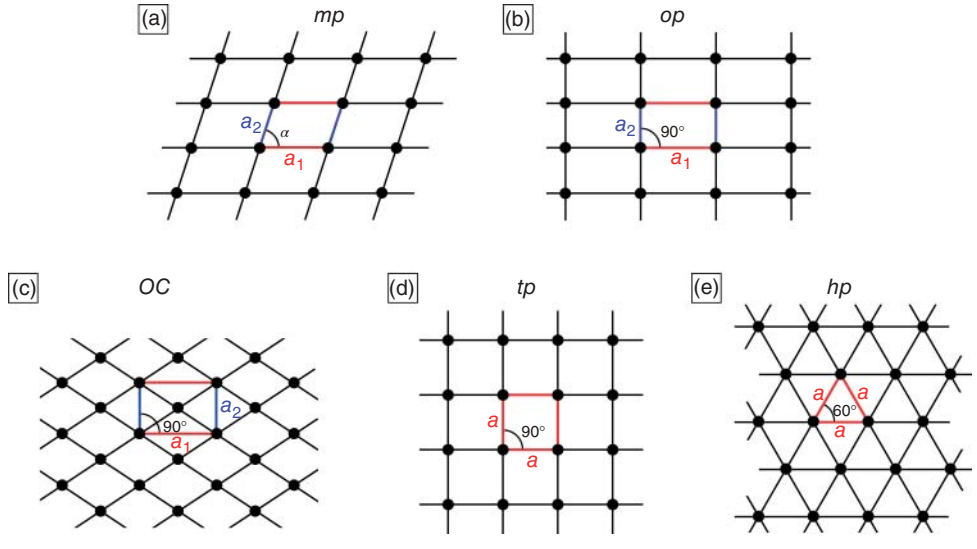

Figure 4.48 (a–e) Conventional cells of the five two-dimensional Bravais lattice types.

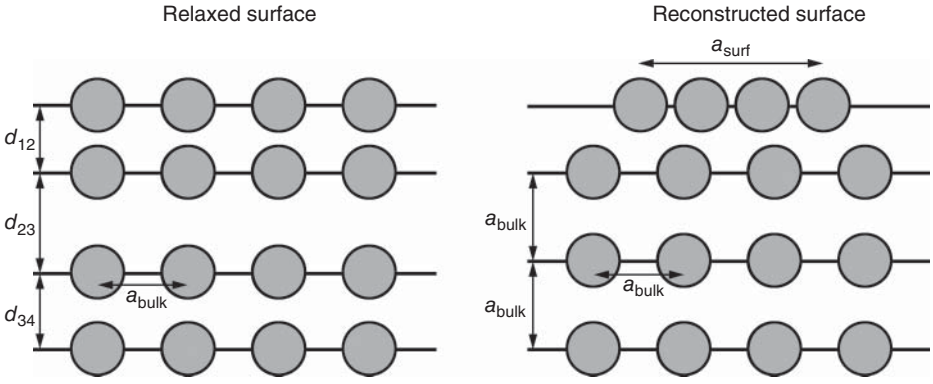

Figure 4.49 Schematic representation of (a) surface relaxation and (b) surface reconstruction. (Adapted from [79].)

A crystal surface distinguishes oneself by an excess energy state relative to the bulk. Let us consider a silicon crystal. In the bulk structure, each silicon atom is tetrahedrally coordinated, that is, each silicon atom is bonded to four neighbors. On the Si (100) surface, each silicon atom has two unsaturated bonds, which are denoted as "***dangling bonds***." The dangling bonds increase the surface energy. A minimization of this excess state of energy will be induced by surface relaxation and/or surface reconstruction.

By surface reconstruction is meant the rearrangement of the atoms in the outer atomic layers of a crystal forming a surface structure with a different periodicity with respect to the bulk lattice. The rigid movement of the surface layers from their bulk positions either perpendicular or parallel to the surface without changing the translational symmetry of the surface layer is denoted as surface relaxation. Figure 4.49 schematically illustrates the phenomena of surface relaxation and surface reconstruction. The real surface structures with respect to the underlying substrate can be classified using the Wood notation [77] or the matrix notation [78].

The general form of Wood's notation can be expressed as

$$S(hkl)\left|\frac{\boldsymbol{a}_S}{\boldsymbol{a}}\right| \times \left|\frac{\boldsymbol{b}_S}{\boldsymbol{b}}\right| - \alpha - A \tag{4.51}$$

Where S is the chemical symbol of the substrate material, (hkl) denotes the crystallographic plane parallel to the substrate, $\boldsymbol{a}$, $\boldsymbol{b}$ and $\boldsymbol{a}_S$, $\boldsymbol{b}_S$ define the corresponding net vectors of the substrate and the surface superstructure, α is the rotation angle between the two nets, and A is the chemical symbol of the overlayer (e.g., adsorbate).

The matrix notation follows directly from the relationship between the two sets of net vectors

$$\begin{aligned}\boldsymbol{a}_S &= m_{11}\boldsymbol{a} + m_{12}\boldsymbol{b}\\ \boldsymbol{b}_S &= m_{21}\boldsymbol{a} + m_{22}\boldsymbol{b}\end{aligned} \tag{4.52}$$

	Ni {001} $2 \times 2 - 0$	$\begin{pmatrix} 2 & 0 \\ 0 & 2 \end{pmatrix}$
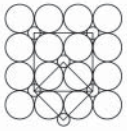	Fe {001} $\sqrt{2} \times \sqrt{2}\ -45° - S$	$\begin{pmatrix} 1 & \overline{1} \\ 1 & 1 \end{pmatrix}$

Figure 4.50 Schematic representation of various surface structures in Wood and matrix notation.

and the surface structure is determined by the matrix $\boldsymbol{M} = \begin{pmatrix} m_{11} & m_{12} \\ m_{21} & m_{22} \end{pmatrix}$.

The schematic surface structures shown in Figure 4.50 illustrate the two commonly applied surface notations.

The knowledge of possible reconstruction structures of a specific crystal surface and their regions of stability are a necessary prerequisite if the crystals are used as substrate materials for growth experiments. Therefore, it is unavoidable to determine experimentally the surface reconstruction phase diagram for the specific material. Figure 4.51 shows the phase diagram for the GaAs (001) surface as a function of temperature and the As_4/Ga beam equivalent pressure (BEP) ratio

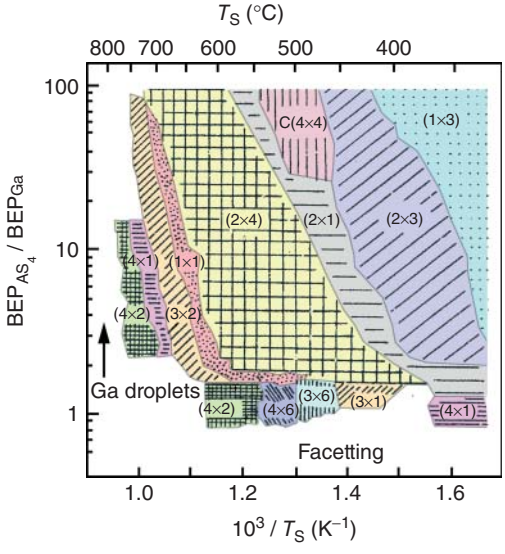

Figure 4.51 Surface reconstruction phase diagram for GaAs (001) as a function of temperature and As_4/Ga BEP-ratio. (By courtesy of L. Däweritz, R. Hey [80].)

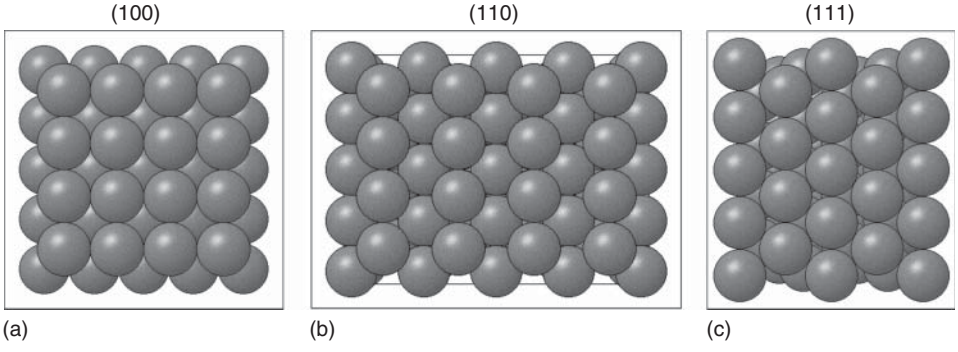

Figure 4.52 (a–c) Low-index faces of an fcc crystal (surfaces drawn with the program "Surface explorer" Hermann, K. [82].)

for MBE experiments. The diagram illustrates that the GaAs (001) surface undergoes various phase transitions. This phase diagram can be used for optimizing the growth conditions for MBE (molecular beam epitaxial) growth of thin films on GaAs (001) substrates.

The properties of materials are influenced by both the atomic structure of the surface and the ***surface morphology***. In Chapter 2, the kinetic processes and mechanisms of crystal growth on flat and rough surfaces were already described. Furthermore, the terminology for terraces, facets, steps, and kinks on surfaces was introduced. In the following section, we illustrate the different surface morphology of low- and high-indexed ideal surfaces. Figure 4.52 shows the atomic arrangement of the main low-index faces of an fcc crystal. The surface unit cell is marked. All three faces are flat faces. High-index crystal faces are called *vicinal faces* because they differ only by a small miscut angle from the fundamental low-index faces. The atomic arrangement of vicinal faces is characterized by a terrace structure separated by steps only or steps with kinks. In order to visualize the composition of high-index faces, the "compact-step notation" [81] was introduced. The surface structure is then designated as

$$w(h_t k_t l_t) \times (h_s k_s l_s) \tag{4.53}$$

In this notation, w is the number of atomic rows in the terrace parallel to the step edge (*w*idth of terrace), $(h_t k_t l_t)$ and $(h_s k_s l_s)$ are the Miller indices of the *terrace* and *step plane*, respectively. A (332) surface of an fcc crystal is designated as $6(111) \times (111)$. It consists of six atom-wide (111) terraces, each separated by a monoatomic (111) step (Figure 4.53a). The stepped surface designation for the kinked (10 8 7) fcc surface is given by $7(111) \times (310)$ (Figure 4.53b).

We should clearly keep in mind that a real low-index surface of an fcc crystal is not always an atomically smooth surface. Atomic steps, kinks, and terraces can be caused by crystal defects such as dislocations. Crystal defects as dislocations, GBs, SFs, and so on can terminate at the surface and mainly influence the atomic morphology. A meanwhile classical method of the early days for the visualization of the surface morphology at an atomic level is the ***surface decoration***

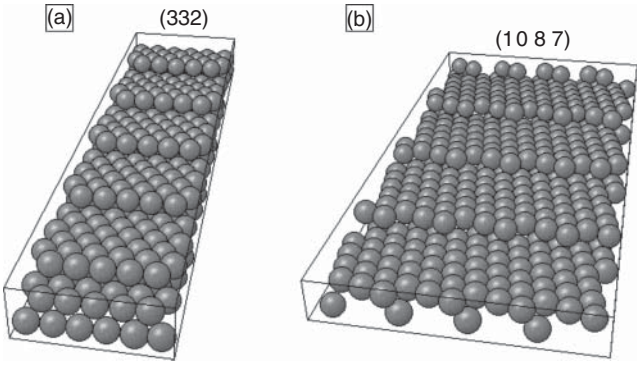

Figure 4.53 High-index faces of an fcc crystal (surfaces drawn with the program "Surface explorer" Hermann, K. [82]): (a) stepped (332) face and (b) kinked (10 8 7) face.

technique (see, e.g., [83, 84]). A typical gold decoration pattern of a NaCl (100) surface is shown in Figure 4.54. In the center of the image, we see a single round and a square spiral around dislocations with a Burgers vector $a/2$ <110> and a <100>, respectively. The various spirals correspond to different dislocations and steps of different height around the dislocations. The end point of the spirals corresponds to the emergence points of the dislocations. The gold decoration method was used to investigate molecular growth processes (e.g., quantitative analysis of step kinetics, interaction of steps and holes).

Nowadays, a tremendous number of modern imaging, diffraction, and spectroscopic methods are applied to analyze the structure of surfaces (for an overview of methods of surface analysis, see, e.g., [85]).

4.1.4 Three-Dimensional defects

Specific combinations of lower dimensional defects such as agglomerations of point defects, clusters of dislocations, and SF tetrahedra can also be considered three-dimensional defects. Fascinating examples of agglomerations of point defects are the so-called *swirl defects* in silicon, which were extensively studied since their discovery in the seventies. It could be shown by HVTEM (high-voltage transmission electron microscopy) that *A-swirls* consist of single dislocation loops or cluster of dislocation loops which were generated by agglomeration of self-interstitials [86]. The structure of *B-swirls* has never been completely identified. It was assumed that *B-swirls* are precursors of *A-swirls* and may consist of globular self-interstitial clusters and carbon impurity atoms. A detailed overview about swirl studies including the impressive picture gallery of TEM micrographs of swirls is given in [87].

Contrary to one- and two-dimensional defects, the various types of bulk defects are not unambiguously defined in the literature. In the following section, we will explain the characteristic features of the most common bulk defects.

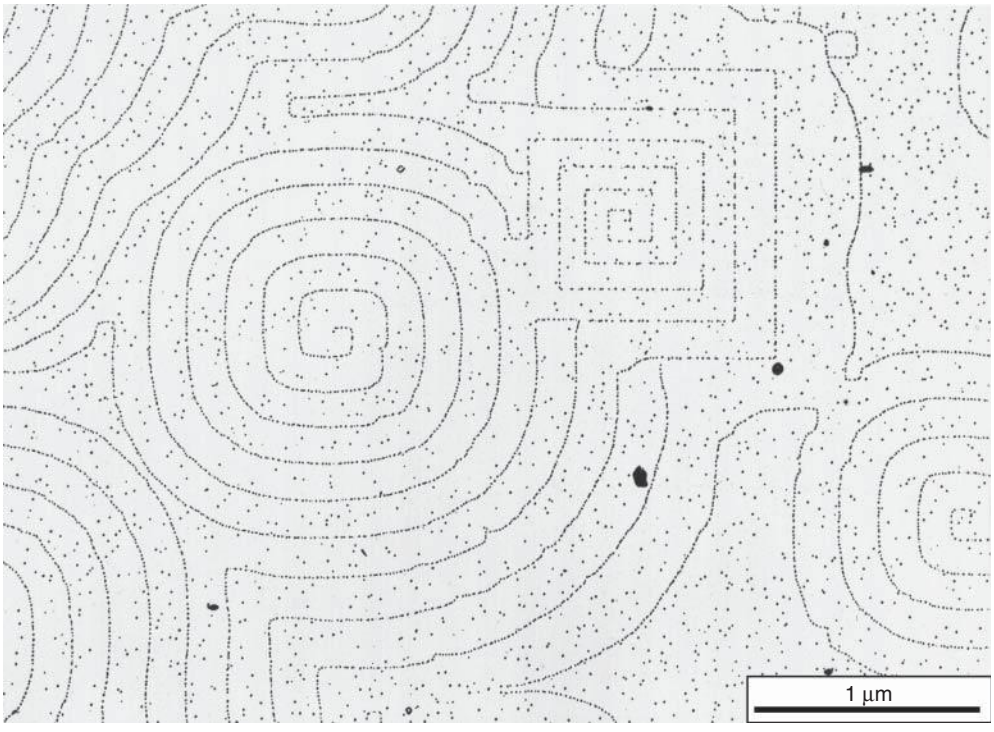

Figure 4.54 Gold decoration pattern of atomic steps around dislocations on a NaCl (100) surface. (By courtesy of K.W. Keller, Halle.)

4.1.4.1 Inclusions

Foreign solid, liquid, or gaseous materials that are trapped within natural or synthetic crystals are denoted as ***inclusions***. In mineralogy and gemology, inclusions are classified after Gübelin [88] and Gübelin and Koivula [89] in three categories.

1) *Protogenic (preexisting) inclusions:* This type of inclusions was already present before the growth of the host. As an example, natural quartz crystals may occur with rutile needles as inclusions. The rutile needles were already present before the host (quartz) started to grow around the inclusion (rutile). Protogenic inclusions are always minerals.
2) *Syngenetic (contemporaneous) inclusions*: Solid, liquid, or gaseous inclusions that are formed during the growth of the host are denoted as syngenetic inclusions. The various forms and shapes of inclusions are often designated by specific terms. Some examples are as follows:
   a. *Negative crystals:* cavities with a definite crystal shape
   b. *Bubbles:* filled bubble-shaped cavities
   c. *Clouds:* aggregates of fine bubbles or cavities
   d. *Veils:* thin sheets or plates of small inclusions

e. *Phantoms:* an outline of the shape of a smaller crystal is visible in the host crystal. This can be caused by a precipitation of a smaller crystal during the growth, which is then embedded in the host crystal or by inclusions of colorizing trace elements or minerals.

Syngenetic inclusions can also consist of combinations of gaseous, liquid, and solid foreign materials. When a syngenetic cavity (primary cavity) is filled with liquid, only a *single-phase inclusion* is given; combinations of gaseous and liquid or liquid and solid foreign materials are denoted as *two-phase inclusions* and of gaseous, liquid, and solid materials as *three-phase inclusions*, respectively. Minerals such as calcite, epidote, feldspar, pyrite, and rutile are typical syngenetic inclusions in quartz.

3) *Epigenetic (postgrowth) inclusions*:These solid, liquid, or gaseous inclusions are formed after the host crystallized. Epigenetic inclusions in minerals can be generated either by exsolution or partly recrystallization of the host crystal. This alteration process as a function of time can happen under varied conditions of temperature and pressure. For example, typical exsolved inclusions in corundum are rutile needles (α-TiO_2), hematite (Fe_2O_3), ilmenite ($FeTiO_3$), and boehmite (γ-AlO(OH)).The most comprehensive treatment of mineral and liquid inclusions in gems is given in the three volumes of the "*Photoatlas of inclusions in gemstones*" [88, 89], which is simultaneously a reference photoatlas library.

The differentiation between protogenetic and syngenetic inclusions is often difficult or impossible. Therefore, one can also find in the literature a classification into primary inclusions (protogenetic and syngenetic) and secondary inclusions (epigenetic). This classification scheme is coincident with that in the field of crystal growth and materials science where ***primary inclusions*** are formed during the crystal growth process and ***secondary*** ones thereafter. The fundamentals and specific conditions for both the formation and prevention of inclusions during the growth process for the different growth techniques (melt growth, flux growth, solution growth, hydrothermal growth, gel growth, and vapor growth) are comprehensively treated in handbooks on crystal growth (see, e.g., [90]). An essential fact is that solid inclusions act as sources of other crystal defects such as dislocations and twins. Parameters that strongly influence the morphology of inclusions are the growth conditions, the structure of inclusions, and the presence of further impurities. The shape of inclusions can vary, for example, from spherical, platelike, dendritic to polyhedral. The formation and characterization of inclusions in $LiAlO_2$ is described and illustrated in detail in Section 4.4.1.

4.1.4.2 Precipitates

In general, a solid phase (precipitate) will be formed from an existing phase (matrix) when the solubility limit of the phase system is exceeded. Precipitates can be formed during the growth process, during cooling after growth, or during various heat treatments at subsequent processing. Precipitation is strongly connected with nonstoichiometry and can be caused by diffusion, agglomeration,

and condensation of point defects. Depending on the materials system, a large diversity of precipitates with respect to size and shape may occur. The size of second phases ranges from very tiny spherical particles and thin platelets up to large polyhedral particles. The interface between the matrix and precipitate can be coherent, semicoherent, or incoherent. It could be shown by means of atomic scale imaging (HAADF-STEM technique) that a θ′-precipitate (Al_2Cu) forms two types of interfaces with the surrounding matrix (aluminum-copper solid solution, α-Cu). One is coherent and the other one semicoherent [91].

Spinel $MgAl_2O_4$ is a compound where both an access of MgO or Al_2O_3 can be accommodated by the formation of point defects and point defect cluster. If the solubility limit is exceeded, precipitations will be formed. Figure 4.55 shows a TEM diffraction contrast image of precipitations of the metastable monoclinic intermediate phase of type I in (001) oriented spinel with an excess of Al_2O_3 ($MgO : Al_2O_3 = 1 : 3$).

The formation of precipitates in nonstoichiometric $MgAl_2O_4$ proceeds from the supersaturated solid solution via a preprecipitation stage, an intermediate structure consisting of two monoclinic phases to the final precipitation of α-Al_2O_3 (for a detailed description of the phases, the orientation relationships and the degree of interface coherence see, e.g., [4]). The precipitates shown in Figure 4.55 are thin platelets. The fringe contrast is similar to that of an SF. However, here the fringe contrast is caused by a small tilt between matrix and precipitate (so-called δ-fringes [40]). The thin monoclinic platelets are preferentially formed at GBs, SFs, and partial dislocations of the spinel matrix.

There exist different suggestions by which mechanism the excess of Al_2O_3 is incorporated into spinel. Recent atomistic simulations by means of DFT have confirmed that point defect clusters formed from antisite defects ($\{V''_{Mg} : 2Al^{\bullet}_{Mg}\}$

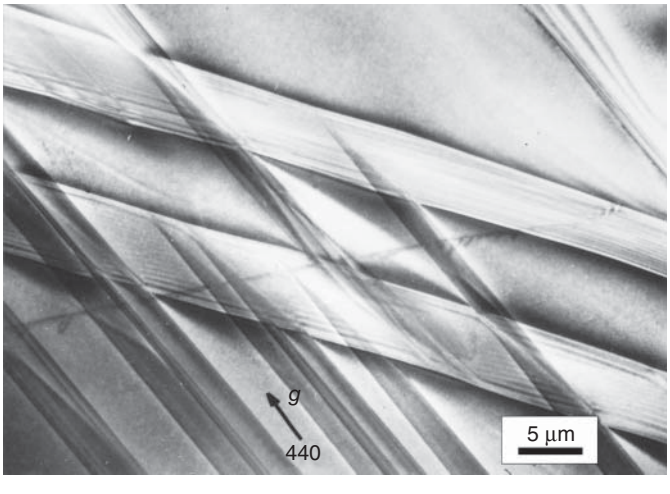

Figure 4.55 Diffraction contrast TEM image of monoclinic precipitates (type I) in (001) oriented $MgAl_2O_4$.

$\{V''_{Al} : 3Al^{\bullet}_{Mg}\}^{x}$ $\{O''_{i} : 2Al^{\bullet}_{Mg}\}^{x}$) play an important role for the incorporation process in spinel [4].

We should be aware of the fact that precipitations of a second phase do not always represent an undesired crystal defect, deteriorating the physical properties of a crystal. Precipitation is a commonly applied process and of great importance in the field of industrial crystallization for the mass production of crystals. The requirements with respect to morphology, purity, crystal size distribution, size range of the crystals and last but not least the yield depend on their specific uses. An example where the formation of precipitates is specifically used to improve the yield strength and hardness of alloys is the process of *age hardening* or *precipitation hardening*. This process is accomplished by a three-step heat treatment (solution treatment, quenching, and aging) where a coherent precipitate (second phase) within the matrix phase is formed. Typical examples where precipitation hardening plays an important role are superalloys. Single-crystal, nickel-based superalloys show excellent creep and fatigue properties at high temperatures and are widely used as structure materials in gas turbines, for example, as turbine blade materials. Nickel-based, single-crystal superalloys consist of ordered cuboidal Ni_3Al precipitates (γ'-phase) and the fcc nickel solid solution matrix (γ-phase). The coexistence of γ-matrix and γ'-precipitates is controlled by the heat treatment of the solution and the cooling rate. Figure 4.56 shows an absorption contrast TEM image of the microstructure of nickel-based superalloy CMSX-10. According to discriminative element concentrations (Al, Cr, Co, Ni, Ta, W, and Re) in the γ- and γ'-phases, the average atomic number $\overline{Z}$ is different for γ and γ' ($\overline{Z}(\gamma) = 31$, $\overline{Z}(\gamma') = 26$). Therefore, the matrix phase γ appears dark and the precipitation phase γ' bright, respectively. The volume fraction of the γ'-phase amounts to about 80%. The bright rectangles or even squares of γ' have edge lengths ranging from 500 nm to 1 μm. The imaged patterns are cross sections of the

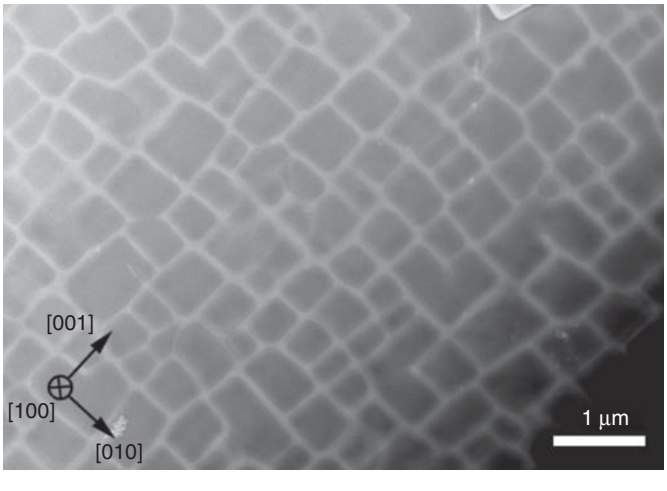

Figure 4.56 TEM absorption contrast image of nickel-based superalloy (CMSX-10).

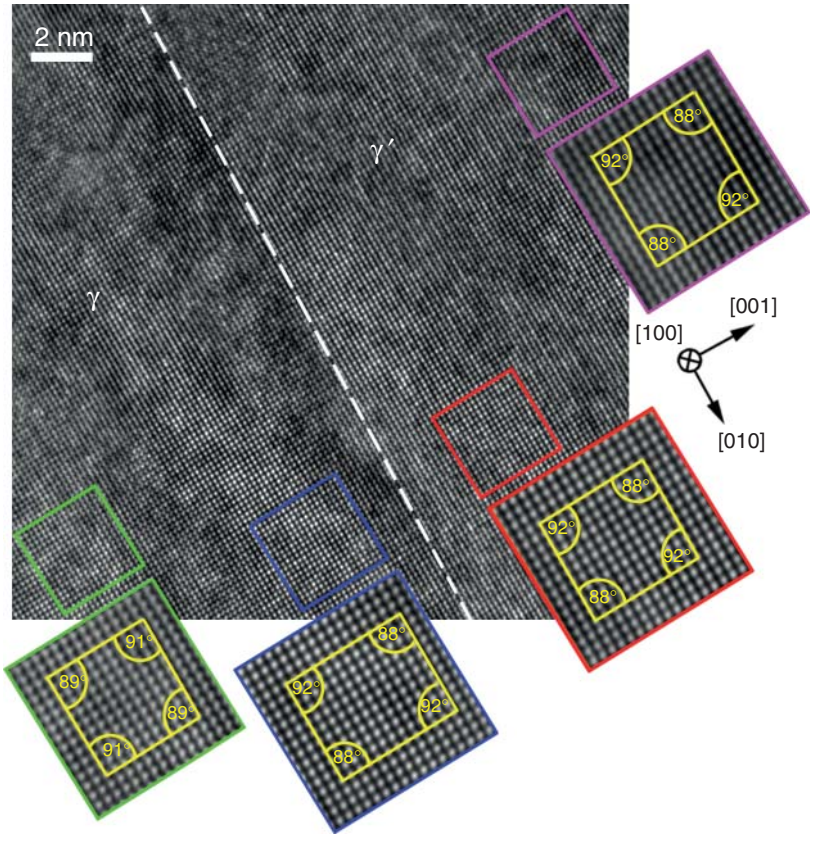

Figure 4.57 HRTEM image of γ/γ′-interface of nickel-based superalloy (CMSX-10).

γ′-precipitates embedded in the γ-matrix. From quantitative analysis of HRTEM images and selected area electron diffraction (SAED) patterns, it was detected that the average γ matrix is slightly tetragonal distorted. The qHRTEM (quantitative high-resolution transmission electron microscopy) analysis has shown that the lattices of γ and γ′ are slightly shear deformed near the γ/γ′-interface. The HRTEM image (Figure 4.57) clearly shows the coherent interface structure confirming the results of diffraction analysis of the lattice parameters parallel and perpendicular to the interface (for details of the analysis, see [71]).

During the aging treatment of precipitation hardening of alloys, nonequilibrium precipitates can also be formed. We will illustrate this for the hardening process of Al-Cu alloys. According to the phase diagram, a mixed crystal α with fcc structure is given at high temperatures, whereas at low temperatures, a phase mixture of $\alpha + \theta$ occurs. The θ-phase consists of tetragonal Al_2Cu. The quenching of the mixed crystal α leads to a supersaturated α-phase. During the aging process, two types of so-called *GP zones* are subsequently formed. The GP-I zones are very thin coherent precipitate layers consisting of one layer of Cu atoms on {100} planes as

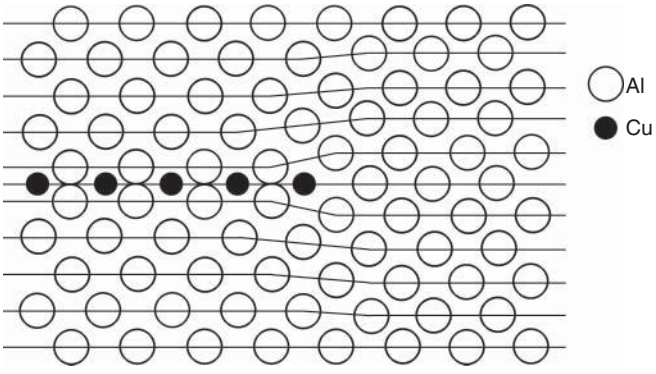

Figure 4.58 Schematic illustration of the GP-I zone in Al-Cu.

illustrated in Figure 4.58. During the progression of aging, more parallel Cu layers on {100} planes will form the also coherent disk-like GP-II zones (θ″-phase) which cause a tetragonal distortion of the structure. After the formation of a further intermediate precipitate θ′, the stable noncoherent equilibrium θ-phase will be reached.

4.1.4.3 **Voids**

In general, the term *voids* is used to designate a smaller or larger hole, that is, an area where atoms are missing. In materials science, the terms, *pore*, *pipe*, and *cavity*, are used for the characterization of *specific* voids formed during the solidification of a material, which is usually accompanied by a shrinkage process. Voids can be generated by

- agglomeration of gas atoms in the crystal lattice (gas bubbles)
- agglomeration of vacancies
- irradiation of crystals with particles (X-rays, electrons, neutrons, etc.)
- ion implantation
- sintering of ceramics.

The size of the voids can range from nanometer- to millimeter-scaled voids. Voids can have a spherical or elongated shape, but polyhedral-shaped voids also occur. In CZ-silicon, octahedral void defects are generated by the agglomeration of vacancies during the growth process. Very often the octahedra are truncated by {100} faces. In addition to single-truncated octahedral voids, double- and triple-adjacent or overlapping voids were observed. The inner walls of the voids are covered with 2–4 mm thick oxide layers. The average size of the voids was about 0.1 μm, the defect density was $10^5 - 10^6$ cm^{-3} [92]. It should be noted that nitrogen impurities as a function of concentration affects both the size and morphology of the voids. Voronkov and Falster [93] figured out that the density of voids ρ_V is proportional to $q^{3/2}C_V^{-1/2}$ where q is the cooling rate at the reaction temperature and C_V is the local vacancy concentration. A detailed description of the existing

problems of defect engineering for void reduction is given in [94]. In the literature, different abbreviations [e.g., D-defects, COPs (crystal originated particles), FPDs, LSTDs, gate oxide integrity (GOI)-defects] are used for the designation of void defects in Si. When a void intersects the silicon wafer surface a pit denoted as "*crystal originated particle*," is generated, which can be analyzed by an AFM (atomic force microscope) or a laser particle counter. One of the specific methods of structural etching for Si can also be applied for the visualization of COPs on the wafer as *flow-pattern defects* (*FPDs*). When voids are detected by light-scattering tomography (LST), they are designated as "LSTDs." As void defects in Si wafers can cause failure of GOI in devices due to the formation of COPs, they are also denoted as GOI-defects.

4.2 Crystal Quality

The ultimate goal of crystal growth and crystal growth technology is the production of high-quality crystals. Titles such as "High-quality crystals of … *substance* … for" or "How to grow high-quality crystals for … ," are often used as headlines for papers on crystal growth and characterization. What are the main criteria defining the quality of a crystal? Are these criteria independent of the compound class and the intended application field? In many papers, the term *quality* is applied in a superficial manner for the rating of a grown crystal. A quality assurance of commercially grown crystals should be based on the authoritative rules and definitions published by the International Organization for Standardization (ISO). The relevant definitions for the quality and quality assurance of a product are published in ISO 9000 [95] and explained below.

- Terms relating to quality:
  Quality: *Degree to which a set of inherent* ***characteristics*** *fulfills* ***requirements****.*
  Requirement: *Need or expectation that is stated, generally implied or obligatory.*
  Characteristic: *Distinguishing feature.*
  Quality characteristic: *Inherent characteristic of a product, process, or system related to a requirement.*
  Grade: *Category or rank given to different quality requirements for products, processes, or systems having the same functional use.*
  Process: *Set of interrelated or interacting activities which transform inputs into outputs.*
  Product: *Result of a process.*There are four generic product categories: services, software, hardware, and processed materials (e.g., grown and processed crystals).
  Customer satisfaction: *Customers perception of the degree to which the customer's requirements have been fulfilled.*
- Terms relating to management:
  Quality control: *Part of quality management focused on fulfilling quality requirements.*

Quality assurance: *Part of quality management focused on providing confidence that quality requirements will be fulfilled.*

According to the ISO 9000 nomenclature, the quality of a grown and/or processed crystal is then described by the following facts: The set of desired inherent characteristics of a crystal to be grown, that is, its main features of the structure/property relationships, is defined by the field of application according to the customer requirements. The specific grading system for the quality assessment is strongly associated with the field of application of the fabricated crystal. The quality of diamond as gemstone will be assessed by means of four grading systems with respect to clarity, color, carat, and cut. Different grading systems are required to assess the quality with respect to optical, thermal, and mechanical properties of thin diamond films grown by CVD (chemical vapor deposition) for technical applications (e.g., optical elements, wavers, dressing, and cutting tools). The grading systems are directly associated with the specific crystal structure/property features required for the specific application of the grown crystals. Strictly speaking, the ISO 9000 system defines the ***quality of a product***, in our case the quality of a grown or processed crystal, by the ***matching degree*** between ***customer's requirement*** and ***customer satisfaction***. It is obvious that a perfect matching between customer requirements and customer satisfaction does not mean the highest quality crystal was grown. The quality degree depends on both the level of customer requirements and the level of the applied grading systems. Now we will discuss the main inherent characteristics of a crystal, that is, the crystal features that are important for a quality assessment.

4.2.1 Criteria of Crystal Quality

Essential crystal features that mainly determine the quality of a crystal are as follows:

- *Degree of crystallinity*
- *Purity degree*
- *Homogeneity degree*
- *Structural perfection*
- *Stress-free crystals*
- *Size and shape*
- *Cost-efficient crystal fabrication*
- *Crystal processing and machining.*

We have seen in Section 1.1 that the ***degree of crystallinity*** can be determined by diffraction experiments which show us whether a single crystal, a textured crystal, a polycrystal, or an amorphous crystal was grown. In addition, the detailed analysis of the diffraction pattern clarifies if a periodic or aperiodic crystal is given. Very important parameters influencing the quality of crystals are ***purity*** and ***homogeneity***. All undesired impurities in a crystal will negatively

affect both the structure quality and the properties of the crystal. On the one hand, we have seen that impurity atoms (extrinsic point defects) can agglomerate and form precipitates or can act as sources of other crystal defects. On the other hand, the doping process is a well-directed diffusion of elemental impurities into the crystal in order to change properties (e.g., electrical conductivity and color) in a desired manner. ***Nonhomogeneities*** in a crystal with respect to the chemical composition will alter structure and properties in an undesired manner. Furthermore, nonhomogeneities may also change the growth rates of different faces. Degree of crystallinity and ***structural perfection*** are closely connected. The main target of most growth experiments is to fabricate a single crystal with high structural and chemical perfection. We have discussed that some defects such as specific precipitates (precipitation hardening) in alloys can improve the properties of materials. The majority of structural defects, however, will bring about a deterioration in the properties. Therefore, the defect analysis of crystals is necessary for the subsequent defect engineering by crystal growers. An essential parameter for the structural perfection closely related to the degree of crystallinity is the so-called ***mosaicity*** of a crystal. It is assumed that a crystal consists of small building blocks which form small-angle boundaries with the adjacent blocks. The two parameters that determine the crystalline perfection is the relative misorientation Δ_ϕ of the blocks and the size of the blocks. It is quite clear that an ideal perfect crystal is formed if $\Delta_\phi = 0$. The mosaicity is measured by rocking curve X-ray diffraction experiments. Crystals that exhibit a high ***stress state*** can be destroyed (e.g., breaking) by a subsequent machining. Furthermore, a high stress state can cause additional structural defects during a machining of the crystal.

Size and ***shape*** are crystal features that strongly depend on both the material class and the customer requirements. Nowadays, the silicon growth technology provides silicon wafers of 450 mm diameter. One of the ever-grown largest protein single crystal of photosystem I, a photosynthetic membrane protein grown under microgravity conditions, was 4 mm long and 1.5 mm in diameter [96]. The size of a majority of protein crystals are measured in micrometers. A specified ***shape of crystals*** is required for many technical applications. In order to avoid a loss of valuable crystal material after crystal growth by means of manifold machining, processing growth techniques that enable the growth of crystals with specified size and shape are commonly applied (for a comprehensive overview on shaped crystal growth, see, e.g., [97]).

Crystal fabrication has to be organized in such a manner that the final product (grown and/or processed crystal) fulfills the requirements and criteria of ***cost-efficiency***.

The ***crystal processing and machining*** maintains all steps (e.g., cutting, polishing, structuring, and doping) from the grown crystal to the final product. During the machining and processing, additional crystal defects can be generated. All machining and processing procedures have to be carried out on a high standard to fulfill the quality requirements (e.g., surface roughness, cutting, and polishing with very precise orientation, for an overview of methods see, e.g., [98]).

4.2.2 Crystal Quality and Application

Diamond crystals are a good example for illustrating how the criteria for classifying crystal quality depend on the field of application. Natural diamond plays an exceptional role among the gemstones because of its beauty caused by its optical properties. The high refractive index ($n_B = 2.407$ for red, Fraunhofer B-line 686.7 nm, and $n_G = 2.415$ for violet, Fraunhofer G-line 430.8 nm) and the high color dispersion (0.044) causes a high brilliance (angle of total internal reflection 24°26′) and the "fire" of well-cut diamonds. When natural as well as synthetic diamonds are used as gemstones, the quality, and connected with it the value of the crystals, is determined by the so-called four Cs, *carat* (1 carat = 0.2 g), *color*, *clarity*, and *cut*. The carat is the most objective of the four Cs because it is measurable. Diamond clarity is graded according to the size, number, and position of the existence of surface defects (blemishes) and internal defects (inclusions). The quality of diamond crystals is differently affected by the various types of defects such as point defects, point defect complexes, dislocations, planar defects (GBs, twins, SFs, and specific platelets), and three-dimensional defects (inclusions and voidites), which were detected in diamond. Natural diamonds are historically divided into four groups. The classification scheme is based on the presence of nitrogen and type of nitrogen defects in a diamond. Approximately 98% of all diamonds belong to ***type I***, which contains a concentration c_N of nitrogen impurities ($c_N > 1$ ppm) detectable by infrared (IR) spectroscopy. ***Type II*** diamonds have a concentration of nitrogen ($c_N < 1$ ppm), which is below the detection limit of IR spectroscopy. The types I and II are subdivided into ***a*** and ***b***. Diamonds of ***type Ia*** have a very high concentration of nitrogen ($c_N \leq 3000$ ppm) in aggregated form. Type Ia diamonds are subclassified into ***IaA*** and ***IaB*** with respect to the predominantly occurring A or B defect centers, respectively. The A-center defect consists of a nearest-neighbor pair of N atoms, whereas the B-center defect is a group of four N atoms surrounding a common vacancy. If both types of defect centers are present in a diamond then the type is denoted as ***IaA/B***. In ***type Ib*** diamonds, there are single nitrogen atoms only surrounded by carbon atoms. This defect type of single substitutional N atoms is called ***C-center***. Only 0.1% of natural diamonds belong to type Ib, which has a concentration of nitrogen impurities ranging from 150 to 600 ppm. Natural type II diamonds occur very rarely. Diamonds of ***type IIa*** have the highest purity grade. Neither nitrogen nor boron impurities occur in a detectable concentration ($c < 1$ ppm). ***Type IIb*** diamonds contain boron impurities ($c_B \leq 50$ ppm), which are present in the diamond structure as single isolating atoms. The boron acts as acceptor and causes a p-type conductivity of the otherwise electrically insulating pristine diamond at room temperature. Typical colors of natural diamonds correlated to the four types are as follows:

Ia: *colorless, brown, pink, violet*
Ib: *brown, yellow, orange*
IIa: *colorless, brown, occasionally pink*
IIb: blue, blue-gray.

Diamond is an insulator at room temperature and has a wide bandgap of 5.47 eV corresponding to a wavelength of 225 nm (deep ultraviolet). Therefore, a chemically homogeneous pristine and nearly perfect diamond should be transparent and colorless. The color of diamond is mainly caused by both extrinsic (substitutional or interstitional impurities) and intrinsic defects (native point defects). A detailed explanation of the fundamentals of point defects as well as the possible physical mechanisms causing the coloration of crystals is given in Section 4.2.1. Specific point defects that cause an optical absorption are called *color centers*. More than 500 color centers are known in diamond formed by both intrinsic and extrinsic point defects [7]. The majority of optical active centers consists of a combination of extrinsic (impurity atoms) and intrinsic point defects (vacancies and interstitials). Most of the impurity-related color centers were detected in synthetic diamonds. They were formed either during the growth process adding dopants or subsequently during ion implantation. Nitrogen is the most important impurity in diamond and is present in at least 50 different color centers. In addition to nitrogen, the following elements forming color centers in diamond: H, He, Li, B, O, Ne, S, Si, P, Ti, Cr, Co, Ni, Zn, As, Zr, Ag, Xe, Ta, W, and Tl. A change of the optical properties of diamond like the absorption of light is strongly related to the presence of nitrogen. Therefore, the physical classification system of diamond is based on the concentration of nitrogen. The specific designation of optical centers in diamond is given by numbered acronyms often correlated to the absorption bands in IR spectroscopy (e.g., A, B, and C centers). Most of the color centers and their influence on the absorption behavior in diamond were identified by different spectroscopic methods [e.g., IR, photoluminescence (PL), cathodoluminescence (CL), Raman and electron spin resonance (ESR) spectroscopy]. These investigations have clarified most of the defect or defect complexes, which are causing a coloration in diamond. It should be noted that a change of color of natural and synthetic diamonds can be released by high-pressure, high-temperature annealing (HPHT) and by ionizing irradiation. This specific treatment induces a change of the point defect structure of the diamond often connected with a color change [99].

Diamond cutting involves the whole processing from a rough diamond to a gemstone by means of shaping and polishing. The term *cut* is often misleadingly used denoting the shape of a diamond. The standard shape of a brilliant diamond is round. All other shapes are called *fancy shapes*. According to the systematically developed cut grading system of the Gemological Institute of America (GIA), the assessment of the overall cut appearance and cut quality of a standard round brilliant diamond includes the aspects of face-up appearance (brightness, fire, and scintillation), design (weight ratio and durability), and craftsmanship (polish and symmetry). The face-up appearance, that is, the appearance when the polished diamond is viewed face-up, is determined by the interplay of *brightness*, *fire*, and *scintillation*. The *brightness* is the extent of internal and external reflections of white light. Nowadays, the term *brightness* is used instead of "brilliance" for the description of reflectivity. The extent of light reflected from the surface of the diamond determines its *luster*. The *luster* of diamond is called *adamantine* and

used as one of the reference types for the luster of minerals and gemstones. The word "adamantine" is derived from the ancient Greek name for diamond "adámas." The higher the refractive index and the better the polish of the gemstone the better is the luster. The *fire* of a diamond is caused by spots of light which are dispersed into the spectral colors. In order to encompass all aspects of *scintillation*, the terms *sparkle* and *pattern* are used. Sparkle describes the flashing spots of reflected white light which are observable when either the diamond, the light source, or the observer are moved. The term *pattern* describes the relative size, arrangement, and contrast of bright and dark areas resulting from internal and external reflections. The weight ratio is the weight of the diamond divided by its diameter. The assessment components "*polish*" and "*symmetry*" should display the effort and care taken for making a beautiful diamond gemstone.

The overall assessment of the quality of both natural and synthetic diamonds is related to the assessment of the 4Cs. The 4Cs are graded according to the worldwide applied scales of the GIA [100].

Nowadays, nearly all synthetic diamonds are grown either by the HPHT method or by the CVD method. The diamond synthesis by means of the HPHT technique is carried out at pressures of 4–6 GPa and temperatures of 1400–1600 °C. The state-of-the-art CVD diamond synthesis allows the growth of thick single-crystalline diamond layers on single-crystal diamond substrates, typically on high-quality HPHT grown plates (type Ib). Freestanding diamond plates are produced by separating the grown layer from the substrates by laser cutting and subsequent polishing. The synthesis takes place at temperatures of 700–1000 °C and pressures below 10 kPa. Main advantages of the diamond CVD synthesis are the high flexibility with respect to size and geometry, high-purity growth conditions leading to a lower density of extended defects and impurities, and last but not least the possibility of controlled doping with impurity elements. It should be noted that high-quality synthetic grown diamonds are comparable in clarity and color to natural diamonds [101, 102]. For enhancing the quality of color and clarity, the synthetic gemstones are postgrowth treated. In addition to an HPHT annealing, low-pressure, high-temperature (LPHT) annealing is applied to improve the physical properties such as color, hardness, and fracture toughness.

The application of diamonds in jewelry is one fascinating field among many others. Diamond is a very promising material for new applications in solid-state physics and material science because of its remarkable physical properties. Diamond is extremely hard and was for a long time the hardest known material (Vickers hardness 10 000 kg mm^2). It was chosen as the reference material for the highest hardness 10 of the Mohs hardness scale. In addition, diamond has a very high thermal conductivity (>1800 W m^{-1} K^{-1}), a very low thermal expansion coefficient (0.8×10^{-6} at 300 K) and is optically transparent over a broadband ranging from the UV to the IR. Diamond is a wide band gap isolator (5.5 eV). For an intrinsic semiconductor, the carrier concentration is too low. Diamond will behave as extrinsic semiconductor when diamond is doped with impurity atoms (B dopant – n-type conductivity, P dopant – p-type conductivity). Owing to the extraordinary mechanical, optical, and thermal properties, synthetic diamond is

a basic material for many industrial applications (e.g., cutting tools, wear resisting coatings, wire saws, lenses, optical windows, heat spreader, and waver). According to the specific application, the fundamentals of quality assurance of diamond are then mechanical, optical, and thermal grading systems. For example, the parameters of thermal conductivity and thermal expansion are decisive for thermal grade CVD diamond. A CVD diamond supplier can offer various grades with respect to the thermal conductivity (e.g., >1200, >1500, >1800 $W\ m^{-1}\ K^{-1}$ [103]).

An eminent important and rapidly growing branch of crystal growth is the unique field of biocrystallization. It is now generally accepted that protein crystallization is not a stochastic event but follows the rules of crystal growth theory where one has to study the different steps from the nucleation stage to the final growth stage as a function of the experimental conditions, particularly of supersaturation. In principle, the crystallization of proteins is mainly based on the same mechanisms as known from the crystallization of small molecules and also from inorganic crystals. However, there are some specific differences. The main one is that protein crystals are composed of a solvent (≈50%). A specified nucleation theory for proteins taking into consideration the main differences between small molecules and proteins was suggested by Nanev [104–106]. In the past years, enormous efforts have been made to improve the methods of crystallizing proteins (for details see, e.g., [96, 107–111]). Essential parameters for optimizing the growth of protein crystals are purity, structural homogeneity, solubility, and stability of the molecular entities. The incorporation of impurities is always a source for the creation of further defects such as dislocations and twins. Systematic studies of the crystallization of various model proteins under microgravity conditions have revealed the following characteristics of those crystals: larger crystal size, less cracks, striations, inclusions, and incorporated impurities [112].

What are the overall criteria for the assessment of crystal quality of protein crystals? The main target of crystal growth of nearly all proteins is to produce a crystalline sample, which enables an X-ray structure analysis with high-resolution structure data. In general, protein crystals are of small size (micrometer-sized) and this is a limiting factor for resolution. Nowadays, an advantage is that the improvements of synchrotron radiation (SR) methods, detectors, and cryocrystallography enable a structure analysis with sufficient resolution of small crystals. Various parameters were used to describe the quality of a protein crystal. But more or less, all parameters are related to the X-ray diffraction analysis (e.g., maximum resolution limit of the diffraction pattern). It is obvious the better the resolution limit the higher the information content about the protein structure. The mosaicity of protein crystals experimentally determined by X-ray rocking curve measurements is also used as a criterion to classify the quality of protein crystals. It should be noted that the parameters for the evaluation of crystal quality in biocrystallography is more or less restricted to the X-ray data. The influence of crystal imperfection on the structural data should also be taken into consideration (for a comprehensive and critical discussion of crystal quality assessment of protein crystals see, e.g., [113]).

4.3
Selected Methods of Crystal Characterization

At the beginning of this chapter, we have explained that an overall crystal characterization means an assessment of the morphology, composition, structure, properties, and last but not least the quality of the fabricated crystal. The multitudinous materials characterization methods compass methods of *imaging*, *diffraction*, *spectroscopy*, *specific thermal*, *electrical*, *magnetic*, and *optical techniques*, and so on which have been described and summarized in subsequent volumes of the "Encyclopedia of Materials Characterization" and books on materials characterization (see, e.g., [114, 115]). Within the scope of this book, we can treat only a few selected characterization methods which play an important role for the characterization of crystals, particularly for the analysis of the defect structure. It should be mentioned that crystal defects in a material can be generated in different manners and stages. First, they can be formed at the various stages of crystal growth (*growth defects*). Second, defects can be generated during the subsequent processing steps of a grown crystal (e.g., slicing, etching, and structuring) during the fabrication of the final application product (e.g., wafer, electronic device, and laser crystal). Then, the defects are called *process-induced defects*. Third, with increasing operation time of an industrially or technologically applied crystal, electronic, or optical device, an aging process may occur. This process is often accompanied with the formation of crystal defects (*aging defects*), which definitely lowers the reliability and lifetime of the crystal or device. Such aging defects often cause a total failure of the crystal or device.

In the following section, we describe three methods which can really be considered powerful workhorses for the characterization and defect analysis of crystals. The requirements of the methods with respect to experiment, theory, and application are quite different.

4.3.1
Etching of Crystals

The method of etching for studying the correlation between growth and morphology of crystals goes back to early investigations of the nineteenth century. Between crystal growth and dissolution and etching of crystals exist a reciprocity relation. Chemical and thermal etching are commonly used for producing *etch pits* on crystal faces. The morphology of etch pits exhibit the face symmetry, that is, the symmetry of one of the 10 two-dimensional point groups (Section 4.1.3.6) and can be applied to determine the point group of a crystal. The possible traps and pitfalls of the method for the determination of the true symmetry of a face are described in the book of Sangwal [116]. For acentric crystals, the different forms of etch pits of parallel but opposite faces can be used to determine the polarity of faces.

Nowadays, the method of wet etching is globally accepted as a cost-efficient, quick, and reliable method for the evaluation of crystal defect types, their distribution, and density in crystals. Despite powerful methods such as laser scattering tomography, X-ray topography (XRT), and TEM, determining the dislocation density by counting the etch pits is still in common use. The method of etching is one step of process control during the manufacture of electronic devices. With the application of new semiconducting systems for the fabrication of new electronic and optical devices, a demand of new preferential chemical etchants is given. For a detailed description of the etching of crystals, the following books and reviews are recommended [117–119].

4.3.2 X-Ray Topography

X-ray diffraction topography shortly denoted as ***XRT*** is a versatile and powerful analytical method for the imaging and characterization of structural and specific growth defects in crystals. XRT is a nondestructive and nonmagnifying method that enables the defect characterization of micrometer-sized crystals up to 300 mm diameter wafers. Various XRT techniques have been applied to numerous classes of materials, such as minerals, metals, semiconductors, polymers, and organic materials including protein crystals. According to the applied X-ray sources, XRT techniques can be divided into *conventional XRT* techniques using X-ray laboratory sources (e.g., X-ray tubes and rotating anodes) and *synchrotron XRT* techniques using an SR source. The advantages of modern SR facilities (e.g., highly collimated beam of high intensity, shorter exposure time, higher lateral resolution) allow the *in situ* characterization of crystal growth processes, the kinetics of crystal defects (e.g., nucleation, propagation, and blocking of dislocations in crystals), phase transitions, etc. An XRT will be obtained if the crystal is oriented to the incident X-ray beam in such a manner that a single set of net planes (*hkl*) satisfies the diffraction condition described by the ***Bragg equation***

$$n \cdot \lambda = 2d \cdot \sin\theta \tag{4.54}$$

where n is the order of diffraction, λ is the X-ray wavelength, d is the interplanar distance, and θ is the Bragg angle or glancing angle. An XRT is the image of the diffracted intensity across the surface of the crystal. XRT can be carried out in *reflection geometry* (*Bragg case*) or in *transmission geometry* (*Laue case*). A topograph obtained in Bragg case provides structural information of the surface region (1–10 μm), whereas a topograph obtained in Laue case provides information about the bulk structure of the crystal.

The XRT of a perfect, unbent crystal of uniform thickness does not produce any contrast. If the diffraction conditions for the X-rays will be changed by thickness variations, misorientations of crystallites, or the strain field of crystal defects, contrast will arise. In general, the obtained contrast mechanisms are divided into *orientation contrast* and *extinction contrast*. Orientation contrast will be obtained

in topographs of twins, GBs, and so on where regions of different orientation are given. Extinction contrast is caused by the strain field of crystal defects and also mainly influenced by absorption processes. The extinction contrast has many similarities with the diffraction contrast in TEM, which will be described in Section 4.3.3. As an example, the application of the invisibility rule for the determination of the Burgers vector of dislocations follows the same scheme in XRT and diffraction contrast imaging in TEM. XRT can be applied for the analysis and imaging of the following defect types:

- point defects and point defect cluster
- dislocations, bunches of dislocations,
- grain boundaries,
- SFs,
- APBs,
- twins
- interfaces
- growth striations, cracks
- macroscopic crystal deformations
- strain fields.

The lateral resolution of XRT using X-ray laboratory sources is in the range of 1–5 and 0.5–2 µm for synchrotron sources. The measurement of the dislocation density is possible only for densities $<10^4\,cm^{-2}$. The following two examples should illustrate the application of XRT for the defect analysis of crystals. Figure 4.59 shows the experimental set up of the Lang topography method (transmission geometry) and a topograph of a 2″ $LiAlO_2$ Czochralski grown (001) wafer. The topograph visualizes that the wafer contains low-angle boundaries, which probably arise from thermal stress during the Czrochalski growth process. The orientation contrast is caused by the misorientation of the different grains forming the GBs.

An example for the extinction contrast is shown in Figure 4.60. The behavior of misfit dislocations in (Si,Ge)/Si layers with respect to nucleation, glide velocity,

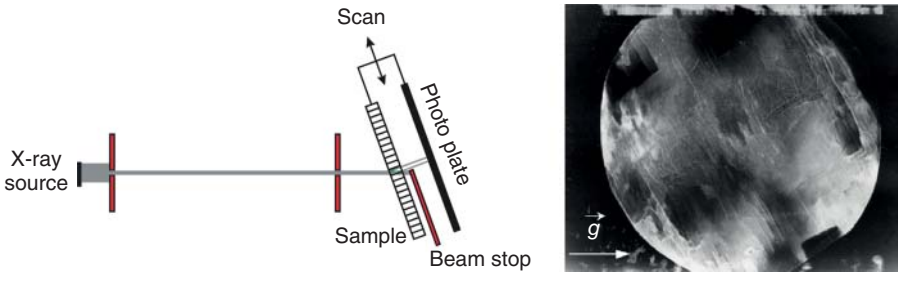

Figure 4.59 Lang topographie (transmission geometry): (a) experimental setup and (b) topograph of a 2″ $LiAlO_2$ (001) wafer, 200 reflection, $MoK_{\alpha 1}$-radiation. (Courtesy of M. Schmidbauer, Leibniz Institute of Crystal Growth, Berlin.)

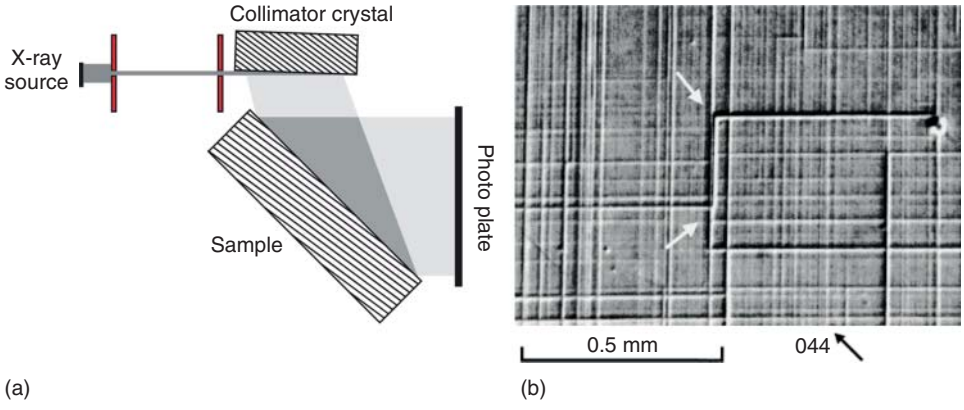

Figure 4.60 Double crystal topography (reflection geometry): (a) experimental setup and (b) topographic evidence of cross slip between different <110> {111} slip systems in (Si,Ge)/Si (044-reflection, $CuK_{\alpha 1}$-radiation). (Reprinted with permission from Köhler, *et al.*, [120].)

and blocking was investigated by means of double crystal topography (reflection geometry, experimental setup Figure 4.60a) using the synchrotron topography beamline ID19 at ESRF (European Synchrotron Radiation Facility) in Genoble, France [120]. The topograph clearly shows the cross slip of the misfit dislocations between different <110> {111} slip systems.

For a comprehensive treatment of fundamentals, theory, and applications of XRT, the reader is referred to the following books and reviews [121–127].

4.3.3
Electron Microscopy

In this section, we give a brief survey of the various methods of electron microscopy for the investigation of structure/property relationships of crystals. Strictly speaking, the interaction process electron/matter as a function of electron energy determines mainly the field of investigation. The applied electron beam energies for the different types of electron-optical methods range from 1 eV to 3 MeV. Microscopes are classified based on specific experimental setups and on whether a *stationary electron beam* or *a scanning electron beam* is used for the image formation. A schematic representation of the various interactions of an electron beam with a crystalline specimen is given in Figure 4.61. First, we will discuss the main scattering events in a TEM. It is common to divide TEM as a function of beam energy (accelerating voltage) in *conventional TEM* (50–200 keV), *medium voltage TEM* (>200–400 keV), and *HVTEM* (500–3000 keV). Depending on the structure to be investigated, for example, crystalline with a periodic ordering of atoms or amorphous with a statistical arrangement of atoms, the incident electron beam is scattered coherently or incoherently by the atomic array. In addition to the undeviated primary beam,

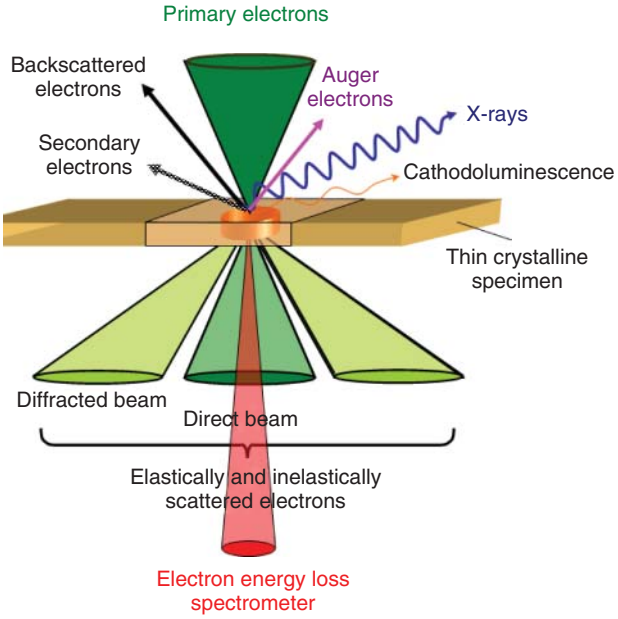

Figure 4.61 Schematic representation of the various interaction processes of an electron beam with a crystalline specimen.

many beams scattered in different directions will leave the exit surface of the crystalline specimen. For a specimen thickness less than the mean free path for *single scattering*, no *multiple scattering* events will occur. The scattering process may be either elastic or inelastic. With inelastic scattering, energy is transferred to the specimen and its electronic state may be changed. The energy transfer may damage the specimen caused by processes such as the ionization of individual atoms. The loss of energy can be measured and is the basis for the determination of the chemical composition by means of electron energy-loss spectroscopy (EELS). An EELS spectrum can be roughly divided into two regions, namely the *low-energy-loss* and *high-energy-loss* ones. Besides the *zero-loss peak* at 0 eV energy loss containing mainly elastically scattered electrons and electrons with extremely low losses (e.g., some 10 meV for phonon excitation), the *low-energy-loss range* (0 – 50 eV) comprises inter/intraband excitations and the excitation of single valence electrons or collective oscillations (plasmons) thereof. The *high-energy-loss range* (50 – typically 2000 eV) results from inner-shell ionizations and is of great importance for the chemical analysis of compounds. When the energy transfer from the incident electron beam to an inner-shell electron is high enough, the atom will be ionized, that is, the inner-shell electron will be excited to a higher energy level or will be entirely ejected from the specimen. The vacancy in the inner shell will be filled by another electron from a higher energy level. The existing energy differences will be counterbalanced by emission of either X-rays or Auger electrons. The created X-rays and Auger

electrons can be used for the spectroscopic microanalysis of the specimen. X-ray analysis can be carried out as wavelength-dispersive X-ray spectroscopy (WDXS) and energy-dispersive X-ray spectroscopy (EDXS). The Auger emission is surface sensitive and mainly used in an SEM, which for this purpose has to be operated under ultrahigh vacuum conditions. Nowadays, in SEM, the energy of the incident beam is in the range of 500 eV to 30 keV. Owing to the lower energy with respect to TEM, the formation of *secondary*, *backscattered*, and *absorbed electrons* is important. Secondary electrons have energies between 0 and 50 eV and may only escape from near-surface specimen regions in depth of approximately 3–10 nm. The energy of BSEs is in the range of 50 eV up to the incident beam energy E_{inc}. In addition to the above-mentioned types of electrons, for specimens with limited thickness, a part of the incident electrons will be transmitted if E_{inc} is high enough. X-rays and Auger electrons will also be emitted as in the energy range for TEM due to the inelastic scattering processes. Another important scattering event of the interaction of the electrons with the solid is the emission of light (CL-cathodoluminescence), which can be applied for the defect analysis particularly of semiconducting materials.

The following enumeration of electron microscopy methods should illustrate the substantial possibilities of electron microscopy for the characterization of solids:

- **Electron microscopy for direct imaging of crystal surfaces**
  - Scanning electron microscopy
  - Emission electron microscopy:
    Special type: UHV (ultrahigh vacuum) photoemission electron microscope with Auger electron spectroscopy (AES)
  - Reflection electron microscopy (REM)
  - Mirror electron microscopy (MEM)
  - Low-energy electron microscopy (LEEM):
    Special type: Spin-polarized low-energy electron microscopy (SPLEEM) for the analysis of magnetic materials.
- **Electron diffraction methods for surface analysis:**
  - Low-energy electron diffraction (LEED, ≈20–200 eV)
  - Reflection high-energy electron diffraction (RHEED, 10–50 keV), *in-situ* characterization of the MBE growth process by means of RHEED.

4.3.3.1 Scanning Electron Microscopy

SEM is definitely the most applied electron microscopy method. It is a non-destructive method where the specimens must be conductive. Nonconductive specimens can be easily coated with a conducting film. A time-consuming and complex specimen preparation is not necessary. Specific SEMs allow the investigations of a sample size of up to 15 cm, which is particularly helpful for semiconductor wafer inspection. In an SEM, an electron beam is focused into a fine probe, which is subsequently used for scanning a selected area of the surface of the specimen. Owing to the interaction process of the electron beam, a number of different types of signals is produced as already described earlier. The signals

Table 4.15 Modes of operation in the SEM and the gained information.

Type of signal	Contrast information	Mode	Spatial resolution
Secondary electrons (SEs)	Specimen topography electric and magnetic fields	Imaging	1 kV 1.2 nm 30 kV 0.4 nm
Backscattered electrons (BSEs)	Compositional crystal orientation (phase analysis)	Imaging	3–4 nm
		Diffraction	EBSD 3–4 nm
Absorbed electrons (AEs)	Topographic compositional	Imaging	1 µm
Transmitted electrons (STE)	Crystallographic defect analysis	Imaging	30 kV 0.34 nm
X-rays	Chemical composition	Spectroscopic	Low atomic number 1–5 µm, High atomic number 0.2–1 µm
Auger electrons	Chemical composition	Spectroscopic	1 µm
Cathodoluminescence	Compositional defect analysis	Spectroscopic	3–4 nm
Electron beam-induced conductivity (EBIC)	Defect analysis	Imaging	3–4 nm

EBSD, electron back-scattering diffraction.

that can be detected and used for imaging, diffraction, and spectroscopy of the specimen are listed in Table 4.15.

This variety of different imaging and spectroscopic modes enables manifold applications of SEM for the characterization of crystals. Particular methods such as EBIC (electron beam-induced conductivity) and CL are valuable tools for the characterization and defect analysis of electronic materials.

4.3.3.2 Transmission Electron Microscopy

TEM and STEM combined with analytical methods of electron microscopy allow a comprehensive analysis of the microstructure and chemical composition of crystals. The information about their structure, chemistry, and materials properties at an atomic level of magnitude can be gained from various TEM/STEM techniques of imaging, diffraction, and spectroscopy. An overview of the main methods of TEM/STEM is illustrated in Figure 4.62. TEM/STEM is a destructive analytical method because electron-transparent specimens have to be prepared from bulk material.

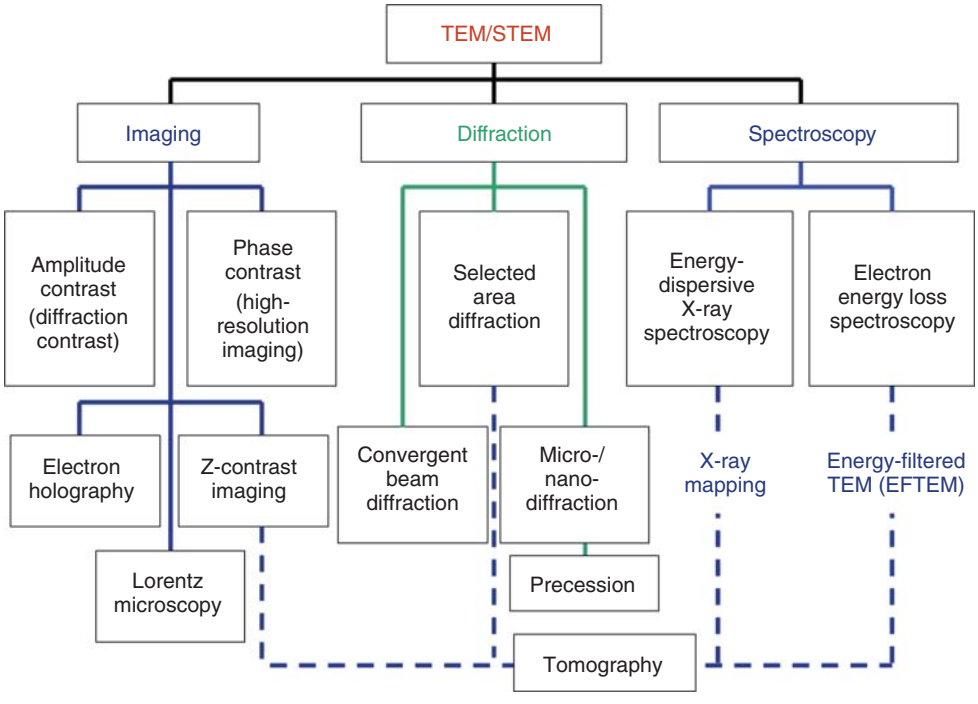

Figure 4.62 Main methods of TEM/STEM.

The main techniques of image formation in a conventional TEM are illustrated in Figure 4.62. For a crystalline object, the incident electrons are scattered coherently in well-defined directions at the atomic arrays and form the diffraction pattern in the back-focal plane of the objective lens. A *bright-field image* in the image plane is formed only if the undiffracted beam is passing through the objective aperture in the back-focal plane. When the image is formed solely by one chosen diffracted beam, a *dark-field image* is obtained. The bright-field image shows the local variations of the intensity of the transmitted beam, and conversely the dark-field image shows the variation of the intensity of the diffracted beam. The bright-field image of a perfect, unbent single-crystalline specimen of uniform thickness does not produce any contrast. But contrast will arise if the diffraction conditions for the electrons will be changed by the following facts:

- thickness variation
- local bending
- presence of crystal defects.

These contrast modes for crystalline materials are denoted as *diffraction contrast* and are widely used for the imaging of crystal defects.

If the image is formed by the interference of many diffracted beams with the undiffracted beam in the image plane in an analogous way as in the light microscope (Abbe theory of image formation), the observed image contrast

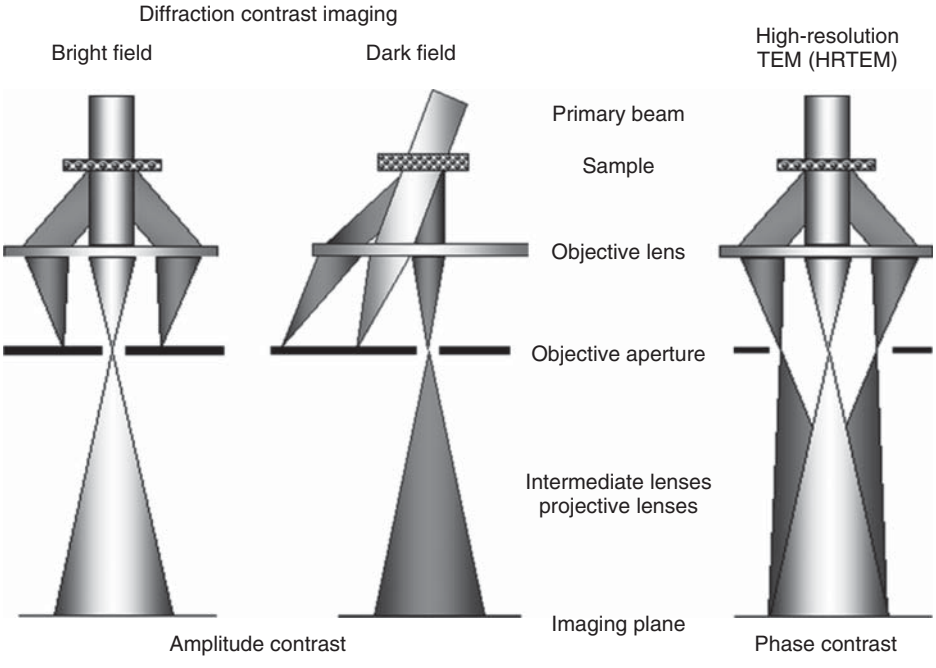

Figure 4.63 Ray paths in a transmission electron microscope.

arises predominantly from phase contrast. An image with atomic resolution may be obtained under suitable experimental conditions with respect to both the electron-optical imaging system and the properties of specimen (Figure 4.63). Figure 4.64 illustrates the different types of image contrast for a single-crystalline thin (In,Ga)As film embedded in GaAs. The system is imaged in crosssection. According to the chosen adjustment of the objective aperture (upper row), the different image contrast types (lower row) arise. In the bright-field diffraction contrast image (lower left), the dark contrast is caused by the strain field between the thin film and the GaAs substrate. The many-beam image (lower middle) shows the projection of the atomic structure of (In,Ga)As film on GaAs in [110] direction. The predominant phase contrast of the image is superimposed by the strain contrast around the layers of thin film. A lattice-fringe image (lower right) is formed if only one or a few diffracted beams interfere with the unscattered beam.

The techniques of diffraction-contrast imaging allow the determination of the nature and crystallography of crystal defects and interfaces. In practice, defect characterization can often be carried out by the application of *contrast rules*, which were derived for the specific types of crystal defects. The contrast rules describe the specific contrast effects for particular imaging conditions. The *invisibility criterion* that we briefly discussed for SFs and APBs (Sections 4.1.3.2 and 4.1.3.3) also plays an important role for the discrimination of dislocations of different character. According to this criterion, a dislocation is invisible when the reciprocal lattice vector $\boldsymbol{g}_{hkl}$, characterizing the imaging reflection *hkl* is

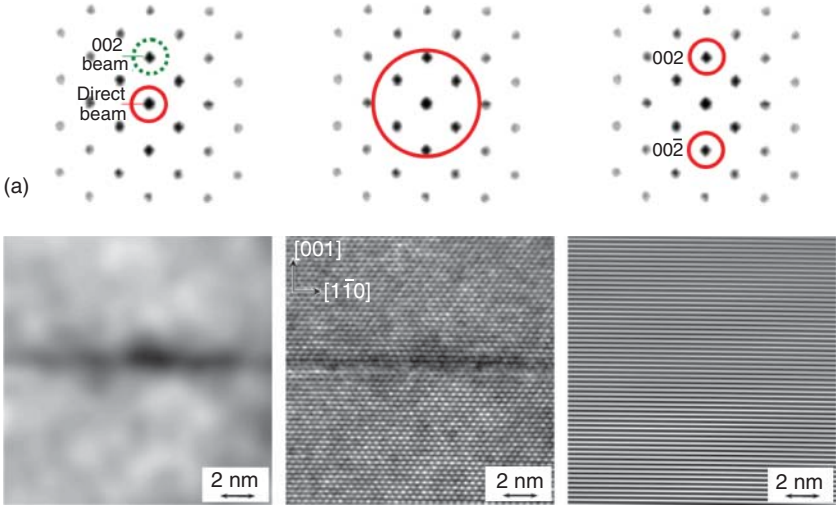

Figure 4.64 Illustration of the imaging process for the system (In,Ga)As on GaAs in cross section (electron beam || [110]) as a function of the size and geometrical position of the objective aperture in [110]. (a) (from left to right): aperture configurations for bright-field-, structure-, and lattice-fringe imaging; and (b) (from left to right): bright-field-, structure-, and lattice-fringe image.

perpendicular to the Burgers vector $\boldsymbol{b}$ of the dislocation.

$$\boldsymbol{g} \cdot \boldsymbol{b} = 0 \quad \text{for} \boldsymbol{g} \perp \boldsymbol{b} \tag{4.55}$$

The dislocation is visible with a maximal contrast ($\boldsymbol{g}\cdot\boldsymbol{b} = \max$) if the Burgers vector $\boldsymbol{b}$ and the reciprocal lattice vector $\boldsymbol{g}$ are parallel to each other ($\boldsymbol{g}||\boldsymbol{b}$). However, this criterion is strictly valid for screw dislocations. For edge and partial dislocations, additional parameters have to be considered (see, e.g., [40]).

The HRTEM allows the imaging of the atomic structure of crystals and crystal defects. Particularly the availability of aberration-corrected TEMs and STEMs enable the detection of the atomic structure of crystal defects such as the core structure of singular dislocations or dislocations in GBs. Very often, the complexity of the scattering and imaging process requires image simulations for the interpretation of HRTEM images. In addition, various methods of qHRTEM can be applied to determine the local strain and chemical composition on atomic scale.

The methods of electron diffraction using a parallel or a convergent beam provide information about the structure of crystals. The classical parallel-beam electron diffraction technique, that is, SAED, is commonly used to measure the degree of crystallinity of the materials as well as the basic parameters of crystal structure (e.g., lattice parameter, type of Bravais lattice) and specimen orientation. Owing to the strong interaction between the electron beam and the crystal potential, the intensities of the diffraction spots in a conventional electron diffraction pattern obtained along a major zone axis are dynamically excited. Therefore, standard

structure analysis methods as used in X-ray diffraction can be applied only when kinematical diffraction conditions are given (e.g., very thin crystals, crystal structures with at least one short axis). An extension for crystal structure analysis starting from electron diffraction intensities as input data is given by means of the precession electron diffraction technique, where the electron beam is rocking over the specimen generating a hollow cone illumination. The convergent-beam electron diffraction (CBED) provides information on the three-dimensional crystal structure and allows the determination of the point and space group of crystals. CBED can also be applied to measure very precisely the lattice parameters as well as the strain state of crystals. Furthermore, CBED can be applied to determine the enantiomorphism and polarity of crystals. In order to study structural features and peculiarities of nanomaterials, the electron nanodiffraction method using both a nanoscale convergent or parallel-beam mode can be used.

The main goal of analytical TEM [EDXS, EELS, energy-filtered transmission electron microscopy (EFTEM)] and STEM (Z-contrast imaging) is the quantitative determination of chemical composition. Dedicated nanoanalytical techniques can be applied to determine the element distribution along a line (X-ray line profile and series of EEL spectra) or in two dimensions (X-ray mapping, EFTEM). Additionally, EELS provides direct information on the local electronic structure of a material. The local chemical bonding can be determined by analyzing the electron-loss near-edge fine structure (ELNES) and comparison with theoretical models. Chemical information on atomic scale can also be obtained using the STEM Z-contrast imaging technique, where a high-angle annular dark-field (HAADF) detector is used for chemical imaging.

Lorentz microscopy and electron holography are very useful techniques for the evaluation of the structure of ferroelectric and magnetic materials as illustrated in Section 4.1.3.5. TEM images represent two-dimensional projections of a three-dimensional structure. In order to get a thorough understanding of the investigated three-dimensional object, very often the exact knowledge of structure and composition in three dimensions is necessary. Various methods of electron tomography in materials science (HAADF-STEM, HRTEM, EDXS, EELS, EFTEM, electron holography) were developed to retrieve the desired information in 3D from a set of 2D-projections. For a more detailed insight into the methods of electron microscopy, the following books are recommended [128–130].

In the following section, we illustrate the combined use of modern electron microscopical TEM/STEM methods for the characterization of grown crystals.

4.4 Materials Engineering by Correlation of Crystal Growth and Characterization

Anna Mogilatenko

The investigation of structure/property relationships of materials is one of the fundamental tasks of material science. The knowledge of the structure–property correlations is the basis for the development of new materials or materials with

improved properties. The process of crystal growth is the starting point for the development of new materials. The data of a comprehensive characterization of crystal quality with respect to structural perfection and physical properties are indispensable for optimizing the growth process. The interplay between crystal growth and characterization as an iterative process is an important step in the manufacture of new materials.

4.4.1
Epitaxial Growth of GaN on $LiAlO_2$ Substrates

In this section, we outline the relationships between structural analysis of crystal defects by TEM and the importance of defect control in crystalline materials using the case study of $LiAlO_2$ substrates for epitaxy of III-nitride films.

III-nitride-based materials (i.e., GaN, AlN, InN, and their ternaries) are currently one of the most important families of semiconducting materials for light emitting diodes (LEDs) and laser diodes (LDs) operating at wavelengths ranging from deep ultraviolet to the infrared region. Furthermore, these materials are considered for high-frequency and high-power transistors. Good stability of GaN-based materials under high voltages, high temperatures, and cosmic radiation makes them attractive for space applications.

Group III-nitrides occur in the following structure types:

- hexagonal wurtzite
- cubic zincblende
- cubic rocksalt.

As already described in Section 1.5, the stacking sequence of basal plane in the wurtzite structure (i.e., along the [00.1] zone axis) corresponds to … AαBβAαBβAαBβ … where each letter pair Aα, Bβ represents the two layers forming a metal-nitrogen atom pair. In contrast, the stacking sequence along the [111] zone axis in the zincblende structure corresponds to … AαBβCγAαBβCγAαBβCγ … ·.

In the past decade, many attempts have been made to grow bulk GaN single crystals with wurtzite structure [131, 132]. However, their growth is still limited to centimeter-sized crystals (Figure 4.65). The growth of large GaN single crystals with low-defect density is a difficult task since this material cannot be grown from the stoichiometric solution by the standard Czochralski or Bridgman growth methods. This restriction arises because of the extreme GaN melting condition, that is, the pressure of 6 GPa and temperature of 2220 °C [133]. As there are no commercially available cheap large-scale GaN substrates for the homoepitaxy, fabrication of GaN-based optoelectronic and electronic devices requires deposition of thin III-nitride layers on *foreign* substrates. Owing to the high lattice mismatch (Table 4.16) between the III-nitrides and commonly used commercial substrates (α-Al_2O_3, SiC, Si), this heteroepitaxial growth results in a large number of defects in the nitride layers (threading dislocations (TDs), inversion domains, SFs, etc.), which drastically affects the device performance.

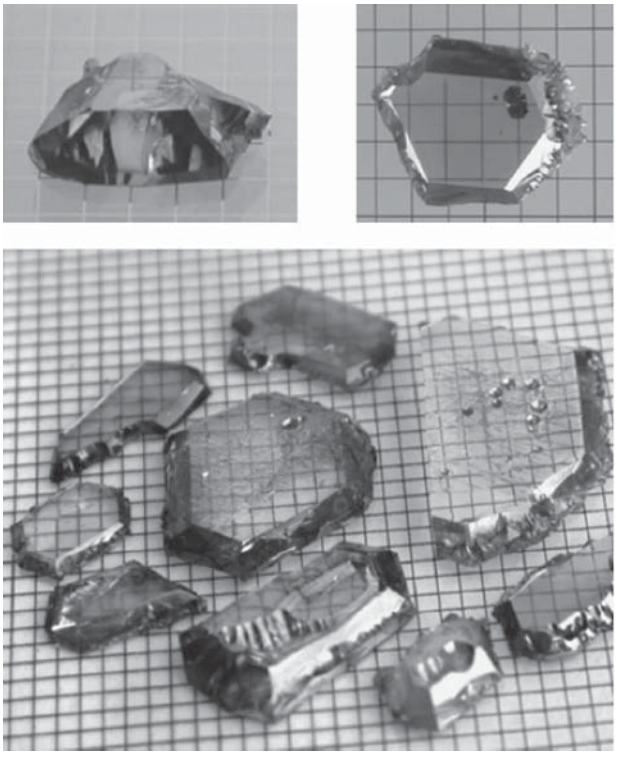

Figure 4.65 GaN single crystals grown by hydride vapor-phase epitaxy on GaN seeds grown by high-pressure solution method. (Reprinted from Grzegory *et al.*, [132] with permission from Elsevier.)

Recently, it has been proposed to grow GaN on a new γ-$LiAlO_2$ substrate [134, 135]. There exist various $LiAlO_2$ modifications, the trigonal α-phase, the monoclinic β-phase, and the tetragonal γ-$LiAlO_2$. In particular, the (100) oriented tetragonal γ-$LiAlO_2$ single crystals with one space group of the enantiomorphic pair $P4_12_12-P4_32_12$ were suggested as possible substrate for the GaN epitaxy (Figure 4.66). Compared to conventional α-Al_2O_3 (sapphire) substrates commonly used for GaN epitaxy, the distinct advantages of γ-$LiAlO_2$ are the possibility to grow GaN in two different orientations [136, 137] (so-called c- and m-plane layers, see Figure 4.66) as well as the self-separation of thick GaN films from the γ-$LiAlO_2$ substrates [138]. Furthermore, the GaN/$LiAlO_2$ system shows a significantly smaller lattice mismatch compared to the above-mentioned commercial substrates (Table 4.16). The crystal quality of substrate material is extremely important because it directly influences the crystal quality of the deposited films which are used for device fabrication. That is why understanding and control of the crystal quality is one of the key issues in materials research.

It has been shown that single-crystalline γ-$LiAlO_2$, 2 in. in diameter, can be grown from melt using the Czochralski method [139]. In the case of γ-$LiAlO_2$

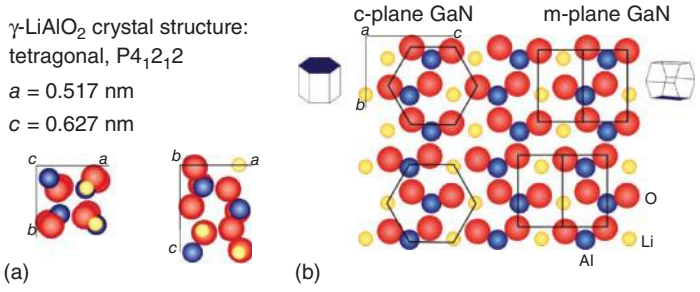

Figure 4.66 (a) Schematic representation of γ-$LiAlO_2$ crystal structure. (b) Sketch of the atom arrangement in (100)-oriented γ-$LiAlO_2$ single crystal superimposed with a schematic presentation of GaN unit cells for so-called c-plane and m-plane orientations.

Table 4.16 Lattice mismatch between GaN and different substrate materials.

Substrate	Crystal structure	GaN orientation	Mismatch
(0001) α-Al_2O_3	Corundum, $R\bar{3}c$	c-Plane	14%
(0001) SiC	Wurtzite, $P6_3mc$	c-Plane	3.4%
(111) Si	Diamond, $Fd\bar{3}m$	c-Plane	17%
(100) γ-$LiAlO_2$	$P4_12_12$	c-Plane	1.4% in *c*-axis and 6.3% in *b*-axis
		m-Plane	1.4% in *c*-axis and 0.1% in *b*-axis

growth, this fabrication process is difficult due to a loss of the volatile Li_2O from the melt as well as from the surface of the growing $LiAlO_2$ single crystal. This unfavorable process results in the formation of voids and inclusions in the single-crystalline $LiAlO_2$ boule. Figure 4.67 shows a photograph of a polished $LiAlO_2$ single-crystal boule. Although pure $LiAlO_2$ single crystal appears transparent and colorless, the core region containing voids and inclusions shows a milky color due to the stronger light-scattering behavior in this region. Using TEM analysis, it was possible to reveal the defect structure in $LiAlO_2$ single crystals and to understand

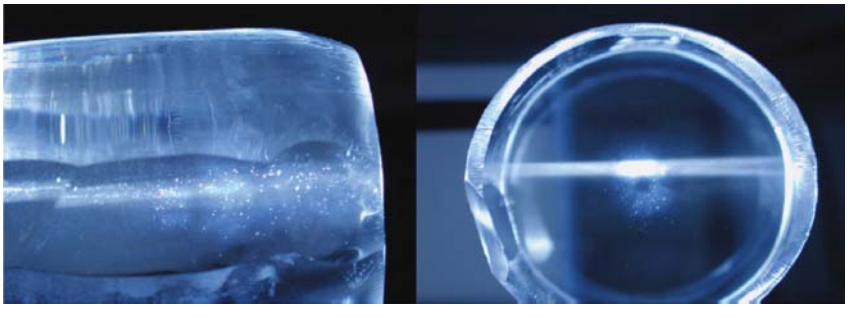

Figure 4.67 Polished γ-$LiAlO_2$ single crystal of 2 in. in diameter in diffuse reflection light [139]. The single-crystal boule contains a core of a milky color due to a high concentration of voids and inclusions. (Reprinted from Veličkov, *et al.*, [139] with permission from Elsevier.)

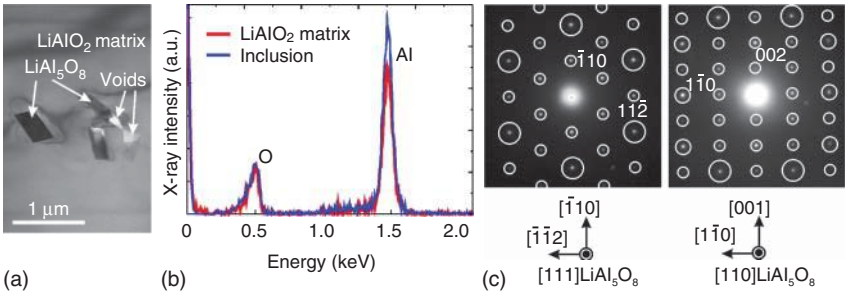

Figure 4.68 (a) Bright-field TEM diffraction contrast image of $LiAl_5O_8$ inclusions and voids in $LiAlO_2$ matrix. (b) EDX spectrum obtained from the inclusions and $LiAlO_2$ matrix. (c) Two exemplary diffraction patterns obtained from different inclusions. The experimental diffraction patterns are overlaid with simulations carried out for the $LiAl_5O_8$ phase.

the formation mechanism of the present inclusions. In particular, three types of 3D-defects were observed in the $LiAlO_2$ single crystals: $LiAl_5O_8$ inclusions, Al_2O_3 precipitates, and voids due to a loss of gaseous Li_2O. A bright-field diffraction contrast TEM image of a $LiAlO_2$ single crystal is shown in Figure 4.68a. As we can see, the single-crystalline $LiAlO_2$ matrix contains a number of crystallites of impurity phase, which are attached to voids. EDXS analysis has proved that the crystallites contain aluminum and oxygen (Figure 4.68b). Unfortunately, lithium detection by EDXS is not possible. Using electron diffraction analysis, the crystallites were assigned to the $LiAl_5O_8$ phase (Figure 4.68c), which can be formed according to the following reaction: $5LiAlO_2 \rightarrow LiAl_5O_8 + 2Li_2O\uparrow$.

The $LiAl_5O_8$ crystallites exhibit an idiomorphic shape. Furthermore, there is no common orientation of crystallites with respect to the surrounding $LiAlO_2$ matrix. From the observations, one can conclude that the $LiAl_5O_8$ crystallites are originally formed in the melt surrounding the growing $LiAlO_2$ single crystal. The $LiAl_5O_8$ formation in the liquid medium allows the development of crystal facets visible in the TEM image. Consequently, the observed $LiAl_5O_8$ crystallites of the idiomorphic shape are ***inclusions***, which were trapped during the growth of the $LiAlO_2$ single crystal at the interface between the laterally growing crystal and the melt.

The presence of the $LiAl_5O_8$ inclusions has a drastic influence on the $LiAlO_2$ crystal quality. In particular, it has been shown that it can lead to the formation of twins in the $LiAlO_2$ matrix (Figure 4.69). The twins are initially formed in the inclusion-rich core region of the $LiAlO_2$ single crystal (Figure 4.69b) and then propagate to the boule edge during the subsequent single-crystal growth. Simultaneously to the Li_2O loss from the melt, a certain Li_2O loss appears directly from the growing $LiAlO_2$ single crystal, which leads to the formation of ***precipitates*** in the single-crystalline matrix. These precipitates can be recognized by the typical "butterfly"-like strain contrast appearing in the diffraction contrast images around coherent or partially coherent precipitates (Figure 4.70a).

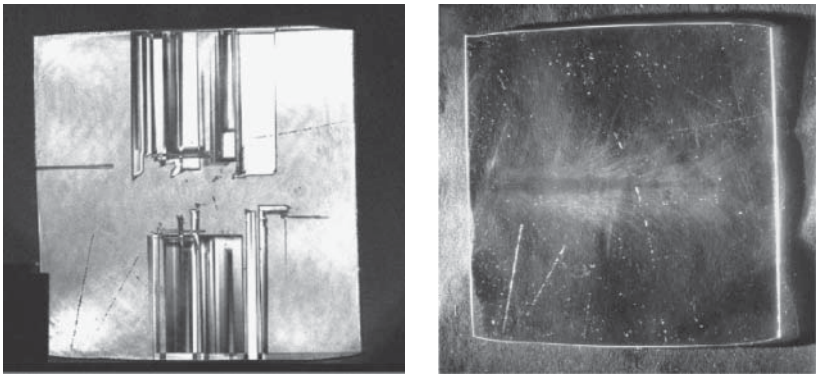

Figure 4.69 (a,b) Optical micrographs of a longitudinal section of a (100) γ-$LiAlO_2$ crystal parallel to the (010) plane between crossed polars (a) and in diffuse reflection light (b). (Reprinted from Veličkov, *et al.*, [139] with permission from Elsevier.)

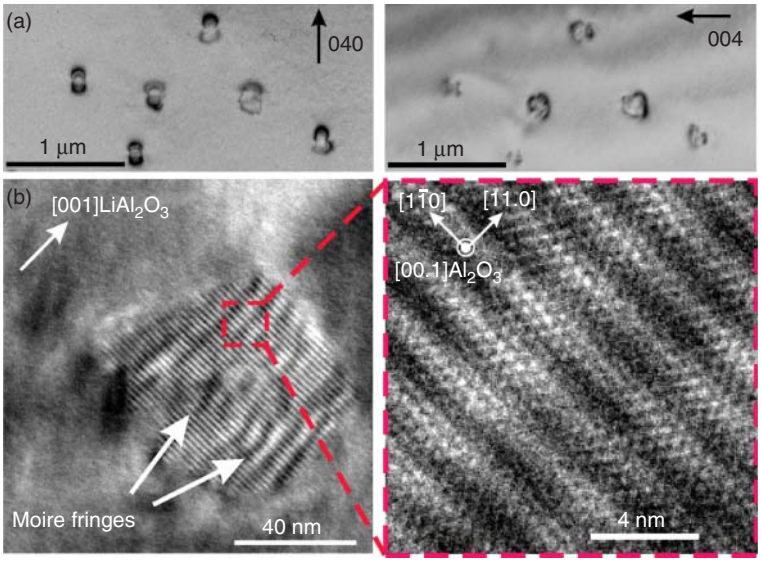

Figure 4.70 (a) Bright-field diffraction contrast and (b) HRTEM images of Al_2O_3 precipitates in $LiAlO_2$ matrix.

HRTEM micrograph in Figure 4.70b shows a magnified image of one of the crystallites. Alternating dark-and-bright fringes observed within the crystallite are the so-called Moire fringes, which appear when two crystals with different lattice plane distances overlap, that is, the matrix crystal $LiAlO_2$ and the unknown precipitate crystal. The distance between the Moire fringes is determined by the lattice plane distances of the host matrix ($LiAlO_2$) and the precipitate itself. Thus, the unknown precipitate phase can be identified based on the experimentally

measured distances between the Moire fringes and the known $LiAlO_2$ lattice plane distances. According to this analysis, the determined lattice plane distances of the precipitates can be assigned to Al_2O_3. This phase can be formed as a result of a complete loss of Li from $LiAlO_2$, that is, $2LiAlO_2 \rightarrow Al_2O_3 + Li_2O\uparrow$. In contrast to the large $LiAl_5O_8$ inclusions, these Al_2O_3 crystallites are much smaller (from 20 to 40 nm in size), do not exhibit a clear faceting, and show a common epitaxial orientation with respect to the substrate $LiAlO_2$ matrix. These observations prove that the Al_2O_3 crystallites are not inclusions, but precipitates, which appear directly in the growing $LiAlO_2$ single crystal and not in the melt around.

As mentioned earlier, the $LiAlO_2$ single crystals contain one more type of 3D defects – ***voids*** (Figure 4.68a). Calculation of the volumetric changes appearing during the Li_2O loss (due to the following reaction $5LiAlO_2 \rightarrow LiAl_5O_8 + 2Li_2O\uparrow$) shows that the $LiAl_5O_8$ volume is about 1.7 times smaller than the volume of the consumed $LiAlO_2$. This explains the presence of core of voids, which is often observed in the $LiAlO_2$ single crystals.

Understanding the origin of defect formation in $LiAlO_2$, single crystals allowed to adjust a special vertical temperature gradient during the Czochralski growth of $LiAlO_2$, so that the Li_2O loss from the melt as well as from the $LiAlO_2$ surface was suppressed and single crystals of high quality were achieved [139]. Nevertheless, a proper adjustment of the steep temperature gradient required for the suppression of the Li_2O evaporation is a challenging process, since it can lead to local thermal stresses in the $LiAlO_2$ single crystals, which favor the formation of misoriented grains. Using XRT it is possible to visualize the misoriented subgrains within a single crystal. This method is based on X-ray diffraction in the crystal lattice. Around the defects, such as dislocation lines within a GB, the crystal lattice is distorted and the diffraction (Bragg) condition is changed, so that the diffracted intensity changes locally and the defect lines become visible. Figure 4.71a shows an X-ray topogram proving that the bulk γ-$LiAlO_2$ single crystal consists of slightly misoriented subgrains. The bright-field TEM image on the right shows an example of a small-angle GB containing periodically arranged dislocation lines. As visible, these GBs act as preferable sites for accumulation of inclusions.

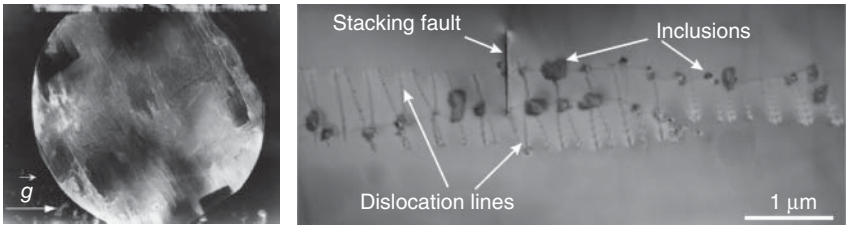

Figure 4.71 (a) X-ray topogram of a (100) $LiAlO_2$ wafer cut from a $LiAlO_2$ single crystal. (Reprinted from Veličkov, *et al.*, [139] with permission from Elsevier.) (b) Bright-field image of a small-angle grain boundary consisting of a network of periodically arranged dislocations decorated by small inclusions.

After development of optimized growth conditions for the growth of high-quality $LiAlO_2$ single crystals, the γ-$LiAlO_2$ boules with the optimized structure were sliced and polished resulting in (100) $LiAlO_2$ wafers of 400 μm in thickness. These wafers were used as substrates for the subsequent growth of GaN layers [137, 138]. As mentioned earlier, depending on the deposition conditions, GaN growth with two different epitaxial orientations is possible on the $LiAlO_2$ substrates (Figure 4.66), known as *polar c-plane orientation* and *nonpolar m-plane orientation*. We will next describe the defect structure of c-plane III-nitride layers on $LiAlO_2$ and conventional sapphire substrates, followed by defect analysis in nonpolar m-plane layers.

α-Al_2O_3 (corundum, also denoted as the gemstone variety of Al_2O_3 as *sapphire*) is one of the substrates generally used for group-III nitride epitaxy. Unfortunately, GaN growth on sapphire results in a high number of so-called TDs, which can be generated during coalescence of slightly misoriented GaN islands or can stem from a defect-rich nucleation layer, which is usually grown at lower temperatures before high-temperature III-nitride deposition [140]. These defects can strongly affect the performance of III-nitride-based devices [141] (i.e., they cause a decrease in efficiency of UV LEDs, an increase in vertical leakage current in electronic and optoelectronic devices, etc.). That is why since the past decade, a large number of research activities have been concentrated on developing special growth procedures resulting in a reduction of threading dislocation densities (TDDs) in III-nitride layers.

Using diffraction contrast TEM analysis, it is possible to reveal dislocations in materials. Figure 4.72 shows cross-sectional dark-field micrographs of a c-plane GaN layer grown on sapphire by metalorganic vapor-phase epitaxy (MOVPE). The micrographs were acquired at two-beam conditions using $11\bar{2}0$ and 0002 diffraction reflections (respectively, Figure 4.71a,b). These images were obtained from the same specimen area. In the micrographs, TDs appear as bright lines in GaN matrix. They originate from the GaN/sapphire interface and propagate along the [0001]GaN direction through the whole GaN layer up to the layer surface.

Three types of perfect dislocations with the dislocation lines arranged along $\boldsymbol{L} = <0001>$ (so-called prismatic dislocations) are known in the wurtzite structure: dislocations of edge type with the Burgers vector $\boldsymbol{b} = 1/3 < 11\bar{2}0 >$ (a-type),

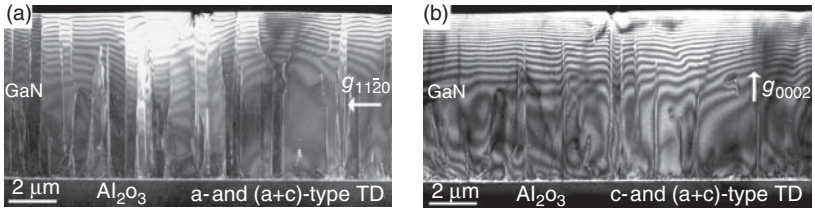

Figure 4.72 Cross-sectional dark-field images of a GaN layer on a sapphire substrate. The images were obtained under two-beam diffraction conditions using (a) $g = 11\bar{2}0$ and (b) $g = 0002$. The images show (a) edge and (b) screw dislocations. Dislocations with a mixed character are visible in both images.

dislocations of screw type with $\boldsymbol{b} = <0001>$ (c-type), and dislocations of mixed type with $\boldsymbol{b} = 1/3 < 11\bar{2}3 >$ ((a + c)-type). Using the invisibility criterion [40], it is possible to distinguish between the different types of dislocations and calculate their density. Although TDs of c-type are visible in the 0002 reflection (Figure 4.72b), TDs of a-type are in contrast for the $11\bar{2}0$ reflection (Figure 4.71a). Dislocations of the mixed character appear in both images. According to this analysis, the total TDD of about $2 \cdot 10^9$ cm^{-2} was calculated in the shown GaN layer on sapphire.

Compared to other semiconducting materials III-nitride-based optoelectronic devices seem to be more tolerant to the high TDDs. For example, for GaAs-based optoelectronic devices TDD as high as 10^5 cm^{-2} can completely damp light emission. In contrast, blue GaN-based LEDs were demonstrated even for a TDD in the range of 10^{10} cm^{-2} [142]. To understand this relatively low electronic activity of TDs in III-nitrides a precise knowledge of atomic structure of TDs is necessary. Thus, many theoretical and experimental studies have been carried out to determine atomic core structures of TDs in GaN [143].

(100)-oriented γ-$LiAlO_2$ shows a lower lattice mismatch to GaN (Table 4.16) as GaN on c-plane sapphire, which was assumed to be favorable for fabrication of GaN layers with a better crystal quality. Growth of thick c-plane GaN layers on γ-$LiAlO_2$ substrates has been demonstrated by hydride vapor-phase epitaxy (HVPE) [144]. This deposition method allows for high growth rates (up to 100 μm h^{-1}) and is often used for fabrication of thick III-nitride layers (from tens to hundreds of micrometers). HVPE growth of GaN requires high growth temperatures in the range of 1000 – 1100 °C. However, it has been shown that γ-$LiAlO_2$ is unstable above 900 °C [138]. Thus, the GaN deposition onto $LiAlO_2$ leads to the gradual substrate decomposition underneath the GaN layer and to the $LiAlO_2$ self-separation from thick GaN layers. This is advantageous compared to planar GaN growth on sapphire substrates, where a tight bonding at the interface often leads to wafer breakage as well as nondefined cleavage of GaN above the interface. The substrate self-separation observed for GaN growth on $LiAlO_2$ can allow the preparation of thick freestanding GaN layers, which could be used as substrates for subsequent GaN homoepitaxy. Consequently, it was proposed that the growth of thick GaN layers on large γ-$LiAlO_2$ substrates might solve the problem of a lack of large-scale GaN single crystals (Figure 4.65). Nevertheless, structural studies have shown that the favorable γ-$LiAlO_2$ decomposition at high temperatures can simultaneously lead to such a disadvantage as contamination of GaN layers by oxygen and lithium. The impurity incorporation favored formation of a number of crystal defects in the layers, as will be shown later.

It was found that during the HVPE growth of GaN on $LiAlO_2$ the substrate decomposition starts even at the early growth stages [71, 138]. This process follows the reaction mentioned above, that is, $5LiAlO_2 \rightarrow LiAl_5O_8 + 2Li_2O\uparrow$. HRTEM analysis (Figure 4.73) proved the presence of the cubic $LiAl_5O_8$ precipitates, which were formed at the GaN/$LiAlO_2$ interface during the GaN layer growth. Notice, that in contrast to the $LiAl_5O_8$ formation in the melt, which played a crucial role during the growth of single-crystalline $LiAlO_2$ boules by

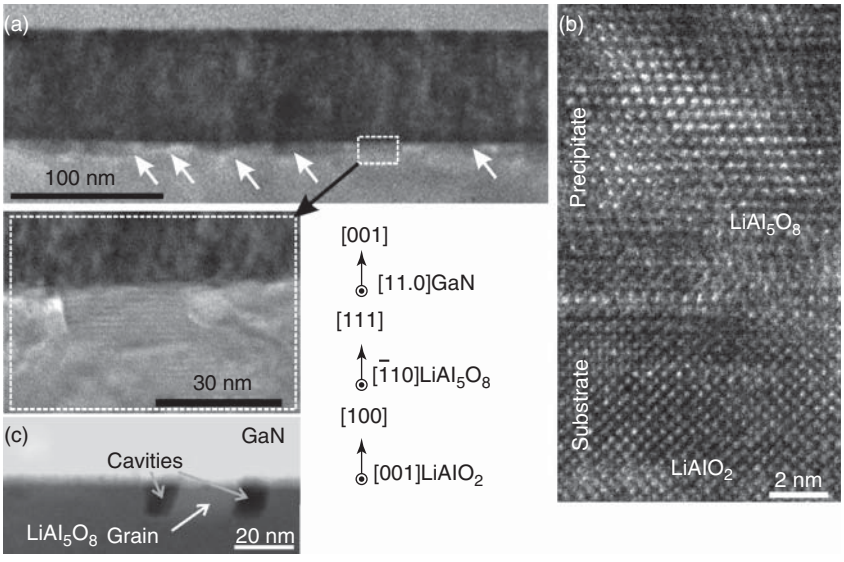

Figure 4.73 (a) Cross-sectional micrograph of an 80 nm thick GaN layer grown on $LiAlO_2$ substrate. Inset shows the presence of interfacial precipitates due to the starting substrate decomposition and the corresponding orientation elation of the GaN layer, the $LiAlO_2$ substrate, and the $LiAl_5O_8$ precipitate. (b) HRTEM micrograph of the interfacial $LiAl_5O_8$ precipitate. (c) Z-contrast image showing the presence of cavities around the $LiAl_5O_8$ precipitates. (Reprinted with permission from Neumann, *et al.*, [71].)

the Czochralski method, these $LiAl_5O_8$ grains are formed in the crystalline $LiAlO_2$ matrix and show a common epitaxial relation to the surrounding matrix (Figure 4.73b). As the $LiAl_5O_8$ volume is smaller compared to the consumed $LiAlO_2$ matrix, the $LiAl_5O_8$ precipitates are surrounded by cavities (Figure 4.73c). Consequently, during the GaN layer growth, the $LiAlO_2$ decomposition leads to the formation of porous GaN/$LiAlO_2$ interface. Owing to a difference in the thermal expansion coefficients of GaN and $LiAlO_2$ as well as the presence of the cavities at the GaN/$LiAlO_2$ interface, the substrate self-separation occurs from thick (hundreds of micrometers) GaN layers during the cooling down procedure. This enables the formation of freestanding GaN substrates [144, 145].

Figure 4.74 shows plan-view and cross-sectional images of a freestanding 230 μm thick GaN layer grown by HVPE on a γ-$LiAlO_2$ substrate. The GaN layer contains macroscopic 3D pinholes (so-called v-pits) of a dodecagonal shape. Their density increases rapidly from the center to the edge of the GaN layer (see dark spots in the colorless GaN wafer in Figure 4.74a). As visible in the cross-sectional view (Figure 4.74c), the 12-sided v-pits are surrounded by pyramids, which originate at the former interface to the $LiAlO_2$ substrate and intersect the whole GaN layer thickness. Although the GaN regions around the pyramids are transparent and colorless, the pyramid material is brown in color. The brown color may indicate a nitrogen-deficiency around the v-pit defects or a presence of impurities, such as oxygen [146]. Indeed, oxygen incorporation

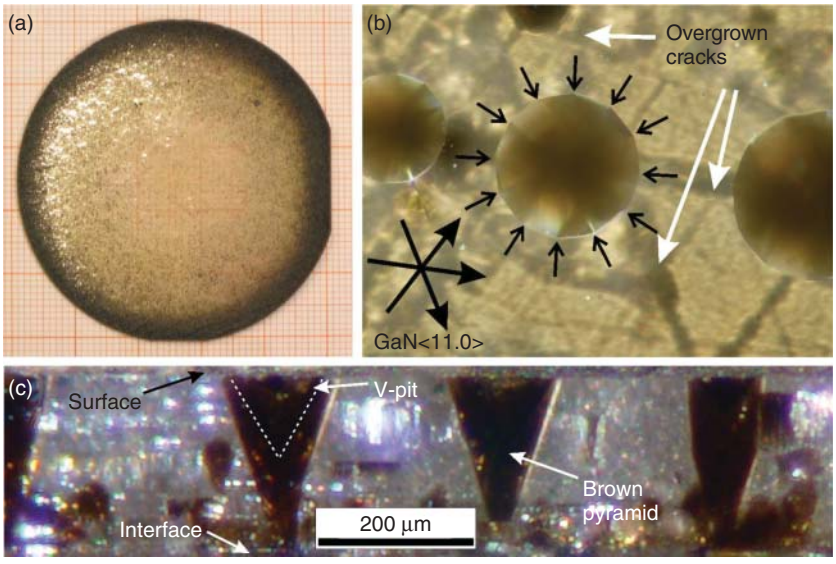

Figure 4.74 (a) Freestanding 2 in. (Reprinted from Richter, E. *et al.*, [145].) (b) Plan-view and (c) cross-sectional photographs of freestanding GaN initially grown on γ-$LiAlO_2$ substrate.

into the growing GaN layers is possible due to the $LiAlO_2$ decomposition at high temperatures [138], which results in a release of Li_2O, which can in turn decompose into Li and O_2.

Obviously, the $LiAlO_2$ decomposition during the GaN growth plays a crucial role in the defect formation of the GaN layers. This conclusion is supported by the fact that the v-pit defects are formed above the cracks in GaN (Figure 4.74b). These cracks appear at early growth stages in thinner GaN layers along the $< 11\bar{2}0 >$ GaN directions and are subsequently overgrown during further growth. However, predominant oxygen incorporation from the substrate into the GaN layer can appear at crack positions which can lead to the formation of the v-pit defects as well as the brown pyramids around them.

Three-dimensional v-pit defects have often been observed in nitride materials [147]. Their formation is strongly correlated to the presence of such defects as TDs and inversion domains in the III-nitride layers. Figure 4.75 shows a cross-sectional image of a c-plane GaN layer on $LiAlO_2$. The first GaN nucleation layer consists of a strongly disturbed columnar structure.

It contains an extremely high defect density, whereas the GaN layer grown above shows a lower defect density. However, this layer contains an inversion domain that is attached to a v-pit defect.

Inversion domains have been frequently observed in group-III nitrides grown on different substrates. The wurtzite crystal structure is noncentrosymmetric. Thus, the positive and the negative c-axis directions, that is, [0001] and $[000\bar{1}]$, are not crystallographically equivalent, and the III-nitride layers grown along [0001] and $[000\bar{1}]$ directions show different physical properties [148]. Conventionally,

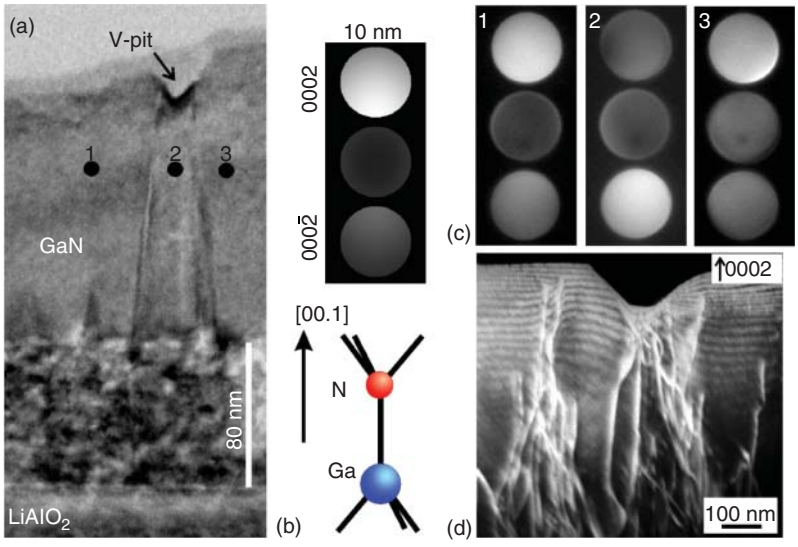

Figure 4.75 (a) Cross-sectional TEM image of a c-plane GaN layer on $LiAlO_2$ substrate. The GaN layer grown on top of the nucleation layer contains an inversion domain, which is attached to a v-pit defect. (b) CBED simulation carried out for Ga-polar GaN viewed in the $[1\bar{1}.0]$ zone axis for a specimen thickness of 10 nm. (c) Experimental CBED images observed at the layer positions 1, 2, and 3 in (a) show a 180° rotation of diffraction pattern in the region of the inversion domain. (d) Cross-sectional dark-field image showing a correlation between threading dislocations in GaN and the v-pit defects. (Reprinted from Mogilatenko, *et al.* [144].)

the positive c-axis direction points from Ga to N atom (Figure 4.76a). As the c-axis is a polar axis, the GaN layers growing in the [0001] growth direction are considered to have Ga-polarity, whereas those grown in the $[000\bar{1}]$ growth direction have N-polarity. GaN layers do not always show a uniform polarity. There are cases when the layer polarity changes locally on the scale of a few nanometers. These regions of different polarity are called inversion domains. Different physical properties of N-polar and Ga-polar material (e.g., different growth and etching rates, impurity incorporation rates) can drastically affect the layer structure [144]. Furthermore, inversion domain boundaries (IDBs) were shown to be strong radiative recombination centers with luminescence intensity of about an order of magnitude higher than that of bulk GaN [148].

Using first-principles calculations of domain wall energies, Northrup *et al.* proposed a structural model of an IDB [149] (Figure 4.76a). Later on, this model has been experimentally confirmed using HAADF (often called *Z-contrast*) imaging [150] (Figure 4.76b).

The presence of inversion domains can be proved by CBED. The CBED images show a 180°-rotation of diffraction pattern in the region of the inversion domain (Figure 4.75c). This proves the rotation of the GaN crystal structure by 180 °C. According to the simulation of the diffracted intensities (Figure 4.75b), the GaN

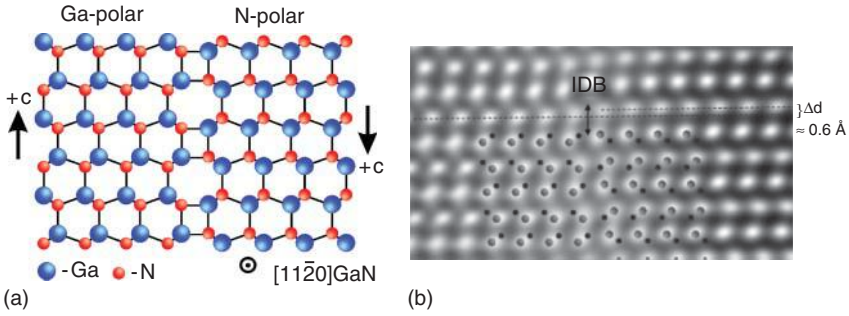

Figure 4.76 (a) Atom arrangement in IDB viewed along the [11.0] zone axis according to [149]. Atom arrangement in GaN structure on the left side from IDB corresponds to Ga-polarity. GaN structure on the right side from IDB is rotated by 180°, which corresponds to N-polarity. (b) HAADF-STEM image of IDB in GaN (b). (Reprinted with permission of Liu, *et al.* [150].)

layer grown by HVPE on the $LiAlO_2$ substrates exhibits Ga-polarity, but contains a number of inversion domains with an N-polarity. The growth rate of Ga-polar material is almost three times higher than that of N-polar GaN [151], which explains the appearance of the v-pit defects. Furthermore, compared to Ga-polar GaN layers, impurity incorporation may be enhanced in N-polar material as well as on nonpolar surfaces of the already formed v-pit defects. This can lead to the preferential incorporation of oxygen impurities in these regions resulting in the formation of brown pyramids around the v-pit defects [144] (Figure 4.74c).

The second source of the v-pit formation in GaN can be the presence of TDs, which can open up within the layer producing open-core defects or nanotubes [151]. At high concentration of point defects in the layers, such as O, Si, Mg, in impurities, the impurity atoms can segregate to the dislocation core and stabilize the formation of nonpolar $\{10\bar{1}1\}$ planes supplying an additional mechanism for the v-pit formation. Indeed, a number of v-pits in GaN on $LiAlO_2$ are not connected to inversion domains but have a bunch of dislocations attached to the v-pit apex (Figure 4.75d).

One of the crucial factors in fabrication of optoelectronic devices based on c-plane-oriented GaN films is the presence of spontaneous and piezoelectric polarization fields, which appear along the polar c-direction. The presence of internal polarization fields along the growth direction results in a poor overlap of electron and hole wave functions that reduces the electron-hole recombination rate and affects the device performance [135]. To solve this problem, the growth along directions different from the polar [00.1] axis, for example, the growth of nonpolar $(11\bar{2}0)$, (1100), and semipolar, for example, $(11\bar{2}2)$, $(10\bar{1}1)$ GaN layers (Figure 4.77), has been extensively investigated in the past decade [152].

The (100) γ-$LiAlO_2$ substrates offer a possibility to grow the so-called nonpolar m-plane layers with a small lattice mismatch (Table 4.16) [135]. Similarly to the polar c-plane layers, TDs are often observed in nonpolar GaN layers. Nevertheless, microstructure of nonpolar GaN layers is different compared to that of the

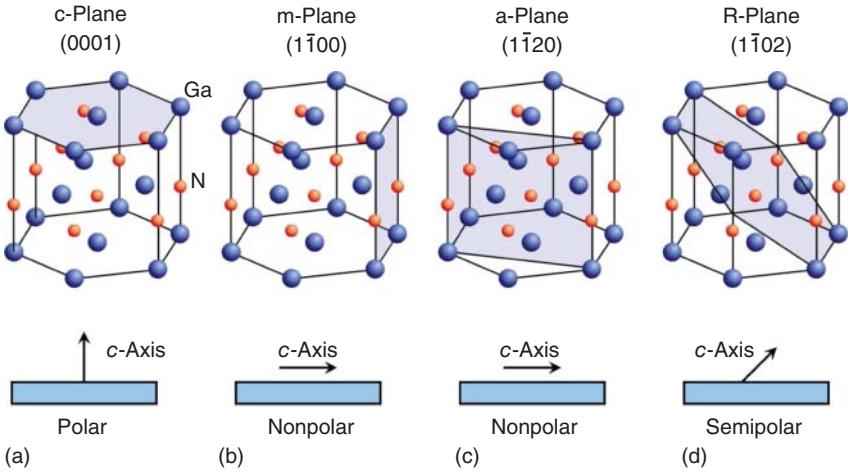

Figure 4.77 (a–d) Notation of some crystal planes in wurtzite GaN structure.

c-plane layers. In particular, the microstructure of nonpolar layers is dominated by planar defects, such as basal plane stacking faults (BSFs) [137], prismatic SFs [153], and prismatic plane boundaries [154]. Figure 4.78 shows plan-view diffraction contrast images revealing the different type of planar defects in the m-plane GaN layers grown on (100)$LiAlO_2$ by MOVPE. Figure 4.78a reveals a complex network of planar defects that can be recognized by a changing thickness fringe pattern, whereas BSFs appear predominantly in contrast for the 10$\bar{1}$0 reflection (BSFs in Figure 4.78c are marked by the dashed arrows and are visible in the magnified inset).

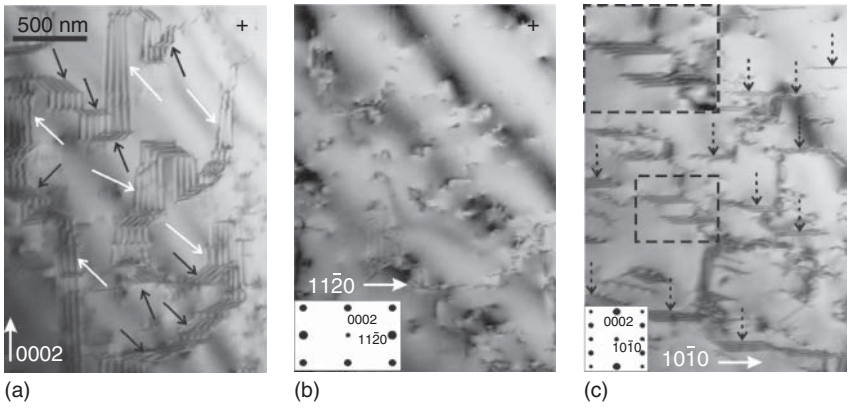

Figure 4.78 Plan-view bright-field images obtained different *g* reflections (a) 0002, (b) 11$\bar{2}$0, and (c) 10$\bar{1}$0. Insets at the bottom of (b) and (c) show sketched diffraction patterns calculated for [11.0] and [01.0] zone axes, respectively. A black cross in the right upper corner of the images marks the same specimen position. (Reprinted with permission of Neumann, *et al.* [137].)

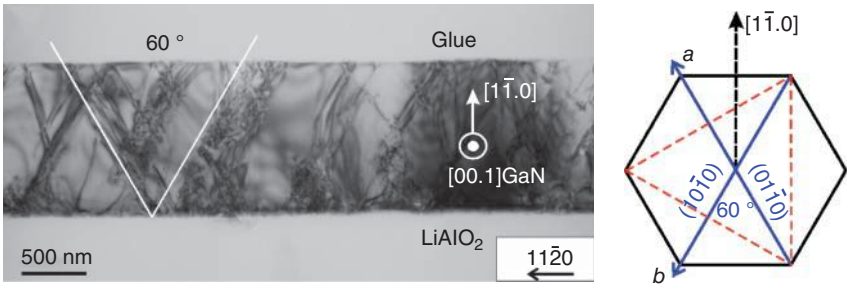

Figure 4.79 (a) Cross-sectional [00.1] GaN bright-field image showing planar defects located on prismatic {10-10} GaN planes. (b) Sketch of {1010} (solid lines) and {1120} (dashed lines) prismatic planes in the wurtzite structure. (Reprinted with permission of Neumann, *et al.* [137].)

In the complex defect network shown in Figure 4.78a, the inclination of the thickness fringes is changed along the network. The different arrangement of the thickness fringes indicates that this network involves planar defects appearing at a number of different defect planes, for example, prismatic planes (see white arrows in Figure 4.78a) as well as differently inclined pyramidal planes (see the black arrows in Figure 4.78b). Two different sets of prismatic planes exist in hexagonal crystal structure: {11$\bar{2}$0} and {10$\bar{1}$0} (Figure 4.79b). Cross-sectional TEM analysis in the [00.1]GaN zone axis allows distinguishing between these two sets of planes. As shown in Figure 4.79a, in the case of m-plane oriented GaN layers, the prismatic planar defects appear at the {10$\bar{1}$0}GaN planes. This is in contrast to the a-plane GaN layers, where the so-called prismatic staking faults are formed at the {11$\bar{2}$0}GaN planes [153].

BSFs are the most frequently observed defects in nonpolar and semipolar GaN layers [137, 155]. As mentioned earlier, stacking sequence of basal plane in the ideal wurtzite structure corresponds to AaBbAaBbAaBb (Figure 4.80a), where each capital letter represents a layer of Ga atoms and the small letter represents a layer of N atoms. This stacking sequence can be locally interrupted and a BSF can be formed, when a single basal layer is inserted into the structure or removed. Three types of BSFs are known in the wurtzite structure: two intrinsic SFs (known as I_1 and I_2) and one extrinsic SF (E). BSF I_1 is formed by removal of a basal plane followed by a slip of a crystal by $1/3 < 1\bar{1}00 >$, which results in the stacking sequence AaBbAaBbCcBbCcBb (Figure 4.80b). This BSF can be described by a displacement vector $\boldsymbol{R} = 1/2[0001] + 1/3 < 1\bar{1}00 >$. BSF of type I_2 can be formed by a slip of one part of the crystal by $\boldsymbol{R} = 1/3 < 1\bar{1}00 >$ (Figure 4.80c), which corresponds to the AaBbAaBbCcAaCcAaCc sequence. An insertion of an extra basal plane gives rise to an extrinsic SF E, which results in a AaBbAaBbCcAaBbAaBb lattice plane sequence (Figure 4.80d) with the displacement vector $\boldsymbol{R} = 1/2[0001]$.

It has been shown that in nonpolar layers, where the basal plane of the wurtzite structure is perpendicular to the growth plane, BSFs nucleate at the substrate

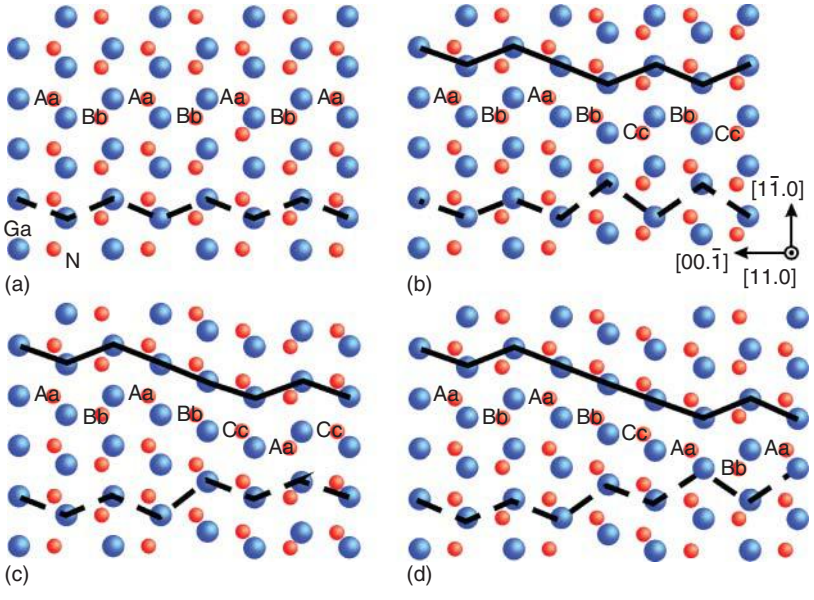

Figure 4.80 Schematic atom arrangement in (a) defect-free wurtzite structure, (b) BSF of type I_1, (c) BSF of type I_2, and (d) BSF of type E. A solid line indicates the atom arrangement in the BSF. A dashed line shows an interruption of the ideal atom sequence in the presence of BSF.

interface and propagate vertically through the layer. They can be connected by prismatic SFs or terminated by partial dislocations. It was considered that the BSF formation takes places mainly during island coalescence [155]. In this case, BSFs are able to compensate for in-plane translation between different nitride nuclei. This is not possible in polar layers, where the basal plane appears as the growth plane. In the latter case, misorientations between different nitride nuclei are compensated by the formation of TDs (Figure 4.72).

Using HRTEM analysis, it is possible to distinguish between the different BSF types resolving the different number of biatomic GaN planes forming a cubic

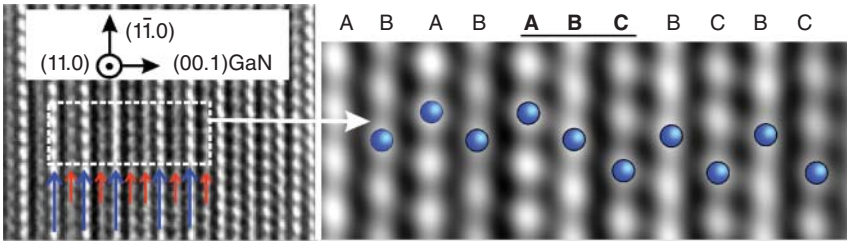

Figure 4.81 HRTEM image of a BSF in m-plane GaN. A Fourier filtered fragment on the right shows the ABABABCBCBC stacking sequence, which is characteristic for intrinsic BSF of I_1-type.

stacking in the hexagonal structure, that is, three biatomic planes for I_1 (ABC), four planes for I_2 (ABCA), and five planes for E (ABCAB). Figure 4.81 shows an HRTEM image demonstrating the presence of I_1 BSFs in the nonpolar m-plane GaN layers grown on $LiAlO_2$. This is the most frequently observed type of BSFs in nonpolar and semipolar nitride layers, most probably due to its low associated strain and formation energy [156] compared to the other types of BSFs.

It has been shown that BSFs provide an additional strong luminescence in GaN layers appearing at about 3.4 eV [157]. This BSF emission reduces the original near band edge emission efficiency degrading luminescent properties of III-nitride-based devices. Thus, elimination of BSFs in non- and semipolar layers becomes an important task.

References

1. Andreas, B., Azuma, Y., Bartl, G., Becker, P., Bettin, H., Borys, M., Busch, I., Gray, M. *et al.* (2011) *Phys. Rev. Lett.*, **106** (3), 030801.
2. IKZ Annual Report 2006/2007, p. 31 *http://www.ikz-berlin.de/publications_folder/report_folder/jbl0706/jb_07_06.pdf*.
3. Kröger, F.A. and Vink, H.J. (1956) in *Solid State Physics*, vol. 3 (eds F. Seitz and D. Turnbull), Academic Press, New York, p. 307.
4. Murphy, S.T., Gilbert, C.A., Smith, R., Mitchell, T.E., and Grimes, R.W. (2010) *Philos. Mag.*, **90** (10), 1297.
5. Tilley, R.J.D. (2008) *Defects in Solids*, John Wiley & Sons, Inc., Hoboken, NJ.
6. Will, S. and Leipertz, A. (1998) in *Diffusion in Condensed Matter* (eds J. Kärger, P. Heitjans, and R. Haberlandt), Vieweg, Braunschweig, Wiesbaden, pp. 219–244.
7. Zaitsev, A.M. (2001) *Optical Properties of Diamond: A Data Handbook*, Springer.
8. Shigley, J.E. and Breeding, C.M. (2013) *Gems Gemol.*, **49** (2), 107.
9. Petrakova, V., Ledvina, M., and Nesladek, M. (2013) Surface doping of diamond and induced optical effects, in *Optical Engineering of Diamond* (eds R. Mildren and J. Rabeau), Wiley-VCH Verlag GmbH, Berlin.
10. Volterra, V. (1907) *Ann. Sci. Ecole Normale Super.*, **24**, 401.
11. Nabarro, F.R.N. (1987) *Theory of Crystal Dislocations*, Dover Publications, New York.
12. Pond, R.C. and Hirth, J.P. (1994) *Solid State Phys.*, **47**, 287.
13. Harris, W.F. (1970) *Philos. Mag.*, **22**, 949.
14. Dash, W.C. (1957) in *Dislocations and Mechanical Properties of Crystals* (eds J.C. Fisher, W.G. Johnston, R. Thomson, and T. Vreeland Jr.,), John Wiley & Sons, Inc., New York, p. 57.
15. Messerschmidt, U. (2010) *Dislocation Dynamics During Plastic Deformation*, Series in Materials Science, vol. 129, Springer.
16. Neumann, W., Schneider, R., Richter, U., Schulze, C., Schumacher, G., Wanderka, N., Bartsch, M., and Messerschmidt, U. (2002) in *Proceedings of 15th International Conference on Electron Microscopy*, vol. 1 (eds J. Engelbrecht, T. Sewell, M. Witcomb, R. Cross, and P. Richards), Microscopy Society of Southern Africa, p. 675.
17. Alexander, H. and Teichler, H. (1991) in *Materials Science and Technology*, Electronic Structure and Properties of Semiconductors, vol. 4 (eds R.W. Cahn, P. Haasen, and E.J. Kramer), Wiley-VCH Verlag GmbH, Weinheim, p. 251.
18. Sutton, A.P. and Balluffi, R.W. (1995) *Interfaces in Crystalline Materials*, Oxford Science Publishing.
19. Christiansen, S.H., Schmidbauer, M., Wawra, H., Schneider, R., Neumann, W., and Strunk, H.P. (2007) in *Lateral*

Alignment of Epitaxial Quantum Dots (ed O.G. Schmidt), Springer, Berlin, p. 127.
20. Wolf, D. and Yip, S. (1992) *Materials Interfaces*, Chapman & Hall, London.
21. Randle, V. (1993) *The Measurement of Grain Boundary Geometry*, IOP Publishing, Bristol, Philadelphia, PA.
22. Priester, L. (2013) *Grain Boundaries, From Theory to Engineering*, Springer Series in Materials Science, vol. 172, Springer, Dordrecht.
23. Bollmann, W. (1970) *Crystal Defects and Crystalline Interfaces*, Springer, Berlin.
24. Ranganathan, S. (1966) *Acta Crystallogr.*, **21**, 197.
25. Grimmer, H. (1974) *Acta Crystallogr.*, **A30**, 685.
26. Grimmer, H. (1984) *Acta Crystallogr.*, **A40**, 108.
27. Grimmer, H. (1989) *Acta Crystallogr.*, **A45**, 320.
28. Grimmer, H. (1990) *Colloq. Phys. Colloq. C1*, **51**, C1–C1555.
29. Warrington, D.H., Radulescu, O., and Lück, R. (1997) *Acta Crystallogr.*, **A53**, 314.
30. Gertsman, V.Y. (2001) *Acta Crystallogr.*, **A57**, 649.
31. Grimmer, H. (1974) *Scr. Mater.*, **8**, 1221.
32. Sutton, A.P. (1984) *Int. Met. Rev.*, **29** (5), 377.
33. Read, W.T. and Shockley, W. (1950) *Phys. Rev.*, **78**, 275.
34. Brandon, D.G. (1966) *Acta Metall.*, **14**, 1479.
35. Thibault, J., Rouviere, J.L., and Bourret, A. (1991) in *Materials Science and Technology*, Electronic Structure and Properties of Semiconductors, vol. 4 (eds R.W. Cahn, P. Haasen, and E.J. Kramer), Wiley-VCH Verlag GmbH, Weinheim, p. 321.
36. Frank, F.C. (1951) *Philos. Mag.*, **42**, 809.
37. Sebastian, M.T. and Krishna, P. (1987) *Cryst. Growth Charact.*, **14**, 103.
38. Baronnet, A. (1992) in *Minerals and Reactions at the Atomic Scale: Transmission Electron Microscopy*, Reviews in Mineralogy, vol. 27 (ed P.R. Buseck), p. 331.
39. Pandey, D. and Krishna, P. (1992) in *International Tables for Crystallography*, vol. C (ed A.J.C. Wilson), Kluwer Academic Publishers, Dordrecht, p. 660.
40. Hirsch, P.B., Howie, A., Nicholson, R.B., and Pashley, D.W. (1965) *Electron Microscopy of Thin Crystals*, Butterworths, London.
41. Jin, Z.H., Dunham, S.T., Gleiter, H., Hahn, H., and Gumbsch, P. (2011) *Scr. Mater.*, **64**, 605.
42. Hesse, D. (1987) *J. Vac. Sci. Technol., A*, **5** (4), 1696.
43. Loiseau, J. (1994) in *Electron Microscopy of Boundaries and Interfaces in Materials Science: Proceedings of the Autumn School of the International Centre of Electron Microscopy* (eds J. Heydenreich and W. Neumann), MPI of Microstructure Physics, Halle, p. 159.
44. Romé de l'Lisle, J.B.L. (1783) *Cristallographie*, vol. 1, Imprimerie de Monsieur, Paris, p. 93.
45. Hahn, T. and Klapper, H. (2003) in *International Tables for Crystallography*, vol. D, Chapter 3.3 (ed A. Authier), Kluwer Academic Publishers, Dordrecht, p. 393.
46. Koch, E. (1992) in *International Tables for Crystallography*, vol. C (ed A.J.C. Wilson), Kluwer Academic Publishers, Dordrecht, p. 10.
47. Grimmer, H. and Nespolo, M. (2006) *Z. Kristallogr.*, **221**, 28.
48. Donnay, J.D.H. (1940) *Am. Mineral.*, **25**, 578.
49. Le Page, Y. (2002) *J. Appl. Crystallogr.*, **35**, 175.
50. Hofmeister, H. (1998) *Cryst. Res. Technol.*, **33**, 3.
51. Senechal, M. (1980) *Sov. Phys. Crystallogr.*, **25**, 520.
52. Salje, E.K.H. (1993) *Phase Transitions in Ferroelastic and Co-Elastic Crystals*, Cambridge University Press.
53. Klassen-Neklyudova, M.V. (1964) *Mechanical Twinning of Crystals*, Consultants Bureau Enterprises, New York.
54. Kelly, A. and Knowles, K.M. (2012) *Crystallography and Crystal Defects*, 2nd edn, John Wiley & Sons, Ltd, Chichester.

55. Christian, J.W. and Mahajan, S. (1995) *Prog. Mater Sci.*, **39**, 1.
56. Rath, B.B., Imam, M.A., and Pande, C.S. (2000) *Mater. Phys. Mech.*, **1**, 61.
57. Neumann, W., Hofmeister, H., and Heydenreich, J. (1994) *Phys. Status Sol.*, **A 146**, 437.
58. Neumann, W., Hofmeister, H., Conrad, D., Scheerschmidt, K., and Ruvimov, S. (1996) *Z. Kristallogr.*, **211**, 147.
59. Gratias, D., Portier, R., and Fayard, M. (1979) *Acta Crystallogr.*, **A35**, 885.
60. Kopezky, C.V., Andreeva, A.V., and Shukomlin, G.D. (1991) *Acta Metall. Mater.*, **39**, 1603.
61. Pond, R.C. and Vlachavas, D.S. (1983) *Proc. R. Soc. London, Ser. A*, **386**, 95.
62. Pond, R.C. (1989) in *Dislocations in Solids*, vol. 8 (ed F.R.N. Nabarro), Elsevier, Amsterdam, p. 1.
63. Aizu, K. (1970) *Phys. Rev. B*, **2**, 757.
64. Janovec, V. and Přívatská, J. (2003) in *International Tables for Crystallography*, vol. D, Chapter 3.4 (ed A. Authier), Kluwer Academic Publishers, Dordrecht, p. 449.
65. Van Aken, B.B., Rivera, H.P., Schmid, H., and Fiebig, M. (2007) *Nature (London)*, **449**, 702.
66. Wadhawan, V.K. (2000) *Introduction to Ferroic Materials*, Gordon and Breach, New York.
67. Shilo, D., Burcsu, E., Ravichandran, G., and Bhattacharya, K. (2007) *Int. J. Solids Struct.*, **44**, 2053.
68. Jia, C.-L., Mi, S.-B., Urban, K.W., Vrejoiu, I., Alexe, M., and Hesse, D. (2008) *Nat. Mater.*, **7**, 58.
69. Laughlin, D.E., Willard, M.A., and McHenry, M.E. (2000) in *Phase Transformations and Evolution in Materials* (eds P. Turchi and A. Gonis), The Minerals, Metals and Materials Society, p. 121.
70. Zheng, Ch. (2009) Investigation of magnetic materials and semiconductor nanostructures by electron holography. PhD thesis. Humboldt University Berlin, Cuvillier Verlag Göttingen.
71. Neumann, W., Kirmse, H., Häusler, I., Mogilatenko, A., Zheng, C., and Hetaba, W. (2010) *Bull. Pol. Acad. Sci.: Tech. Sci*, **58** (2), 235.
72. Lichte, H. and Lehmann, M. (2008) *Rep. Prog. Phys.*, **71**, 1.
73. Schmid, H. (2008) *J. Phys. Condens. Matter*, **20**, 434201.
74. Spaldin, N.A., Fiebig, M., and Mostovoy, M. (2008) *J. Phys. Condens. Matter*, **20**, 434203.
75. Schmid, H. (2001) *Ferroelectrics*, **252**, 41.
76. Litvin, D.B. (2008) *Acta Crystallogr.*, **A64**, 316.
77. Wood, E.A. (1964) *J. Appl. Phys.*, **35**, 1306.
78. Park, R.L. and Madden, H.H. (1968) *Surf. Sci.*, **11**, 188.
79. Michaelides, A. and Scheffler, M. (2012) in *Surface and Interface Science: Concepts and Methods*, vol. 1 (ed K. Wandelt), Wiley-VCH Verlag GmbH, p. 13.
80. Däweritz, L. and Hey, R. (1990) *Surf. Sci.*, **236**, 15.
81. Lang, B., Joyner, R.W., and Somorjai, G.A. (1972) *Surf. Sci.*, **30**, 440.
82. Hermann, K. (2010) *Crystallography and Surface Structure*, Wiley-VCH Verlag GmbH, Weinheim.
83. Keller, K.-W. and Höche, H. (1987) in *Electron Microscopy in Solid State Physics* (eds H. Bethge and J. Heydenreich), Elsevier, Amsterdam, p. 437.
84. Bethge, H. (1962) *Phys. Status Solidi A*, **2/3**, 775.
85. Brune, D., Hellborg, R., Whitlow, H.J., and Hunderi, O. (eds) (1997) *Surface Characterization: A Users'Source Book*, Wiley-VCH Verlag GmbH.
86. Föll, H. and Kolbesen, B.O. (1975) *Appl. Phys.*, **8**, 310.
87. Föll, H. Hyperscript, Defects in Crystals, *http://www.tf.uni-kiel.de/matwis/amat/def_en/metamod/preface.html* (accessed 25 February 2014).
88. Gübelin, E.J. (1953) *Inclusions as a Means of Gemstone Identification*, GIO, Los Angeles, CA.
89. Gübelin, E. and Koivula, J. (1986) *Photoatlas of Inclusions in Gemstones*, vol. 1, Opinio Verlag, Basel, (2005) vol. 2, (2008) vol. 3).
90. Dhanaraj, G., Byrappa, K., Prasad, V., and Dudley, M. (eds) (2010) *Handbook on Crystal Growth*, Springer.

91. Bourgeois, L., Medhekar, N.V., Smith, A.E., Weyland, M., Nie, J.-F., and Dwyer, C. (2013) *Phys. Rev. Lett.*, **111**, 046102.
92. Itsumi, M. (2003) in *Crystal Growth Technology* (eds H.J. Scheel and T. Fukuda), John Wiley & Sons, Ltd, Chichester, p. 205.
93. Voronkov, V.V. and Falster, R. (1998) *J. Cryst. Growth*, **194**, 76.
94. Falster, R., Vorenkov, V.V., and Mutti, P. (2003) in *Crystal Growth Technology* (eds H.J. Scheel and T. Fukuda), John Wiley & Sons, Ltd, p. 225.
95. ISO (2005) ISO 9000:2005. *Quality Management Systems: Fundamentals and Vocabulary*, International Organization for Standardization (ISO) (Management standards pages), *www.iso.org* (accessed 21 February 2014).
96. Fromme, P. and Grotjohann, I. (2009) The crystallization of photosynthetic membrane proteins, in *Membrane Protein Crystallization* (ed L. DeLucas), Academic Press, San Diego, CA.
97. Tatarchenko, V.A. (2010) in *Handbook on Crystal Growth* (eds G. Dhanaraj, K. Byrappa, V. Prasad, and M. Dudley), Springer, p. 205.
98. Scheel, H.J. and Fukuda, T. (eds) (2003) *Crystal Growth Technology*, Part 5: Crystal Machining, John Wiley & Sons, Ltd, Chichester, p. 529.
99. De Weerd, F. and Collins, A.T. (2007) *New Diamond Front. Carbon Technol.*, **17**, 291.
100. GIA Brochure. The Four Cs of Diamond Quality, *http://gia4cs.gia.edu/en-us/four-cs-guide.htm* (accessed 21 February 2014).
101. Wang, W., D'Haenens-Johansson, U.F.S., Johnson, P., Moe, K.S., Emerson, E., Newton, M., and Moses, T.M. (2012) *Gems Gemol.*, **48** (2), 80.
102. Eaton-Magaña, S. and D'Haenens-Johansson, U.F.S. (2012) *Gems Gemol.*, **48** (2), 124.
103. Diamond Materials Advanced Diamond Technology. *The CVD Diamond Booklet*, Diamond Materials GmbH, Freiburg, (2008) *www.diamond-materials.com/download* (accessed 21 February 2014).
104. Nanev, C.N. (2007) *Cryst. Res. Technol.*, **42**, 4.
105. Nanev, C.N. (2008) *Cryst. Res. Technol.*, **43**, 914.
106. Nanev, C.N. (2012) *Cryst. Res. Technol.*, **47**, 1195.
107. McPherson, A. (1990) *Eur. J. Biochem.*, **189**, 1.
108. Gutiérrez-Quezada, A.E., Arreguín-Espenosa, R., and Morena, A. (2010) *Handbook of Crystal Growth*, Springer-Verlag, p. 1587.
109. Bergfors, T.M. (ed) (2009) *Protein Crystallization*, IUL Biotechnology Series, 2nd edn, International University Line, La Colla, CA.
110. Derewenda, Z.S. (2010) *Acta Crystallogr., Sect. D*, **66**, 604.
111. Rupp, B. (2010) *Biomolecular Crystallography, Principles, Practice, and Applications to Structural Biology*, Garland Science, Taylor & Francis Group, New York.
112. McPherson, A., Malkin, A.J., Kuznetsov, Y.G., Stan Koszelak, S., Wells, M., Jenkins, G., Howard, J., and Lawson, G. (1999) *J. Cryst. Growth*, **196**, 572.
113. Rossmann, M.G. and Arnold, E. (eds) (2001) *International Tables for Crystallography F, Crystallography of Biological Macromolecules*, Kluwer Academic Publishers, Dordrecht, Boston, MA, London.
114. Brundle, C.R., Evans, C.A. Jr., and Wilson, S. (eds) (1992) *Encyclopedia of Materials Characterization*, Butterworth-Heinemann, Boston, MA.
115. Zhang, S., Li, L., and Kumar, A. (2009) *Materials Characterization Techniques*, CRC Press.
116. Sangwal, K. (1987) *Etching of Crystals, Theory, Experiment and Application*, North-Holland, Amsterdam.
117. Heimann, R.B. (1982) in *Crystals: Growth, Properties and Applications*, vol. 8 (ed J. Grabmaier), Springer-Verlag, Berlin, p. 173.
118. Weyher, J.L. (1994) in *Handbook on Semiconductors*, vol. 3 (ed S. Mahajan), Elsevier, Amsterdam, p. 995.
119. Weyher, J.L. and Kelly, J.J. (2010) *Handbook of Crystal Growth*, Springer-Verlag, p. 1453.

120. Köhler, R., Pfeiffer, J.-U., Raidt, H., Neumann, W., Zaumseil, P., and Richter, U. (1998) *Cryst. Res. Technol.*, **33** (4), 593.
121. Lang, A.R. (1992) in *International Tables for Crystallography*, vol. C (ed A.J.C. Wilson), Kluwer Academic Publishers, Dordrecht, p. 113.
122. Tanner, B.K. (1976) *X-Ray Diffraction Topography*, Pergamon, Oxford.
123. Bowen, D.K. and Tanner, B.K. (1998) *High Resolution X-Ray Diffractometry and Topography*, Taylor & Francis, London.
124. Köhler, R. (1994) *Appl. Phys. A*, **58**, 149.
125. Authier, A. (2001) *Dynamical Theory of X-Ray Diffraction*, Oxford Science Publishing.
126. Raghothomachar, B., Dudley, M., and Dhanaraj, G. (2010) *Handbook of Crystal Growth*, Springer-Verlag, p. 1426.
127. Moore, M. (2012) *Crystallogr. Rep.*, **18** (3), 207.
128. Bethge, H. and Heydenreich, J. (eds) (1987) *Electron Microscopy in Solid State Physics*, Elsevier, Amsterdam.
129. Amelinckx, S. (1997) *Electron Microscopy, Principles and Fundamentals*, Wiley-VCH Verlag GmbH, Weinheim.
130. Williams, D.B. and Carter, C.B. (2009) *Transmission Electron Microscopy, A Textbook for Materials Science*, Springer Science.
131. Paskova, T., Hanser, D.A., and Evans, K.R. (2010) *Proc. IEEE*, **98** (7), 1324.
132. Grzegory, I., Łucznik, B., Boćkowski, M., and Porowski, S. (2007) *J. Cryst. Growth*, **300**, 17.
133. Utsumi, W., Saitoh, H., Kaneko, H., Watanuki, T., Aoki, K., and Shimomura, O. (2003) *Nat. Mater.*, **2**, 735.
134. Hellmann, E.S., Liliental-Weber, Z., and Buchanan, N.E. (1997) *MRS Internet J. Nitride Semicond. Res.*, **2**, 30.
135. Waltereit, P., Brandt, O., Trampert, A., Grahn, H.T., Menniger, J., Ramsteiner, M., Reiche, M., and Ploog, K.H. (2000) *Nature*, **406**, 865.
136. Mogilatenko, A., Neumann, W., Richter, E., Weyers, M., Velickov, B., and Uecker, R. (2007) *Springer Proc. Phys.*, **120**, 45.
137. Neumann, W., Mogilatenko, A., Wernicke, T., Richter, E., Weyers, M., and Kneissl, M. (2010) *J. Microsc.*, **237**, 308.
138. Mogilatenko, A., Neumann, W., Richter, E., Weyers, M., Velickov, B., and Uecker, R. (2007) *J. Appl. Phys.*, **102**, 023519.
139. Veličkov, B., Mogilatenko, A., Bertram, R., Klimm, D., Uecker, R., Neumann, W., and Fornari, R. (2008) *J. Cryst. Growth*, **310**, 214.
140. Moram, M.A., Ghedia, C.S., Rao, D.V.S., Barnard, J.S., Zhang, Y., Kappers, M.J., and Humphreys, C.J. (2009) *J. Appl. Phys.*, **106**, 073513.
141. Kneissl, M., Kolbe, T., Chua, C., Kueller, V., Lobo, N., Stellmach, J., Knauer, A., Rodriguez, H., Einfeldt, S., Yang, Z., Johnson, N.M., and Weyers, M. (2011) *Semicond. Sci. Technol.*, **26**, 014036.
142. Ponce, F.A. and Bour, D.P. (1997) *Nature*, **386**, 351.
143. Belabbas, I., Ruterana, P., Chen, J., and Nouet, G. (2006) *Philos. Mag.*, **86**, 2241.
144. Mogilatenko, A., Neumann, W., Richter, E., Weyers, M., Velickov, B., and Uecker, R. (2008) *Phys. Status Solidi C*, **5**, 3712.
145. Richter, E., Hennig, C., Zeimer, U., Weyers, M., Tränkle, G., Reiche, P., Ganschow, S., Uecker, R., and Peters, K. (2006) *Phys. Status Solidi C*, **3** (6), 1439.
146. Shin, T.I. and Yoon, D.H. (2005) *Cryst. Res. Technol.*, **40**, 827.
147. Hellman, E.S. (1998) *MRS Internet J. Nitride Semicond. Res.*, **3**, 11.
148. Stutzmann, M., Ambacher, O., Eickhoff, M., Karrer, U., Pimenta, A.L., Neuberger, R., Schalwig, J., Dimitrov, R., Schuck, P.J., and Grober, R.D. (2001) *Phys. Status Solidi B*, **228**, 505.
149. Northrup, J.E., Neugebauer, J., and Romano, L.T. (1996) *Phys. Rev. Lett.*, **77**, 103.
150. Liu, F., Collazo, R., Mita, S., Sitar, Z., Pennycook, S.J., and Duscher, G. (2008) *Adv. Mater.*, **20**, 2162.
151. Liliental-Weber, Z., Jasinski, J., and Washburn, J. (2002) *J. Cryst. Growth*, **246**, 259.
152. Scholz, F. (2012) *Semicond. Sci. Technol.*, **27**, 024002.
153. Vennéguès, P., Mathal, F., and Bougrioua, Z. (2006) *Phys. Status Solidi C*, **3**, 1658.

154. Jasinski, J., Liliental-Weber, Z., and Maruska, H.P. (2003) *Mater. Res. Soc. Symp. Proc.*, **764**, C6.6.

155. Vennéguès, P., Chauveau, J.M., Bougrioua, Z., Zhu, T., Martin, D., and Grandjean, N. (2012) *J. Appl. Phys.*, **112**, 113518.

156. Stampfl, C. and Van de Walle, C.G. (1998) *Phys. Rev. B*, **57**, 52.

157. Liu, R., Bell, A., Ponce, F.A., Chen, C.Q., Yang, J.W., and Khan, M.A. (2005) *Appl. Phys. Lett.*, **86**, 021908.

Index

a

ABC notation 124
Abelian groups 53
acentric crystals 382
adamantine 379–380
age hardening. *See* precipitation hardening
aging defects 382
albite twin law 348
ambient phase
– growth from melt 191–192
– growth from solutions 192–193
– growth from vapor 193
American Mineralogist Crystal Structure Database (AMCSD) 156–157
amorphous solid 10
anisotropy 3
annealing twins 347, 351
anti-Frenkel defect 304, 307
antiphase boundaries 151, 340–342
anti-Schottky defect 304
antisite defect 304–305
antisymmetry operation 103
aperiodic crystals 5
aqueous solutions 296, 298
aristotype 145, 148, 149
assembly of zones 22
associativity 52
asymmetrical grain boundary 329
ATHENA 157
atomic scale imaging 371
Auger electron spectroscopy (AES) 293
Auger emission 387
axial glides 72

b

$Ba_8Al_{16}Ge_{30}$ 135, 136
ball and stick model, of C_{60} fullerene 137
Bärnighausen tree 145, 147–148, 150
basal plane stacking faults (BSFs) 405–408
bicrystal 354
Bilbao Crystallographic Server (BCS) 88, 153
biocrystallization 381
Biological Macromolecule Crystallization Database (BMCD) 155
Blickrichtungen symmetry directions 41
Bond number 217
Bragg equation 383
Bravais–Friedel–Donnay–Harker (BFDH) law 20
Bravais–Friedel rule 20
Bravais lattice 61–62, 64, 364
Bravais–Miller indices (hkil) 24
Brazil twins 345–346
Bridgman growth method 234–243
bright-field image 389, 405
bubbles 369
Buckminsterfullerene 137
buckyball. *See* Buckminsterfullerene
bulk crystal growth from metallic solutions 253
– solute, synthesis, diffusion method (SSD) 259–260
– traveling heater method (THM) 255–257
– – in microgravity environment 257–259
– traveling solvent method (TSM) 253
bulk oxide crystals 232
buoyancy convection 215–216
Burgers circuit 316–317
Burgers vector 315–320

c

cadmium telluride (CdTe) 221, 222, 235, 261
– ampoule wall influence, during crystal growth experiments-detached growth 241–243
– crystal growth

Introduction to Crystal Growth and Characterization, First Edition.
Edited by Klaus-Werner Benz and Wolfgang Neumann.
© 2014 Wiley-VCH Verlag GmbH & Co. KGaA. Published 2014 by Wiley-VCH Verlag GmbH & Co. KGaA.

cadmium telluride (CdTe) (*contd.*)
– – by Markov method in semi-closed ampoules 264–266
– – by sublimation traveling heater method in closed ampoules 262–264
– melt structure 240–241
– peculiarities, with respect to bulk crystal growth 239–240
– related compounds growth by vertical Bridgman method 237–238
– typical growth defects 240
calomel 126
Cambridge Crystallographic Data Center (CCDC) 154
Cambridge Structural Database (CSD) 152, 154–155
carbon nanotubes (CNTs) 143–146
C-center 378
chain-like molecules 127
chair conformation 128
chalcopyrite structure 120–121
characteristic and noncharacteristic forms 59
chemical potential 173–174, 199
chemical vapor deposition (CVD) 279–286, 376, 380–381
chlorinated copper phthalocyanine (CuPc) 133
clathrates 134–135
Clausius–Clapeyron equation 196
clean surfaces 363
climb 323
closed ampoule PVT system 260–261
closed crystal forms 35
closest homogeneous sphere packing 110
closure 52
clouds 369
cocrystallization with metal organic compounds 143
coherent interface 327–328
coherent twin plane 349
coincidence site lattice (CSL) 332–333, 354
– misorientation scheme 330
colinear interstitialcy diffusion 311
color center 307, 311–313, 379
commensurate interface 328
commensurate-modulated crystal 6
commutative groups. *See* Abelian groups
complication rule 22
composite lattice 331
composite symmetry 354
compound twins 350
conformation 126
conformational polymorphism 124
conjugate/reciprocal twins 350
conjugate element 55
conservative antiphase boundary 340
contrast rules 390
convergent-beam electron diffraction (CBED) 392
coronene 130–131
coset decomposition 54–55
critical numbers 215
critical shear stress 321
cross slip 322, 323
– multiple 324
crystal axes systems, crystal systems, and crystal families 14–15
crystal characterization methods 382
– electron microscopy 385–392
– etching of crystals 382–383
– X-ray topography (XRT) 383–385
crystal-chemically isotypic structures 107–108
crystal class. *See* point groups
crystal defects 301–303
– crystal characterization methods 382
– – electron microscopy 385–392
– – etching of crystals 382–383
– – X-ray topography (XRT) 383–385
– crystal quality 375–376
– – application 378–381
– – criteria 376–377
– materials engineering by crystal growth and characterization correlation 392–393
– – epitaxial growth of GaN on $LiAlO_2$ substrates 393–408
– one-dimensional defects 314
– three-dimensional defects 368
– – inclusions 369–370
– – precipitates 370–374
– – voids 374–375
– two-dimensional defects (planar defects) 326–328
– – antiphase boundaries 340–342
– – crystal surfaces 363–368
– – domain boundaries 355–362
– – grain boundaries 328–336
– – stacking faults 336–340
– – twins 342–354
– zero-dimensional defects 303–313
crystal faces and zones 15–23
crystal lattices 12–14
– structures database 157
crystalline state 1–12
crystallographic databases and computer programs 152–156
Crystallographic Information File (CIF) 153
crystallographic orbit 90

crystallographic space groups 71–76
– International Tables For Crystallography 76–93
– space group symmetry mathematical description 93–101
Crystallography Open Database (COD) 153, 156
crystal originated particles (COPs) 375
crystal pattern 60
crystal processing and machining 377
crystal quality 375–376
– application 378–381
– criteria 376–377
crystal size and shape 377
crystal structures 104–109
– inorganic structure types examples 112–126
– molecular crystals examples 126–145
– sphere packings 108–112
– symmetry relations between crystal structures 145–152
crystal surfaces 363–368
CRYSTMET 152, 154
CsCl structure 116
Cu_3Au structure 117–118
CuAu structure 116–118
cubic closest packing 109
cubic crystal class crystal forms 160
cubic point groups 46
cubic twins 350
cyclic group 54
cyclohexane 128
Czochralski crystal growth process 224–234

d

dangling bonds 365
dark-field image 389
Dauphiné twin 345–347
Dauphiné twins 150–151
defect analysis. *See* crystal defects
deformation fault 337–338
deformation twinning. *See* mechanical twins
degree of crystallinity 376–377
degree of polymerization 129
degress of freedom (DOF) 330
deltoid-dodecahedron 163
deltoid-icositetrahedron 164
derivative lattice 330
detached crystal growth. *See* detached solidification
detached solidification 241
dewetting 241
diagonal glides 73
diamond crystals 378–381
diamond glides 73
diamond structure 113–114
diffraction contrast 389
diffuse interfaces 327
diffusion coefficient 257
dihedron 46
dimensionless numbers 215. *See also* Prandtl number; Rayleigh number; Schmidt number
direct interstitial mechanism 311
disclinations 315
disdodecahedron 59
dislocation core 315
dislocation density 318–319
dislocation line 315–316
dislocations 315
– multiplication 324
dispiration 315
displacement field 318
displacement shift complete (DSC) lattice 332–333
displacement vector 336–337
dodecahedrane 133, 134
domain boundaries 355–362
domain switching 356–357
dome 36–38, 46
dopant striations 211
double-ellipsoidal mirror furnace 251
double glides 73
dovetail twin of gypsum 345, 347

e

edge dislocation 315–316, 318, 323
effective charge of defect 305
electron acceptor 307
electron donors 307
electron energy-loss spectroscopy (EELS) 386, 392
electron holes 307
electron-loss near-edge fine structure (ELNES) 392
electron microscopy 385–387
– scanning electron microscopy (SEM) 387–388
– transmission electron microscopy (TEM) 388–392
enantiomorphism 48, 49
endohedral fullerenes 141, 143
energy-dispersive X-ray spectroscopy (EDXS) 396
enthalpy 172, 176
epigenetic (postgrowth) inclusions 370
epilayers. *See* epitaxy
epitaxial growth techniques 266–270
– liquid phase epitaxy (LPE) 270–278

epitaxial growth techniques (*contd.*)
– vapor phase epitaxy (VPE) 279–295
epitaxy 222–223
equilibrium cooling 272
etching of crystals 382–383
eutectic point 199–200
excess electrons 307
exohedral fullerenes 141
extinction contrast 384
extrinsic point defects 305
extrinsic semiconductors 308
extrinsic stacking faults 337–338

f

factor group 55, 99
fancy shapes 379
Faraday induction law 248
ferroelastics 348, 361
ferroelectric phase 355–357
ferroic phase 355–356, 361
ferromagnetic and ferrimagnetic materials 358–359
ferrotoroidic crystal 361–362
Fick's law 206
flat faces
– defect-induced growth kinetics 189–190
– growth kinetics 188–189
float zone crystal growth process 244–253
fluid flow damping in semiconductor melts
– rotating magnetic fields 247–248, 250
– static magnetic fields 246–247
fluorite structure 119–120
flux growth 295–297
Frank's rule 320–321
Frank-Read source 324–325
Frank–van derMerwe growth mechanism 267, 268
free energy 172, 191
Frenkel defect 304, 307, 310
Friedel's Law 46, 48
fullerenes 137, 139–141
– ball and stick model 141
fullerides 142–143
– ball-and-stick representation 143
fullerites 126, 141, 142

g

gallium arsenide (GaAs) 221–225, 230
– growth, by horizontal Bridgman and horizontal gradient freeze technique 235–236
gas hydrates 134
gas source molecular beam epitaxy (GSMBE) 292
Gemological Institute of America (GIA) 308
general position 89
generators 51
geometrical crystallography 12
– crystal axes systems, crystal systems, and crystal families 14–15
– crystal faces and zones 15–23
– crystal lattices 12–14
– crystallographic databases and computer programs 152–156
– crystal structures 104–109
– – inorganic structure types examples 112–126
– – molecular crystals examples 126–145
– – sphere packings 110–112
– – symmetry relations between crystal structures 145–152
– indexing in hexagonal crystal family 24–25
– morphological symmetry of crystals 25–40
– – crystallographic point groups 40–52
– – group theory 52–59
– structural symmetry 60
– – crystal lattices motifs, and crystal structures, 60
– – crystallographic space groups 71–99
– – generalized crystallographic symmetry 101–103
geometric crystal class 39
giant fullerenes 140
Gibbs–Curie–Wulff theorem 181–182
Gibbs–Thomson equation 174–176, 182
glide 321
glide direction 321
glide elements and system 321
glide reflections 72–76, 97
GR1 color center 313
grain boundaries 328–336
graphene 144
graphite structure 115
Grashof number 216
great circles 28
group theory 52–59
growth accident 351
growth fault 337
growth mechanism and solidification 171
– flow regime principles in growth melts 214–215
– – buoyancy convection 215–216
– – Marangoni convection 216–218
– kinetic processes and growth mechanism 182–183

– – crystal growth from ambient phases on rough surfaces 190–193
– – crystal growth molecular kinetic theory 183–185
– – crystal growth on flat surfaces 193–195
– – interfaces and roughening of surfaces 185–189
– – vapor–liquid–solid (VLS) mechanism 189–190
– nucleation processes 171–175
– – equilibrium shape of crystals 180–182
– – heterogeneous nucleation 177–178
– – homogeneous nucleation 175–177
– – metastable zone regime 179–180
– phase diagrams and segregation principles 195–196
– – constitutional supercooling and morphological stability 212–214
– – phase diagrams with continuous miscibility in solid and liquid phases 196–200
– – segregation and segregation coefficients 201–212
growth melts and flow regime principles 214–215
– buoyancy convection 215–216
– Marangoni convection 216–218
growth techniques, in correlation with related growth mechanism 221–223
– II-VI compounds bulk crystal growth from vapor 260–262
– – CdTe crystal growth by Markov method in semi-closed ampoules 264–266
– – CdTe crystal growth by sublimation traveling heater method in closed ampoules 262
– aqueous solutions 296–298
– epitaxial growth techniques 266–270
– – liquid phase epitaxy (LPE) 270–278
– – vapor phase epitaxy (VPE) 279–295
– flux growth 295–298
– melt growth techniques
– – bulk crystal growth from metallic solutions 253–260
– – Czochralski crystal growth process 224–234
– – float zone crystal growth process 244–253
– – growth method after Bridgman 234–243
– Verneuil technique 295–296
growth twins 347–348
Guinier–Preston (GP) zone 328, 373–374

h

habit 32
Hägg notation 124
half-crystal position 183
h–c notation 124
hecatonicosahedron 138
helical dislocations 323
hemihedries 59
heteroepitaxial layers 222, 266, 269
heterofullerenes 141
heterogeneous nucleation 177–178
heterogeneous primary nucleation 172
heterophase boundaries 327
hettotype 145, 149
hexa-cesium C_{60}-fulleride 143
hexagonal closest packing 109
hexagonal crystal family indexing 24–25
hexagonal layer of circles 109
hexagonal pyramids 36
hexaicosahedron 138
hexakisoctahedron form 59
Heywang equation 245
high-angle annular dark-field (HAADF) 392
high-angle grain boundaries 329
higher fullerenes 140
high pressure method (HPB) 238
high resolution transmission electron microscopy (HRTEM) 3–4, 6, 7, 133, 335–336, 338, 340–342, 347, 352–354, 358, 373, 391, 397, 400, 407
high-temperature annealing (HPHT) 380
high-voltage transmission electron microscopy (HVTEM) 368
HKUST-1 135, 137
holohedral point groups (holoedries) 48
homeotypic structures 108
homoepitaxial layers 222, 266
homogeneous nucleation 175–177
homogeneous primary nucleation 172
homogeneous sphere packing 109, 111
homophase boundaries 327
horizontal gradient freeze (HGF) 235
hydrogen vapor phase epitaxy (HVPE) 286–288

i

icosahedral symmetry 139
ideal crystal 4, 302
ideal structure 302
imperfect crystal 302
imperfect dislocation. *See* partial dislocation
inclusions 369–370, 396
incoherent interface 327
incoherent twin plane 349

incommensurate interface 328
incommensurate-modulated crystal 6
Incommensurate Structures Database (ICSDB) 157
indium phosphide (InP) 230
induction period of nucleation 179
Inorganic Crystal Structure Database (ICSD) 105, 152, 156
integral extinctions 90
interface plane scheme 330
interfaces 327–329
International Tables For Crystallography 76–93
International Technology Roadmap for Semiconductors (ITRS) 228
International Union of Crystallography (IUCr) 11
interstices 109
interstitialcy mechanism 311–312
interstitial impurities 304, 305
interstitials 303, 311–312
intrinsic point defects 305, 310
intrinsic primary GB dislocations 333
intrinsic stacking faults 337–339
inverse element 53
inversion 37, 96–97
inversion boundaries. *See* inversion twins
inversion domains 403
inversion twins 343
invisibility criterion 390
isoconfigurational structures 107
isolated pentagon rule (IPR) 140
isomers 127
isomorphic groups 53, 55
isopointal structures 107
isotopy 107
IUCr 153

j

Jagodzinski–Wyckoff notation. *See* h–c notation
jogs 323
Journal of Applied Crystallography 153

k

kinetic processes and growth mechanism 182–183
– crystal growth from ambient phases on rough surfaces 190–193
– crystal growth molecular kinetic theory 183–185
– crystal growth on flat surfaces 193–195
– interfaces and roughening of surfaces 185–189
– vapor–liquid–solid (VLS) mechanism 189–190
kinetic roughening 188–189
kinks 323. *See also* half-crystal position
Kossel crystal 182, 183
Kossel–Stranski model 188
Kröger–Vink notation 305–307
Kyropoulos technique 233–234

l

Laplace/capillary pressure 174
laser lift-off process 288
lattice complexes 90
lattice defects, of crystal 302
lattice periodicity 34
lattice transformations 68–71
Laue classes 46
law of constancy of interfacial angles 15, 20
law of rational indices (Haüy's law) 18–19
layer displacement fault 338
line defects 314
liquid crystals 11
liquid-encapsulated Czochralski (LEC) 230–231
liquid phase epitaxy (LPE) 223–224, 258, 270–278
long period antiphase boundary structures (LPSs) 342
long period polytypes (LLP) 125
lonsdaleite 114
Lorentz force 246–248, 250, 360
Lorentz microscopy 359–361
low-angle grain boundaries 329
low gravity environment experiments 250
low-pressure, high-temperature (LPHT) annealing 380

m

macroscopic homogeneity 3
macroscopic twin 345, 347
Marangoni convection 216–218, 246, 252
Marangoni number 252
Markov method 264–266
Marseille Protein Crystallization Database (MPCD) 156
mass conservation equation 257
materials engineering by crystal growth and characterization correlation 392–393
– epitaxial growth of GaN on $LiAlO_2$ substrates 393–408
matrix notation 365–366
maximal isomorphic subgroups 92
maximal nonisomorphic subgroups 91
mechanical twins 349–354

melt growth techniques
– bulk crystal growth from metallic solutions 253–260
– Czochralski crystal growth process 224–234
– float zone crystal growth process 244–253
– growth method after Bridgman 234–243
merohedral twins 344–345
merohedries 59
metalorganic molecular beam epitaxy (MOMBE) 292
metalorganic vapor phase epitaxy (MOVPE) 223, 288–291
micropulling 232–233
microsegregation 211–212
Miller indices 18–19, 22–23
MINCRYST Crystallographic and Crystallochemical Database for Mineral and their Structural Analogs 157
mineralogical databases 157
mineralogy database 157
minimal nonisomorphic supergroups 92
misfit 327
mixed dislocations 318
molecular beam epitaxy (MBE) 291–295
molecular configuration 126
molecular constitution 126
mono-ellipsoidal mirror furnace 250–251
monomers 129
mosaicity 377
moving phase boundary 207
multiferroics 362
multiple twinned particles (MTPs) 347
multiple twins 345–346
multiplicity 89
multiwalled nanotubes (MWNTs) 144

n
N3 color center 313
NaCl structure 115–116
nanobuds 145
nanocones 145
nanocrystalline materials 5
nanopeapods 145
nantiomorphic point groups 48
naphthalene 129–130
National Institute of Standards and Technology (NIST) Crystal Data 157
– Surface Structure Database (SSD) 158
Navier–Stokes equations 214–215, 246
negative climb 323
negative crystals 369
node rule 319
Nomarski differential interference contrast (NDIC) 249
noncolinear interstitialcy diffusion 311
nonconservative antiphase boundary 341
noncrystallographic point group symmetry 138–145
nonhomogeneities 373–377
nonsubstantial defects 302
normal freezing 202–204
normal subgroup 55, 99
n-type conductivity 307
nucleation processes 171–175
– equilibrium shape of crystals 180–182
– heterogeneous nucleation 177–178
– homogeneous nucleation 175–177
– metastable zone regime 179–180
Nucleic Acid Database (NDB) 155
NV-color center 313, 314

o
OBLIQUE program 347
occupation modulation 7
octahedral voids 110–111
octahedron 161
octane 127
octanitrocubane 133–134
ogdohedries 59
O-lattice 332–333
one-dimensional defects 302, 314
open ampoule PVT system 261
O-points 333
order of group 53
orientation contrast 383–384
Ostwald–Miers regime 179, 180

p
packing density 109
packing polymorphism 124
paraelectric phase 355–356
parallel lattice twins. *See* merohedral twins
paramagnetic state 358–359
partial dislocation 319
partial lattice translation 336
Patterson function 77, 84, 87
Pauling File 156
Pearson's Crystal Data (PCD) 156
pedion 35
Peierls–Nabarro stress 321
penetration twin 345
pentagon-dodecahedron 162
pentagon-hexecontahedron 138
pentagon–icositetrahedron 59
perfect dislocations 318
perfect single crystal 4, 302

pericline twin law 348
periodic bond chains (PBC) method 20, 186
periodicity 4
perovskite structure 121–122
Pfann's law 205
phantoms 370
phase diagrams and segregation principles 195–196
– constitutional supercooling and morphological stability 212–214
– phase diagrams with continuous miscibility in solid and liquid phases 196–200
– segregation and segregation coefficients 201–212
phase identification special database 158
phase transformation twins 348–349
phthalocyanines 131–132
physical vapor transport (PVT) 222–223, 260–261
pinacoid 37, 38
plane molecules 129
plastic crystals 11
platonic hydrocarbons 133
point configuration. *See* crystallographic orbit
point defects. *See* zero-dimensional defects
point groups 39–52
point symmetry
– elements 38
– operations 38
polycrystal 5
polyethylene 128–129
polyhedral molecules 133
polymerization 129
polymorphism and polytypism 124–126
polysynthetic twin. *See* multiple twins
polytypes 124
polytypism 124
porphyrins 131–132
positive climb 323
Powder Diffraction File (PDF), of the International Center for Diffraction Data (ICCD) 158
Prandtl number 215–216
precipitates 370–374, 396
precipitation hardening 372
Predicted Crystallography Open Database (PCOD) 156
primary nucleation 172
primitive lattice 14
primitive circle (the primitive) 28
proper subgroups 54
Protein Data Bank (PDB) 152, 154
protogenic (preexisting) inclusions 369
pseudo-merohedral twins 151, 344–347
p-type conductivity 307

q
quadratic voids 112
quantitative high-resolution transmission electron (qHRTEM) 373
quasicrystals (QCs) 9–10
quasi-fullerenes 137
quotient group. *See* factor group

r
Ramsdell notation 124
Rayleigh number 215–216
real crystal 302
realgar 126
real structure 302
reciprocal lattice 3, 62–63, 65–68
reentrant angles 348
reflection 36–37
reflection conditions 90
reflection high-energy electron diffraction (RHEED) 293–294
reflection twins 343, 345, 350
restricted multiplicity of rotation axes law 34
rhomb-dodecahedron 160
rhombohedron 37, 38
rotationals 212
rotations 315
rotation twins 343, 350
rotoinversion 97–98
– and rotoreflection 37–40
roughening transition 186

s
$Sc_3N@C_{80}$.Ni(OEP).2 benzene 143
scanning electron microscopy (SEM) 387–388
scanning transmission electron microscopy (STEM) 143, 335, 336
Schmidt number 215–216
Schottky defect 304, 307, 310–311
screw dislocation 315–318, 322–323
screw rotations 72, 96, 97, 315
secondary ion mass spectroscopy (SIMS) 293
secondary nucleation 172
segregation and segregation coefficients 201–212
selected area electron diffraction (SAED) 373, 391
self-conjugate element 55
self-energy of dislocation 320
self-interstitials. *See* interstitials
semi-closed ampoule PVT system 261

semicoherent interface 327–328
serial extinctions 90
shape factor 176
sharp interfaces 186, 327
Shockley partial dislocations 320
silicon (Si) 227–228
silicon carbide (SiC) 222
simple twins 345
SINCris 154
single-walled nanotubes (SWNTs) 144
site-symmetry group 89
slip 321–322, 339
small circles 28
solute, synthesis, diffusion method (SSD) 259–260
space group diagrams 85. *See also* crystallographic space groups
space group visualizer (SGV) (3D) 93–94
space lattice 12–13
special position 89
sphenoid 35, 36, 46
sphere packings 108–112
– closest homogeneous sphere packing 110
– homogeneous sphere packing 109, 111
spherical projection 27, 28
spinel structure 122–124
stacking faults 336–340
stagnant layer model 290–291
steady-state diffusion equation 257
Stefan's flow 263
step cooling 272
stereographic projection 27–30, 33–35
Stirling's formula 308
Stranski and Krastanov mechanism 267, 268
stress state 377
structural perfection 377
structural symmetry 60
– crystal lattices, motifs, and crystal structures 60
– crystallographic space groups 71–99
– generalized crystallographic symmetry 101–103
structural unit model 335
STRUCTURE TIDY 105
Strukturbericht designation 105, 106
sublattice 331
sublimation traveling heater method (STHM) 262–264
substantial defects 302
substitutional impurities 304–305
sulfur 126
super cooling 272
superlattice 331
superreflections 118
supersaturation 173
superstructures 117
surface decoration technique 367, 368
Surface explorer program 367, 368
surface relaxation and surface reconstruction 364–365
swirl defects 368
symmetrical grain boundary 329
symmetry 3
– morphological symmetry of crystals
– – crystallographic point groups 40–52
– – group theory 52–59
– relations between crystal structures 145–152
– structural symmetry 60
– – crystal lattices, motifs, and crystal structures 60
– – crystallographic space groups 71–99
– – generalized crystallographic symmetry 101–103
symmetry operations of first and second kind 95
symmorphic space groups 74–75, 89
synchrotron X-ray topography 383
syngenetic (contemporaneous) inclusions 369–370

t

tautozonal faces 20
tetartohedries 59
tetragonal disphenoid 37–38
tetragonal ferroelectric phase 355
tetragonal pyramids 36
tetrahedral-pentagondodecahedra 59
tetrahedral voids 110–111
tetrahedrane 133
tetrahedron 161
tetrakishexahedron 162
tetrakishexahedron form 59
texture 5
three-dimensional defects 303, 368
– inclusions 369–370
– precipitates 370–374
– voids 374–375
three-periodic twins 344
Tiller equation 203
tilt boundary 328, 333
tolerance factor 122
translation 13, 315
transmission electron microscope (TEM) 5–6, 143, 318, 324, 334, 338, 340–341, 358–359, 368, 371, 372, 385–392, 395, 396, 398, 403

traveling heater method (THM) 255–257
– in microgravity environment 257–259
traveling solvent method (TSM) 253
trigonal dipyramid 37, 38
trigonal pyramids 36
triple point 196–197
trisoctahedron 164
tristetrahedron 163
trivial subgroups 54
transdlation domains. *See* antiphase boundaries
twin components. *See* twins
twin elements 349
twin law 342–343
twin obliquity 343–344
twins 342–354
twist boundary 329
two-dimensional defects 303, 326–328
– antiphase boundaries 340–342
– crystal surfaces 363–368
– domain boundaries 355–362
– grain boundaries 328–336
– stacking faults 336–340
– twins 342–354
type I striations 257
type II striations 258–259

u

urea 131

v

vacancies 109, 303, 308, 310–312
vapor–liquid–solid (VLS) mechanism 189–190
vapor phase epitaxy (VPE) 223
– chemical vapor deposition (CVD) 279–286
– hydrogen vapor phase epitaxy (HVPE) 286–288
– metalorganic vapor phase epitaxy (MOVPE) 288–291
– molecular beam epitaxy (MBE) 291–295
veils 369
velocity of dislocations 321
vertical gradient freeze (VGF) 235–237
vicinal faces 185, 194, 367
vicinal surfaces 194
voids 109–112, 374–375, 398
Volmer–Weber mechanism 267, 268

w

Weiss symbols 16, 18
wet etching 383
wetting function 178
Wiki Crystallography Database (WCD) 158
WinXMorph program 20, 139, 140, 164
Wood's notation 365–366
Wulffe rule. *See* Gibbs–Curie–Wulff theorem
Wulff net 28, 30
wurtzite structure 118–119
Wyckoff letter 89
Wyckoff position 90
Wyckoff sets 90

x

X-ray photoemission spectroscopy/ultraviolet photoemission spectroscopy (XPS/UPS) 293
X-ray topography (XRT) 383–385

y

Young relation 177

z

zeolite structures database 157
zero-dimensional defects 302
Zhdanov notation 124
zincblende (sphalerite) structure 118–119
zonal extinctions 90
zone 20
– law. *See* assembly of zones
zone axis 20–21
zone circle 30, 32
zone melting 204–206
zone refining 204

WILEY END USER LICENSE AGREEMENT

Go to www.wiley.com/go/eula to access Wiley's ebook EULA.